AN ELECTROCHEMICAL STUDY OF THE OXIDATIVE DISSOLUTION OF SYNTHETIC NICKEL-IRON-SULPHIDE MINERALS IN AQUEOUS MEDIA

by

Terence Edwin Warner B.Sc.(Hons.) Dip.Min.Eng.

Submitted in accordance with the requirements
for the degree of Doctor of Philosophy.

The University of Leeds,
Department of Mining and Mineral Engineering

December, 1988

To my mother and late father

ABSTRACT

Pentlandite ($Fe_{4.5}Ni_{4.5}S_8$) and violarite ($FeNi_2S_4$) were synthesized by dry in vacuo techniques. The products were analysed by reflected light microscopy, powder X-ray diffraction and electron microprobe analysis. The synthetic pentlandite was found to have an average stoichiometry of $Fe_{4.35}Ni_{4.65}S_8$. A partial phase segregation of pentlandite into heazlewoodite and pyrrhotite was observed. The synthetic violarite grains showed a zonal separation into a $Fe_{1.2}Ni_{1.8}S_4$ core, and a $Fe_{0.5}Ni_{2.5}S_4$ rim. Trace amounts of pyrite and millerite were also detected.

From a critical review of the thermodynamic data in the literature, several Eh-pH diagrams were constructed for the Fe-Ni-S aqueous system. These were compared with mineralogical evidence obtained from naturally occuring mineral assemblages.

A study of the oxidative dissolution of pentlandite by electrochemical techniques was made to clarify the mechanism by which pentlandite is leached in acid $FeCl_3$ solution. The techniques used included: potentiometry, linear sweep cyclic voltammetry, intermittent galvanostatic polarization, chronopotentiometry and chronoamperometry. The products were analysed using scanning electron microscopy, powder X-ray diffraction, electron microprobe analysis, atomic absorption spectroscopy and gravimetric analysis. The fitting of experimental results to a simple electron transfer model via the Sand equation was tested and found to be inappropriate.

A mechanism for the oxidative dissolution of pentlandite is postulated. In acid solution, pentlandite decomposes spontaneously, liberating aqueous metal ions and H_2S. Under potentiostatic conditions akin to $FeCl_3$ leaching, pentlandite is oxidized directly to elemental sulphur, without the formation of any intermediate phases. The lack of formation of violarite indicates that the system is substantially perturbed from equilibrium due to slow solid state diffusion of metal atoms within the sulphur sub-lattice. The formation of metastable amorphous sulphur as the alternative product is further evidence of this perturbation. The physical properties of the sulphur product layer cause an impediment to mass transport between the bulk aqueous solution and the mineral surface. However, the oxidation involves an intrinsically slow electron transfer for the S^o,Fe^{2+},Ni^{2+} / $Fe_{4.5}Ni_{4.5}S_8$ couple which, within the potential range relevant to $FeCl_3$ leaching, is rate determining for an appreciable part of the reaction. The implication for extractive hydrometallurgy is discussed.

The use of a convolution transform of voltammetric currents with a $(\pi t)^{-1/2}$ function as applied to simple electron transfer is described. In addition, the derivation of a functional form for the treatment of chronoamperometric data is given. These models were applied in the determination of the heterogeneous electrochemical parameters and diffusion coefficients for the $FeCl_3/FeCl_2$ couple in 1M HCl solution on platinum at 293K, using computer controlled chronoampermetric techniques. The results show quasi-reversible behaviour (at 293K), which implies that electron transfer for this couple would not be rate determining in the leaching of pentlandite.

CONTENTS

PREFACE

Extractive hydrometallurgy is essentially concerned with the production of metals from ore minerals (or similar inorganic material produced from an intermediate step, eg. matte, anode slimes), whereby at least some of the chemical reactions occuring during the sequence of operations are carried out in aqueous solution (180). Such technology often enables the economic recovery of metals from ores which would otherwise be of too low grade or of such mineralogical complexity to afford extraction by conventional pyrometallurgical treatment.

An understanding of the mechanism during the dissolution of these minerals is crucial in the optimization and development of new processing routes to achieve enhanced yields, recovery rates, overall energy efficiency, selective leaching, and by no means least of all in the reduction of environmental pollution.

Concerning the extractive metallurgy of nickel, there is at present a considerable overcapacity in the industry. This was essentially caused by the more recent exploitation of nickel latterite ores. These constituted approximately 45% of nickel produced in 1979 (the remainder being essentially sulphide). This has had the effect that exploration of new deposits is focussed on those associated with gold and platinum group metals (PGM). Hence the need for industrial processes which cater for the extraction and separation of both valuables. An example of this recent practice is that operated at Impala Platinum Ltd, South Africa, in which nickel (and copper) is extracted as a "by-product" from what is considered to be a PGM ore, by the Sherritt Gordon

Process which involves pressure hydrometallurgical technology.

In recent years much attention has been directed towards chloride hydrometallurgy. For example, the use of cupric chloride as a leachant for chalcopyrite (an important copper sulphide ore mineral) in the CLEAR process; The Falconbridge chlorine leach process for the treatment of Ni-matte via a chlorine "potential-pump"; and the Cymet process in which ferric chloride is used as a leachant for copper-sulphide minerals (with the possibility of extending its use to other base-metal sulphides eg. lead/zinc sulphide); are a few important examples. In addition, much interest lies in extending the use of these leachants to other chalcogenide systems eg. anode slimes (containing PGM), and in the treatment of low grade and complex sulphide ore.

The use of acid ferric chloride as a possible leachant for Ni-Fe-S minerals (principally pentlandite $Fe_{4.5}Ni_{4.5}S_8$) has been investigated by previous workers, notably, Kelt, and Tzamtzis, using conventional chemical techniques. There are several desirable benefits for the processing of pentlandite in this medium, including the opportunity for the direct leaching of such concentrates as opposed to the production of an intermediate matte (viz. Ni_3S_2); the recovery of elemental sulphur (including a reduction in environmental pollution); and a desired possibility of operating at relatively low temperatures and at atmospheric pressure.

The results of their work indicate that the reaction rate is very slow, and that the nickel dissolution is incomplete. This was inferred in terms of a mixed-kinetic

regime involving mass transport control of the oxidant $FeCl_3$ from the bulk aqueous solution to the pentlandite surface through a progressively thickening sulphur product layer. Although the basic aims of these investigations were achieved, their conclusions presented further questions regarding the dissolution mechanism.

In this present work these problems were explored through the use of a series of electrochemical techniques. Since pentlandite and violarite ($FeNi_2S_4$) are known to be electronic conductors on account of the appreciable metallic bonding within their crystal lattices, much beneficial information concerning the dissolution mechanism can be revealed through various electrochemical techniques including, cyclic voltammetry, chronopotentiometry and chronoamperometry. In these techniques, electrochemical oxidation or reduction is induced on the mineral surface by using a three electrode configuration. Cyclic voltammetry gives information regarding electron transfer, diffusion, and rate constants; whilst chronoamperometry and chronopotentiometry may produce in addition, observable solid state phase changes in the mineral sample.

Results from these techniques lead to the conclusion that the oxidative dissolution mechanism involves an intrinsically slow electron transfer process for the S^o,Fe^{2+},Ni^{2+} / $Fe_{4.5}Ni_{4.5}S_8$ couple, which within the potential range relevant to ferric chloride leaching is rate determining for an appreciable portion of the reaction. The continuation of the present treatment of such ores via an intermediate Ni-matte is therefore concluded to be a more viable approach.

FIGURES

TABLES

ACKNOWLEDGEMENT

I would like to thank my supervisors, Dr. N.Taylor of the Department of Physical Chemistry, and Dr. N.M.Rice, of the Department of Mining and Mineral Engineering, for their advice and encouragement throughout the course of this work. Thanks are also due to Prof. P.Gray, and Prof. P.A.Young, for the provision of joint laboratory facilities, and in particular for their inter-departmental cooperation which created the opportunities for much of this work.

Particular acknowledgement is made here to the following:

Dr.P.D.Battle and Miss.S.Nixon, of the Department of Inorganic Chemistry, for conducting powder X-ray diffraction analysis, and assistance in the interpretation of the data.

Dr.T.Boddington, of the Department of Physical Chemistry, for assistance with the mathematical aspects of this work.

Prof.A.R.Burkin, of Imperial College, London, for a discussion on the hydrometallurgical extraction of nickel, and for practical advice on the synthesis of sulphide minerals. Imperial College, February, 1986.

Dr.E.Condliffe, of the Department of Earth Sciences, for operational and analytical assistance with electron microprobe analysis.

Mr.D.L.Dean, of the Department of Mining & Mineral Engineering, for operational assistance with reflected light microscopy.

Falconbridge Nikkelverk-Aktieselskap, Kristiansand, Norway, for sending literature on their current industrial process.

Mr.C.J.Gascoigne and Mr.M.Holmes, of the School of Chemistry, for their glass blowing services.

INCO Limited, Ontario, Canada, for the donation of natural specimens of nickel-iron-sulphide minerals.

Mr.A.Hedley, of the School of Chemistry, for conducting atomic absorption spectroscopy and gravimetric analysis.

Dr.G.Hornung, of the Department of Earth Sciences, for providing the facilities and operational assistance with powder camera X-ray diffraction analysis.

Mr.P.A.Halford-Maw and Mr.D.G.Mills, of the Department of Physical Chemistry, for assistance with instrumentation and computer operation.

Kambalda Nickel Operations, Western Mining Co. Limited., Australia, for the donation of natural specimens of nickel-iron-sulphide minerals.

Kwinina Nickel Refinery, Western Mining Co. Ltd., Western Australia, for sending literature on their current industrial processes.

Mr.S.R.Lloyd, of the Department of Mining and Mineral Engineering, for practical assistance during the synthesis of the metal sulphides.

Dr.Mustughaochia, of the Department of Ceramics, for the use of two horizontal tube furnaces.

Mr.A.Nichells and Mr.J.P.Harrington, of the Department of Metallurgy, for the operational and analytical assistance with scanning electron microscopy.

Mr.C.Reyner, of the School of Chemistry, for the fabrication of experimental equipment.

Sherritt Gordon Mines Limited, Fort Saskatchewam, Alberta, Canada, for the donation of nickel powder and natural specimens of nickel-iron-sulphide minerals, and for sending literature on their current industrial processes.

Dr.C.J.Stanley, of the British Museum (Natural History), London, for a discussion on the mineralogy of nickel-iron-sulphide minerals, and for the provision of natural specimens of nickel-iron-sulphide minerals on behalf of the British Museum. British Museum, February, 1986.

Dr.M.R.Thornber, of CRISO, Division of Minerals and Geochemistry, Floreat Park, W. Australia, for sending literature and information concerning the mineralogy and geochemistry of nickel-iron-sulphide deposits.

Prof.D.Vaughan, then Reader of the Department of Geological Sciences, University of Aston, for discussions of the mineralogy and surface alterations of nickel-iron-sulphide minerals. University of Aston, May 1986 and September 1987.

I would like to take this opportunity to thank my collegues, Mr.R.Luo, Mr.L.K.Witika, and Dr.S.Wallace for the many informal discussions concerning this work. Finally, I wish to acknowledge the Science and Engineering Research Council for the provision of a Studentship in the form of a Research Quota Award.

T.E.W.

ABBREVIATIONS

RDE	rotating disk electrode
mss	monosulphide solid-solution
MO	molecular orbital
AO	atomic orbital
SCE	saturated calomel electrode
SHE	standard hydrogen electrode
MS	metal sulphide (of nominal stoichiometry)
XRD	X-ray diffraction
EMPA	electron microprobe analysis
SEM	scanning electron microscopy
emf	electromotive force
PPL	plain polarized light
XP	crossed polars
EDXA	energy dispersive X-ray analysis
PTFE	polytetrafluoroethylene
SEI	solid electrolyte interface
hcp	hexagonal close packed
ccp	cubic close packed
M	metal atom
IGP	Intermittent galvanostatic polarization
ESCA	electron spectroscopy for chemical analysis
RE	reference electrode
WE	working electrode
CE	counter electrode

1 INTRODUCTION

1.1 EXTRACTIVE HYDROMETALLURGICAL PROCESSES FOR THE LEACHING OF NICKEL-IRON-SULPHIDE MINERALS

1.1.0 Introduction

The major producers of nickel sulphide ore among the western nations are: Canada, [192]; Australia, [61]; South Africa,[30]; Botswana,[19]; Zimbabwe,[15]; and Finland,[6].*

The most relevant nickel sulphide minerals contained in such concentrates are: pentlandite and nickeliferous pyrrhotite (96) and to a lesser degree: millerite, violarite and polydymite, whilst nickeliferous pyrite (bravoite) is essentially restricted to a secondary product of other base metal ores, e.g. lead/zinc sulphides of Mill Close Mine, Derbyshire (28). However, regional variation does occur, i.e. the importance of violarite as an ore mineral in the Kambalda deposits of Western Australia is illustrated by the fact that the Durkin Shoot contained in excess of 1 million tonnes of supergene ore (91), (cf. Section 1.4.2). Likewise, currently mined supergene ore from the Foster Shoot (608 stope) contains 52% violarite (95).

Heazlewoodite rarely occurs in nature. However, the metal-rich nickel sulphide phase approximating to heazlewoodite in composition, is the major component of Bessemer furnace matte from Thompson, Manitoba (97); converter matte from the Falconbridge smelter in Sudbury, Ontario (98); and Flash Smelter matte from Kalgoorlie, Western Australia (99), (cf. Figure 1.1.3).

In order to describe the possible hydrometallurgical reaction routes available for the decomposition of these

---

* Figures in parentheses denote nickel metal production in 000's tonnes per annum, relating to the year 1980 (94).

minerals the reader is referred to the appropriate E_h-pH diagrams in Section 1.5. For a comprehensive review of the extractive metallurgy of nickel, the reader is referred to the recent work by Burkin (152), and Boldt & Queneau (174).

This résumé will essentially relate to the more economically important phases: pentlandite, heazlewoodite and millerite. The author considers that reference to these phases is quite adequate in illustrating the general effects by which changes in the thermodynamic parameters: E_h and pH induce on the Fe-Ni-S aqueous system. However, for categorical details of the influence of thermodynamic and kinetic factors on this system, the reader is referred to Sections: 1.4.2, 1.5 and 1.7.

Examination of such E_h-pH diagrams reveals that pentlandite and heazlewoodite could decompose by four principal reaction paths (96):

(a) Alkali Oxidation

$$Fe_{4.5}Ni_{4.5}S_8 + 32H_2O = 4.5Fe^{2+} + 4.5Ni^{2+} + 8SO_4^{2-} + 64H^+ + 66e \quad (1.1.1)$$

$$Ni_3S_2 + 8H_2O = 3Ni^{2+} + 2SO_4^{2-} + 16H^+ + 18e \quad (1.1.2)$$

(b) Acid Oxidation (4)

$$Fe_{4.5}Ni_{4.5}S_8 = 4.5Fe^{2+} + 4.5Ni^{2+} + 8S^o + 18e \quad (1.1.3)$$

$$Ni_3S_2 = 2NiS + Ni^{2+} + 2e \quad (1.1.4)$$

$$NiS = Ni^{2+} + S^o + 2e \quad (1.1.5)$$

(c) Acid Decomposition

$$Fe_{4.5}Ni_{4.5}S_8 + 18H^+ = 4.5Fe^{2+} + 4.5Ni^{2+} + 8H_2S + H_2 \quad (1.1.6)$$

$$NiS + 2H^+ = Ni^{2+} + H_2S \quad (1.1.7)$$

$$Ni_3S_2 + 6H^+ = 3Ni^{2+} + 2H_2S + 2H_2 \quad (1.1.8)$$

(d) Reduction

$$Fe_{4.5}Ni_{4.5}S_8 + 16H^+ + 16e = 4.5Fe^o + 4.5Ni^o + 8H_2S \quad (1.1.9)$$

$$Ni_3S_2 + 4H^+ + 4e = 3Ni^o + 2H_2S \quad (1.1.10)$$

Route (a) leads to the successful Sherritt Gordon Ammonia Pressure Leach Process. Route (c) leads to the successful but now obsolete Falconbridge Matte Leach Process, and the Amax HCl Leach of Sulphide Precipitates (181). Route (b) leads to the new Falconbridge Chlorine Leach Process, and the SLN $FeCl_3/Cl_2$ Leach Process (112). A combination of route (b) with the simultaneous but separate (cathodic) reduction of aqueous Ni^{2+} to metallic nickel, leads to the INCO Direct Electro-refining of Nickel Matte Process. Route (d) has not been reported and may be unobservable in acid media since nickel is a metal with too low a hydrogen over-potential to permit Reactions (1.1.9) and (1.1.10) to continue after the first traces of nickel are formed (96).

There are no economic metallurgical processes for the direct extraction of nickel from nickel-iron sulphide ores. Prior to any hydro or pyrometallurgical treatment, beneficiation is achieved by appropriate communition and sulphide froth-flotation to yield a corresponding sulphide concentrate.

The "pyrometallurgical" processing of nickel sulphide concentrates essentially involves an oxidizing roast to oxidize the iron and remove excess sulphur. The calcine is matte smelted in a reverberatory, electric or flash furnace and partially blown in a converter to further oxidize out any iron and yield a Ni-Cu matte (cf. Figure 1.1.3). The traditional separation of nickel from copper was achieved by the now obsolete Orford "tops and bottoms" smelting with sodium sulphate, whereby Ni_3S_2 was tapped from the "bottoms" (110) or, alternatively by slow cooling of the matte with subsequent separation of Ni_3S_2 and Cu_2S by appropriate beneficiation. The nickel sulphide may then be roasted to oxide, sintered and reduced to crude nickel by smelting in a hearth furnace with coke, then cast into anodes to be refined electrolytically. Alternatively, the oxide may be reduced by roasting in a rotating kiln with hydrogen then purified by the Mond-Langer Nickel Carbonyl Process (109).

Such pyrometallurgical routes as described above, particularly the reduction of the matte to metal, consume large amounts of energy yet produce a crude product which requires further treatment. This together with problems of inherent atmospheric pollution strongly favours a more direct method which is afforded by a hydrometallurgical approach.

1.1.1 Alkali-Ammonia Leach

The hydrometallurgical processing of nickel sulphide concentrates is currently restricted to the Sherritt Gordon Ammonia Pressure Leach Process at Fort Saskatchewan, Alberta, Canada. However, the process is operated under license at Impala Platinum Limited for Ni-matte treatment in South Africa; and also under license at Kwinana Nickel Refinery (Western Mining Co. Ltd.), Kwinana, Western Australia. This latter plant is reported to now run on an all-matte feed, for reasons of energy efficiency (102). The process is illustrated in Figure 1.1.1, and described in the literature (103),(104),(105).

The chemistry involves essentially an oxidizing ammonia leach at an elevated temperatute (352 to 363K) and pressure (824 to 870kPa), whereby the sulphides, which are carried in aqueous suspension, come into contact with free ammonia and air. The dissolved oxygen oxidizes both metal and sulphur in the mineral, with the latter forming various intermediate metastable oxy-sulphur anions (thionates, thiosulphates and sulphamates) and ultimately sulphate.

$NiS + H_2O + 2O_2 = NiO + SO_4^{2-} + 2H^+$ (1.1.11)

$NiO + 2NH_4^+ + 4NH_3 = Ni(NH_3)_6 + H_2O$ (1.1.12)

The ammonia provides the complexing agent for holding the nickel in solution until it is hydrogen reduced to metal. Advantage is taken of the fact that while all four metals (Ni,Fe,Cu,Co) form soluble ammine complexes, there is a marked difference in their resistance to hydrolysis and oxidation. The ammine complexes of iron(II) are easily hydrolysed and then oxidized in ammonical solutions, thus iron is readily removed as hydrated ferric oxide and discarded. Furthermore, its precipitation also performs a vital role of purifying the leach liquor by absorbing from solution various contaminant elements, i.e. arsenic and selenium. The products are high grade nickel powder, precipitated copper sulphide, cobalt powder by an auxillary route, and ammonium sulphate as a commercial by product.

1.1.2 Acid-Chloride Leach

Much attention has focused in recent years on chloride hydrometallurgy for the treatment of base metal sulphides (96),(101),(106). Chloride hydrometallurgy offers several advantages over sulphate hydrometallurgy (101). In general, metal chlorides are easier to separate and the metals are recovered using less energy (eg. the separation of $CoCl_4^{2-}$ from $Ni^{2+}(aq)$ by solvent extraction). Furthermore, hydrochloric acid has a much higher activity in salt solutions and can be readily recovered from solution by distillation or by pyrohydrolysis of several metal chlorides (eg. $MgCl_2$). Chlorine is also readily recycled. It is liberated at inert anodes at low overpotentials, and at a lower overall electrode potential than oxygen; and yet is a more powerful oxidant than oxygen.

These processes are essentially based on an acid chloride medium with or without various oxidants. However, direct non-oxidative acid leaching of nickel-iron sulphide concentrates is inefficient (101), e.g. the leaching of Kambalda nickel-iron sulphide concentrates containing pyrrhotite under such conditions yields only about 10% of their nickel content in solution, even with prolonged leaching and excess acid. The reaction is retarded due to the excess sulphur liberated during pyrrhotite dissolution forming a protective surface coating on the nickel containing minerals (100). This may be prevented by an initial "activation" procedure wherein the concentrates are roasted for 1 hour at 1023 to 1073K in a reducing atmosphere of hydrogen or methane to remove excess sulphur from pyrrhotite and pyrite (100). Nonetheless, this presents additional financial costs not only in terms of energy but also in the removal of substantial amounts of iron from aqueous solution, in the handling of H_2S, and HCl regeneration.

Such problems have led to an intermediate smelting step to remove iron as an oxide with the consequent production of a nickel-copper matte low in iron, and sulphur deficient. This provides the feed material to a variety of acid-chloride hydrometallurgical processes as outlined above. The choice of process is largely dictated by the composition of the matte, especially with respect to its Cu, Co and precious metals content. These processes will now be described in further detail.

The Hybinette Process was a long standing practice employed at Kristiansand, Norway, since the early 1910's. It involved essentially an oxidizing roast of nickel-copper matte from which copper was separated by a sulphuric acid leach. The resulting leach residues were converted to a "reduced matte" and nickel anodes in reduction furnaces and electric furnaces respectively. Electro-nickel was then obtained from these anodes, whilst the "reduced matte" was used to cement the copper contamination from the subsequent impure electrolyte.

During the 1950's Falconbridge Nikkelverk A/S Kristiansand, developed a direct non-oxidative HCl leach for nickel-copper matte in an urgent attempt to diversify their company's product line. A commercial scale pilot plant was constructed in which nickel sulphide (Ni_3S_2) was selectively leached (98%Ni, 2%Cu) with 7.5M HCl at 70°C for 12 hours then crystallized as nickel chloride crystals.

$$Ni_3S_2 + 6HCl = 3NiCl_2 + 2H_2S + H_2 \qquad (1.1.13)$$

These in turn were hydrolysed to nickel oxide, then hydrogen reduced to "Nickel 98" (108). The remaining copper sulphide was treated accordingly by a separate route.

However, by 1981, the new Falconbridge Chlorine Leach Process (98) developed to superceed the old Hybinette Process was fully operational (cf. Figure 1.1.2). The main feed to the process is converter matte from the Falconbridge smelter in Sudbury, Ontario, with a typical composition of: 35-40%Ni, 30-35%Cu, 22-24%S, 2-3%Fe, 0.9-1%Co. The matte is leached with chlorine recovered from the electrowinning circuit whilst the temperature of the leach solution is held at boiling point (383K). Nickel is leached selectively at this stage by controlling the redox potential of the slurry.

Although the chlorine ultimately provides the oxidative power, the actual oxidative leaching of Ni_3S_2 involves a reaction with cupric ions. Thus the redox potential is governed by the ratio of the Cu^{2+}/Cu^{+} couple which in turn can be controlled by an automatically linked matte feed mechanism which determines the amount of total copper and nickel brought into contact with the chlorine. The net effect is that about 92% of the nickel enters solution whilst essentially all the copper and sulphur contained in the matte is present in the leach residue as CuS. The main chemical reactions are as follows:

$$Cu^{2+} + Cl_2 = 2Cu^{2+} + 2Cl^- \qquad (1.1.14)$$

$$Ni_3S_2 + 2Cu^{2+} = 2NiS + Ni^{2+} + 2Cu^+ \qquad (1.1.15)$$

$$NiS + 2Cu^{2+} = Ni^{2+} + 2Cu^+ + S^o \qquad (1.1.16)$$

$$Cu_2S + S^o = 2CuS \qquad (1.1.17)$$

However, the leach liquor contains about $50gdm^{-3}$ Cu, which is reduced to $0.2gdm^{-3}$ by precipitation as CuS with additional quantities of matte in seperate precipitation tanks.

The resulting nickel chloride solution with a relatively low HCl activity, is purified (iron removed by oxyhydrolysis, and cobalt by solvent extraction) prior to the electrowinning of high grade nickel metal. The copper sulphide leach residues, which contain some nickel are treated via an auxillary route.

SLN have developed a similar process for treating a Ni-rich matte containing little or no Cu (112), viz. 75%Ni, 1.5%Co, 2-4%Fe. Chlorine is likewise passed through the slurry, but in this case it is the Fe^{3+}/Fe^{2+} couple which participates in the oxidative dissolution of Ni_3S_2 whereby the E_h is controlled at 700mV, and the temperature at 380K. This overcomes NiS passivation and oxidizes sulphide sulphur to the elemental form. This process like the Falconbridge Chlorine Leach Process provides a leach solution containing little free HCl which is suitable for direct electrowinning after purification ($FeCl_3$ is partially extracted with TBP, whilst Ni^{2+} is separated from Co^{2+} and residual iron by ion-exchange).

The INCO Thompson Refinery at Manitoba, Canada produces 135 tonnes of electro-nickel (99.98%Ni) per day by the direct electrorefining of nickel matte anodes (113), (114), (115). These are cast from bessemer-matte containing: 74.3%Ni, 2.6%Cu, 0.51%Co, 0.25%Fe and 20.4%S; comprising of the major phases: heazlewoodite, chalcocite and nickel.

Anodic dissolution of this matte brings into solution, ideally: $75gdm^{-3}$ Ni^{2+}, $0.6gdm^{-3}$ Cu^{2+}, $0.1gdm^{-3}$ Co^{2+}, and $0.05gdm^{-3}$ Fe^{2+}. The sulphide anodes corrode at approximately 94% current efficiency, the remaining 6% of the anode current being consumed in the evolution of oxygen, with an increase in the anolyte acidity from pH 3.25 to 1.9. A sulphate-chloride electrolyte is used, chloride ions ($45-50gdm^{-3}$) are present to improve the conductivity and anode corrosion.

The anodes dissolve to leave a residue containing approximately 33% of the original nickel content, together with elemental sulphur in the slimes; while the cell potential difference rises from 2.2 to 4.2V. The anolyte is removed and purified by precipitation of contaminant ions before the electrowinning of nickel at the cathode.

The Cymet Process (116) (in many ways analogous to a hybrid of the SLN and INCO processes) was developed for the proposed treatment of chalcopyrite concentrates, but may equally be applicable to nickel-iron sulphide concentrates, i.e. pentlandite and violarite.

The Cymet process basically involves the dissolution of chalcopyrite (in slurry form) to cuprous chloride, ferrous chloride and sulphur; by a combined treatment with acid ferric chloride at 348 to 353K (previously generated by the seperate anodic oxidation of ferrous chlodide) and anodic leaching. These anodic currents are theoretically balanced by the cathodic electrowinning circuit for copper and iron in separate cathode compartments. The principal reactions involved are:

$$6FeCl_3 + 2CuFeS_2 = 2CuCl + 8FeCl_2 + 4S^o \quad (1.1.18)$$

$$CuFeS_2 + 3HCl = CuCl + FeCl_2 + 2S^o + 3H^+ + 3e \quad (1.1.19)$$

$$6FeCl_2 + 6Cl^- = 6FeCl_3 + 6e \quad (1.1.20)$$

$$3CuCl + 3e = 3Cu^o + 3Cl^- \quad (1.1.21)$$

$$3FeCl_3 + 6e = 3Fe^o + 6Cl^- \quad (1.1.22)$$

$$3H^+ + 3Cl^- = 3HCl \quad (1.1.23)$$

Overall reaction: $3CuFeS_2 = 3Cu^o + 3Fe^o + 6S^o$ (1.1.24)

In tests carried out on the anodic dissolusion of Cu-Ni concentrates (chalcopyrite, pentlandite and pyrrhotite) at pH 0.5, the material dissolved with approximately the theoretical efficiency until about 70% of the nickel was dissolved. At this point the efficiency decreased due to a substantial increase in sulphur concentration and a substantial decrease in slurry density. However, at pH 3.5

the reaction was assisted by the oxidative reaction of the Fe^{3+}/Fe^{2+} couple directly on the minerals concerned (116).

From the above resume it is apparent that at present the processing of nickel-iron-sulphide minerals is essentially restricted to the production of an intermediate matte, principally to upgrade the material with respect to the removal of iron and excess sulphur. However, with variety and advances in the technology concerning the removal of aqueous iron chloride (e.g. goethite precipitation, solvent extraction (TBP), and extraction of Ni^{2+} and Co^{2+} from such solutions by ion-exchange), there arises an opportunity to possibly engineer a route for the direct leaching of these minerals. An appropriate medium would be acid-chloride for the reasons illustrated above, whilst either a Fe^{3+}/Fe^{2+} or a Cu^{2+}/Cu^{+} couple (101) could provide the necessary potential (at least in thermodynamic terms) to instigate oxidation.

The conversion of sulphide to elemental sulphur, rather than to sulphate (viz. Sherritt Gordon Process), is important in reducing unneccessary further oxidation and the consequental removal of sulphate from the system; both at a substantial chemical/energy expense (116). Unfortunately, it is the formation of such a sulphur product layer that appears to be the cause for the incomplete dissolusion of pentlandite in such media (4), (14). This kinetic problem forms the subject matter for further discussion in Section 1.7, and is indeed the essence of the treatise of this work.

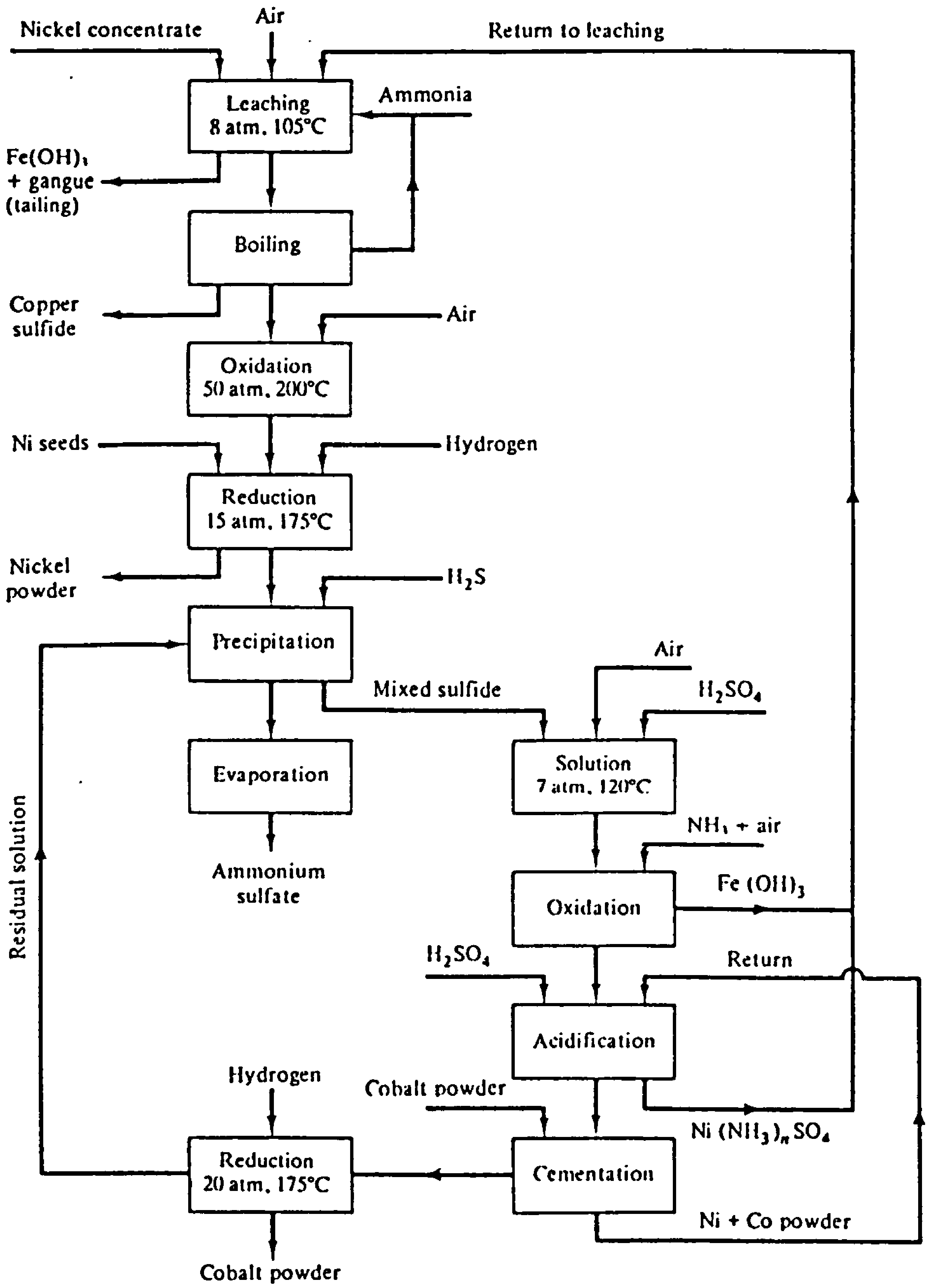

Figure 1.1.1

Flow-sheet for the Sherritt Gordon Process (179)

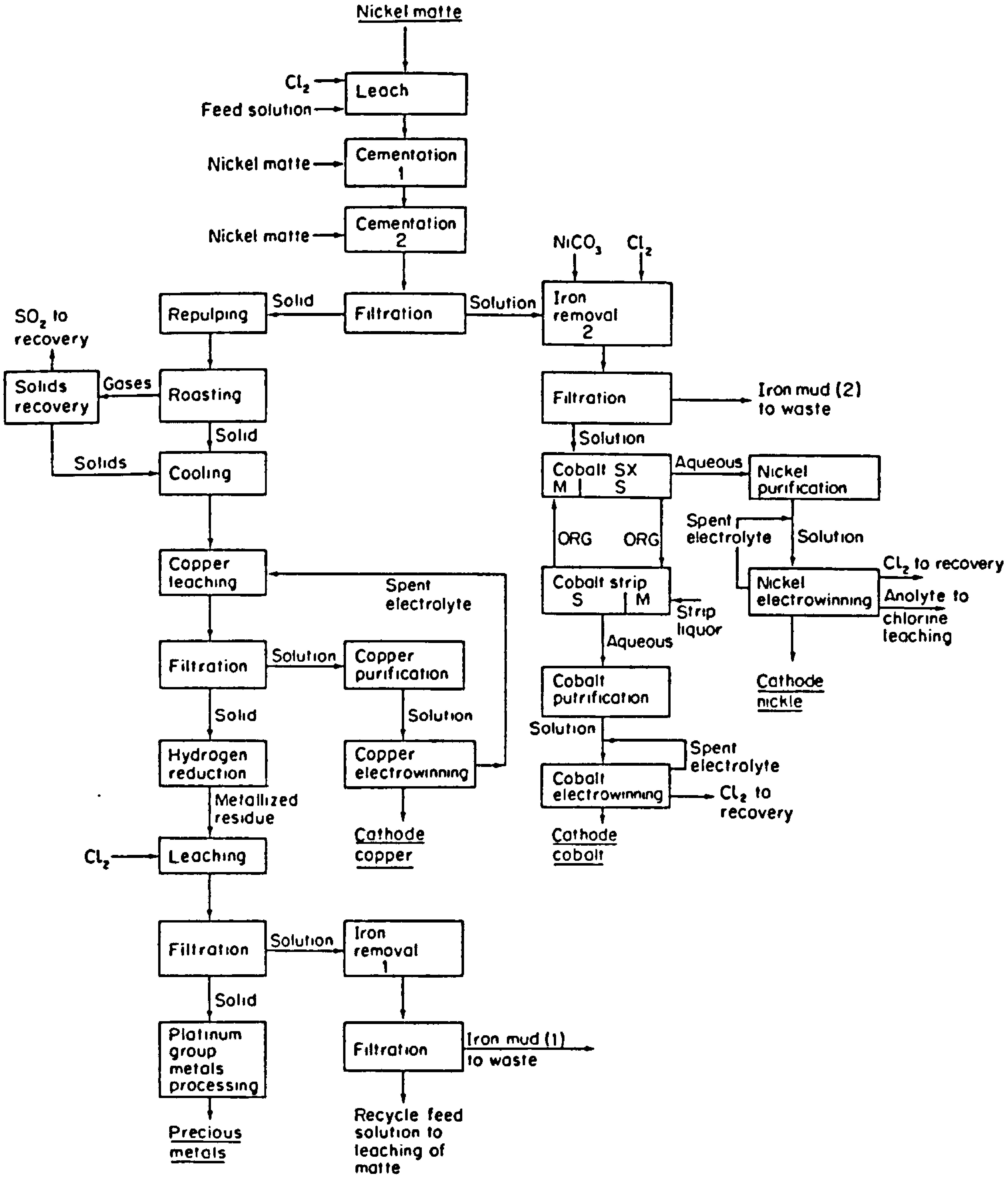

Figure 1.1.2

Flow-sheet for the Falconbridge chlorine leach process (152)

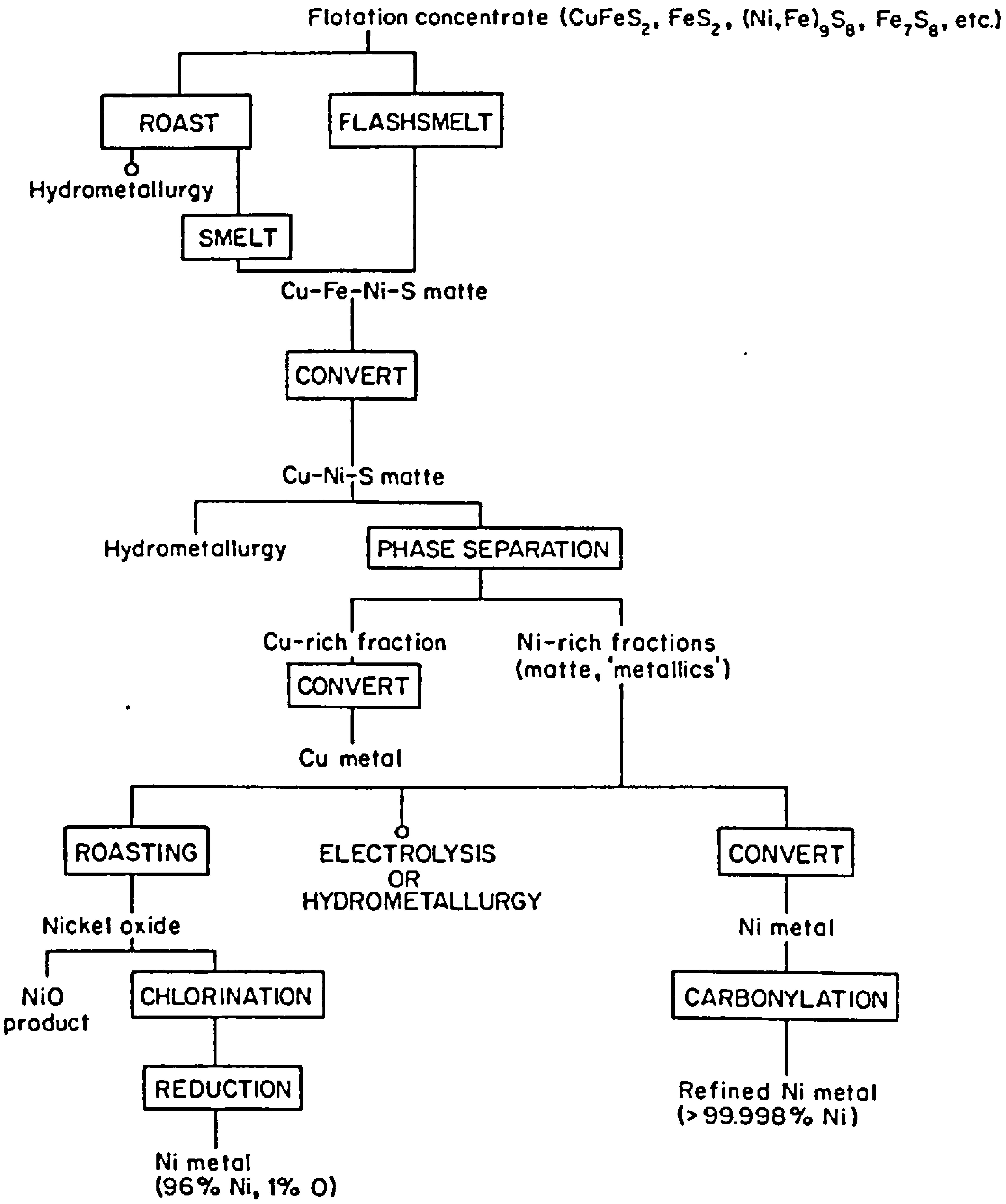

Figure 1.1.3

Pyrometallurgical treatments of nickel sulphides (152)

1.2 PHASE EQUILIBRIA

1.2.1 Iron-Nickel-Sulphur Ternary System

The phase equilibria in the Fe-Ni-S ternary system are directly applicable to ore mineralogy, particularly with regards to ore genesis, since many massive nickel-sulphide ore-bodies have formed from immiscible sulphide melts in mafic and ultramafic magmas (cf. Section 1.4). An appreciation of the Fe-Ni-S system across a wide range of temperatures and compositions was fundamently important in the design of a suitable procedure for the dry synthesis of these minerals; cf. Section 2.1. A résumé of phase equilibria in the Fe-Ni-S ternary system through the temperature range of 1100°C to 200°C is given below.

General phase relations within the system were first characterized by Lundqvist (33), then extended by the high temperature work of Kullerud (12),(29),(30); the sulphur rich system by Clark and Kullerud (19), Shimazak (21), Vaughan and Craig (25), Craig (7),(11), Misra and Fleet (23); with the central and sulphur deficient regions by Kullerud (3), Naldrett et al (10), Graterol and Naldrett (31), Shewman and Clark (8), Misra and Fleet (13); and low temperature relations by Craig (32). The Ni-S binary system is described in a comprehensive report by Kullerud and Yund (20). A partial incorporation of the Ag-Fe-Ni-S quaternary system is given by Mandziuk and Scott (16).

A complete account of all the condensed phases and fields of stability within this temperature range is unnecessary and emphasis will be placed on those most relevant to the present work. The reader is therefore referred to the literature for a discussion of other phases present. For a general review, see Vaughan and Craig (18) and Barton and Skinner (72). Phase diagrams depicting the various assemblages stable at specified temperatures are given in Figures 1.2.1 to 1.2.9.

At 1100°C the phase relations show that the central portion of the Fe-Ni-S system is dominated by a large field containing homogeneous liquid and vapour, which extends from about 45.5% to 84% (mass) Ni along the Ni-S side of the phase diagram, then diverges just short of the Fe-S boundary at between 53.5% to 55%, and 66% to 71% (mass) Fe. The divergence of the homogeneous liquid field is caused by the protrusion of the pyrrhotite solid solution. This first occurs with the crystallization of pyrrhotite ($Fe_{1-x}S$) at 1190°C in the Fe-S binary system (72). On cooling, the pyrrhotite field extends along the Fe-S boundary between 36.5% and 43.5% (mass) S, though more significantly into the ternary system corresponding to 14% (mass) Ni at 1100°C. The pyrrhotite solid solution field is separated from the homogeneous liquid by a divariant field containing pyrrhotite solid solution and liquid. Above the central field containing homogeneous liquid, and extending close to the sulphur corner lies a divariant field comprised of two immiscible liquids; one rich in sulphur with the other rich in metal. Below the central field containing homogeneous liquid and extending to the Fe-Ni boundary lies a divariant field containing homogeneous liquid and a complete alpha-type solid solution of iron and nickel metal.

On cooling, various changes take place in the phase relations. Below 1007°C vaesite (NiS_2) condenses, which on further cooling incorporates an increasing amount of iron into solid solution as $(Ni,Fe)S_2$ till a maximum is reached corresponding to 29.8% (mole) FeS_2 at 729°C (19). The protrusion of the pyrrhotite solid solution extends further across the ternary system yet with a constriction on the limits of its sulphur content, whilst eventually meeting the Ni-S boundary at 992°C. This solid solution series has a NiAs structure and is complete from $Fe_{1-x}S$ to $Ni_{1-x}S$ below 992°C. It is normally referred to as the mono sulphide solid solution (mss) of the Fe-Ni-S system. The mss begins to decompose in the Ni-rich region at 379°C as stoichiometric αNiSinverts from the high temperature NiAs structure to the low temperature millerite structure: βNiS (20). Nonetheless metal deficient compositions of the $\alpha Ni_{1-x}S$ solid solution retain the high temperature structure such that the mss remains continuous across the system even though, at 300°C the field has narrowed to about 30% of its width at 600°C with respect to its sulphur mass composition limits (10). Below 282°C the end member species $\alpha Ni_{1-x}S$ decomposesto form polydymite (Ni_3S_4) and stoichiometric millerite (βNiS) (20). Between 275°C and 250°C a immiscibility gap appears in the mss in the vicinity of 25% (mass) Ni and 35% (mass) Fe (32),(2). Between 250°C and 200°C a second immiscibility gap forms in the region 30.5% to 22% (mass) Fe (32) which corresponds to the same immiscibility gap reported at 300°C by Misra and Fleet (13). Betweeen 225°C and 200°C this immiscibility gap has expanded sufficiently to enable pyrite and pentlandite to coexist (18) and account for the synthesis of pyrite-pentlandite assemblages below 212°C by the sequential annealing of mss in the compositional range Fe:Ni:S = 40:20.5:39.5 to 35.3:25:39.5 respectively, initially to permit pyrite nucleation at 400°C then pentlandite exsolution below 200°C (32).

Phase diagrams below 200°C remain uncertain due to the difficulties in obtaining equilibria at relatively low temperatures. However, a possible sequence for the destiny of the mss is the retreat of the Ni-rich mss to form an Fe-bearing millerite. A continued breakdown of the central mss "island" initially into a pyrite-pentlandite assemblage on the Fe-rich side, and a pyrite-millerite assemblage on the Ni-rich side, with the consequent formation of a pyrite-pentlandite-millerite assemblage on further cooling (57), (51), (31).The continued breakdown of Fe-rich mss and subsequent formation of the pentlandite-pyrrhotite-pyrite assemblage is discussed in Section 1.4.

The eutectic between vaesite and the high temperature form of millerite ($\alpha Ni_{1-x}S$) appears at 985°C, such that below this temperature these two phases coexist in equilibrium. However, at 356°C a sulphide phase of intermediate stoichiometry, i.e. polydymite, is in equilibrium with vaesite and alpha-millerite (20); which will be referred to later in conjunction with violarite.

Along the Fe-S boundary the $Fe-Fe_{1-x}S$ eutectic appears at 988°C (72). Below this temperature the central field of the homogeneous liquid gradually shrinks and retreats from the Fe-S boundary towards the Ni-S boundary in the wake of the advancing mss.

At 862°C the high temperature, the nonquenchable phase $(Ni,Fe)_{3-x}S_2$ condenses out of the mss + central homogenous liquid divariant field (3), (viz. the incongruent melting point of the binary phase $Ni_{3-x}S_2$, at 806°C to yield $\alpha Ni_{1-x}S$

+ Liquid (20); before the central homogeneous liquid disappears entirely at 635°C, corresponding to the Ni - $Ni_{3\mp x}S_2$ eutectic in the Ni-S binary system (20).

The cubic binary phase $Ni_{3\mp x}S_2$ shows a wide range of composition from 23.5 to 30.5%(mass) sulphur at 600°C, and exists down to 556°C in the Ni-S system where stoichiometric Ni_3S_2 inverts to the low temperature hexagonal heazlewoodite. Simultaneously, the $(Ni,Fe)_{3-x}S_2$ solid solution which shows a deficiency of metal with respect to the ideal stoichiometry, widens its domain rapidly in the direction of increasing metal to sulphur ratio whilst approaching the Ni-S boundary with a corresponding preference for nickel over iron held in solid solution. This "migration" and depletion of iron culminates in the $(Ni,Fe)_{3\mp x}S_2$ solid solution joining the Ni-S boundary at the incongruent melting point of the binary $Ni_{3\mp x}S_2$ phase, viz. 806°C. However, by virtue of the Fe contained in solid solution, the $(Ni,Fe)_{3+x}S_2$ solid solution phase remains extended into the ternary system below the high-low inversion temperature for stoichiometric Ni_3S_2 in the pure Ni-S binary system; viz. 556°C. Nonetheless, on cooling below 556°C its domain becomes constricted due to the advance of the hexagonal stoichiometrc Ni_3S_2 + cubic solid-solution $(Ni,Fe)_{3\mp x}S_2$ + vapour divariant field from the Ni-S boundary. This eliminates the $(Ni,Fe)_{3\mp x}S_2$ solid solution at a temperature just above 500°C, and is replaced by an assortment of fields with tie lines from heazlewoodite to mss, pentlandite, and the Ni-Fe solid solutions. These phase phenomena regarding the cubic (Ni,Fe)3∓xS2 solid solution have direct implication in the interpretation of the products formed during the annealing of synthetic pentlandite at 550°C (cf. Section 2.1.1).

At 650°C a divarient field exists on the sulphur deficient side of the mss comprising of mss + $(Ni,Fe)_{3\mp x}S_2$ + vapour. On cooling to 610°C these phases condense to form stoichiometric pentlandite $Fe_{4.5}Ni_{4.5}S_8$ (3). The Fe to Ni atomic ratio is initially unity but on cooling, a pentlandite solid solution extends asymetrically on either side of this composition. Even though this solid solution is somewhat constricted at lower temperatures, pentlandite is considered a stable phase at 25°C.

On further cooling in the sulphur rich portion of the Fe-Ni-S system, pyrite becomes stable at 743°C. Below this temperature tie lines exist from FeS_2 to mss, corresponding to the equilibrium between FeS_2 and $Fe_{1-x}S$ in the Fe-S binary system, whilst enclosing a $(Fe,Ni)S_2$ (nickeliferous-pyrite) + mss + vapour divariant field in the Fe-Ni-S ternary system. Likewise, below 985°C tie lines exist from NiS_2 to mss corresponding to the equilibrium between NiS_2 and $\alpha Ni_{1-x}S$ in the Ni-S binary system (20) and enclosing a $(Ni,Fe)S_2$ + mss + vapour divariant field in the ternary system.

Tie lines connecting FeS_2 to NiS_2 are established at 729°C, enclosing a $(Fe,Ni)S_2$ + $(Ni,Fe)S_2$ + mss + vapour univariant field. At this temperature pyrite contains 7.7% (mass) NiS_2 in solid solution (27), and vaesite contains 29.8% (mole) FeS_2 in solid solution (19). A series of synthetic fusion products between FeS_2 and NiS_2 has been attempted. Polished sections and X-ray patterns of the products shows that although FeS_2 and NiS_2 were homogeneous products, all intermediate members consisted of a mechanical mixture of the two without any observable solid solution. The naturally occuring mineral bravoite $(Fe,Ni)S_2$ with an intermediate composition between that of pyrite and vaesite, i.e. Fe:Ni (atomic) ratio approximately equal to unity, (28) has been described by Shimazaki (21) as being metastable under normal, geological and experimental conditions (cf. Section 1.4.2).

With decreasing temperatures from about 500°C the mss corner of the $(Fe,Ni)S_2$ + $(Ni,Fe)S_2$ + mss + vapour univariant field shifts sufficiently towards more Ni-rich compositions, such that at 461°C violarite of composition $Fe_{0.92}Ni_{2.08}S_4$ condenses from these phases (7),(22). Solid solution in the violarite phase extends simultaneously upon further cooling to stoichiometric $FeNi_2S_4$ at approximately 350°C, and towards the Ni-S boundary which is reached at 356°C with the formation of polydymite, viz. NiS_2 - Ni_3S_4 - $\alpha Ni_{1-x}S$ equilibrium (20).This homogeneous $FeNi_2S_4$- Ni_3S_4 solid solution appears to be thermodynamically stable down to at least 200°C (7). At lower temperatures with the breakdown of the mss below 300°C, phase relations involving violarite are still uncertain since conflicting evidence is available from experimental studies in the literature and the examination of natural assemblages (25).

Some confusion existed in the past over whether or not the violarite solid solution extends further at low temperatures from $FeNi_2S_4$ to Fe_3S_4 (greigite), another naturally occuring thiospinel mineral. However, if this was the case then pyrite and millerite would almost certainly not represent a stable assemblage by application of the phase rule; as is remarked later. Furthermore, the consensus of Vaughan and Craig (25) is that although electron microprobeanalysis of natural samples indicates that this solid solution is complete from Ni_3S_4 to Fe_3S_4, conclusions from bonding models (cf. Section 1.3.2) and the fact that compositions more Fe-rich than $FeNi_2S_4$ have never been synthesized (excluding a vague quotation of Fe_2NiS_4 by Hulliger (26)) suggests that such compositions are metastable.

Similar arguments exist as to whether tie lines can be drawn at low temperatures from violarite to pentlandite (23) with the consequence that the naturally occuring pyrite - millerite assemblage is metastable, or whether they should be drawn from pyrite to millerite to permit a thermodynamically stable coexistance of pyrite and millerite (32). This latter alternative is preferred by Vaughan and Craig (25). These controversies will be pursued further with regard to supergene alteration of pentlandite in Section 1.4.2, and speculative thermodynamic data in Section 1.5.1.

1.2.2 Iron-Nickel-Silver-Sulphur Quarternary System.

Phase relations within the quaternary Ag-Fe-Ni-S system can be described by use of tetrahedral symmetry. Argentopentlandite $Ag(Fe,Ni)_8S_8$ has recently been defined as an independent mineral species by Rudashevskiy et al (35). The existence of a solvus between argentopentlandite and normal pentlandite is not understood (16), even though the crystal structure and bonding theories discussed in Section 1.3.1 suggest that continuous solid solution is possible between $(Fe,Ni)_9S_8$ and $Ag(Fe,Ni)_8S_8$. However, both natural and synthetic normal pentlandites contain less than the limit of

Ag detectable by electron microprobe i.e.<0.05% (mass), even when coexisting with argentopentlandite or other Ag-bearing phases. Naturally occuring argentopentlandite is restricted to Cu-rich zones of magmatic Cu-Ni-Fe sulphide ores where it is in direct contact with chalcopyrite (71), from which in some samples it has probably exsolved (52).

Silver in quantities of up to 14% (atomic) do not alter the solid-solution limits or tie-line relationships within the Fe-Ni-S ternary system at least not between 300 to 600°C. Likewise the solubility of Ag in the phases encountered at 600°C, i.e. mss, pentlandite, taenite (Fe,Ni) is below electron microprobe detection limits i.e.<0.05% (mass) (16). Consequently a projection from Ag onto the Fe-Ni-S base in the Ag-Fe-Ni-S quarternary system at 600°C reveals similar phase relations to the central part of the Fe-Ni-S ternary system, in conjunction with additional stable phases of Ag and/or argentite (Ag_2S) which occur in 3-dimensional regions (within the tetrahedron) of appropriate ambient sulphur fugacity (S_2) over a given assemblage. The divariant volume Ag + Ag_2S + mss + vapour, intersects with the Fe-Ni-S ternary base parallel with the mss field, such that towards the sulphur rich region lies the mss + Ag_2S + vapour trivariant volume, whilst towards the sulphur deficient region lies the mss + Ag + vapour trivariant volume (cf. Figure 1.2.10).

Projected above the mss + pentlandite + vapour divariant field of the Fe-Ni-S ternary system at 600°C, lies the mss + pentlandite + Ag + vapour divariant field of the Ag-Fe-Ni-S quaternary system (cf. Figure 1.2.12). However, on cooling to approximately 455°C these phases condense to form stoichiometric argentopentlandite $AgFe_5Ni_3S_8$ with the consequental establishment of the argentopentlandite + pentlandite + mss + vapour divariant field. This field extends across the entire bottom part of the argentopentlandite solubility field with an ever increasing slope of tie lines between argentopentlandite - pentlandite, and argentopentlandite - mss, as the Fe:Ni ratio decreases. Since argentopentlandite is always in equilibrium with pentlandite of lower Fe:Ni (atomic) ratio, it follows that the substitution of Ag into the pentlandite structure lowers the activity of FeS in argentopentlandite relative to that in pentlandite of the same Fe:Ni (atomic) ratio, i.e. $Fe_{5.625}Ni_{3.775}S_8$ (16). However, whilst argentopentlandite ($AgFe_5Ni_3S_8$) is only just thermodynamically stable at 455°C; pentlandite ($Fe_{5.625}Ni_{3.375}S_8$) with the same Fe:Ni (atomic) ratio is thermodynamically stable at 500°C (2).

At 400°C the range of solid solution between Fe and Ni is smaller, but displaced towards more Fe-rich compositions in argentopentlandite than in normal pentlandite (cf. Figure 1.2.11). Below approximately 358°C argentopentlandite coexists with Ag or Ag_2S. At 300°C the argentopentlandite solid-solution composition ranges from Fe:Ni (atomic) ratio 1.07 to 4.10, and Ag% (atomic) 3.80 to 5.88 (16).

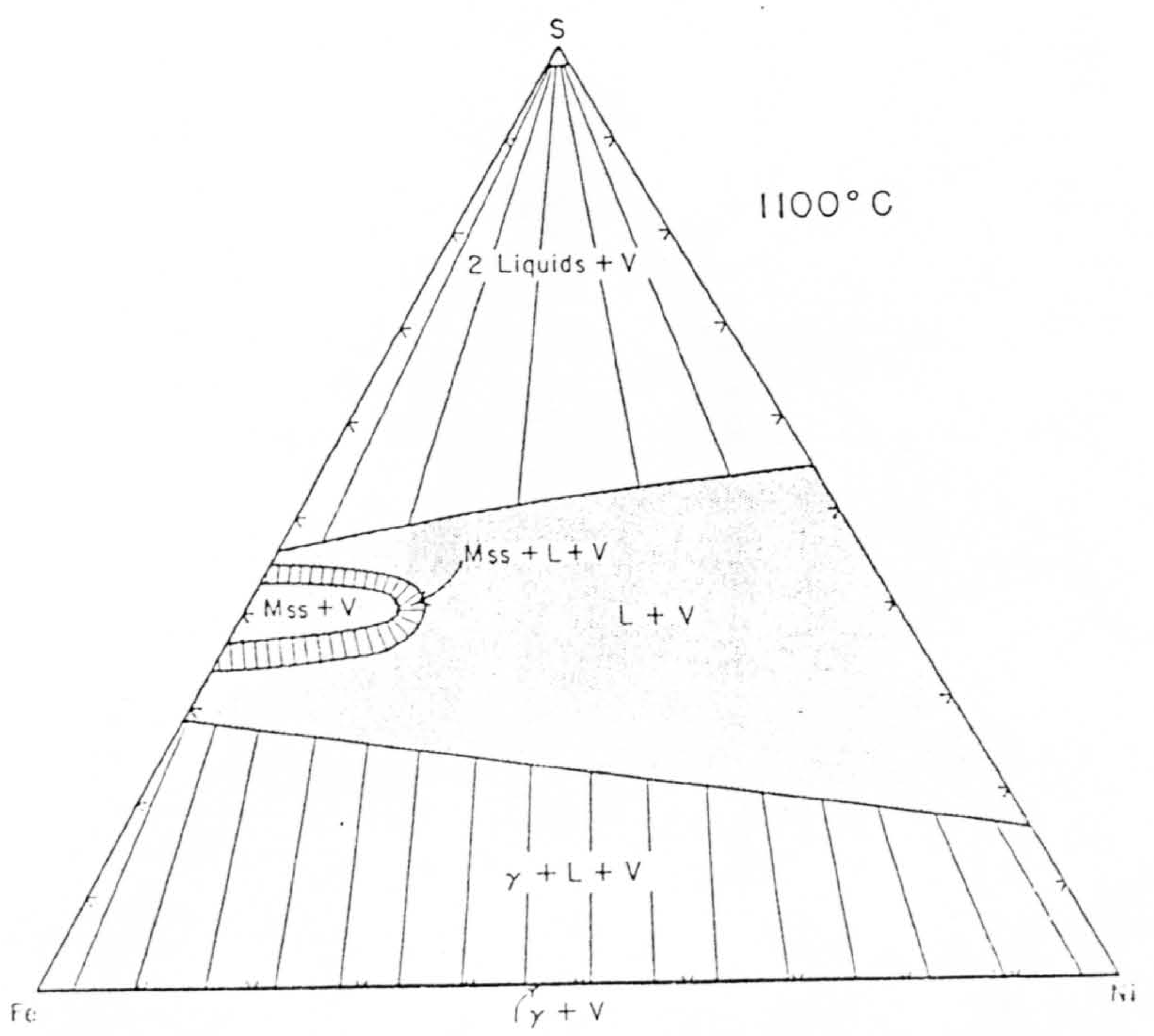

Figure 1.2.1

Isothermal Fe-Ni-S phase diagram 1100°C (12)

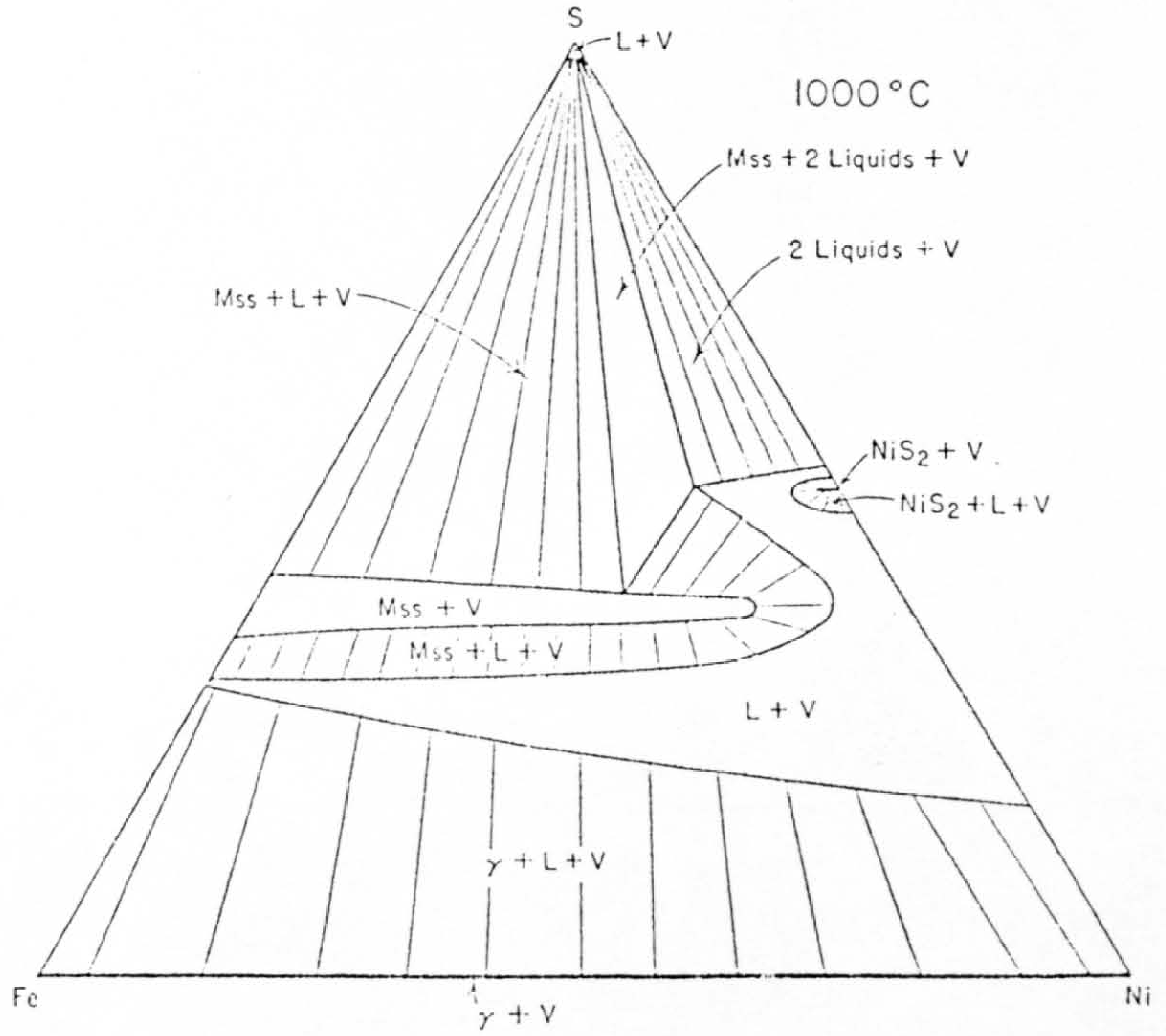

Figure 1.2.2

Isothermal Fe-Ni-S phase diagram 1000°C (12)

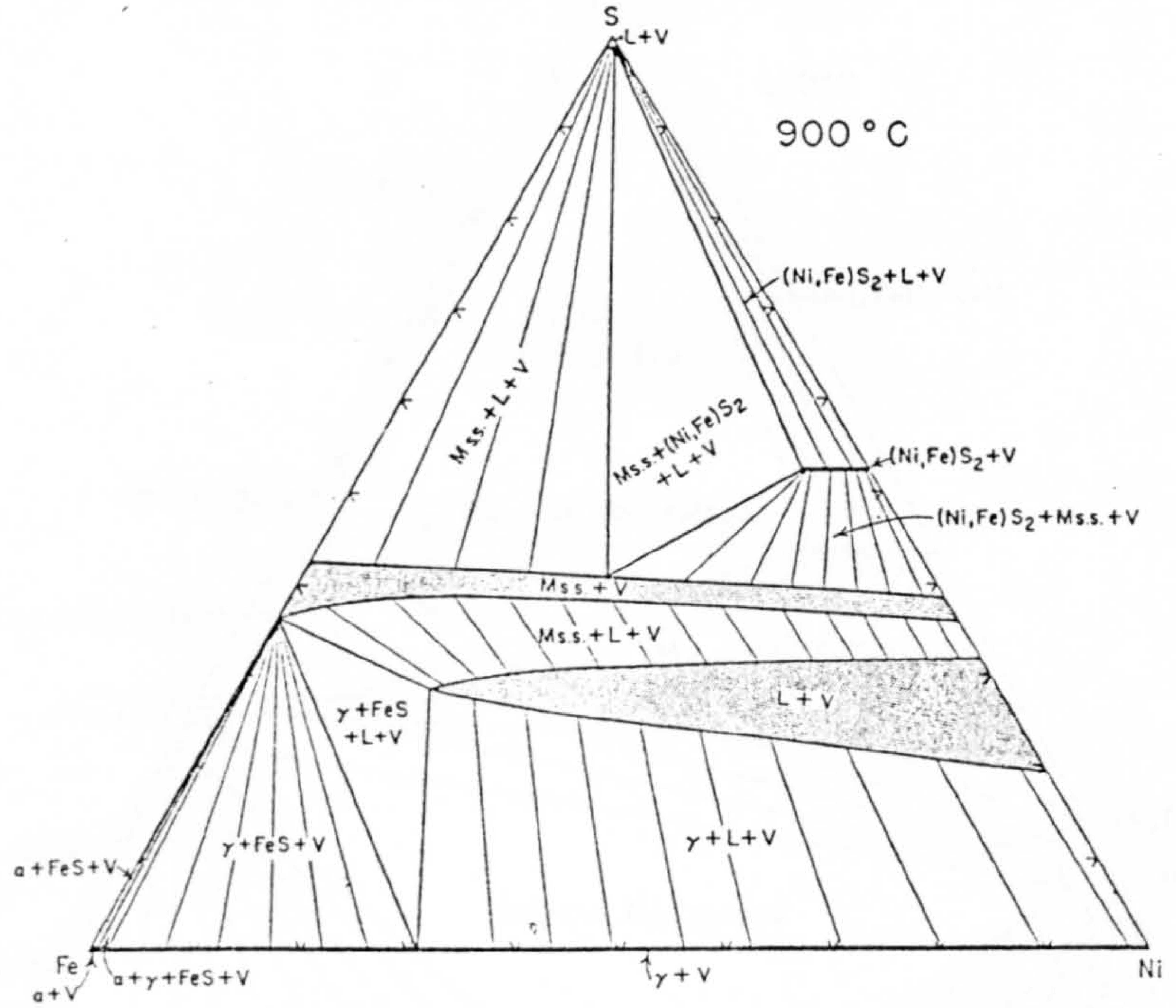

Figure 1.2.3

Isothermal Fe-Ni-S phase diagram 900°C (12)

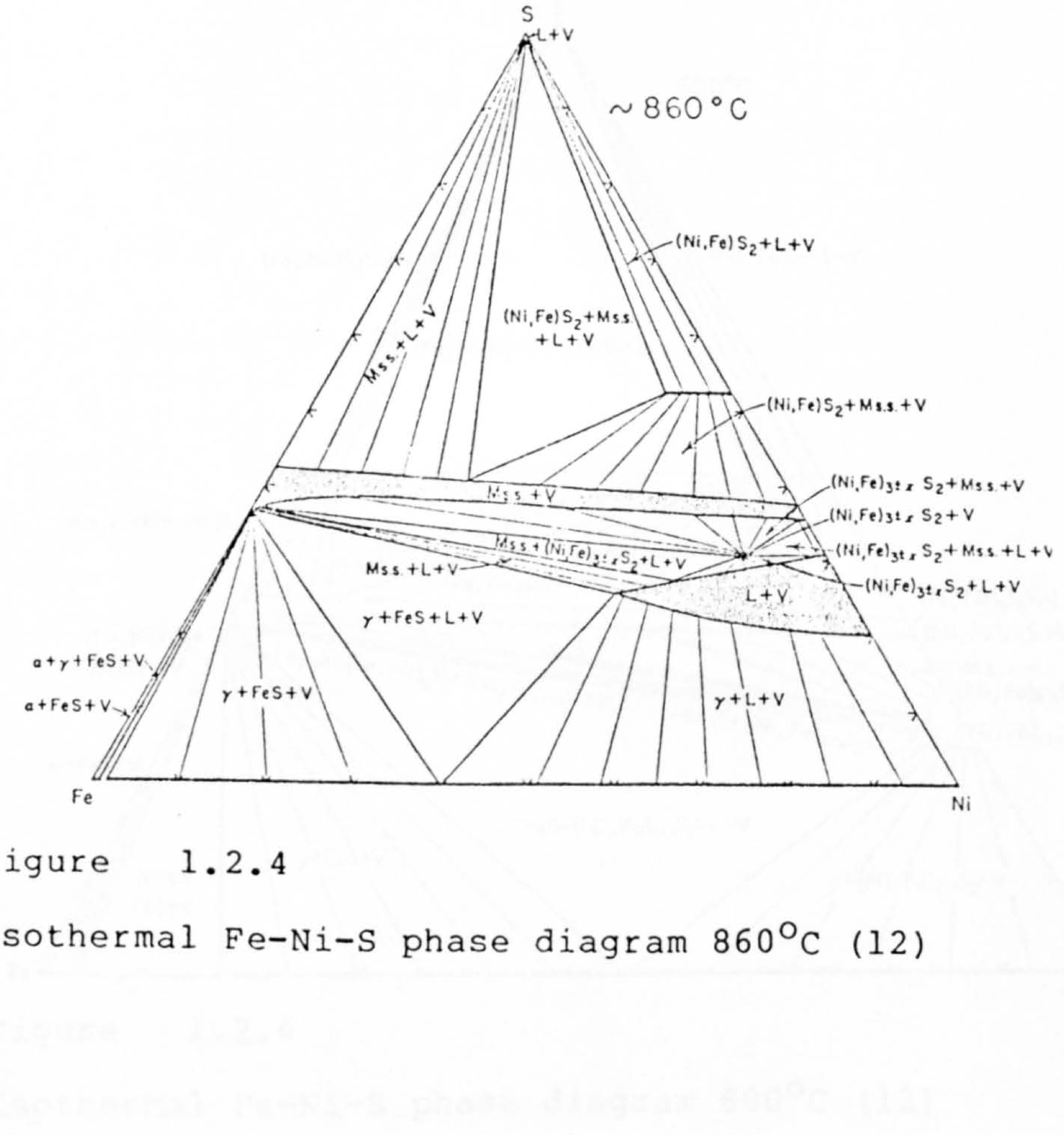

Figure 1.2.4

Isothermal Fe-Ni-S phase diagram 860°C (12)

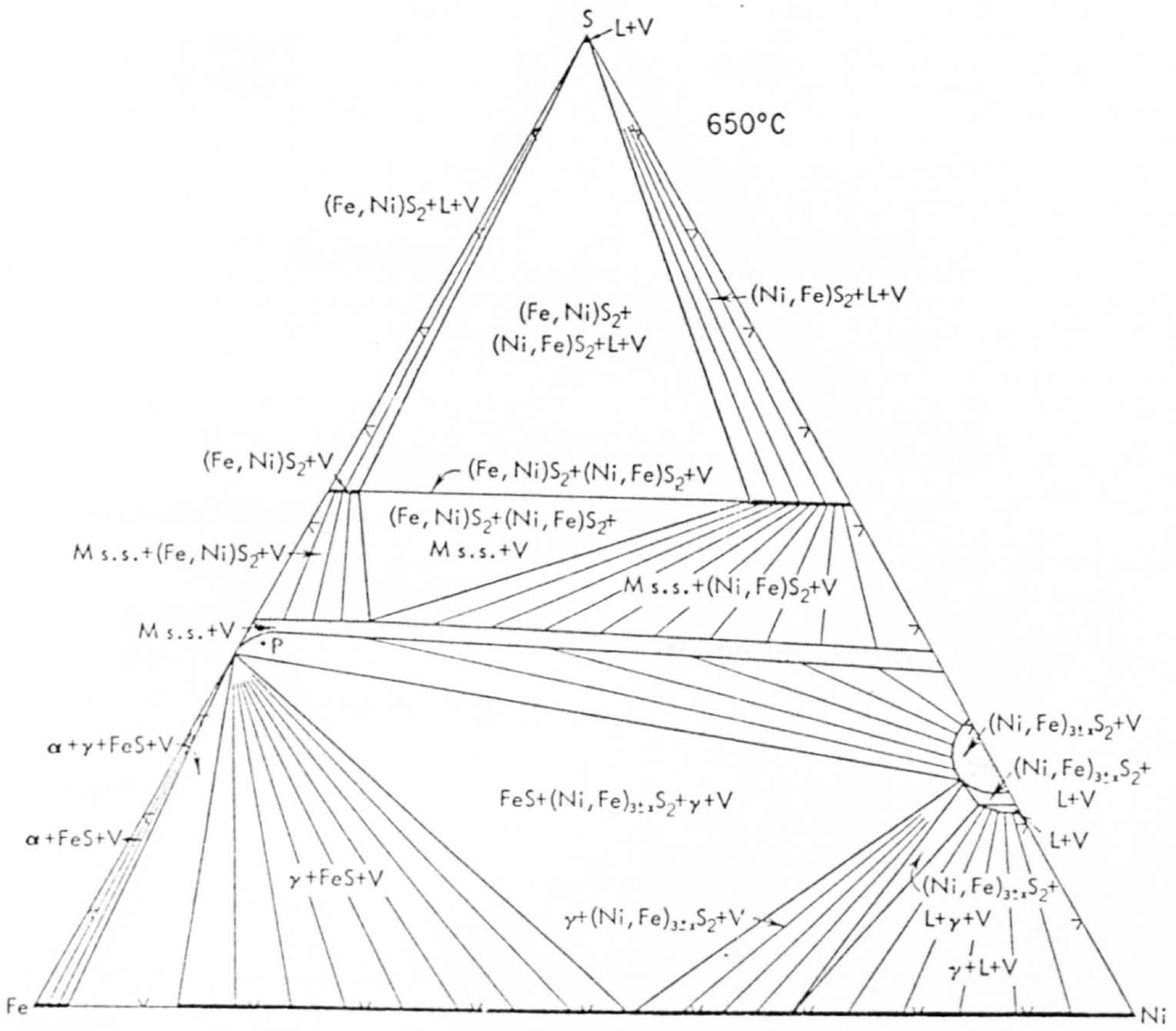

Figure 1.2.5

Isothermal Fe-Ni-S phase diagram 650^{o}C (12)

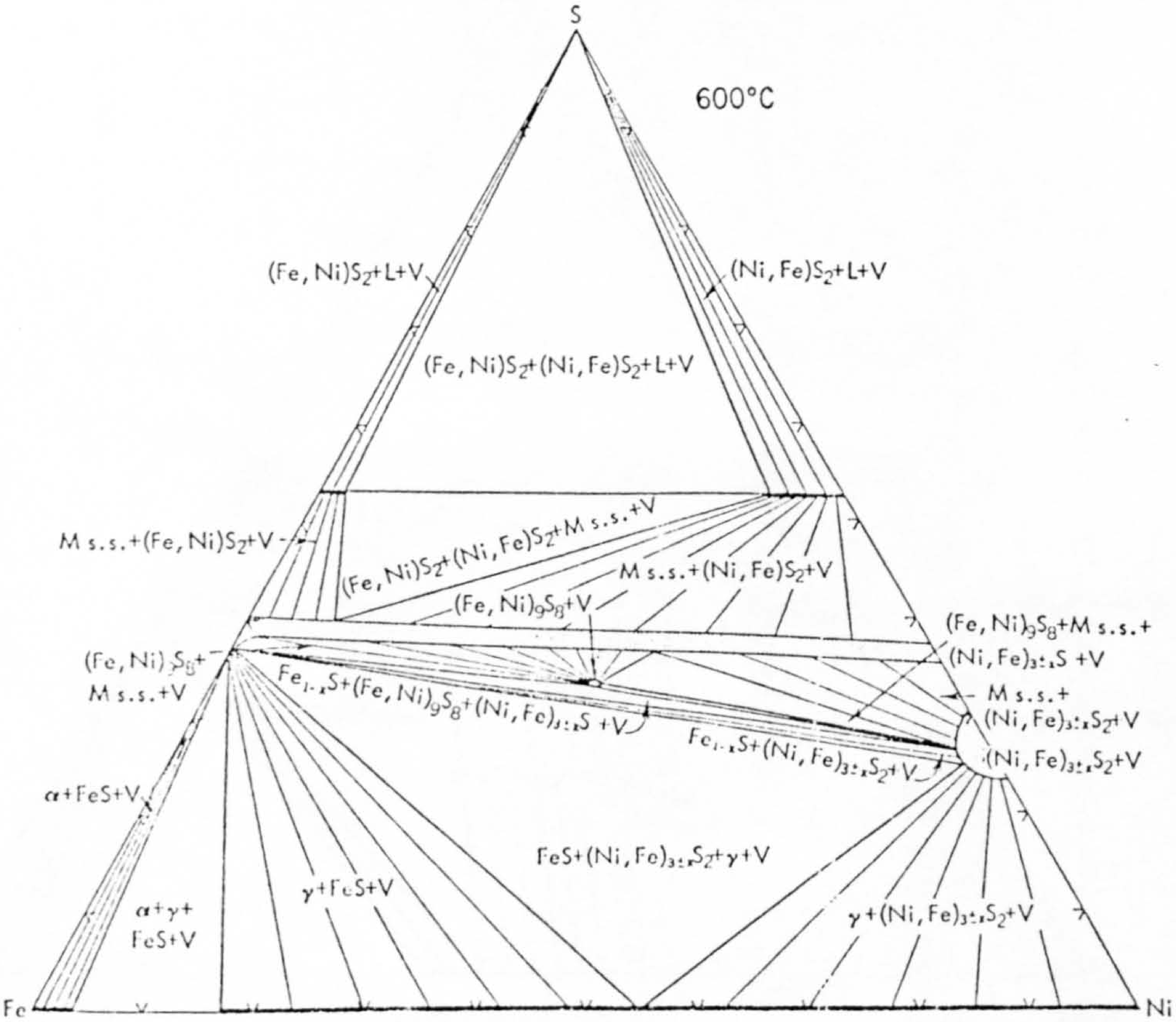

Figure 1.2.6

Isothermal Fe-Ni-S phase diagram 600^{o}C (12)

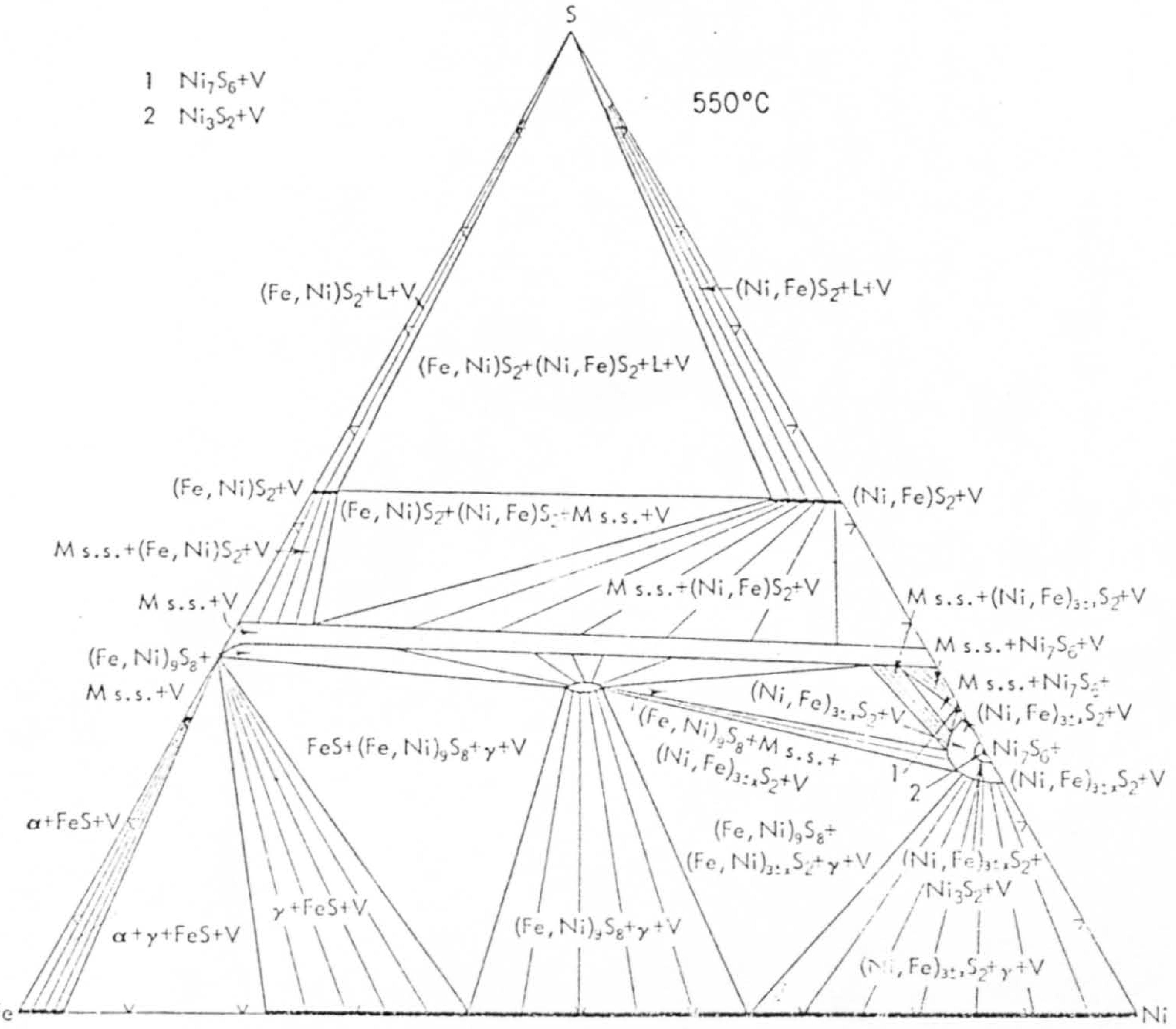

Figure 1.2.7

Isothermal Fe-Ni-S phase diagram 550°C (12)

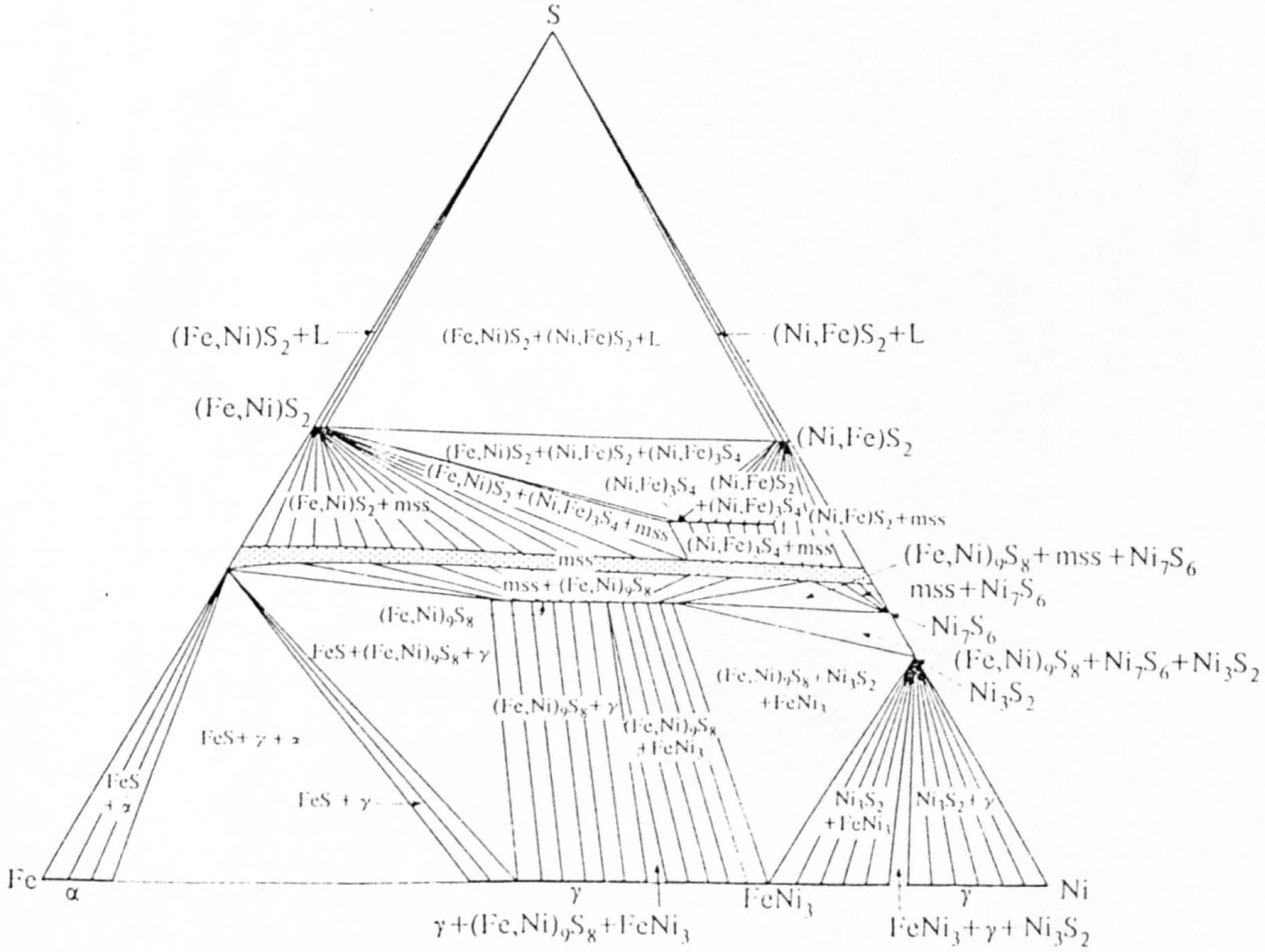

Figure 1.2.8

Isothermal Fe-Ni-S phase diagram 400°C (18)

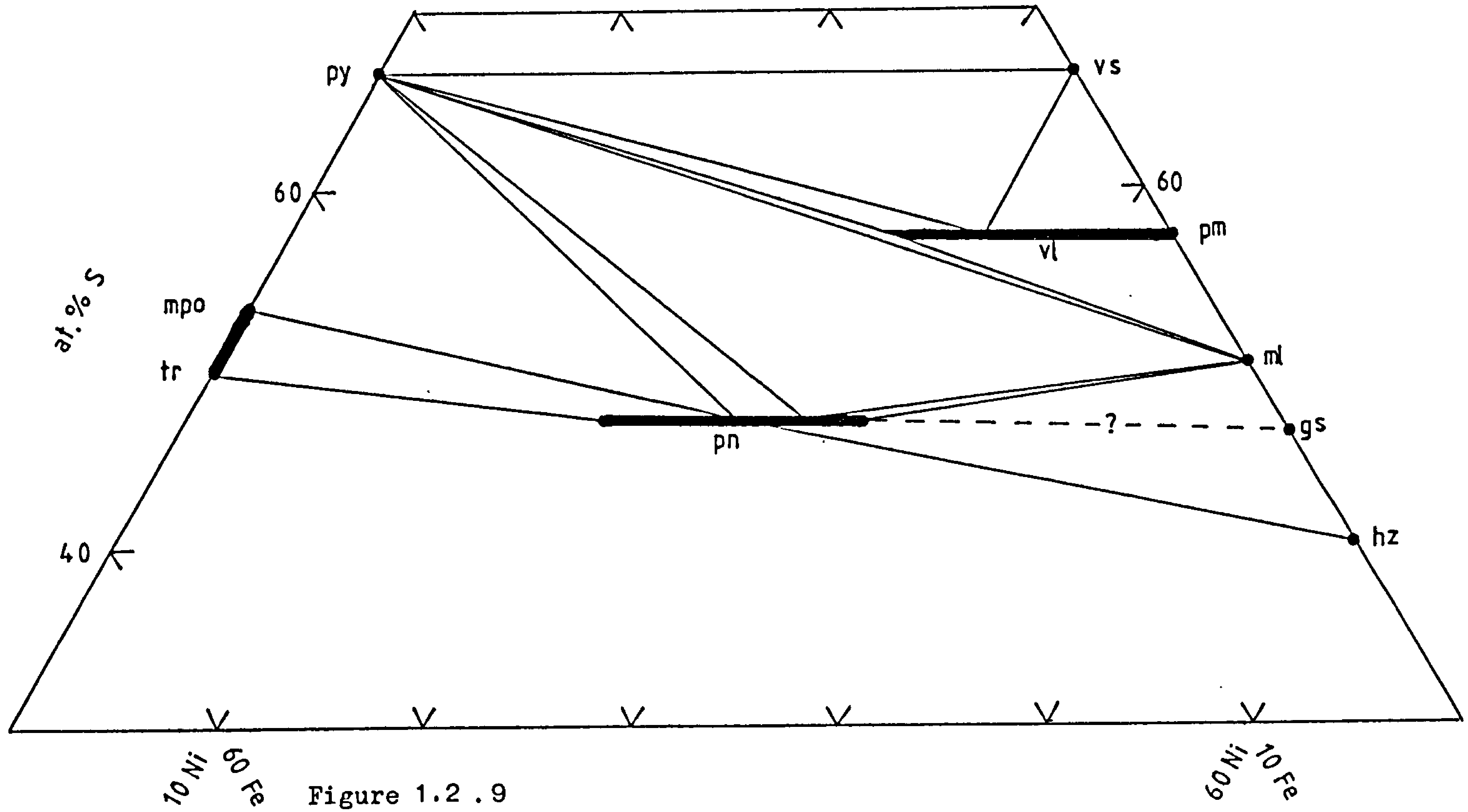

Figure 1.2 .9

Speculative phase diagram for a portion of the Fe-Ni-S system at 298K. Compositions are in atomic percentages. Tie lines to sulphur and Fe-Ni alloys are not shown. Abbreviations: gs, godlevskite; hz, heazlewoodite; ml, millerite; mpo, monoclinic pyrrhotite; pm, polydymite; pn, pentlandite; py, pyrite; tr, troilite; vl, violarite; vs, vaesite. (Based on Vaughan and Craig (18), Graterol and Naldrett (31)).

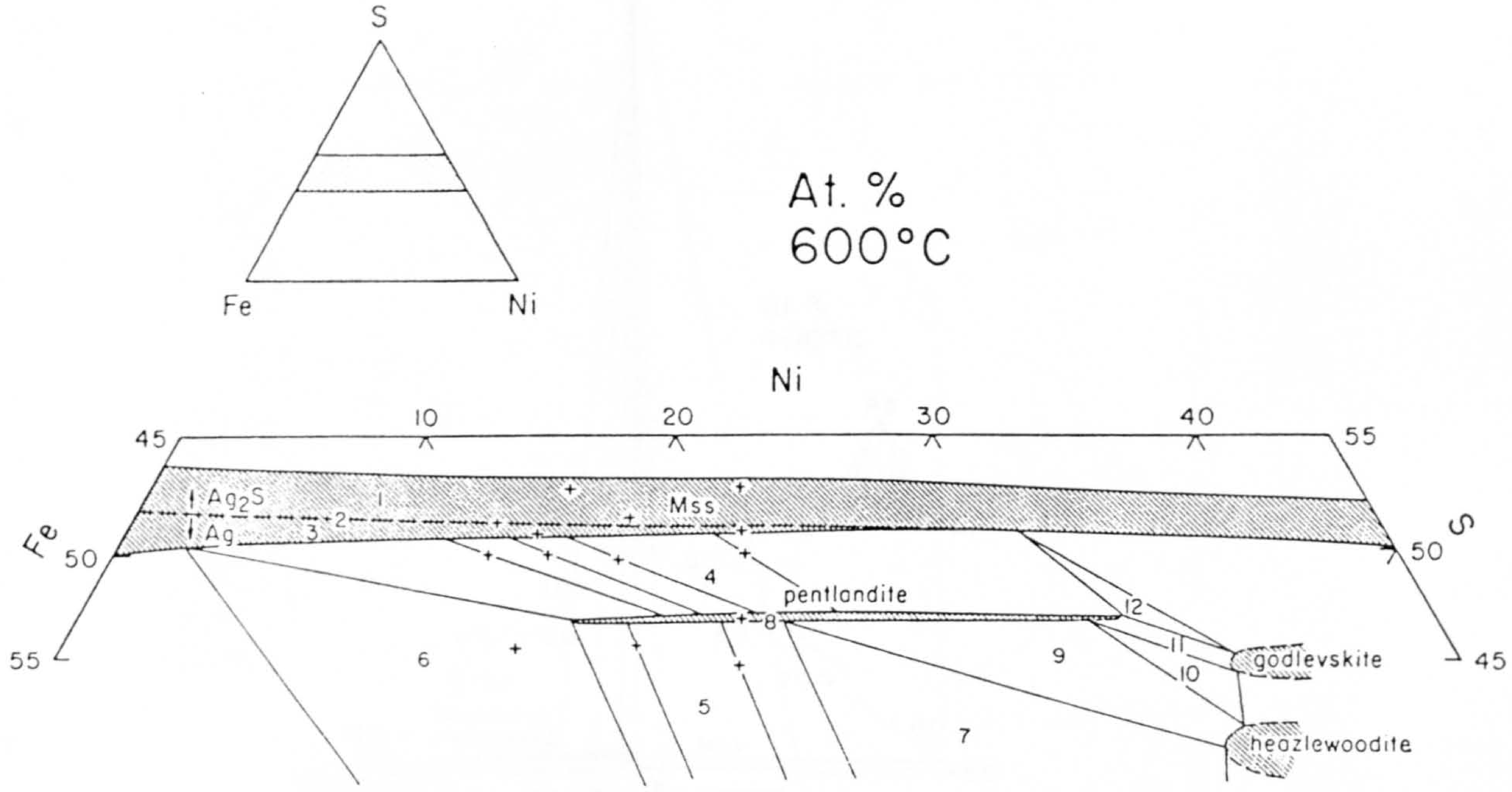

Figure 1.2.10

Isothermal Ag-Fe-Ni-S phase diagram 600^{o}C. Projection of phase relations from Ag onto the central part of the ternary Fe-Ni-S base in the Ag-Fe-Ni-S system. The dashed line traces the Ag/Ag_2S equilibrium across the mss field. Numbers identify equilibrium assemblages given below. Vapour coexists with all phases. (1) Ag_2S + mss; (2) Ag_2S + Ag + mss; (3) Ag + mss; (4) Ag + mss + pn; (5) Ag + pn + FeNi; (6) Ag + mss + pn + FeNi; (7) Ag + pn + FeNi + hz; (8) Ag + pn; (9) Ag + pn + hz; (10) Ag + pn + hz + gs; (11) Ag + pn + gs; (12) Ag? + mss + pn + gs.

(After Mandziuk and Scott (16)).

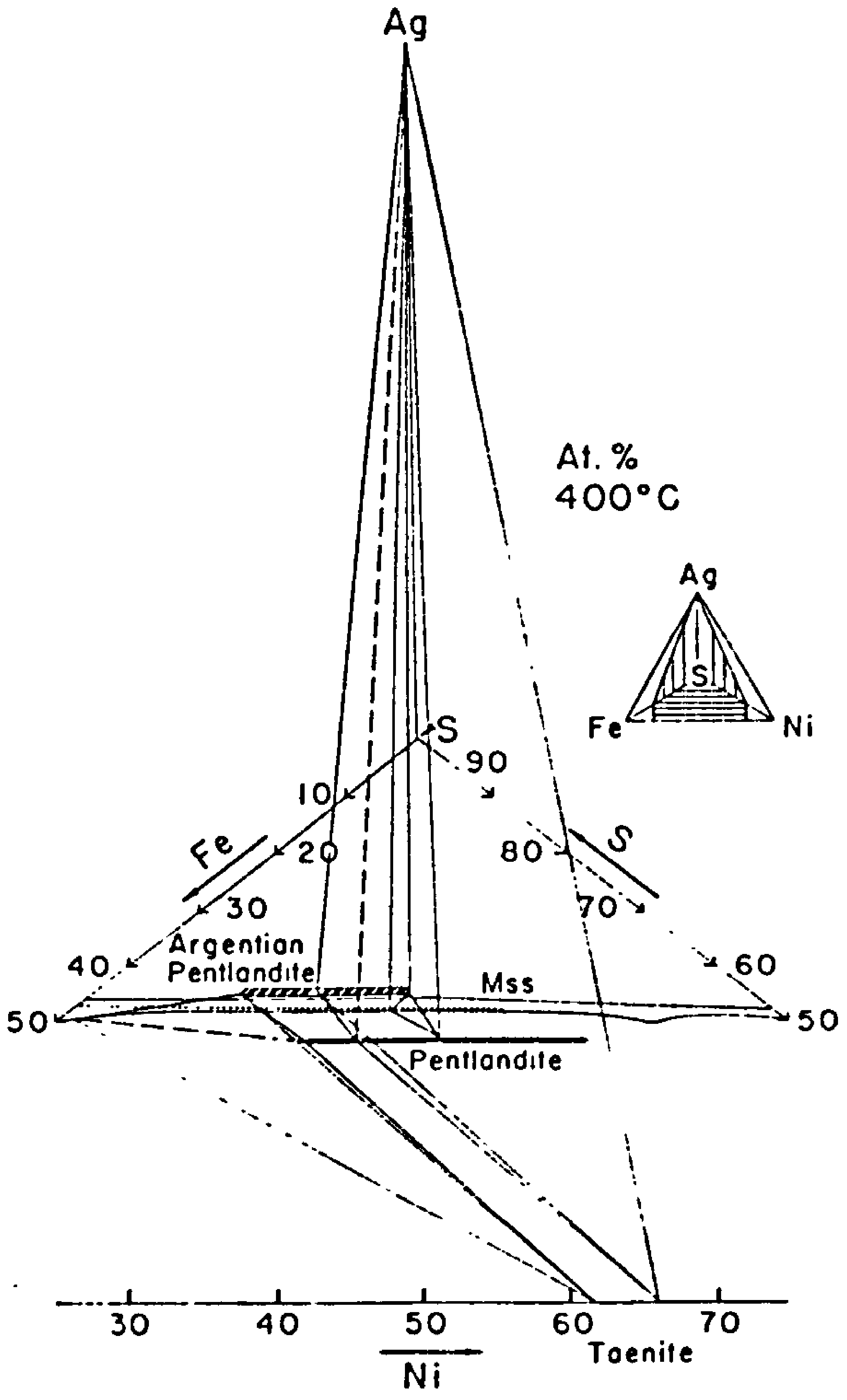

Figure 1.2.11

Solubility limits and phase relations involving argentopentlandite in the lower central part of the Ag-Fe-Ni-S system at 400^{o}C. The dotted line traces the projected position of the Ag/Ag_2S equilibrium on the ternary Fe-Ni-S base. Three univariant prisms are shown:

(1) argentopentlandite + mss + pentlandite + taenite + vapour.

(2) argentopentlandite + Ag + pentlandite + taenite + vapour.

(3) argentopentlandite + mss + pentlandite + Ag + vapour.

(After Mandziuk and Scott (16)).

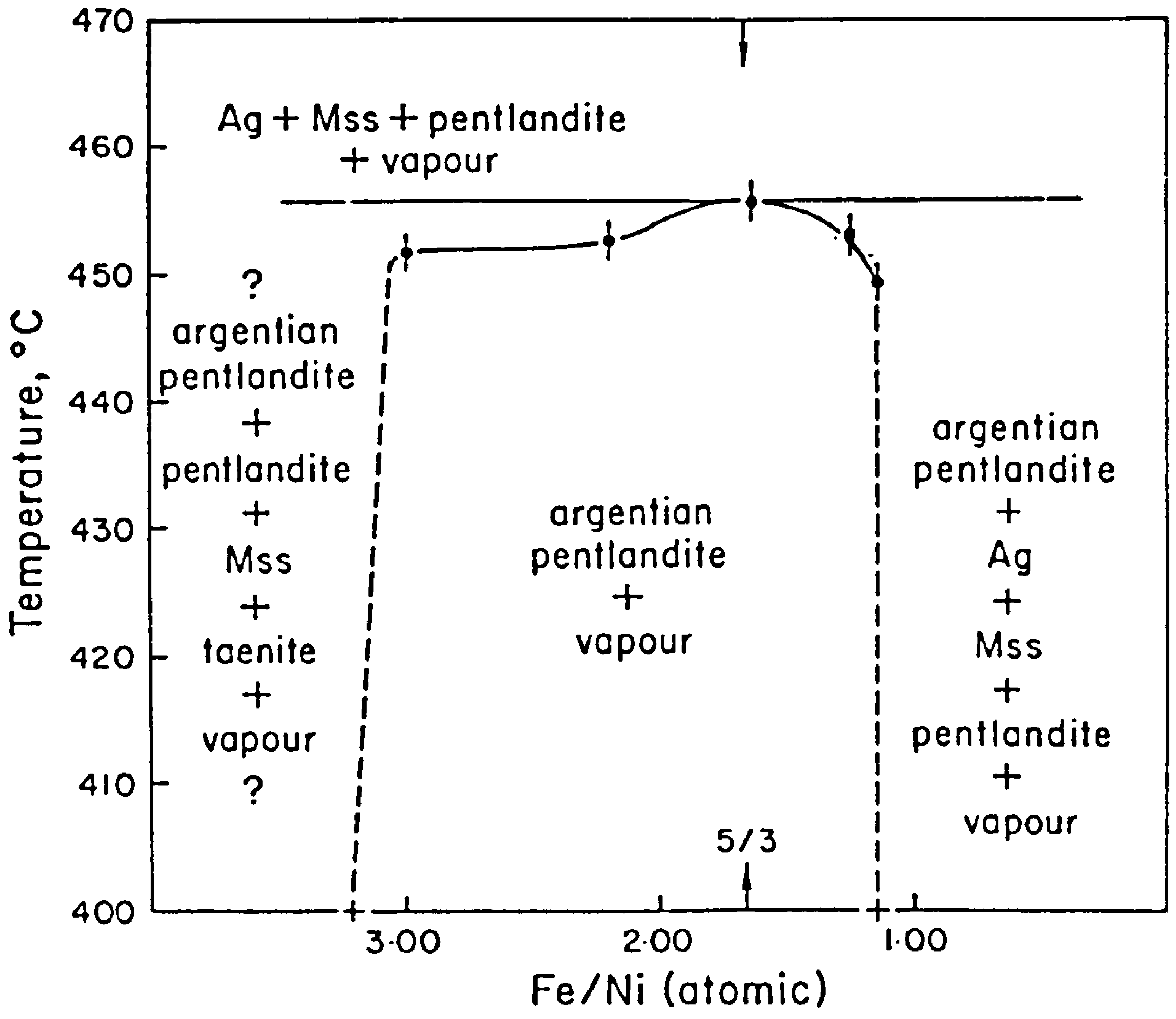

Figure 1.2.12

Section locating the upper thermal stability of argento-pentlandite $Ag(Fe,Ni)_8S_8$ with variable atomic Fe/Ni ratios. (After Mandziuk and Scott (16)).

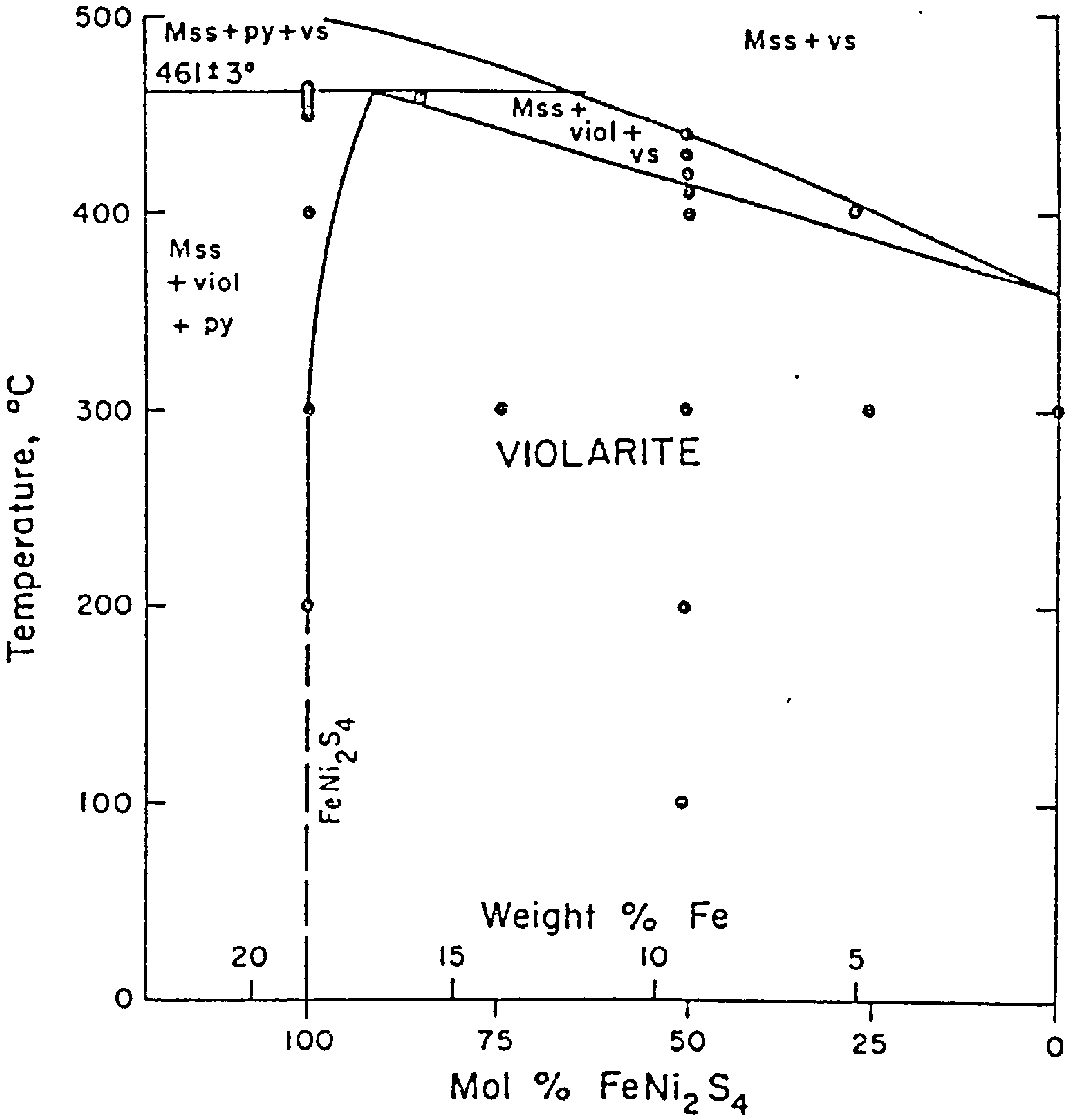

Figure 1.2.13

Section along the $FeNi_2S_4$ - Ni_3S_4 solid solution join.

(After Craig (7)).

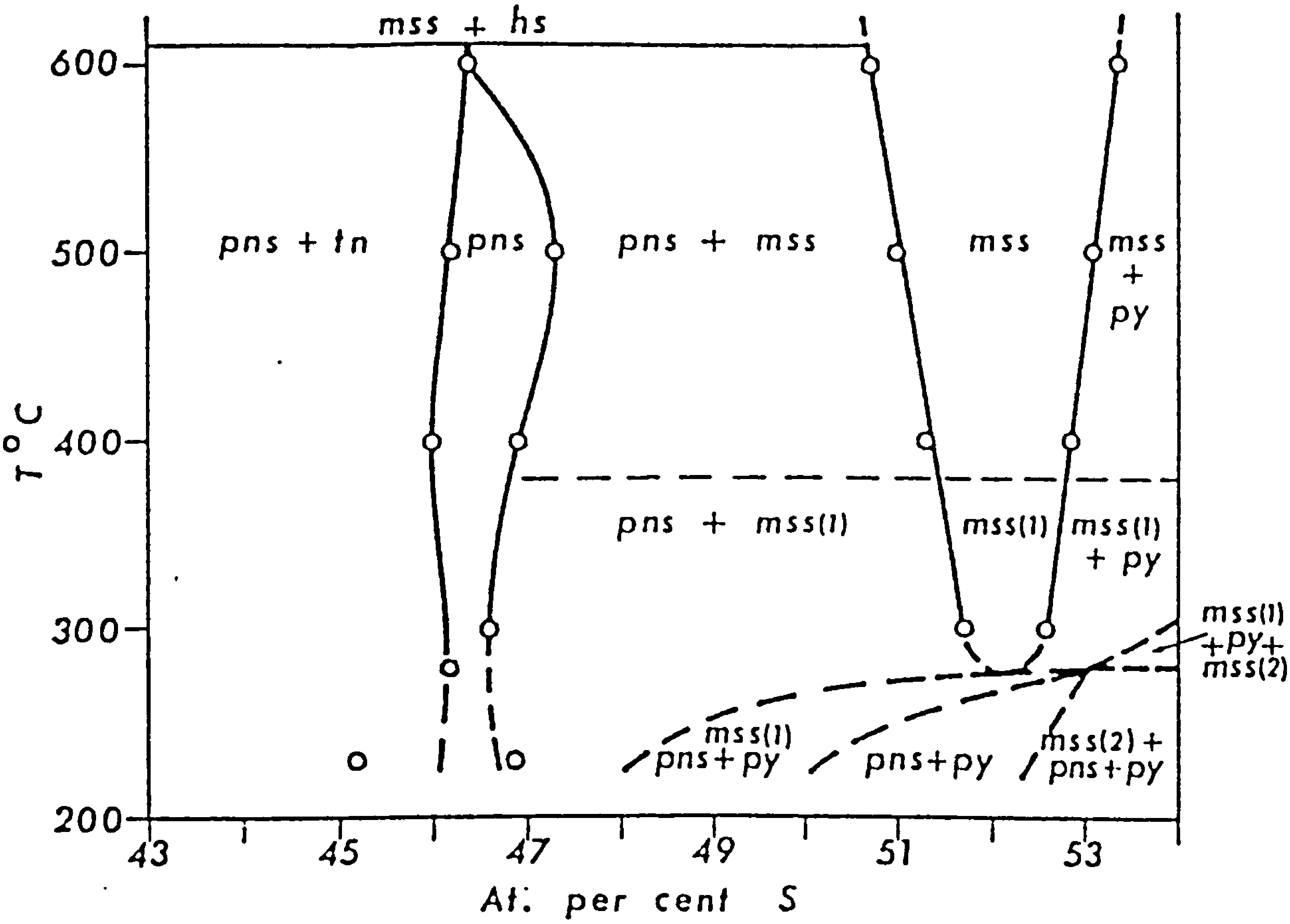

Figure 1.2.14

Section across the pentlandite - Mss solubility field at Fe:Ni = 1:1 with variable atomic % sulphur. (After Misra and Fleet (13)).

1.3 CRYSTAL STRUCTURES AND CHEMICAL BONDING

1.3.0 Introduction

The crystal structures of pentlandite and violarite share an almost identical sulphur sublattice. Their differences lie essentially in their respective stoichiometry and coordination numbers. The similarity of the sulphur sublattice has a profound influence on the composition of subsequent products of the oxidative alteration of pentlandite in nature, viz. the formation of violarite as an intermediate phase (cf. Section 1.4.2).

1.3.1 Pentlandite

The crystal structure of pentlandite was first determined from X-ray powder data by Lundqvist et al, (37) and later confirmed by Pearson and Buerger (40) and Knop and Ibrahim (41), refined by Rajamani and Prewitt (38). Further work with regards to cation distribution from ^{57}Fe-Mössbauer speectroscopy studies and proposed bonding models have been reported by Knop et al (42),(44), Tsukimura and Nakazawa (45), Vaughan and Ridout (43); and extended to argentopentlandite by Hall and Stewart (39).

The pentlandite structure is illustrated in Figure 1.3.1. Pentlandite is a cubic mineral, with a unit cell containing 36 metal and 32 sulphur atoms and a nominal cell perameter a_o = 1.005nm. Pentlandite is isostructural with Co_9S_8, belonging to the space group $O^5{}_h$- Fm3m.

The structure is composed of an almost cubic close-packed framework of sulphur atoms forming the stacking sequence ABCABC... The metal atoms are distributed among the interstices of the sulphur sublattice such that 4 metal atoms are accommodated in 4(b) octahedral sites out of a possible 32 vacancies, whilst 32 metal atoms occupy 32(f) tetrahedral (trigonally distorted) sites out of a possible 64 vacancies availabe in the unit cell; vis à vis 32 sulphur atoms distributed over 8(c) and 24(e) equipoints in four and five-fold coordination by metal atoms respectively.

A complete ordering with respect to octahedral and tetraherdal sites could only be possible if the Fe:Ni atomic ratio was either 1:8 or 8:1. However, the ratios observed in natural pentlandites are far from this, and those of synthetic pentlandite only lie between 1:1.53 and 1.98:1 respectively at 400°C (8); cf. Section 1.3.1. Regardless of whether the 4(b) sites are occupied exclusively by 4Fe or 4Ni or a mixture of both, the 32(f) sites must consequently always accommodate both Fe and Ni. These predictions manifest themselves in the mössbauer studies by Knop et al (42), and Vaughan and Ridout (43). The ^{57}Fe-mössbauer spectrum at 300K shows a small unsplit peak due to octahedral Fe, with a superimposed symmetrical quadrupole doublet from Fe in distorted (f) sites. The absence of a paramagnetic moment on (f)Fe in an external field of 3 Tesla at 4.2K suggests delocalization of d electrons with a formal oxidation state <2+, and indicates the irrelevance of formal valency when describing the covalently bonded (f)Fe atoms. Thus the Fe atom in the slightly distorted FeS_4 tetrahedron is engaged in appreciable covalent bonding utilizing sd^3 hybridized orbitals as well as perhaps the rather higher sp^3 hybridized orbitals as suggested by Knop et al (42); viz. T_d point group symmetry.

Mossbauer studies on a series of pentlandites $(Fe,Co,Ni)_9S_8$ with varying Co:Ni ratios from Co_8FeS_8 to

$Co_3FeNi_5S_8$ reveals that the isomer shift for (f)Fe decreases steadily with increasing cell parameter: a_o = 0.9941nm to 1.0021nm, yet with a simultaneous increase in d electrons per stoichiometric formula (nd = 62 to 67) (44). The decrease in isomer shift for (f)Fe is due to the increased nd, which more than compensates for the volume shrinkage. This trend clearly illustrates that the 3(f) atoms neighbouring a fourth (f) atom at the apex of the 3 mutually perpendicular axis (forming a cubic cluster of 8 tetrahedrally coordinated metal atoms within the lattice) have a significant effect on the isomer shift of one another; i.e. some of the 3d electrons from Co and Ni at the 32(f) sites are delocalized and thus able to affect the isomer shift of an (f)Fe atom. A bonding model has been proposed to account for this delocalization (18),(39),(42),(44), cf. Figures 1.3.2 and 1.3.3.

Anti-bonding sigma molecular orbitals (t_2^*) arise from the overlap of essentially sd^3 and perhaps sp^3 hybridized atomic orbitals on the (f) metal with sp^3 hybridized atomic orbitals on 4(c) sulphur atoms. These anti-bonding sigma molecular orbitals (t_2^*) are in close enough proximity (0.2533nm) with identical t_2^* MO's on 3 adjacent (f) metal atoms at the corner of the cube cluster to overlap with one another and allow the electrons (3 unpaired electrons in the case of Co) to form 3 metal-metal bonds. The summation of these t_2^* MO's across the lattice constitutes a band whose electrons are delocalized around the M_8 cube cluster and possibly throughout the entire crystal lattice. In $Fe_{4.5}Ni_{4.5}S_8$ the net result of electron contribution to the t_2^* MO is also 3 unpaired electrons;

viz. Co_8 cube cluster in Co_9S_8.

The ^{57}Fe mössbauer spectrum reveals a larger isomer shift for the 4(b)Fe atoms, than that for the 32(f)Fe atoms. This is to be expected since both are coordinated to sulphur ligands but (b)Fe has less s-character in its bonding MO's attributed to octahedral sp^3d^2, than has (f)Fe with tetrahedral sd^3 or sp^3 (42). The isomer shift lies between those for octahedrally coordinated high spin Fe^{2+} in FeS and low spin Fe^{2+} in FeS_2, although much closer to the former (44). Work by Rajamani and Prewitt (38) on comparing bond lengths indicates that (b)Fe is probably high spin. Vaughan and Ridout (43) favour the low spin situation on account of the absence of quadrupole splitting and the cubic site symmetry, which is in agreement with similar work by Goncharov and Tomilov (92).

A plausable bonding model for (b) site metals involves the overlap of sp^3d^2 with sp^3d hybridized atomic orbitals on 6(e) sulphur atoms, with the formation of e_g and t_{1u} bonding orbitals, t_{2g} non-bonding orbitals, and partially filled e*g anti-bonding orbitals. In the case of high spin (b)Fe^{2+} the e_g^* MO's are half filled with 2 unpaired electrons, or in the case of low spin (b)Co^{2+} with only 1 lone electron. When summed up over the entire lattice, these e_g^* MO's constitute an anti-bonding sigma band. Furthermore, the magnetic and electrical properties of pentlandite (i.e. pauli-paramagnetism and high electrical conductivity) suggest an overlap of the sigma anti-bonding band (formed from e_g^* MO's on octahedral site metal atoms) with the sigma anti-bonding band (formed from the t_2^* MO's on tetrahedral site metal atoms). The orientation of these anti-bonding MO's on the appropriate (b) and (f) site metal atoms does indeed favour such an overlap. This could give a single broad, yet partially filled composite s and d band, accounting for these physical properties. This possibility of extensive delocalization of electrons may account for the intermediate spin-state on (b)Fe.

In the $(Fe,Co,Ni)_9S_8$ solid solution series, the compositions are generally confined to the range between Co_9S_8 and $Fe_{4.5}Ni_{4.5}S_8$ such that the Fe:Ni ratio remains appreciably at unity (51). This suggests a need to retain an overall d electron configuration of 63 per stoichiometric formula.

Pentlandite compositions with variable Fe:Ni ratios lying on either side of the ideal stoichiometric $Fe_{4.5}Ni_{4.5}S_8$ do exist as a solid solution series although they are thermally less stable (cf. Section 1.2). Such deviations inevitably lead to a departure from the ideal total d electron configuration of 63 electrons per stoichiometric formula viz. Co_9S_8. However, this need not cause a change in the d-electron population of the metal cube cluster since excess Ni could be ordered into (b) sites creating vacancies in (f) sites, whilst excess Fe could enter unoccupied (f) sites. Thus, the structural formula for pentlandite could be represented as $^{VI}(Fe,Ni)^{IV}(Fe,Ni,*)_8S_8$ where (*) represents a tetrahedral vacancy in Ni-rich compositions or excess cations in Fe-rich compositions.

An irreversible (albeit partially reversible) thermal expansion of the pentlandite lattice is reported to occur whilst annealing natural pentlandite at 150 to 200°C under laboratory conditions (42),(47). This is further evident by natural pentlandite having a smaller lattice parameter than synthetic pentlandite of an identical composition (47). Although the mechanism is not fully substantiated, it is reported that cation migration occurs between (b) and (f) sites, yet with much discrepancy in the literature over the relative migrations of Fe and Ni.

Rajamani and Prewitt are adamant that for natural (Frood) pentlandite $Fe_{3.97}Ni_{4.84}Co_{0.07}S_8$ an isothermal expansion on annealing at 150 to 200°C coincides with an enrichment of high spin Fe^{2+} from (f) to (b) sites relative to the initial natural mineral (47), vis à vis creation of (f) site vacancies with (b)Ni ordered into some of them, which would enable this Ni-rich pentlandite to obtain an ideal d-electron configuration for the cube cluster for the high temperature phase (38). These observations appear to contradict those of other workers. Tsukimura et al (45) have determined the distribution of Fe and Ni in synthetic $Fe_5Ni_4S_8$ and natural/annealed (Sudbury) pentlandite $Fe_{4.40}Ni_{4.57}Co_{0.03}S_8$ by X-ray powder method employing the anomolous dispersion of Fe K_{beta} and Cu K_{alpha} radiations, which are consistant with the ^{57}Fe mössbauer study by Knop (42) on natural (Sudbury) pentlandite $Fe_{4.20}Ni_{4.74}Co_{0.06}S_8$ annealed at 200°C. Annealing causes a net migration of Fe from (b) to (f) sites, whilst in the synthetic Fe-rich pentlandite Fe is concentrated in (f) sites.

A possible mechanism for the irreversible thermal expansion of natural pentlandite is the disordering of metal atoms between nonequivalent sites in the lattice, i.e. isochemical substitutional disordering transitions (viz. second order phase transitions) (73). However, the precise mechanism is likely to be a complex function of the initial mineral, i.e. composition, ore genesis (thermal history, metamorphisim); with the possibility of an irreversible spin transition: low-high spin Fe(b) (47),(62).

Further work is needed concerning this transition, particularly with regards to different compositions at various temperatures and pressures with a view to gaining an enhanced understanding of the electronic structure before and after the transition. Neutron diffraction studies may reveal the absolute location of Ni and Fe, within the lattice. However, the obtainment of thermodynamic data (enthalpy and entropy changes) concerning this transition would be of direct relevance to this present work. This would enable a more accurate determination for the free energy of formation of pentlandite (stoichiometric or otherwise) at 298K. An important implication of constructing E_h-pH diagrams at 298K from free energy data for pentlandite obtained from the extrapolation of thermodynamic data at temperatures above 473K, is that they are highly speculative (76), (cf.Section 1.5). Similar studies may need to be performed to check the low temperature thermodynamic data of violarite.

Since synthetic pentlandite appears to retain the high temperature structure of annealed natural pentlandite at room temperature, this suggests that either synthetic pentlandite with the cation distribution of the high temperature phase is metastable at 298K, or that the phase transition for natural pentlandite is truely irreversible at atmospheric pressure implying that the low temperature phase (natural pentlandite) is in fact metstable at 298K and

103kPa.

If a consistent population of 56 d electrons in the metal cube cluster was the sole reason for the stability of the pentlandite structure, then argentopentlandite of stoichiometry $AgFe_4Ni_4S_8$ would be predicted as the most thermodynamically stable of that series (since Ag is known to exclusively occupy (b) sites). However, the solid solution field in argentopentlandite extends only from (atomic ratio) Fe:Ni = 1.12 to 3.21 (16); whilst $AgFe_5Ni_3S_8$ is thermodynamically the most stable of the series. This suggests that perhaps the total number of outer-shell s and d electrons is the most critical factor in stabilizing the pentlandite structure, rather than just the d electrons; especially since Co_9S_8, $Fe_{4.5}Ni_{4.5}S_8$, and $AgFe_5Ni_3S_8$ which are the most stable species in their respective series, all have a total of 81 outer-shell d and s electrons per stoichiometric formula (16).

In argentopentlandite Ag exclusively occupies the 4(b) sites which is predicted on account of its larger cationic radius, but there is a lack of definite evidence in the literature for nominating a particular oxidation state to Ag. Lattice dimension considerations suggest Ag is monovalent ($4d^{10}$) (38). The metal-metal bonds in the cubic cluster are longer in argentopentlandite ($Ag_{0.99}Fe_{4.88}Ni_{3.17}S_{8.00}$) than those in normal pentlandite ($Fe_{4.15}Ni_{4.74}Co_{0.15}S_{8.0}$), 0.2670nm and 0.2533nm respectively (39). This fact, coupled with the reduced reflectivity (52) suggests that argentopentlandite may have significantly different electrical properties from those of normal pentlandite (39). However, such data for $AgFe_5Ni_3S_8$ are not available in the literature.

The author concludes from the literature that the thermal stability of the pentlandite lattice is dependant on a consistent outer-shell electronic configuration when summed up over all the metal atoms within the unit cell. The most thermodynamically stable compositions are the stoichiometric: Co_9S_8, $Fe_{4.5}Ni_{4.5}S_8$, $AgFe_5Ni_3S_8$ which contain a consistant 81 outer-shell d and s electrons. These electrons are extensively delocalized throughout the lattice i.e. engaged in the metal-metal bonds of the cubic cluster, the covalent metal-sulphur bonds, and in the partially filled s-d conduction band.

Nonetheless, the cubic cluster with its assigned d electrons is an important parameter in explaining the thermodynamic stability of non-stoichiometric compositions, and may bear a role in the low temperature ordering of the cations among octahedral and tetrahedral sites.

1.3.2 Violarite

Violarite is a member of the thiospinel series $(Fe,Co,Ni,Cu)_3S_4$. The violarite ($FeNi_2S_4$) to polydymite (Ni_3S_4) solid solutions and the pure iron metastable analogue greigite (Fe_3S_4) all share the inverse spinel structure as illustrated in Figure 1.3.4. The thiospinel structure is composed of a cubic close-packed sulphur lattice (viz. pentlandite) forming a cubic unit cell. 16 metal atoms are accommodated in 16(b) octahedral (trigonally distorted) sites from a possible 32 vacancies; whilst 8 metal atoms occupy 8(f) tetrahedral sites from a possible 64 vacancies available within the unit cell. The unit cell constitutes 8 AB_2S_4 formula units such that A and B represent tetrahedral and octahedral cation sites respectively. Each sulphur atom is four-coordinated to 3 cations in (b) sites and 1 cation in an (f) site (33).

Violarite was originally assigned to the space group Fd3m, however, single-crystal precision X-ray studies on the analogous mineral indite ($FeIn_2S_4$) (viz. high-spin (f)Fe^{2+}), show a lower symmetry F43m than that formally assigned to spinel (54). It seems possible that similar violations of symmetry occur in other members of the thiospinel series, which would be consistent with evidence that the octahedrally coordinated metal atoms are "off-centre" and displaced along [111] directions, resulting in a trigonal distortion of the (b) sites.

The ^{57}Fe mössbauer spectrum of $(Fe,Ni)_3S_4$ with varying Fe:Ni ratios have been studied by Vaughan and Craig (53). Townsend et al (22) have studied a natural and synthetic violarite by magnetic susceptibility, thermoelectric power, and mossbauer spectroscopy.

X-ray powder data (22) suggests a metallic character for violarite $(Ni_{1.63}Fe_{1.01}Co_{0.33})S_{4.02}$ since the cell parameter (a_o = 0.945nm) is low viz. the metallic spinels: Co_3S_4 (a_o = 0.9399nm) and Ni_3S_4 (a_o = 0.948nm), vis à vis semiconducting spinels: Fe_3S_4 (a_o = 0.987nm) and $FeCr_2S_4$ (a_o = 0.9989nm). The absence of magnetic ordering down to 5K, together with the temperature independent susceptibility (>120K) and the low thermoelectric power confirms that violarite is a Pauli-paramagnetic metal cf. pentlandite. The ^{57}Fe-mössbauer spectrum of synthetic violarite ($Fe_{1.22}Ni_{1.81}S_{3.97}$) reveals a symmetrical quadrupole doublet which indicates that Fe is present in only one site. However, at 300K the isomer shift

(0.18mms^{-1}) in violarite is lower than that for (b)Fe in pentlandite (viz. 0.65mms^{-1}), whilst it is somewhat closer to the value for the isomer shift for (f)Fe in pentlandite (viz. 0.37mms^{-1})(42), and (b)Fe in localized low-spin pyrite (viz. 0.30mms^{-1}) (60). Hence, Fe^{2+} in violarite could be in tetrahedral sites with delocalized electrons, or in octahedral sites with essentially a localized low-spin configuration. Quadrupole splitting at 300K (0.59mms^{-1}) suggests (b)Fe^{2+} since the octahedral and not the tetrahedral site is distorted from cubic symmetry (22). However, even this is inconclusive since tetrahedral sites may be distorted by the Jahn-Teller effect. Vaughan and Craig (53) assume low-spin (b)Fe^{2+}, as supported by the correlation in isomer-shift (0.28mms^{-1}) and quadrupole-splitting (0.54mms^{-1}) with those for low-spin Fe^{2+} in pyrite (0.31mms^{-1} and 0.61mms^{-1} respectively) at 300K. Hence violarite may be represented as: $Ni^{3+}(Fe^{2+},Ni^{3+})_2S^{2-}$. With a successive decrease in the Fe content across the series from $FeNi_2S_4$ to $Fe_{0.25}Ni_{2.75}S_4$ there is a systematic decrease in isomer-shift and increase in quadrupole-splitting (0.29mms^{-1} to 0.23mms^{-1} and 0.54mms^{-1} to 0.61mms^{-1} respectively). This could be interpreted as the result of changes in the occupancy of the nearby surrounding cation sites producing slightly more asymmetric electronic environments around the nucleus, and slight changes in the s electron density at the nucleus.

Closer examination of the spectra reveals a slight asymmetry in the quadrupole-doublet amounting to 18+/-4% of the overall intensity. It is possible that this second doublet represents a partial occupation of Fe in tetrahedral sites in violarite as well as a predominance in the octahedral sites. Tetrahedral coordination is feasible as described earlier (22), and such Fe should be comparable to that in the tetrahedral sites in pentlandite due to the similar metallic and Pauli-paramagnetic behaviour of the two phases. Furthermore, such a substitution would not effect the electron occupancy of the sigma anti-bonding band in violarite as referred to later in this section, since both (b) and (f) site metals partake in its construction.

By comparison, the ^{57}Fe mössbauer spectrum of greigite (Fe_3S_4) contrasts strongly with that of violarite (43). The spectrum at 4.2K has been interpreted as three sets of magnetic hyperfine spectra corresponding to Fe in three different sites in the spinel structure. The isomer-shifts, quadrupole-splittings and hyperfine fields of these three different types of Fe are consistent with the assignment of high-spin Fe^{2+} and Fe^{3+} in slightly distorted (f) sites with electron hopping yielding a mean valancy of 2.5 (66); and Fe^{3+} in regular (b) sites. Greigite is therefore an inverse thiospinel: $Fe^{3+}(Fe^{2.5+},Fe^{2.5+})S^{2-}$ viz. magnetite.

The bonding in thiospinel crystals is essentially of a similar nature to that described in the previous section for pentlandite (62),(63). sd^3 hybridized atomic orbitals on tetrahedral site metal atoms overlap with sp^3 hybridized atomic orbitals on four tetrahedral site sulphur atoms to form $3t_2$ and a_1 bonding and anti-bonding sigma MO's; whilst the d_z2 and $d_x2_{-y}2$ atomic orbitals on tetrahedral metal atoms remain as 2e non-bonding MO's. Likewise, sp^3d^2 hybridized atomic orbitals on octahedral site metal atoms overlap with sp^3 hybridized atomic orbitals on six tetrahedral site sulphur atoms to form $2e_g$, $3t_{1u}$ and a_{1g} bonding and anti-bonding sigma MO's, whilst the d_{xy}, d_{xz}, and d_{yz} atomic orbitals on the tetrahedral metal atoms remain as $3t_{2g}$ non-bonding MO's. Pi bonding has been ignored in this simplified scheme.

The extent to which these various orbitals are filled depends on the valence and spin states of the metals involved. A schematic MO/Band energy level diagram for Ni_3S_4, $FeNi_2S_4$ and Fe_3S_4 is illustrated in Figure 1.3.5. In Ni_3S_4 and $NiFe_2S_4$ the non-bonding 2e and t_{2g} levels are considered as being full, whereas the higher energy anti-bonding e_g^* and t_{2g}^* levels overlap with one another to form partially filled anti-bonding sigma bands containing delocalized electrons from cations in both (b) and (f) sites; viz. pentlandite.

In traversing the series from Ni_3S_4 to $FeNi_2S_4$ the electronic structures remain fundamentally the same, except for a drop in the number of electrons contained in the sigma anti-bonding band, from 6 to 4 per formula unit respectively. Furthermore, the systematic changes in the physical properties across the series can be directly attributed to the electron occupancy of this band. Likewise, the systematic increase in the cell parameter from $FeNi_2S_4$ (0.9465nm) to Ni_3S_4 (0.9489nm) correlates with the increasing electron occupancy of the sigma anti-bonding band, enhancing the degree of anti-bonding character in the metal-sulphur bonds. The systematic decrease in reflectance at 589nm from $FeNi_2S_4$ (R%= 47) to Ni_3S_4 (R%= 44) correlates with a decrease in the number of empty levels available in the sigma anti-bonding band to which electrons may be exited during photo absorption. The lower thermal stability limit of polydymite (353°C) compared to violarite (461°C) relates to the greater electron occupancy of the sigma anti-bonding band in polydymite, presumably weakening the metal-sulphur bonds.

The electronic structure of greigite contrasts strongly with the polydymite-violarite series. Fe^{2+} is in a high spin state (43) and high spin Fe^{3+} is in both (b) and (f) sites. These unpaired electrons become coupled anti-ferromagnetically at lower temperatures. This substantial localization of 3d electrons accounts for the enhanced ionic nature of the mineral and for its larger cell parameter than in the violarites; whilst the larger number of electrons in anti-bonding orbitals contributes to its instability.

It has been suggested that the lack of synthetic solid solutions between $FeNi_2S_4$ and Fe_3S_4 is due to this fundamental difference in electronic structure. Such compositions that do occur in nature are likely to be metastable as was mentioned in Section 1.2 and discussed further in Section 1.4.2 on supergene alteration.

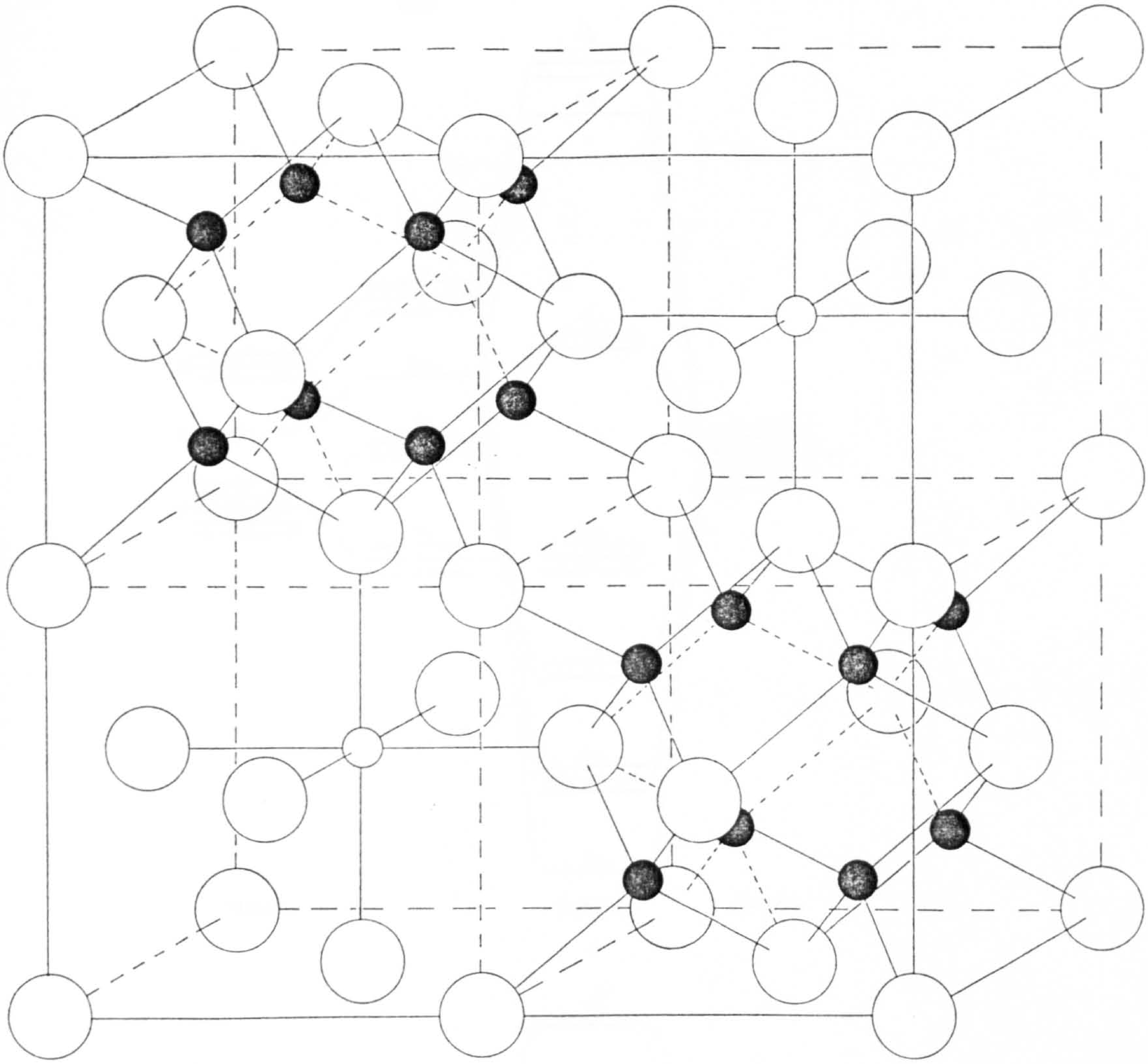

Figure 1.3.1

The crystal structure of pentlandite $(Fe,Ni)_9S_8$: Half the unit cell is shown.

◯ = sulphur atoms forming the ccp sulphur sublattice.

○ = interstitial octahedrally coordinated metal atoms.

● = interstitial tetrahedrally coordinated metal atoms.

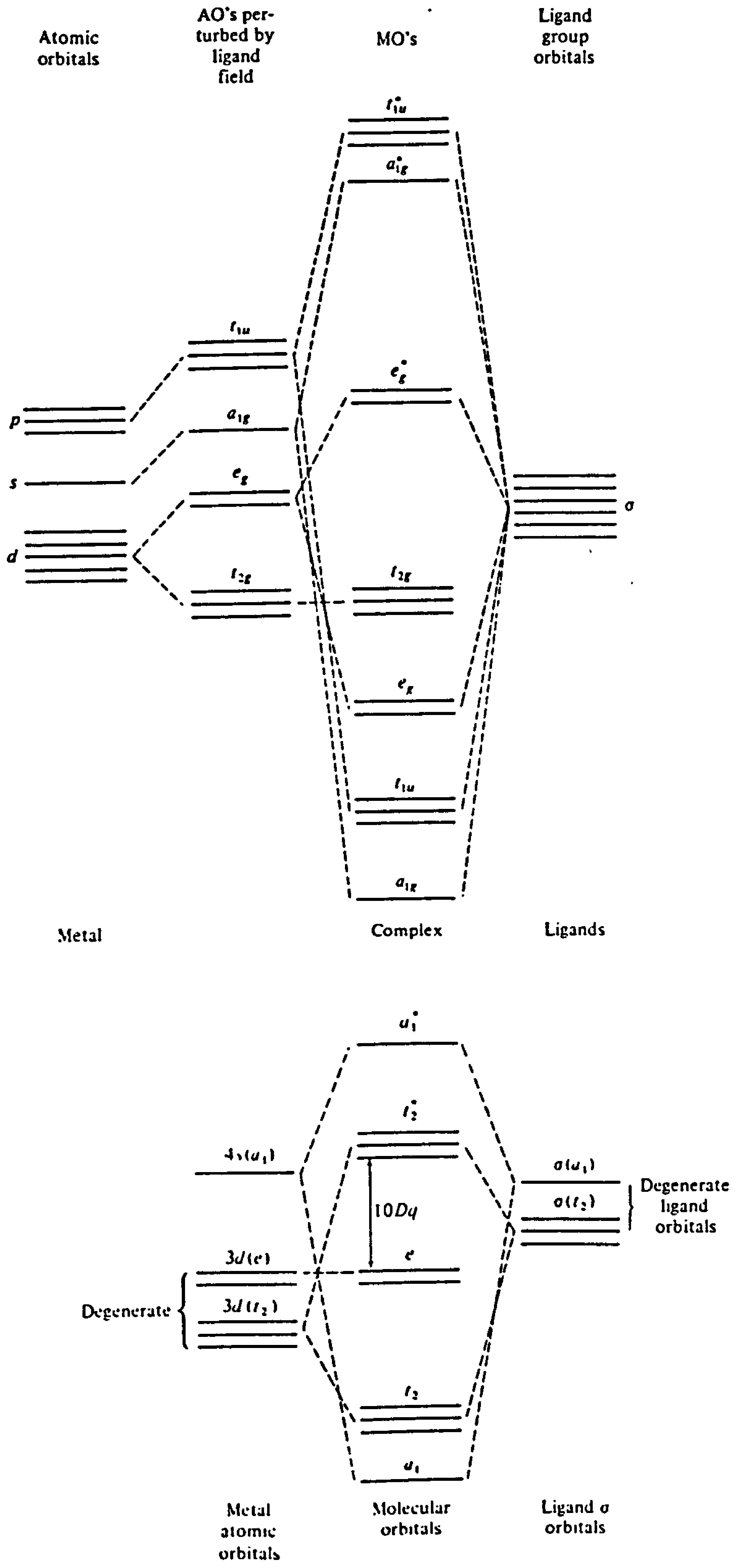

Figure 1.3.2

Molecular orbital diagrams for octahedral (top) and tetrahedral (bottom) complexes. Pi bonding has been excluded. (After Huheey (134)).

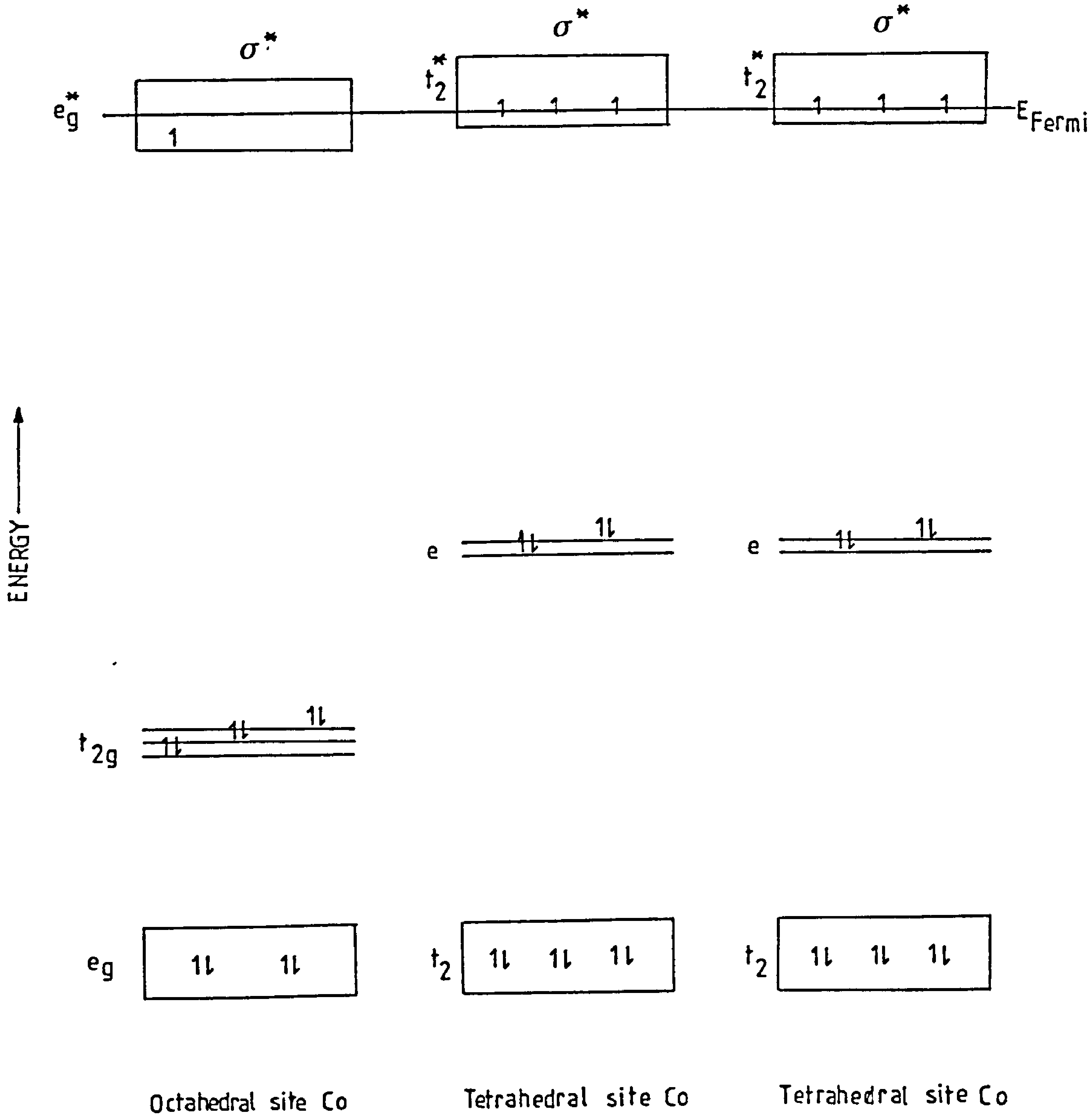

Figure 1.3.3

Schematic MO/Band Energy Level Diagram of Pentlandite showing the sigma MO's derived from the metal 3d atomic orbitals in Co_9S_8 (isoelectronic with $Fe_{4.5}Ni_{4.5}S_8$). Conduction band is formed through the interactions of sigma antibonding MO's between adjacent tetrahedral site cobalt atoms, together with those neighbouring onto octahedral site cobalt atoms. (Based on Rajamani and Prewitt (133)).

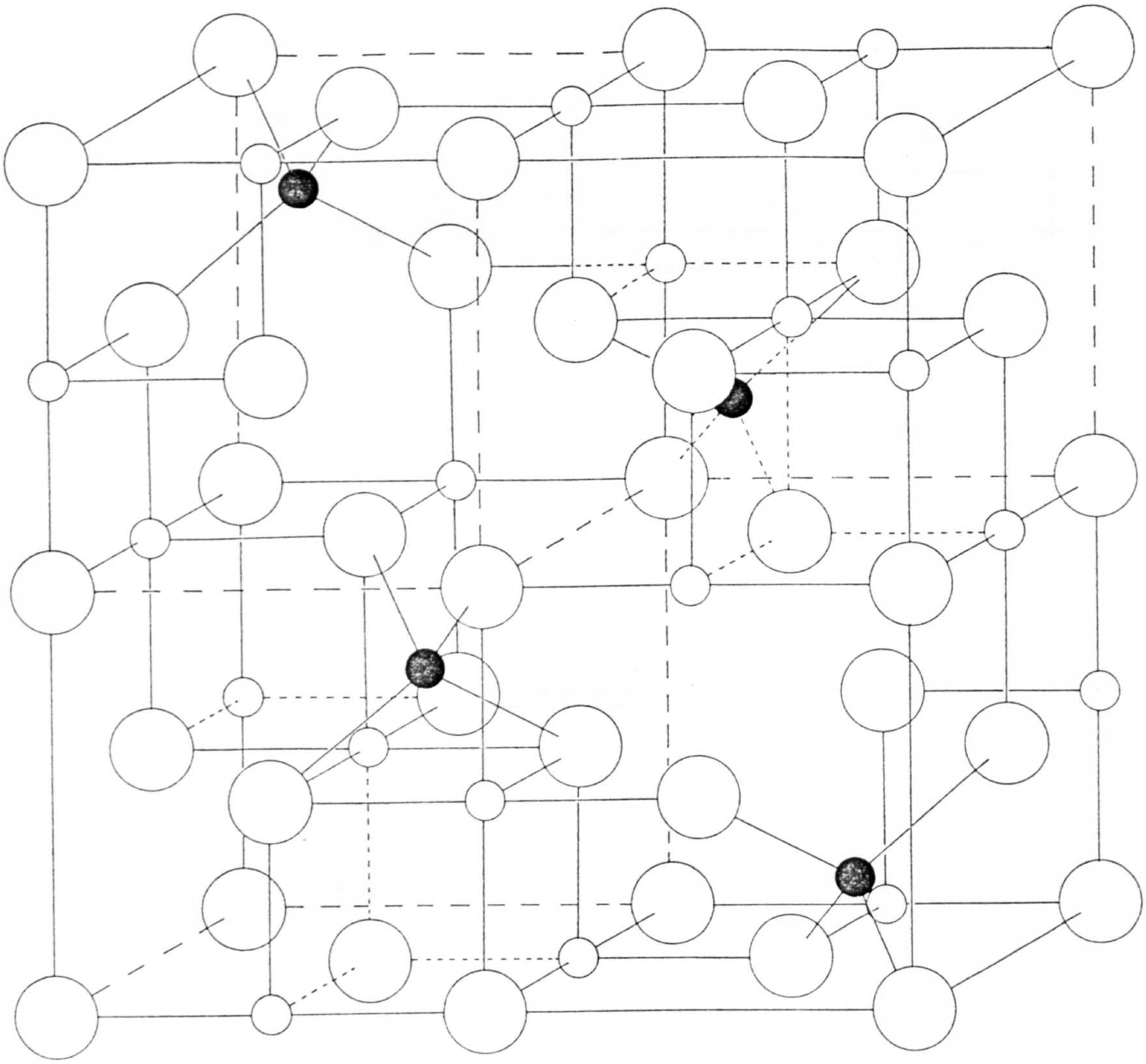

Figure 1.3.4

The crystal structure of violarite $(Fe,Ni)_3S_4$: Half the unit cell is shown.

◯ = sulphure atoms forming the sulphur sublattice.

○ = interstitial octahedrally coordinated metal atoms.

● = interstitial tetrahedrally coordinated metal atoms.

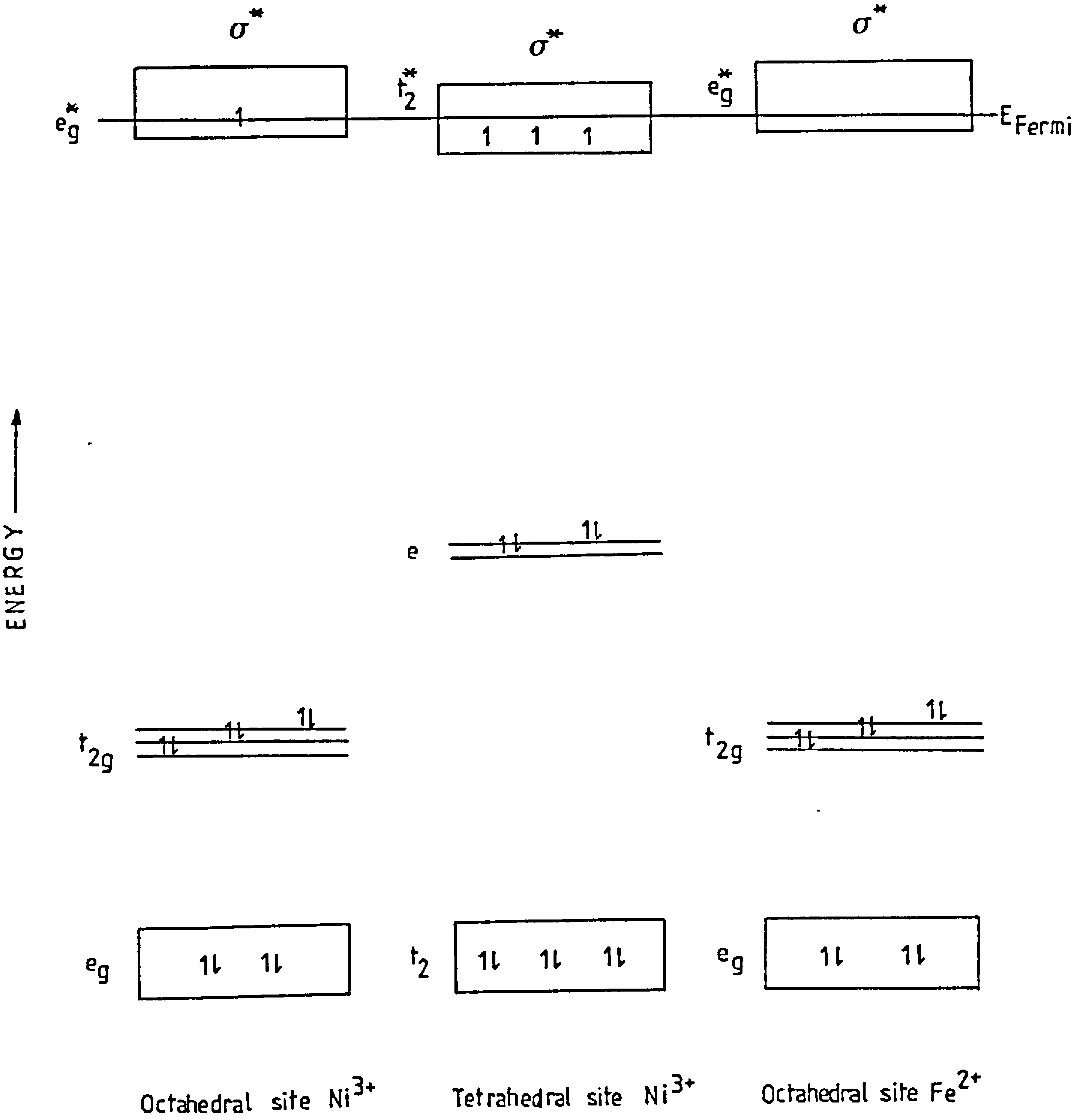

Figure 1.3.5

Schematic MO/Band Energy Level Diagram of Violarite showing the sigma MO´s derived from the metal 3d atomic orbitals in $FeNi_2S_4$.

(Based on Vaughan and Craig (53)).

1.4 ORE PARAGENESIS

1.4.1 Pentlandite Exsolution

The bulk compositions of the sulphide fraction of most nickel ore bodies lie within the mss (often Fe-rich) domain of the Fe-Ni-S system at high temperatures, up to approximately 1100°C (36) (cf.Section 1.2). On cooling below 610°C pentlandite becomes a stable phase in the ternary system, whilst simultaneously the sulphur defficient edge of the mss field retreats towards more sulphur-rich compositions (2),(10),(13); such that below approximately 450°C many sulphide bulk compositons fall outside the mss domain and subsequently lie within the divariant region containing mss + pentlandite + vapour. Such a bulk sulphide composition at this lower temperature now has the neccessary thermodynamic driving force to instigate substantial substitutional ordering amongst the constituent atoms of the mss to favour a strutural transformation culminating in the segregation of the high temperature disordered mss phase into the low temperature ordered pentlandite and pyrrhotite phases (albeit that during the initial stages at relatively high temperatures a predominantly Fe-rich mss is exsolved; viz. nickeliferous pyrrhotite) (48).

When this process occurs at relatively high temperatures (>300°C), the diffusion rates are sufficiently high to enable adequate diffusion of Ni outwards through the mss to enable segregation of the pentlandite into veinlets between the grains of mss. Consequently, the remaining mss acquires a higher Fe:Ni ratio culminating in the segregation of monoclinic pyrrhotite (<1% mass Ni), often with the more nickeliferous hexagonal pyrrhotite (<2% mass Ni) contained within the core of the remaining mss (66). However, below approximately 150°C diffusion rates are insufficient for the exsolving pentlandite to migrate to the grain boundaries of the mss, resulting in a second variety of pentlandite exsolution texture consisting of crystallographically oriented lamellae which often coarsen into "flames" within the ultimately exsolved pyrrhotite (<0.5% mass Ni) (9),(49),(50).

In summary and in general, pyrrhotite-pentlandite-pyrite-chalcopyrite-magnetite constitutes a typical mineral assemblage of an unaltered primary Fe-rich nickel-sulphide ore associated with mafic and ultramafic igneous rocks. However, subsequent alteration processes, often at low temperature, may create a new assemblage which, unlike the old, is determined more by kinetic restraints, and less by the thermodynamic parameters imposed by a change in the potential / chemical environment at these low temperatures.

1.4.2 Supergene Alteration

1.4.2.1 Low Temperature Assemblages

As mentioned in Section 1.2.1, violarite is thermally stable below 461°C in the presence of an equilibrium vapour. Consequently, violarite may form as a hypogene phase by primary direct crystallization from $(Fe,Ni)S_2$, $(Ni,Fe)S_2$ and mss; or by secondary exsolution from an initially homogeneous mss phase.

However, in many occurances violarite is generally considered a supergene mineral formed as a result of surficial alteration of Fe-Ni-S minerals, in particular pentlandite (7),(cf. Figure 1.4.1). This conclusion is drawn from a combination of evidence regarding phase equilibria studies and naturally occuring mineral assemblages. The reader may recall the equivocal phase relations below 200°C in the Fe-Ni-S ternary system, in particular the allocation of a tie line between violarite and pentlandite, versus pyrite and millerite as cited at the close of Section 1.2.1, (cf. Figure 1.2.9). Grounds for the consideration of the former arise through the suggestions of Misra and Fleet (23) that the common development of violarite as a secondary phase on pentlandite during deuteric and meteoric alteration constitutes an equilibrium assemblage. However, there is a strong possibility that the occurrence of secondary violarite may represent a metastable assemblage (in the "dry" Fe-Ni-S system), reflecting on the relative ease of the transition of pentlandite to violarite compared with the failure of pyrite to nucleate during low-temperature alteration. This situation would also allow, and account for, the apparent thermodynamically stable hypogene pyrite-millerite-pentlandite assemblages reported in massive nickel bearing sulphide ores such as the Marbridge ore deposite (31) and the hypogene pyrite-millerite assemblage at Black Swan, Western Australia.

A further hypothesis for a metastable violarite-pentlandite assemblage, vis à vis metastable violarite-pyrrhotite assemblage, arises from a similar failure of pyrite to nucleate at 200°C in attempts to synthesize pyrite-pentlandite assemblages from mss (32). (This can be achieved by first annealing at 400°C to permit pyrite nucleation before annealing at 200°C to allow pentlandite exsolusion as discussed in Sections 1.2.1 and 1.4.1). This suggests that difficulties of pyrite nucleation at temperatures envisaged during supergene alteration, may persist along the entire sulphur-rich boundary of mss (32).

The construction of the pyrite-millerite tie lines can be facilitated by assuming that an Fe-bearing millerite is in equilibrium with pyrite and violarite, as is suggested from the mineral analysis of the Marbridge ore deposit (31), and/or that the violarite in the required univariant field (pyrite-millerite-violarite-vapour) contains a greater Ni:Fe (atomic) ratio than the nominal 2:1. The author is inclined to prefer the later proposition since the solid-solution of Fe in millerite at low temperatures may be metastable (66), whilst a contraction in the composition limits of violarite from nominal $FeNi_2S_4$ to $Fe_{1-x}Ni_{2+x}S_4$ is consistant with the upper thermal stability limit for violarite at 461°C, viz. $Fe_{0.92}Ni_{2.08}S_4$ (7). Unfortunately, low temperature data on the thermal stability limits of violarite and the extent of Fe solubility in millerite are unavailable in the literature to allow a more conclusive comment. Assuming that the above hypothesis is correct, the apparent metastable occurance of violarite with pentlandite will be described in more detail.

In Section 1.3 the crystal structures of pentlandite and violarite reveal that they share an almost identical sulphur sublattice. This suggests that pentlandite can be converted into violarite with the minimum of reorganization by removal of excess cations and redistribution of the remainder among tetrahedral and octahedral sites within the sulphur sublattice (23). In an idealized example, assuming a fully disordered structure, the net effect is that $10Fe^{2+}$ and $2Ni^{2+}$ would be leached from tetrahedral and octahedral sites respectively within the pentlandite unit cell, with a further 6Fe and 6Ni atoms migrating from tetrahedral to octahedral sites to form the violarite unit cell; viz. the anodic reaction:

$$Fe_{4.5}Ni_{4.5}S_8 = 2FeNi_2S_4 + 2.5Fe^{2+} + 0.5Ni^{2+} + 6e \qquad (1.4.1)$$

This constitutes substantial cation migration from tetrahedral to octahedral sites involving preferential migration of Fe with respect to Ni, with the consequential ordering of Fe into octahedral sites within the recipient violarite. This solid-state transition is accompanied by a 17% volume decrease in the unit cell (based on the respective cell parameters (23)) resulting in characteristic shrinkage cracks within supergene violarite (cf. Figure 1.4.1). Furthermore, these cracks run parallel with the octahedral cleavage planes [111] of the pentlandite precursor, whilst the retention of this texture is further evidence of pseudomorphic replacement. These observations suggest that the alternative possibility of sulphurization of pentlandite to violarite is an unlikely mechanism in such deposits; whilst the selective leaching of metal atoms is considered the dominant process.

Violaritization of pentlandite is observed through the transition zone of the massive pyrrhotite-pentlandite ore at Kambalda, Western Australia (65). Initially small specks of violarite are randomly present in the pentlandite exhibiting shrinkage fractures with decreasing depth. Then pentlandite is progressively replaced by violarite whose specks enlarge and coalesce, often into thin crystallographically oriented plates that are parallel to the octahedral cleavage planes of the pentlandite host, until the entire pentlandite is replaced by violarite. However, when pentlandite grains are surrounded by gangue minerals, the development of violarite is inhibited (56).

Ramdour (68) suggests that bravoite can also occur in pentlandite as a supergene alteration product; as in the deposit at Horback, Schwarzwald, Germany. Much confusion exists in the early literature as a consequence of an apparent difficulty in distinguishing between violarite and bravoite; e.g. Buddington's unknown mineral "X" which he inferres as bravoite, may from the textural evidence he describes, be in fact violarite (86). However, when violarite and bravoite form together, violarite seems to form mainly a network along octahedral cleavage planes, filled in by bravoite. This may infer that violarite forms as an intermediate in the formation of bravoite. Ramdour was adamant that bravoite is of widespread occurance as a product of the incipient decomposition of pentlandite, yet typically absent in pentlandite mined at great depth. However, he cautiously describes an inclusion of bravoite found within a pentlandite grain, present in the Mokaia meteorite (New Zealand) as being probably secondary in origin; vis à vis alternative migration of sulphur during the meteorite's history in space (93).

The reader may note that bravoite is considered a metastable phase (cf. Section 1.2.1) often formed hydrothermally at low temperatures, generally either meteoricly or in euxenic sedimentary environments (68), viz. greigite.

An important feature of supergene violarite particularly with regards its genesis is the frequent departure from ideal stoichiometry $(Fe,Co,Ni)_3S_4$, both in terms of the common occurance of sulphur deficiency (59) (viz. retention of the sulphur content of the precurser mineral) and a variable Fe content often exceeding the nominal $FeNi_2S_4$ composition. A further and often diagnostic feature of supergene violarite is the occurance of distinct textural variations corresponding to various unique peripheral mineral assemblages, as will be described below. These observations and interpretations have been extensively reported in the literature, especially that concerning the Kambalda deposit of Western Australia (56),(65),(67),(77).

Besides the ubiquitous alteration of pentlandite as already described above, supergene violarite can also be attributed to the alteration of at least two other sulphide minerals, namely: monoclinic pyrrhotite and millerite. In monoclinic pyrrhotite, violarite is observed to have grown as a marginal comb-like alteration with a typically lamellar texture inherited from the pyrrhotite twin lamellae i.e. [001]. It is important to note that violaritization of pyrrhotite proceeeds inwards from grain boundaries and outwards from fractures, and that the replaced violarite is often richer in Fe than the blocky violarite formed within pentlandite; whilst low cobalt contents reflect the negligible presence of this element in the parent pyrrhotite. The development of violarite is often preceded by a front of smythite (a metastable phase approximating in composition to $(Fe,Ni)_9S_{11}$ (66)) which apparently represents an intermediate alteration state between monoclinic pyrrhotite and violarite (65),(67). This is consistent with the structural requirements in such a transformation since monoclinic pyrrhotite and smythite share essentially the same NiAs type structure whilst the h.c.p. sulphur sublattice common to both will require an atomic rearrangement on its subsequent transformation to the c.c.p. of violarite. It is reported that the energies involved are not great, and that these reactions may be reversible (57).

$$0.33Fe_7S_8 + 1.1Ni^{2+} = 00.66Ni_{1.7}Fe_{1.6}S_4 + 1.3Fe^{2+} + 0.4e \quad (1.4.2)$$

Pyrrhotite immediately adjacent to violaritized pentlandite grains shows a greater degree of alteration than pyrrhotite some distance away. This implies that the violaritizing pentlandite is the source of the Ni^{2+} required for the violaritization of pyrrhotite (24). Furthermore, assuming a constant sulphur content (as is evident from preferential siderite precipitation rather than secondary pyrite or pyrrhotite, suggesting low aqueous sulphur activities) this coupled reaction may explain why the alteration of pyrrhotite is often incomplete; since the amount of pentlandite originally present in the assemblage is inadequate to supply the neccessary amount of Ni (56).

Millerite, when occuring in the pentlandite-millerite ore assemblage often shows partial violaritization. However, the replacement textures are not as readily diagnostic as those from pentlandite and pyrrhotite violaritization. Nevertheless, the violarite does contain a characteristically high Ni content with a Ni:Fe (atomic) ratio = 6:1 or greater (approaching the composition of polydymite) reflecting on the composition of its precursor (56). The source of Fe is linked infallibly with the violaritization of associated pentlandite, where incidently there is a marked preferential leaching of Fe over Ni (8), since pyrrhotite is excluded from this assemblage (as explained earlier in this section) and pyrite is stable at these oxidative potentials (76),(65), (cf. Sections 1.4.2.2 and 1.5).

$$20.8NiS + 2.6Fe^{2+} = 5.2Ni_{2.7}Fe_{0.5}S_4 + 6.8Ni^{2+} + 8.4e \qquad (1.4.3)$$

This subsequent release of Ni^{2+} during the above alteration may explain the origin for the Ni^{2+} required for the late stage bravoitic pyrite that occurs as encrustations and veinlets in the pentlandite-millerite-pyrite assemblage of Ottershoot, Kambalda (8), and the formation of very late stage secondary millerite in the pyrite-pentlandite-millerite assemblage of zone II,No.3 deposit, Marbridge(31).

The above examples reveal quite categorically that the composition of the supergene violarite is a functon of its precuring mineral, which accounts for the often anomolous non-stoichiometry and compositional variation among such alteration products. Furthermore, the relative ease of structural transformations during these processes implies that many of the products of such reactions do occur in a metastabe state, such that the course of the reaction is governed not exclusively by thermodynamic equilibria but by kinetic constraints. This leads to the consensus that in the supergene alteration of pentlandite to violarite, for certain violarite compositions at least, (e.g. $Fe_{1+x}Ni_{2-x}S_4$) the transformation may indeed have occured metastably.

However, it must be born in mind that during the supergene alteration of these primary assemblages, Ni and Fe are likely to be removed as ionic aqueous species. Consequently we are concerned with the Fe-Ni-S-H-O aqueous system (albeit that the water may be removed after the alteration) in which the transformation of certain stoichiometries of pentlandite to violarite might occur reversibly, representing a state of equilibrium dependant on the inherent thermodynamic conditions, i.e. potential, and the activities of associated aqueous species (cf. Section 1.5). It is important to point out that what may constitute a metastable assemblage in the Fe-Ni-S system, does not necessarily prevail as such in the aqueous Fe-Ni-S-H-O system, whereby such an assemblage might be thermodynamically stable under these aqueous conditions. Nontheless, the subsequent removal of water after supergene alteration, in a perhaps hitherto stable pentlandite-violarite-aqueous assemlage, would indeed suggest a state of metastability from the light of speculative low-temperature phase relations in the Fe-Ni-S system (cf. Section 1.2.1 and Figure 1.2.9).

1.4.2.2 An Electrochemical Model

A mechanism based on an electrochemical model has been proposed by Thornber (57),(80),(81),(76),(83) and enhanced by others (56),(8),(24),(65),(84) for the supergene alteration of the massive Ni-Fe sulphide deposits at Kambalda, Western Australia. For full details the reader is referred to the literature quoted above. A summary of the mechanism is given below with particular focus on factors of electrochemical interest relevant to hydrometallurgy, whilst relating changes in potential to the sequence of alterations as already described above.

The model is based on the fact that the massive sulphide ore body conducts electricity (cf. Section 1.3) and due to its surrounding environment consequently behaves like a giant electrochemical cell with anodic reactions occuring at depth and cathodic reactions taking place near the surface (87); whilst ionic transport through the ground waters completes the circuit (cf. Figure 1.4.2). The thermodynamic driving force for such weathering processes is the cathodic reduction of atmospheric molecular oxygen. Aereation of rain and surface water results in dissolved oxygen coming into contact with sulphides either above or close to the water table, such that the oxygen activity is relatively high in this region. Oxygen reduction probably takes place preferentially on the surface of primary pyrite since an appreciable cobalt content ensures electrical conductance whilst its inert nature provides an ideal surface on which the reduction of oxygen can take place (80). Thus the aqueous interface at the top of the sulphide ore body acts as an "electron-sink" with respect to the sulphide ore below.

$$O_2(g) = O_2(aq) \qquad (1.4.4)$$

$$O_2(aq) + 2H_2O(l) + 4e = 4OH^-(aq) \qquad (1.4.5)$$

Consumption of free electrons creates a potential gradient (self-potential) from +0.3V in the shallow weathered ore to -0.3V in the primary ore at some 200m in depth, promoting anodic conditions in the conductive sulphide body at depth. The sequence of oxidative reactions is a function of the relative stabilities (thermodynamic and possibly kinetic) of the respective sulphides. This may best be described by reference to Figures 1.5.1 to 1.5.7. Observations cited earlier in this section indicate that pentlandite is the least stable of the sulphide minerals in the supergene environment, and subsequently is the first to react at the lowest oxidation potential by being altered to violarite, with Fe and Ni being released into the ground water. This region constitutes the border between the primary and transition zones, at some 160m in depth.

Simultaneously within the transition zone, the increased nickel activity causes the pyrrhotite to become unstable and it takes up Ni from the solution to form violarite. As described earlier, in disseminated ore, grains of pentlandite and pyrrhotite may remain intact when surrounded by gaunge minerals which inhibit the movement of electrons and elements to complete the chemical reaction, and thus represent pockets of chemical disequilibrium (56). However, this process generally continues until all of the pentlandite is altered to violarite, then at a higher oxidation potential any remaining pyrrhotite alters to pyrite until the pyrrhotite is completely consumed and the supergene assemblage of violarite-pyrite is formed. Within the supergene enrichment zone, violarite undergoes cation exchange whereby much of its Fe is replaced by Ni and may proceed till the composition approaches that of polydymite.

The base of the oxide zone, which approximately coincides with the water table, marks the point where violarite appears to be unstable and where it is ultimately replaced by nickel carbonates and iron oxides (65), with sulphur entering solution as sulphate and subsequently carried away in the ground water, viz. 0.05M $SO_4^{2-}(aq)$. This position in the supergene profile also coincides with the point where atmospheric oxygen has access to the sulphides, presenting the possibility of direct oxidative leaching of the violarite (56). This is feasible on account of the fact that violarite does indeed appear unstable in the presence of oxygen, as is evident by rapid tarnishing of freshly cut specimens and polished sections of violarite when exposed to the air.

However, the alternative electrochemical mechanism is fervently quoted in the literature (80),(65) as a continuing episode in the oxidative weathering of massive sulphides at Kambalda, though occuring at higher oxidation potentials. This possibility represents the major anodic reaction with regards to current appropriation for the ore body since it entails a substantial increase in the oxidative state of the sulphur atoms corresponding to the release of an appreciable number of electrons.

Even if molecular oxygen has intimate access, there is likey to be a strong tendency for a galvanic coupling between pyrite and violarite (83). Dissolved oxygen would induce an attack on the less stable violarite phase by an electrochemical mechanism that causes the violarite-electrolyte interface to become anodic, whilst the adjacent more noble pyrite surface becomes cathodic. Electrons are conducted between these two sulphide phases such that molecular oxygen is preferentially reduced on the pyrite surface (which is cathodically preserved) while anodic dissolution of Ni^{2+} and Fe^{2+} would ensue on the violarite surface. The released aqueous Ni^{2+} may migrate to, and be adsorbed in, the supergene enrichment zone, or alternatively be precipitated as various carbonates. The presence of wall rock, particularly carbonates, acts as a pH buffer for the appreciable amounts of acid generated at the base of the oxide zone (8). This, together with hydroxide produced from the cathodic reduction of oxygen, results in a sufficiently high pH for the decomposition of nickel carbonates: gaspeite ($NiCO_3$), and reevesite ($Ni_6Fe_2(OH)_6CO_3.4H_2O$).

It is reported that near the anodic violarite surface the pH is low (i.e.<4)(83). If however, the bulk aqueous environment is buffered at pH >6, then part of the ferrous iron will be oxidized to ferric and hydrolyzed in situ (82) producing psuedomorphic goethite. Furthermore, it is observed that violarite dissolves preferentially along the planes that enhance either the blocky pentlandite or platelike pyrrhotite morphology from which the violarite originally formed (82).

$$FeNi_2S_4 + 16H_2O = Fe^{2+} + 2Ni^{2+} + 4SO_4{}^{2-} + 32H^+ + 30e \quad (1.4.6)$$

$$Fe^{2+} + 2H_2O = FeOOH + 3H^+ + e \quad (1.4.7)$$

Supergene alteration of the more Ni-rich pentlandite-millerite-pyrite primary assemblage (as described earlier in this section) follows a similar mechanism to that for the pentlandite-pyrrhotite-pyrite primary assemblage as described above. The essential difference is that Fe^{2+} released during the oxidation of the Ni-rich pentlandite is incorporated in the oxidation of millerite to form a Ni-rich violarite. Thus, a violarite-pyrite supergene assemblage is formed which although more Ni-rich than that formed from the more ubiquitous pentlandite-pyrrhotite-pyrite primary assemblage, nonetheless undergoes further oxidation by an identical mechanism (76).

A most remarkable feature of this phenomenon is that the initial product of the pentlandite alteration (i.e. violarite) is itself an excellent conductor of electricity (cf. Section 1.3.2). This enables the conduction of electrons through the supergene enrichment zone (where the pentlandite has now vanished) allowing a continuation of the self-potential with sustained anodic oxidation within the transition zone beneath.

The persistance of violarite over a considerable range of the supergene profile together with the fact that violarite occurs as a stable phase in the synthetic Fe-Ni-S system (cf. Section 1.2.1), suggests that violarite may have a substantial stability field in a supergene environment (81). This contravenes the thermodynamic calculations derived from the appropriate Nernst functions based on the values for the free energy of formation of pentlandite and violarite at 298K and 101kPa by Craig and Naldrett (85). Such data implies that violarite does not exist as a thermodynamically stable entity in the Fe-Ni-S aqueous system. However, this low temperature thermodynamic data is likely to be inaccurate, especially for pentlandite, for reasons deduced in Section 1.3.1 and exemplified in Section 1.5.1. Likewise, thermodynamic data estimated from room temperature electrochemical studies is probably not reliable either, since conditions at the mineral/ electrolyte interface cannot always be described by application of the Nernst function, as many electrode reactions are not at equilibrium (76), (cf. Section 1.6). For instance, it is generally accepted that the reaction between sulphides and sulphate is irreversible in the electrochemical sense (81), (i.e. slow electron transfer). Considerable overpotentials are therefore required to form sulphate from sulphides, and sulphate cannot be reduced in an aqueous environment because of the preferential reduction of water. This phenomenon may likewise account for the "observed" stability of violarite at higher potentials than those expected from the high temperature thermodynamic data (81). Alas, thermodynamic data need to be obtained from another angle of attack for a concise understanding of the Fe-Ni-S aqueous system at 298K, (cf.Section 1.5).

Although some 2500 million years have passed since the emplacement of the massive sulphide bodies at Kambalda, the oxidative weathering as described here is a far more recent event in geological time, considered to have initiated from the Early Tertiary Period (circ. <65 million years) (80). Nonetheless, in terms of reaction rates this represents a very slow geochemical change in the Ni-Fe-S phases, such that there is sufficient time for the solid-state diffusion of metal atoms within the sulphur-sublattice to obtain a more equal precedence with the otherwise more rapid processes at the mineral/electrolyte interphase (76), thus enabling the formation of violarite from pentlandite. Furthermore, the corresponding electrical currents persisting over such geological time would be of an equally small magnitude, thus requiring a minimal overpotential, hence representing near equilibrium conditions for the phase transition (cf. latter part of Section 1.7).

A unique opportunity has arisen from a study of the abandoned diamond drill core samples of primary sulphide ore from the Sudbury basin (69). These had been left on the ground, exposed to atomspheric weathering for a period of perhaps 25 years. Inspection revealed that violarite is rapidly formed from pentlandite and subsequently leached by further oxidation. This is almost a negation of the previous statement for the time scale of the alteration events at Kambalda, yet nonetheless, 25 years does represent a significant length of time at least in relation to hydrometallurgical processes, to preclude a similar mechanism. Furthermore, such atmospheric weathering occurs in an open system allowing continuous removal of the generated sulphuric acid, which if allowed to accumulate would inevitably destroy the violarite almost as quickly as it is formed (69). This tallies with the observation that at a pH <6 (E_h = 0.0 to +0.2V) violarite is further oxidized to oxide material (76), (cf. Section 1.5).

The fact that violarite remains in these exposed drill samples till all the pentlandite has been replaced, even though atmospheric conditions maybe considered constant, does indeed suggest the possibility of an electrochemical intervention during the oxidation. Furthermore, chalcopyrite remains unaltered until the violarite (and pentlandite) is leached away (69), presenting the possibility of galvanic coupling between these sulphide phases.

1.4.2.3 Argentopentlandite

The supergene alteration of argentopentlandite is less well documented in the literature than that of pentlandite. However, a Finnish sample of exsolved argentopentlandite from chalcopyrite reveals substantial supergene alteration textures. The initial stages of alteration develop along fractures and grain boundaries. Analysis (X-ray scanning images and electron microprobe profiles) suggests that Ag and Fe are depleted from argentopentlandite, whilst Ni remains in situ and apparently produces cubic nickelsulphide (viz. polydymite/vaesite). Ag and Fe are expelled almost completely, the former being enriched (up to 100%) in the boundary zones between unaltered argentopentlandite and the alteration products; yet Fe is leached from the system (71).

In a highly altered sample from Bird River, Manitoba, the argentopentlandite is rimmed and cut by crystallographically oriented blades of an unidentified Ag-Fe-Ni-sulphide(s) together with acanthite (Ag_2S) (52).

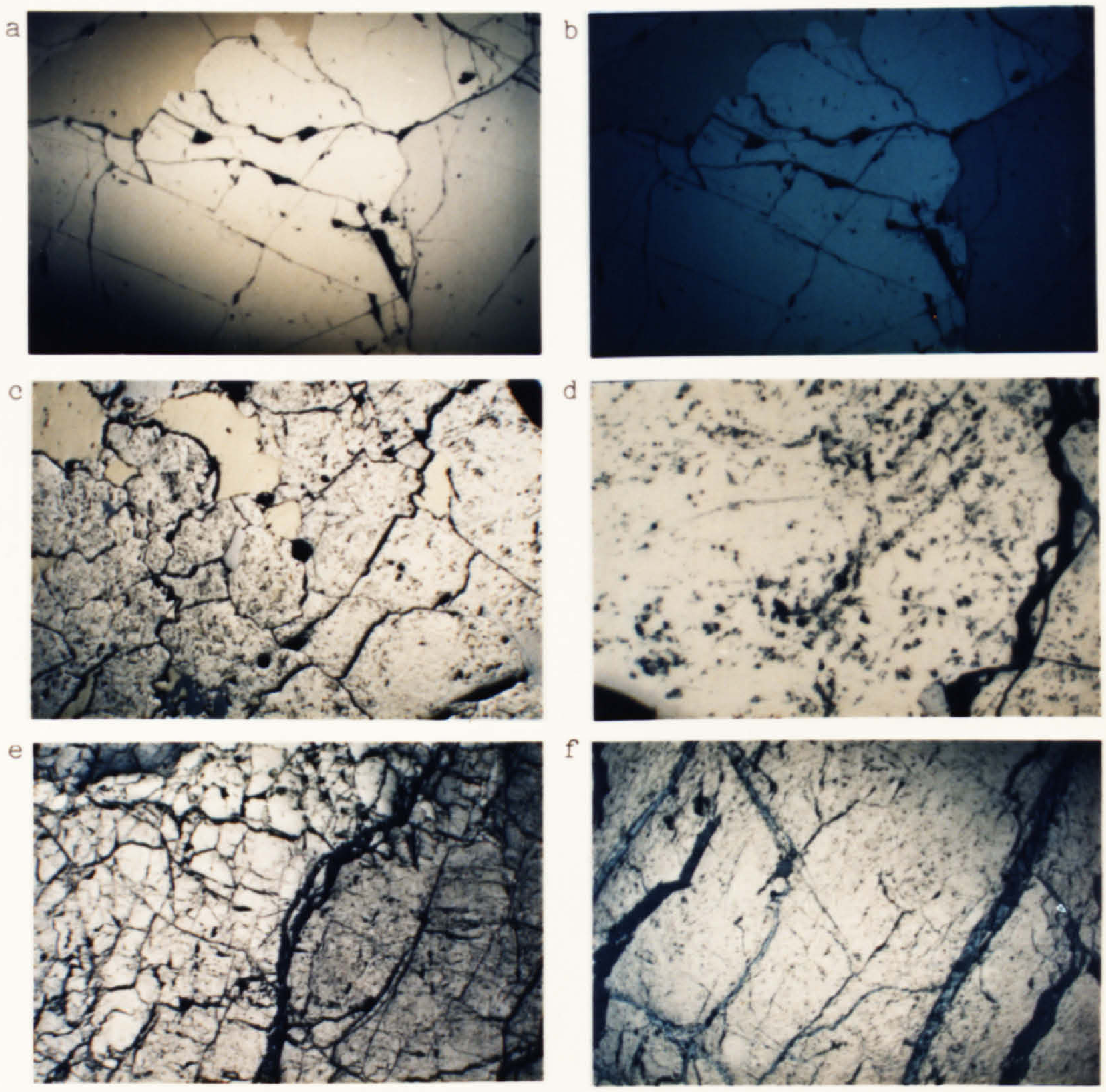

Figure 1.4.1

Reflected Light Microscopy: Natural Specimens

(a). Pentlandite/pyrrhotite, Thompson, Manitoba, x200,PPL. Yellow grain (top left) = chalcopyrite; beige coloured grains with octahedral cleavage (centre) = pentlandite, dark grain (right) = pyrrhotite.

(b). Specimen (a), x200XP.

(c). Violarite alteration of pentlandite, Sudbury, Ontario, x140 PPL. Alteration of pentlandite (white) giving rise to incipient violarite (violet/grey spots) formation.

(d). Specimen (c), x200,PPL. Violaritization occurs preferentially along the octahedral cleavage cracks in the pentlandite.

(e). Violarite, Kambalda (Z28892) x140,PPL. Pyrite (left), violarite (right), $(Fe,Ni)CO_3$ (dark grey central line).

(f). Specimen (e), x200,PPL. Violarite with magnetite (blue), $(Fe,Ni)CO_3$ (dark grey) veins.

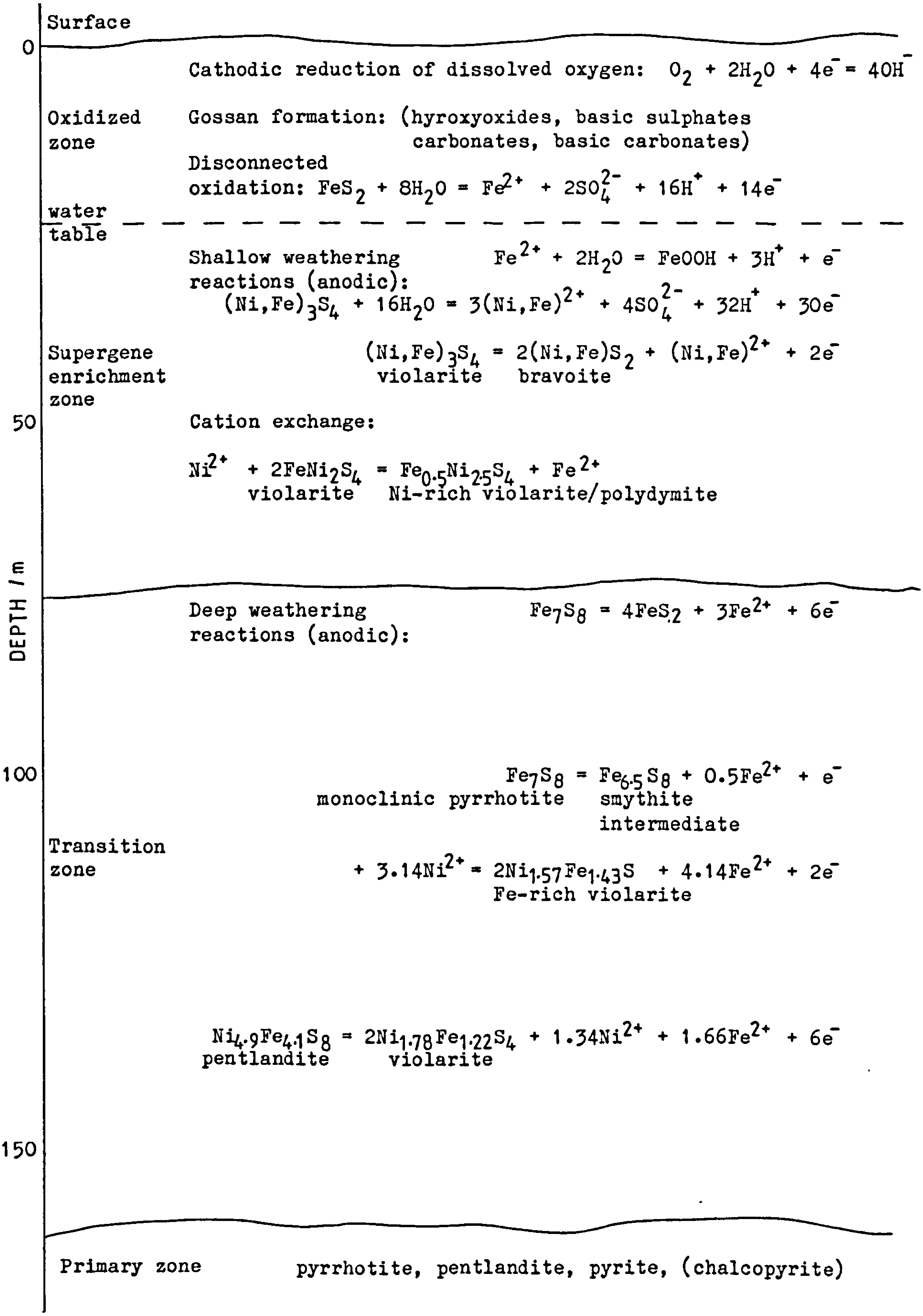

Figure 1.4.2

Idealized schematic representation of the alteration processes in the Kambalda supergene profile. (Based on Thornber (57), (80)).

1.5 SULPHIDE EQUILIBRIA IN AQUEOUS SYSTEMS: THERMODYNAMIC-ELECTROCHEMICAL CONSIDERATIONS

1.5.1 Speculative Thermodynamic Data

1.5.1.0 Introduction

One of the conclusions from section 1.4.2 was the need for more accurate thermodynamic data for pentlandite and violarite in order to gain a more realistic insight into the Fe-Ni-S aqueous system. A brief appraisal of the experimental difficulties envisaged in such a quest was given in Sections 1.4.2.2 and 1.3.1. In this section a speculative estimation of the standard free energy of formation of these two phases at 298K is proposed; together with a comparison of such data with those of other workers, resulting in a satisfactory alignment with mineralogical observations.

1.5.1.1 Iron-Nickel Alloys

A knowledge of thermodynamic equilibria in the Fe-Ni binary system, particularly at 298K would permit a more accurate understanding of the equilibria involving the ternary phases: pentlandite and violarite, together with those of the Fe-Ni-S aqueous system. Unfortunately the knowledge regarding phase relationships appears to be restricted to temperatures above approximately 473K (127),(128). Nonetheless, the ordered phase $FeNi_3$ (awaruite) has been ascribed as having $\Delta H^o_{298} = -16.74 kJmol^{-1}$ and $\Delta S^o_{298} = -0.52 Jmol^{-1}K^{-1}$ for the mutual solubility between iron and nickel at 298K (129).

More realistic perhaps, are the results from compositional studies of iron meteorites (130). These are composed of iron-nickel alloys which contain only small amounts of other elements. More important is the fact that they have cooled with a slow rate of about 1K per million years, thus presenting a closer state to thermodynamic equilibrium than for alloys prepared by man. From such investigations (130) it is suggested that the ordered FeNi phase (taenite) exists below 557K; although thermodynamic data were not given.

However, since iron and nickel share a similar atomic mass (Fe = 55.847gmol^{-1} and Ni = 58.71gmol^{-1}) together with a similar atomic radius (Fe = 0.116nm and Ni = 0.115nm) it is conceivable that the bonds between Fe-Ni may share similar energetics with those between either Fe-Fe or Ni-Ni; although the ordered phase implies that Fe-Ni bonds are favoured, thus suggesting $\Delta H^{o}{}_{f298}$FeNi(c) < 0. Since the creation of an ordered phase from the elements is accompanied by a minimal change in entropy, then as a first approximation $\Delta S^{o}{}_{f289}$FeNi(c) $\sim$ 0. Therefore, the author concludes that stoichiometric FeNi is likely to exist as a stable ordered phase at 298K with the speculation that $\Delta G^{o}{}_{f298}$FeNi(c) <0.

1.5.1.2 Pentlandite

In Section 1.3.1 it was revealed that a second order phase transition in pentlandite which occurs between 323K and 473K would in principle prevent the direct extrapolation of thermodynamic data at temperatures above 473K to 298K. However, Craig and Naldrett (85) measured the partial pressure of S_2(g) over the assemblage: FeNi and $(Fe,Ni)_9S_8$ at 773K and 673K as 1.01×10^{-9}Pa and 1.61×10^{-13}Pa respectively. Presumably, by applying Van't Hoffs' isochore to this data, Craig and Naldrett obtained the Gibbs-

Helmholtz function for the reaction:

$2.25FeNi(c) + S_2(g) = 0.25(Fe,Ni)_9S_8(c)$ (1.5.1)

as:

$\Delta G^o = -338067 + 166.1T$ /Jmol^{-1} (T = 298 to 773K) (1.5.2)

and estimated the absolute standard entropy of pentlandite as: 505.43Jmol^{-1}K^{-1} at 298K.

Taking$\Delta G^o{}_{f298}S_2(g)$ = 79.73kJmol^{-1} and $\Delta G^o{}_{f298}FeNi(c)$ = 0 (cf.Appendix C.1), whilst solving the above function at 289K leads to $\Delta G^o{}_{f298}(Fe,Ni)_9S_8(c)$ = -835.2kJmol^{-1}. Not surprisingly this value is in close agreement with the value similarly calculated by Thornber(76) viz.-836.9kJmol^{-1} based on the same source reference viz. (85); even though Thornber erroneously divided by 4.184 instead of multiplying for the conversion of calories to joules (125).

However, this extrapolation of thermodynamic data ignores the characteristic abrupt change in heat capacity (126) for pentlandite at the transition temperature (viz. between 323K and 473K) and the accompanying entropy changes for the corresponding formation reactions; besides the assumption that the enthalpy and entropy changes of formation are temperature independant. Therefore it is not surprising, as mentioned previously in Section 1.4.2.2 that calculations for the appropriate Nernst functions based on the thermodynamic data given by Craig and Naldrett (85) imply that violarite does not exist in the aqueous system, contrary to geological observations.*

Consequently, Thornber (76) suggested a manipulation of the free energy data to fit the mineralogical evidence; thus he obtained a self-consistant set of data by using pyrite ($\Delta G^o{}_{f298}$ = -160.2kJmol^{-1}) as an anchor value, although he does not describe the "exact" criteria he used in selecting such data. More specifically, he obtains $\Delta G^o_{f298}(Fe,Ni)_9S_8(c) = -770.0kJmol^{-1}$ which is inconsistant with the value for the following inequality where pyrrhotite, troilite and heazlewoodite (whose free energy data are known with a reasonable degree of accuracy, cf. Appendix C.1) are the hypothetically presumed phases metastable with respect to pentlandite at 298K and 101kPa.

$$FeS + Fe_7S_8 + 1.5Ni_3S_2 = Fe_{4.5}Ni_{4.5}S_8 \qquad \Delta G^o < -790.1kJmol^{-1} \qquad (1.5.3)$$

Thus faced with the lack of more viable data, the arithmetic mean between the value for this inequality viz. $-790.1kJmol^{-1}$ and the value previously derived from Craig and Naldrett (85) viz. $-835.2kJmol^{-1}$, was adopted as the standard free energy of formation for pentlandite at 298K viz. $\Delta G^o_{f298}Fe_{4.5}Ni_{4.5}S_8(c) = -813kJmol^{-1}$.

1.5.1.3 Violarite

Craig (7) constructed the Gibbs-Helmholtz function for the formation of violarite by a combination of the $S_2(g)$ partial pressure data for the pyrite + vaesite + mss assemblage at 873K (1.6kPa) and for the pyrite + violarite + mss assemblage at 723K (1.6Pa) and 673K (0.1Pa)

---

* From the previous page: For a comparison, adopting free energy data given by Craig and Naldrett (85) (cf. Appendix C.1) implies that the following equilibria in Appendix C.2: violarite/pentlandite, millerite [55], and pyrite,polydymite/violarite [56] are metastable with respect to pyrite,polydymite/pentlandite [57]. However, adopting the authors' "selected speculative values" for pentlandite and violarite (cf. Appendix C.1), results in the contrary. An identical situation arises for the equilibria where hydrogen sulphide and sulphate are neither consumed nor produced viz. violarite/pentlandite [74] and pyrite,vaesite/violarite [89] vis á vis pyrite/ pentlandite [90].

with an estimated entropy of formation for violarite: $\Delta S^o{}_{f298}FeNi_2S_4(c) = 192.46Jmol^{-1}K^{-1}$.

$Fe(c) + 2Ni(c) + 2S_2(g) = FeNi_2S_4(c)$ (1.5.4)

$\Delta G^o = -291102 + 175.3T$ (T = 273 to 723K) (1.5.5)

Taking $\Delta G^o{}_{f298}S_2(g) = 79.73kJmol^{-1}$ (cf. Appendix C.1) whilst solving the above function for 298K leads to $\Delta G^o{}_{f298}FeNi_2S_4(c) = -319.0kJmol^{-1}$ (which is identical to thatas calculated by Thornber (76) likewise based on the same data). Craig's estimate (7) for the entropy of violarite at 298K is derived from the average value for the two reactions:

$FeS_2(c) + 2NiS(s) = FeNi_2S_4(c)$ (1.5.6)

and

$FeS(c) + NiS(c) + NiS_2(c) = FeNi_2S_4(c)$ (1.5.7)

using available entropy data for the binary phases, whilst assuming that the entropy change for these reactions is zero! The author suggests that a more accurate estimate is obtainable if one considers that the free energy change rather than the entropy change is assumed as being zero for the particular reaction:

$FeS_2(c) + 2NiS(c) = FeNi_2S_4(c)$ (1.5.8)

at 298K; by exploiting circumstantial evidence of certain phase phenomena pressumed at temperatures near 298K as decribed here in detail below.

The phase equilibria studies, mineralogical observations and synthesis experimentation as reviewed in Sections 1.2.1, 1.3.2, 1.4.2.1 and 2.1.2, suggest that stoichiometric violarite ($FeNi_2S_4$) is thermodynamically unstable with respect to Ni-rich violarite, pyrite and millerite at 298K (cf. Figure 1.2.9). Since $FeNi_2S_4$ exists as a stable phase at 473K (7) it may be assumed that $FeNi_2S_4$ is only just unstable at 298K (at least as an approximation), thus the decomposition reaction can be considered as being near to stoichiometric equilibrium at 298K: i.e.

$$FeNi_2S_4 = (1-x)Fe_{1-x}Ni_{2+x}S_4 + (2x-x^2)FeS_2 + (x+x^2)NiS \quad (1.5.9)$$

where $\Delta G^o{}_{298} < 0$ and $x > 0$ at 298K,

thus:

$$Fe_{1-x}Ni_{2+x}S_4 = (1-x)FeS_2 + (2+x)NiS \quad (1.5.10)$$

where $\Delta G^o{}_{298} = 0$ and $x > 0$ at 298K.

Since the bonding in nominal violarite is almost identical to that in Fe-deficient violarite, and in particular since both these phases share an almost identical structure, with the only significant differences being the ratio and ordering of Fe/Ni within the sulphur-sublattice (cf. Section 1.3.2), it is reasonable therefore to assume that each has a similar enthalpy and entropy of formation at 298K. Furthermore, if "x" is relatively small at 298K as is indeed proposed, then the approximate value for $\Delta G^o{}_{f298}FeNi_2S_4(c)$ can be derived from the following equilibrium:

$$FeNi_2S_4 = FeS_2 + 2NiS \quad (1.5.11)$$

where $\Delta G^o{}_{298} = 0$ and $x = 0$ (which is presumed exact for a particular temperature between 298 and 473K). This leads to the following inequalities at 298K:

$$\Delta G^o{}_{f298}FeNi_2S_4(c) > \Delta G^o{}_{f298}FeS_2(c) + 2\Delta G^o{}_{f298}NiS(c) \quad (1.5.12)$$

$$\Delta G^o{}_{f298}Fe_{1-x}Ni_{2+x}S_4(c) < \Delta G^o{}_{f298}FeS_2(c) + 2\Delta G^o{}_{f298}NiS(c) \quad (1.5.13)$$

Thus adopting the free energy data for pyrite and millerite as cited in Appendix C.1, yields the following speculative inequalities:

$\Delta G^{o}{}_{f298}FeNi_2S_4(c) > -343.1kJmol^{-1}$ (1.5.14)

$\Delta G^{o}{}_{f298}Fe_{1-x}Ni_{2+x}S_4(c) < -343.1kJmol^{-1}$ (1.5.15)

This result is comparable with the value deduced by Thornber (76) ($-348.4kJmol^{-1}$), yet takes into consideration the metastability of nominal violarite vis à vis stability of Ni-rich violarite at 298K. However, since the above result is expressed as an inequality, it is considered appropriate to take the mean between this inequality and the value estimated by Thornber (76) thus arriving at:

$\Delta G^{o}{}_{f298}Fe_{1-x}Ni_{2+x}S_4(c) = -346kJmol^{-1} \quad (x > 0)$ (1.5.16)

although the "true" value may indeed be more negative. Nonetheless, when this value is adopted in conjunction with the respective free energy data (cf. Appendix C.1) for the following equilibrium:

$Fe_{1-x}Ni_{2+x}S_4 + (1-x)Ni^{2+} = Ni_3S_4 + (1-x)Fe^{2+}$ (1.5.17)

it yields $\Delta G^{o}{}_{298} = 0$ (when $x = 0$) which embraces the notion of such an equilibrium existing during the supergene enrichment (cf. Section 1.4.2) whereby such a process would appear to be dependant on the ratio of the Fe^{2+}/Ni^{2+} aqueous activities.

1.5.2 Electrochemical Equilibria (E_h-pH Diagrams)

E_h-pH diagrams are a useful portrayal of the equilibria involved in the leaching of metal-sulphides. The dissolution equilibria of the Fe-Ni-S aqueous system can be viewed in a way analogous to the Pourbaix diagrams for the M-H_2O system, although the thermodynamic treatment involves a further two components (cf. Figures 1.5.1 to 1.5.7).

To illustrate this (131), it is convenient for the sake of simplicity to consider first the nature of the equilibria between a two component metal-sulphide phase MS(c) in contact with an aqueous solution containing its conjugate ions: $M^{n+}(aq)$ and $S^{2-}(aq)$ (albeit in acid solution H_2S per se). The electrode potential of the metal-sulphide / aqueous interface can be expressed by the Nernst function in a similar fashion to that for the corresponding metal/ aqueous interface, by considering the equilibrium between the metal component of the MS(c) phase with that of its conjugate aqueous metal cation $M^{n+}(aq)$ viz.

$$M^{n+}(aq) + ne = M(MS) \qquad (1.5.18)$$

$$E_h = E^o - \frac{2.3RT}{nF}\lg a_{M(MS)} + \frac{2.3RT}{nF}\lg a_{M^{n+}(aq)} \qquad (1.5.19)$$

where activities are with respect to the standard state (i.e. $a_{M(MS)}$ is the activity of elemental metal in the two component phase MS).

According to the Gibbs Phase Rule ($F = C-P+2$), provided that only one metal-sulphide phase exists in the two component M-S system, then there will be one degree of freedom at constant temperature and pressure, which can be identified with the chemical potential of the metal component $\mu_{M(MS)} = -RT\ln a_{M(MS)}$; thus representing an independent variable in terms of equation (1.5.19).

This chemical potential is related to the stoichiometry of the metal-sulphide phase such that an upper and lower limit corresponds to the compositional limits of the solid-solution $M_{1+x}S$ as described in a two component phase diagram. Thus the electrode potential of a metal-sulphide is an indeterminate value within a range of defined upper and lower limits (the actual value in many cases being also a function of pH). For a metal-sulphide system where only one phase exists (eg. PbS), the lower limit ($\mu_{M(MS)} = 0$) corresponds to the electrode potential of the elemental metal/metal ion couple, whilst the upper limit ($\mu_{M(MS)} = 1$) corresponds to the electrode potential of the elemental sulphur/sulphide ion couple. Furthermore, when the metal-sulphide phase only exists as stoichiometric MS i.e. without the accompanyment of a solid solution (and where the conjugate metal ion has a formal oxidation state of 2+), it can adopt an indeterminant electrode potential between the corresponding upper and lower limits (even where these limits relate to the incorporation of a second metal-sulphide phase) without influencing the equilibrium reaction for the solubility product viz.

$$MS(c) = M^{2+}(aq) + S^{2-}(aq) \qquad (1.5.20)$$

Thus, this equilibrium predominates because of the integrity of the conjugate aqueous ions at any electrode potential within the confindments of the corresponding upper and lower limits; although the upper limit is itself a function of pH.

It follows, that the electrode potential can also be written in terms of an electrochemical reaction for sulphur, although the intervention of $H^+(aq)$ in the formation of H_2S in acid solution necessitates a pH dependance on the electrode potential viz.

$$S(MS) + 2H^+(aq) + 2e = H_2S(aq) \qquad (1.5.21)$$

$$E_h = E^o - 2.3\frac{RT}{2F}\lg a_{S(MS)} - 2.3\frac{RT}{F}pH - 2.3\frac{RT}{2F}\lg a_{H_2S(aq)} \qquad (1.5.22)$$

where activities are with respect to the standard state. (i.e. $a_{S(MS)}$ is the activity of elemental sulphur in the metal-sulphide phase). Furthermore, the activity of aqueous hydrogen sulphide is related to the fugacity of gaseous hydrogen sulphide in contact with the aqueous phase via its solubility viz.

$$H_2S(g) = H_2S(aq) \qquad (K \sim 0.1) \qquad (1.5.23)$$

i.e.

$$\mu H_2S(aq) - \mu H_2S(g) = RT\ln f_{H_2S}(g) - RT\ln a_{H_2S}(aq) \qquad (1.5.24)$$

Thus:

$$S(MS) + 2H^+(aq) + 2e = H_2S(g) \qquad (1.5.25)$$

$$E_h = E^o - \frac{2.3RT}{2F}\lg a_{S(MS)} - \frac{2.3RT}{F}pH - \frac{2.3RT}{2F}\lg f_{H_2S} \qquad (1.5.26)$$

Moreover, in this stoichiometric MS case, the electrode potentials of equations (1.5.19) and (1.5.26) are identical because of the thermodynamic links between $a_{S(MS)}$ and $a_{M(MS)}$ in the solid metal-sulphide phase, and between $a_{M^{2+}(aq)}$ and $f_{H_2S(g)}$ in the aqueous and gaseous phases respectively.

At a constant aqueous composition, the two component M-S system is invariant in electrochemical potential when there are two solid phases (e.g. metal + sulphide, sulphur + sulphide, or two different sulphides) in equilibrium with each other; i.e. elemental metal + elemental sulphur + metalsulphide cannot coexist; at constant temperature and pressure (cf. Section 1.2).

A comprehensive list of the Nernst functions for the various equilibria in the Fe-S, Ni-S, and Fe-Ni-S aqueous systems is given in Appendix C.2, which is based on the free energy data given in Appendix C.1. However, the reader should note that for violarite (cf. Section 1.5.1.3) viz. $\Delta G^o_{f298}Fe_{1-x}Ni_{2+x}S_4 = -346kJmol^{-1}$; that since "x" is assumed to be small and the precise value is unknown, the value of zero was adopted as an approximation in order to simplify the stoichiometry and computation for the relevant Nernst functions.

The Standard Electrode Potential E(T) for the couple R/O to which the Nernst function relates is inaptly named since by definition (IUPAC, Stockholm Convention 1953) is relative to the Standard Hydrogen Electrode (SHE) at temperature (T), such that it "is" the difference in these two electrode potentials, and therefore a "Cell Potential" per se.

An ambiguity arises because this convention presupposes nothing about the standard free energies of formation at temperature (T) for the "individual" constituents of the equilibrium electrochemical reaction. It only conveys the notion of an "overall change" in the standard free energy (which is inherent in all thermodynamic understanding). Thus, it avoids the arduous and somewhat philosophical question of ascribing a standard enthalpy of formation and standard entropy for the electron and for even such terms as the aquated hydrogen ion at temperature (T), which it circumvents as being zero! This is idiologically unsound in "absolute" terms since it erroneously implies:

$$0.5H_2(g) = H^+(aq) + e \qquad \Delta G^o(T) = 0 \; ! \qquad (1.5.27)$$

However, this approach is unnecessary if one accepts the notion that the equilibrium EMF refers to that of the whole "cell" and not specifically to either of the two electrodes.

Furthermore, this leads to two different approaches in relating standard free energy data for aquated redox species as a function of equilibrium cell EMF, e.g. for the simple $M^+(aq)/M(c)$ couple, the conventional approach implies:

$$\Delta G^o{}_f(T)M^+(aq) = -(-nFE^o(T)cell) \qquad (1.5.28)$$

whilst the absolute approach (via the appropriate Born-Harber cycle) implies:

$$\Delta G^o{}_f(T)M^+(aq) = -(-nFE^o(T)cell) + \Delta G^o{}_f(T)H^+(aq) \qquad (1.5.29)$$

Thus, the conventional cell equilibrium EMF data are fundamentally incompatable with the Born-Harber free energy data.

Fortunately, the free energy data (119) given in Appendix C.1, relate to the conventional approach, such that the Nernst Functions in Appendix C.2 which express "E_h" as an implicit function of the SHE are compatable.

It is important to realize that equilibria more anodic than the oxygen/water equilibrium and more cathodic than the water/hydrogen equilibrium are thermodynamically meaningless since the aqueous phase which includes $H^+(aq)$ doesnot exist under these circumstances! Nonetheless, equilibria drawn outside the aqueous domain, particularly in the cathodic region, though representing a quasi-thermodynamic situation are useful since they give a plausible indication of which reactions may occur at appropriate hydrogen overpotentials, and/or hydrogen overpressures. However, the latter needs to be fairly excessive inorder to achieve this objective, whilst devolving a certain lack of credibility at least in puritanical terms for changes in "Standard" Free Energy.

For the E_h-pH diagrams that describe ternary systems, e.g. Fe-Ni-S aqueous system; it is particularly important to appreciate that the lines portrayed in these digrams refer to specific equilibria, whilst the concept of a field of stability for a predominating phase has to be treated within the context of these equilibria. This is clearly illustrated in the example for the equilibrium (in strong alkali) between the two ternary phases: pentlandite and violarite (cf. Figure 1.5.3), which incorporates a third binary phase: millerite, and has a pH dependance as given by Nernst function [55] in Appendix C.2. Nonetheless the practical advantage of labelling such domains (mainly for ease of clarity) was exploited for the diagrams given in this work.

The activities of aqueous ionic species are often treated by other workers (e.g. Peters (96)), as though they are independant variables in the Nernst Function for the metal-sulphide aqueous system; i.e. they are arbitarily ascribed various values for the portrayal of E_h-pH diagrams. However, they are quite often interdependant through complex formation equilibria, e.g. ferric sulphate complex ions, which involve the following equilibria:

$Fe^{3+}(aq) + SO_4^{2-}(aq) = FeSO_4^{+}(aq)$ lgK = 2.24

$Fe^{3+}(aq) + 2SO_4^{2-}(aq) = Fe(SO_4)_2^{-}(aq)$ lgK = 0.94

It is only for the sake of convenience that these equilibria are ignored.

Although orthodox E_h-pH digrams show reversible equilibria reactions in which all the species as determined by thermodynamic criteria are present, in reality they yield little practical information with regard to hydrometallurgical leaching and supergene alteration processes (especially for ternary systems) for the reasons described below.

The obtainment of equilibrium between three solid phases (which is a requirement of Gibbs Phase Rule for an invariant electrode potential in the ternary system (131)), is a far slower process in comparison with the equilibrium between just two such phases. Therefore, it is more suitable to consider pseudo-two (solid) phase equilibria. However, many of these are still unlikely to occur for kinetic reasons, therefore transitions which are known to occur, together with those between phases which are structurally similar enough to theoretically afford an observable rate of reaction present a more practical choice; e.g. pentlandite/violarite, pentlandite/ orthorhombic sulphur, violarite/orthorhombic sulphur. Similar reasoning appears in the selection of the metastable phases: $\alpha FeO(OH)$ and $Ni(OH)_2$ vis à vis Fe_2O_3 and NiO respectively. The presence of hydrogen sulphide as a reactant is eliminated since it is unavailable as a reactant in any significant quantity neither in any conceivable leaching process for nickel-iron-sulphides, nor in the envisaged supergene alteration of pentlandite. See Figures 1.5.4 to 1.5.7.

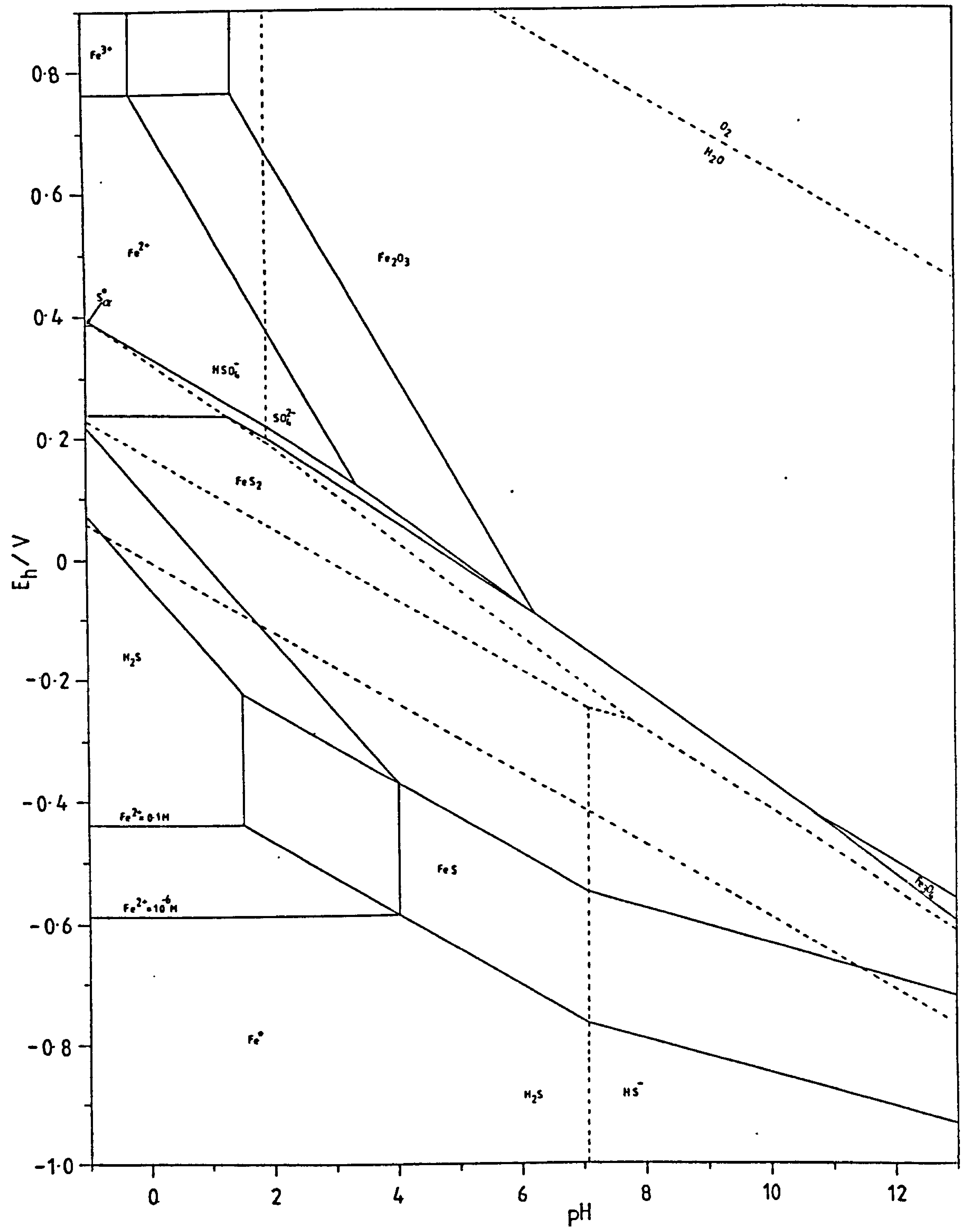

Figure 1.5.1

Eh-pH diagram for the Fe-S-H_2O system at 298.15K and 101.325kPa. Activities of aqueous sulphur species = 0.1M. Activities of aqueous iron species = 0.1M and 10^{-6}M. All reactions reversible.

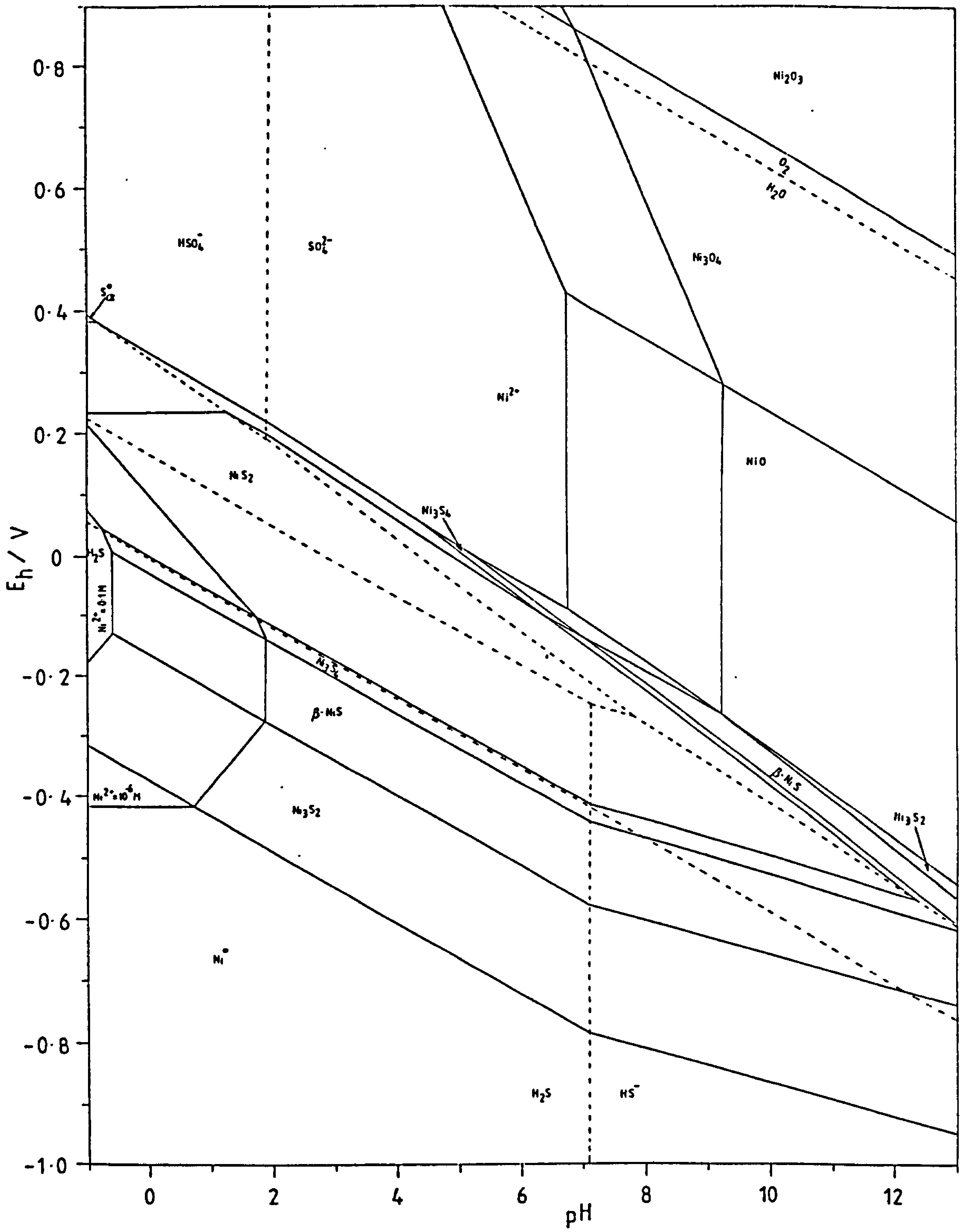

Figure 1.5.2

Eh-pH diagram for the Ni-S-H_2O system at 298.15K and 101.325kPa. Activities of aqueous sulphur species = 0.1M. Activities of aqueous nickel species = 0.1M and 10^{-6}M. All reactions reversible.

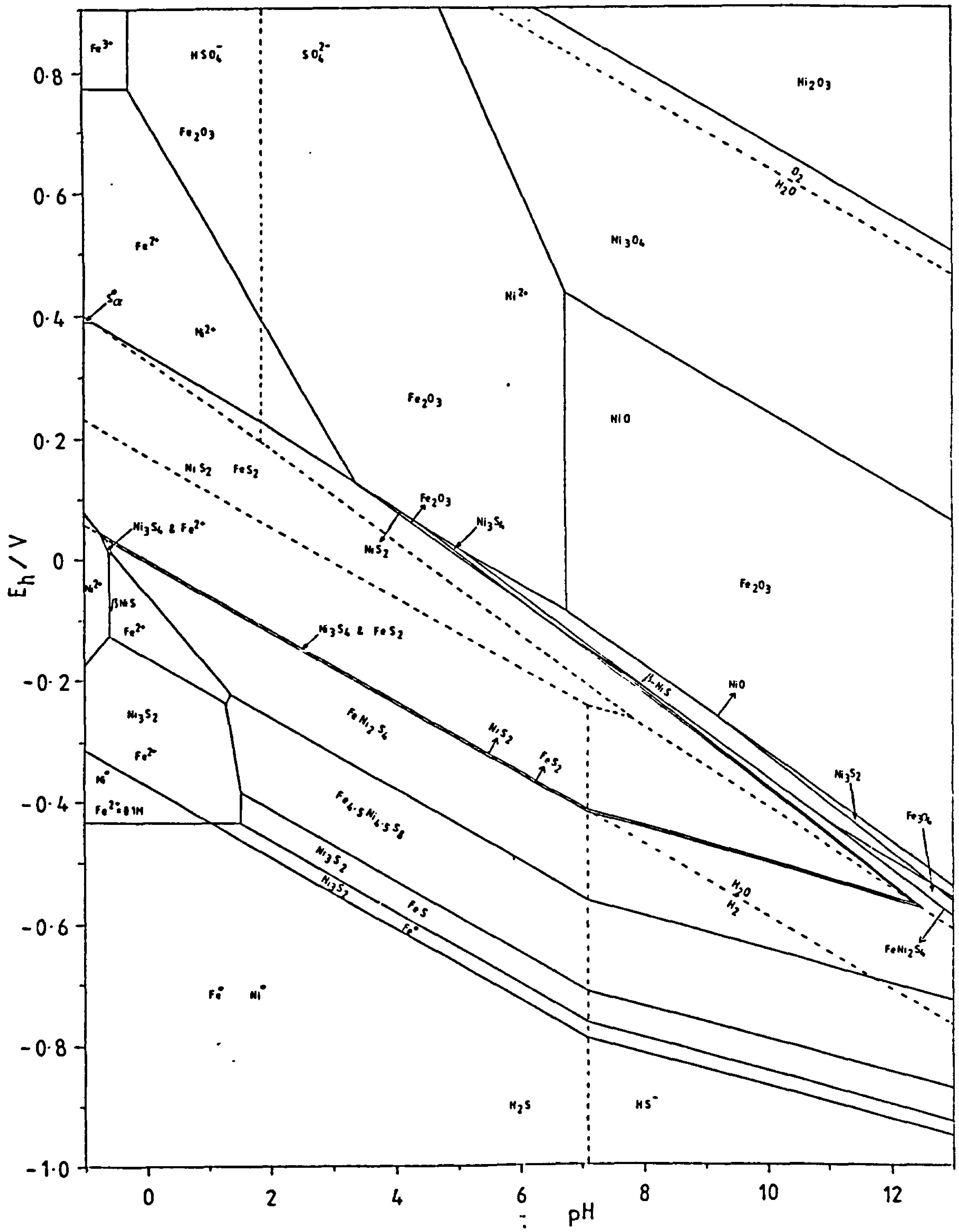

Figure 1.5.3

Speculative Eh-pH diagram for the Fe-Ni-S-H_2O system at 298.15K and 101.325kPa. Activities of aqueous sulphur species = 0.1M. Activities of aqueous iron and nickel species = 0.1M. All reactions reversible.

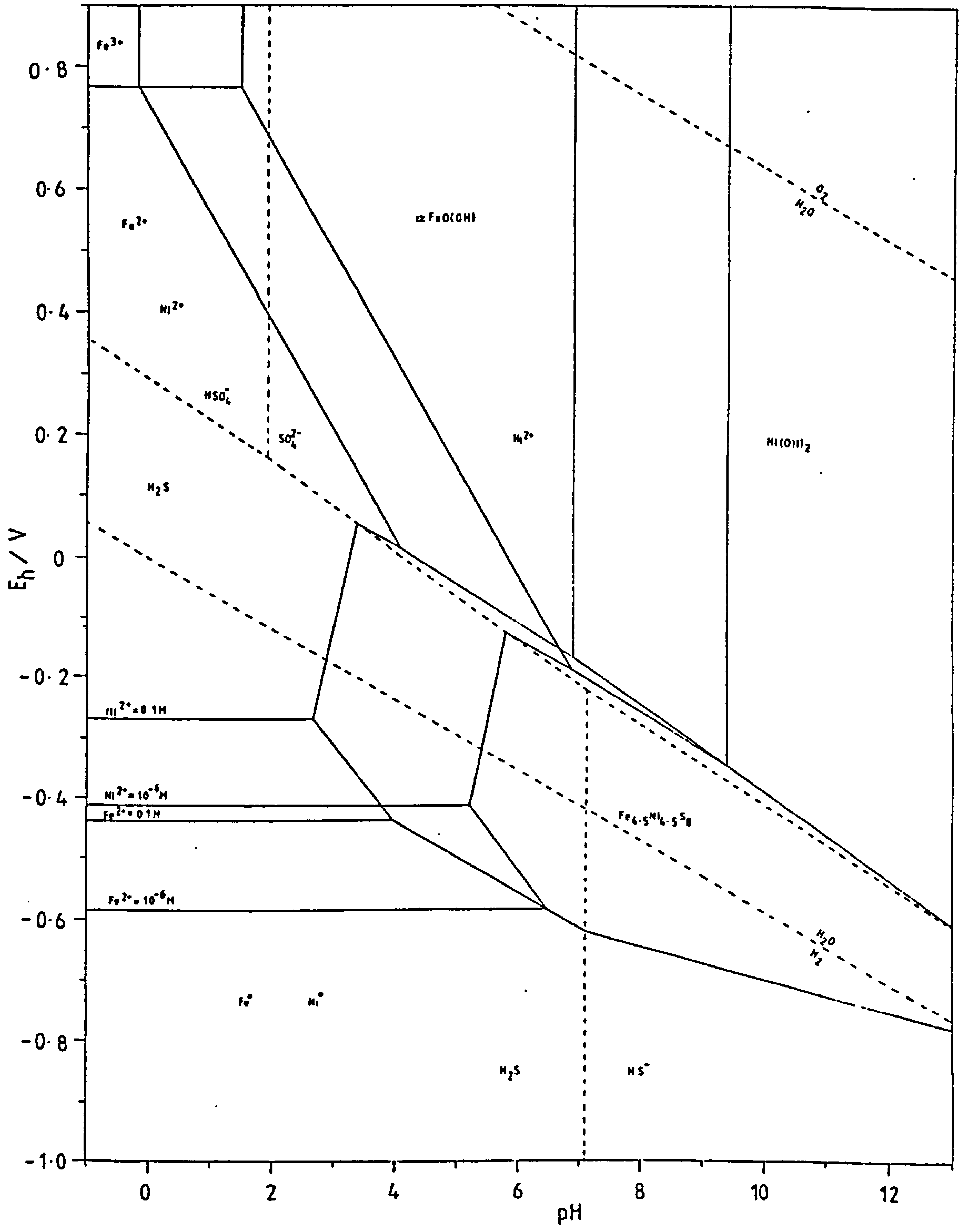

Figure 1.5.4

Speculative Eh-pH diagram for the Fe-Ni-S-H_2O system at 298.15K and 101.325kPa. Activities of aqueous sulphur species = 10^{-6}M. Activities of aqueous iron and nickel species = 0.1M and 10^{-6}M. Metastable equilibria: with $Fe_{4.5}Ni_{4.5}S$ as the only metal-sulphide phase. H_2S not consumed. α-FeO(OH) and $Ni(OH)_2$ as metastable products.

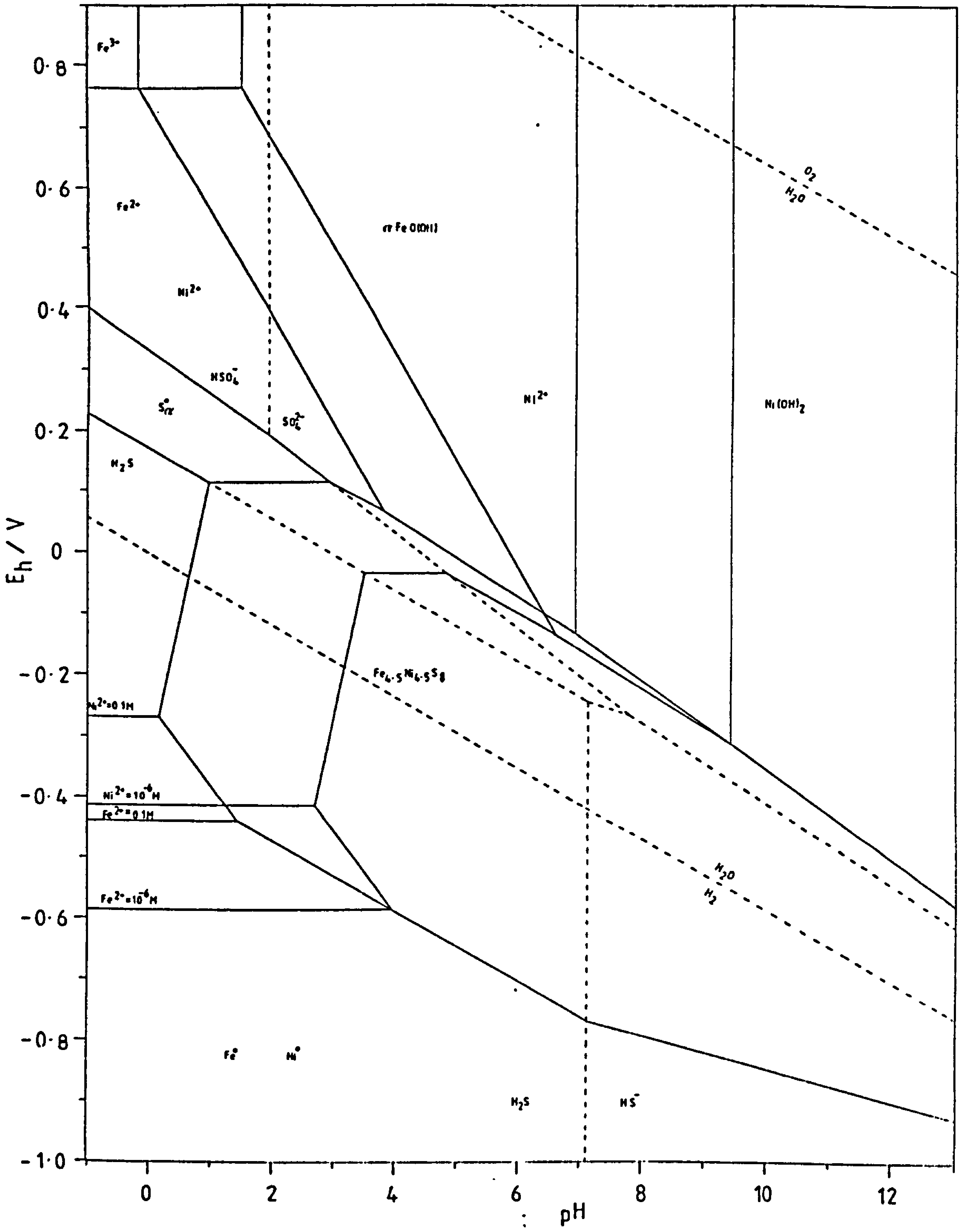

Figure 1.5.5

Speculative Eh-pH diagram for the Fe-Ni-S-H_2O system at 298.15K and 101.325kPa. Activities of aqueous sulphur species = 0.1M. Activities of aqueous iron and nickel species = 0.1M and 10^{-6}M. Metastable equilibria: with $Fe_{4.5}Ni_{4.5}S_8$ as the only metal-sulphide phase. H_2S not consumed. α-FeO(OH) and $Ni(OH)_2$ as metastable products.

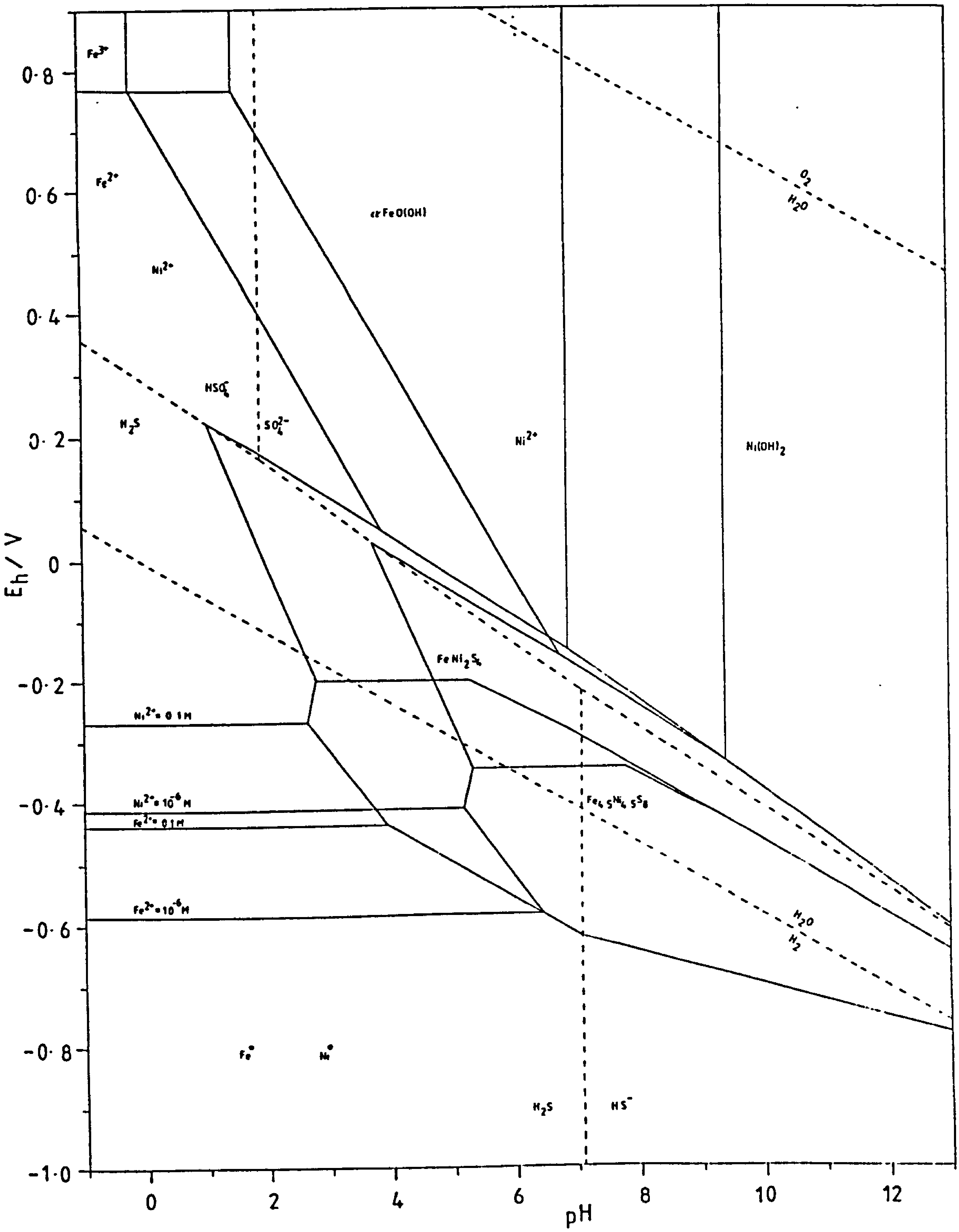

Figure 1.5.6

Speculative Eh-pH diagram for the Fe-Ni-S-H_2O system at 298.15K and 101.325kPa. Activities of aqueous sulphur species = 10^{-6}M. Activities of aqueous iron and nickel species = 0.1 and 10^{-6}M. Metastable equilibria: with $Fe_{4.5}Ni_{4.5}S_8$ and $FeNi_2S_4$ as the only metal-sulphide phases. H_2S not consumed. α-FeO(OH) and $Ni(OH)_2$ as metastable products.

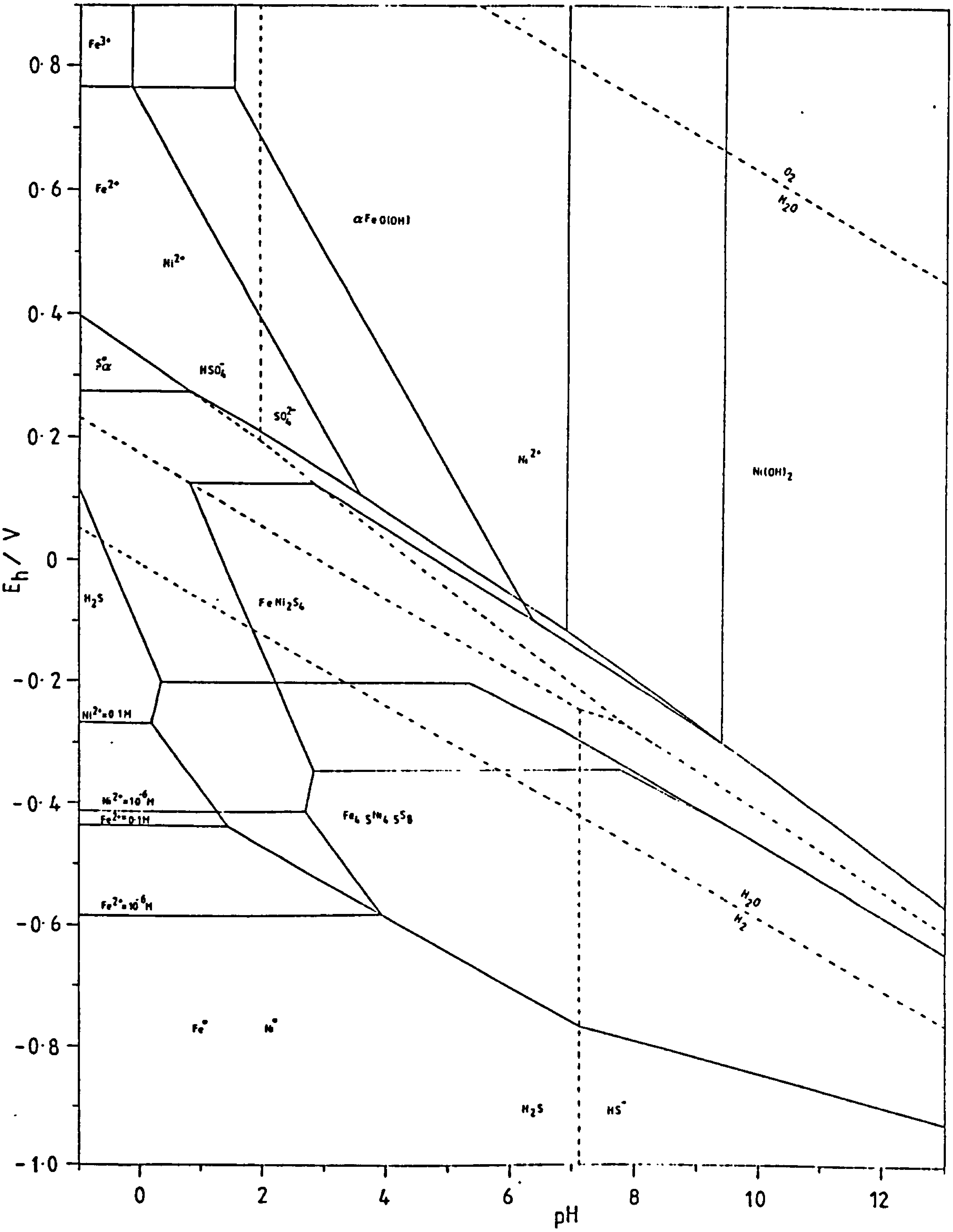

Figure 1.5.7

Speculative Eh-pH diagram for the Fe-Ni-S-H_2O system at 298.15K and 101.325kPa. Activities of aqueous sulphur species = 0.1M. Activities of aqueous iron and nickel species = 0.1 and 10^{-6}M. Metastable equilibria: with $Fe_{4.5}Ni_{4.5}S_8$ and $FeNi_2S_4$ as the only metal-sulphide phases. H_2S not consumed. α-FeO(OH) and $Ni(OH)_2$ as metastable products.

1.6 FUNDAMENTAL CONCEPTS OF ELECTROCHEMICAL KINETICS

1.6.0 Introduction

An important aspect to the understanding of electrochemical kinetics is the fundamental relationship between the rate of the electron transfer and the potential at the electrode. This is discussed here in terms of the Butler-Volmer treatment. For a more comprehensive account, the reader is referred to Bard and Faulkner (173), Atkins (126), and the Southampton Electrochemistry Group (175).

This relationship is obtained via the postulate that the forward and backward rate constants for electron transfer (k_f and k_b) adhere, to Arrhenius's equation and to the predictions of simple activated complex theory, i.e.

$$k_f = \frac{kT}{h} e^{-\Delta\bar{G}_f^{\ddagger}/RT} \qquad (1.6.0.1)$$

and

$$k_b = \frac{kT}{h} e^{-\Delta\bar{G}_b^{\ddagger}/RT} \qquad (1.6.0.2)$$

The activation free energies $\Delta\bar{G}_f^{\ddagger}$ and $\Delta\bar{G}_b^{\ddagger}$ have a dependence on the interfacial potential difference, such that they can be expressed in terms of separate chemical and electrical components, in which the chemical components are assumed to be potential independent:

$$\Delta\bar{G}_f^{\ddagger} = \Delta G_f^{\ddagger} + (\Delta G_f^{\ddagger})_e \qquad (1.6.0.3)$$

$$\Delta\bar{G}_b^{\ddagger} = \Delta G_b^{\ddagger} + (\Delta G_b^{\ddagger})_e \qquad (1.6.0.4)$$

To obtain an explicit relationship with potential, the electrical components to the activation energies are assumed to be fixed fractions of the overall standard electrical free energy change $(\Delta G^{o})_{e}$, and sum to $(\Delta G^{o})_{e}$ i.e.

$$(\Delta G_{f}^{\ddagger})_{e} = \alpha(\Delta G^{o})_{e} \qquad (1.6.0.5)$$

and

$$(\Delta G_{b}^{\ddagger})_{e} = -(1-\alpha)(\Delta G^{o})_{e} \qquad (1.6.0.6)$$

where α is the charge transfer coefficient.

From the relationship between the standard electrical free energy change and the potential difference, i.e.

$$(\Delta G^{o})_{e} = (Z_{B}-Z_{A})F(E-E^{o}) \qquad (1.6.0.7)$$

(where E and E^{o} are with respect to a reference electrode) equations 1.6.0.1 and 1.6.0.2 yield

$$k_{f} = \frac{kT}{h} e^{-\Delta G_{f}^{\ddagger}/RT} \cdot e^{\alpha(Z_{B}-Z_{A})F(E-E^{o})/RT} \qquad (1.6.0.8)$$

$$k_{b} = \frac{kT}{h} e^{-\Delta G_{b}^{\ddagger}/RT} \cdot e^{-(1-\alpha)(Z_{B}-Z_{A})F(E-E^{o})/RT} \qquad (1.6.0.9)$$

where $\frac{kT}{h} e^{-\Delta G_{f}^{\ddagger}/RT}$ and $\frac{kT}{h} e^{-\Delta G_{b}^{\ddagger}/RT}$

are the forward and backward standard heterogeneous rate constants (k^{o}_{f} and k^{o}_{b}). Thus

$$k_{f} = k^{o}_{f}\, e^{\alpha(Z_{B}-Z_{A})F(E-E^{o})/RT}$$

$$k_{b} = k^{o}_{b}\, e^{-(1-\alpha)(Z_{B}-Z_{A})F(E-E^{o})/RT}$$

where the symbols have identical meaning with those in Section 1.6.2.

Alternatively, expressing the rate constants in terms of electric current, yields the Butler-Volmer equation

$$i = i_o[e^{\alpha(Z_B-Z_A)F(E-E^o)/RT} - e^{-(1-\alpha)(Z_B-Z_A)F(E-E^o)/RT}]$$

where i_o (which = $(Z_B-Z_A)F(C_A{}^o)^{\alpha}(C_B{}^o)^{1-\alpha}k^o$) is the exchange current density.

Section 1.6.2 describes a model for simple electron transfer at a planar electrode as based on the combination of the mathematical treatments for concentration polarization via diffusional processes (as described by Fick's Second law), and activation polarization via the Butler-Volmer relationship for current and potential (or more explicitely via the alternative equivalent relationships in terms of the standard heterogeneous rate constant). The solutions to the differential equations obtained from Fick's Second law applied to this scheme, are described in terms of a convolution transform of the current with a $(\pi t)^{-1/2}$ function (obtained through the use of Laplace transform methods; cf. Bard & Faulkner (173)).

This treatment yields functional forms relevant to a variety of electrochemical techniques, e.g. cyclic voltammetry, chronoamperometry and chronopotentiometry. Furthermore, many of these equations are initially derived for any regime of electron transfer (i.e. fast or slow electron transfer). The Cottrell and Sand relationships are then evolved as a natural consequence of the specific limiting case of purely diffusional conditions. In Section 3.5, the Sand relationship (as expressed in terms of the convoluted current), is used to test the data captured from chronopotentiometric experiments on the anodic dissolution of pentlandite in aqueous solution, for the adherence of this system to the simple diffusional model.

Section 1.6.2 includes also, the treatment of chronoamperometric data via a novel method, employing a step equation, hitherto unreported, as derived in Appendix G. This treatment was used to determine the heterogeneous electrochemical parameters for the hydrometallurgically important $FeCl_3/FeCl_2$ couple, on a platinum electrode, as discussed in Section 3.7.

For a description of the basic experimental principles and theory of the electrochemical techniques used in this work, the reader is referred to Section 2.2. Likewise, details concerning the apparatus and instrumentation are given in Section 2.3. Finally, a description of the electrical double layer, and the concept of a mixed potential are given in Sections 1.6.1, and 1.6.3 respectively.

1.6.1 The Electrical Double Layer

A homogeneous bulk phase has by definition no spacial variation in its physical properties. However, at the interface between two such phases this condition no longer applies. The example of the interactions at the interface between an inert metal electrode and an aqueous redox couple will now be considered.

Anisotropic forces arise at the interface due to the incomplete valency requirements of the atoms in the metal surface and abrupt changes in the solvation sheaths of the ionic species in the solution. This normally gives rise to preferential adsorption of aqueous species, and preferred orientations of the dipolar water molecules at the interface.

When the system is at equilibrium, electrons are distributed within the metal so as to oppose exactly the charge created on the aqueous side and therefore maintain the conservation of charge. The resulting segregation of positive and negative charge is called the electrical double layer, and is responsible for the creation of a potential difference across the interface. The structure of the layer can be viewed as two parallel sheets of opposite charge. This conceptual view is analogous to the capacitive element in an electric circuit. The double layer does indeed exhibit a capacitance which has real consequences in experimental work with the passage of non-faradaic current across the interface (cf. Section 3.7).

The structure of the electrical double layer is particularly important when the system is perturbed from equilibrium. Under these conditions, the electrical double layer may be envisaged in simplest terms as incorporating the electroactive species in structural configurations which in the case of slow electron transfer depart considerably in amount from those at equilibrium (open-circuit).

In the more recent Stern-Grahame model, a distinction is made between two planes of adsorbed ions (cf. Figure 1.6.1). The inner layer, is at most, only a couple of molecular diameters in thickness and contains solvent molecules and specifically adsorbed ions (which are generally considered to be unsolvated). The locus of their centres defines the position of the Inner Helmholtz Plane (IHP). The Outer Helmholtz Plane (OHP) represents the plane of closest approach of non-specifically adsorbed species. The diffuse layer is the region extending from the OHP to the bulk solution. The properties of the diffuse layer can be described in terms of an equilibrium between thermal motion and the long range coulombic interactions of the ions with the charge on the electrode.

The "structure" of the electrical double layer has direct implications for electrode kinetics, since this is the region where the electron transfer reaction occurs. Consequently, a knowledge of the potential gradient across the "entire" interfacial region, and the relative position of the reactant species during the electron transfer reaction is important in kinetic studies. The Butler-Volmer relationship assumes that the whole of the potential difference between the "bulk" metal and the "bulk" solution (excluding any obvious iR drop within these "bulk" phases) is utilized in driving the electron transfer reaction. However, this driving force is solely determined (at least in this model) by the potential difference between the metal surface and the OHP. Within this narrow region the potential gradient is large with a typical order of magnitude $10^5 Vm^{-1}$. Electron transfer occurs via electron tunnelling across this narrow region. The effect of applied potential is to alter the relative energies of the donor and acceptor electron levels, and allow tunnelling to occur between filled donor and empty acceptor levels of the same energy.

In the consideration of the oxidative dissolution of a metal-sulphide, the structure is further complicated by the lack of knowledge in the properties of the metal-sulphide in the vicinity of the interfacial region. For instance, metal concentrations within the sulphide sub-lattice may vary within this region. This may be accompanied by changes in electronic conductance (e.g. a transition from electrical to semi-conductor properties), and perhaps changes in solid state diffusion. More fundamentally, the reactant species is in the solid phase (i.e. a metal atom within a sulphur sub-lattice). The electron transfer reaction is therefore accompanied by the breakage of metal-sulphur chemical bonds within the crystal structure, and the incorporation of the metal ions into the aqueous phase.

1.6.2 Simple Electron Transfer (E_n)

The objective of this section is to describe the treatment of electrochemical data for the E_n case using a convolution transform of the current with a $(\pi t)^{-1/2}$ function. The methods, in the first instance, are generally applicable to a variety of techniques, including chronoamperometry, cyclic voltammetry and chronopotentiometry, and are not limited to any particular regime of the heterogeneous parameters involved. In addition, they are relevant to any ratio of initial bulk concentrations of the electroactive species involved, provided that the initial potential is determined solely by the above concentrations. Furthermore, this treatment shows how the Cottrell and Sand relationships are evolved as a natural consequence of the specific limiting case of purely diffusional conditions.

The description of the treatment for the E_n case will relate to the following general reaction scheme

$$A^{Z_A} - (Z_B - Z_A)e \xrightarrow[\alpha,\ D_A,\ D_B]{k_f,\ k_b,\ k^o,\ E^o} B^{Z_B}$$

The parameters have their usual electrochemical meaning, where A is the reactant and B is the product. The electroactive species (A) and (B) may be either oxidizing or reducing with any initial bulk concentrations.

To account for concentration polarization, diffusion to a planar electrode of area A located at $x = 0$ is assumed to be the only source of mass transport as described by Fick's second law and expressed by the second order partial differential linear equations appropriate to this scheme:

$$\frac{\delta C_{A(x,t)}}{\delta t} = D_A \frac{\delta^2 C_{A(x,t)}}{\delta x^2} \qquad (1.6.1)$$

$$\frac{\delta C_{B(x,t)}}{\delta t} = D_B \frac{\delta^2 C_{B(x,t)}}{\delta x^2} \qquad (1.6.2)$$

These equations are solved for semi-infinite one dimensional linear diffusion subject to the following initial and boundary conditions:

at $t = 0, \quad x \geqslant 0$

$$C_{A(x,0)} = C_A^{\infty}, \qquad C_{B(x,0)} = C_B^{\infty} \qquad (1.6.3)$$

(i.e. an initial homogeneous distribution of electroactive species A and B throughout the solution for all x).

at $t \geqslant 0$

$$\lim_{x \to \infty} C_{A(x,t)} = C_A^{\infty}, \quad \lim_{x \to \infty} C_{B(x,t)} = C_B^{\infty} \qquad (1.6.4)$$

(i.e. semi-infinite diffusion for all t).

Notation for concentrations at the electrode are given in short as:

$$C_{A(0,t)} = C_A^{o}, \qquad C_{B(0,t)} = C_B^{o}$$

During an experiment the concentration gradients are equivalent to the electrical current (i), thus the conservation of charge is described by the relationship:

at $x = 0, \quad t \geqslant 0$

$$-i(t) = z_A F A D_A \frac{\delta C_{A(0,t)}}{\delta x} + z_B F A D_B \frac{\delta C_{B(0,t)}}{\delta x} \qquad (1.6.5)$$

and for the conservation of mass:

at $x = 0, \quad t \geqslant 0$

$$D_A \frac{\delta C_{A(0,t)}}{\delta x} + D_B \frac{\delta C_{B(0,t)}}{\delta x} = 0 \qquad (1.6.6)$$

The application of Laplace transform methods, and some algebraic manipulation, yields the following spacial dimensionless linear integral equation with variable coefficients:

$$C_A{}^o = C_A{}^\infty - \frac{1}{(Z_B-Z_A)FAD_A{}^{1/2}} \left[\frac{1}{\pi^{1/2}} \int_0^t \frac{i(u)}{(t-u)^{1/2}} du \right] \quad (1.6.7)$$

$$C_B{}^o = C_B{}^\infty - \frac{1}{(Z_A-Z_B)FAD_B{}^{1/2}} \left[\frac{1}{\pi^{1/2}} \int_0^t \frac{i(u)}{(t-u)^{1/2}} du \right] \quad (1.6.8)$$

where u is the time at which the current i(u) was measured. The semi-integral term in square parenthesis is the convoluted current summed over t = 0 to t = t, and is denoted as

$$i * \frac{1}{(\pi t)^{1/2}}$$

and as I_1 for short[‡], hence:

$$C_A{}^o = C_A{}^\infty - \frac{I_1}{(Z_B-Z_A)FAD_A{}^{1/2}} \quad (1.6.9)$$

$$C_B{}^o = C_B{}^\infty - \frac{I_1}{(Z_A-Z_B)FAD_B{}^{1/2}} \quad (1.6.10)$$

Thus the transformed current data (I_1) can be used directly by these equations to obtain $C_A{}^o$ and $C_B{}^o$. Equations (1.6.9) and (1.6.10) hold for any potential/time profile. Under the specific conditions during the experiment where $C_A{}^o$ or $C_B{}^o$ become zero (i.e. purely diffusion controlled conditions) I_1 reaches maximum (limiting) values

---

[‡] The capture of i(t) data and subsequent computation of I_1 was facilitated by the use of the commercially available CONDECON 300 System (EG&G,PAR) which is a combined hardware/ software package designed to be used with an IBM PC computer

$$\lim_{C_A^o \to 0} I_1 = I^A{}_{lim} = (Z_B-Z_A)FAD_A{}^{1/2}C_A{}^{\infty} \tag{1.6.11}$$

$$\lim_{C_B^o \to 0} I_1 = I^B{}_{lim} = (Z_A-Z_B)FAD_B{}^{1/2}C_B{}^{\infty} \tag{1.6.12}$$

To complete the analysis of the I_1 data the heterogenous parameters need to be determined ultimately as functions of potential. These are introduced in the form:

$$i(t) = (Z_B-Z_A)FA[k_f(E)C_A{}^o - k_b(E)C_B{}^o] \tag{1.6.13}$$

where the forward and backward potential dependent heterogeneous rate constants k_f and k_b are not assumed at this stage to have any particular "form" of variation with potential. From equations (1.6.9), (1.6.10) and (1.6.13) the following relationship between the current i(t) and its "history" I_1 is derived:

$$i(t) = (Z_B-Z_A)FA\left\{k_fC_A{}^{\infty} - \frac{k_fI_1}{(Z_B-Z_A)FAD_A{}^{1/2}} - k_bC_B{}^{\infty} + \frac{k_bI_1}{(Z_A-Z_B)FAD_B{}^{1/2}}\right\} \tag{1.6.14}$$

or in terms of I_{lim}

$$i(t) = (I^A{}_{lim} - I_1)\left\{\frac{k_f}{D_A{}^{1/2}}\right\} + (I^B{}_{lim} - I_1)\left\{\frac{k_b}{D_B{}^{1/2}}\right\} \tag{1.6.15}$$

This holds generally for the E_n case. Various functional forms will be derived for particular conditions.

The potential E^o is defined here as the potential E at which the ratio $C_B{}^o/C_A{}^o$ is unity. Potential can be introduced explicitly via, for example, the Butler-Volmer relationship for current, or via the equivalent relationships:

$$k_f = k^o e^{\alpha\xi} \qquad (1.6.16)$$

$$k_b = k^o e^{-(1-\alpha)\xi} \qquad (1.6.17)$$

where $\xi = (Z_B-Z_A)F(E-E^o)/RT$ is a "reduced" emf (1.6.18) and α is the charge transfer coefficient.

The exchange current density (i_o) is then defined in terms of the standard heterogeneous rate constant (k^o) by the following relationship:

$$i_o = (Z_B-Z_A)F(C_A{}^o)^{\alpha}(C_B{}^o)^{1-\alpha} k^o$$

Introducing potential into equation (1.6.14) thus gives:

$$\frac{i(t)}{k^o} = I^A{}_{lim}\left\{\frac{e^{\alpha\xi}}{D_A{}^{1/2}}\right\} + I^B{}_{lim}\left\{\frac{e^{-(1-\alpha)\xi}}{D_B{}^{1/2}}\right\} - I_1\left\{\frac{e^{\alpha\xi}}{D_A{}^{1/2}}\right\} - I_1\left\{\frac{e^{-(1-\alpha)\xi}}{D_B{}^{1/2}}\right\} \qquad (1.6.19)$$

This expression holds for "any" variation of potential with time, e.g. as in the techniques of cyclic voltammetry (linear and non-linear sweep), chronoamperometry etc.

Nernstian behaviour is defined as when the concentration of the reactant and product species at the electrode surface is governed solely by the Nernst equation; as in the case when electron transfer is fast.

In the Nernstian case electron transfer is intrinsically fast in both directions (i.e. k_f and k_b are both large: k_f, k_b >> i). In this case i(t) can be ignored with respect to each of the terms on the right hand side of equation (1.6.15) and similarly $i(t)/k^o$ in equation (1.6.19). Hence simple algebraic manipulation of equation (1.6.19), yields the polarographic relationship

$$E = E_{1/2} + \frac{RT}{(z_B-z_A)F} \ln\left\{\frac{I_1 - I^B{}_{lim}}{I^A{}_{lim} - I_1}\right\} \qquad (1.6.20)$$

where $$E_{1/2} = E^o + \frac{RT}{(z_B-z_A)F} \ln(D_A/D_B)^{1/2} \qquad (1.6.21)$$

In contrast to the Nernstian case, in the irreversible case (i.e. $k_f >> k_b$), the Butler-Volmer relationship yields

$$i(t) = (z_B-z_A)FAk^oC^o{}_A \, e^{-\alpha(z_B-z_A)F(E-E^o)/RT} \qquad (1.6.22)$$

and hence from equation (1.6.19) the irreversible polarographic relationship

$$E = E^o - \frac{RT}{\alpha(z_B-z_A)F} \ln\left\{\frac{D_A{}^{1/2}}{k^o}\right\} - \frac{RT}{\alpha(z_B-z_A)F} \ln\left\{\frac{i(t)}{I^A{}_{lim} - I_1}\right\} \qquad (1.6.23)$$

In the Nernstian case, note that all the I(t) data for any potential/time profile, can be assessed on the same plot. $E_{1/2}$ is obtained from the condition:

$$(I^A{}_{lim} + I^B{}_{lim})/2 = I_1 \qquad (E = E_{1/2}) \qquad (1.6.24)$$

or, somewhat more simply, via the maximum in dI_1/dE and also in the deconvolution dI_1/dt in the specific case of linear sweep cyclic voltammetry (LSCV). Note that dI_1/dE and the deconvolution (dI_1/dt) are obtained via differentiation of equation (1.6.20), yielding the "sech squared" and equivalent forms. dI_1/dE is thus symmetric about $E_{1/2}$. Furthermore, for any potential/time profile:

$$(dI_1/dE)_{max} = RT(I^A{}_{lim} - I^B{}_{lim})/4(z_B-z_A)F \qquad (1.6.25)$$

and in the specific case of LSCV:

$$(dI_1/dt)_{max} = (z_B-z_A)dE/dt(I^A{}_{lim} - I^B{}_{lim})/4 \qquad (1.6.26)$$

Equation (1.6.20) is expressed in terms of both of the electroactive species (A) and (B). If either of these species is initially absent from the bulk solution, then from equations (1.6.11) or (1.6.12) $I^{A}_{lim} = 0$ or $I^{B}_{lim} = 0$ (See Figure 1.6.1).

In contrast to the Nernstian case, when electron transfer is in the quasi-reversible regime (where $i \sim i_o$) the term on the left hand side of equation (1.6.18) cannot be ignored with respect to any other term. I_1 now varies with time and hence for example, in a cyclic voltammetric sweep or in multiple sweeps, plots of I_1 versus E do not "overlay" each other. Likewise, dI_1/dE and the deconvolutions in LSCV etc., are now displaced either side of the half-wave potential.

At a constant potential k_f and k_b are fixed (as in chronoamperometry) and equation (1.6.14) leads to a linear relationship between i(t) and I_1

$$i(t) = I^{A}_{lim}\left\{\frac{k_f(E)}{D_A^{1/2}}\right\} + I^{B}_{lim}\left\{\frac{k_b(E)}{D_B^{1/2}}\right\} - I_1\left\{\frac{k_f(E)}{D_A^{1/2}} + \frac{k_b(E)}{D_B^{1/2}}\right\} \tag{1.6.27}$$

or, in terms of γ and β for short,

$$i(t) = \gamma - \beta I_1$$

where $$\gamma = I^{A}_{lim}\left\{\frac{k_f}{D_A^{1/2}}\right\} + I^{B}_{lim}\left\{\frac{k_b}{D_B^{1/2}}\right\}$$

and $$\beta = \frac{k_f}{D_A^{1/2}} + \frac{k_b}{D_B^{1/2}}$$

yielding k_f, k_b, D_A, D_B (see Section 3.7)

Still considering the Nernstian case; within this regime an expression for i(t) in terms of the convoluted current (I_1) is obtained as follows.

Since

$$I_1 = i(t) * \frac{1}{(\pi t)^{1/2}} \qquad (1.6.28)$$

then as a general relationship:

$$i(t) = \frac{d}{dt}\left\{ I_1 * \frac{1}{(\pi t)^{1/2}} \right\} \qquad (1.6.29)$$

or,

$$i(t) = I_{1(t=0)} \frac{1}{(\pi t)^{1/2}} + \left\{ \frac{dI_1}{dt} * \frac{1}{(\pi t)^{1/2}} \right\} \qquad (1.6.30)$$

Since in the case of chronoamperometry I_1 is independent of time at the Nernstian limit, then

$$\frac{dI_1}{dt} = 0$$

hence,

$$i(t) = \frac{I_1}{(\pi t)^{1/2}} \qquad \text{for all } t \qquad (1.6.31)$$

Furthermore, at the extremes of potential:

$$\lim_{E \to \infty} I_1 = I^A{}_{\lim}, \qquad \text{etc.} \qquad (1.6.32)$$

This yields the equivalent Cottrell relationship:

$$\lim_{E \to \infty} i(t) = \frac{I^A{}_{\lim}}{(\pi t)^{1/2}} = \frac{(Z_B - Z_A) FAD_A{}^{1/2} C_A{}^{\infty}}{(\pi t)^{1/2}} \qquad (1.6.33)$$

If electron transfer is "not intrinsically fast" then Cottrell behaviour is still observed under two conditions.

Firstly, in the region "well past" the polarographic wave, i.e. when $I_1 \rightarrow I_{1im}$ and hence $dI_1/dt \rightarrow 0$. Secondly, in the latter stages of any decay irrespective of the rate of electron transfer. Thus from equation (1.6.34), calculation shows a 1% deviation of the current from the "Cottrell value" at $(t \,.\, k_f/D_A{}^{1/2}) = 60$. Nonetheless, the Cottrell relationship allows only the diffusion coefficients to be determined.

However, the linearity of i with I_1 in equation (1.6.27) allows k_f, k_b, D_A and D_B to be determined in principle in any regime of electron transfer.

There is an alternative to using the above linear relationship which does not rely experimentally on convolution of the current time relationship, and which has the experimental advantage of not being dependent on the charging current once this has decayed.

This is obtained as follows. In general, for simple electron transfer (173), the variation of i with t for a chronoamperometric experiment turns out to be:

$$i(t) = \gamma e^{\beta^2 t} \operatorname{erfc} \beta t^{1/2} \qquad (1.6.34)$$

where γ and β have the same meaning as in equation (1.6.27). However, equation (1.6.34) as it stands is not useful for parameter determination directly, because of the difficulty in determining erfc $\beta t^{1/2}$. However, a functional form, hitherto unreported, is obtained directly from this expression as given by equation (1.6.35),(cf. Appendix G).

$$\frac{\Delta Q}{\Delta i} = \left\{\frac{2}{\pi^{1/2}}\frac{\gamma}{\beta}\right\}\frac{\Delta t^{1/2}}{\Delta i} + \frac{1}{\beta^2} \qquad (1.6.35)$$

where $$Q = \int_{t_1}^{t_2} i(t)\, dt,$$

and $\Delta t = t_2 - t_1$,

and $\Delta i = i(t=t_2) - i(t=t_1)$.

Equation 1.6.35 can be written in an alternative algebraic form

$$\frac{\Delta i}{\Delta t^{1/2}} = \beta^2 \frac{\Delta Q}{\Delta t^{1/2}} - \frac{2\gamma\beta}{\pi^{1/2}}$$

This has the advantage that the heterogeneous rate constant appears in the gradient. Furthermore, statistical treatment can be carried out with the equations in this form yielding a weighting of the deviations proportional to $(\Delta t^{1/2})^2$. This has the effect of placing more importance on the short time data.

The criterion for chronopotentiometry is that the current is controlled. If i now follows a simple power functional form of time: $i = at^n$ (where a and n are independent constants). Then $I_1(t)$ is obtained as follows, in terms of the gamma function

$$I_1 = i * \frac{1}{(\pi t)^{1/2}} = \frac{a\Gamma(n+1)\ t^{(n+1/2)}}{\Gamma(n+3/2)} \qquad (1.6.36)$$

For the specific case where the current is kept constant, (i.e. for when n = 0 and i = a).

$$I_1 = \frac{a\Gamma(1)\ t^{1/2}}{\Gamma(3/2)} = \frac{2it^{1/2}}{\pi^{1/2}} \qquad (1.6.37)$$

i.e. in the specific case above, I_1 increases with the square root of time, and at the limit where $I_1 = I_{1im}$, t has a characteristic value t_s

$$\lim_{I_1 \to I_{1im}} t = t_s$$

and at this limit the potential becomes infinite

$$\lim_{t \to t_s} E = \infty .$$

This yields the Sand relationship:

$$I^A{}_{1im} = 2i_c\left\{\frac{t_{s(A)}}{\pi}\right\}^{1/2} = (Z_B-Z_A)FAD_A{}^{1/2}C_A{}^{\infty} \qquad (1.6.38)$$

The Sand time (t_s) yields I_{1im} and hence a route to D_A, and D_B, irrespective of the rate of electron transfer.

Furthermore, in the Nernstian case where I_1 is a function of E only, E has the following functional form obtained directly from the polarographic relationship (equation 1.6.20):

$$E(t) = E_{1/2} + \frac{RT}{(Z_B-Z_A)F} \ln\left\{\frac{I_1 - 2i_b(t_{s(B)}/\pi)^{1/2}}{2i_f(t_{s(A)}/\pi)^{1/2} - I_1}\right\} \qquad (1.6.39)$$

If either of the species is initially absent in the bulk solution, such that either $I^A{}_{1im} = 0$ or $I^B{}_{1im} = 0$, then $E_{1/2}$ (in equation 1.6.39) = $E_{1/4}$. For example, in the case when $C_B{}^{\infty} = 0$, equation (1.6.39) becomes:

$$E(t) = E_{1/4} + \frac{RT}{(Z_B-Z_A)F} \ln\left\{\frac{I_1}{2i(t_s/\pi)^{1/2} - I_1}\right\} \qquad (1.6.40)$$

which can be expressed in terms of time t

$$E(t) = E_{1/4} + \frac{RT}{(Z_B - Z_A)F} \ln\left\{\frac{(t/t_s)^{1/2}}{1 - (t/t_s)^{1/2}}\right\} \qquad (1.6.41)$$

(cf. Figure 1.6.2)

Note that $E_{1/4}$ in the chronopotentiometric wave (i.e. Equation 1.6.40) is identical to the polarographic half-wave potential $E_{1/2}$ (in Equation 1.6.20). Furthermore, for all other ratios of $C_A^{\infty}/C_B^{\infty}$, the partial wave potential for the chronopotentiometric wave is expressed as $E_{1/x}$, where x lies within the range $2<x<4$.

1.6.3 Mixed Potential

The concept of a mixed potential is important in explaining many hydrometallurgical reactions, e.g. the interaction between an electronic conducting chalcogenide and the oxidizing chemical species during the dissolution of metal ions.

The mixed potential is governed by the kinetic restraints imposed by two interacting electrochemical processes, such that each process provides the thermodynamic driving force for the other. The system is therefore thermodynamically unstable and the mixed potential represents a departure from equilibrium.

The two processes (one being anodic and the other cathodic) are considered as occuring at seperate sites on the electrode surface and therefore partition the total electrode area into a cathodic region (A_c) and an anodic region (A_a), such that $A_a + A_c = A_{total}$.

The mixed potential results from the fact that the anodic and cathodic regions are in electrical contact (i.e. short circuited), so that the mixed potential (E_m) lies between the equilibrium potentials E_a and E_c of the two processes (cf. Figure 1.6.4). The mixed potential therefore defines the overpotential for each of the two processes (η_a and η_c) in the interacting system (since $\eta = E - E_{eq}$). The position of E_m is determined by the kinetics of "each" process such that it corresponds to the potential at which the anodic current exactly balances the cathodic current:

$$E = E_m \quad \text{where} \quad i_a = -i_c$$

Note, that this equality does not necessarily apply to current densities (i.e. A_a need not equal A_c). When current densities are reported in this respect, they must be normalized in terms of the total area A_{total}.

If A_a and A_c are separate and distinguishable surfaces yet electrically in contact (e.g. two conducting minerals in electrical contact), the system is called a galvanic couple. If A_a and A_c are part of the same surface, but only occupy different domains, then the system is called a corrosion couple.

The mixed potential is a transitory phenomenon and therefore a fuction of time (i.e. the current/potential curves if Figure 1.6.4 may change with time). In a closed system E_m may vary until such time that: $E_m = E_a = E_c$. However, the relative position of E_m between the standard equilibrium potentials for the anodic and cathodic processes, can give an indication of the magnitude of the exchange current density of the corroding system, provided that the kinetic parameters (k^o and α) of one of the redox couples is known.

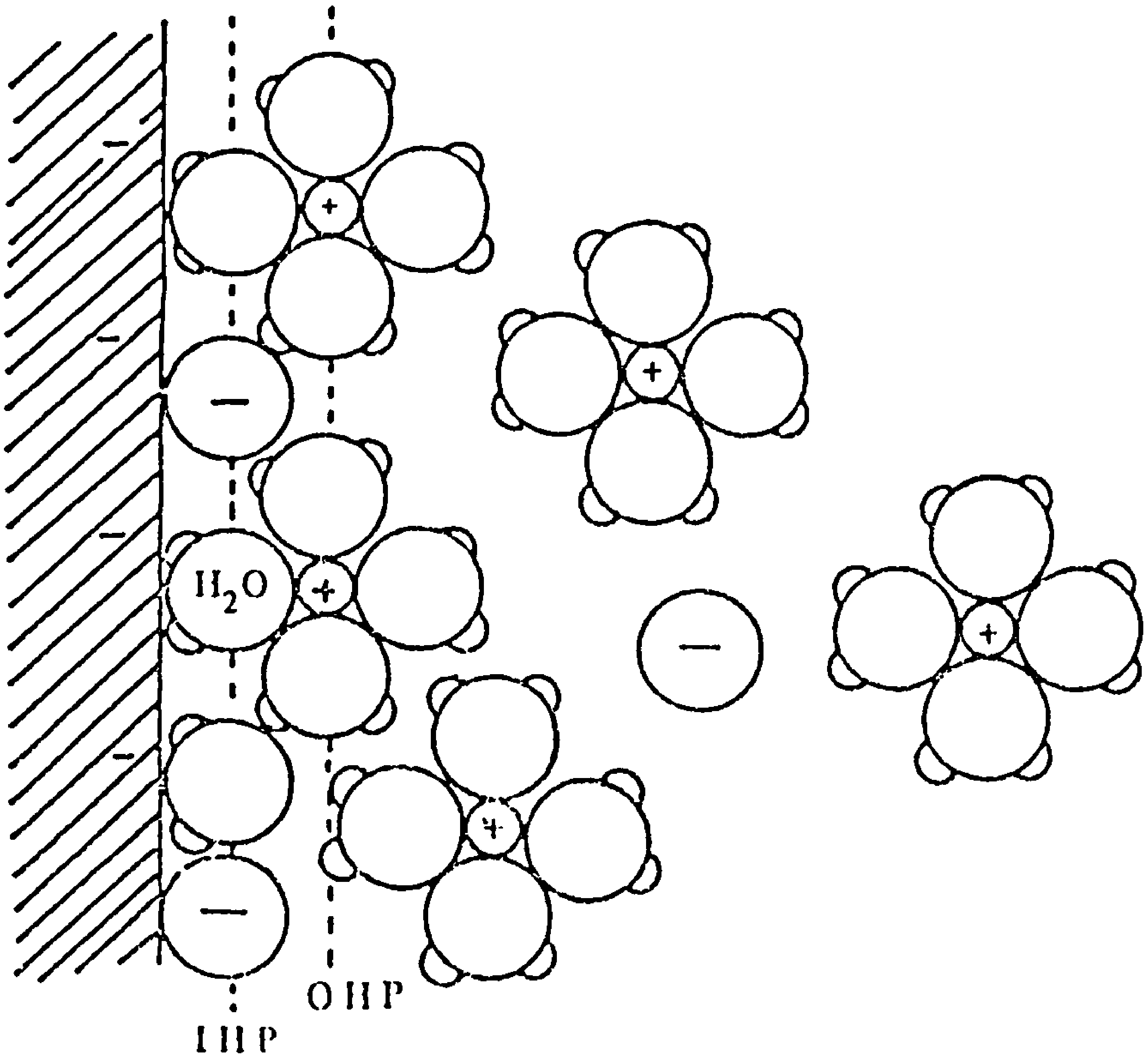

Figure 1.6.1

Stern-Grahame model of the interfacial region in the immediate vicinity of the electrode. IHP is the inner Helmholtz plane, OHP is the outer Helmholtz plane (175).

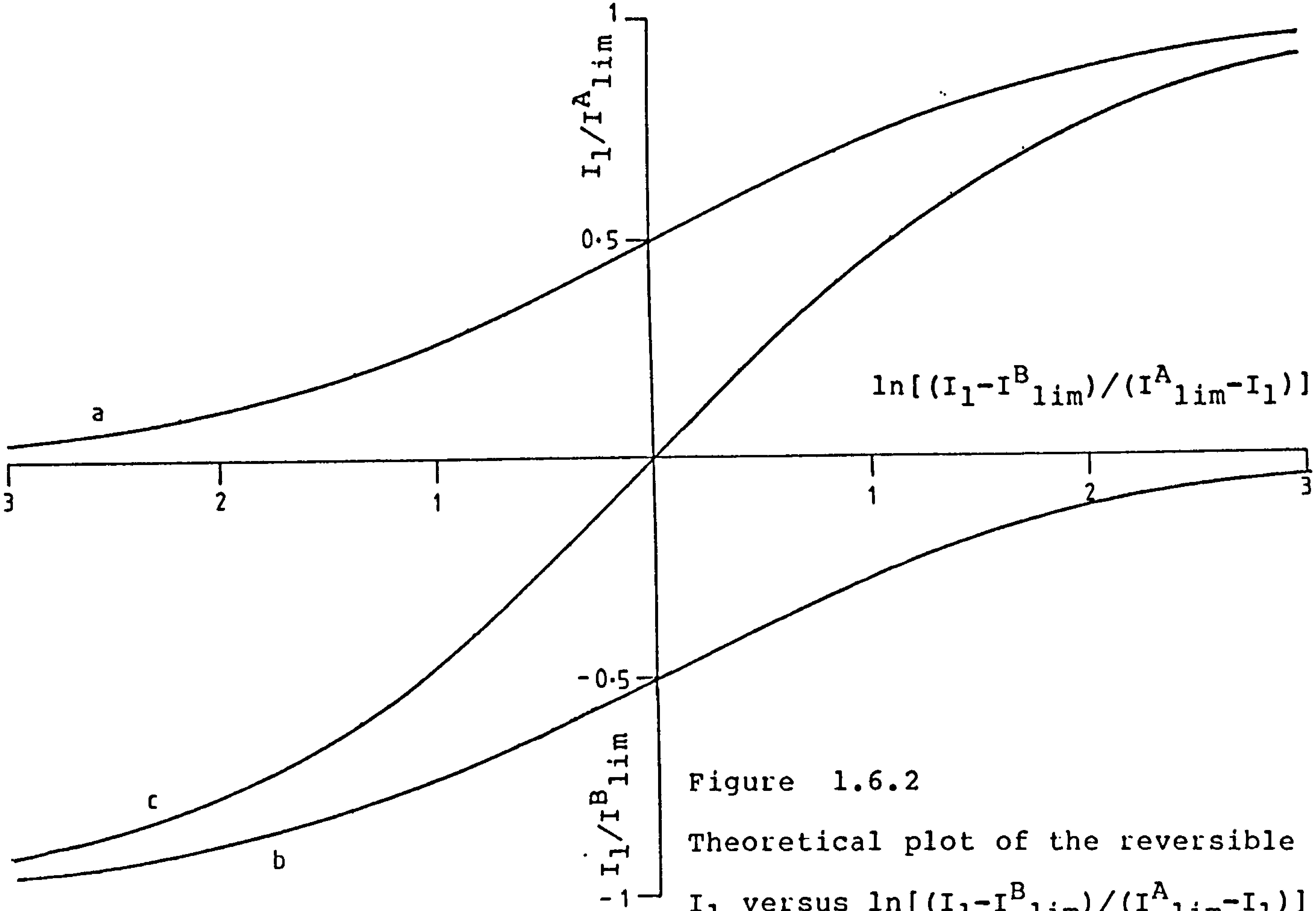

Figure 1.6.2

Theoretical plot of the reversible polarographic relationship: I_1 versus $\ln[(I_1-I^B{}_{lim})/(I^A{}_{lim}-I_1)]$, (cf. Equation 1.6.20). (a) $C_B{}^{\infty} = 0$; (b) $C_A{}^{\infty} = 0$; (c) $C_A{}^{\infty} = C_B{}^{\infty}$, where $D_A = D_B$. x-axis is in intervals of $RT/(Z_B-Z_A)F$ Volts.

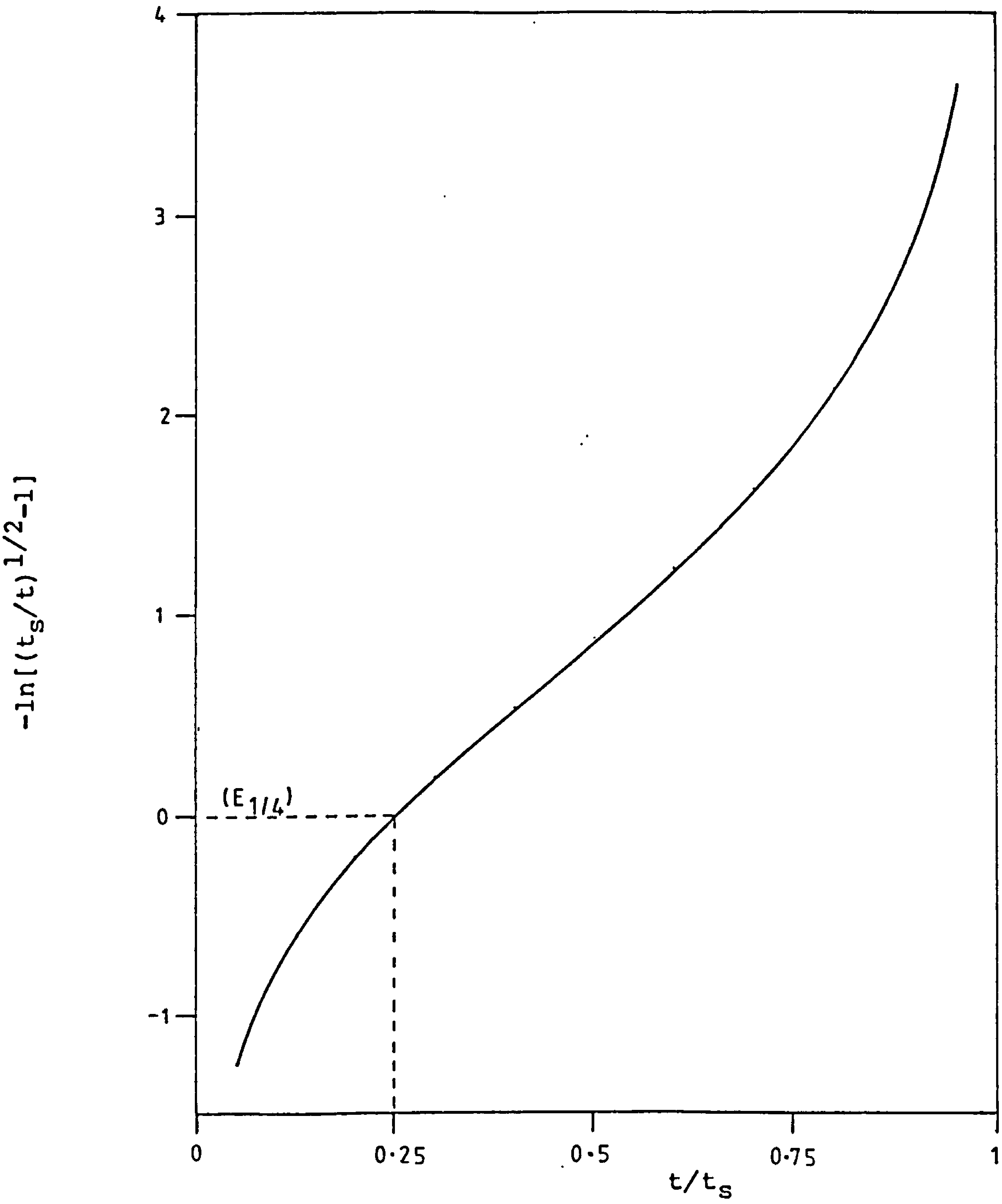

Figure 1.6.3

Theoretical plot of the reversible chronopotentiometric relationship: $-\ln[(t_s/t)^{1/2}-1]$ versus t/t_s, where $C_B^{\infty} = 0$ (cf. Equation 1.6.41).

y-axis is in intervals of $RT/(Z_B-Z_A)F$ Volts.

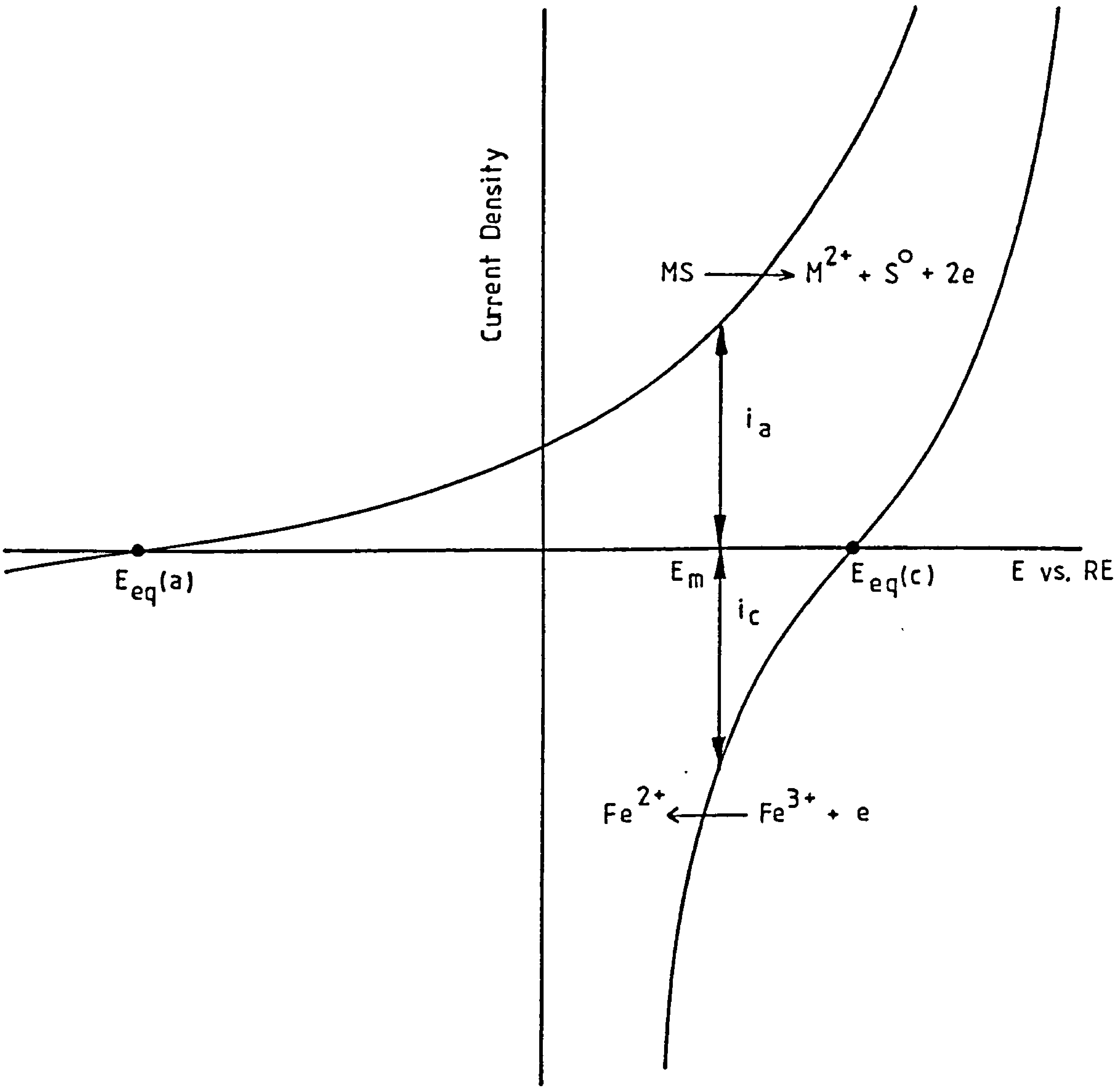

Figure 1.6.4

Schematic i-E curves showing the concept of mixed-potential for the interaction between a S^o,M^{2+} / MS and the Fe^{3+} / Fe^{2+} couples.

E_{eq}(a) is the equilibrium potential for the anodic reaction $MS = M^{2+} + S^o + 2e$.

E_{eq}(c) is the equilibrium potential for the cathodic reaction $Fe^{3+} + e = Fe^{2+}$.

E_m is the mixed-potential (the potential at which $i_a = -i_c$).

1.7 THE OXIDATIVE DISSOLUTION OF NICKEL-IRON-SULPHIDE MINERALS IN AQUEOUS MEDIA: A LITERARY REVIEW

1.7.0 Introduction

A summary of the extractive hydrometallurgical processes for the leaching of nickel-iron-sulphides was given in Section 1.1 ipso facto indicating that the "direct" oxidative dissolution of pentlandite in acid media is impractical. In Section 1.4.2 the geological occurance of supergene violarite as an alteration product from pentlandite was discussed in terms of an electrochemical model. In Section 1.5 an attempt was made at defining the thermodynamic equilbria in the Fe-Ni-S aqueous system, as portrayed in a series of E_h-pH diagrams.

A comprehensive résumé of previous chemical leaching studies prior to 1974 is found in the works of Kelt (4) and Tzamtzis (14). This section will briefly review these, whilst generally concentrating on more recent studies.

1.7.1 Acid decomposition

Dyson and Scott (100) investigated the acid leaching of metal sulphide concentrates, typical to those of Kambalda. A sample of pentlandite (containing 10% pyrite) was found to be readily attacked at 373K by 1M HCl or H_2SO_4 solution, and could be completely dissolved without the nead for fine grinding, by a moderate excess of acid. It is of interest to note that dissolution is preceded by an induction period of several minutes. By comparison, violarite is reported to be insoluble under these conditions. The poor acid leaching results for pentlandite when in the presence of pyrrhotite containing concentrates, was ascribed to the inhibiting effect of a sulphur layer formed on the pentlandite surface.

However, the origin of this layer was from the excess sulphur liberated during pyrrhotite dissolution, and has nothing to do with the reactivity of pentlandite per se.

Jibiki (143) studied the acid decomposition reaction on compounds and minerals in the Fe-Ni-S system; which were synthesized from metal powders in an atmosphere of H_2S at 873K. Synthetic pentlandite $(Fe,Ni)_{9\mp x}S_8$ with an equimolar Fe/Ni ratio but with various sulphur activities, was leached in 0.1M HCl at 303K. The increase in concentration of Fe and Ni in solution was found to be linear with time.

The analytically determined dissolution rates of these compounds in 0.1M HCl solution at 303K was plotted against the synthesis P_{H_2S}/P_{H_2} ratio. From this data, for P_{H_2S}/P_{H_2} ratios up to 0.01, pentlandite dissolves faster than the other compounds, but then decreases as the sulphur activity increases. Once the phase $(Fe,Ni)_{1-x}S$ starts to appear (at higher H_2S/H_2 synthesis ratios), the dissolution rate drops sharply, whilst further increases in sulphur activity lead to further decreases in the dissolution rate. The material synthesized at $P_{H_2S}/P_{H_2} = 57.9$ was virtually insoluble under the applied leaching conditions.

In an experiment where pentlandite was leached in 1M HCl solution at 313K the initial dissolution of nickel was briefly accelerated and then stopped, by the introduction of oxygen. The iron dissolution rate was similar, although the brief acceleration of nickel appeared to be missing. The re-introduction of helium into the system did not reactivate the pentlandite surface within an experimental period of 260 minutes. It was generally found that the higher the sulphur activity in the compounds, the more susceptable the compounds were to inhibition. Jibiki concluded that the presence of such oxidants must be avoided in the acid dissolution of these compounds. He proposed that the formation of an oxide-film on the sulphide surface may be responsible for this behaviour. However, this seems highly implausible at pH = 0.

1.7.2 Oxidative Dissolution

Conventional chemical studies by Kelt (4) and Tzamtzis (14) were performed on the dissolution of pentlandite in acid-ferric chloride solution.

In Kelt's work (4), 1g samples of synthetic pentlandite with a particle size range -180 +125μm was leached with 0.2 dm^3 of 0.1M $FeCl_3$ in the temperature range 303K to 363K. The dissolution occured in two stages; the rate of the first being faster than that of the second. The rates of dissolution of iron and nickel were similar, especially at higher temperatures. The reaction produced orthorhombic sulphur and a small amount of sulphate (the latter species due to the free access of air to the reacting system). No new Fe-Ni-S phases were identified. The value for the apparent activation energy for the dissolution of nickel varied from 67 to 46 kJmol^{-1}, indicating that the reaction rate was controlled by a mixed regime. The initial value of 67 kJmol^{-1} suggested a predominance of chemical control in the initial stage. "The nucleation of orthorhombic sulphur" was suggested as a possible reaction, (ibid. p145). At 305K, <50% Ni had been extracted in 400 hours, whilst at 336K, approximately 50% Ni was extracted in 40 hours. The leach attack occured only at exposed surfaces. At lower temperatures, pyrrhotite (present as an impurity) appeared to be leached preferentially to pentlandite, although with less disparity at higher temperatures and in the latter stages of the reaction. Kelt concluded that "pentlandite was leached in ferric chloride by oxidation at a surface" (ibid. p145).

Tzamtzis (14) conducted a similar study, and not surprisingly obtained similar results. The dissolution of pentlandite in $FeCl_3$ occured in two stages. The apparent activation energy of 46 to 29 $kJmol^{-1}$ for the dissolution of nickel indicated a mixed kinetic regime. It was inferred that chemical control predominates in the initial stage. However, like Kelt, Tzamtzis was inadvertently indecisive as to whether it is "the reaction of pentlandite with the ferric chloride" (although the actual rate determining "step" for this coupled reaction is not specified), (ibid. p176), or "the oxidation of the sulphide sulphur to elemental sulphur" (ibid. p194), which is the main rate determining step during the initial stage of reaction.

The second stage was inferred as being predominantly diffusion controlled, and interpreted in terms of mass transport of the oxidant species ($FeCl_3$) through a sulphur product layer developing around the pentlandite grains. An alternative explaination for the kinetics of this second stage of the reaction was offered by the simple fact that insufficient $FeCl_3$ was available in the bulk solution to complete the reaction (ibid. p178)! Furthermore, Tzamtzis was in fact aware of the accompanying drop in the potential of the solution as stated in his "Conclusion" (ibid. p195). The $FeCl_3$ concentration did not have any affect on the rate of leaching until about 20% of the nickel was dissolved, after which it became an important factor in terms of mass transport effects (ibid. p177).

In experiments where insufficient $FeCl_3$ was available, it was concluded from the sulphur mass balance that hydrogen sulphide was evolved. This was subsequently confirmed by an experiment under controlled conditions. However, his equation 4.5 for this latter reaction does not balance (ibid. p181) , since this reaction is an oxidative process accompanied with the evolution of hydrogen. The high rate of nickel dissolution was inferred in terms of the lack of formation of a sulphur layer around the pentlandite grains, under these conditions.

In an experiment where 1g of synthetic pentlandite of particle size range -125 +90 μm, in 0.1M $FeCl_3$, 0.1M HCl solution at 353K, stirrer speed 16.7 Hz; 50% nickel extraction was not achieved until after 30 hours. The addition of chloride ions to the bulk solution had a favourable effect on the dissolution rate in the latter stage of the reaction. The addition of hydrogen peroxide favoured the rate of formation of sulphate.

Tzamtzis acknowledges the electrochemical mechanism in describing the formation of supergene violarite from pentlandite, yet goes on to state: "but the electrochemical corrosion is not important in the dissolution of pentlandite by ferric chloride", ibid. p190; without offering any evidence for this assertion.

In Tzamtzis's comparison of his work with that of Kelt's, he makes an erroneous statement relating to the number of moles of electrons transferred in the oxidative dissolution of pentlandite to Fe^{2+}, Ni^{2+}, S^o (ibid. p192).

Kelt is originally correct to this respect.

Greig (140) investigated the leaching of various metal sulphide concentrates ($d_{50} < 35\mu m$), including pentlandite and violarite, with a variety of oxidants in chloride media at 363K with a retention time of 24 hours. Sulphide sulphur was converted to mixtures of elemental sulphur and sulphate, with elemental sulphur being the predominant species.

When leaching in HCl/Cl_2, a high molar ratio of Cl_2/Ni was required for an acceptable nickel extraction. Leaching in HCl/O_2 yielded a high nickel extraction for both pentlandite and violarite. However, details of product sulphur speciation are not given, although the reader is lead to believe that sulphate may predominate. Leaching in $HCl/FeCl_3$ required a molar ratio: $FeCl_3/Ni = 4$ for 90% extraction. Similar, if not greater extractions were obtained for lower ratios (especially for violarite) by sparging with oxygen, although an analysis for sulphate is not given. Leaching in $HCl/CuCl_2$ required a large molar ratio: $CuCl_2/Ni = 8$ for 85% extraction. Sparging with oxygen showed similar effects as in the $HCl/FeCl_3$ leaching described above.

It was generally found that nickel extraction decreased dramatically on reducing the retention time and lowering the leach temperature.

Hubli et al (141) investigated a ferrous chloride / oxygen process for Ni-Cu-S concentrates (incl. pentlandite, bravoite, millerite, violarite and chalcopyrite). Optimum conditions for a nickel extraction of 94-99% were obtained by employing the theoretical amount of $FeCl_2$ at pH 2 (HCl) under 377 kPa O_2 pressure at a temperature of 383K in 8 hours. 8% (mass) of the total sulphur present in the concetrate was oxidzed to sulphate. The major portion of the sulphur present was converted into elemental sulphur.

Subramanian et al (144) studied the effect of low chloride addition to oxygen pressure leaching of Fe-Ni-Cu-S concentrates at 383K. Addition of low concentrations of chloride (0.5-10 gdm^{-3}) did not significantly affect the rate of dissolution of pentlandite, but appeared to favour the formation of elemental sulphur. This was attributed to the possible leaching action by $FeCl_3$ or $CuCl_2$ intermediates.

An early paper by Wells (145) showed the importance of the measurement and comparison of open-circuit potentials for a variety of metal-sulphide minerals in variety solutions. Later on in 1960, Sato (146) showed that for certain binary metal sulphide phases, the first step in an electrode reaction can be identified by the measurement of the open-circuit potential of the mineral in contact with a solution containing its assumed oxidation or reduction product ions.

In 1961, Woodcock (147) produced a general review of the oxidative dissolution of metal sulphides in aqueous solution, where he emphasized the importance of electrochemical phenomena during dissolution. In 1972, Wadsworth (148) extended this review and offered evidence in support of the claim that "while electrochemical processses are clearly in evidence and appear to be fundamental to the leaching process, in most instances the kinetics observed are explainable on the basis of processes that do not involve charge transfer. At low temperature, mass-transport through reaction products seems to predominate, while at high temperatures dissolution kinetics can be explained by normal surface kinetics and appear to be independent of surface potentials".

Muir et al (149) studied the formation of sulphur from the ammonia/oxygen leach of copper and nickel sulphides. Linear anodic sweep voltammetry showed that precipitated NiS oxidized at approximately -150mV vs. SHE, with a discrepancy of nearly 50mV between different batches; whilst synthetic (pyro) NiS oxidized at the much higher potential of +500mV vs. SHE. This clearly showed that the reactivity of the NiS depends upon its history and method of preparation. These results correlated with the observation that in an ammonia/ oxygen leach, elemental sulphur can be obtained from freshly precipitated NiS, but not from synthetic (pyro) NiS.

Together with the work on CuS, it was concluded that the rate of formation of sulphur is electrochemically controlled under the stated conditions. Although the production of sulphate is thermodynamically favoured, the overpotentials associated with its formation appeared to be about 1.2V higher than the overpotential for the formation elemental sulphur at 303K. Therefore sulphur is a kinetically rather than a thermodynamically favoured product.

Price et al (150) performed a chronopotentiometric study on the anodic dissolution of Ni_3S_2 , βNiS, and a commercial nickel matte. They concluded that the matte as well as both compounds decompose with loss of nickel ions through the series of phase changes:

$Ni_{1.5}S_2 \longrightarrow Ni_{1.2}S_2 \longrightarrow NiS_2 \longrightarrow S^o + Ni^{2+}$

Much of the evidence for this sequence of intermediate metal deficient phases lies solely in the interpretation of small inflections in the chronopotentiometric wave, and the application of a simple diffusional model through use of the Sand equation to the solid state (cf. Section 1.6.2). From this analysis Price derives a diffusion coefficient $D(Ni^{2+}) = 3x10^{-12}ms^{-1}$ for the solid state diffusion during stage (I) of the reaction in $100kgm^{-3}$ H_2SO_4 solution at 323K.

Nonetheless, the chronopotentiometric results show that relatively high potentials in the range 0.8 to 1.1V vs. SCE are required to drive these reactions at the rates imposed by the applied constant current.

Thornber (76) carried out an electrochemical study on pentlandite and violarite as a thermodynamic inquiry into the stability relations during certain geological alteration events. Aspects of his work have already been discussed in Sections 1.4.2 and 1.5.1.

Working electrodes were prepared from synthetic violarite and naturally occuring pentlandite from Nepean, W. Australia. Traces of pyrrhotite were dissolved from the latter with concentrated hydrochloric acid whilst cathodically protecting the pentlandite. Electrochemical experiments were performed at 298K in a conventional three-elctrode cell under an atmosphere of nitrogen. An electrolyte of 0.1M NaCl at a variety of pH's (0 to 8) was chosen to give a similarity to a natural ground-water system. The electrochemical techniques used were: cyclic voltammetry with a potential sweep rate of $6.7mVs^{-1}$, and intermittent galvanostatic polarization (IGP) with 1s pulses of applied anodic/cathodic current densities in the range 0.01 to 8mAcm^{-2}. The variation of pH during these experimentswas continuouslymonitored.

Thornber's IGP experiments were performed to gain a knowledge of the potential of the metal sulphide surface during the interrupted period of open-circuit, with a view to obtaining a better estimation of the potential at which a particular reaction is initiated. (The choice of 1s appears rather arbitrary, whilst the uncertainty of the response time of the potential recorder for much shorter periods would be questionable, see section 2.2.3 for details). Nonetheless, a summary of Thornber's findings is given below; whilst the results of these experiments are shown in Figures 1.7.1 and 1.7.2.

The cyclic voltammograms of pentlandite and violarite showed that appreciable anodic currents (i.e. > 0.1mA), are not obtained until significantly high potentials of about 1V are reached. (Although Thornber realized the kinetic significance of this observation with respect to the obtainment of thermodynamic data (81), he did not make any reference to its direct implication to an hydrometellurgical attempt at the oxidation of these minerals under these conditions. Furthermore, the reader is left to guess the working electrode area, and what potential scale the potentials relate to. The current author assumes 1cm^2 and SHE, respectively).

Figure 1.7.3 shows a hypothetical representation of a section through a pentlandite or violarite / electrolyte interface as it reacts during a cathodic / anodic cycle of the voltammetric experiments. The sequence begins with the ideal unreacted sulphide/electrolyte interface at an anodic open-circuit potential, being reduced to a metal-rich surface with the evolution of H_2S. Some chemisorption of hydrogen is proposed at these potentials, with ultimately the evolution of hydrogen from the reduction of water.

On the positive sweep, the metal on and in the surface is oxidized into the solution, to leave a sulphur-rich surface. Sulphur enrichment progressively gives a "porous" elemental sulphur coated surface if the $pH < 4$. Progressively more metal is leached into solution, and dissolution through the sulphur layer forming on the surface probably limits the reaction rate. Orthorhombic sulphur was identified by powder XRD.

The reactions being forced on the mineral/electrolyte interface did not involve the formation of metal hydroxides, although at higher pH values some hydrolysis of metals would be expected. At $pH > 4$ the sulphur undergoes oxidation to sulphate. At lower pH's the anodic reaction leaves the surface rich in sulphur, which is subsequently reduced to H_2S during the cathodic sweep.

Because of the similarity in the bulk crystal structures of pentlandite and violarite, Thornber suggests that the pentlandite and violarite crystal surfaces which are depleted in metal atoms would be very similar. Thus he inferred that the electrochemical properties of the mineral/electrolyte interface are similar for both minerals. He proceeded to state that "at lower pH values violarite does appear to undergo a form of near-reversible reaction near its rest potential, whereas the pentlandite appears to be stabilized by some form of polarization" (ibid. p265).

Thornber emphasised that for there to be any correlation between the equilibrium relations of the bulk mineral (as portrayed by the E_h-pH diagrams) with the reacting mineral/ electrolyte interface; then rapid diffusion between the solid bulk of the mineral and the reaction interface would need to occur. Although solid-state diffusion at the temperature and conditions of the experiment could not be expected to maintain precedence with changes at the mineral/ elctrolyte interface, Thornber suggested that geological time might allow the mineral crystal composition to equilibrate with the surface.

No data is available for the diffusion of metals in pentlandite or violarite. However, by comparison with pyrrhotite, Thornber adopted a diffusion coefficient at 298K of $10^{-21}m^2s^{-1}$, and arrives at an ionic flux (J) of $10^{-9}molm^{-2}s^{-1}$. Since the diffusing metal species are assumed to carry a divalent positive charge, this represents a current density of $2JF = 2x10^{-4}Am^{-2}$. During the supergene process, the solid-state diffusion currents flowing over geological periods of time would therefore be very low. Hence, they would require a much smaller overpotential than those required in the electrochemical experiments, and therefore represent near equilibrium conditions during the phase transformation. The pH of the environment during supergene alteration is likely to be in the range 7 to 8.5. (Presumably at lower values of pH, if indeed such values could exist geologically, the oxidizing influence of H^+(aq) would predominate with the oxidation of pentlandite to H_2S).

Concerning the hydrometallurgical implications of this work, Thornber envisaged the following industrial process:

"Acid leaching of pentlandite and violarite should be possible at low temperatures if some means could be devised whereby the potential of the sulphides could be made alternately oxidizing and reducing so that metal could be removed as M^{2+} and excess sulphur dissolved as H_2S". The current author concludes that at least in thermodynamic terms this is equivalent to a direct acid leach of pentlandite where H^+(aq) acts as an oxidant; although the scheme may be of some hypothetical use for violarite.

Liao Pinjm, used cyclic voltammetric techniques to study the oxidation of the violarite surface. Within the pH range 5.6 to 9.2, violarite was oxidized to nickel and ferrous sulphate with an overpotential of approximately 0.6V. At pH > 9.2 violarite formed an insoluble film on the violarite surface, comprized of hydrated iron oxides, which retard the reaction (164).

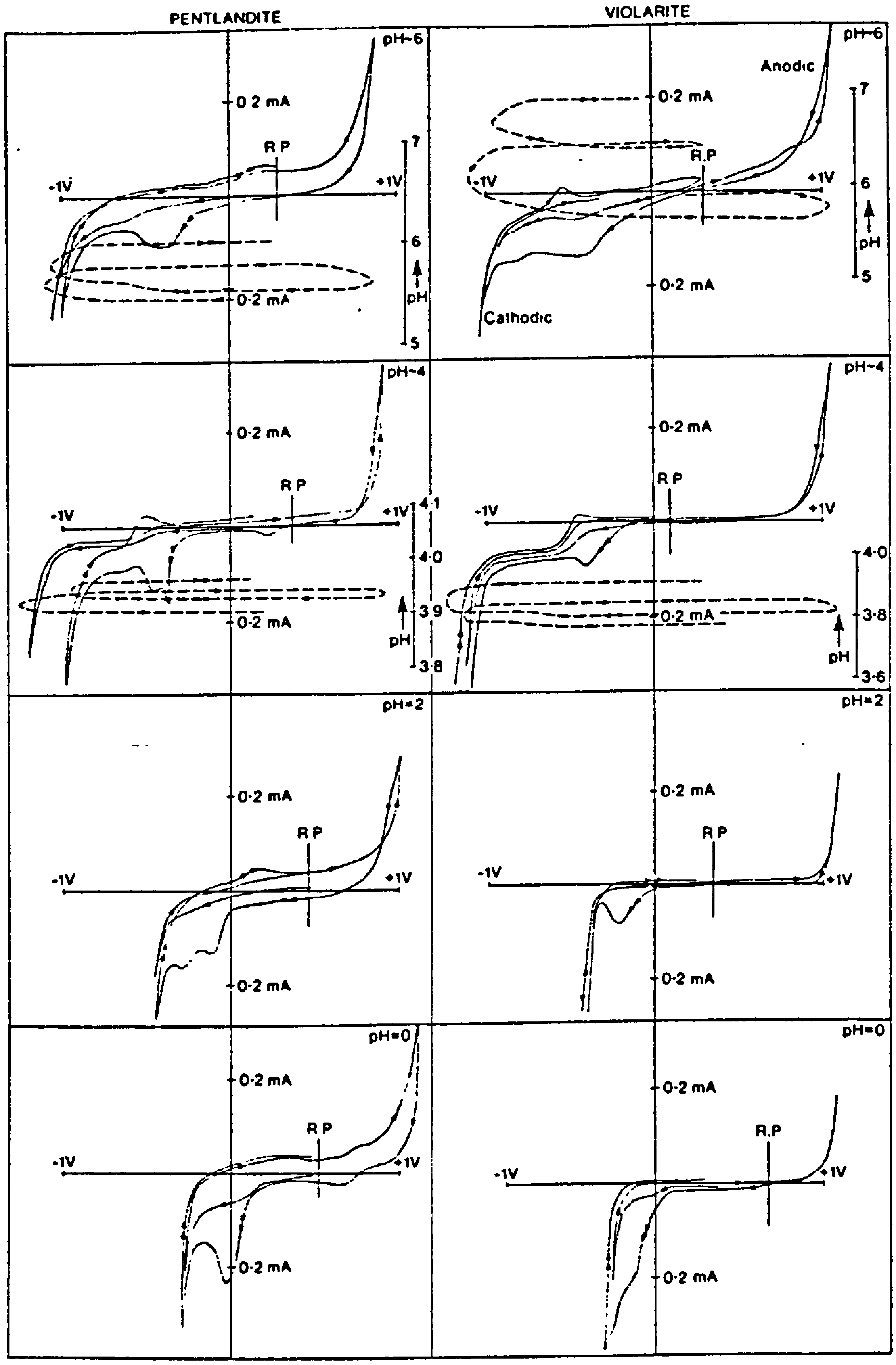

Figure 1.7.1

Cyclic voltammograms of pentlandite and violarite in 0.1M NaCl solution and various pH values. Solid lines indicate current; dashed lines, pH values. (After Thornber (76)).

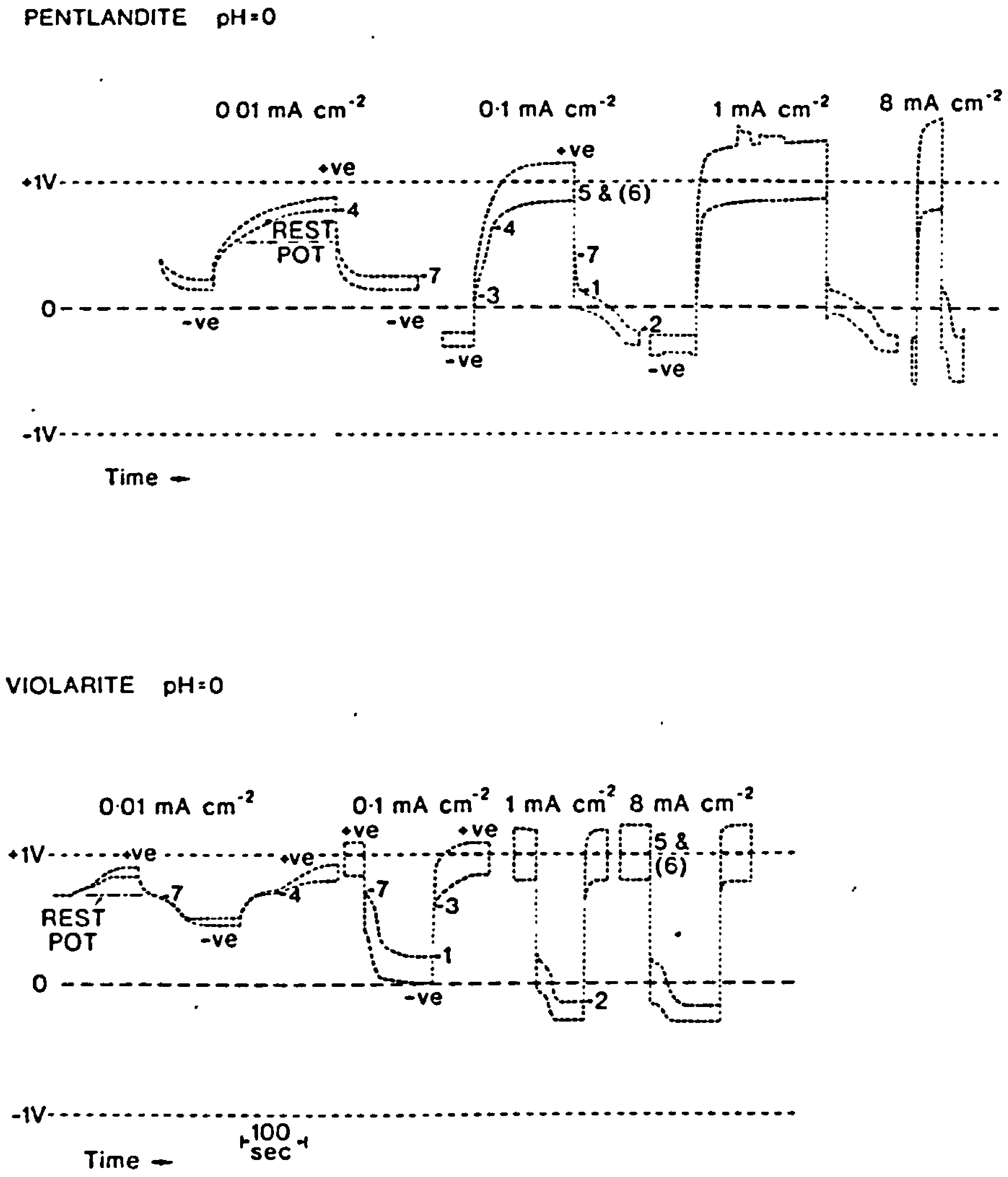

Figure 1.7.2

IGP traces for (a) pentlandite and (b) violarite, at pH = 0. (After Thornber (76)).

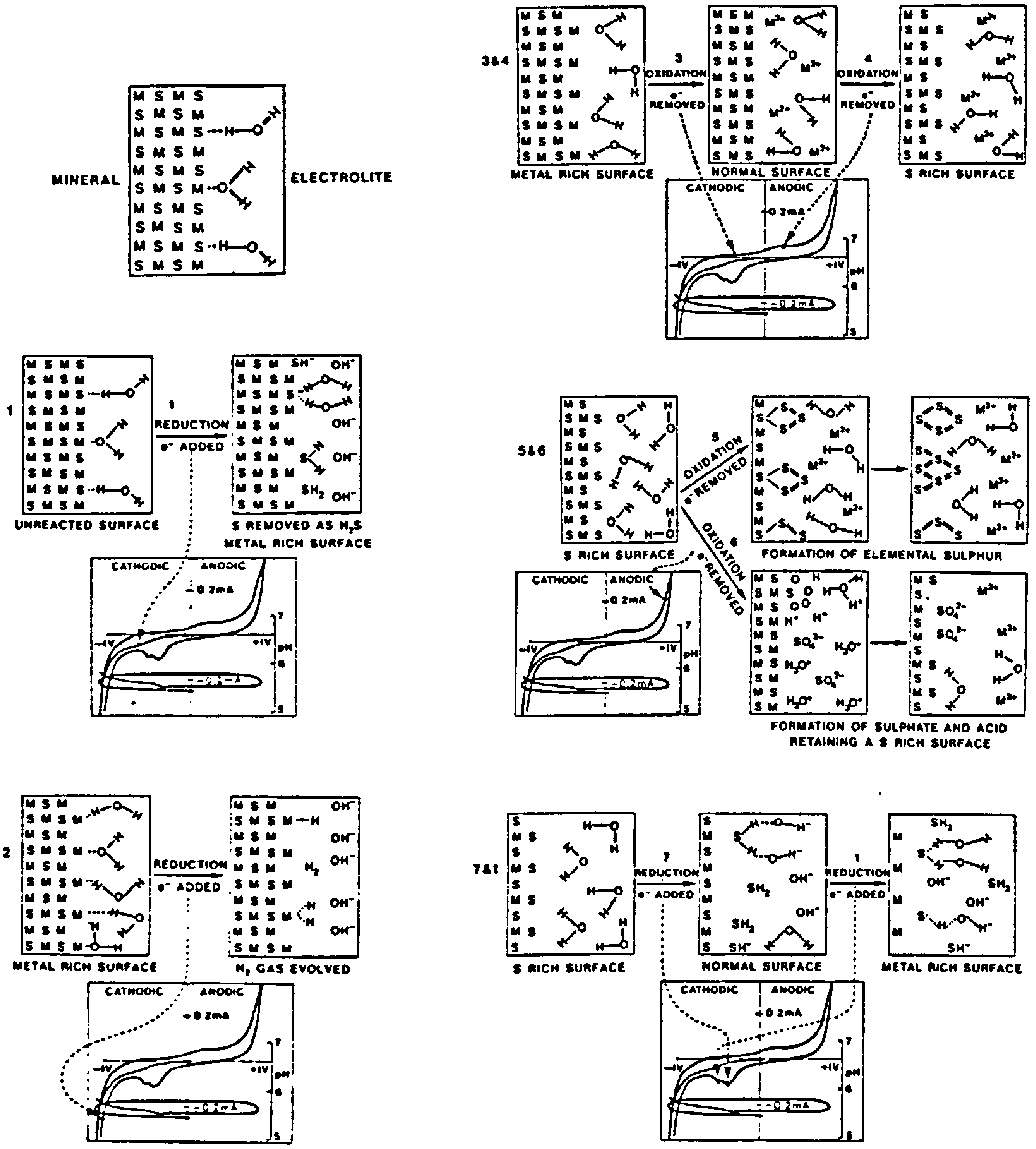

Figure 1.7.3

Hypothetical representation of a section through a pentlandite (or violarite) surface/electrolyte interface as it reacts during a cathodic-anodic potential cycle. Numbers in on this figure relate to those on the IGP traces in Figure 1.7.2.

(After Thornber (76)).

2 EXPERIMENTAL

2.1 SYNTHESIS OF NICKEL-IRON-SULPHIDES: PREPARATORY TECHNIQUES AND PRODUCT ANALYSIS

2.1.0 Introduction

The feasibility of growing single crystals of practical size (i.e. >4mm in diameter) for electrochemical experimentation was investigated from the existing literature.

Crystal growth via a transport medium e.g. halogen, appears successful for metal sulphides of the pyrite structure (77). Euhedral crystals 3-4mm in diameter, of FeS_2, CoS_2, and NiS_2 have been grown by vapour transport with chlorine in sealed silica tubes in a thermal gradient. The use of halogen reduces the otherwise high sulphur fugacity required for the formation of volatile sulphide species. The primary reaction is the temperature dependant equilibrium:

$$MS_2(s) + Cl_2(g) = MCl_2\ (g) + (2/x)S_x(g) \qquad (2.1.1)$$

In the crystal growth of the $Fe_xCo_{1-x}S_2$ and $Ni_xCo_{1-x}S_2$ solid solutions (78) (also of pyrite structure), bromine is more suitable for vapour transport than either chlorine or iodine on thermodynamic grounds. The free energies of formation of the volatile species: $FeBr_2$, $CoBr_2$ and $NiBr_2$ are fairly similar, and hence reduce the preferential transport of FeS_2, that occurs when using chlorine. Iodine is unsuitable since the free energy changes for the formation of the corresponding metal iodides are negative only above 827°C. However, even with bromine, temperatures >677°C are required, and it is therefore unsuitable for crystal growth of the lower temperature minerals:

pentlandite, <610°C; violarite, <461°C; argentopentlandite, <455°C (cf. Section 1.2).

A vapour-liquid transport technique has been employed for the single crystal growth of the thiospinels: $CoCr_2S_4$ and $FeCr_2S_4$, by reacting $CrCl_3$ with CoS and FeS respectively (79). Unfortunately this technique does not lend itself to violarite synthesis due to the high temperatures involved and unfavourable stoichiometries. Single euhedral crystals of monosulphide solid solution (mss), approximately 0.1mm in diameter have been grown by sublimation in thermal gradients of $500^{o}Cm^{-1}$ at temperatures >900°C for 1 week in a vertical furnace (9).

From Section 1.2 it is evident that neither crystals of violarite nor pentlandite can be grown directly from a melt under conditions of equilibrium vapour pressure. Violarite has enhanced complications concerning its low thermal stability limit (which eliminates the possibility of using the above growth techniques), and the kinetic competition from pyrite nucleation (cf. Section 2.1.2). Pentlandite may lend itself to crystal growth by sublimation; however, due to its relatively low thermal stability (viz. 610°C) this may prove unsuccessful (cf. Section 1.2.1). Consequently, in this current work synthesis was directed at obtaining polycrystalline material with a homogeneous phase from starting elements of known purity.

2.1.1 Synthesis of Pentlandite ($Fe_{4.5}Ni_{4.5}S_8$)

Three 100g batches of pentlandite, namely: SynPn1, SynPn2, SynPn3, were synthesized (with an increasing degree of success) by heating together iron, nickel, and sulphur powder in the appropriate stoichiometric ratio with mass percentages: 32.554%, 34.223%, and 33.223% respectively; in an evacuated double bulbed fused "96%" silica glass vessel (39mm I.D., 43mm O.D.) similar to that described by Ferreira (1) (cf. Figure 2.1.1) with dry sulphide synthesis techniques developed from those of Kullerud (15).

The starting materials were Johnson Matthey "Specpure" sulphur and iron powder, with nickel powder (Sample No. 9976-S) donated by Sherritt Gordon Mines Ltd. (cf. Section 2.5 for analyses). All materials prior to, and at various intermediate stages during the synthesis were stored in a vacuum desiccator. The iron and nickel powders were reduced in a stream of hydrogen: 0.2dm^3 per minute, and argon: 1.5dm^3 per minute (controlled by appropriate gas-flow meters) at 600^{o}C for 5 hours to remove any oxygen contamination. This was achieved by placing the metal powders in silica "boats" enclosed within an air-tight stainless steel tube, subsequently purged with argon: 1.5dm^3 per minute for 1 hour at 200^{o}C prior to initiating the reduction.

After this prescribed period of reduction at 600^{o}C, the furnace was switched off and the contents allowed to cool to <200^{o}C in the same reducing atmosphere, after which a slight positive pressure of argon (0.1dm^3 per minute) sufficed, to accomplish further cooling to ambient temperature. Failure to cool in a reducing atmosphere, along with the substitution of cheaper "white-spot" nitrogen in place of argon during an earlier attempt, resulted in visible oxidation of iron with formation of a black powder, viz. magnetite. The successfully reduced iron was only mildly sintered, and therefore readily ground to a coarse powder with an agate pestle and mortar. The sulphur powder was deemed to be of sufficiently high purity to allow it to be used directly without the necessity of pre-drying (5). The effect of any moisture content on the weighings was therefore considered to be negligible, whilst any moisture that was present would be adequately removed during subsequent evacuation. The interior of the silica vessel, prior to use, was cleansed with a small volume of concentrated sulphuric acid followed by distilled water and finally ethanol (absolute); then dried under the hot tap whilst under vacuum (water-pump).

The powders were weighed in a glass "boat" to an accurracy of +/-0.5mg using a Mettler AC 100 balance. The sulphur powder was poured into the lower bulb of the vessel, whilst the nickel and iron powders were transferred into the upper bulb using a specially adapted funnel and a magnet. The use of a double bulb was adopted from the precept that if the metal and sulphur are physically separated such that the reaction occurs only via sulphur vapour as opposed to the liquid, then the reaction proceeds at a more controlable rate with a diminished possibility of an explosive reaction, since the reaction is highly exothermic (18).

The vessel was necked, then evacuated using a rotary-pump and two mercury diffusion pumps with two liquid air traps, to a pressure <0.08Pa (0.0006 torr) (2); then sealed in an oxygen-natural gas flame. The sealed vessel was placed in a horizontal Kanthal wound tube furnace (Carbolite CTF2 1200) capable of operating up to 1200°C; with the bulb containing the metal powder in the hottest zone, whilst the sulphur was located in the relatively cooler region of the furnace. The temperature was controlled by a Gallenkamp QPL 397 HJ temperature control unit with a NiCr/NiAl thermocouple.

The silica vessel was inserted in an intermediate mullite furnace liner (50mm I.D., 60mm O.D.) whose coefficient of expansion is similar to that of silica, yet with a higher softening temperature.

This served as a precaution against the possibility of the silica vessel expanding under the influence of internal pressure, which might on cooling, cause the alumina furnace liner to fracture (a problem more relevant during the synthesis of mss, cf. Section 2.1.2). As an additional safeguard to the contents of the vessel, the mullite tube was fixed at both ends with silicon rubber bungs such that the vessel could be contained in an inert atmosphere of argon (0.1dm^3 per minute). This was desirable in order to prevent oxidation occuring to the product in the event of a fracture to the vessel during synthesis, especially whilst cooling.

The temperature was slowly raised (100^{o}C per hour) to approximately 500^{o}C. The temperature profile of the furnace implies that the bulb containing the sulphur was near to 444.6^{o}C, thus inducing an internal sulphur vapour pressure of approximately 101kPa at that point.

Due to the low vapour pressure of iron and nickel (at the temperatures envisaged during synthesis) homogenization of the phase is inevitably achieved through solid state diffusion of the metal atoms, such that a reduction of the intergranular vapour space by initial fusion of the charge should enhance the rate of equilibration (13),(5),(17).

Consequently, it was desirable to at least partially melt the charge. As may be recalled from Section 1.2.1, at 610°C pentlandite thermally decomposes to $(Fe,Ni)_{1-x}S$ + $(Ni,Fe)_{3\mp x}S_2$. At higher temperatures this latter phase becomes metal deficient such that by 862°C (the incongurent melting point) it too, thermally decomposes to yield mss and a metal rich Fe-Ni-S liquid ("central homogeneous liquid"). This corresponds to a strong thermal effect at 862°C in the Differential Thermal Analysis of synthetic pentlandite and the melting effects in natural pentlandite (Frood mine, Sudbury) viz. 864°C to 881°C (3), (cf. Figure 2.1.2).

Once all the sulphur had diffised into the metal, which could be observed by the disappearance of the yellow coloured vapour (<3 days), the temperature was increased steadily to approximately 900°C to instigate fusion within the charge. After 18 hours at this temperature the charge was slowly cooled to ambient temperature. Slow cooling was initially considered to be desirable in order to reduce the thermal shock to the vessel, especially during the sulphide phase transitions, thus attempting to prevent subsequent fracturing. However, as reveалled later in this section, such a practice may be detrimental to the homogeneity of the product.

On inspection, the vessel was found to have fractured in the vicinity of the sulphide in both the synthesis of "SynPn1" and "SynPn2". In "SynPn1" this resulted in oxidation to the product, thus requiring a repetition of the synthesis*. During the second attempt (i.e. "SynPn2") a non-

---

* "SynPn1" was reannealed in a similar fashion to that of "SynPn2" and used in experimental work.

return valve was attached to the argon outlet of the furnace tube, thus preventing an insurgance of air caused by a drop in internal pressure, in the advent of a fracture to the vessel.

As a consequence of this precaution, the charge (SynPn2) remained intact during cooling except for a thin dark coloured film which occured irregularly along the posterior of the otherwise lustrous metallic sulphide slab. This film (possibly oxide) was effectively removed by gentle scraping with a stainless steel spatula.

The product was immensely porous and brittle. The presence of at least two distinct shades of yellow suggested an appreciable level of inhomogeniety; as was to be expected after such a brief reaction period. The anterior surface, when viewed under a low powered binocular microscope, revealed a "columnar" structure reminiscent of its previous molten state. This confirmed that a temperature of 900^{o}C is sufficient to at least partially melt the charge (cf. Section 1.2.1).

In order to form compact homogeneous "slugs" suitable for electrode construction (cf.Section 2.3.3.3), the product was dry-ground with an agate pestel and mortor (the use of solvents during grinding being considered unnecessary). 50g of the subsequent powder was placed inside a "96%" silica glass tube (11mm I.D., 14mm O.D.). A plug of silica wool was inserted to compress the sulphide powder, which also served to prevent the escape of powder during evacuation and provided a convenient thermal buffer during sealing.

Once sealed, the silica tube was placed inside that of another (20mmI.D.,22mmO.D.) and likewise evacuated and sealed. This ensured a continued isolation of the contents from the atmosphere in the event of a rupture to the inner tube during the annealing stage. This procedure was then repeated for the other 50g of product. The pair of double sealed tubes were placed at the "hot zone" in a vertically orientated tube furnace and slowly heated to 950°C in order to fuse the contents.

It is reported that annealing below 500°C requires considerable time in order to obtain a homogeneous product (30); whilst annealing above 610°C,with subsequent rapid cooling (quenching) through the phase transition at 610°C, results in the formation of two condensed phases. Kullerud (3) states that these can be distinguished by reflected light microscopy with oil immersion in which one phase appears isotropic with the other anisotropic; yet he reports that X-ray diffraction "confirms" that both are pentlandite! He suggests that this textural difference is the result of disequilibrium, which can be prevented by slow cooling through this phase transition (3). A similar problem was encountered by Kelt (4) in her attempt to produce a homogeneous pentlandite by rapid cooling from 1200°C, which yielded a mixture of pentlandite and pyrrhotite. For these reasons, after 1 hour at 950°C the charge was slowly cooled to 550°C (66) and annealed at this temperature for 40 days; after which time the furnace was switched off and the charge left to cool to room temperature.

The contents of the tubes had fused together to form a "slug", though this was of varying texture. The top end proved to be very porous and friable, whilst the middle and lower sections were far more compact.

These textural differences are further revealed in the results from reflected light microscopy (cf. Figure 2.1.3), powder-XRD (cf. Appendix D), and EMPA (cf. Appendix E). See Figure 2.1.4 for a schematic longitudinal cross-section of the "slug".

The top portion was mainly comprised of the anisotropic phase monosulphide solid-solution (mss) with a stoichiometry approximating to $Fe_{0.74}Ni_{0.21}S$. This was interspersed with minor amounts of an exsolved isotropic phase, namely: Ni-rich pentlandite of composition $Fe_{4.4}Ni_{4.6}S_8$.

The middle and lower portions, which accounted for a far greater percentage of the total volume of the charge, were essentially composed of stoichiometric pentlandite ($Fe_{4.5}Ni_{4.5}S_8$); with minor amounts of the Fe-containing, metal-deficient, isotropic, high-heazlewoodite solid-soluton ($Fe_{0.2}Ni_{2.7}S_2$).

From these results it is evident that the charge has segregated into a metal deficient portion at the top and a metal rich portion in the middle and lower sections. This phenomenon was dictated by the equilibrium phase relationships at 950°C in which the more dense and metal rich "central homogeneous liquid" had sunk to the bottom, with the less dense and metal deficient monosulphide solid-solution (presumably still solid at 950°C) floating on top (cf. Section 1.2.1 for phase equilibria in the Fe-Ni-S system). Annealing at 550°C for 40 days had little apparent effect in obtaining equilibration. This suggests that solid state diffusion of Fe and Ni within this system, and at this moderately high temperature, is rather slow.

The two tubes of "SynPnl" (which were reannealed simultaneously with "SynPn2") yielded identical results. Nonetheless, the lower portion of the two rods which consisted of pentlandite with minor amounts of iron containing high-heazlewoodite solid solution, were kept and used in experimental work and therein referred to as SynPn1.

In an attempt to circumvent this problem of segregation, the inhomogeneous product (SynPn2a) was reannealed yet again, although this time in a "horizontal" tube furnace*. The temperature was raised to only 850°C (for 1 hour) which should effectively sinter the grains without inducing significant melting which occurs at temperatures > 862°C; before annealing at 550°C for 38 days.

A third batch of pentlandite (SynPn3) was prepared in a similar fashion to that of "SynPn2", although this charge (whilst still in the double silica vessel) was heated to only 600°C. This moderate temperature was considered sufficient since a prerequisite of the synthesis at this stage was the attainment of a controlled reaction between sulphur and metal without inducing a fracture to the vessel. The homogenization was orchestrated in the subsequent annealing stage, conducted within the narrower double-sealed tubes as described earlier (viz. the reannealing of SynPn1). Thus, "SynPn3" was re-annealed simultaneously with the second re-annealing of "SynPn2".

The final products after annealing revealed that the charge had slumped and thereby adopted the mould of the silica tube. This phenomenon may however, be due to creep

---

* Aknowledgement is given to Dr. Mustughachia of the Department of Ceramics, for the use of two "laboratory built" horizontal tube furnaces with substantially long and well defined "hot-zones".

rather than actual fusion, since 850^{o}C should not be sufficient to cause the latter.

Results from Powder XRD and EMPA, on a cross-sectional sample taken from the centre of the rod (cf. Appendices D.1 and E.1), reveal that the major phase is pentlandite with only trace amounts of mss, whilst $(Ni,Fe)_{3\mp x}S_2$ was not detected by either technique. EMPA reveals that the stoichiometry of pentlandite in the lower regions of the cross-section is $Fe_{4.3}Ni_{4.7}S_8$, whilst that near the top occurs within the range: $Fe_{4.3}Ni_{4.7}S_8$ to $Fe_{4.4}Ni_{4.6}S_8$. Furthermore, the mss $(Fe_{0.78}Ni_{0.17}S)$ is essentially concentrated near the top. Reflected light microscopy reveals a more porous texture in the upper regions.

As a first order of approximation from the above analyses, the percentage yield of pentlandite is approximately 95%. These results are typical of those of other workers, namely: Kelt(4), Tzamthis(14), Thornber (76), and Kullerud (3); though none of these workers offer any explaination as to the apparent inadvertent metal deficiency of this assemblage (i.e. the absence of heazlewoodite vis à vis pyrrhotite / mss). However, it is conceivable that the pentlandite is metal-rich, although this was neither inferred from either the EMPA or the powder XRD results (cf. Appendices E and D respectively); nor is it favoured from crystal structure and chemical bonding considerations (cf. Section 1.3.1). The presence of $(Ni,Fe)_{3\mp x}S_2$ in "vertically" annealed charges, together with a knowledge of phase equilibria within the Fe-Ni-S system (cf. Section 1.2.1), suggests that this phase is also likely to occur in conjunction with mss in the horizontally annealed charge; its apparent absence is therefore unexplained. The possibility of an effective partial removal of metal by the formation of oxides is unlikely since another metal sulphide i.e. Synthetic mss, has been prepared with success by similar techniques elsewhere in this current work (cf. Section 2.1.2).

2.1.2 Synthesis of Violarite ($FeNi_2S_4$)

100g of violarite was synthesized by a two-step process in a similar manner to that described by Craig (7). During his work on violarite stability relations, he observed that if the synthesis is attempted by direct reaction of the elements at either 300°C or 400°C, then the result is a product comprised predominantly of pyrite, vaesite and mss, with only a trace amount of the desired violarite. Extensive regrinding and longer annealing periods produced little improvement on the yield. To circumvent the rapid formation and metastable preservation of pyrite and vaesite he employed a two-step process involving the initial preparation of an mss and its subsequent reaction with additional sulphur. In this work a similar regime to Craig's was adopted in conjunction with the apparatus described in the previous section (2.1.1).

100g of mss with a net stoichiometry of $FeNi_2S_{3.25}$ was prepared by heating together iron, nickel and sulphur powder with mass percentages: 20.128%, 42.319%, and 37.553% respctively, with the sulphur segregated from the metal as described in Section 2.1.1. This stoichiometry was chosen to correspond to a desired atomic ratio of Fe:Ni = 1:2, whilst also allowing the composition to lie within the domain of mss down to a temperature of at least 300°C; based on the thermal stability limits of mss as defined by Naldrett et al (10). The temperature was slowly raised to approximately 500°C till all the sulphur had diffused into the metal, then gradually increased further over a period of 6 hours to 1100°C and held at that temperature for 1 hour. Tzamtzis (14) reported that initial fusion of the charge at high temperature considerably reduces the length of time required for the synthesis. This should therefore avoid the necessity of an intermediate grind and prolonged annealing as was performed by Craig (7), and Naldrett et al (10). Thus, after 1 hour at 1100°C the furnace* was switched off and the contents left to cool for 18 hours to ambient temperature.

From the Fe-Ni-S phase relationships in Section 1.2, it is apparent that below 275°C, homogeneous mss breaks down to form a solid emulsion exsolution texture comprised of two mss phases: $(Fe,Ni)_{1-x}S$ and $(Ni,Fe)_{1-x}S$ (8). This presented an uncertainty as to whether the cooling rate would be sufficiently fast enough to prevent the formation of these two phases, or if quenching of the charge below 280°C is indeed necessary (as was practiced by Tzamtzis below 600°C (14)). However, it was anticipated that a homogeneous mss

---

* Above 1050°C there is an irreversible change from vitreous silica (of which 96.5% of the reaction vessel is composed) to β-cristobalite. β-cristobalite should not initially harm the vessel since its coefficient of thermal expansion is similar to that of vitreous silica. However, on cooling, the β-cristobalite changes either to α-quartz via β-quartz at 570°C, or to α-cristobalite at about 270°C. These phase changes are accompanied by large volume changes and consequently they are not compatible with the low expansion vitreous substrate, which will inevitably result in shattering the vessel on cooling. Fortunately, the initial irreversible process occurs rather slowly, so any β-cristobalite produced at 1100°C during the one hour should be negligible. It is reported that the maximum servicetemperature for "96%" silica glass is 900°C (117).

should prevail on account of the kinetic restraints (i.e. slow solid-state diffusion) impeding the obtainment of equilibria under the prevailing parameters of temperature and time.

During cooling the vessel had severely shattered, although the product remained intact. The sulphide "slab" had a deep yellow colour with a bright metallic lustre, although some parts of the surface had an optically thin film (presumably oxide) showing the interference colours: blue/violet. The inheritance of a miniscus around the edge of the slab implies that the charge had solidified from a molten state.

A sample of the product was taken for analysis. Powder XRD data (cf. Appendix D.3) indicates the sole presence of mss. However, the peaks are rather broad; i.e. the characteristic d_{102} lattice spacing yields a distribution of values ranging from 0.1973nm to 0.2036nm (cf. Figure 2.1.5). These extremities correspond to Ni-rich and Fe-rich mss respectively (2). Since the metal to sulphur ratio has a profound affect on the d_{102} values (2), quantitative information regarding these mss composition limits cannot be extrapolated from the data of other workers. Nonetheless, the existance of a continuous spectrum between these two values ($2\theta = 44.5$ to 46^{o}) means that the cooling profile had just surpassed the critical rate for which mss breaks down into two Mss phases of different composition (cf. Section 1.2.1).

EMPA data (cf. Appendix E.3) revealed only homogeneous mss ($FeNi_2S_{3.25}$), indicating that the scale of phase segregation is below the resolution limit of the EMPA.

Chemical analysis (cf. Sections 2.4.5 and 2.4.6) confirmed a bulk composition of 20.2% (mass) Fe, 41.1% (mass) Ni, and 37.1% (mass) S; corresponding to the desired stoichiometry of $FeNi_2S_{3.25}$. 92.025g of mss was ground and reacted with 23.077% additional sulphur powder (i.e. 7.975g), each being separately contained in the two compartments of the silica vessel as described in Section 2.1.1.

Although the upper thermal stability limit of violarite ($Fe_{0.92}Ni_{2.08}S_4$) is 416°C, for $FeNi_2S_4$ it lies some where between 300°C and 400°C. An attempted synthesis by Craig (7) at 400°C resulted in the formation of considerable amounts of pyrite, formed because of the extension of the pyrite-Mss tie lines between mss ($FeNi_2S_{3.25}$) and violarite ($FeNi_2S_4$) at this temperature; cf. Section 1.3. Since the violarite produced at 400°C contains less iron than is indicated by the formula $FeNi_2S_4$ some of this pyrite is stable; whilst the additional portion is presumed to be a metastable product resulting from a rapid initial reaction of the mss and sulphur. Subsequently, insufficient sulphur is left to permit a complete reaction of the mss. Just as with the attempts of a direct one-step synthesis from the elements, re-equilibration (i.e. breakdown of the pyrite) is exceedingly slow.

As a consequence of the work done by Craig (7),(11), the charge in this present work was annealed at 295°C for 34 days, since at this lower temperature, tie lines from pyrite are excluded from the compositional changes of $FeNi_2S_{3.25}$ to $FeNi_2S_4$; (cf. Figures 9, and 10).

Since violarite is reported to be thermally stable down to at least 200°C (7), quenching of the charge was thought to be unnecessary; thus the furnace was switched off and the contents allowed to cool to room temperature.

The product (SynVlla) was mildly sintered and therefore highly friable, with a morphology reminiscent of the previous mss grains. The colour was predominantly of a dull violet/grey, whilst the larger crystals showed more of a metallic luster.

Powder XRD data (cf. Appendix D.4) revealed the presence of minor amounts of pyrite and millerite. Reflected light microscopy showed that the core of some grains was comprised of an anisotropic phase (cf. Figure 2.1.3). EMPA (cf. Appendix E.4) revealed in addition, a distinct compositional segregation between two violarite phases within the individual violarite grains. The core of such grains was composed of Ni-deficient violarite ($Fe_{1.2}Ni_{1.8}S_4$) with the rim composed of Ni-rich violarite ($Fe_{0.5}Ni_{2.5}S_4$) approaching that of polydymite. The radial distribution of Ni and Fe (cf. Figure 2.1.6) indicates an abrupt peripheral change between these two compositions rather than a continual variation in solid-solution.

Since $Fe_{1.2}Ni_{1.8}S_4$ is regarded as a metastable phase (cf.Section 1.2.1) this textural feature is considered to be a kinetic phenomenon. A possible mechanism for this phenomenon is an internal friction caused by mechanical stress during cooling vis à vis decrease in molar volume (unit-cell parameter) from $Fe_{0.5}Ni_{2.5}S_4$ to $Fe_{1.2}Ni_{1.8}S_4$ (if such a trend (53) is extrapolatable beyond $FeNi_2S_4$ to more Fe-rich compositions, namely: $Fe_{1.2}Ni_{1.8}S_4$). It is interesting to note that Vaughan and Craig (53) emphasise that compositions more Fe-rich than $FeNi_2S_4$ have not yet been synthesized!

The product (SynVlla) was ground and inserted into 8mm I.D. and 6mm I.D. silica tubes by a similar procedure to that described in the previous section (cf. Section 2.1.1). It is not advisable to attempt to melt the product, since as stated earlier, the re-equilibration of the decomposition products (pyrite and millerite), is exceedingly slow (7). Therefore the charge was sintered at 295°C for 38 days in an attempt to produce a compact rod of homogeneous violarite suitable for electrode construction.

After this time, the tubes were removed from the furnace and allowed to cool fairly rapidly to ambient temperature. The annealed product (SynVllb) was particularly friable. Powder XRD showed only trace amounts of pyrite and millerite (cf. Appendix D). However, EMPA (cf. Appendix E) of the violarite grains revealed the same compositional/textural phenomenon as before, although to a less severe extent, i.e. a core of Ni-deficient $Fe_{1.1}Ni_{1.9}S_4$ surrounded by a rim of Ni-rich $Fe_{0.90}Ni_{2.1}S_4$.

To investigate this phenomenon further, the 6mm I.D. silica tube which had not yet been opened, was reannealed at 295°C for 4 days, then quenched with dry ice. The annealed product (SynVllc), was analysed by EMPA, from which the "Fe/Ni maps" revealed that the same phenomenon still persisted (cf. Figure 2.1.7).

In a final attempt to produce a less porous electrode, a portion of "SynVllb" was ground and pelletized using a hydrostatic technique. A pressure of 280MPa was applied which yielded compact pellets of 6mm diameter and approximately 10mm in length. These were then inserted into a 8mm I.D. silica tube, evacuated and sealed as described above, annealed at 295°C for 7 days, and then quenched with dry ice. The sintered pellets (SynV11d) were surprisingly more friable than those of previous batches, and had an average density of $3740kgm^{-3}$, which yields an average relative density for the pellets of 79% (cf. Appendix B.2).

This lack of fusion reflects on the slow solid-state diffusion of Fe and Ni within this phase; compared with the satisfactory preparation of pellets of AgCuSe by application of this pressure alone (153).

Although the synthesis of polydymite (Ni_3S_4) is not an integral part of this work a brief mention is perhaps worthwhile in the context of violarite synthesis. Craig (7) found that attempts to synthesize homogeneous violarites more nickel rich than $Fe_{0.25}Ni_{2.75}S_4$ resulted in the formation of substantial amounts of NiS_2 and residual mss in addition to the spinel phase. In effect, he suggests that this is due to the sluggish formation of the spinel phase being superceded by the alternative nucleation of vaesite at higher sulphur fugacities.

Kullerud and Yund (20), during attempts to synthesize homogeneous polydymite, found that the best results were obtained with nickel and sulphur as starting materials, rather than millerite or vaesite intermediates reacted with additional sulphur. Nonetheless only 80% polydymite, contaminated with NiS_2 and $\alpha Ni_{1-x}S$, was produced even after annealing for eight months at 300°C with three regrinds.

However, Lundqvist (64) reports that it is possible to synthesize polydymite merely by boiling whilst stongly agitating under oxidizing conditions (air) for at least

1 hour, the primary precipitation ($Ni(SH)_2$) obtained from the boiling mixture of concentrated aqueous $Na_2S_2O_3$ added to dilute aqueous $NiSO_4$.

2.1.3 Synthesis of Argentopentlandite ($Fe_5Ni_3AgS_8$)

Mandziuk and Scott (16) have described a two-step process for the synthesis of argentopentlandite involving the initial preparation of mss and its subsequent reaction with the appropriate amount of silver. However, they appear to have overlooked the fact that if $(Fe,Ni)_8AgS_8$ is prepared in this manner, then the intermediate nickel-iron sulphide with the desired composition $(Fe,Ni)_8S_8$ (i.e. metal to sulphur atomic ratio = 1:1) lies outside the domain of mss (10),(50). For temperatures below the thermal stability limit of pentlandite ($Fe_{4.5}Ni_{4.5}S_8$) viz. 610°C, the tie lines on the corresponding ternary phase diagrams indicate that the composition $(Fe,Ni)_8S_8$ will exist as a solid mixture of mss and pentlandite. However, this may not affect the overall regime since these two phases are among the products of the thermal decomposition of argentopentlandite at approximately 455°C which, although somewhat slow, is nevertheless reversible. Even with the possibility of quenching the charge from a high temperature, the production of a metastable "$Fe_5Ni_3S_8$" is rather dubious on account of the phase relations as described in Section 1.3; (i.e. this composition occurs within the divariant field containing the phases: mss, vapour and the non-quenchable $(Ni,Fe)_{3\mp x}S_2$; at temperatures above 610°C). Furthermore, this two-step procedure is rather tedious, so the alternative option of a more direct synthesis of argentopentlandite, likewise described by the above workers

(16), was adopted.

100g of argentopentlandite was synthesized by heating "Specpure" silver crystalline pieces (obtained from Johnson Matthey Ltd.), iron, nickel and sulphur powder (cf. Section 2.5) with the mass percentages: 13.159%, 34.065%, 21.487%, and 31.289% respectively; by a similar procedure as described for the synthesis of pentlandite in Section 2.1.1. Once all the sulphur had diffused into the metal at 500°C, the temperature was gradually raised (100°C per hour) to 850°C and held there for 2 hours to instigate at least partial fusion within the charge and to promote solid-state reaction and homogenization. The charge was then slowly cooled to ambient temperature.

The vessel had fractured, and a dark coloured film was visible in patches along the otherwise bright metallic yellow/white sulphide slab where it was in intimate contact with the fractured vessel; viz. synthesis of pentlandite (Section 2.1.1). This film was gently scraped off. Close to the partition between the two glass bulbs, and resting on the sulphide slab, lay a "nest" of lustrous black crystals, with a physical appearance corresponding to that of acanthite (Ag_2S), which may have formed by sublimation at this cooler end of the vessel. The sulphide "slab" was visibly inhomogeneous, whilst the "frozen" inverted miniscus indicated a previous molten state.

The product was then converted into a "slug" suitable for electrode construction by the procedure as described in Section 2.1.1. The temperature of the charge (whilst in a vertically orientated furnace) was raised to 850°C and held at that temperature for 3 hours to ensure adequate fusion.

It was then slowly lowered to 440°C and annealed at this temperature for 34 days in an attempt to achieve homogenization, before slowly cooling to ambient temperature.

On visual inspection of the annealed product, it was clearly evident that a similar problem of segregation had occured whilst annealing in a vertical position as was concluded in Section 2.1.1 for pentlandite. The top of the rod was immensely porous and friable with a dull grey colour, whilst the middle and lower sections were more compact, with a large dispersion of small grains of elemental silver, which gave this region of the rod an overall white metallic luster. EMPA on a section from the bottom of the rod, revealed a minor phase of stoichiometry approximating to $Fe_{4.3}Ni_{4.7}Ag_{0.1}S_8$ (cf. Appendix E).

This unsuccessful product was reannealed in a horizontal furnace, as in the case during the synthesis of pentlandite (cf. Section 2.1.1). In synthesizing argentopentlandite, one is at a dilemma as to what temperature to select during the annealing. If the charge is annealed much "above" 400°C then there is a risk of encroaching on the decomposition temperature of 455°C, which should obviously be avoided. However, annealing much "below" 400°C will inevitably extend the time required for satisfactory homogenization, due to the slower solid-state diffusion rates at lower temperarures. Thus, the temperature was initially raised to, and held at, 850°C for 15 minutes, before lowering and annealing at 400°C for 66 days. After such time the furnace was switched off and the charge allowed to cool to room temperature.

The product (SynAgPnlb) was golden/brown coloured, with a distinct lack of the previous metallic silver sheen. The charge had slumped and adopted the mould of the silica tube. Powder XRD results reveal that the predominant phase is argentopentlandite, with a minor amount of mss. However, elemental silver was not detected (cf. Appendix D.2).

EMPA was conducted across the face of a cross-sectional sample taken from the middle of the rod. The major phase (approx. 85%) was Fe-deficient argentopentlandite, with a composition varying slightly from $Fe_{4.8}Ni_{3.2}AgS_8$ at the top of the cross-section, to $Fe_{4.7}Ni_{3.3}AgS_8$ at the bottom (i.e. the side which was previously in contact with the silica tube). In all cases the atomic ratio for Ag:S was distinctly 1:8 (cf. Appendix E.2). Two minor phases were detected; firstly, an Fe-rich mss with a stoichiometry approximating to $Fe_{0.71}Ni_{0.23}S$, which was more randomly distributed throughout the cross-section than in the equivalent specimen of synthetic pentlandite (SynPn3, cf. Section 2.1.1). Secondly, elemental silver, which was likewise randomly distributed, although some concentrated patches were observed near the bottom of the cross-section.

The absence of normal pentlandite (by either Powder XRD or EMPA) is noted, although its "metastably preserved existence" vis à vis monosulphide solid-solution and elemental silver, would have been assumed from equilibrium phase relations in the Fe-Ni-Ag-S ternary system above 550°C (cf.Section 1.2.2). Note, the similar phenomenon surrounding the absence of heazlewoodite in synthetic pentlandite (SynPn3), (cf. Section 2.1.1).

It is concluded that the product (SynAgPnlb) contains approximately 85% of the desired phase, namely argentopentlandite. The failure in obtaining an homogeneous product has been ascribed by other workers to the very sluggish nucleation of this phase (16); perhaps this is due to the presence of four components in this "ternary" phase (i.e. Fe,Ni,Ag,S). Consequently, this material is considered suitable only for certain electrochemical experiments.

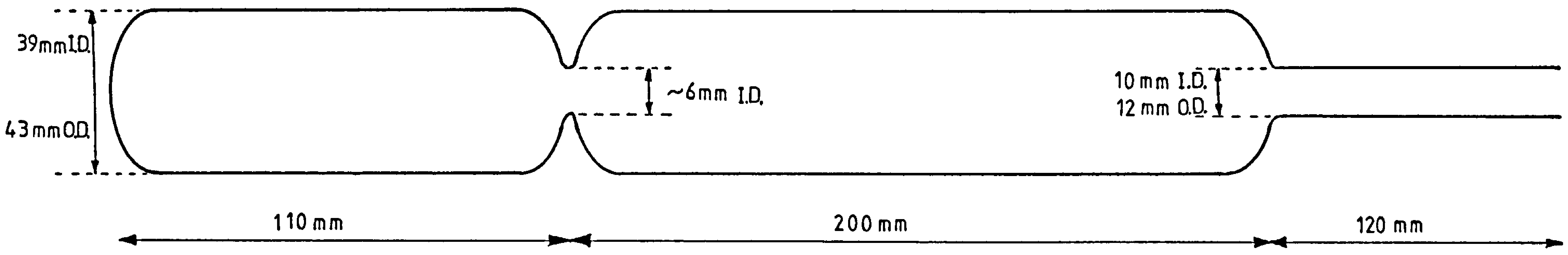

Figure 2.1.1

Double bulbed fused 96% silica glass vessel

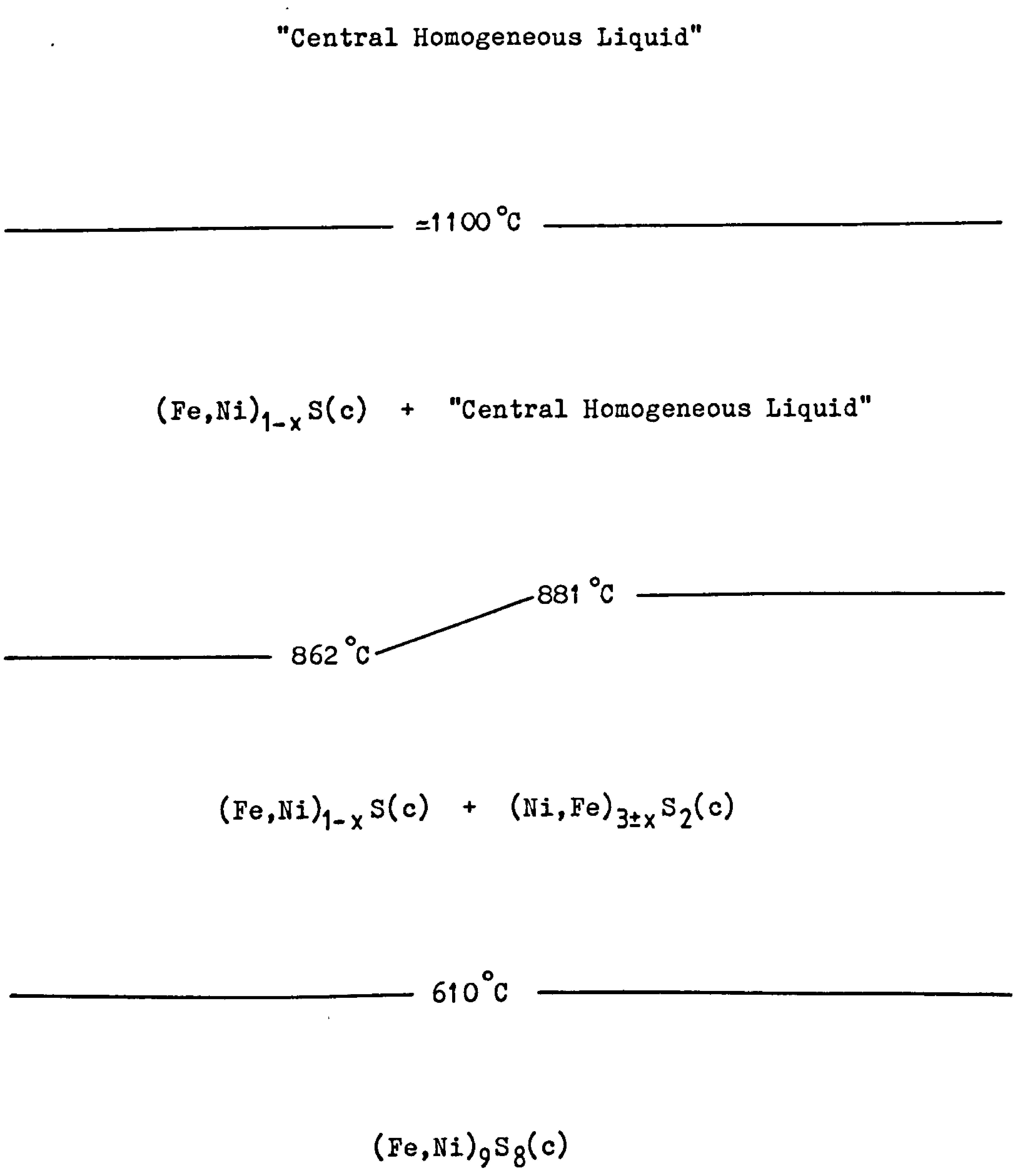

Figure 2.1.2

Schematic phase diagram showing the various thermal decomposition products of pentlandite at equilibrium vapour pressure as a function of temperature.

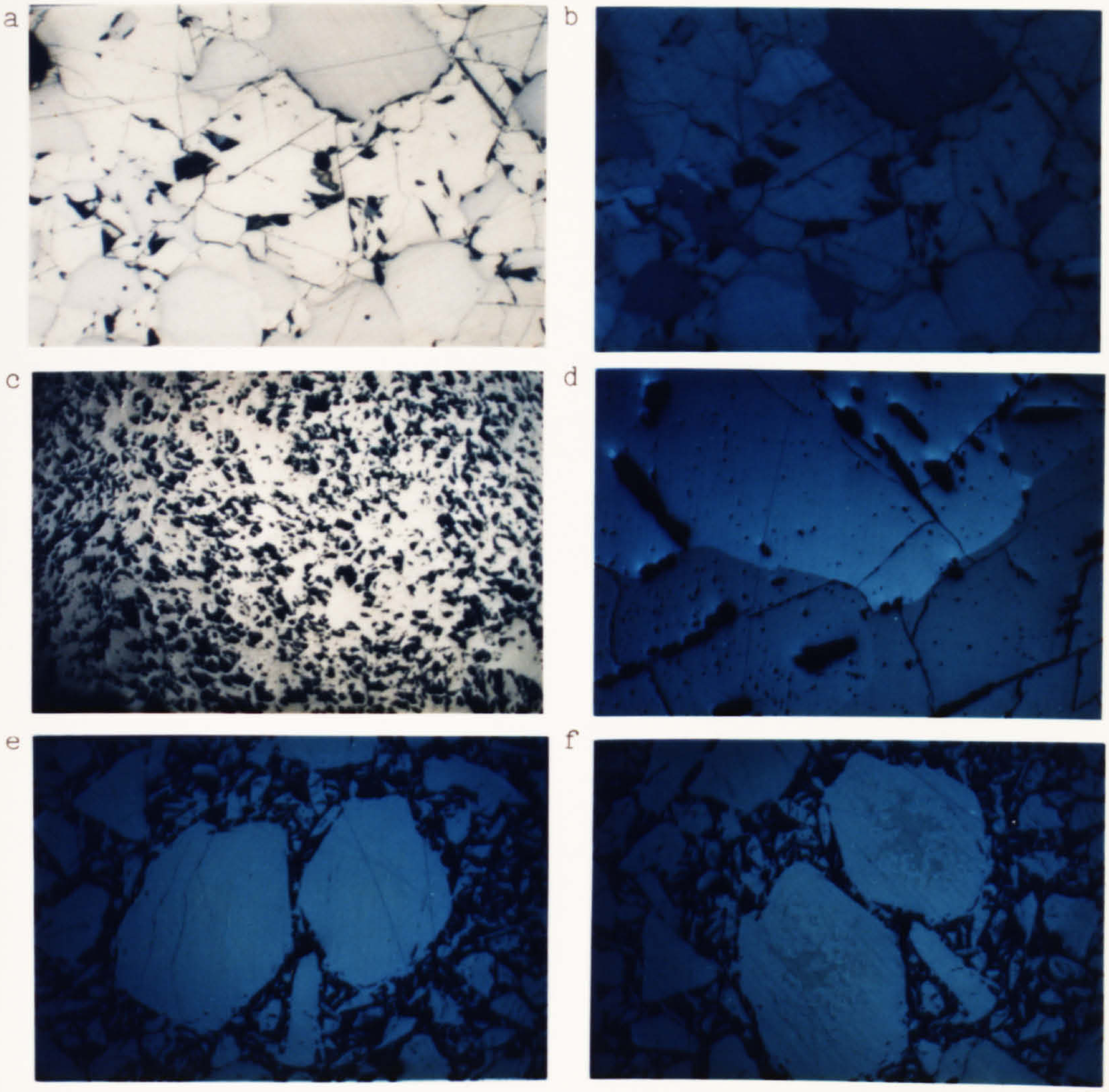

Figure 2.1.3

Reflected Light Microscopy: Synthetic Specimens

(a). SynPn2a(top) x400,PPL. Pale yellow grains with octahedral cleavages = pentlandite. Bounded by darker grains = pyrrhotite (mms).

(b). SynPn2a(top) x400,XP. Isotropic grains = pentlandite, anisotropic grains = Pyrrhotite (mms).

(c). SynPn2a(bottom) x140,PPL. Porous pentlandite mass, with no other phases detected.

(d). Synthetic mss x140,XP. Mss grains with different degrees of extinction reflecting different crystallographic orientations for this anisotropic phase.

(e). SynVl1a x200,XP. Isotropic violarite grains.

(f). SynVl1a x200,XP. Specimen (e) rotated 315° shows the large violarite grains with an anisotropic core (unreacted mss ?).

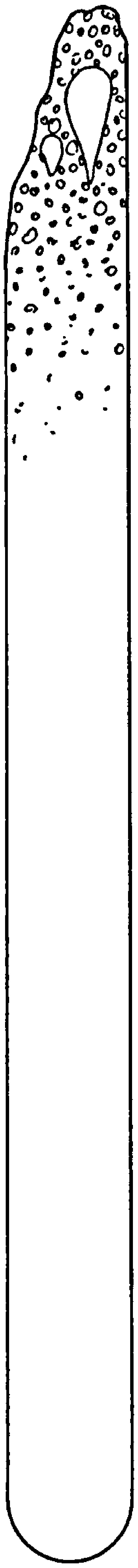

Figure 2.1.4

Schematic longitudinal cross-section of the fused synthetic pentlandite slug ("SynPn2a") showing textural and compositional differences after fusion/annealing in the vertical tube furnace.

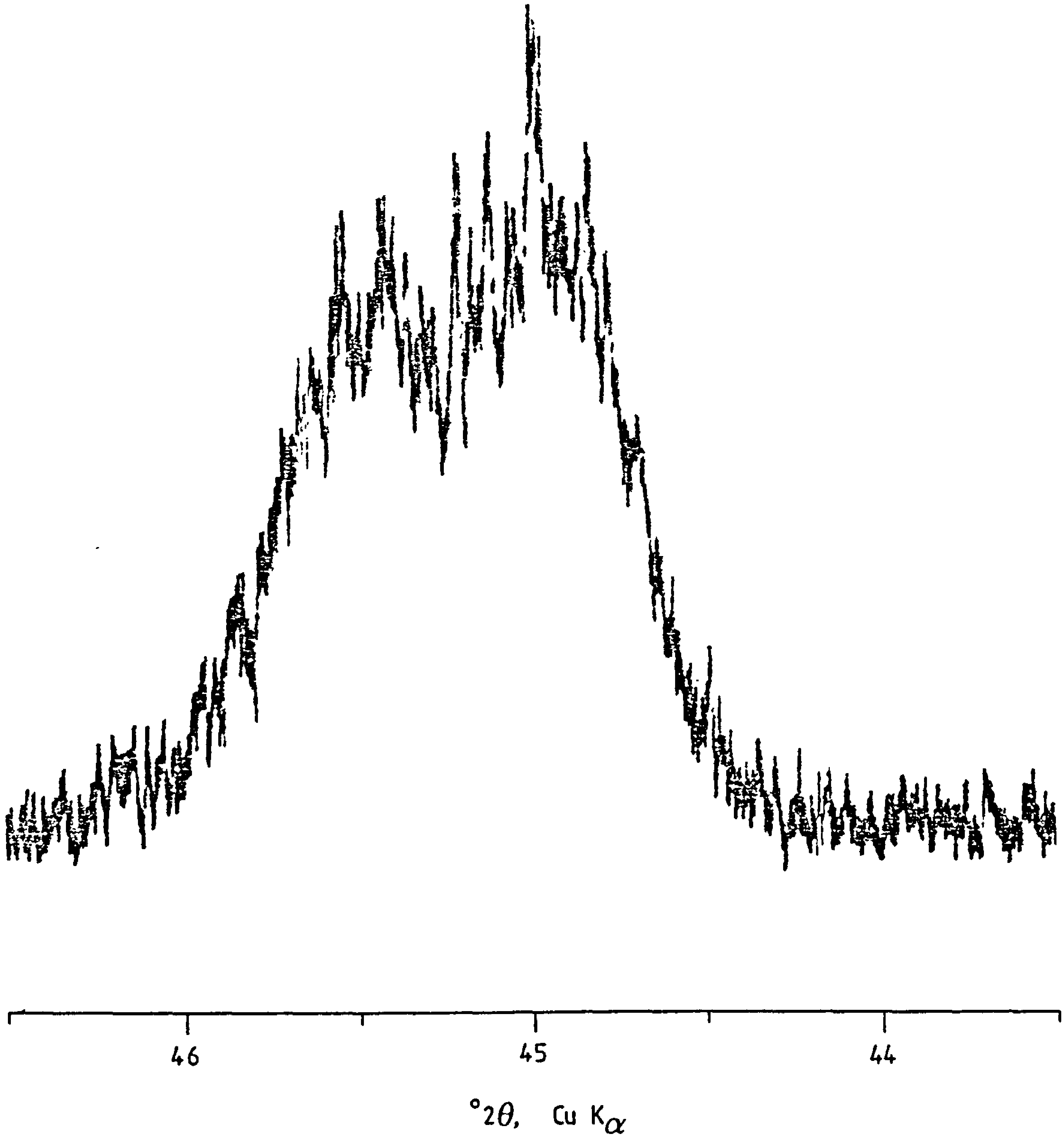

Figure 2.1.5

d_{102} X-ray powder diffraction peak of synthetic Mss ($FeNi_2S_{3.25}$). The abscissa is °2θ for CuK_α radiation; the peak intensity is not calibrated.

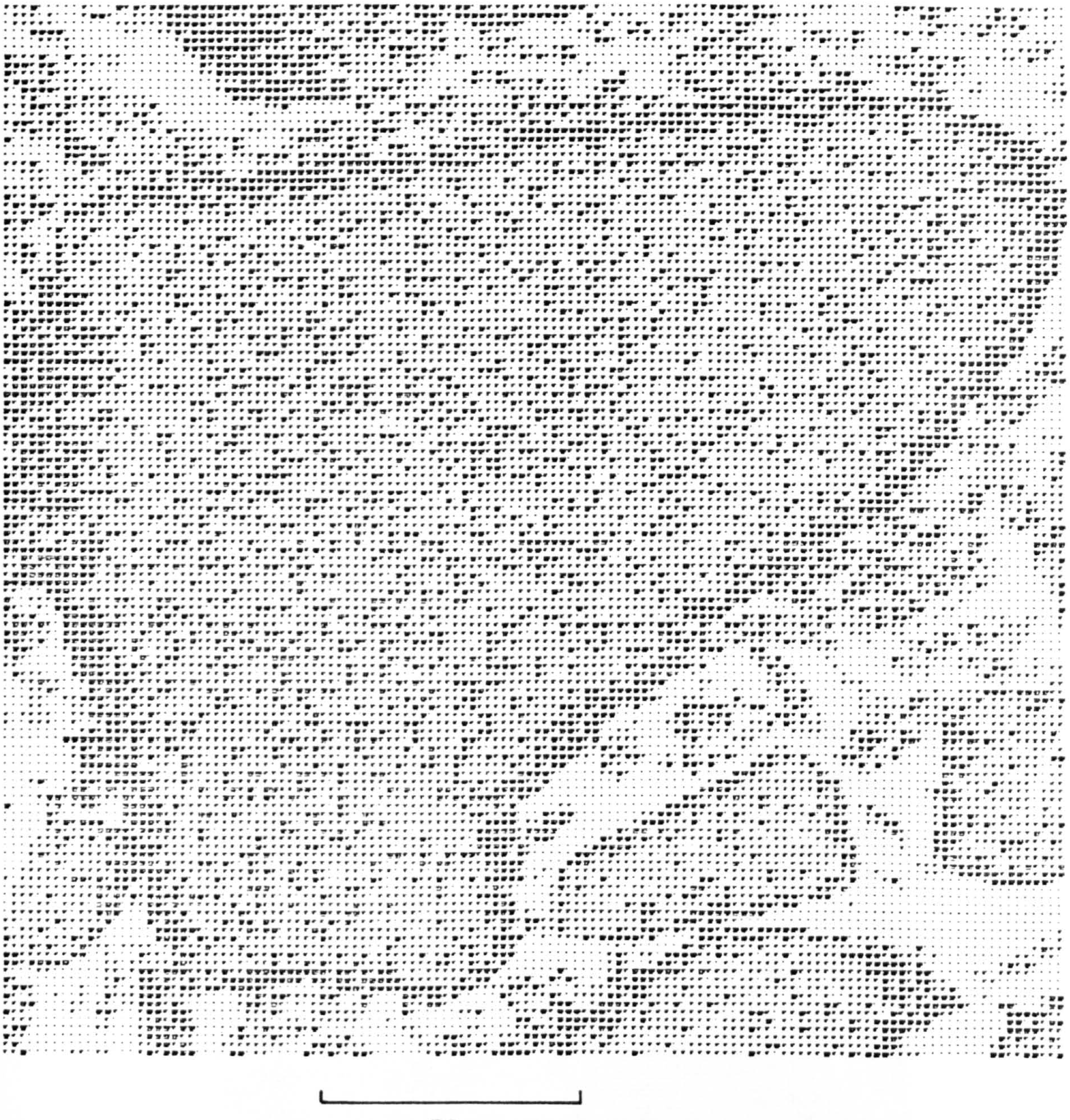

Figure 2.1.6

Electron Microprobe Analysis Ni Map of synthetic violarite ("SynVl1a"). Dark shading represents Ni-rich / (Fe-poor). Map reveals that the violarite grains are comprised of an Fe-rich core ($Fe_{1\cdot2}Ni_{1\cdot8}S_4$) with a Ni-rich rim ($Fe_{0\cdot5}Ni_{2\cdot5}S_4$). The radial distribution of Ni indicates an abrupt peripheral change between these two compositions.

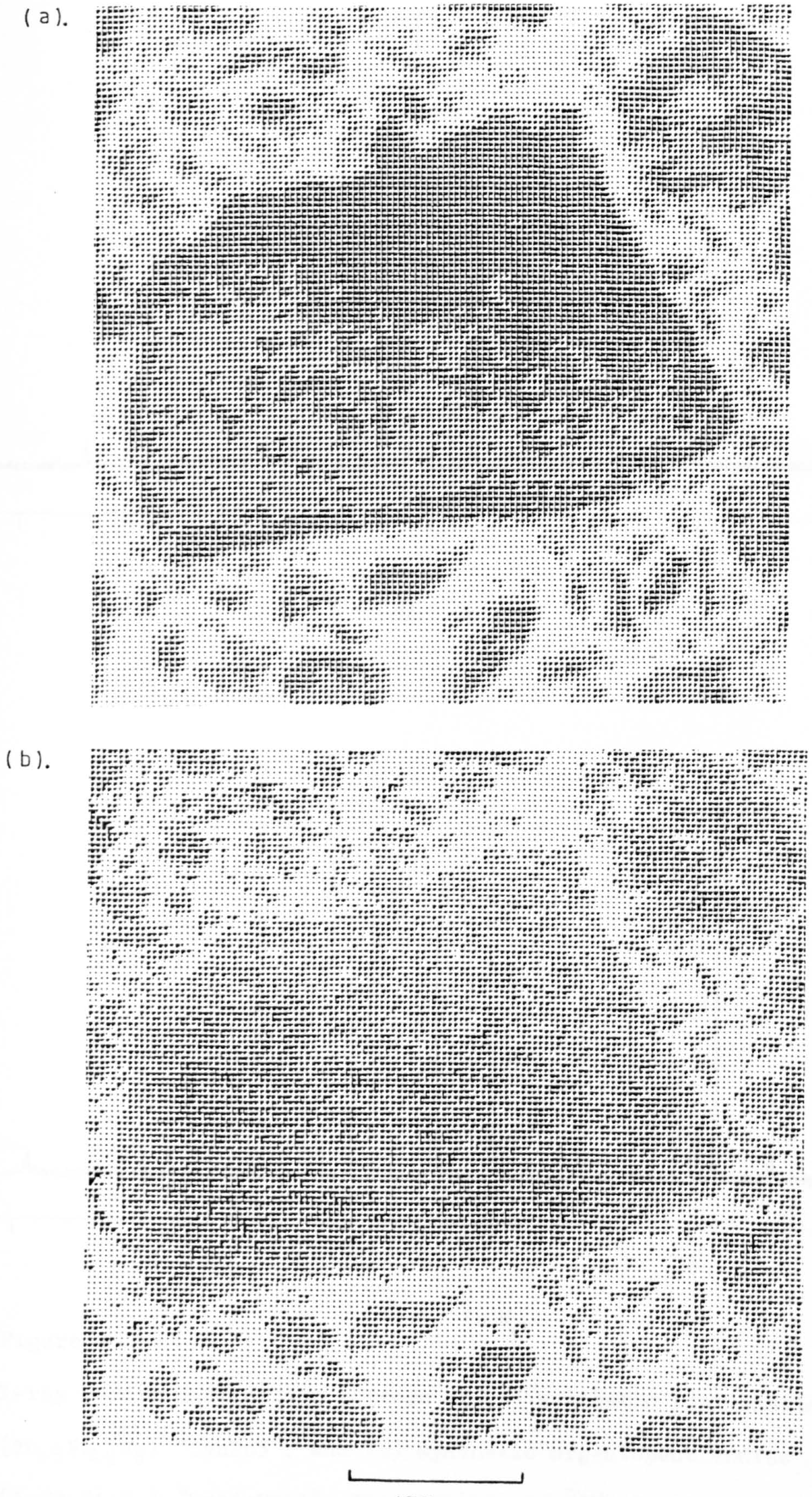

Figure 2.1.7

Electron Microprobe Analysis digitized maps of a typical synthetic violarite grain ("SynV11c") after quenching from 295 °C.

(a) Ni-map, (b) Fe-map.

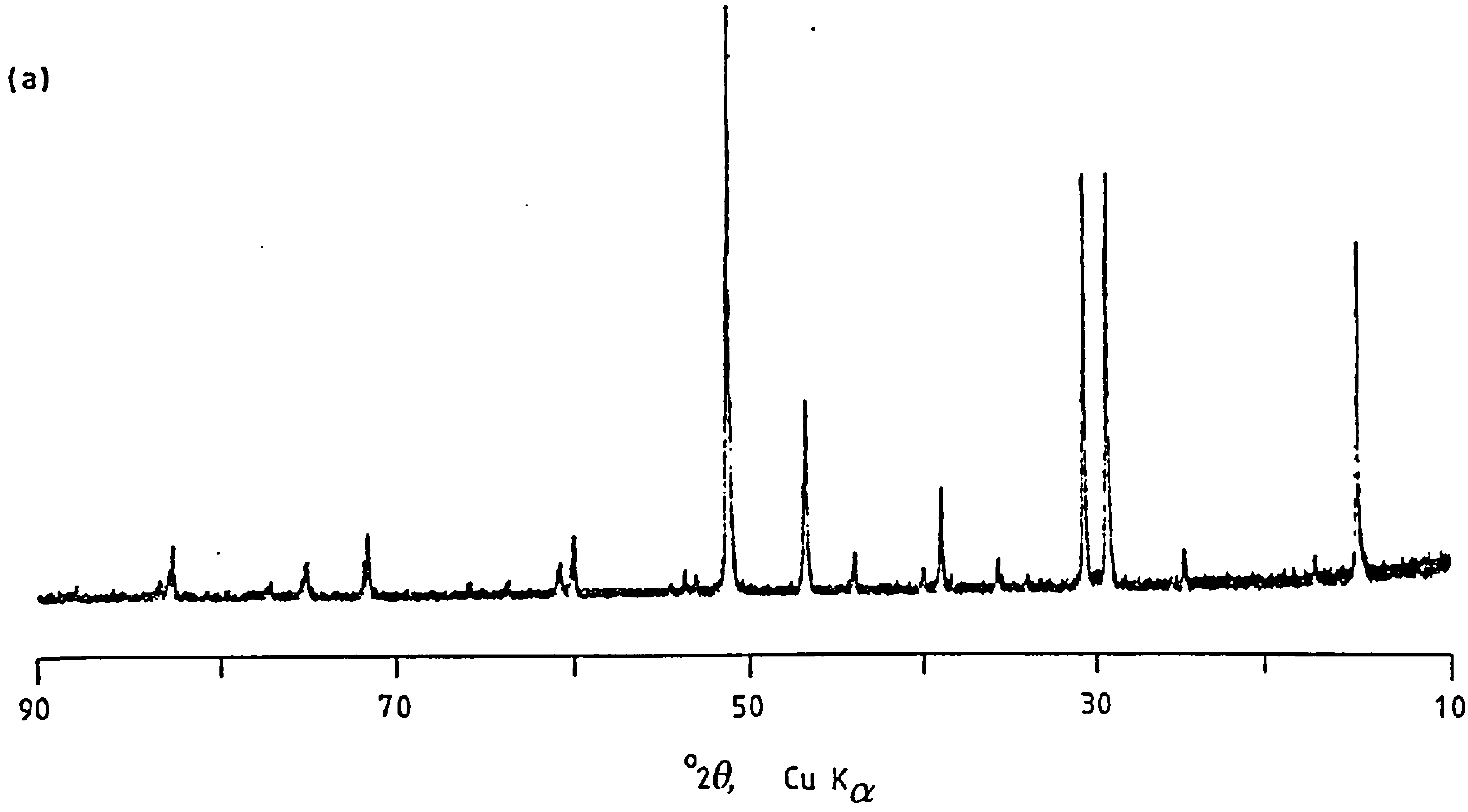

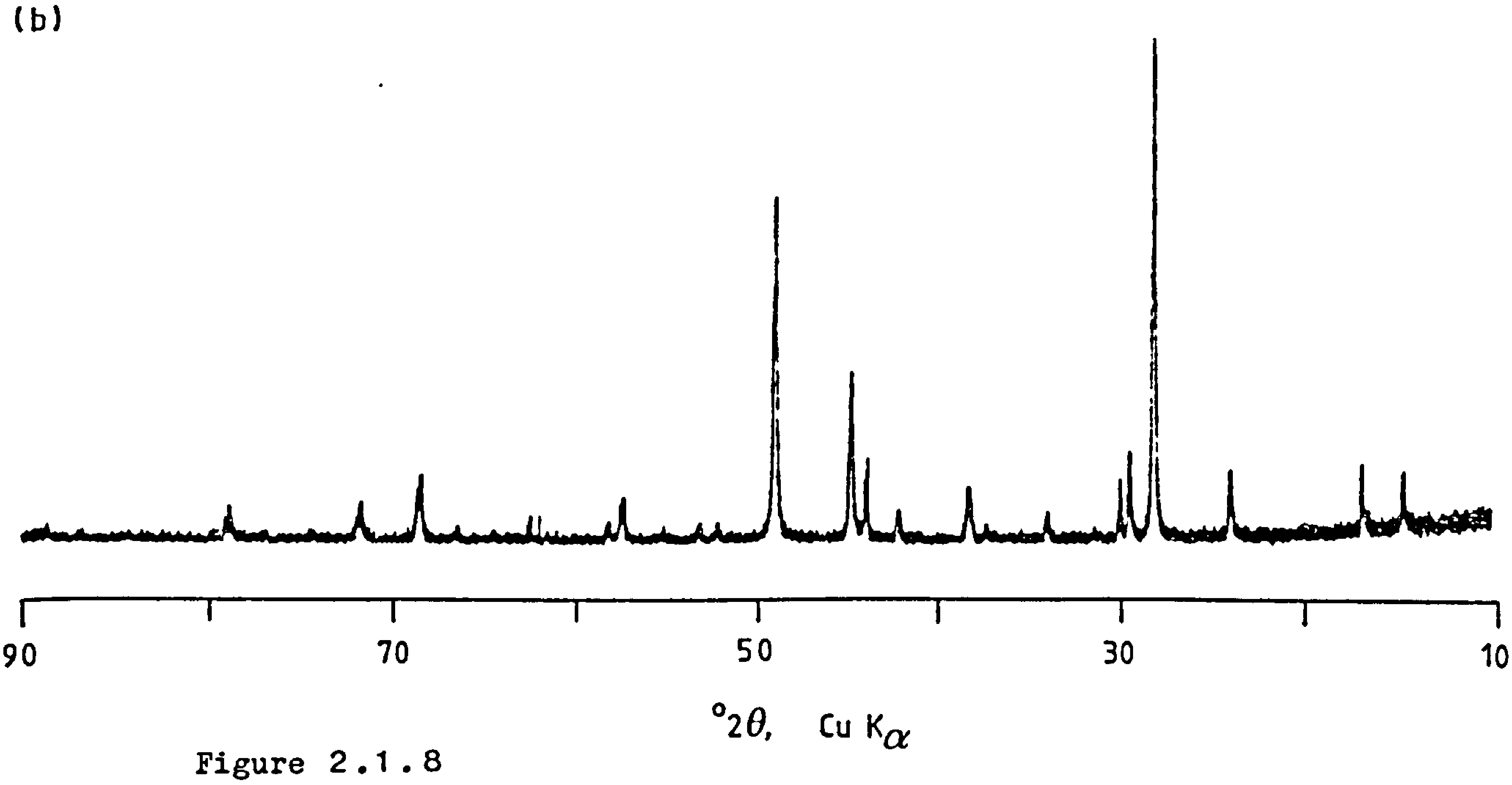

Figure 2.1.8

X-ray powder diffraction pattern of (a) synthetic pentlandite ($Fe_{4.5}Ni_{4.5}S_8$) "SynPn3"; and (b) synthetic argentopentlandite ($AgFe_5Ni_3S_8$) "SynAgPn1b". The abscissa is °2θ for CuK_α radiation; the peak intensities are not calibrated.

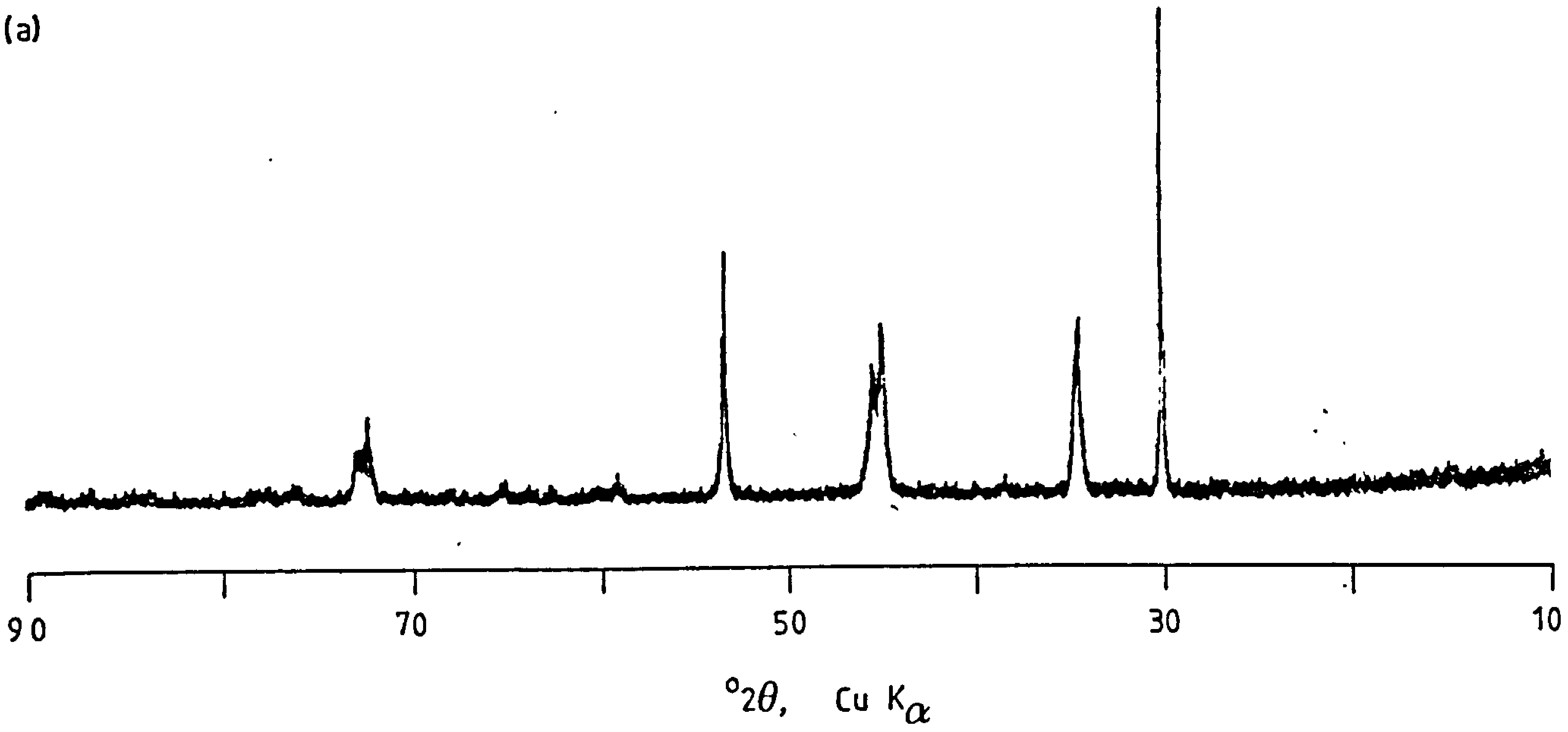

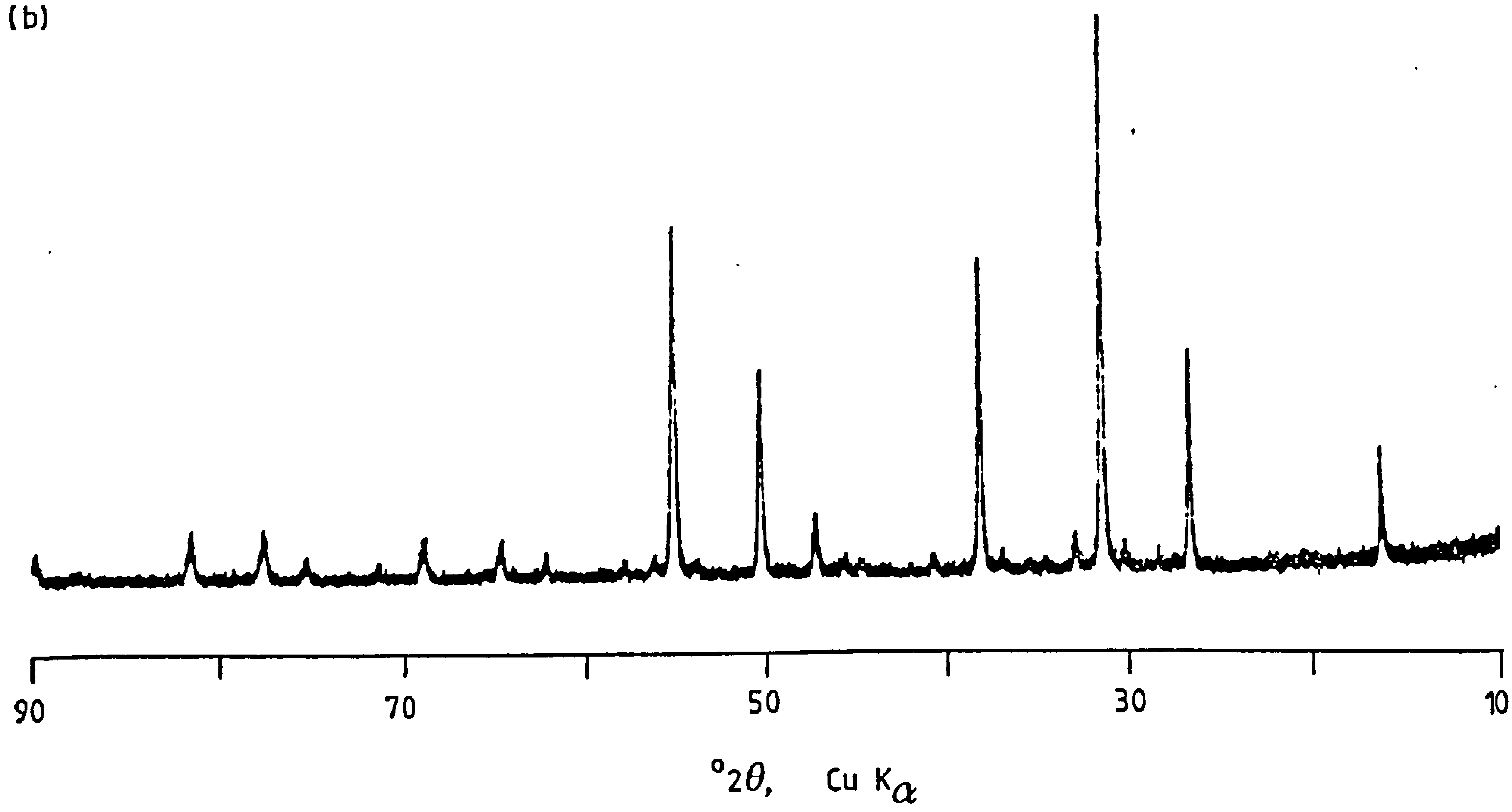

Figure 2.1 . 9

X-ray powder diffraction pattern of (a) synthetic monosulphide solid solution ($FeNi_2S_{3.25}$) "SynMss"; and (b) synthetic violarite ($FeNi_2S_4$) "SynV11b". The abscissa is °2θ for CuK_α radiation; the peak intensities are not calibrated.

2.2 ELECTROCHEMICAL TECHNIQUES

2.2.0 Introduction

This section describes the basic principles and theory of the electrochemical techniques used in this work, whilst details concerning apparatus and instrumentation are given in Section 2.3. It is important to stress that the electrochemical techniques discussed in this work are not intrinsically unique or isolated experiments. They are essentially variants of a perturbed E-i-t system in which the variables E (potential) or i (current) are controlled in a prescribed manner, whilst the other variable (i or E) is monitored simultaneously as a function of time (cf. Section 1.6.2 and Figure 2.2.1).

2.2.1 Potentiometry

In potentiometric experiments the potential of the working electrode (metal-sulphide/aqueous interface) is measured with respect to a reference electrode (usually saturated calomel) as a function of the electrolyte composition. This constitutes a two electrode system in which ideally, no external current is flowing, and hence no net faradaic reaction can occur.

Depending on the nature of both the working electrode and the electroactive species in solution, the potential may be governed by the thermodynamics of the system in which case the potential is defined by the Nernst function as an equilibrium potential (cf. Section 1.5.2). Alternatively, and more common to this work, the potential may be governed by the kinetic restraints of the system and may for example correspond to the steady-state interaction of two processes and thereby be kinetically defined as a "mixed-potential".

In corrosion studies this if commonly referred to as the corrosion potential (cf. Section 1.6.3).

2.2.2 Chronopotentiometry

In chronopotentiometric experiments the potential of the working electrode is continuously monitored as a function of time during polarization by an externally imposed current. This technique involves the use of a three-electrode system as illustrated in Figure 2.2.2.

A constant current is "instantaneously" applied between the working and counter electrodes with a galvanostat, whilst the potential is measured between the working and reference electrodes. This produces a constant rate of electrochemical oxidation (or reduction), i.e. the concentration "gradient" at the electrode surface is kept constant. The potential of the working electrode varies with time as the concentration ratio $C_A{}^o/C_B{}^o$ changes at the electrode surface. Eventually, the concentration of the electroactive species drops to zero at the electrode interface such that its flux to the interface alone is now insufficient to maintain the applied current. At this moment the electrode potential rises (or falls) rapidly until an additional oxidative (or reductive) process occurs. The time from the initial onset of polarization to the "sudden" rise (or fall) in potential is called the "Sand time" (t_s). The Sand time is related to the concentration and diffusion coefficient of the electroactive species through the Sand equation. A diagnostic test for a diffusion controlled process is that the product $i_c\ t_s{}^{1/2}$ remains constant, irrespective of the value for the applied constant current (i_c), (see Section 1.6.2).

This technique has previously been used for investigating intermediate solid state phase changes and in determining diffusion coefficients in other metal-sulphide systems including: heazlewoodite (Ni_3S_2), and millerite (NiS), (150); chalcocite (Cu_2S), and digenite (Cu_9S_5), (156), (157); bornite (Cu_5FeS_4), and chalcopyrite ($CuFeS_2$), (158), (159).

2.2.3 Intermittent Galvanostatic Polarization (IGP)

IGP is a varient of constant current chronopotentiometry, in which the system alternates periodically between closed and open-circuit (76), (160), (161), (162). This technique allows known amounts (or pulses) of anodic or cathodic charge to be passed across the working electrode/aqueous interface, whilst enabling the measurement of potentials both in closed and open-circuit.

Suitable values of imposed current density are applied as a rectangular wave form (cf. Section 2.3.2 for details of instumentation). The current "pulse" (i.e. the magnitude of the applied current density and the time spent per cycle in closed-circuit) needs to be selected such that the initial faradaic process (in systems in which there are several) can be observed. If too large a current density is applied, then the potential will inevitably rise to the next faradaic process within the first cycle, so that the effects of the first process may not be observed in the subsequent period of open-circuit. The closed-circuit potential corresponds to the faradaic process which is sustained by the applied current density, and by this virtue includes the corresponding overpotential. This overpotential may comprize of several components depending on the nature of the system, eg. charge transfer (activation), diffusion (concentration), nucleation, or any ohmic resistances (ionic/ electronic).

The current pulse is followed by a "suitable" period in open-circuit. However, the interpretation of the open-circuit potential vis à vis time spent in open-circuit is the cause of some disparity between the intentions and actual attainment of previous workers. Their objective has been to determine the potential accompanying the faradaic process whilst the reaction is "briefly" sustained through the discharge of the double layer capacitance (cf. Section 1.6.4) and therefore with a zero iR drop (i.e. when no externally imposed current is flowing). Such information would be of great mechanistic importance. However, the time scale over which this is applicable is governed by the value of the electrical double layer capacity and might typically be of the order 100μs to 1ms. This aspect appears to have been overlooked by these workers who arbitarily select 1s for the open-circuit duration. Consequently, the potential values "captured" on their traces may not necessarily relate to any physical significance apart from the transitory position of the pen, or at most, the diffusional drift in concentration of electroactive species at the electrode.

Alternatively, if a sufficiently longer period in open-circuit is allowed for the obtainment of reproducible and definite "potential-arrests", these may now be interpreted in terms of an equilibrium (or mixed) potential between speices generated during the preceeding faradaic reaction and that of the solution. Such observations have proved valuable in this work as a means of identifying the product species.

It is concluded that Horvath and Hackl's statement (161) concerning the theoretical basis of IGP that "the potential obtained at the current-free periods corresponds to the equilibrium potential of an electrode reaction", is an over generalization; although it may be true for certain systems, e.g. simple electron transfer for a single process.

After a suitable number of cycles (i.e. when sufficient product has formed to enable a definite potential arrest) the polarity of the cell was reversed to allow a novel variant of the cathodic stripping technique to be implemented.

2.2.4 Chronoamperometry

Chronoamperometric experiments involves the use of a three-elctrode system as illustrated in Figure 2.2.3. The potential of the working electrode is "instantaneously" changed (either anodically or cathodically) from the rest potential (i.e. from where the net faradaic current is zero) to a fixed value with respect to the reference electrode. This applied potential creats a current between the working and counter electrodes, which is continuously monitored. Initially the current is very large due to the non-faradaic current in charging the double layer capacitance, but rapidly decays exponentially (cf. Section 1.6.1).

If the applied potential is in the region of mass transport control (i.e. electron transfer is either intrinsically or extrinsically fast), then the oxidation (or reduction) of the electroactive species at the working electrode creates a concentration gradient with respect to the bulk phase. This leads to a net flux of electroactive species towards the interface such that the current is proportional to the concentration gradient (which is assumed to be linear, and decreases with time). This yields an $i = f(t^{-1/2})$ relationship called the Cottrell equation. The constancy of the product $i_c\ t^{1/2}$ is a test for diffusion control (see Section 1.6.2).

If the applied potential is in the region of electron transfer control (i.e. electron transfer is slow or C_A^{∞} is large; hence $I^A{}_{lim}$ is large), the current tends towards a steady state. The values of current density extrapolated to $t = 0$ can be plotted according to the appropriate form of the Butler-Volmer equation (e.g. the Tafel equation at large overpotentials), (cf. Section 1.6.0).

For i-t profiles in between these two extremes, the system is considered as being of mixed control (i.e. mass transport and electron transfer occur at comparable rates).

2.2.5 Cyclic Linear Sweep Voltammetry

Linear sweep voltammetry or more precisely linear potential sweep chronoamperometry, is as the latter name suggests, a variant of chronoamperometry in which the potential is varied linearly with time. In this work, the potential was normally scanned from the rest-potential using the potentiostat in sweep mode, whilst the current was continuously monitored as a function of applied potential (i.e. as an implicit function of time), cf. Section 2.3.2.

As the potential is scanned, net oxidation (or reduction) of the electrochemical species is induced resulting in an anodic (or cathodic) current. As the applied potential increases, the enhanced rates of electron transfer cause a decrease in the concentration of the electroactive species at the electrode and hence an increase in the flux (or current) of the electroactive species towards the electrode interface. As the potential increases beyond the anodic (or cathodic) half-wave potential, the concentration of the electroactive species drops to almost zero. As a result of this, the flux (or current) of the electroactive species reaches a maximum (i_p) which corresponds to the peak potential (E_p). Beyond the peak potential, the flux (or current) decreases as the depletion effect occurs.

It is helpful, to consider the i-E-t surface to understand this technique (see Figure 2.2.4). On the E-t plane, an excursion is made at an angle dependant upon the scan rate. The projection of this line onto the i-E-t surface reveals the current profile as described above.

If the potential scan is instantaneously reversed, the oxidation (or reduction) process continues initially, though at an ever diminishing rate. Once the cathodic (or anodic) half-wave potential is reapproached the product species obtained from the oxidation (or reduction) becomes unstable and thus undergoes a "net" reduction (or oxidation) resulting in a cathodic (or anodic) current. The shape of this reversed current transient is similar to that of the forward scan. This technique of reversed potential scan is called cyclic linear sweep voltammetry, or cyclic voltammetry for short.

Cyclic voltammetry is particularly useful for preliminary mechanistic investigations. Much qualitative information can readily be obtained from the cyclic voltammogram e.g. the reaction sequence together with the potential regions at which they occur, and an indication of their reversibility. Two prominant diagnostic features for fast electron transfer are that the square root of the scan rate is proportional to the peak curent density (i_p and that the peak potential (E_p) is independant of the scan rate. For a detailed description in terms of the convoluted current see Section 1.6.2).

In this work, the potential was normally scanned at low rates (typically 5 or 10mVs^{-1}) because of the reasonably high electrical double layer capacity on the metal-sulphides which would otherwise cause sufficiently large non-faradaic currents to flow to mask the finer detail on the cyclic voltammogram. Low scan rates were also required in the obtainment of kinetic parameters for the quasi-reversible $FeCl_3/FeCl_2$ couple.

Various adaptations of cyclic voltammetry were exploited in this work, e.g. a comparison between the behaviour of aqueous couples on platinum and nickel-iron-sulphides; and the effects on the reverse scan from successivily greater anodic excursions.

2.2.6 Cathodic Stripping Voltammetry

Cathodic stripping voltammetry is a combination of chronoamperometric and linear voltammetric techniques (cf. Sections 2.2.4 and 2.2.5). This technique allows the working electrode/aqueous interface to be polarized at a constant anodic potential for a known length of time such that oxidation can be induced at a prescribed potential. The amount of anodic charge passed during, the reaction can be calculated by integrating the i-t transient by use of the trapezoidal rule. This period is instantaneously followed by linearly scanning the potential in a cathodic direction (10mVs^{-1}).

By repeating the experiment at different applied potentials for the initial polarization, information can be obtained from the cathodic linear sweep voltammogram concerning changes in product formation pro rata with applied potential.

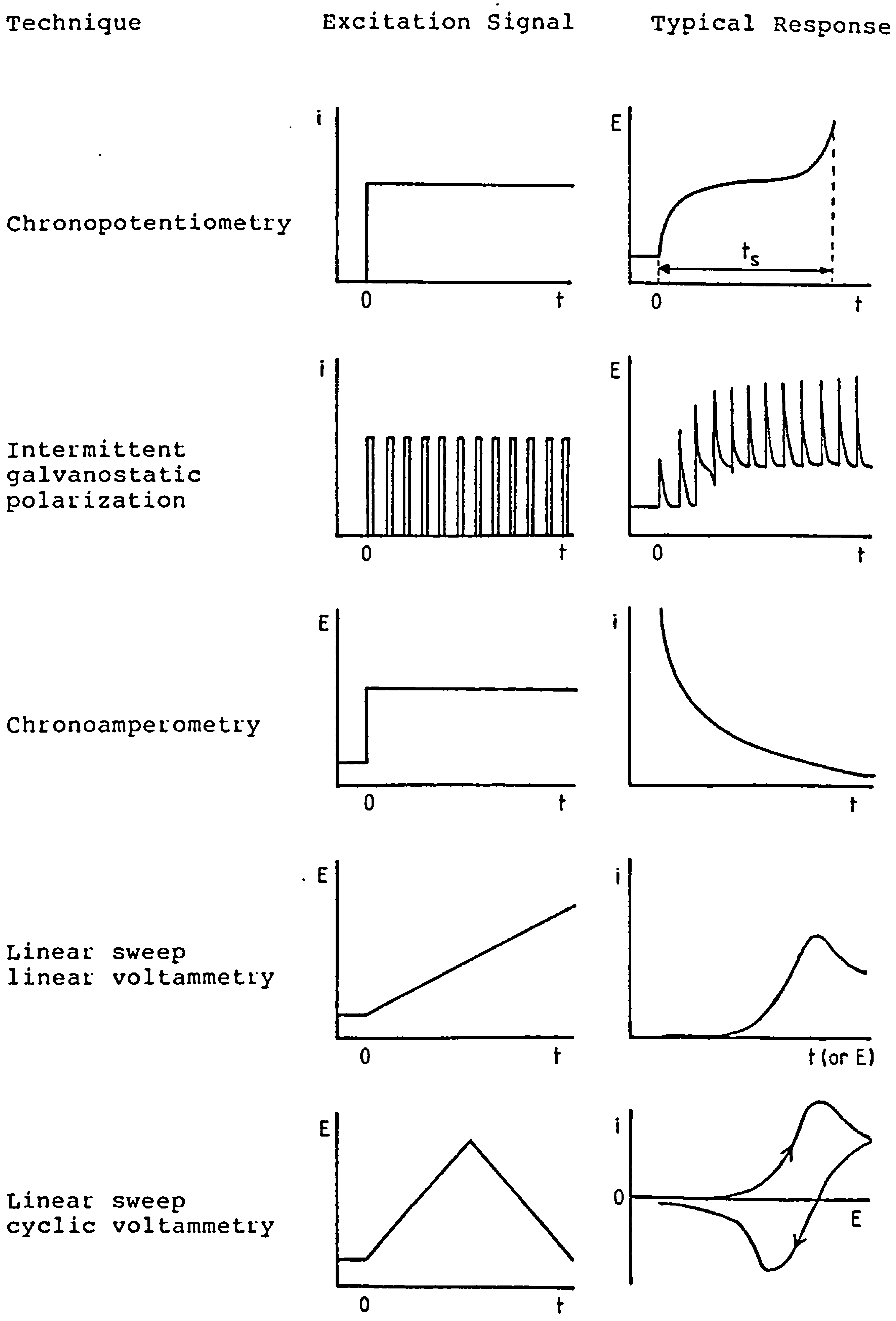

Figure 2.2.1

Excitation and response E-i-t profiles for the various electrochemical techniques used in this work.

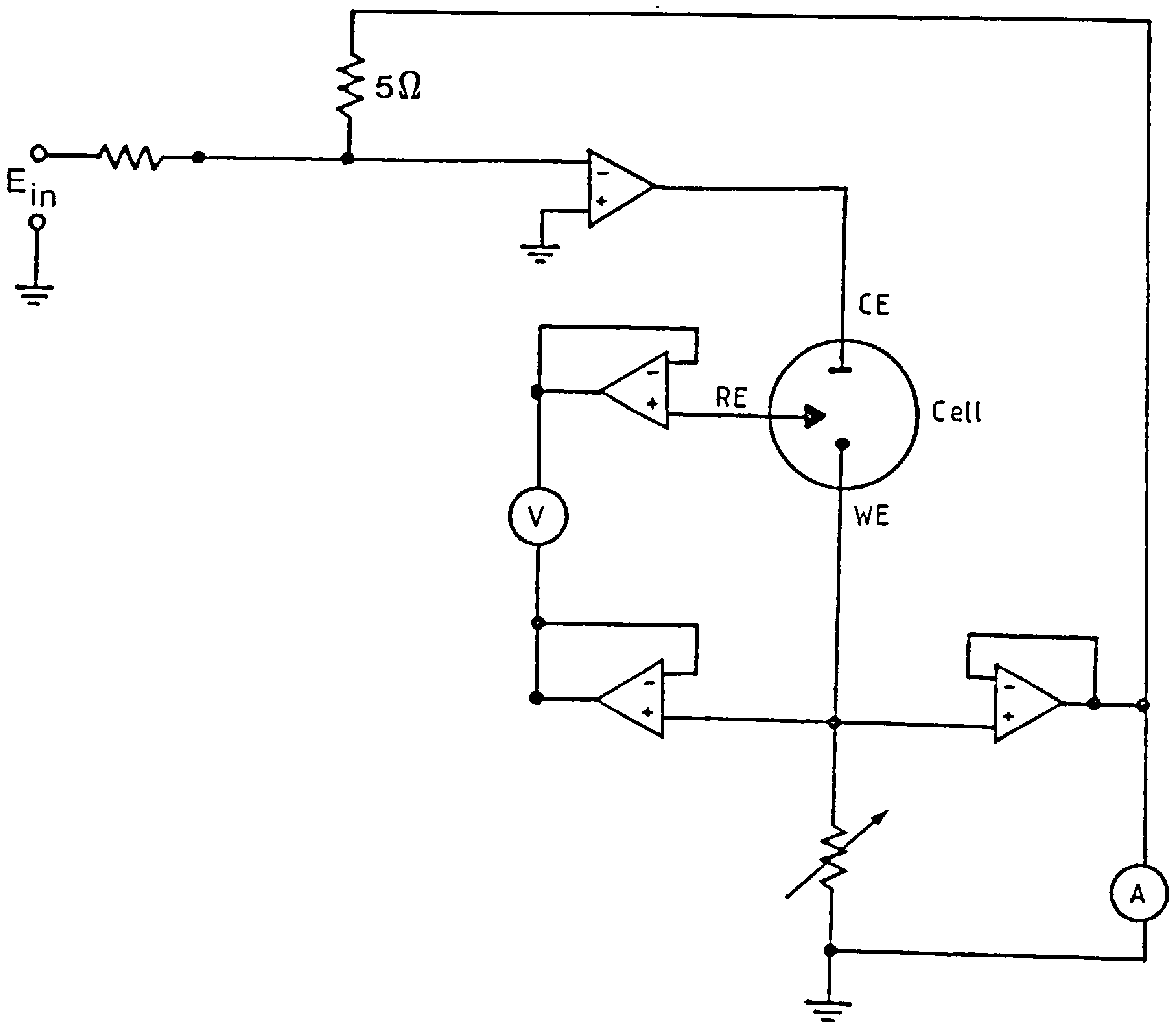

Figure 2.2.2

Schematic circuit diagram of the apparatus in chronopotentiometry, i.e. the principle operation of a galvanostat.

E_{in} = input potential

WE = working electrode

RE = reference electrode

CE = counter electrode

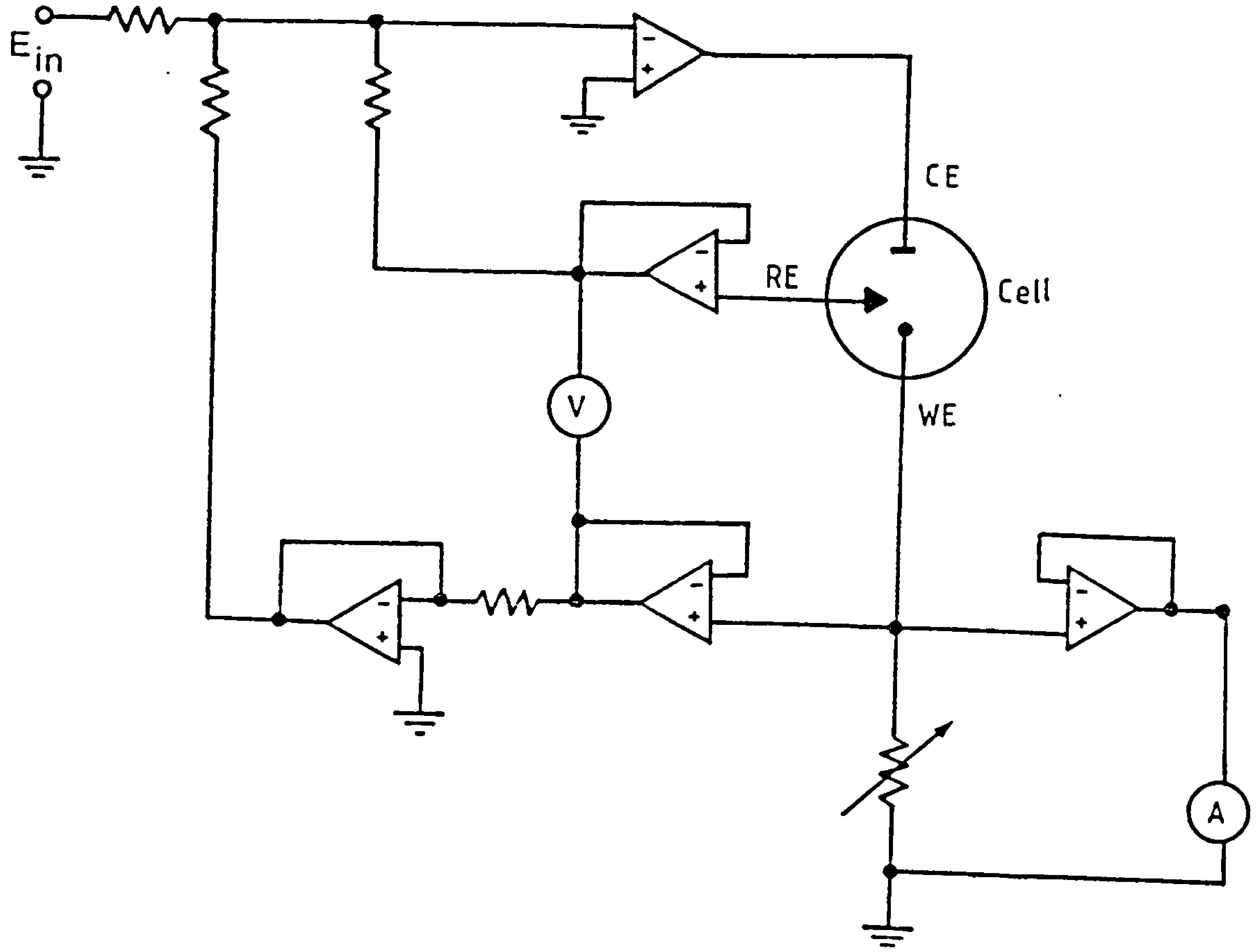

Figure 2.2.3

Schematic circuit diagram of the apparatus in chronoamperometry (including linear sweep cyclic and linear voltammetry), i.e. the principle operation of a potentiostat.

E_{in} = input potential

WE = working electrode

RE = reference electrode

CE = counter electrode

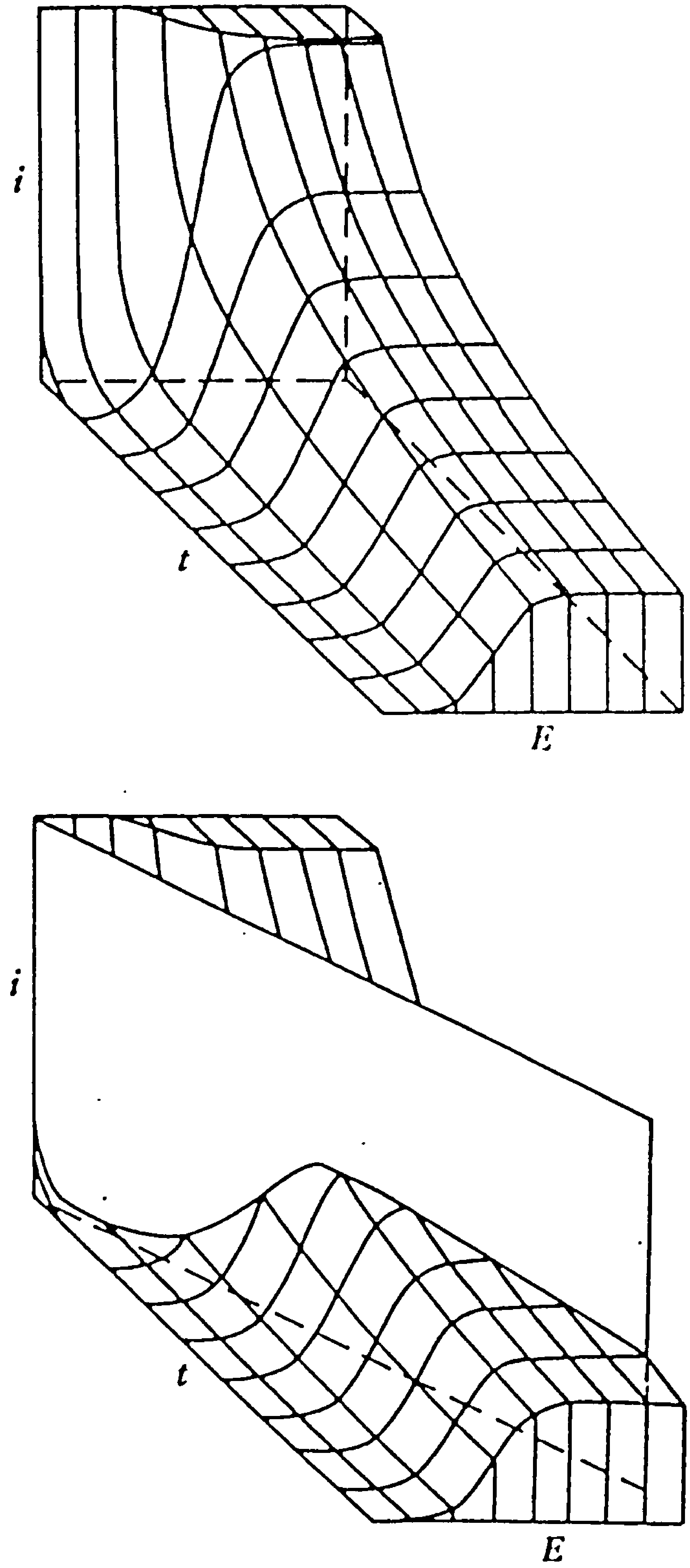

Figure 2.2.4

(a) Representation of a portion of the i-E-t "surface" for a Nernstian reaction. Potential axis is in units of 0.06/n V

(b) Linear potential sweep across the surface.

2.3 ELECTROCHEMICAL APPARATUS AND METHODOLOGY

2.3.1 Electrochemical cell

The majority of electrochemical measurements were made using a conventional three-electrode cell configuration enclosed within a Metrohm vessel with a volume of $0.1dm^3$ (cat. 6.1418.220), with a working electrolyte volume of $0.05dm^3$. A Metrohm vessel lid (cat. 6.1414.010) equiped with five Q.F. 14/23 female joints provided ports for the working, counter and reference electrodes, together with the thermometer and gas disperser unit (see Figure 2.3.1).

The cell was thermostatically controlled by circulating water at the required temperature from a waterbath using a Gallenkamp thermo-stirrer model 85 via polypropylene tubing to and from the thermostatic jacket of the Metrohm vessel. The temperature of the working electrolyte could be maintained to within ±0.5K in the temperature range from ambient to 353K, and was measured with a mercury thermometer of 0.1K graduations.

The tip of the reference electrode (or salt-bridge) was placed approximately 10mm from the working electrode. The use of a Luggin capillary was considered unnecessary in this work since the supporting electrolyte commonly used was either 1 molar hydrochloric or perchloric acid; both of which have a sufficiently high conductivity to ensure a negligible iR drop. The counter electrode was placed at a similar distance from the working electrode.

A larger unpartitioned "electrolysis cell" was used in experiments where the possibility of solid-state phase changes in the mineral was investigated (notably chronopotentiometry). This cell comprised of a $0.7dm^3$ glass vessel with a thermostatic jacket and a sealable flanged pyrex lid Q.F. MAF4/41. The Q.F. female glass ground joints in the lid provided ports for the working and counter electrodes, salt-bridge, thermometer and gas disperser unit (see Figure 2.3.2). A modified design of working electrode was used (cf. Figure 2.3.3), which was placed opposite the counter electrode to minimize field distortions. A working electrolyte volume of $0.5dm^3$ provided the opportunity for aqueous sampling during electrolysis. The electrolyte was stirred by a magnetic bead.

2.3.2 Instrumentation and Data Aquisition

The majority of the experiments were performed using an EG & G PAR model 362 potentiostat/galvanostat. The potential control range was -9.999 to 9.999V, with potential scan rates ranging from 0.0001 to $0.5Vs^{-1}$. When operating in galvanostatic mode, cathodic or anodic currents could be applied in the range 10^{-6}A to 1A.

For the IGP experiments an EG & G PAR model 175 universal programmer was used to trigger the galvanostat via an inlet modification to the model 362; thus enabling the generation of a square or rectangular current wave form. Expansion of this wave form to enable short pulses of current followed by longer spells in open-circuit over and above those permitted by the two multipliers, was achieved by first generating a suitable triangular potential wave form with the model 175, such that the positive apex of this wave triggered the 2.0V threshold modification on the model 362 at the desired intervals. A correction for a small offset in the "zero" current (which often occured when in operation, i.e. when the "ON" button on the model 362 was surpressed) was made by applying an appropriate potential from a Eurotherm millivolt source type 039, connected to the "EXT IN" on model 362. This was particularly important since the systems investigated in this work often involved small exchange current densities.

Measurement of current and potential were made using a high input impedance Keithley model 171 digital multimeter and a Keithley model 616 digital electrometer respectively. Current and potential profiles were recorded on a Brown Boveri multi channal X-t chart recorder Servogor model 460, and a Bryans X-Y recorder model 2600A4.

Rapid accummulation of cyclic voltammograms was facilitated by photocopying a sufficient number of "blank" i/E axes with a selection of labelled scales, followed by careful alignement on the X-Y recorder prior to the run. A similar method was exploited in portraying the E-f(t) profiles obtained from IGP. The E-f(t) trace was first recorded on a plain paper scroll on the X-t chart recorder. A transparent acetate sheet with the corresponding axis was then superimposed upon the E-f(t) trace during photocopying.

For electrochemical experiments requiring convolutive techniques and for certain chronoamperometric experiments of short duration, a fast data-capture system was used. This was based upon a twin-channel 12-bit analogue-to-digital converter (conversion time 50μs) and an Amstrad PC1640HD20 microcomputer. The potentiostat model 363 was operated in a conventional mode except for being triggered by the computer via the inlet modification as mentioned above. The current response and applied potentials were stored on a magnetic disk. Data capture/convolutive analysis software was provided by the commercially available CONDECON software package (originally developed in the Department of Physical Chemistry, University of Leeds) written in Marco 80 assembler language which allowed a minimum acquisition time of 100μs per point. In all experiments 2000 data points were routinely captured, equally spaced in time, with a time interval appropriate to the time-scale of the particular experiment. The CONDECON software package allowed the current response originally captured to be convoluted as a function of time, and displayed in a variety of functional forms relevant to kinetic and mechanistic diagnosis (cf. Section 1.6.2). Desired functions were obtained for graphical display using a Graphtec model MP1000 plotter.

2.3.3 Electrode Fabrication and Use

2.3.3.1 Reference Electrode

A Metrohm saturated calomel electrode model 6.0702.100 was used to measure the emf of the working electrode for temperatures up to 353K. This was introduced directly into the working electrolyte of the electrochemical cell when operating in chloride media. When operating in alternative media (especially in perchlorate solution) the reference electrode was connected to the cell via a salt-bridge. This was constucted from a glass "U"-tube with 2 Q.F. 14/23 male glass ground joints and vycor plugs (supplied by EG&G) affixed at either end, and filled with 1M NH_4NO_3 (aq) solution. This avoided the precipitation of $KClO_4$, which might have interferred with the emf measurement, besides being deleterous to the plug itself, at thereference / working electrolyte interface. NH_4^+(aq) and NO_3^-(aq) ions have very similar mobilities in the temperature range 273 to

373K (163), and therefore create a minimal liquid junction potential: e.g. +26mV in sat. (4.17M) KCl(aq)/1M NH_4NO_3; and -28mV in 1M NH_4NO_3 / 1M $HClO_4$ at 298K (cf. Appendix A). Thus, in a typical cell containing these two liquid junction potentials in series, the net E_J = -2mV and can therefore be ignored.

This particular model of calomel electrode was chosen since its mercury/aqueous interface could be sufficiently confined within the Metrohm cell such that its temperature could be assumed identical to that of the elctrolyte/working electrode. When operating the "electrolysis-cell", the reference elctrode was introduced into a seperate Metrohm cell containing saturated KCl(aq) solution at an identical temperature and connected via a suitable salt bridge.

The electrode potential for the saturated calomel electrode with respect to SHE is given as a function of temperature (154):

$$E(T) = 0.2420 - 0.00076(T-298) \ / \ V \qquad (2.3.1)$$

However, for the philosophical reasons discussed in Section 1.5.2 concerning electrode potentials vis à vis cell potentials, and the approximations concluded in Appendix A.1 concerning liquid junction potentials, together with the uncertainty as to whether or not the above quoted SCE potential includes the corresponding liquid junction potential; all potential measurements in this work refer specifically to the cell i.e. with respect to the SCE including a specified salt-bridge and at a given temperature, unless otherwise stated.

The upper operational temperature limit for the calomel electrode is approximately 353K.

2.3.3.2 Counter Electrode

A counter electrode was fashioned from Specpure platinum sheet of dimensions: 10x10x0.1mm. This was spot-welded to a 100mm length of 0.1mm diameter platinum wire which was in turn spot-welded to a suitable length of copper wire. This wire was then inserted into a 125mm length of 6mm diameter soda glass tube with the lower end subsequently fused on to the platinum wire. A sufficient length of platinum wire was left exposed to prevent the fused glass/platinum joint coming into contact with the electrolyte, thus avoiding seapage through the joint during operation.

When operating the "electrolysis-cell" a similar counter electrode was used, though of proportionally larger dimensions.

2.3.3.3 Working Electrode

The working electrode had a plane surface and was comprised of a cylindrical block of the sulphide mineral (or in some experiments platinum) affixed with an electrical contact and insulated such that only the desired face of the mineral was exposed to the electrolyte (see Figure 2.3.4).

Approximately 8mm length sections of synthesized sulphide were cut by spark erosion using a Sparcatron model SM24. This method was favoured over the use of a circular diamond saw since a finer cut is achieved without the risk of fracture. One of the faces was ground on 600 grit silicon carbide paper, washed in ethanol, dried, then joined to a 6mm diammeter copper cylinder using low resistivity (0.05Ωm) silver loaded epoxy adhesive (RS Components Ltd.). Once cured, the sulphide block was ground to a diammeter of 6mm and set in epoxy resin (cf. Section 2.4.1 for details). This resin is chemically inert in hydrochloric and perchloric acid solutions, but experienced swelling in sulphuric acid solution at temperatures >333K resulting in loss of electrical insulation. Once hardened, the resin was machined to 8mm diammeter, creating a readily interchangable electrode pellet for insertion into a PTFE sleeve. A reliable seal was obtained with PTFE tape. Electrical contact was made by screwing a stainless steel rod through the sleeve and into a M4 screw thread at the rear of the copper block. Physical support for use within the cell was achieved with a tappered PTFE collar near the top of the rod.

This design of working electrode proved experimentally successful. Examination of its electrical properties (by sandwiching a mineral specimen between two copper blocks with silver loaded epoxy adhesive) revealed ohmic behaviour in the current range 0-1A, with a resistivity for pentlandite = 5.2×10^{-4} Ωm and violarite = 6.5×10^{-4} Ωm (assuming a negligable contribution from the adhesive and copper). The M4 screw thread also provided a convenient mounting of the electrode pellets for examination of the mineral surface by SEM and EMPA.

The design was compatable for use with a Metrohm rotating disk electrode (RDE) model 628, which enabled the working electrode to be rotated at a variety of speeds, typically 20Hz. The RDE was used in experiments where it was desirable to enhance mass transfer in the aqueous phase which might otherwise have had a rate determining effect on the current density.

2.3.3.4 Glass Electrode

A Metrohm combined glass electrode model 6.0203.100 was normally used to measure the pH of the working electrolyte. However, when operating in perchloric acid solution, in order to prevent the precipitation of $KClO_4$ in the porous plug of the combined electrode, a Kent EIL glass pH electrode model 33 1070 130 was used in conjunction with a suitable salt-bridge (cf. Section 2.3.3.1).

A Pye Unicam pH meter model 291 was used to determine the pH, after calibration with appropriate buffer solutions.

2.3.4 General Experimental Prodedure

The majority of the experiments involved a similar procedure whether operating the Metrohm or the electrolysis cell. Details of the apparatus are described in Sections 2.3.1, 2.3.2 and 2.3.3.

In a typical experiment the cell was first brought to thermal equilibrium, whilst the electrolyte was purged with "white-spot" nitrogen to displace the oxygen. In experiments which required the electrolyte to be convection free, the nitrogen bubbler was later retrieved and a nitrogen atmosphere above the electrolyte maintained at a positive pressure to ensure the continuation of a low oxygen activity within the electrolyte.

The exposed face of the working electrode was ground on 1000 grit silicon carbide paper then thoroughly washed with distilled water. Polishing was normally avoided since other workers have reported that this may cause the mineral to become passivated prior to the experiment (131). The working electrode was then introduced into the cell and its open-circuit potential was measured with respect to a saturated calomel reference electrode.

After selecting the various parameters for the ensueing experiment, polarization was initiated and the response of the system was recorded (see Sections 2.2 and 2.3.2).

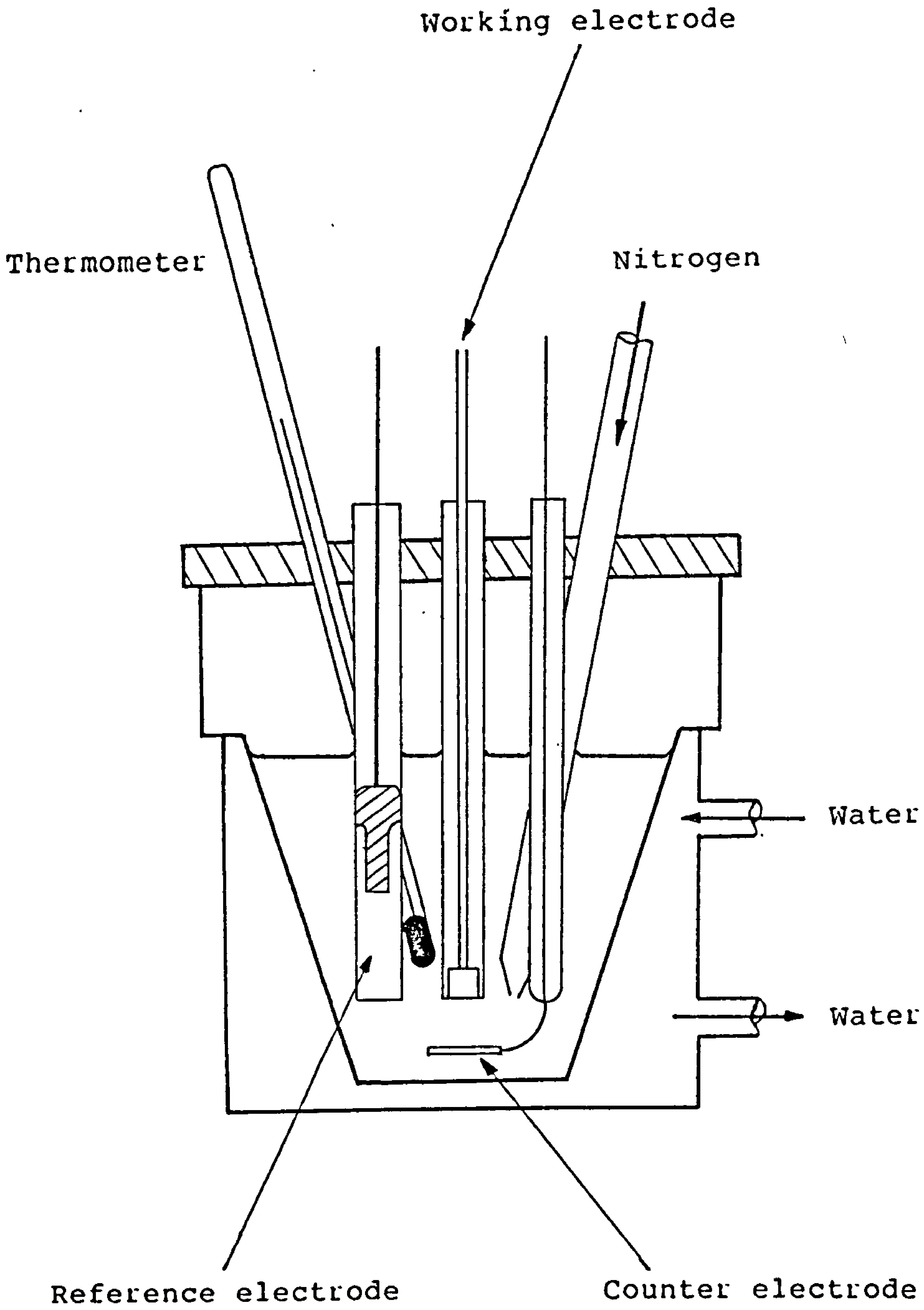

Figure 2.3.1

Schematic diagram of the Metrohm vessel

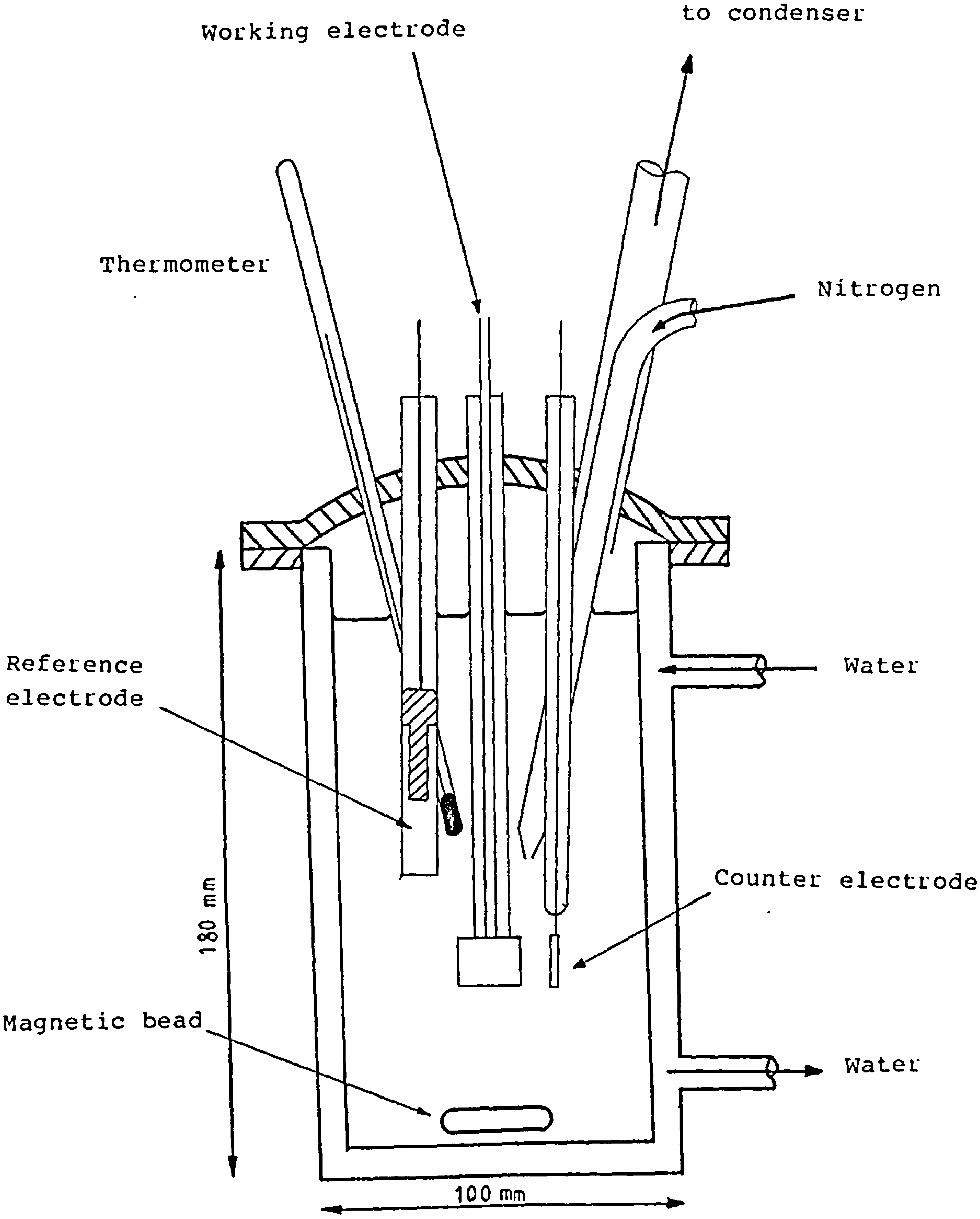

Figure 2.3.2

Schematic diagram of the "electrolysis cell"

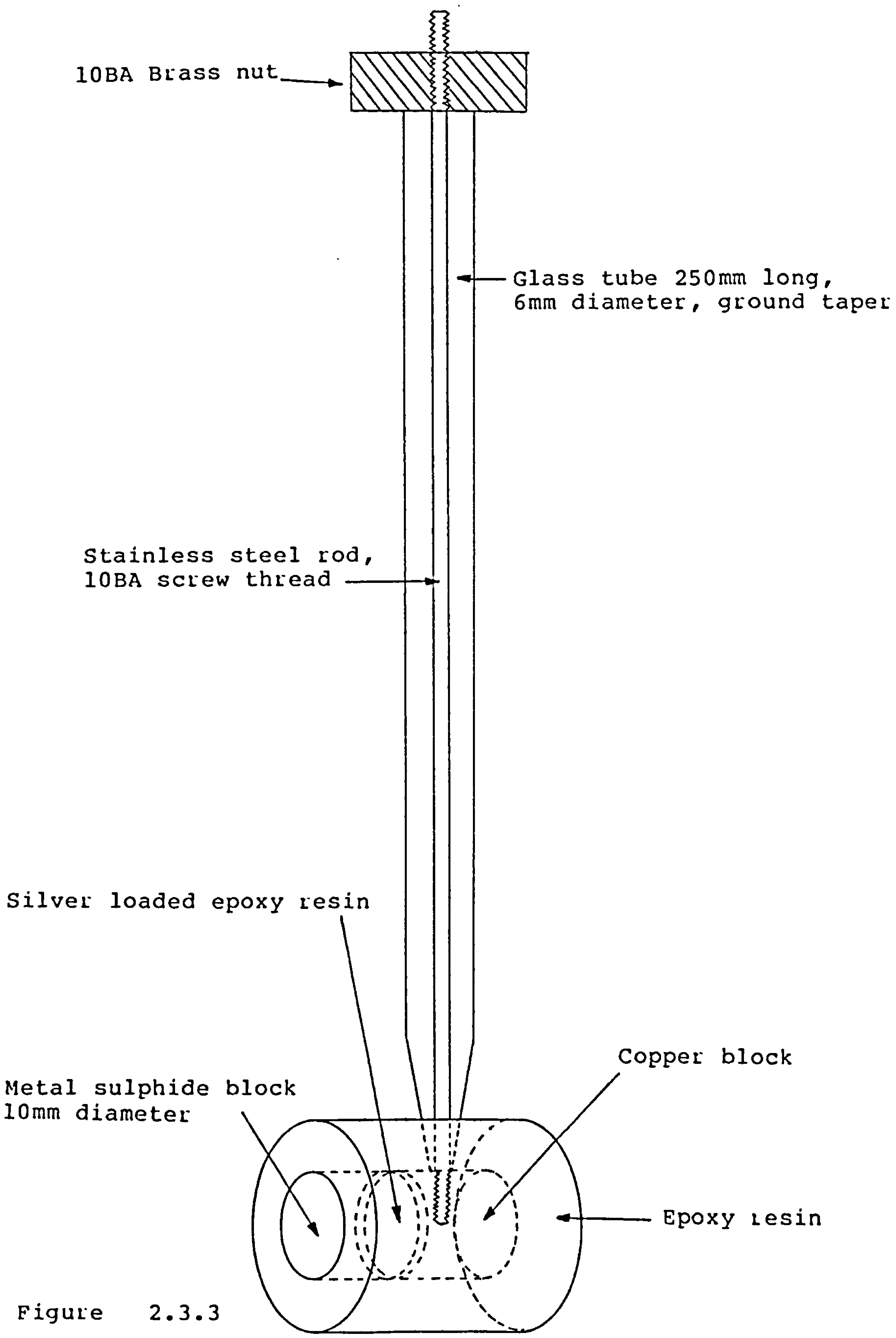

Figure 2.3.3

Schematic diagram of the working electrode

(as used in the electrolysis cell").

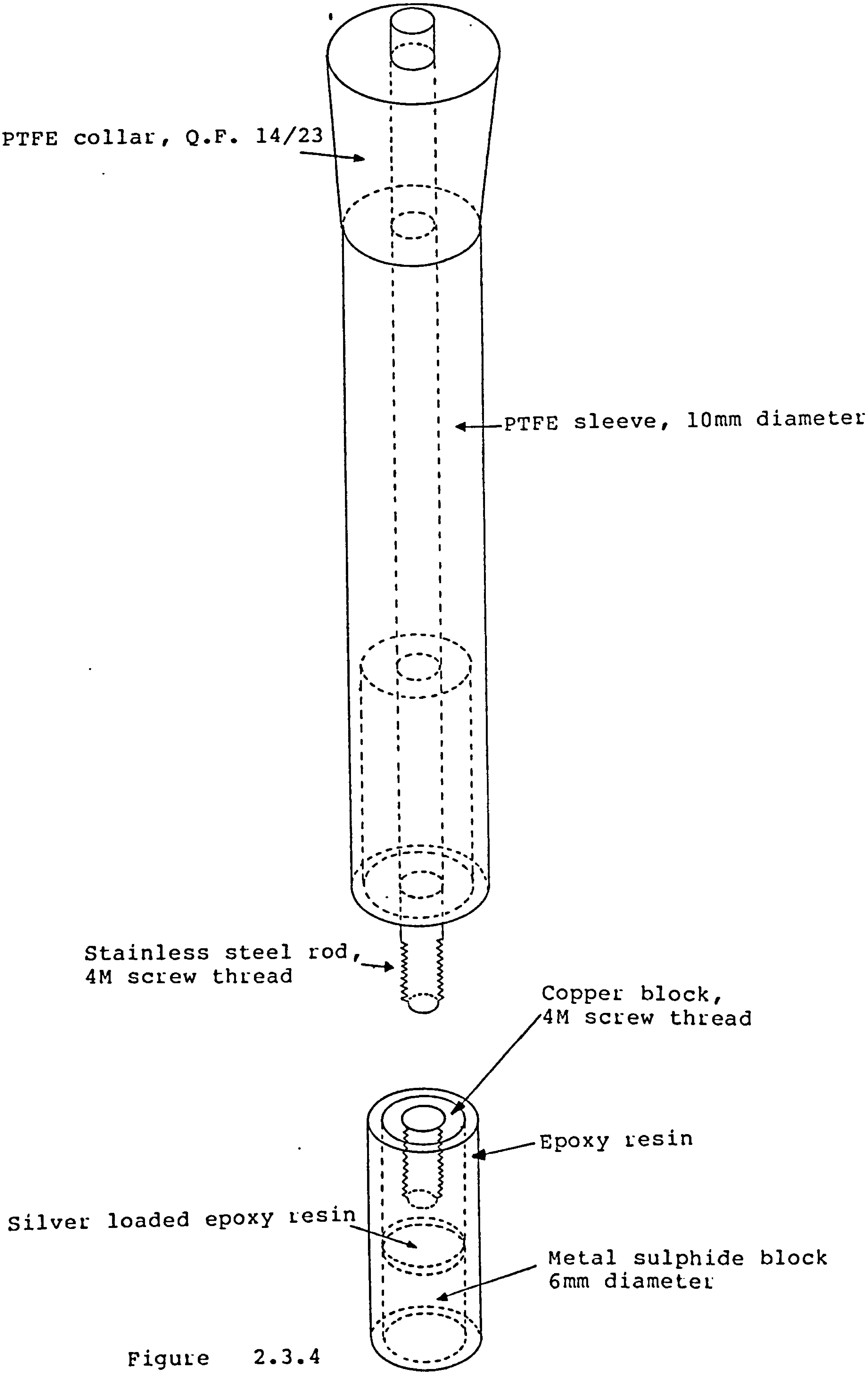

Figure 2.3.4

Schematic diagram of the working electrode

(as used in the Metrohm cell).

2.4 ANALYTICAL TECHNIQUES

2.4.1 Reflected Light Microscopy

A Vickers M55 microscope was used in the identification of the phases present in natural, synthetic and electrolysed mineral specimens and in the determination of their morphology and textural relationships. See Ramdohr (68) for a comprehensive treatise on ore mineralogy. The incident light was from a xenon bulb with a marco filter. Observations were made in either plane polarized light or crossed polars. Lense magnifications were x35, x70, x100, x200 (relative to the 35mm negative). Photographs were taken with the aid of a camera attachment.

Flat polished mineral sections were prepared by setting the mineral specimens in epoxy resin. This technique was favoured over the alternative use of thermal setting resins since it eliminates the possibility of any phase changes which may occur at the relatively high temperatures and pressures applied to thermal setting resins. Suitable specimens were selected and cut using either a circular diamond saw or by spark erosion (see Section 2.3.3.3). The desired face for observation was ground flat using wet 600 grit silicon carbide paper, then thoroughly washed and dried. The specimen was then placed face downwards concentricly in a polyethylene mould which was previously greased with petroleum jelly. The resin was prepared by mixing 8 parts of araldite resin MY 778 with 1 part of araldite hardener HY 951 (supplied by B & K Resins Ltd.) in a sealable plastic bag. This method permits the exclusion of air during mixing, thus reducing air bubble entrainment in the resin. The resin was then poured to fill the mould and any air bubbles were enticed to the surface with a metal wire. After 24 hours the desired face was ground flat using wet 400 and 600 grit silicon carbide paper on a rotating cast-iron lap. This was proceeded by polishing with 6 and 1 μm diamond paste on a rotating cloth lap.

The optical properties of colour and reflectivity were observed in plane polarized light. These were often diagnostic, eg. the characteristic violet colour of violarite. In crossed polars the optical property of reflection anisotropy was used to distinguish between isotropic and anisotropic phases. Under crossed polars, isotropic phases remain in darkness in all orientations of the microscope stage (eg. the cubic phases: pentlandite, violarite and high-heazlewoodite); whist anisotropic phases exhibit reflection anisotropy and thereby reflect some light (eg. pyrrhotite and heazlewoodite).

During the preparation of perpendicular cross-sections of electrolysed material, severe plucking of product material was encountered during the grinding and polishing stages. This resulted in major focusing problems and poor reflectivity of the regions concerned.

2.4.2 Scanning Electron Microscopy (SEM)

A Camscan Series 3 scanning electron microscope* was used in the study of the surface morphology of synthetic and electrolysed specimens. The operating parameters were: beam energy 20kV, beam current 0.15mA. A qualitative compositional analysis was obtained by energy dispersive

---

* Acknowledgement is given to Mr.A.Nichells and Mr.J.Harrington of the Department of Metallurgy, for operational and analytical assistance in the use of this instrument.

X-ray analysis (EDXA) using a Link Systems analytical 860 Series.

Synthetic mineral specimens were set in epoxy resin and prepared in a similar fashion as described in Section 2.4.1. In the analysis of electroysed samples it was found that the 6mm diameter electrodes (cf. Section 2.3.3.3) were most convenient for insertion into the instrument. Advantage was made of the 4M screw thread in the rear of the electrode for satisfactory mounting on specially adapted 4M bolts. Prior to analysis, all specimens were carbon coated using an Emscope TB500 carbon fibre flash coating unit. This was considered more favourable to the alternative use of gold since adequate dissipation of charge was achieved without the interference of the $S_{K\alpha}$ radiation by $Au_{M\beta}$, which might otherwise be deleterious to the analysis.

However, where high resolution photography was required the samples were gold coated using an Emscope SC500 gold spluttering unit.

2.4.3 Powder X-Ray Diffraction (XRD)

A Philips X-Ray Powder Diffractometer* was used in the identification of the phases present in synthetic and electrolysed specimens. The operating parameters were: nickel-filtered $Cu_{K\alpha}$ radiation of mean wavelength 0.15418nm at 35kV and 55mA. The diffraction angles corresponding to the various peak diffraction intensities were converted into lattice spacings (d/nm) by use of the Bragg equation ($\lambda = 2d\sin\theta$), and ascribed relative intensities (I). Peaks less

---

*Acknowledgement is given to Miss S.Nixon and Dr.P.D.Battle of the Department of Inorganic Chemistry, for conducting the analysis and for assistance in the interpretation of the analytical data.

than 5% (area) were denoted as trace intensities (t). Comparision of these data was made with those in the ASTM Handbook (155) and those of other workers.

Approximately 0.5g of sample material was required for the analysis. Synthetic material was readily obtained as broken fragments. However, in the analysis of the product layer from electrolysed specimens, the material was carefully scrapped from the electrode surface using a surgical blade. In order to obtain sufficient quantities, the electrolysis had to be repeated several times.

A minor complication can arise in the interpretation of the diffraction pattern due to the presence of split peaks which are particularly apparent at larger diffraction angles. This is caused by the presence of a doublet in the Cu_{K_α} radiation which arises through the transitions $K_{\alpha 1}$ (2p-1s) and $K_{\alpha 2}$ (2s-1s) where $K_{\alpha 1}$ predominates over $K_{\alpha 2}$ with wavelengths: 0.15405nm and 0.15443nm respectively. Where this problem arose, the mean value for the diffraction angle was adopted in conjunction with the mean wavelength for the radiation.

A Siemens Kristalloflex 2 powder camera* was used in the identification of phases present in the product layer. This technique was particularly useful since only a small amount of material was required. Operating parameters were: nickel-filtered Cu_{K_α} radiation at 30kV and 25mA, with an exposure time of 2.5 hours. The geometry of the camara is such that the diffraction angles can be obtained directly by measuring

---

* Acknowledgement is given to Dr.G.Hornung of the Department of Earth Sciences, for operational assistance in the use of this instrument.

the distance (4θ) in millimeters between the respective pairs of bands from the developed film.

2.4.4 Electron Microprobe Analysis (EMPA)

A Joel JXA-50A Electron Probe Microanalyser* fitted with a Link 860-500 energy dispersive system was used in the compositional analysis of synthetic and electrolysed specimens. The operating parameters were: beam energy 20kV, beam current 1nA giving 3000 counts per second into the detector. Spectrum livetime 100s. Beam penetration depths in Fe-Ni-S compounds are of the order of 1-2 μm, which represents the approximate depth of analysis on the surface. The elemental standards used were: Fe, S, pyrite; Ni, Ag, pure metals. Apparent concentrations were corrected for atomic number, absorption and fluorescence using Link ZAF4/FLS software. To determine elemental distributions, a Digitized EDS mapping technique was used with a Link Digimap proprietary software.

Synthetic mineral specimens were set in epoxy resin and prepared in a similar fashion as described in Section 2.4.1. Electrolysed samples were analysed in either of two ways. For cross-sectional analysis the electrodes were cut perpendicularly with a circular diamond saw, then set in epoxy resin and subsequently prepared as above. Unfortunately, problems were encountered in the polishing stage due to the plucking of loose product material. For analysis normal to the electrode surface, no preparation was necessary apart from the procurement of a suitable specimen

---

* Acknowledgement is given to Dr.E.Condliffe of the Department of Earth Sciences, for operational and analytical assistance in the use of this instrument.

holder. Prior to analysis, all specimens were carbon coated using an Emscope carbon fibre flash coating unit, in order to prevent a build up of charge during the analysis.

A small analytical error can arise when analysing Fe in the presence of Ni and vice versa. Ni_{K_α} has an energy of 7.472keV which is very close to the Fe_{K_α} absorption edge of 7.111keV. This leads to strong absorption of Ni_{K_α} by Fe and secondary fluorescence of Fe_{K_α}. The net effect is that this can lead to an increase in the apparent Fe concentration whilst reducing that for the nickel. More relevant to this work is to note that EMPA assumes a perfectly flat/smooth surface normal to the incident beam. However, these conditions could not always be met, either because of the porous nature of the bulk synthetic phase or that of the product layer. Consequently, a rough surface changes the X-ray take-off angle and therefore changes the absorption path length, and hence effects the absorption correction factor in the software. This second factor in particular imposes a limitation on the reported compositions to two significant figures.

2.4.5 Atomic Absorption Spectroscopy (AAS)

A Perkin Elmer model 272 atomic absorption spectrophotometer* was used in the determination of nickel, iron and silver concentrations in aqueous solution after suitable dilution or evaporation and comparison with appropriate standard solutions. The characteristic wavelengthes used were: Fe, 248.3nm; Ni, 232.0nm; and Ag, 328.1nm.

Prior to the analysis of solid material, a known mass of the solid was first digested in oxidizing acid media (either hydrogen peroxide / sulphuric acid or, aqua-regia).

2.4.6 Gravimetric Analysis

Gravimetric analysis* was used in the determination of sulphate in aqueous solution. The procedure was adopted from that of Vogal (139) and involves the addition of an excess of barium chloride in order to precipitate barium sulphate. After filtration and drying, the mass of the precipitate was determined on an appropriate balance.

This technique was extended to the analysis of elemental sulphur in solid material after prior combustion of the solid in oxygen to form sulphate.

---

* Acknowledgement is given to Mr.A.Hedley of the School of Chemistry, for conducting both of these analyses.

2.5 PURITY OF MATERIALS

2.5.1 Sulphur Powder, Batch No.S93593.

"Specpure" Johnson Matthey Chemicals Limited, England.
Spectroscopic Analysis:
Element detected / parts per million by mass

Bismuth	50
Germanium	2.0
Calcium	0.5
Copper	0.5
Silicon	0.5
Aluminium	0.3
Iron	0.3
Sodium	0.3
Titanium	0.3
Magnesium	0.2
Indium	0.05
Boron	0.03

2.5.2 Iron Powder, Batch No.S92701B.

"Specpure" Johnson Matthey Chemicals Limited, England.
Spectroscopic Analysis:
Element detected / parts per million by mass

Aluminium	<1
Calcium	<1
Copper	<1
Nickel	<1
Silicon	<1

2.5.3 Nickel Powder, Sample No.9976-S.

Sherritt Research Centre, Canada.
Chemical Analysis:
Element detected / parts per million by mass

Cobalt	730
Copper	4
Iron	75
Sulphur (Total)	290
Carbon	74

2.5.4 Silver Crystalline Pieces, Batch No.90996

"Specpure" Johnson Matthey Chemicals Limited, England.
Spectroscopic Analysis:
Element detected / parts per million by mass

Iron	1
Magnesium	<1
Sodium	<1

2.5.5 Platinum Sheet, Batch No.29986

"Puratronic" Johnson Matthey Chemicals Limited, England.
Spectroscopic Analysis:
Element detected / parts per million by mass

Palladium	6
Iron	4
Copper	2
Silver	2
Silicon	1

2.5.6 Sulphur Broken Lump, Batch No. S70343

"Specpure" Johnson Matthey Chemicals Limited, England.
Spectroscopic Analysis:

Element detected /	parts per million by mass
Boron	0.01
Calcium	0.04
Iron	0.06
Magnesium	0.02
Manganese	0.06
Silicon	0.6
Sodium	0.02

2.5.7 Platinum wire

"Puratronic" Johnson Matthey Chemicals Limited, England.
Spectroscopic Analysis:

Element detected /	parts per million by mass
Palladium	3
Rhodium	3
Nickel	2
Copper	1

2.5.8 Hydrochloric acid

"AnalaR" BDH Limited, Poole, England.
Assay(HCl) 31.5-33.0%

2.5.9 Perchloric acid

"AR" East Anglia Chemicals, Hadleigh Ipswich Suffolk.
Assay 71-73%

3 RESULTS AND DISCUSSION

3.0 INTRODUCTION

This section shows the results (often displayed in graphic form) for a series of electrochemical experiments performed on pentlandite and violarite in aqueous media. Synthetic minerals were used since sufficiently large and contaminant free specimens of natural minerals were unavailable (particularly for pentlandite, cf. Section 1.4.1). However, an additional quantity of naturally occuring violarite from Kambalda, Western Australia, was available for comparative work.

Experimental work was orientated towards discovering what processes occur under anodic conditions in various electrolytes of acid pH (typically 1M hydrochloric acid solution), within the temperature range 293 to 353K. Acid conditions were employed to enable direct comparison with acid ferric chloride leaching (in which acid pH is essential for the solubility of ferric and ferrous iron). Acid pH also provides the thermodynamiclly favourable conditions for the industrially desirable formation of elemental sulphur vis á vis sulphate in neutral/alkali pH. Behaviour in the potential region of 0.2 to 0.6V vs. SCE is particularly important since the equilbrium potentials for the common hydrometallurgical oxidants (eg. $FeCl_3$ and $CuCl_2$) occur in this region. The relevant hydrometallurgical processes (cf. Section 1.1.2) typically operate in the temperature range 348 to 383K. However, because of the technical difficulties of performing experiments at such temperatures, a compromise was reached by operating at temperatures up to 353K.

Initially, a correlation of open-circuit potentials (both as a function of pH and in the presence of additional aqueous redox couples) was performed prior to investigations by voltammetric techniques. Cyclic voltammetry, both with and without the presence of additional redox couples was then conducted on the various minerals, and on platinum for comparison. A comparison of results was also made of rotating disk and static electrode experiments to distinguish between diffusion limitation in the solid and the electrolyte near the mineral surface. Intermittent galvanostatic polarization (IGP) was performed in an attempt to identify the product species from measurement of regularly interspersed open-circuit potentials.

The studies described above were considered a prerequisite to those of chronopotentiometry and chronoamperometry, from which quantitative information can be obtained concerning reaction stoichiometry and kinetic parameters for diffusional processes. Since intermediate solid-state phase changes are known to occur in pentlandite under geological conditions, chronopotentiometry was performed on pentlandite in acid media to investigate this phenomenon under conditions more akin to hydrometallurgical extraction. Here, in particular, analytical techniques such as powder camara XRD, electron microprobe analysis, scanning electron microscopy and atomic absorption spectroscopy proved vital in identifying the products of the reaction both quantitativly and morphologically, and in establishing the reaction profile.

Chronoamperometry was conducted on the minerals primarily to compare and confirm the conclusions drawn from the earlier voltammetric studies within this work.

Finally, a study was made to determine the kinetic parameters of the industrially important $FeCl_3/FeCl_2$ couple using the techniques theoretically derived in Section 1.6.2.

3.1 POTENTIOMETRY

Pentlandite adopts a definite rest-potential of approximately -0.410V vs. SCE in 1M hydrochloric acid solution at 353K. At lower temperatures this potential is less negative, though it tends to drift towards more negative values with time. From previous work on acid decomposition discussed in Section 1.7.1, where pentlandite is known to be readily leached in such media (particularly at high temperature, viz. 373K), it is evident that this potential corresponds to the acid decomposition of pentlandite. This suggests a mixed-potential regime (cf. Section 1.6.3) incorporating the reduction of hydrogen ions in the acid solution to hydrogen gas, together with the oxidation of pentlandite to hydrogen sulphide, aqueous ferrous and nickel ions; as predicted from the metastable equilibrium discussed in Section 1.5:

$$4.5Fe^{2+} + 4.5Ni^{2+} + 8H_2S + 2e = Fe_{4.5}Ni_{4.5}S_8 + 16H^+ \quad (3.1.1)$$

$$E_h = 0.158 + 0.473pH + 0.133lg[Fe^{2+}] + 0.133lg[Ni^{2+}]$$
$$+ 0.236lg[H_2S]$$

In contrast to pentlandite, measurements ofthe open-circuit potential of violarite in 1M HCl solution in the temperature range 293 to 353K gave poor reproducibility, with values occuring in the range of 0.1 to 0.4 V vs. SCE. The thermodynamic relationships described in Section 1.5 show that it is impossible for hydrogen ions to oxidize this sulphur rich phase (viz. M_3S_4), and that the alternative dissolution with the generation of hydrogen sulphide would require reducing conditions. Therefore, in a closed aqueous system of acid pH, free from imposed oxidizing or reducing conditions, (and in which H_2S is unavailable as a reactant) violarite is metastable with respect to sulphur disproportionation:

$$4FeNi_2S_4 + 23H^+ + 4H_2O = 8Ni^{2+} + 4Fe^{2+} + 15H_2S + HSO_4^- \tag{3.1.2}$$

hence the association of an ill-defined potential.

Sato (146) states in a fundamental paper on metal sulphide dissolution in 1960 that: "Of all the complexities of the oxidation reactions of a sulphide mineral, the most crucial and the least understood part is the first step of the heterogeneous reaction through which the solid sulphide is partially or totally dissolved into the surrounding solution upon breaking up its crystal bonds........ The understanding of this first-step reaction mechanism is essential in the discussion of the rate of reaction and the activation potential levels for the oxidation of sulphide minerals". He then goes on to describe a procedure for the identification of the first-step oxidation or reduction reaction of a sulphide mineral by the measurement of the single electrode potential of the sulphide mineral in solutions containing its assumed oxidation or reduction product ions. The first step reaction is that which best fits the observed data with respect to the potential, pH dependence and change in activities of the chemical species involved.

This is clearly a thermodynamic approach (i.e. through the establishment of the Nernst potential) for what is essentially a kinetic problem. Consequently, this approach is only applicable to systems which portray a state of thermodynamic equilibrium. It is important to note that his studies were restricted to binary compounds of which Cu_2S, PbS, Ag_2S and ZnS gave satisfactory conclusions, although results from the sulphur rich phases: pyrrhotite and FeS_2 were inconclusive.

Such equilibrium studies on pentlandite are excluded because of the metastability of pentlandite in acid media as described above. However, a correlation of open-circuit potentials as a function of pH was performed on natural violarite in a solution containing 0.001M Ni^{2+}, 0.001M Fe^{2+} and 0.1M $SO_4{}^{2-}$ at 291K. pH was adjusted with perchloric acid (see Figure 3.1.1). The rest potentials are very sensitive to the dissolved O_2 concentration, where an atmosphere of 101kPa O_2 raises the potential by approximately 0.13V, and also enhances reproducibility.

Figure 3.1.2 shows the results of a similar experiment on synthetic violarite and on platinum for comparison, with equal amounts of ferrous and ferric iron in solution. 1M $NaClO_4$ was added to the solution in order to maintain a constant ionic strength, to enable comparison of potentials at different pH values without extraneous effects from changes in the ionic strength of the solution accompanying the addition of acid. The potentials on violarite tally with the "101kPa O_2" potentials in Figure 3.1.1, suggesting that the latter are due to the indirect oxidation by O_2 (or other trace oxidants) on violarite through a Fe^{3+}/Fe^{2+} couple. Furthermore, these potentials lie just negative of the equilibrium Fe^{3+}/Fe^{2+} potentials on platinum.

The experimental procedure as described by Sato (146) for the identification of the first step of the reaction is clearly inapplicable here. The evidence suggests a mixed-potential regime incorporating the reduction of aqueous ferric ions to ferrous (with or without the additional action of an O_2 "pump"). In the pH region <1.5, the independence of the mixed-potential on pH can be interpreted by the involvement of the S^o, Fe^{2+}, Ni^{2+} / $FeNi_2S_4$ couple within the "mixed-potential regime" (i.e. oxidation of violarite to elemental sulphur). Likewise, in the pH region >1.5, the mixed potential dependence on pH ($dE/dpH = -0.027$ V decade^{-1}) can be interpreted in terms of the $SO_4{}^{2-}$, Fe^{2+}, Ni^{2+} / $FeNi_2S_4$ couple (i.e. oxidation of violarite to sulphate). Note that since these are non-equilibrium potentials, dE/dpH is not expected to correspond to the Nernstian slope of -0.063 V decade^{-1}.

The observation that electrode potentials of sulphide minerals, particularly those of polysulphides, were very similar to the oxidation potential of the solution were made as long ago as 1914 by Wells (145). In this current work, pentlandite and violarite adopt the same rest potential in 1M HCl solution containing 0.05M $FeCl_3$ and 0.05M $FeCl_2$ at 298K, as that on platinum, i.e. +0.450V vs. SCE. The rest potentials on pentlandite, violarite and platinum at the higher temperature of 343K and with various $FeCl_3/FeCl_2$ ratios in 1M HCl solution, are shown in Table 3.1.1 and Figure 3.1.3.

These results are viewed in terms of the concept of a mixed potential as described in Section 1.6.3. Since the $FeCl_3/FeCl_2$ couple is known to be quasi-reversible (at least on platinum) i.e. there is reasonably fast electron transfer (cf. Section 3.7), Figure 1.6.4 provides a means for the interpretation of these results. The increase in disparity between the mixed potentials on the metal sulphides and the equilibrium potentials on platinum at higher $FeCl_3/FeCl_2$ ratios (see Figure 3.1.3) may be due to a greater positive shift in "equilbrium" potential of the latter process, compared with that of the former; i.e. the metal sulphide experiences a greater "overpotential" and hence a greater anodic current. Nonetheless, the mixed potentials on pentlandite and violarite are remarkably close to the equilibrium potential for the $FeCl_3/FeCl_2$ couple, even at 343K and $[FeCl_3]/[FeCl_2] = 100$; compared with copper under identical conditions (viz. $E_{mixed} = -0.23V$ vs. SCE (293K)).

The different mixed potential values on violarite and pentlandite may, at least in part, be explained ("assuming" similar kinetics for each) by the higher "equilibrium" potential for the S^o, Fe^{2+}, Ni^{2+} / $FeNi_2S_4$ couple compared with the S^o, Fe^{2+}, Ni^{2+} / $Fe_{4.5}Ni_{4.5}S_8$ couple (cf. Section 1.5). Hence a smaller overpotential occurs for violarite dissolution compared with that for pentlandite.

Even greater parity is observed with the $CuCl_2/CuCl$ couple, see Table 3.1.1. This is expected for two reasons. Firstly, the $CuCl_2/CuCl$ couple is known to be more reversible than the $FeCl_3/FeCl_2$ couple (at least on platinum and chalcopyrite(165)). Secondly, if the existance of a mixed-potential regime as cited above is correct, then because of the lower equilibrium potential of the $CuCl_2/CuCl$ couple a smaller anodic current is expected giving a greater similarity between the mixed and equilibrium potentials.

From this series of rest potential measurements and an understanding of the concept of mixed potential, there is strong evidence that the exchange current density for the S^o, Fe^{2+}, Ni^{2+} / $Fe_{4.5}Ni_{4.5}S_8$ (or $FeNi_2S_4$, Ni^{2+}, Fe^{2+} /

$Fe_{4.5}Ni_{4.5}S_8$) and S^o, Fe^{2+}, Ni^{2+} / $FeNi_2S_4$ couples is small.

Furthermore, since the concentrations of metal atoms within the pentlandite and violarite crystal lattices are very large (cf. Appendix B), this implies that the heterogeneous rate constants for these couples are very small. Thus, it is quite pertinent to suggest that the oxidative dissolution of pentlandite and violarite in acid media (at least during the initial stages of reaction and in the temperature range 293 to 343K) involves slow electron transfer for the S^o,Fe^{2+}, Ni^{2+} / $Fe_{4.5}Ni_{4.5}S_8$ (or $FeNi_2S_4$, Ni^{2+},Fe^{2+} / $Fe_{4.5}Ni_{4.5}S_8$) and S^o, Fe^{2+}, Ni^{2+} / $FeNi_2S_4$ couples per se.

Table 3.1.1 Open-Ciruit Potential Measurements

W.E.	T/K	Working electrolyte	E/V vs. SCE
SynPn3	293	1M HCl	-0.224
SynPn3	353	1M HCl	-0.410
SynVllb	293	1M HCl	approx. 0.1 to 0.4
SynVllb	353	1M HCl	approx. 0.1 to 0.4
SynPn3	293	1M $HClO_4$	-0.210
SynPn3	353	1M $HClO_4$	-0.370
SynVllb	293	1M $HClO_4$	approx. 0.1 to 0.4
SynVllb	353	1M $HClO_4$	approx. 0.0 to 0.4
SynPnl	343	1M HCl, 0.001M $FeCl_3$, 0.099M $FeCl_2$	0.355
SynVllb	343	1M HCl, 0.001M $FeCl_3$, 0.099M $FeCl_2$	0.383
Pt	343	1M HCl, 0.001M $FeCl_3$, 0.099M $FeCl_2$	0.383
SynPnl	343	1M HCl, 0.010M $FeCl_3$, 0.090M $FeCl_2$	0.428
SynVllb	343	1M HCl, 0.010M $FeCl_3$, 0.090M $FeCl_2$	0.434
Pt	343	1M HCl, 0.010M $FeCl_3$, 0.090M $FeCl_2$	0.436
SynPnl	343	1M HCl, 0.050M $FeCl_3$, 0.050M $FeCl_2$	0.490
SynVllb	343	1M HCl, 0.050M $FeCl_3$, 0.050M $FeCl_2$	0.499
Pt	343	1M HCl, 0.050M $FeCl_3$, 0.050M $FeCl_2$	0.503
SynPnl	343	1M HCl, 0.090M $FeCl_3$, 0.010M $FeCl_2$	0.522
SynVllb	343	1M HCl, 0.090M $FeCl_3$, 0.010M $FeCl_2$	0.560
Pt	343	1M HCl, 0.090M $FeCl_3$, 0.010M $FeCl_2$	0.566
SynPnl	343	1M HCl, 0.099M $FeCl_3$, 0.001M $FeCl_2$	0.544
SynVllb	343	1M HCl, 0.099M $FeCl_3$, 0.001M $FeCl_2$	0.590
Pt	343	1M HCl, 0.099M $FeCl_3$, 0.001M $FeCl_2$	0.635
SynPn3	293	1M HCl, 0.05M $CuCl_2$, 0.05M CuCl	0.233
SynVllc	293	1M HCl, 0.05M $CuCl_2$, 0.05M CuCl	0.233
Pt	293	1M HCl, 0.05M $CuCl_2$, 0.05M CuCl	0.233
SynPn3	343	1M HCl, 0.05M $CuCl_2$, 0.05M CuCl	0.289
SynVllc	343	1M HCl, 0.05M $CuCl_2$, 0.05M CuCl	0.289
Pt	343	1M HCl, 0.05M $CuCl_2$, 0.05M CuCl	0.289

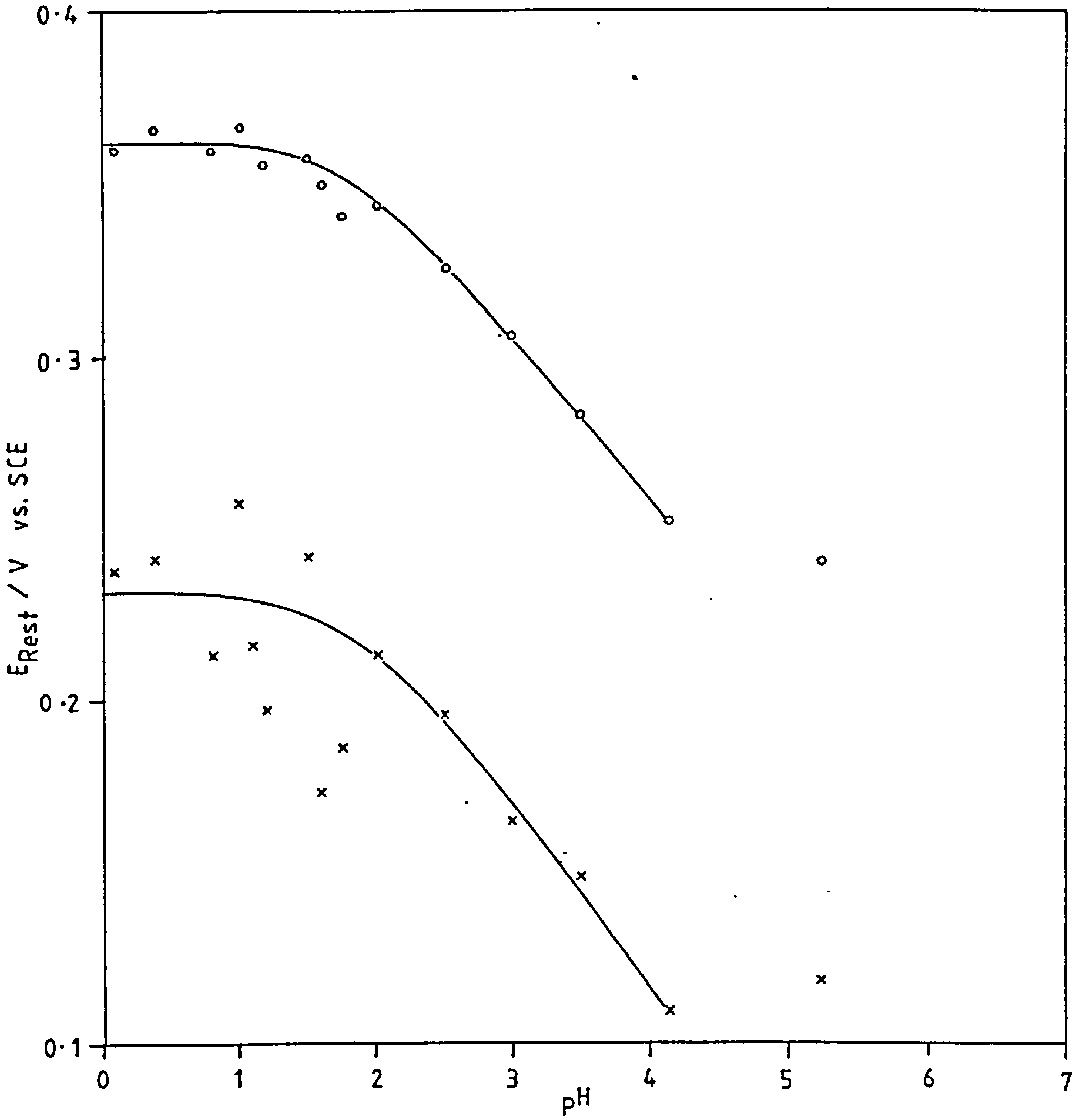

Figure 3.1.1

Effect of pH on the open-circuit potential for natural violarite (Z28892) at 291K in aqueous solution containing the envisaged oxidized conjugate ionic species. Solution composition: 10^{-3}M $NiSO_4$, 10^{-3}M $FeSO_4$, 0.098M Na_2SO_4. pH adjusted with perchloric acid.

o = O_2 purge (101kPa), × = N_2 purge (101kPa).

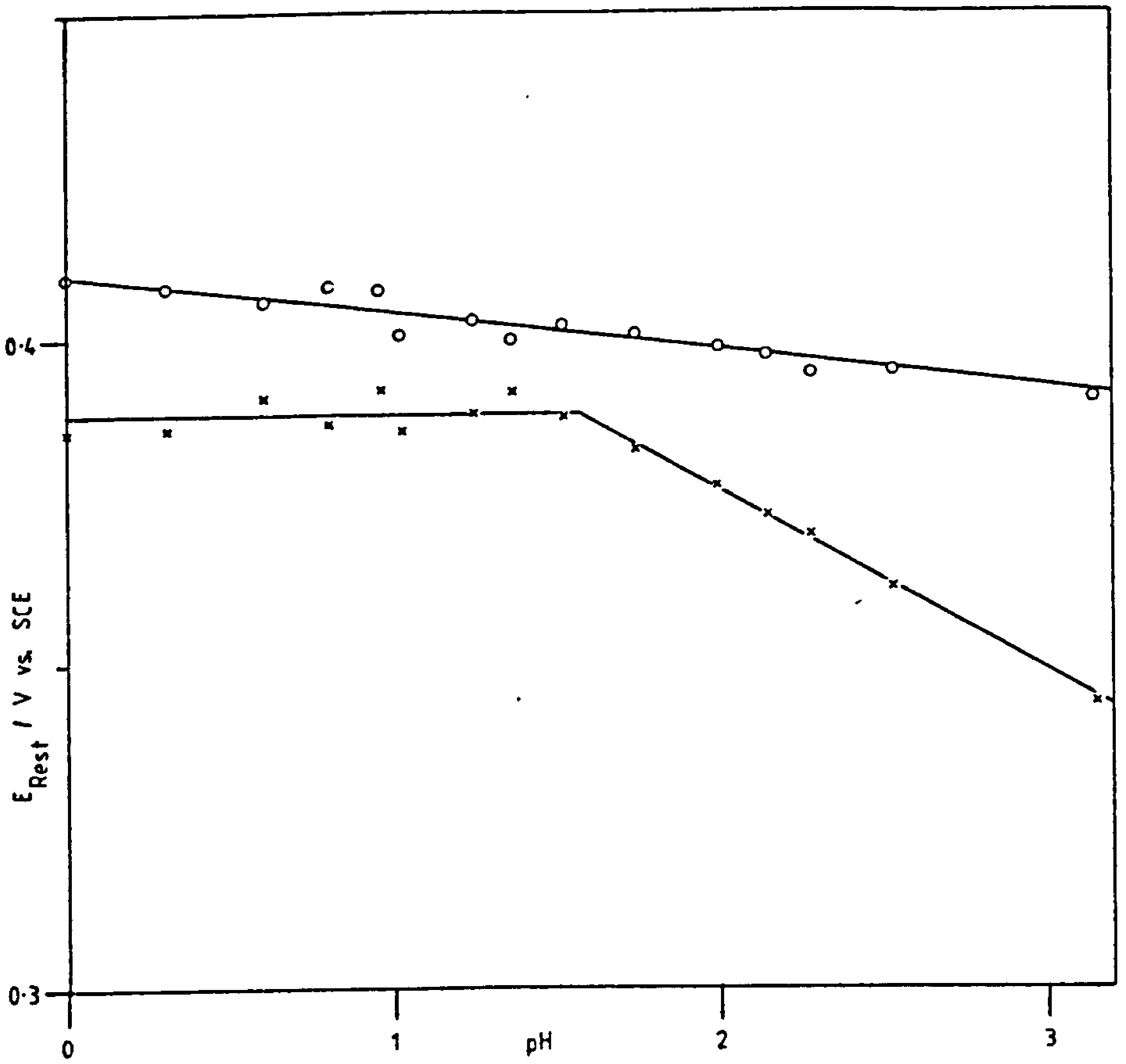

Figure 3.1.2

Effect of pH on the open-circuit potential for violarite (SynVl1b) at 291K, in aqueous solution containing equal amounts of ferrous and ferric iron. Solution composition: $5\text{x}10^{-4}$M Fe^{3+}, $5\text{x}10^{-4}$M Fe^{2+}, 10^{-3}M Ni^{2+}, 0.1M $SO_4{}^{2-}$, 1M $NaClO_4$. pH adjusted with perchloric acid. N_2 purge.

× = violarite, o = platinum.

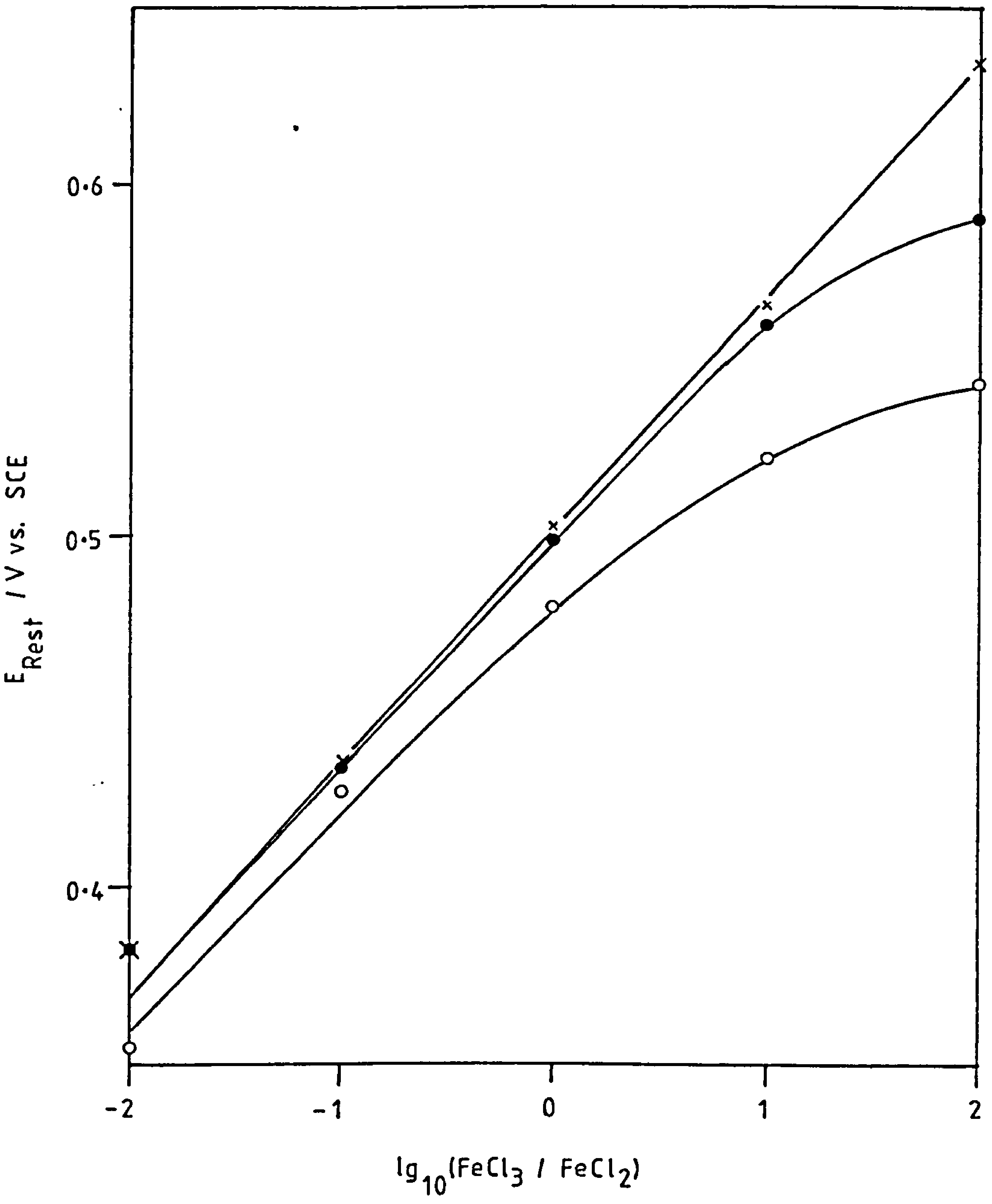

Figure 3.1.3

Correlation of open-circuit potential with various $FeCl_3/FeCl_2$ ratios at 343K, in 1M HCl solution. Total iron concentration = 0.1moldm^{-3}. RDE = 20Hz.

× = platinum, ● = violarite, o = pentlandite.

3.2 LINEAR SWEEP CYCLIC VOLTAMMETRY

3.2.1 Pentlandite

The voltammetric "window" for 1M HCl solution at 343K on platinum is shown in Figure 3.2.1. Chlorine is liberated at E >1.0V vs. SCE, and hydrogen at E <-0.2V vs. SCE.

Figures 3.2.2 to 3.2.5 show cyclic voltammograms for pentlandite in 1M HCl and in 1M $HClO_4$ solution at temperatures 293 and 353K. The most striking feature of these results is that reasonable rates of oxidative dissolution (i.e.>100Am^{-2}) were not obtained until relatively high potentials (viz. >0.8V vs. SCE), irrespective of temperature or solution composition. Thus implying that a large anodic overpotential is required for the oxidation of this mineral. In this high potential region, the anodic currents were accompanied by the visible formation of yellow coloured elemental sulphur. However, the sulphur was not crystalline but showed plastic/elastic properties indicating an amorphous allotrope (166). The surface of the pentlandite proper, showed a metallic violet/ grey coloured tarnish. The formation of violarite as an intermediate phase was considered a likely explanation to these visual observations at this stage in the work. These phenomena were studied and are described in greater detail in Section 3.5.

The initial small anodic current (just positive of the rest potential) is interpreted as the oxidative dissolution of pentlandite accompanied by the formation of H_2S (see Section 3.1 and Equation 3.1.1). This feature is more prominent at higher tempertures. Figure 3.2.76 shows SEM images of the pentlandite surface after an anodic excursion from the rest-potential to 0.7V vs. SCE in acid solution at 343K. It is evident that the pentlandite surface has been etched, whilst no elemental sulphur was detected by EDXA. This suggests the predominance of the above reaction, at low potentials.

Since it is impossible to reduce pentlandite in aqueous media (cf. Section 1.5), any cathodic currents arising during the cathodic excursion must be due either to the reduction of oxidation products formed during the anodic excursion, or to the reduction of species in the electrolyte. The cathodic currents below approx. 0V vs. SCE are inferred, at least in part, from the reduction of elemental sulphur:

$$S^o + 2H^+ + 2e = H_2S \qquad (3.2.1)$$

The reduction of violarite at the interface was also considered a possibility at this stage in the work. The predominant cathodic current below approx. -0.4V vs. SCE is due to the reduction of $H^+(aq)$ to H_2 on the pentlandite surface.

Figure 3.2.6 shows that even at higher scan rates, significant currents (i.e. $>100Am^{-2}$) are still not observed until >0.8V vs. SCE. Quantitative analysis (i.e. the determination of kinetic parameters) cannot be performed on these voltammetric waves since conventional voltammetric peaks for single processes are not obtained (see Figures 3.2.7 and 3.2.8). At these large potentials other processes occur, e.g. Cl^-/Cl_2 (by olfactive observation) and possibly the formation of sulphate, which contribute to the observed current and therefore complicate the analysis. Furthermore, these high potential voltammograms show a drop in current on successive anodic excursions, which indicates that the product(s) of oxidation formed during the initial anodic excursion have a passivating effect on further mass/charge transfer.

Figures 3.2.9 to 3.2.16 illustrate the effects on the reverse (cathodic) scan of progressively greater anodic excursions. Cathodic currents in the potential region 0 to -0.3V vs. SCE region are not observed until the anodic excursions extend beyond 0.2V vs. SCE. Thereafter the cathodic currents increase pro rata with the extent of anodic polarization. The occurance of two cathodic peaks in the potential region 0 to -0.3V vs. SCE may be attributed to the reduction of elemental sulphur and an intermediate phase e.g. violarite. Alternatively, these peaks may be attributed to the reduction of different allotropes of sulphur, or even the reduction of an impurity phase e.g. pyrrhotite. This problem is resumed in Section 3.3.

A brief experiment to investigate the effect of visible light on the pentlandite/aqueous interface during anodic polarization showed that no photoelectric currents were evident (cf. Figure 3.2.17).

The impossibility of reducing pentlandite in aqueous media, was exploited by investigating the electron transfer reaction for the aqueous redox couples $FeCl_3$/$FeCl_2$ and $CuCl_2$/CuCl on a corroding pentlandite surface and on platinum for comparison. $FeCl_3$ and $CuCl_2$ are important leachants for the dissolution of base metals from sulphide ore minerals and mattes. Thus, it is important to gain a knowledge (at least in qualitative terms) of their heterogeneous kinetic rate parameters on a common electrode surface i.e. platinum, and then to compare these with those on the corroding mineral surface, ipso facto revealing the mineral surface's ability to participate in charge transfer.

Figures 3.2.18 and 3.2.19 show cyclic voltammograms for the $FeCl_3/FeCl_2$ on platinum at 303 and 343K respectively. The current densities are not particularly indicative of quasi-reversible behaviour, but nonetheless are reproducible on succesive scans. (for quantitative details of the heterogeneous kinetic parameters of the $FeCl_3/FeCl_2$ couple see Section 3.7).

Figures 3.2.20 to 3.2.22 show cyclic voltammograms for the $FeCl_3/FeCl_2$ couple on differnt batches of synthetic pentlandite at 292K. These show relatively large currents during the first anodic excursion from the mixed potential. Subsequent anodic/cathodic perturbations result in progressively reduced, though still sustainable, anodic and cathodic currents. Since these features are common to all three samples of pentlandite, they can not be attributed to the inclusion of an impurity phase i.e. pyrrhotite or heazlewoodite (cf. Section 2.1).

Within the potential range studied, the observed current density (i_{obs}) is comprized of the following components:

$$i_{obs} = i_a(Fe_{4.5}Ni_{4.5}S_8) + i_a(FeCl_2) + i_c(FeCl_3) \qquad (3.2.2)$$

Since at potentials <0.8V vs. SCE, $i_a(Fe_{4.5}Ni_{4.5}S_8)$ is very small (as illustrated by the above work), its contribution to i_{obs} within this potential range can be ignored.

Therefore, examination of i_{obs} at potentials cathodic of the mixed potential should give a valuable indication of the surface's ability to participate in electron transfer.

Figures 3.2.23 to 3.2.32 show the results from a series of such experiments, in which the effects on i_{obs} during successive cathodic cycles are studied with progressively greater anodic excursions. The results show a consistent trend in which smaller current densities are observed pro rata with the extent of anodic polarization.

At higher temperatures (viz. 343K) the same phenomenon occurs, though to a less drastic degree (cf. Figures 3.2.33 to 3.2.35). Experiments with the $CuCl_2/CuCl$ couple indicate that this couple involves fast electron transfer whether on platinum, pentlandite or violarite surfaces (cf. Figures 3.2.36 and 3.2.37).

These results suggest the formation of a passive film, which thereafter retards electron transfer and/or mass transport at the pentlandite surface. However, such changes to the mineral surface were too subtle to be detected by EMPA. It was hoped that this particular work would be run in conjunction with electron spectroscopy for chemical analysis (ESCA) for the identification of surface species. Unfortunately, this was beyond the financial constraints of this present work, but may provide a stimulating area for future research. Nonetheless, if such studies were embarked upon, comparative work on various surfaces would be crucial because of the "ex-situ" nature of this sensitive technique.

Comparison with similar work on chalcopyrite ($CuFeS_2$) is appropriate here (167),(165),(168),(169),(170),(171),(142). Parker (167) concludes that the oxidation of chalcopyrite is limited by transport of ions through an unstable film of semi-conductor metal deficient polysulphide. To this same phenomenon McMillan (168) suggests an iron deficient copper sulphide species which he terms a "solid electrolyte interface" (SEI). Nonetheless, both groups of workers attribute the retardation of the dissolution kinetics to electron transfer and ionic mass transport through such an intermediate film. They overlook the possibility that the physical properties of plastic sulphur (as observed on the chalcopyrite surface by Biegler & Swift (171)) may allow the sulphur product layer to form a sufficiently dense layer that may just as plausibly account for the low rates of dissolution.

Parker (167) states that electron transfer from corroding $CuFeS_2$ to Fe^{3+} or Cu^{2+} in solution is a "very slow" process, which for the reduction of ferric sulphate is rate limiting. This is contradictory to his results which indicate a "large exchange current density" for the $CuCl_2/CuCl$ couple on corroding $CuFeS_2$, with a mixed potential "very similar" to the equilibrium potential (i.e. that on Pt) for this couple. Nonetheless, electron transfer rates decrease in the series:

$$CuCl_2 > FeCl_3 > Fe_2(SO_4)_3$$

which Parker uses to explain why the dissolution of $CuFeS_2$ is faster with $CuCl_2$ rather than $FeCl_3$, even though on purely thermodynamic grounds the reverse would have been expected.

In the presence of uncoated "cathodic" sites (within the specimen) for electron transfer e.g. FeS_2, electron transfer to the oxidants is much faster (i.e. a galvanic effect) such that the reaction is then subject to the limitation of the "anodic" process by the slow diffusion of ions at the anodic sites. (The present author is also aware that greater cathodic currents can be induced through galvanic coupling, an effect produced solely by increasing the "cathodic area" irrespective of whether or not the alternative "cathodic" sites are coated! cf. Section 1.6.3). Furthermore, such a system becomes comparable with anodic polarization experiments in which the "cathodic" current is introduced via the rear of the mineral (with minimal iR drop) such that the kinetics are determined by the anodic processes at the mineral/aqueous interface.

However, Parker (167) concludes that oxidation of $FeCl_2$ and $FeSO_4$ on corroding $CuFeS_2$ is limited by the "supply of holes" to the semi-conductor surface, so that the oxidation of Fe^{2+} has a limiting current. This is why addition of $FeCl_2$ to a $FeCl_3$ leach of $CuFeS_2$ has negligible Nernstian effect on the mixed potential and hence negligible effect on the rate of oxidation of $CuFeS_2$. This latter observation was also made by Hirato (169).

In a later paper (170) on the $CuCl_2$ leaching of $CuFeS_2$ at 343K, Hirato concludes that the leaching rate is proportional to $[CuCl_2]^{0.5}$ $[CuCl]^{-0.5}$. The present author infers that this is equivalent to the statement that the rate of $CuCl_2$ dissolution of $CuFeS_2$ is dependent on the Nernstian potential of the solution, and therefore on the rate of electron transfer of the Cu^+, Fe^{2+}, S^o / $CuFeS_2$ couple per se.

Referring to the present work on pentlandite, there is no additional analytical evidence to suggest a metal deficient SEI. Even so, a change from metallic to semi-conductor properties at the surface of corroding pentlandite could be inferred from the above results, although this must remain a conjectural issue.

A more feasible explanation is that amorphous sulphur, which is known to occur as one of the products of oxidation, influences events here. This could be achieved by decreasing the effective area of the electrode and/or by producing a passive film which hinders ionic mass transport in the aqueous phase adjacent to the pentlandite surface.

This conclusion does not retract from that drawn in Section 3.1, i.e. that the oxidative dissolution of pentlandite in acid media in the temperature range 293 to 343K, and in the potential range relevant to the $FeCl_3$ and $CuCl_2$ leachants (0.2 to 0.7V vs. SCE) involves slow electron transfer for the S^o, Fe^{2+}, Ni^{2+} / $Fe_{4.5}Ni_{4.5}S_8$ couple per se. It merely creates an additional kinetic problem for the dissolution mechanism i.e. ionic mass transport (notably that of the oxidant species in conventional chemical leaching) through a semi-permeable layer of amorphous sulphur. It is therefore possible that at a later stage of the reaction, this mass transport process becomes comparable with, and ultimately predominates over the electron transfer process and thereby becomes rate determining.

3.2.2 Violarite

Figures 3.2.38 to 3.2.44 show cyclic voltammograms for violarite in 1M HCl and in 1M $HClO_4$ solution at a variety of temperatures. The features are in many ways similar to those for pentlandite. Reasonable rates of oxidation are not obtained until relatively high potentials (viz. +0.8V vs. SCE), although greater currents are sustainable on successive excursions in the very high potential region (cf.

Figures 3.2.45 and 3.2.45). This latter phenomenon may be associated with the observation that less elemental sulphur (though still amorphous) appeared to form on violarite, implying perhaps a greater formation of sulphate and/or greater ease in the oxidation of chloride on the violarite surface.

A few features arise in the cyclic voltammograms for violarite which are different to those for pentlandite. When the potential is initially scanned cathodic from the rest potential, a cathodic current is generated. However, potentials in the region 0.4 to -0.3V vs. SCE are insuffuciently negative for the evolution of hydrogen on the violarite surface. Furthermore, these currents cannot be attributed to the reduction of elemental sulphur, since at this stage in the cycle none is present. Therefore, the reduction of violarite to hydrogen sulphide is implicated:

$$FeNi_2S_4 + 8H^+ + 2e = 2Ni^{2+} + Fe^{2+} + 4H_2S \qquad (3.2.2)$$

The predominant cathodic current at potentials <-0.4V vs. SCE is due to the reduction of the acid solution with hydrogen evolution. On the return (anodic) scan, the initial anodic current (with a peak at approx. 0V vs. SCE at high temperatures) is attributed to the oxidation of a metal rich surface (as discussed in Section 1.7.2, within the critcal review of the work by Thornber (76)).

An almost characteristic feature of violarite (vis à vis pentlandite) is a "prewave" during the anodic excursion at approximately 0.5V vs. SCE, with the appearance of associated cathodic currents on the reverse (cathodic) scan. This feature was studied by a series of cyclic voltammograms with a variety of scan rates to progressively greater anodic potentials (see Figures 3.2.47 and 3.2.57). These results clearly show an association between the cathodic wave and the anodic "prewave".

The linear voltammogram in Figure 3.2.58 illustrates how this "prewave" may be regarded as a superimposed anodic process in addition to the main anodic oxidation of violarite. Experiments captured on a more sensitive current range (cf. Figures 3.2.59 to 3.2.61) showed that the peak currents are proportional to the square root of the scan rate which is one of the diagnostic features of fast electron transfer (cf. Section 2.2.5 and Figure 3.2.62). With reference to Figure 3.2.59, at 303K the peak separation for the trace "C" (i.e. E_p(C) - E_p(-C)) was approx. 65mV indicating a one electron transfer process. The half-wave potential ($E_{1/2}$) for trace "C" was 0.45V vs. SCE.

At 323K, the peak potentials (E_p) are more independent of the scan rate than at 303K, indicating increased reversible behaviour at this higher temperature. At 323K, the cathodic currents are of a smaller magnitude vis á vis anodic currents, suggesting that the oxidized species has a greater mobility to leave the surface of the violarite. However, a comparison between rotating disk and static electrode experiments showed that diffusion of the electroactive species in the electrolyte near the mineral surface was not rate limiting (see Figures 3.2.63 and 3.2.64). It is possible that the rate limiting currents are governed by the rate of formation of the electroactive species by a preceding reaction.

The above discussion strongly implicates the presence of a ferric/ferrous couple. Since iron is absent from the bulk solution, the oxidation of ferrous iron at the violarite surface as released by a preceding reaction (e.g. the main anodic oxidation process of violarite) is suggested here as the explanation for the superimposed "prewave" during the anodic polarization of violarite.

Figures 3.2.65 to 3.2.75 show cyclic voltammograms for the $FeCl_3/FeCl_2$ couple on the violarite surface. These experiments are similar to those performed on pentlandite in Section 3.2.1, where the effects on the observed current density during successive cathodic cycles are studied with progressively greater anodic excursions.

These results indicate that the observed current densities decrease pro rata with the extent of anodic polarization, though not quite as rapidly as those on pentlandite. The effects of an amorphous sulphur film are again implicated. However,the more facile electron transfer on violarite may be due to a different morphology of the sulphur product and/or the production of alternative and less passivating products of oxidation i.e. bisulphate.

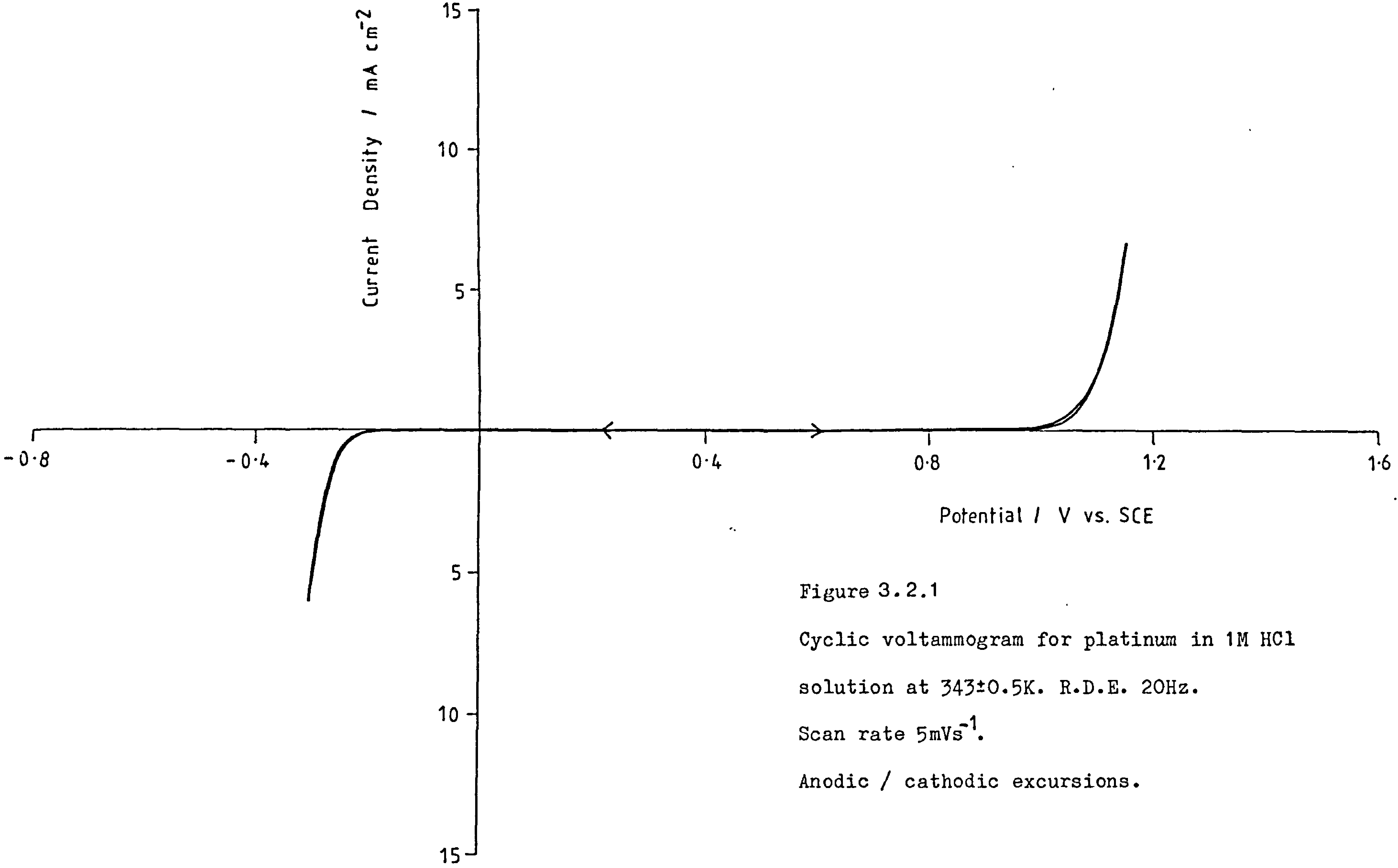

Figure 3.2.1

Cyclic voltammogram for platinum in 1M HCl solution at 343±0.5K. R.D.E. 20Hz. Scan rate 5mVs^{-1}. Anodic / cathodic excursions.

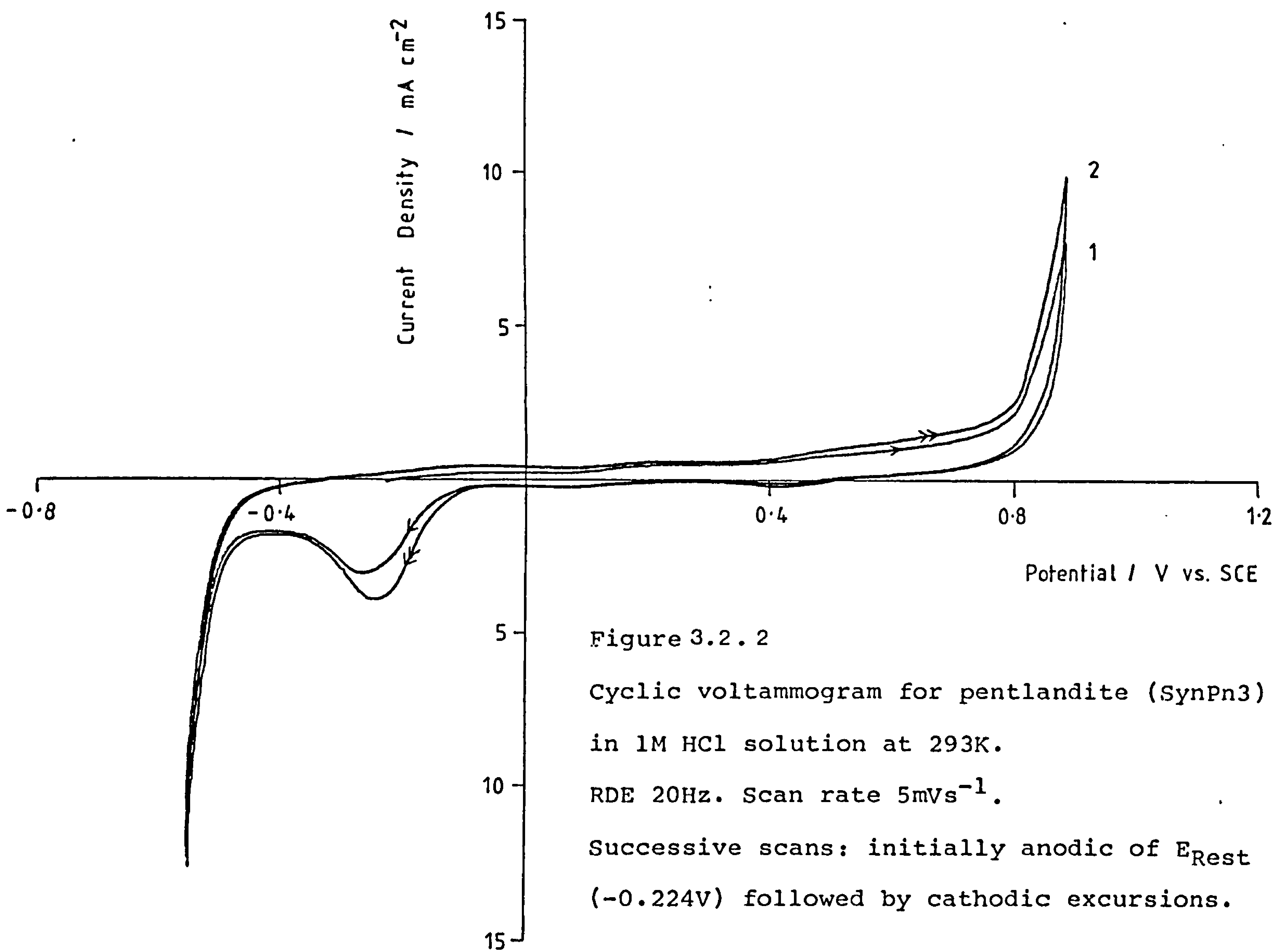

Figure 3.2.2

Cyclic voltammogram for pentlandite (SynPn3) in 1M HCl solution at 293K.

RDE 20Hz. Scan rate 5mVs^{-1}.

Successive scans: initially anodic of E_{Rest} (-0.224V) followed by cathodic excursions.

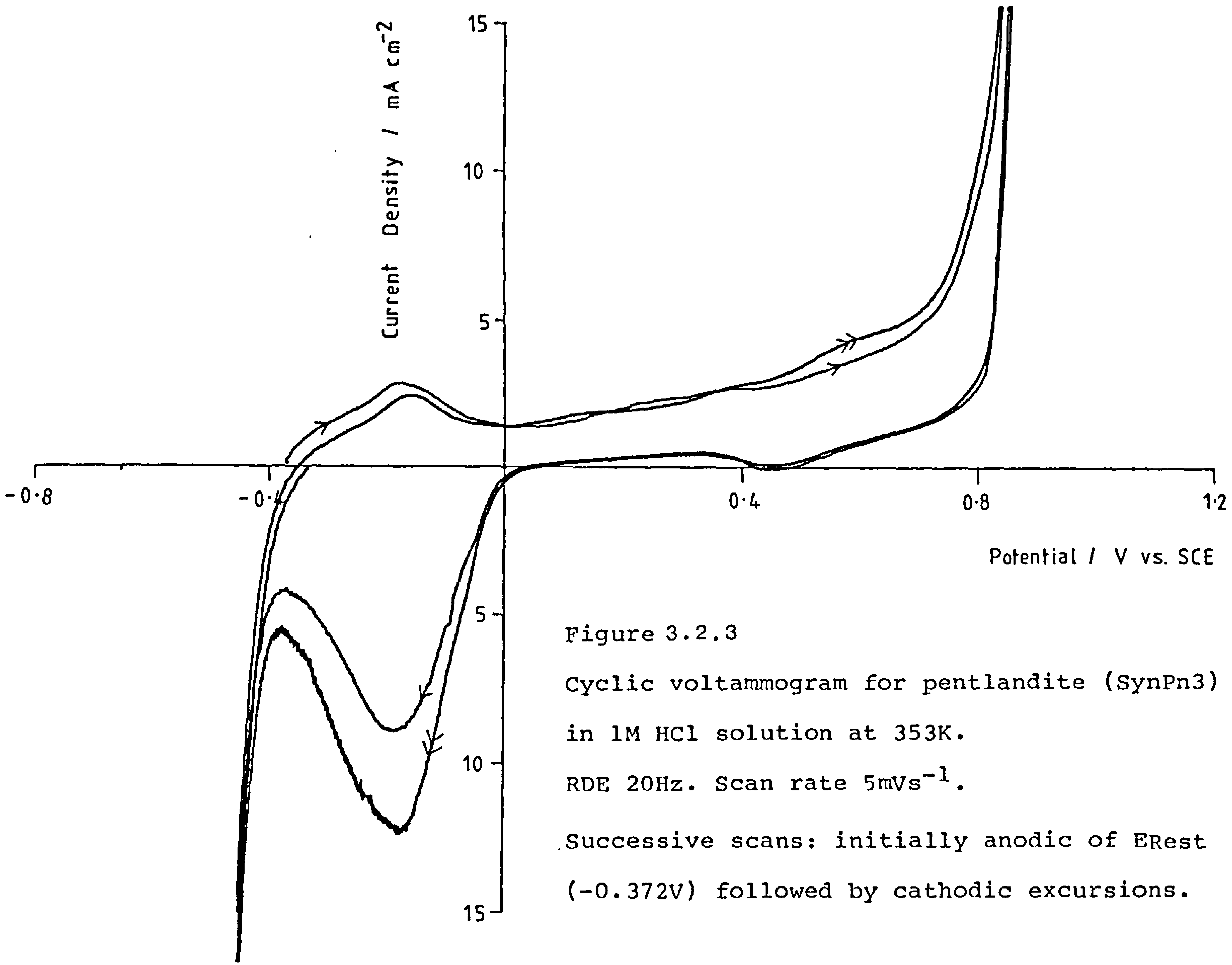

Figure 3.2.3

Cyclic voltammogram for pentlandite (SynPn3) in 1M HCl solution at 353K.

RDE 20Hz. Scan rate 5mVs^{-1}.

Successive scans: initially anodic of ERest (-0.372V) followed by cathodic excursions.

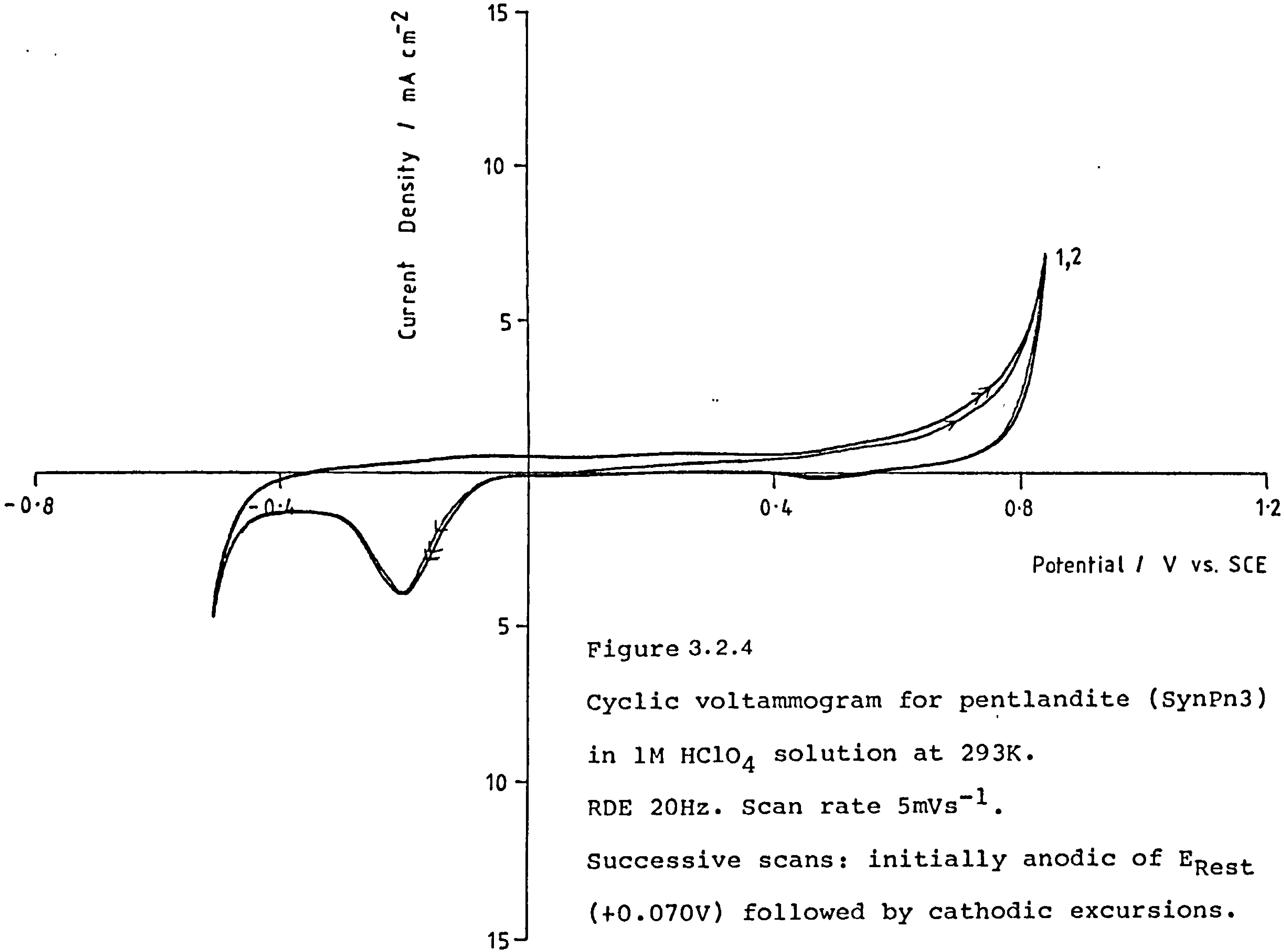

Figure 3.2.4

Cyclic voltammogram for pentlandite (SynPn3) in 1M $HClO_4$ solution at 293K.

RDE 20Hz. Scan rate 5mVs^{-1}.

Successive scans: initially anodic of E_{Rest} (+0.070V) followed by cathodic excursions.

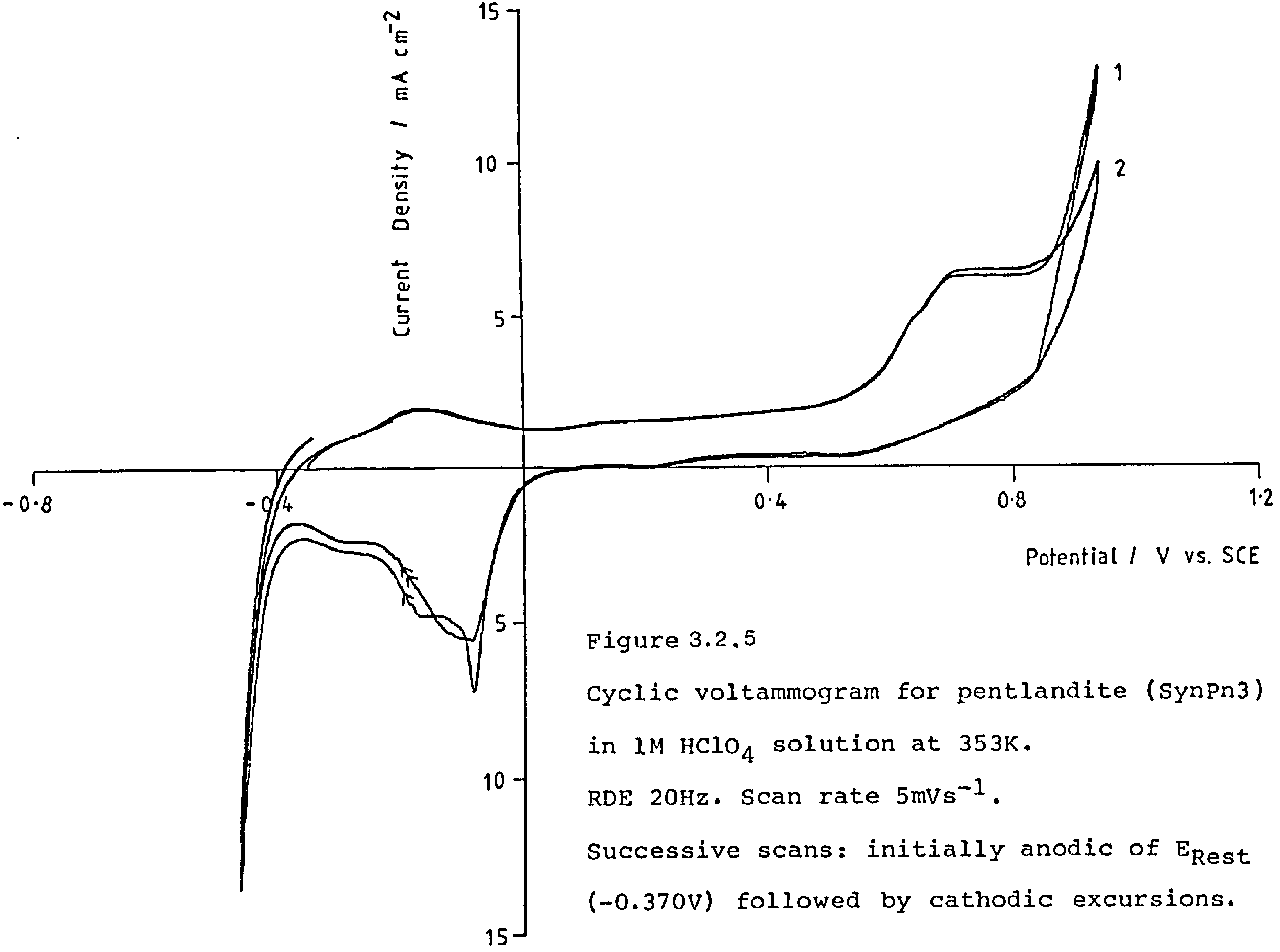

Figure 3.2.5

Cyclic voltammogram for pentlandite (SynPn3) in 1M $HClO_4$ solution at 353K.

RDE 20Hz. Scan rate 5mVs^{-1}.

Successive scans: initially anodic of E_{Rest} (-0.370V) followed by cathodic excursions.

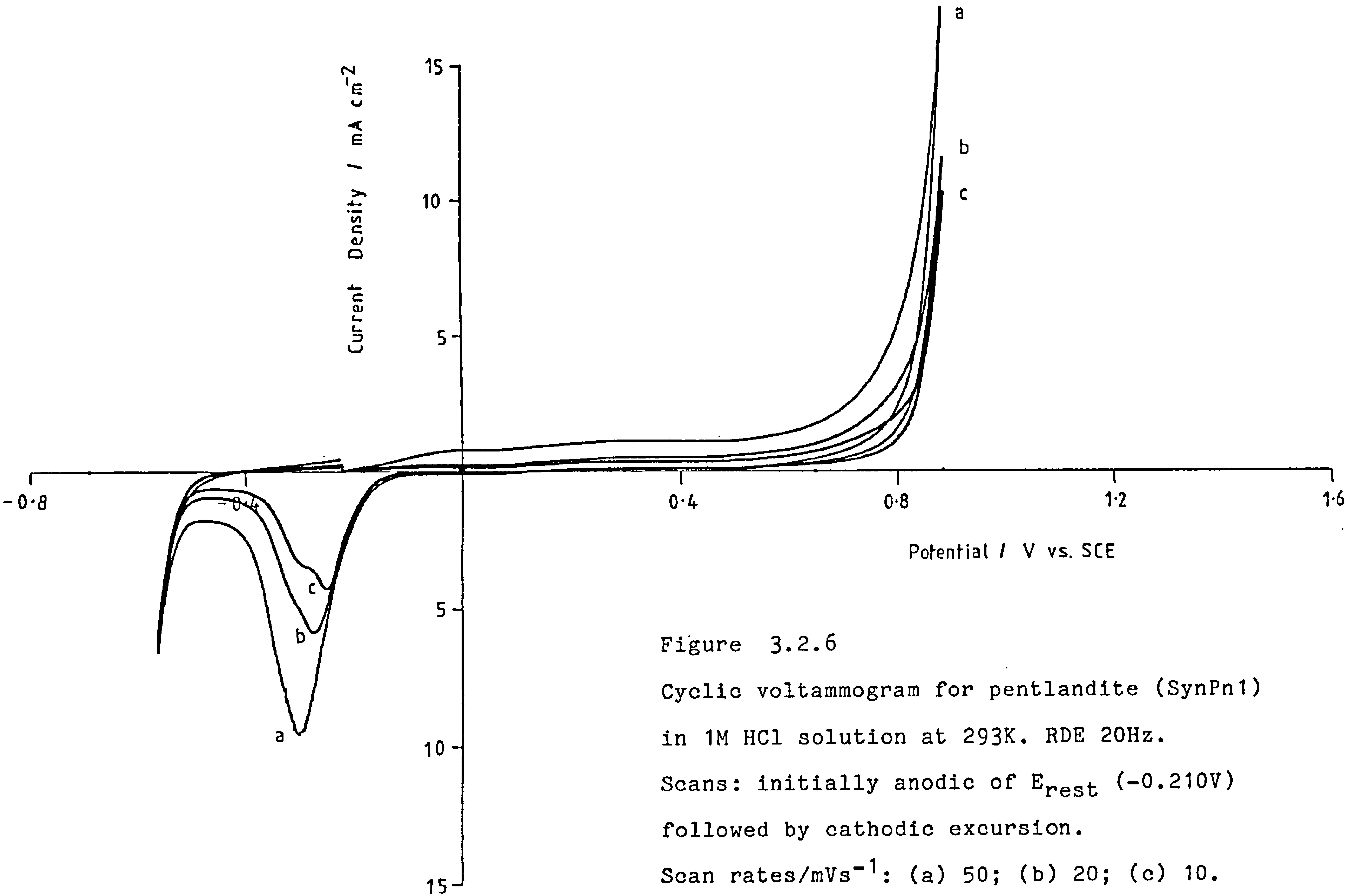

Figure 3.2.6

Cyclic voltammogram for pentlandite (SynPn1) in 1M HCl solution at 293K. RDE 20Hz.

Scans: initially anodic of E_{rest} (-0.210V) followed by cathodic excursion.

Scan rates/mVs^{-1}: (a) 50; (b) 20; (c) 10.

Figure 3.2.7

Linear voltammogram for synthetic pentlandite ("SynPn3") in 1M HCl solution, 298±0.5K.

R.D.E. 20Hz. Scan rate 50mVs^{-1}.

Successive scans: anodic of E_{Rest} with open circuit between each scan.

Figure 3.2.8

Linear voltammogram for synthetic pentlandite ("SynPn3") in 1M HCl solution, 343±0.5K. R.D.E. 20Hz. Scan rate 50mVs^{-1}. Successive scans: anodic of E_{Rest} with open circuit between each scan.

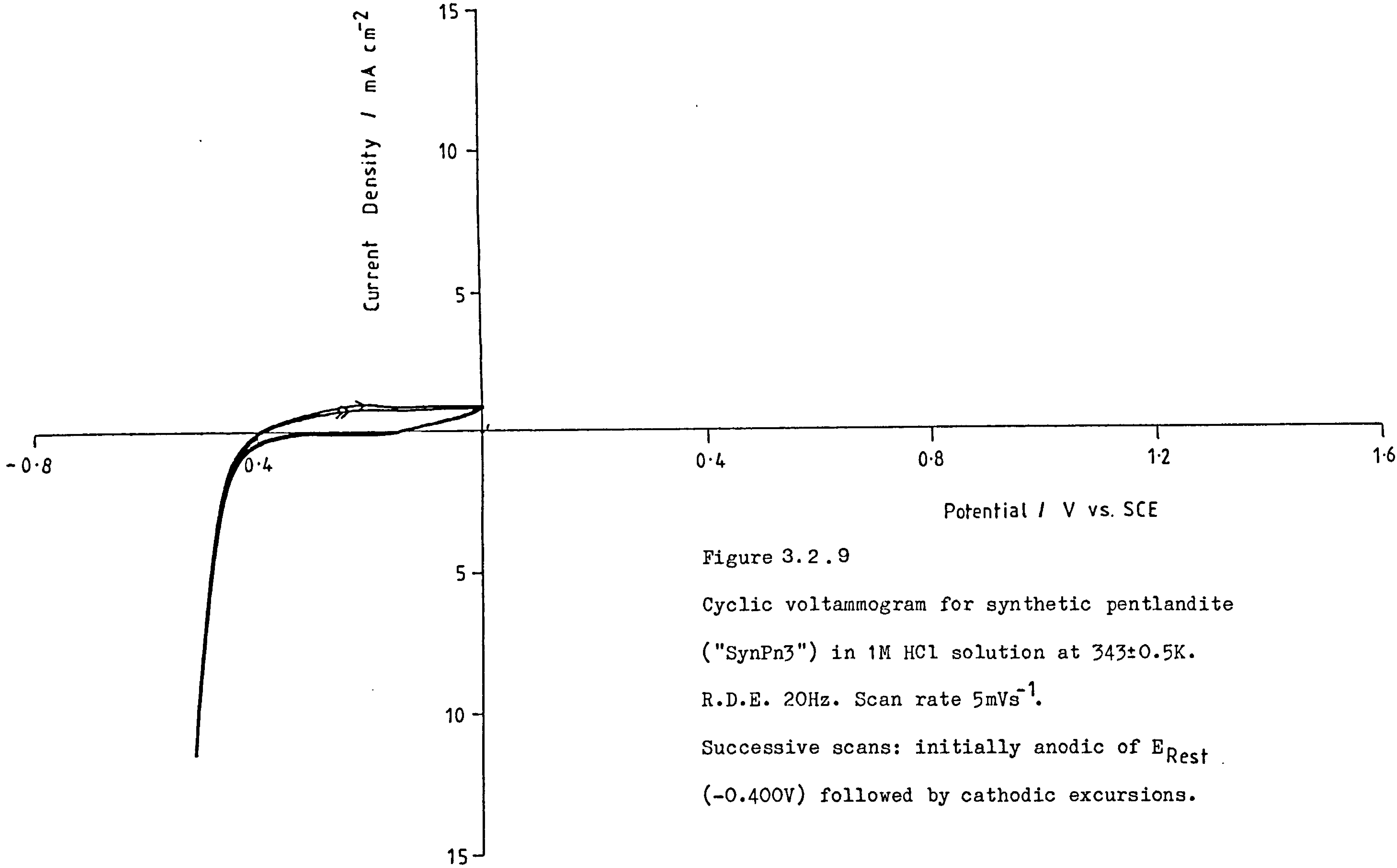

Figure 3.2.9

Cyclic voltammogram for synthetic pentlandite ("SynPn3") in 1M HCl solution at 343±0.5K. R.D.E. 20Hz. Scan rate 5mVs^{-1}. Successive scans: initially anodic of E_{Rest} (-0.400V) followed by cathodic excursions.

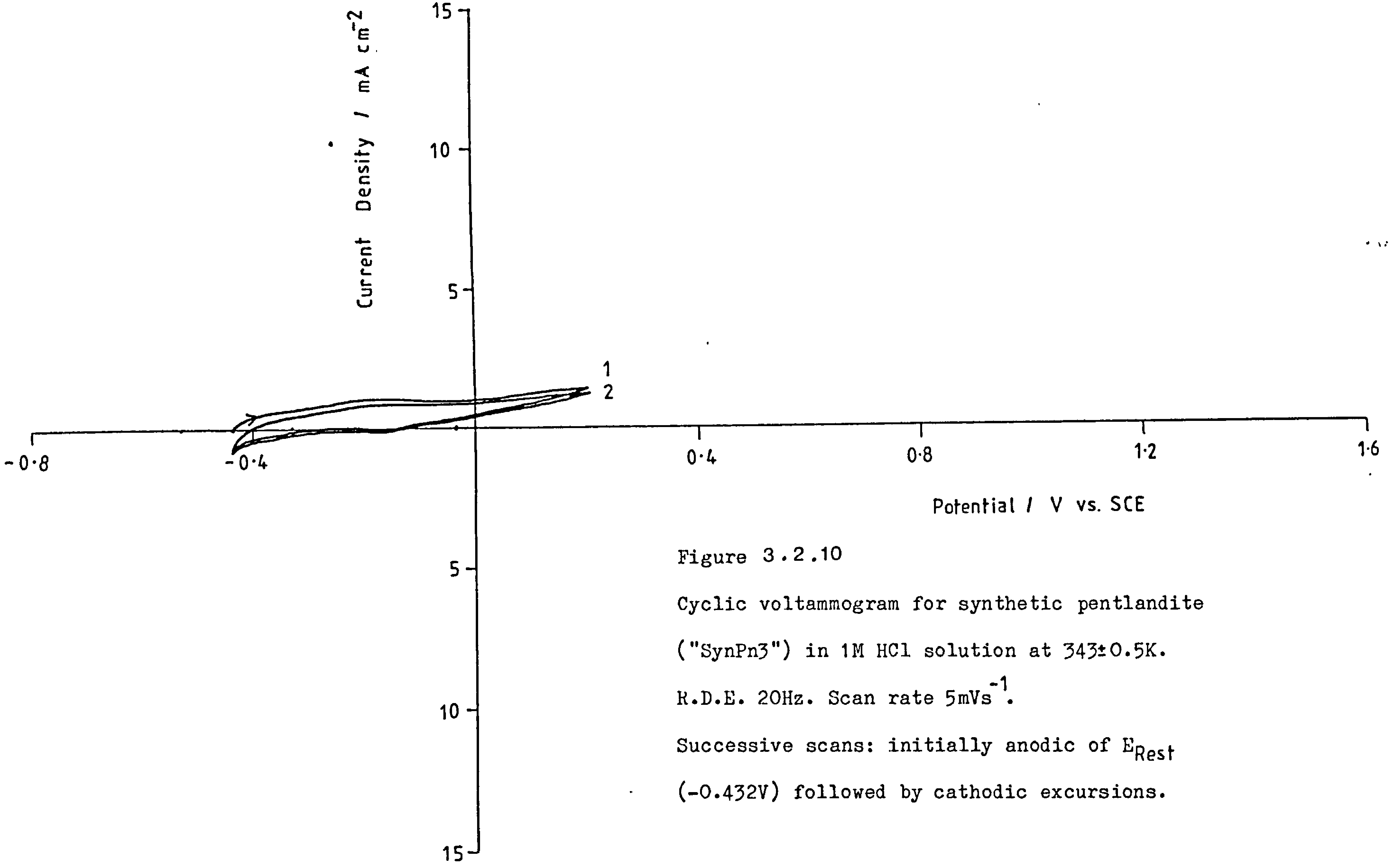

Figure 3.2.10

Cyclic voltammogram for synthetic pentlandite ("SynPn3") in 1M HCl solution at 343±0.5K. R.D.E. 20Hz. Scan rate 5mVs^{-1}. Successive scans: initially anodic of E_{Rest} (-0.432V) followed by cathodic excursions.

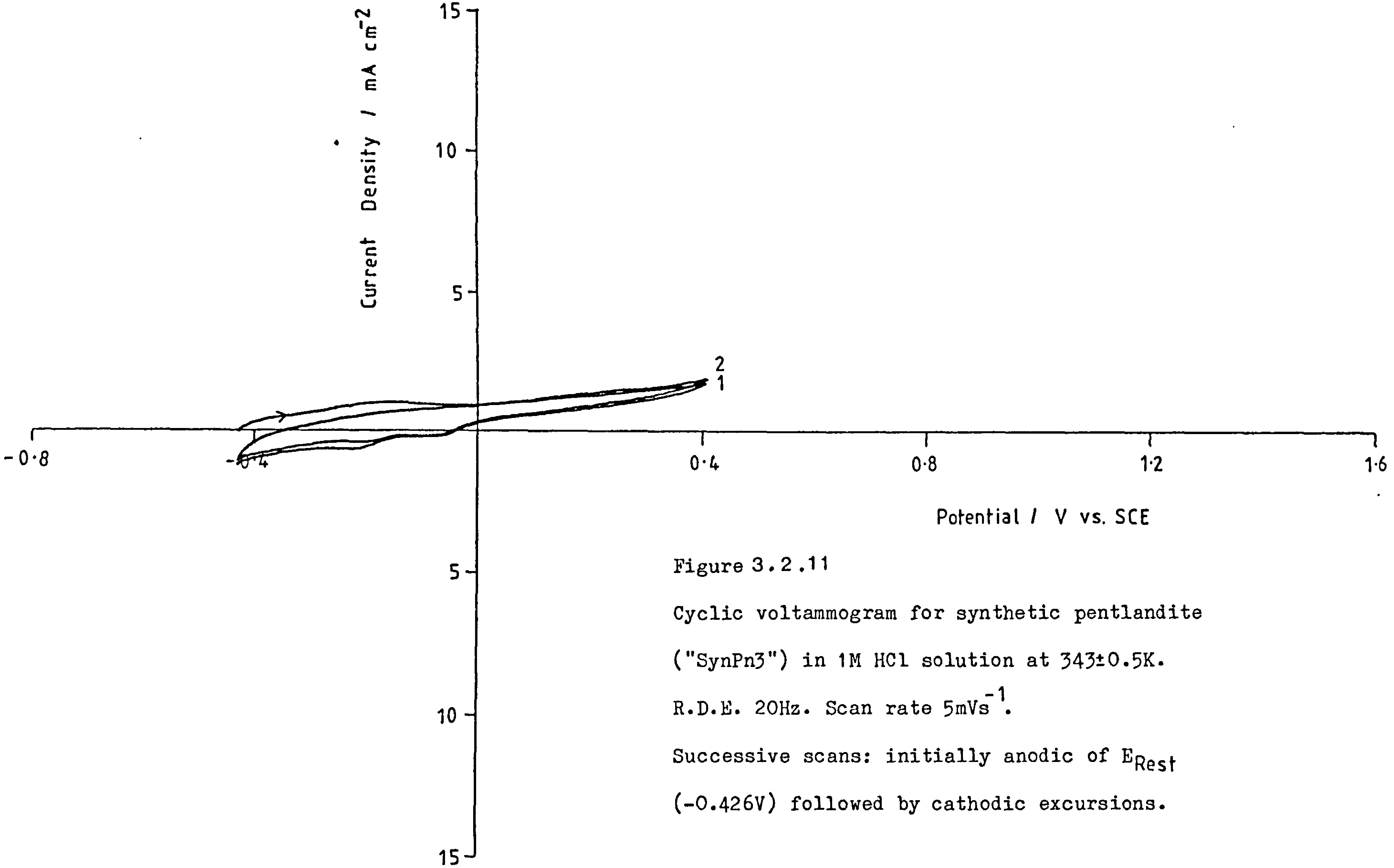

Figure 3.2.11

Cyclic voltammogram for synthetic pentlandite ("SynPn3") in 1M HCl solution at 343±0.5K.

R.D.E. 20Hz. Scan rate 5mVs^{-1}.

Successive scans: initially anodic of E_{Rest} (-0.426V) followed by cathodic excursions.

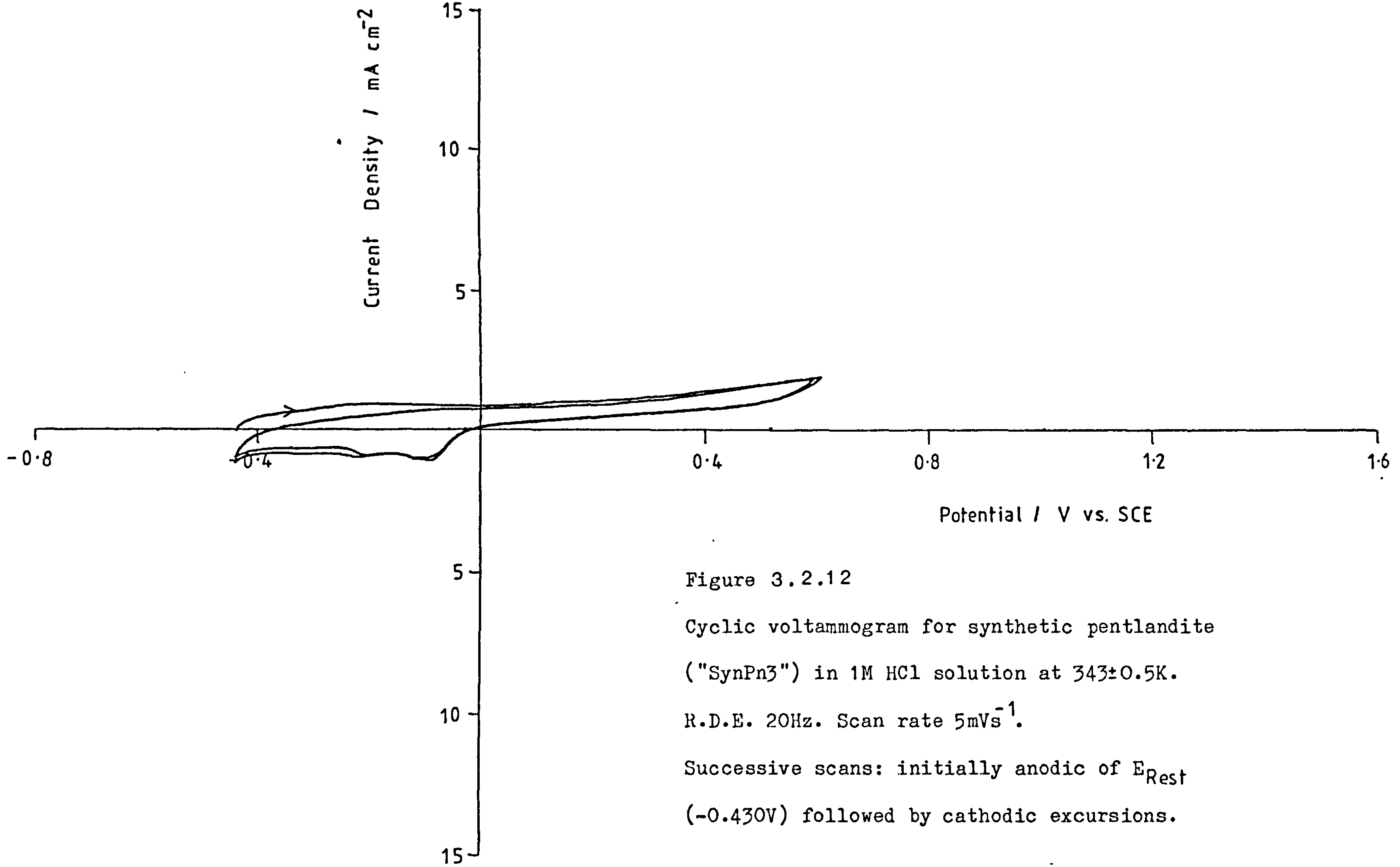

Figure 3.2.12

Cyclic voltammogram for synthetic pentlandite ("SynPn3") in 1M HCl solution at 343±0.5K.

R.D.E. 20Hz. Scan rate 5mVs^{-1}.

Successive scans: initially anodic of E_{Rest} (-0.430V) followed by cathodic excursions.

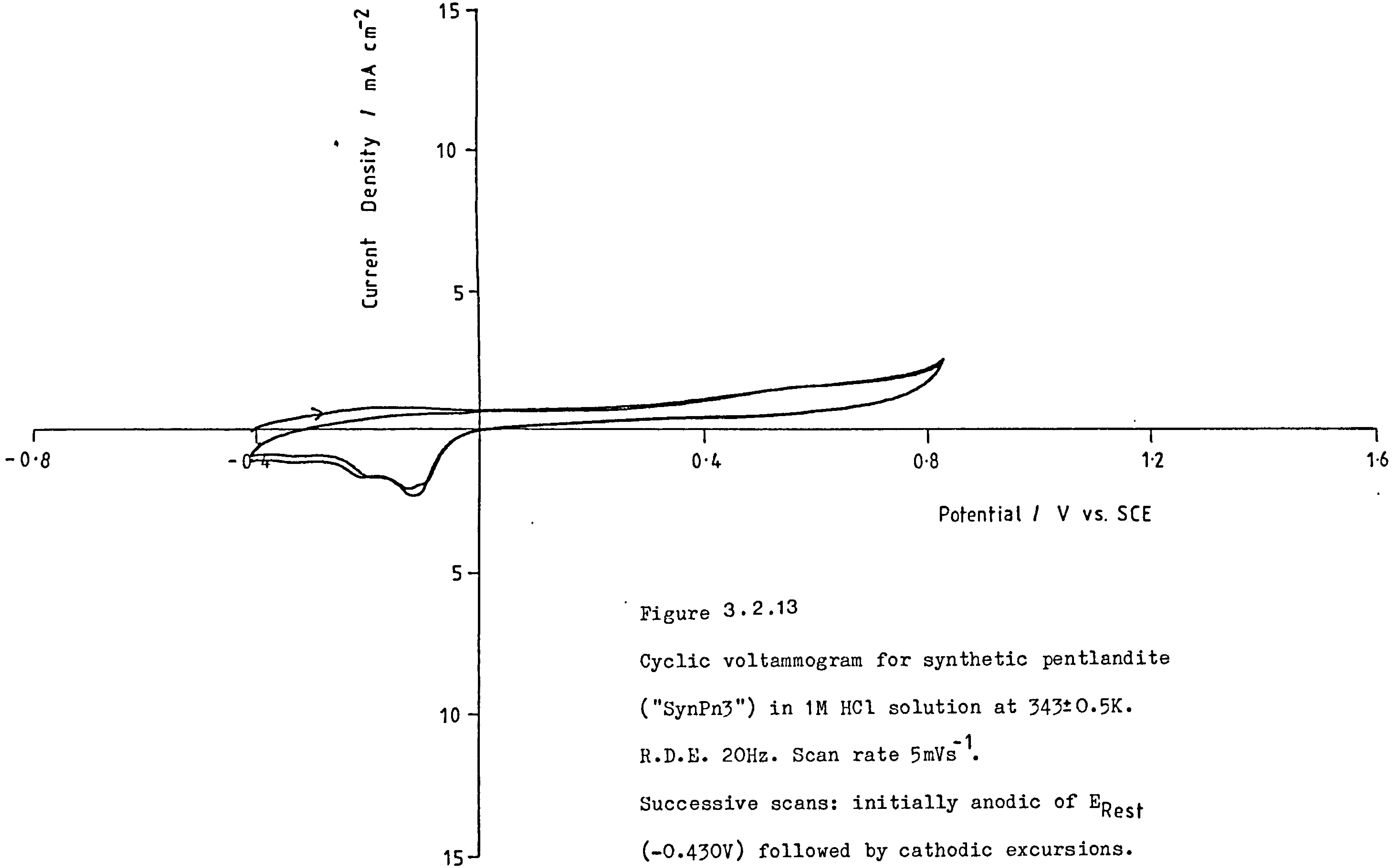

Figure 3.2.13

Cyclic voltammogram for synthetic pentlandite ("SynPn3") in 1M HCl solution at 343±0.5K. R.D.E. 20Hz. Scan rate 5mVs^{-1}. Successive scans: initially anodic of E_{Rest} (-0.430V) followed by cathodic excursions.

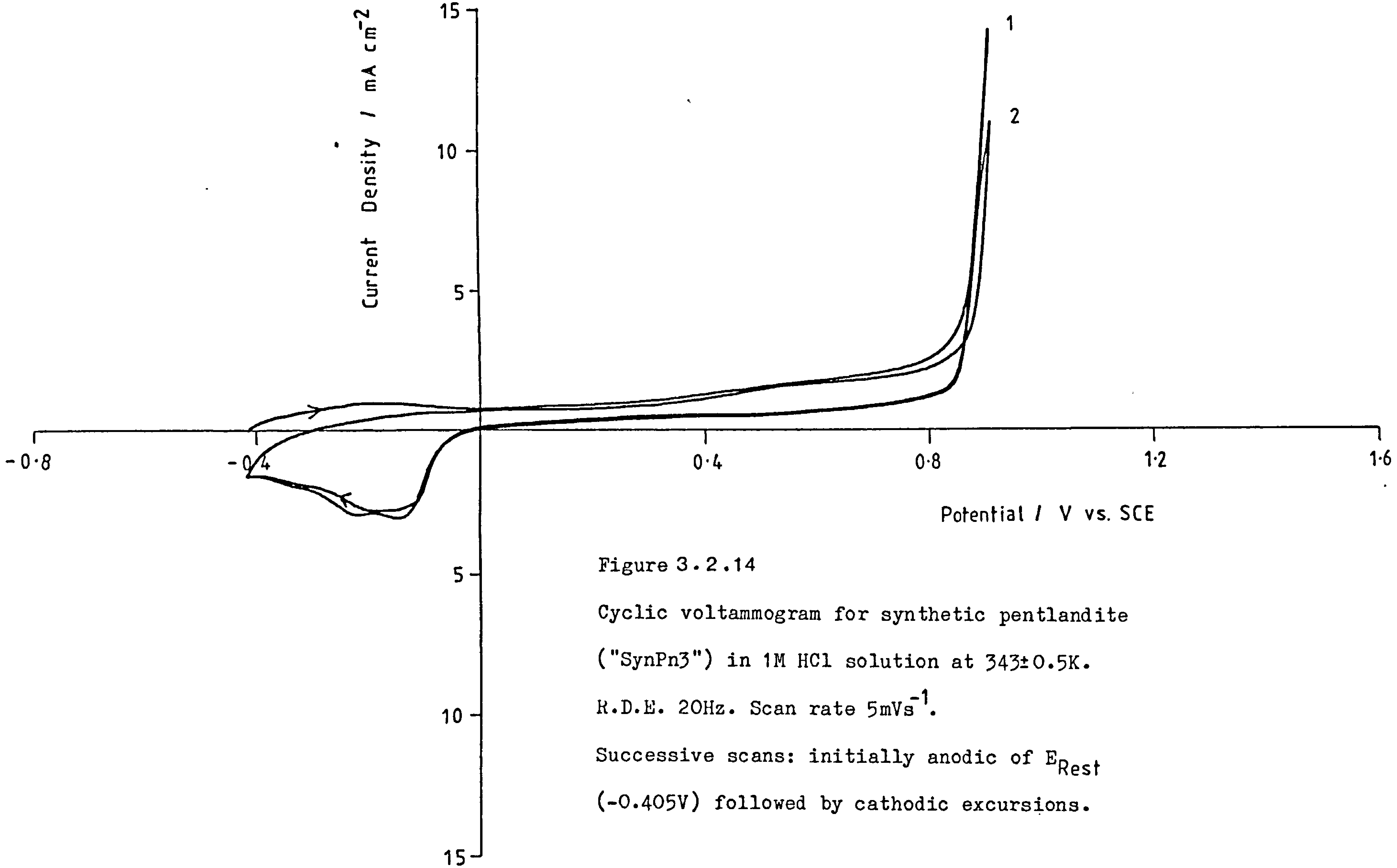

Figure 3.2.14

Cyclic voltammogram for synthetic pentlandite ("SynPn3") in 1M HCl solution at 343±0.5K.

R.D.E. 20Hz. Scan rate 5mVs^{-1}.

Successive scans: initially anodic of E_{Rest} (-0.405V) followed by cathodic excursions.

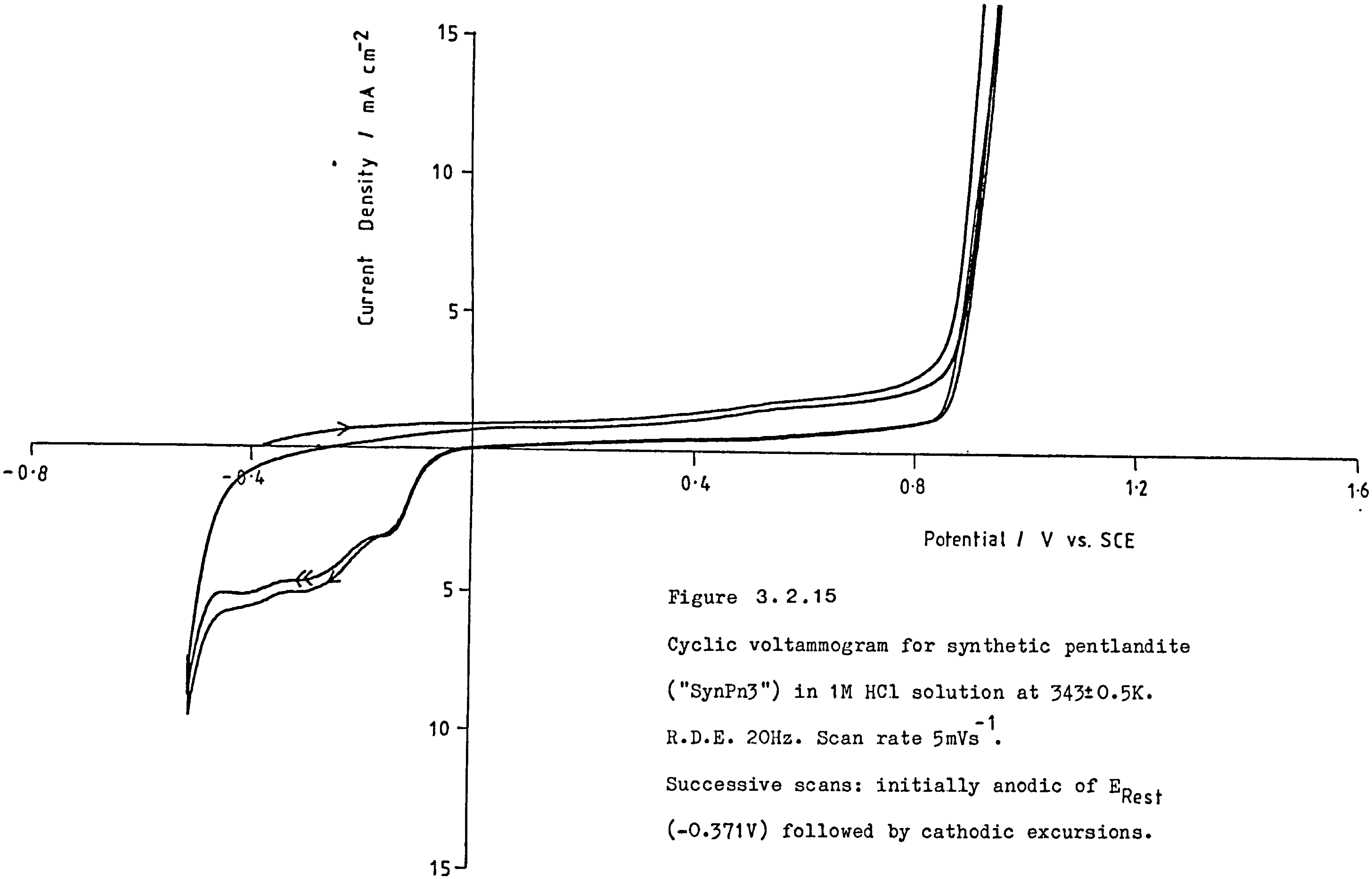

Figure 3.2.15

Cyclic voltammogram for synthetic pentlandite ("SynPn3") in 1M HCl solution at 343±0.5K.

R.D.E. 20Hz. Scan rate 5mVs^{-1}.

Successive scans: initially anodic of E_{Rest} (-0.371V) followed by cathodic excursions.

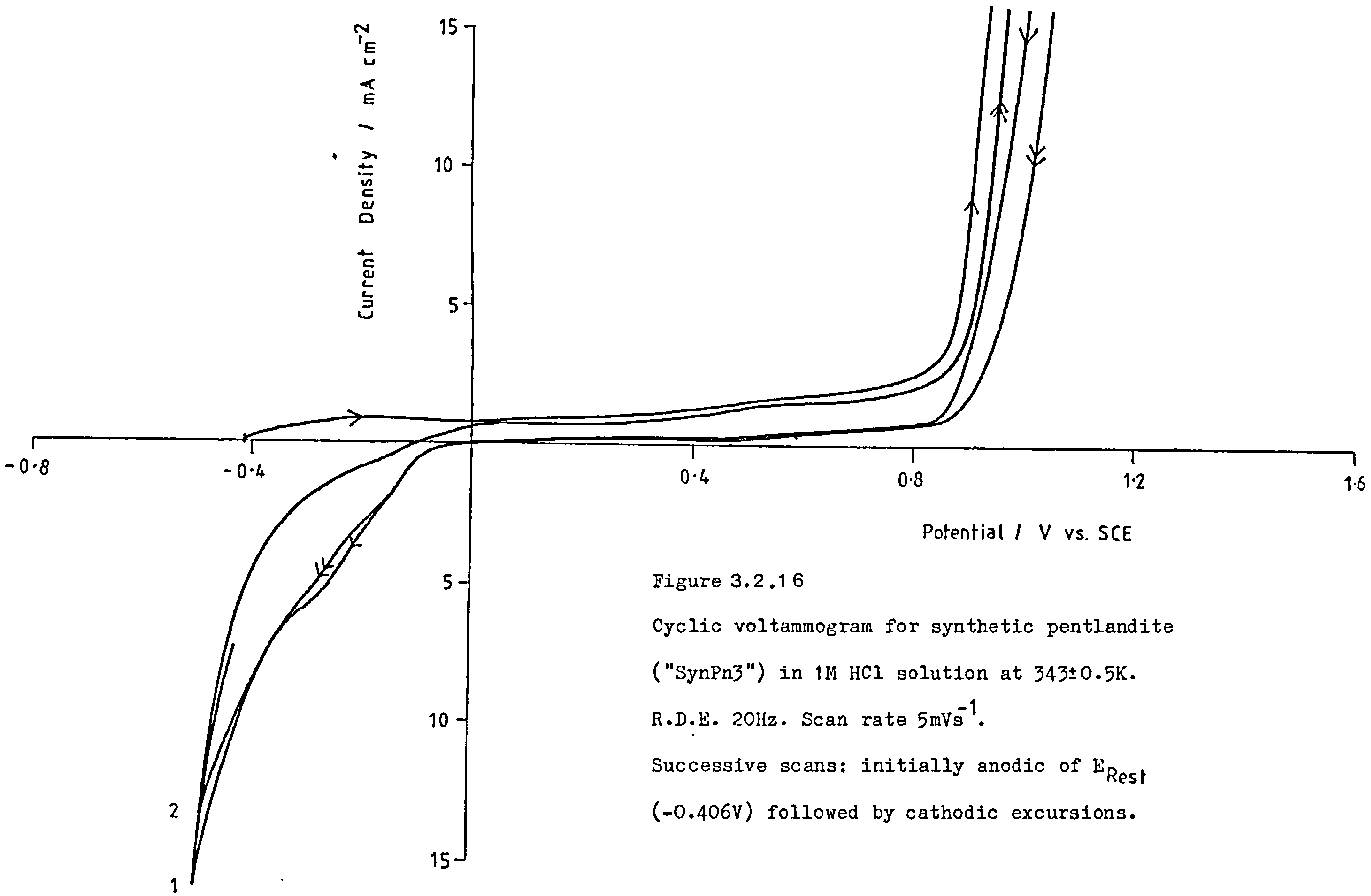

Figure 3.2.16

Cyclic voltammogram for synthetic pentlandite ("SynPn3") in 1M HCl solution at 343±0.5K. R.D.E. 20Hz. Scan rate 5mVs^{-1}. Successive scans: initially anodic of E_{Rest} (-0.406V) followed by cathodic excursions.

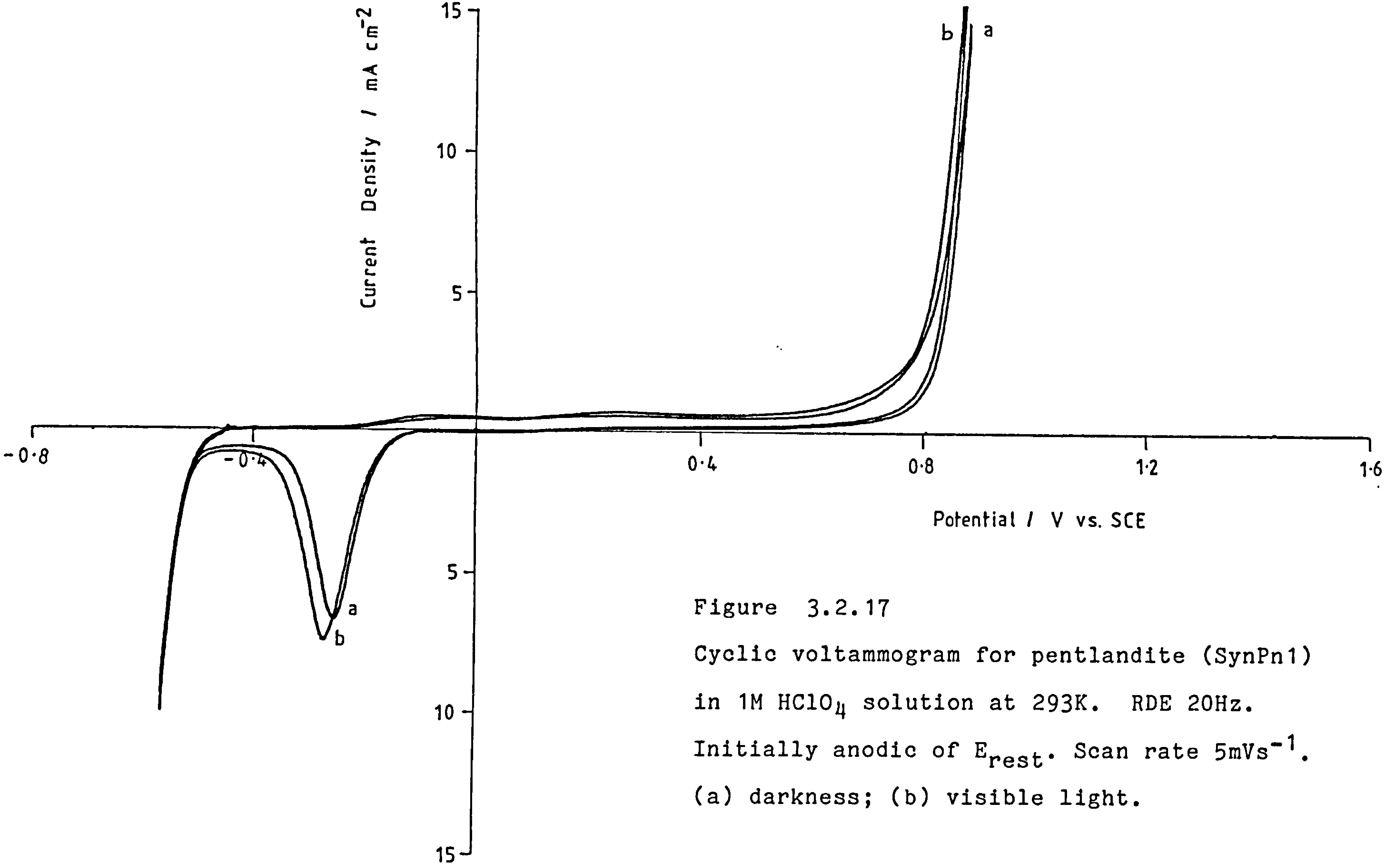

Figure 3.2.17

Cyclic voltammogram for pentlandite (SynPn1) in 1M $HClO_4$ solution at 293K. RDE 20Hz. Initially anodic of E_{rest}. Scan rate $5 mVs^{-1}$. (a) darkness; (b) visible light.

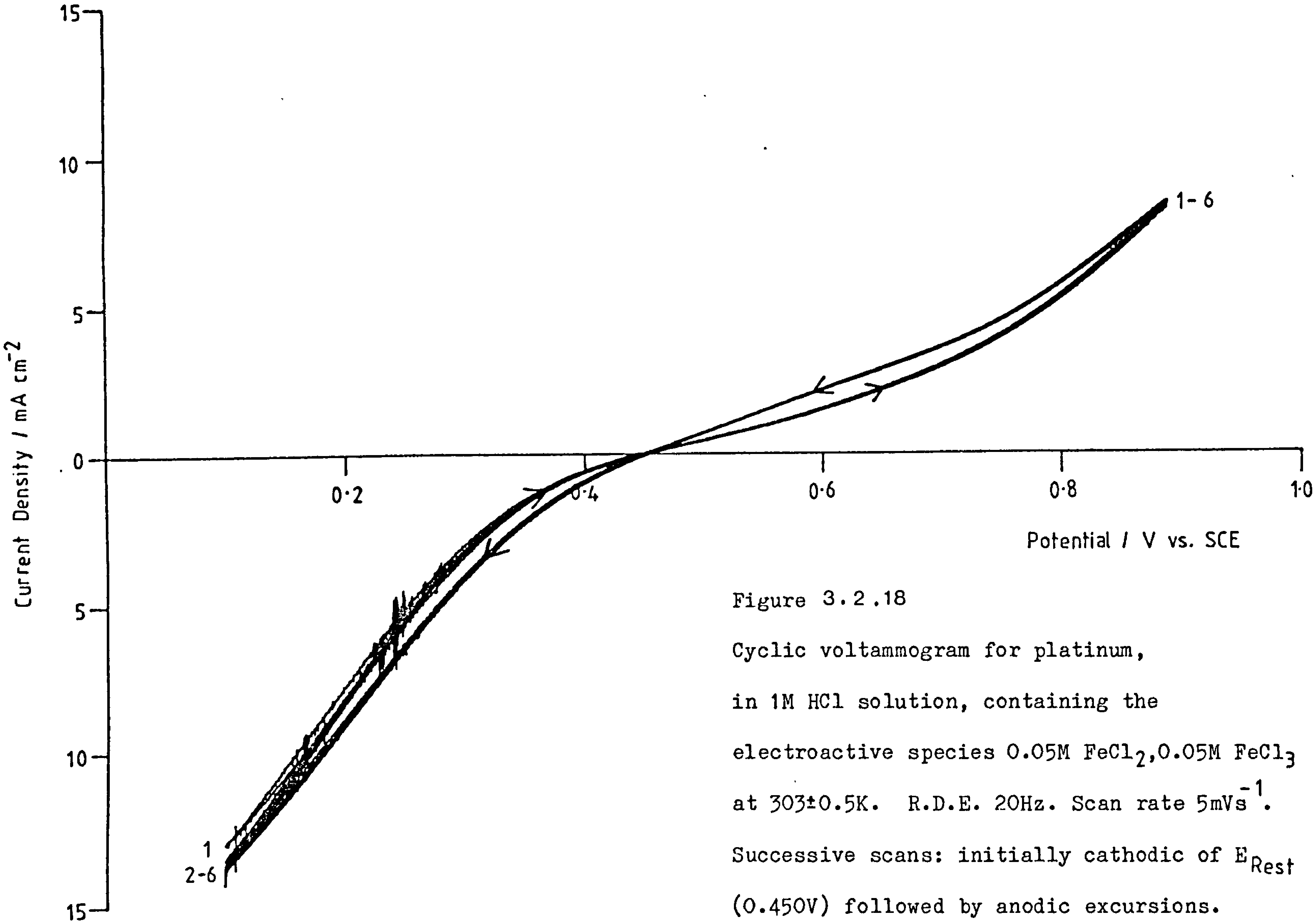

Figure 3.2.18
Cyclic voltammogram for platinum, in 1M HCl solution, containing the electroactive species 0.05M $FeCl_2$,0.05M $FeCl_3$ at 303±0.5K. R.D.E. 20Hz. Scan rate $5mVs^{-1}$. Successive scans: initially cathodic of E_{Rest} (0.450V) followed by anodic excursions.

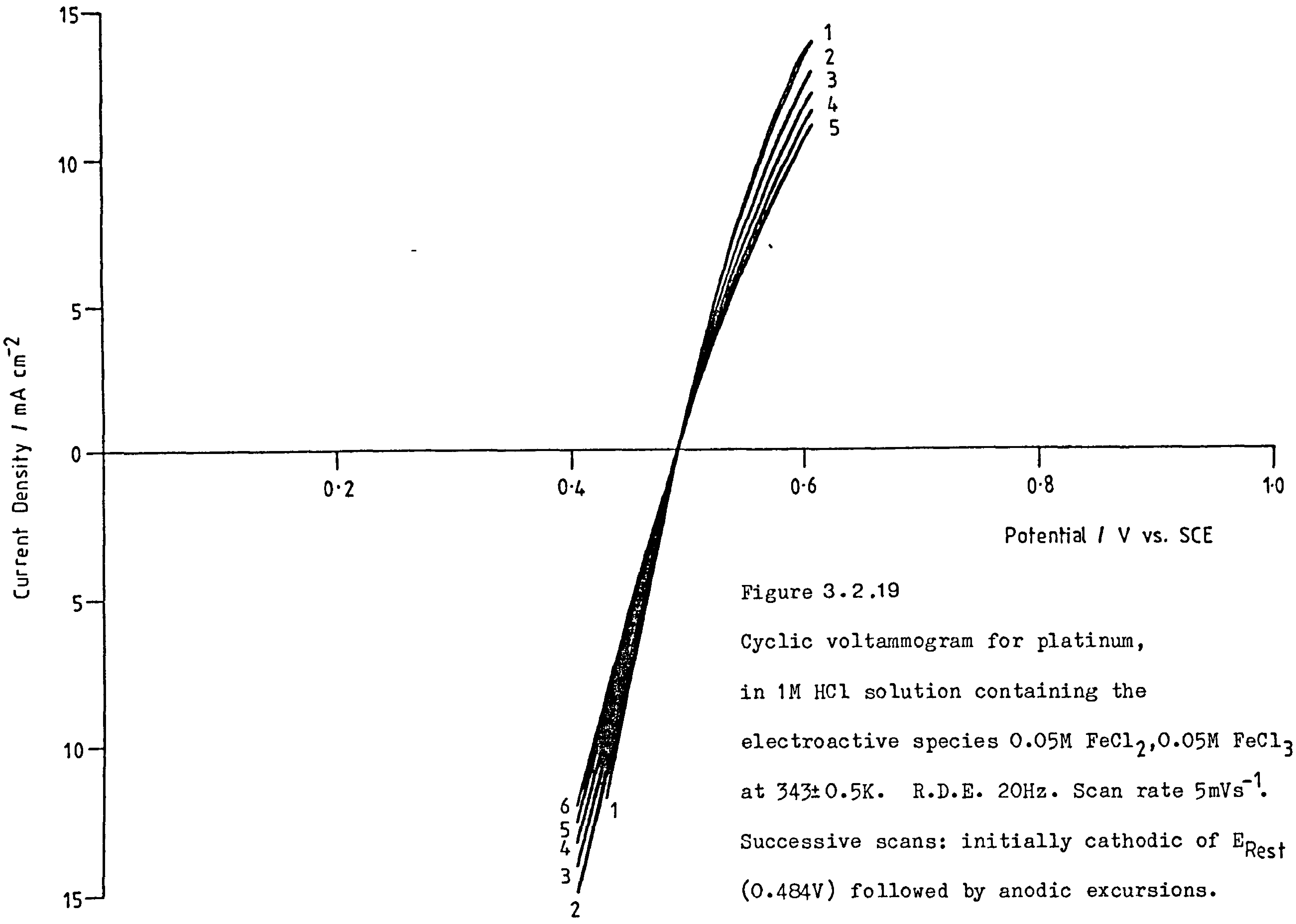

Figure 3.2.19

Cyclic voltammogram for platinum, in 1M HCl solution containing the electroactive species 0.05M $FeCl_2$, 0.05M $FeCl_3$ at 343±0.5K. R.D.E. 20Hz. Scan rate $5 mVs^{-1}$. Successive scans: initially cathodic of E_{Rest} (0.484V) followed by anodic excursions.

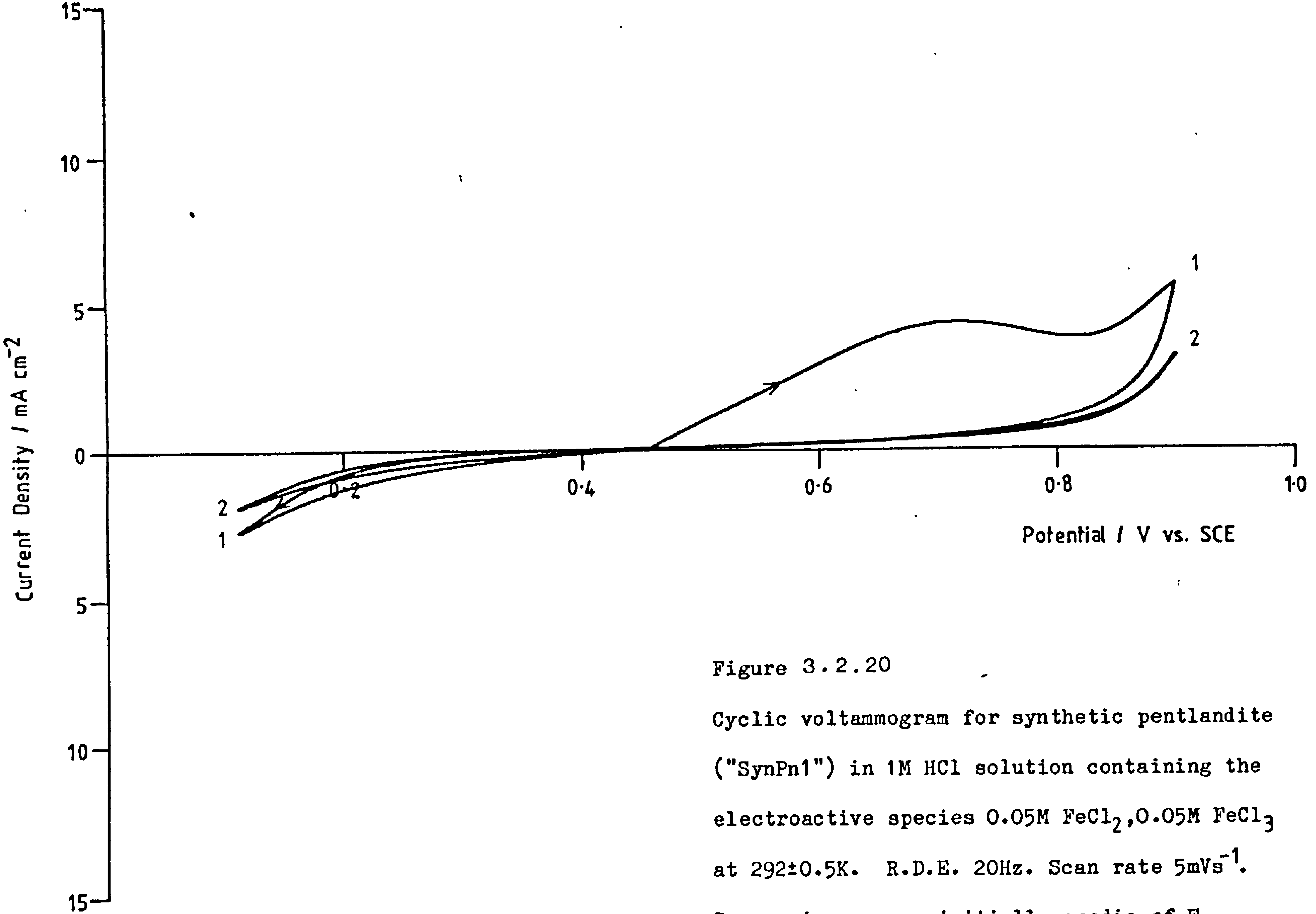

Figure 3.2.20

Cyclic voltammogram for synthetic pentlandite ("SynPn1") in 1M HCl solution containing the electroactive species 0.05M $FeCl_2$,0.05M $FeCl_3$ at 292±0.5K. R.D.E. 20Hz. Scan rate $5mVs^{-1}$. Successive scans: initially anodic of E_{Rest} (0.447V) followed by cathodic excursions.

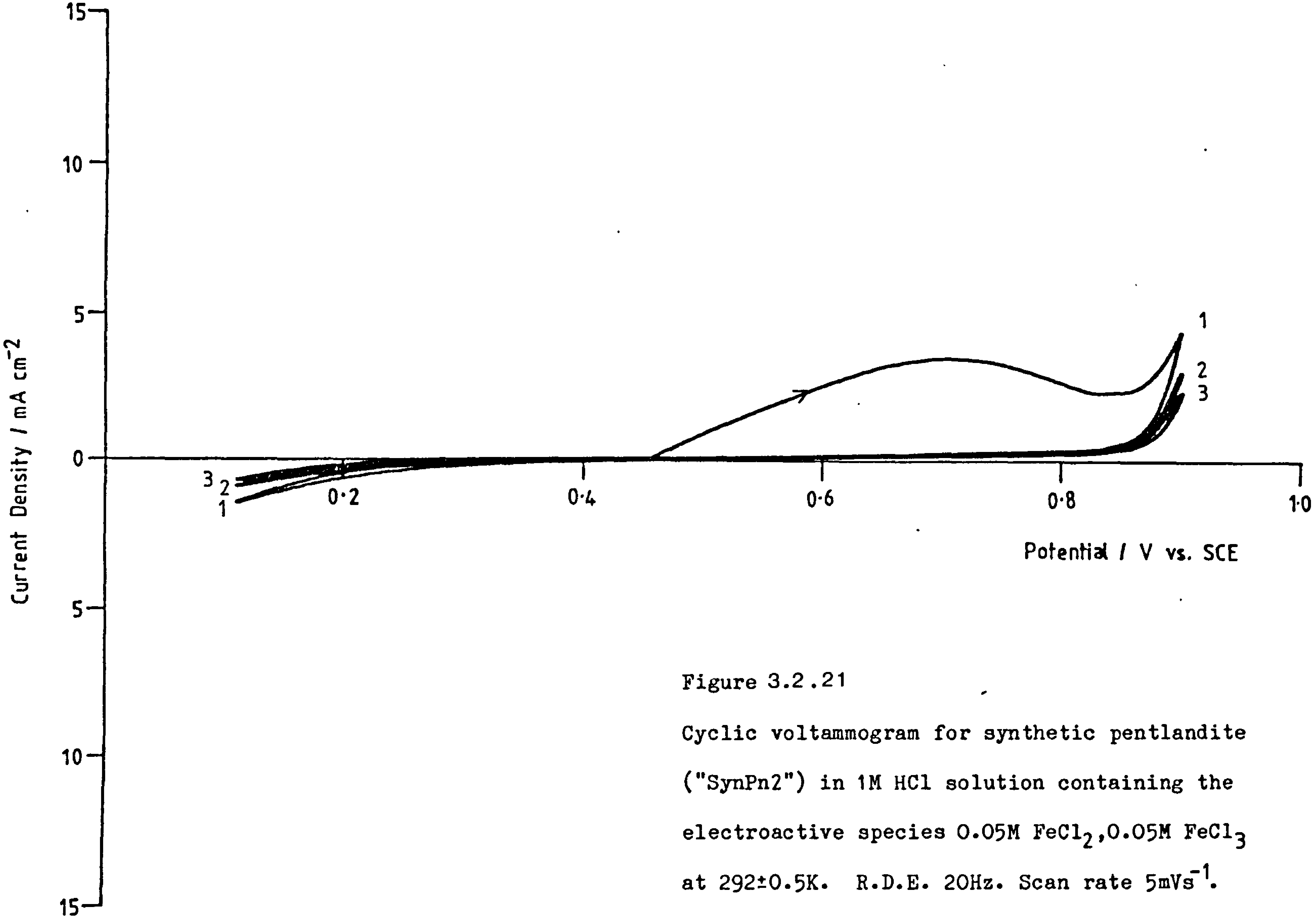

Figure 3.2.21

Cyclic voltammogram for synthetic pentlandite ("SynPn2") in 1M HCl solution containing the electroactive species 0.05M $FeCl_2$,0.05M $FeCl_3$ at 292±0.5K. R.D.E. 20Hz. Scan rate $5mVs^{-1}$. Successive scans: initially anodic of E_{Rest} (0.447V) followed by cathodic excursions.

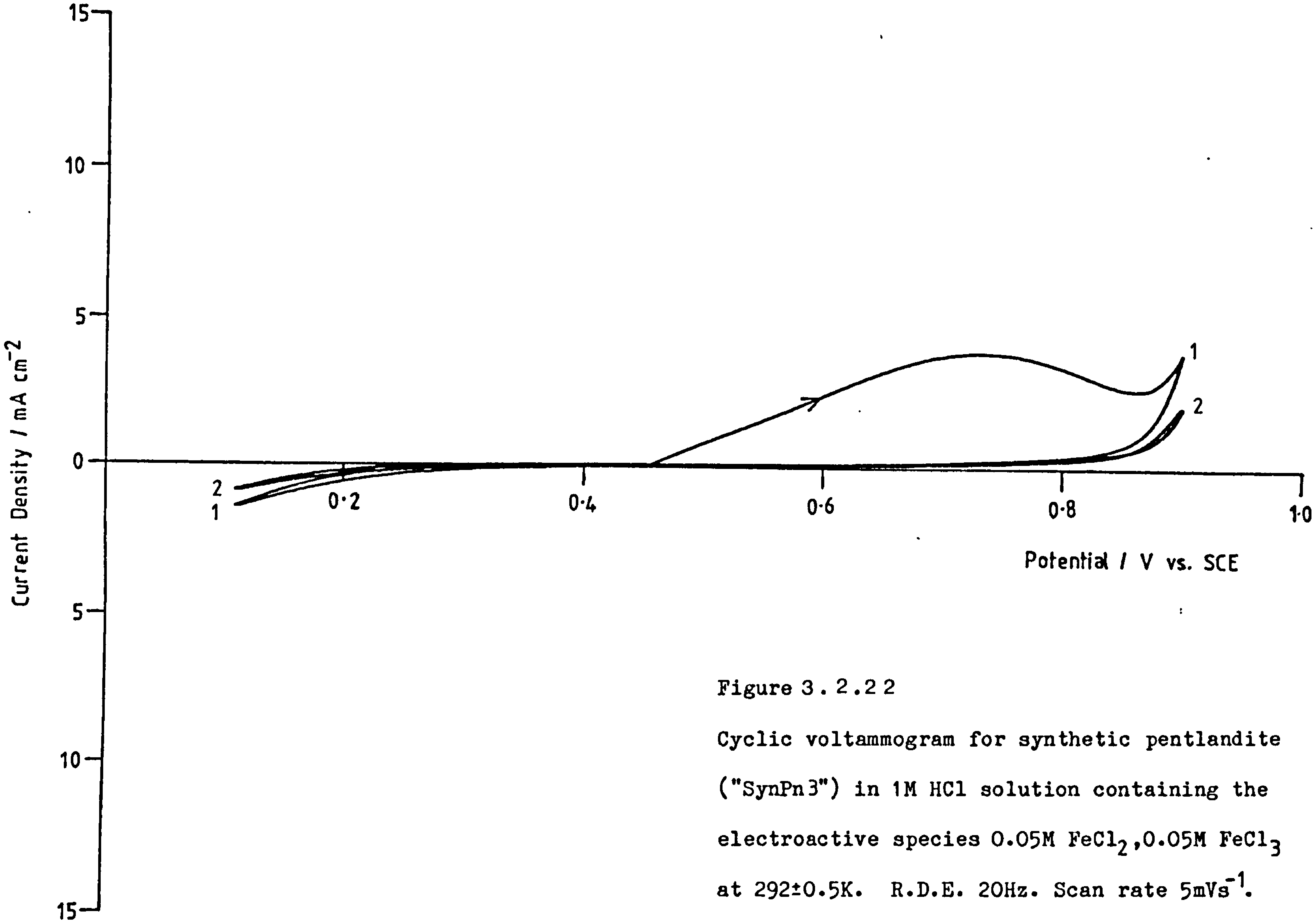

Figure 3.2.22

Cyclic voltammogram for synthetic pentlandite ("SynPn3") in 1M HCl solution containing the electroactive species 0.05M $FeCl_2$,0.05M $FeCl_3$ at 292±0.5K. R.D.E. 20Hz. Scan rate $5mVs^{-1}$. Successive scans: initially anodic of E_{Rest} (0.447V) followed by cathodic excursions.

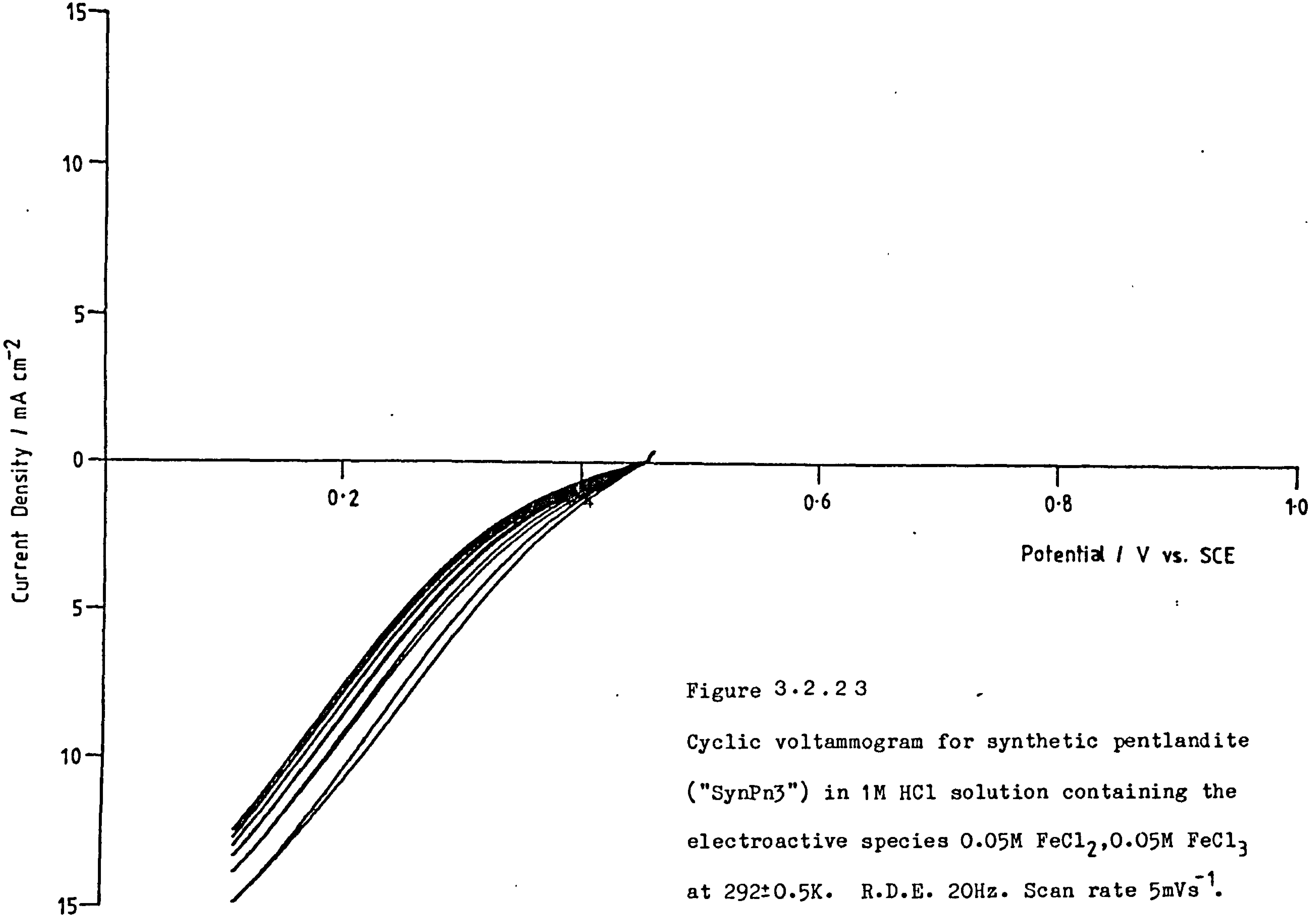

Figure 3.2.23

Cyclic voltammogram for synthetic pentlandite ("SynPn3") in 1M HCl solution containing the electroactive species 0.05M $FeCl_2$,0.05M $FeCl_3$ at 292±0.5K. R.D.E. 20Hz. Scan rate $5mVs^{-1}$. Successive scans: cathodic of E_{Rest} (0.447V).

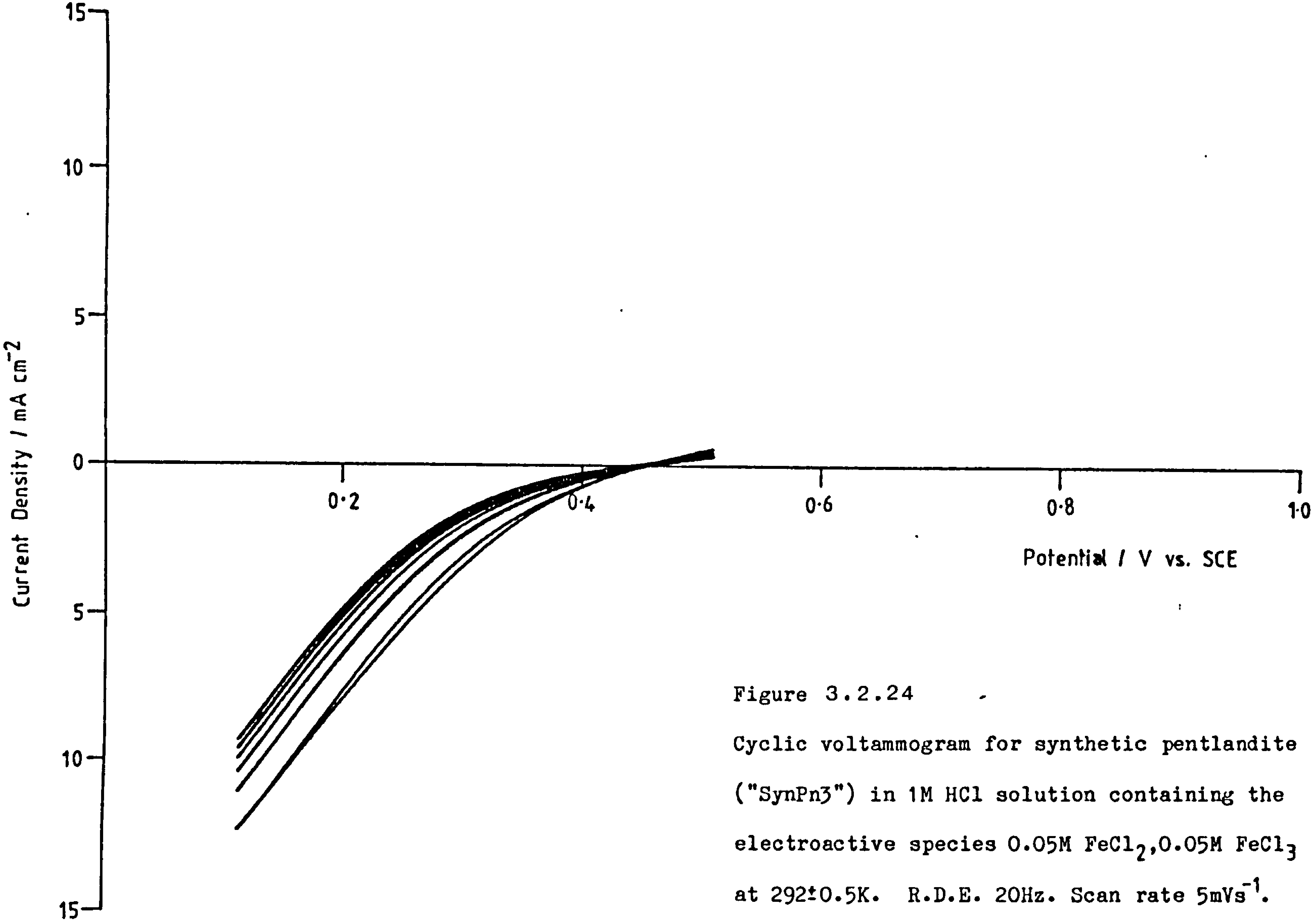

Figure 3.2.24

Cyclic voltammogram for synthetic pentlandite ("SynPn3") in 1M HCl solution containing the electroactive species 0.05M $FeCl_2$,0.05M $FeCl_3$ at 292±0.5K. R.D.E. 20Hz. Scan rate $5mVs^{-1}$. Successive scans: initially cathodic of E_{Rest} (0.447V) followed by anodic excursions.

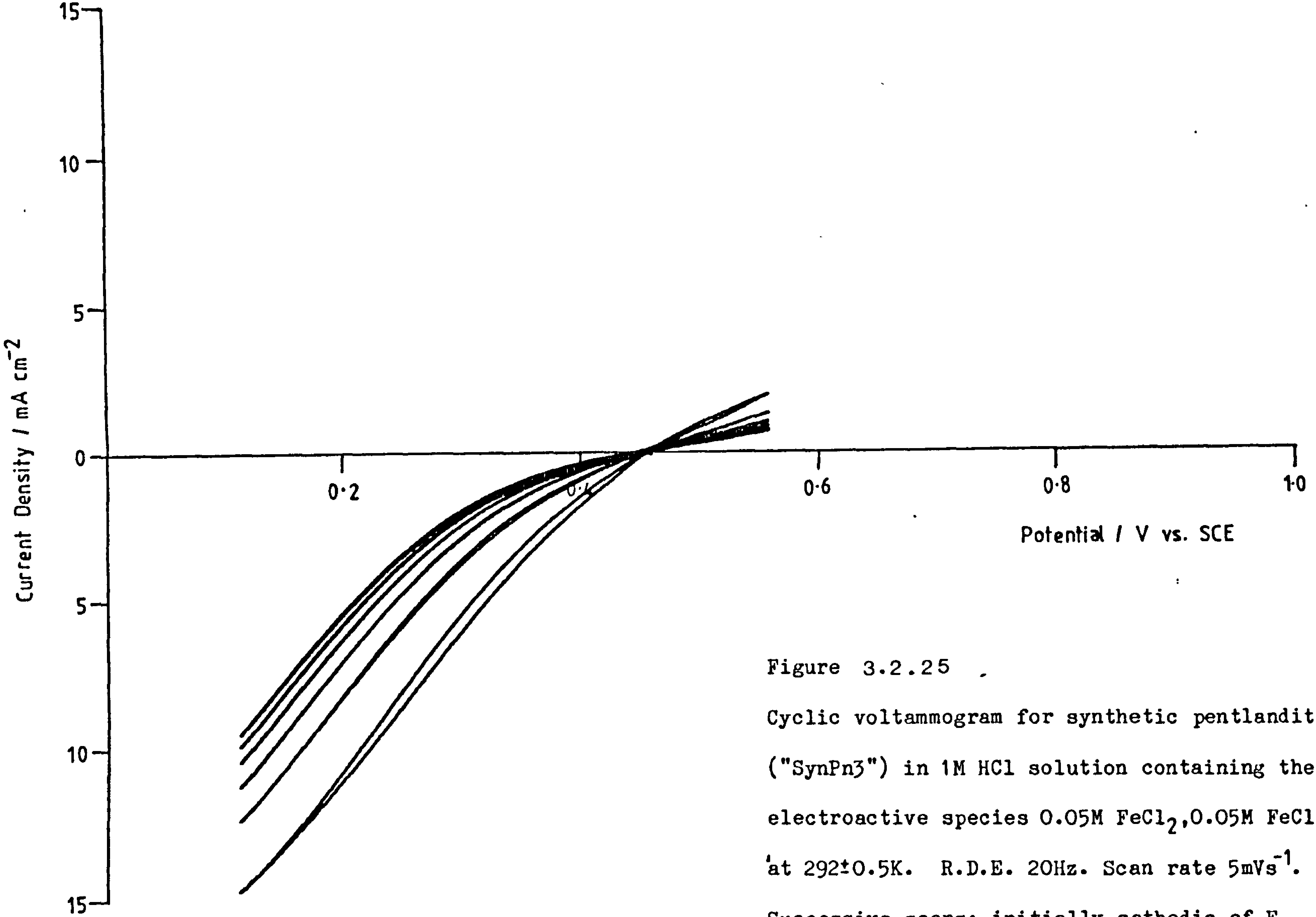

Figure 3.2.25

Cyclic voltammogram for synthetic pentlandite ("SynPn3") in 1M HCl solution containing the electroactive species 0.05M $FeCl_2$,0.05M $FeCl_3$ at 292±0.5K. R.D.E. 20Hz. Scan rate $5mVs^{-1}$. Successive scans: initially cathodic of E_{Rest} (0.447V) followed by anodic excursions.

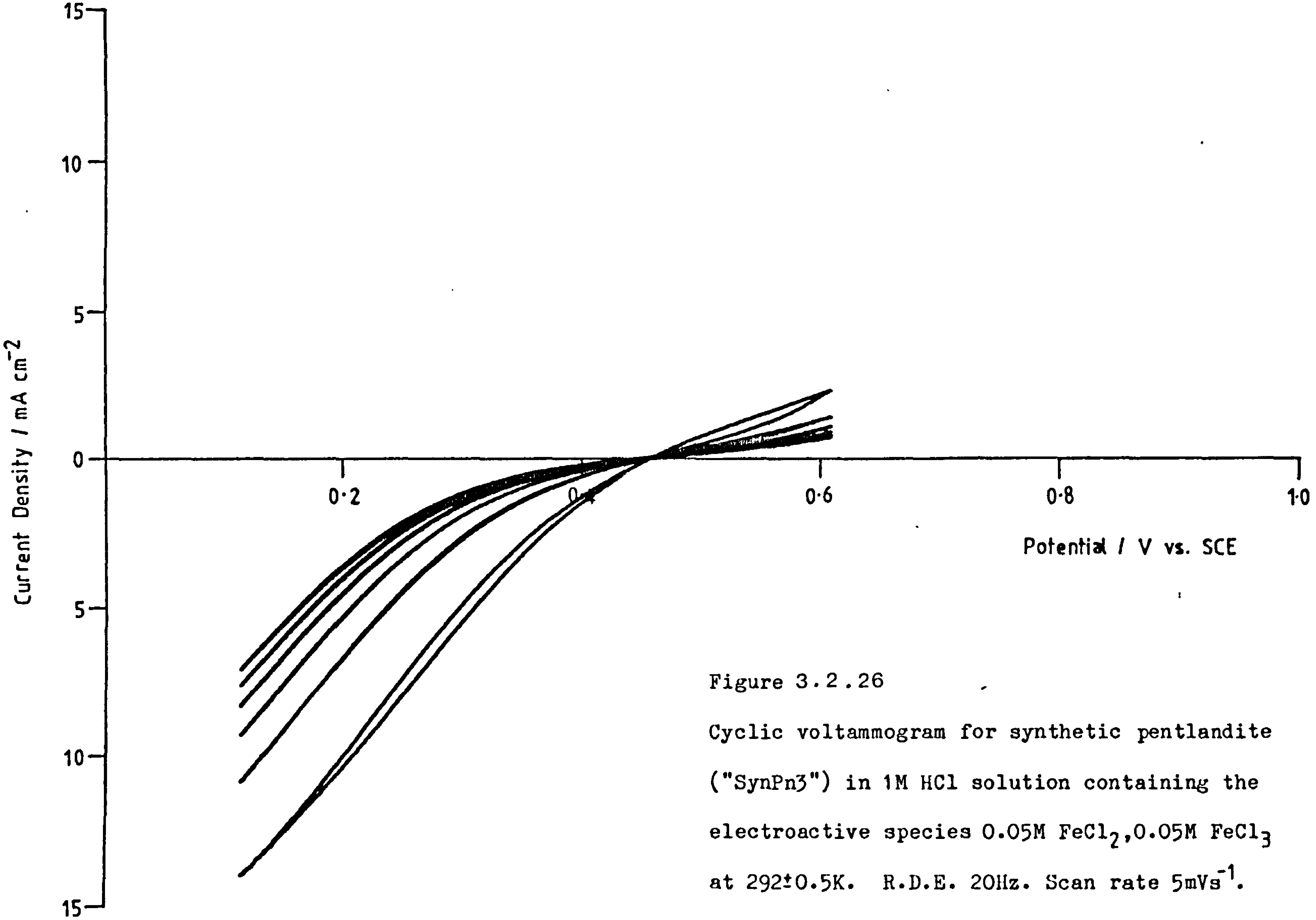

Figure 3.2.26

Cyclic voltammogram for synthetic pentlandite ("SynPn3") in 1M HCl solution containing the electroactive species 0.05M $FeCl_2$,0.05M $FeCl_3$ at 292±0.5K. R.D.E. 20Hz. Scan rate 5mVs^{-1}. Successive scans: initially cathodic of E_{Rest} (0.447V) followed by anodic excursions.

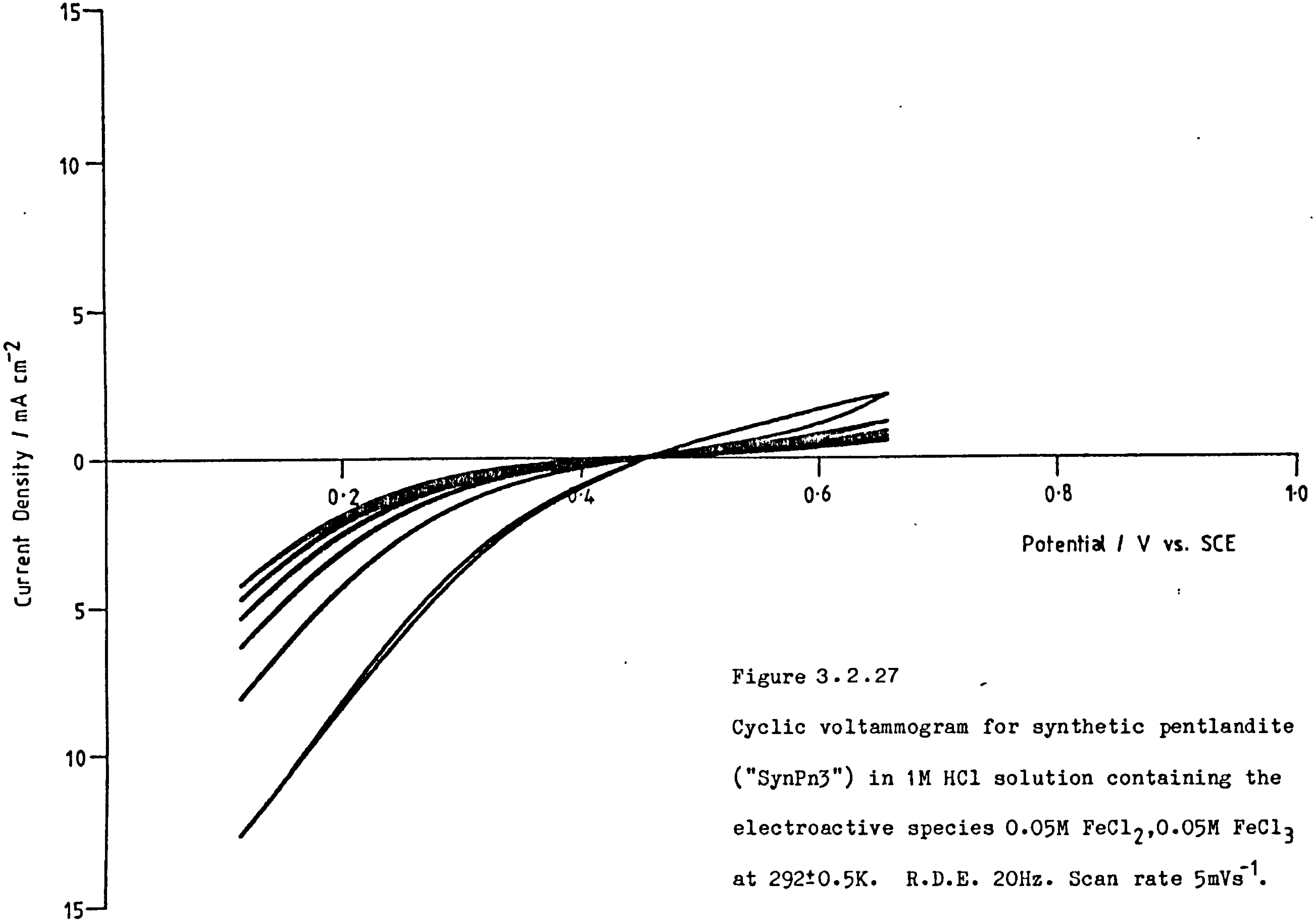

Figure 3.2.27

Cyclic voltammogram for synthetic pentlandite ("SynPn3") in 1M HCl solution containing the electroactive species 0.05M $FeCl_2$,0.05M $FeCl_3$ at 292±0.5K. R.D.E. 20Hz. Scan rate $5mVs^{-1}$. Successive scans: initially cathodic of E_{Rest} (0.447V) followed by anodic excursions.

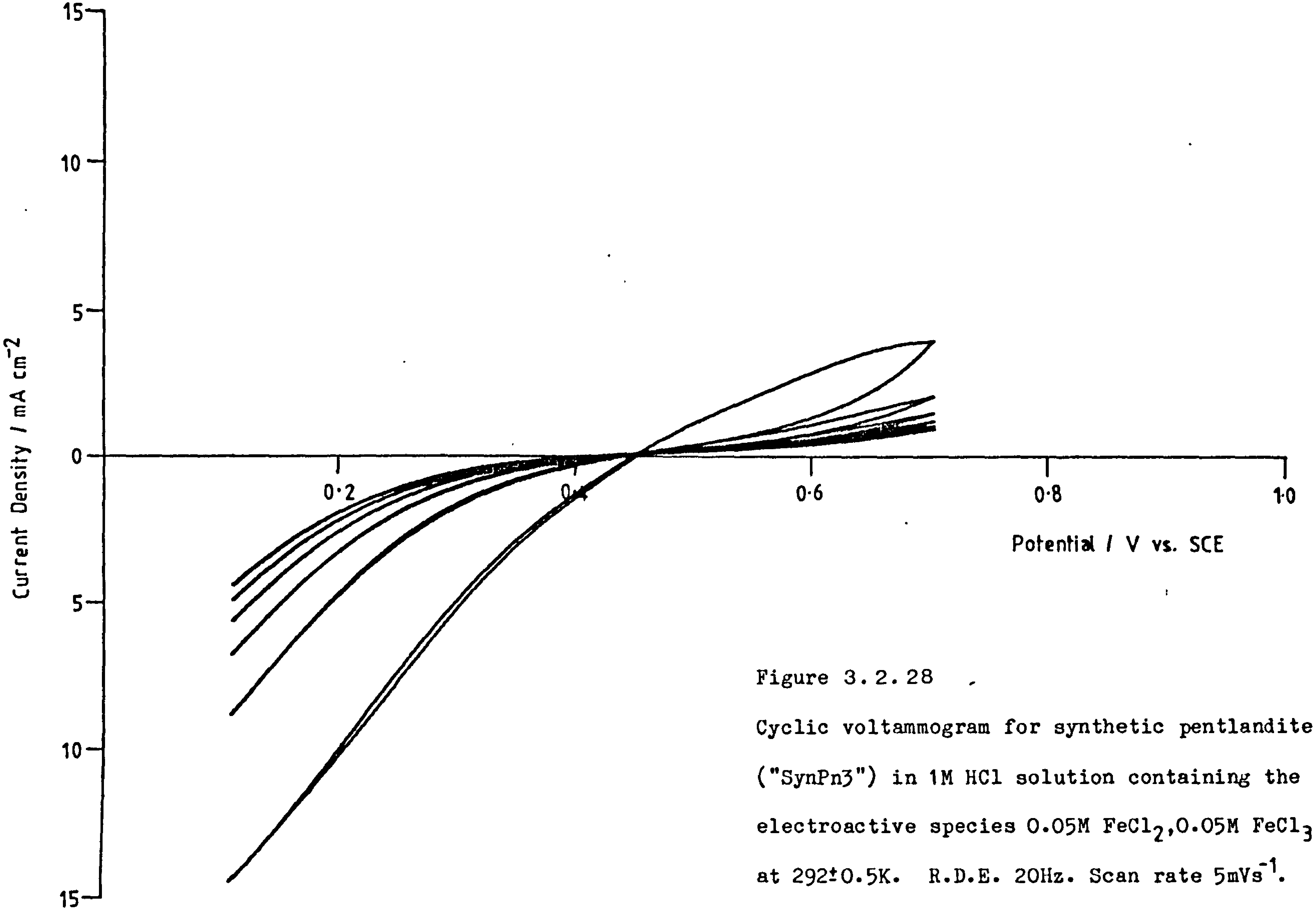

Figure 3.2.28

Cyclic voltammogram for synthetic pentlandite ("SynPn3") in 1M HCl solution containing the electroactive species 0.05M $FeCl_2$,0.05M $FeCl_3$ at 292±0.5K. R.D.E. 20Hz. Scan rate $5mVs^{-1}$. Successive scans: initially cathodic of E_{Rest} (0.447V) followed by anodic excursions.

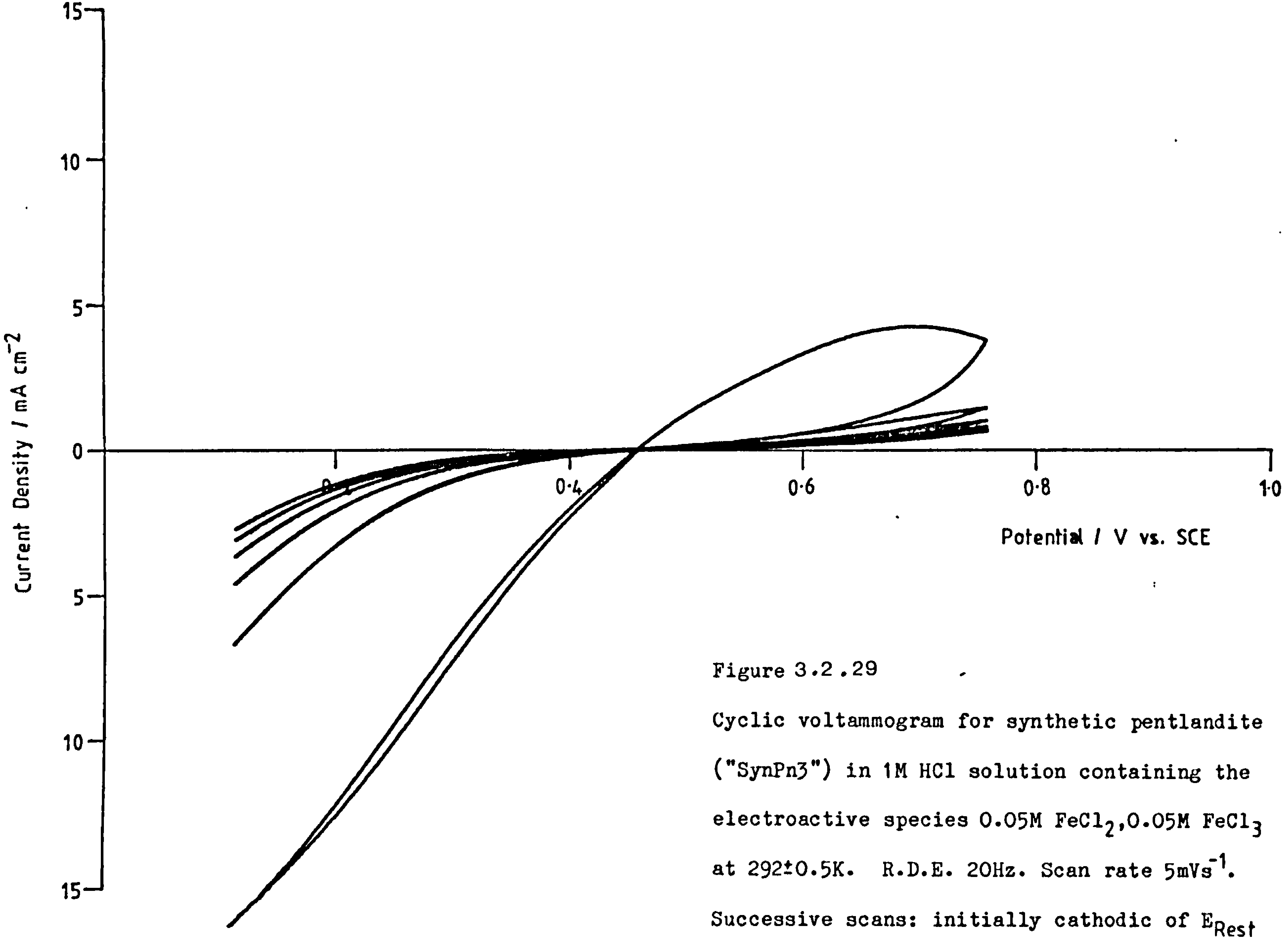

Figure 3.2.29

Cyclic voltammogram for synthetic pentlandite ("SynPn3") in 1M HCl solution containing the electroactive species 0.05M $FeCl_2$,0.05M $FeCl_3$ at 292±0.5K. R.D.E. 20Hz. Scan rate $5mVs^{-1}$. Successive scans: initially cathodic of E_{Rest} (0.447V) followed by anodic excursions.

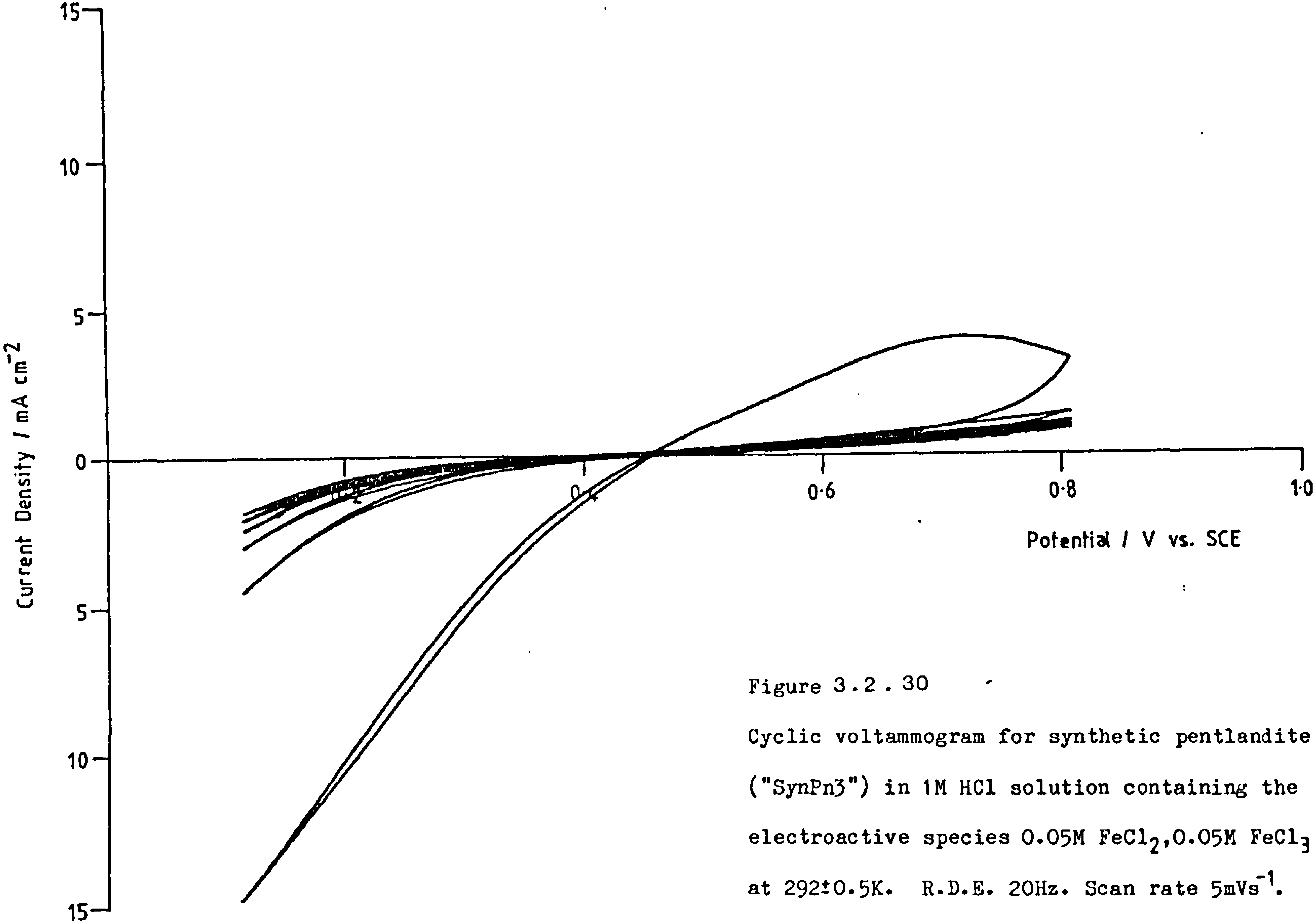

Figure 3.2 . 30

Cyclic voltammogram for synthetic pentlandite ("SynPn3") in 1M HCl solution containing the electroactive species 0.05M $FeCl_2$,0.05M $FeCl_3$ at 292±0.5K. R.D.E. 20Hz. Scan rate $5mVs^{-1}$. Successive scans: initially cathodic of E_{Rest} (0.447V) followed by anodic excursions.

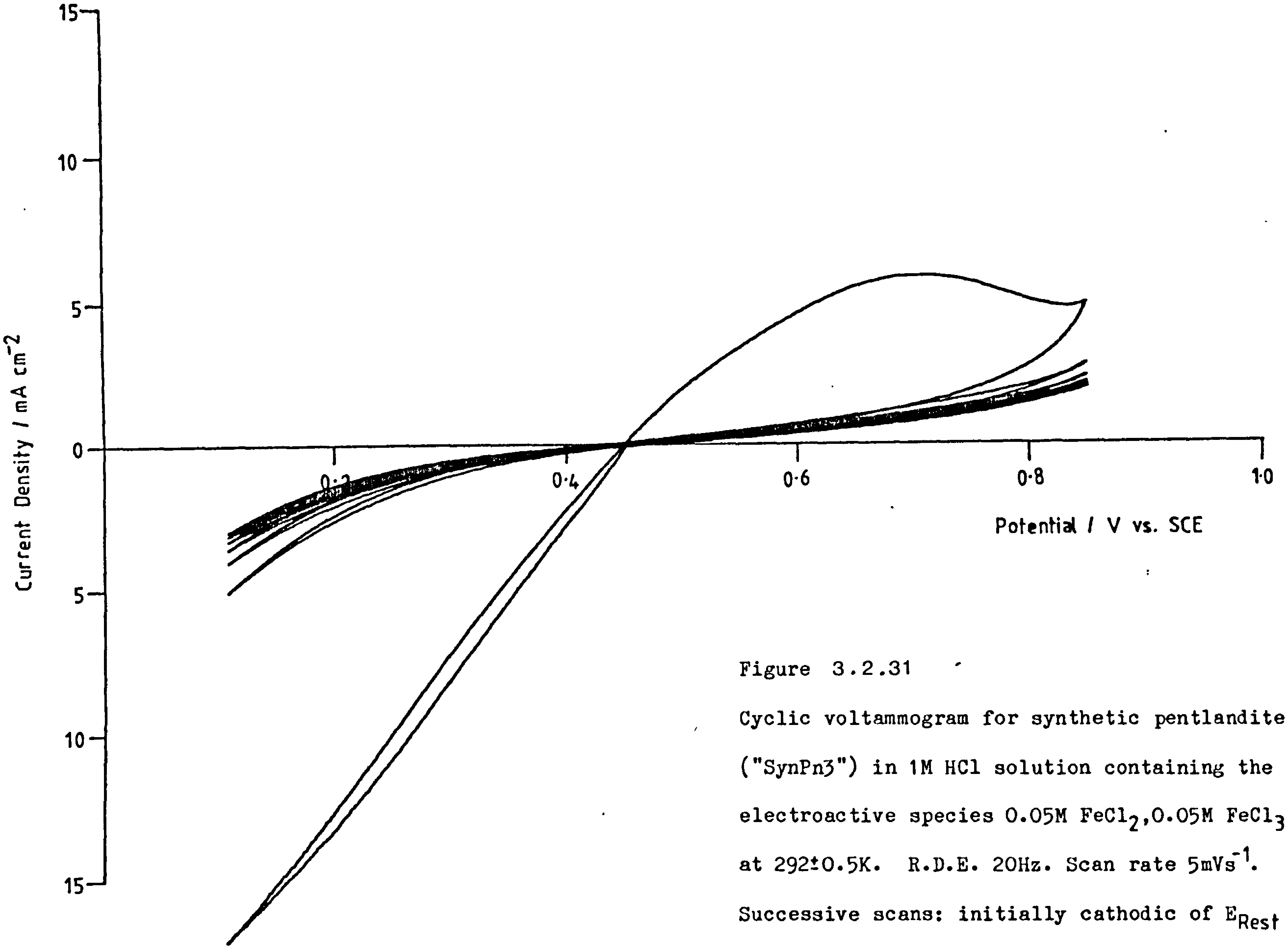

Figure 3.2.31

Cyclic voltammogram for synthetic pentlandite ("SynPn3") in 1M HCl solution containing the electroactive species 0.05M $FeCl_2$, 0.05M $FeCl_3$ at 292±0.5K. R.D.E. 20Hz. Scan rate $5 mVs^{-1}$. Successive scans: initially cathodic of E_{Rest} (0.447V) followed by anodic excursions.

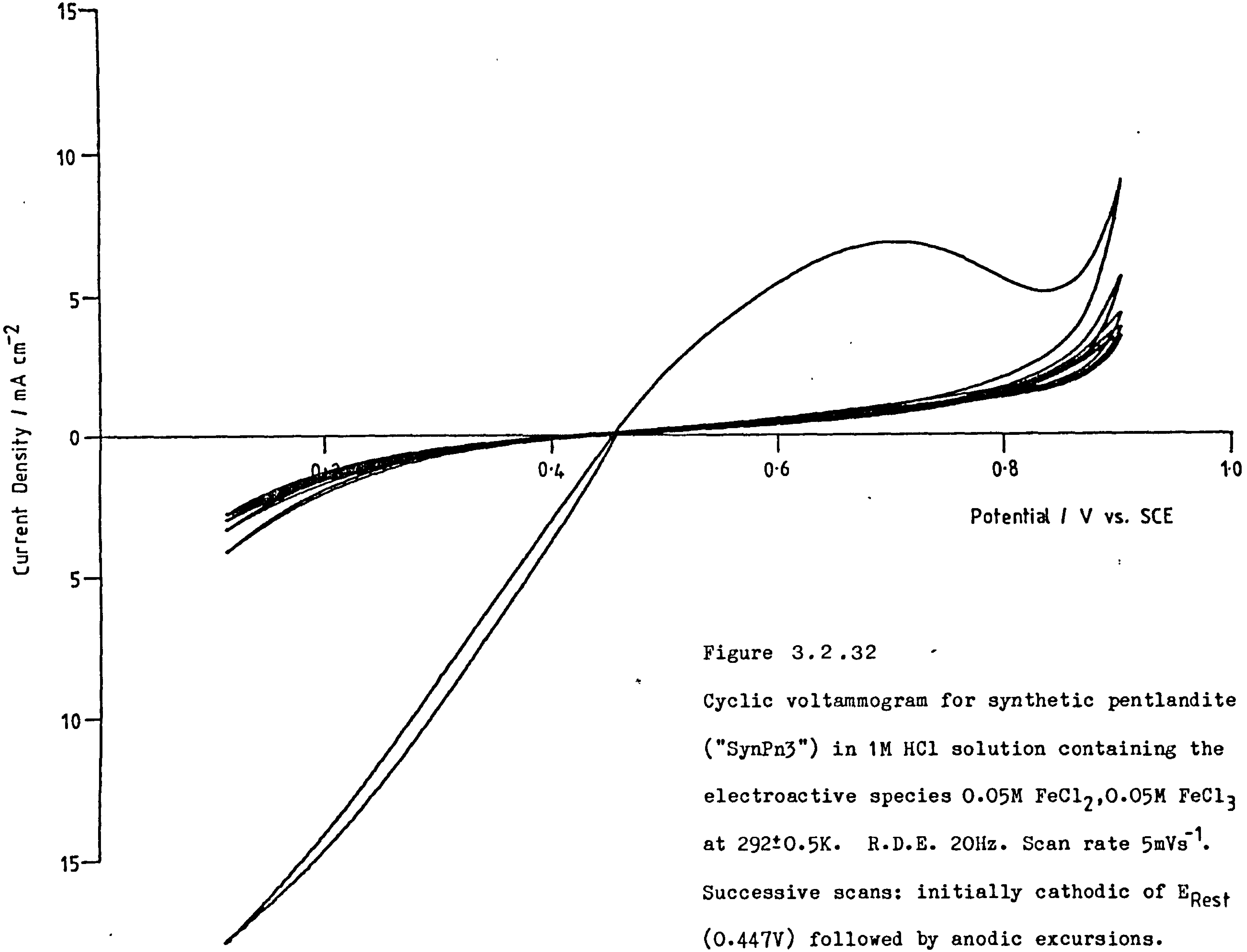

Figure 3.2.32

Cyclic voltammogram for synthetic pentlandite ("SynPn3") in 1M HCl solution containing the electroactive species 0.05M $FeCl_2$,0.05M $FeCl_3$ at 292±0.5K. R.D.E. 20Hz. Scan rate 5mVs^{-1}. Successive scans: initially cathodic of E_{Rest} (0.447V) followed by anodic excursions.

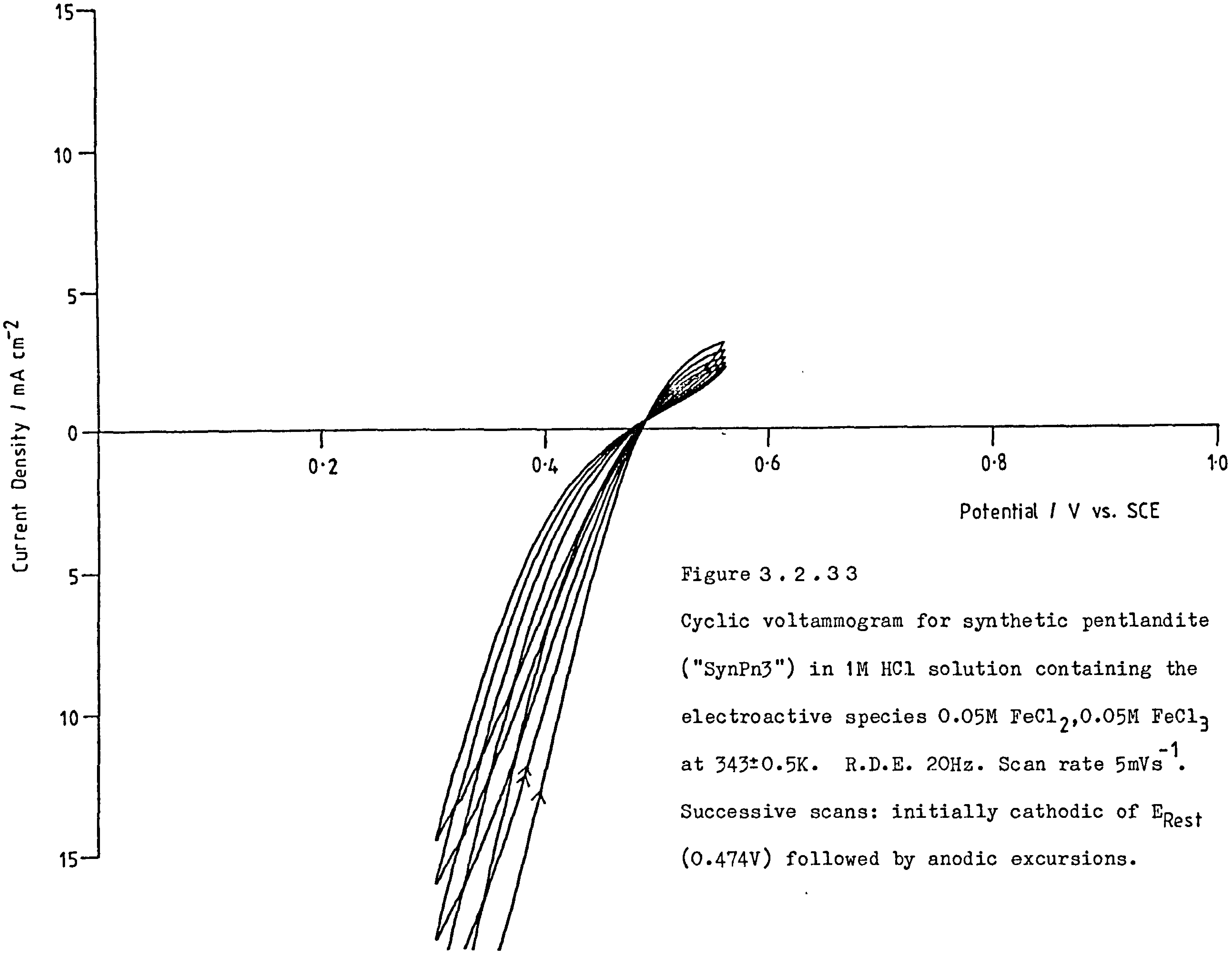

Figure 3.2.33

Cyclic voltammogram for synthetic pentlandite ("SynPn3") in 1M HCl solution containing the electroactive species 0.05M $FeCl_2$, 0.05M $FeCl_3$ at 343±0.5K. R.D.E. 20Hz. Scan rate 5mVs^{-1}. Successive scans: initially cathodic of E_{Rest} (0.474V) followed by anodic excursions.

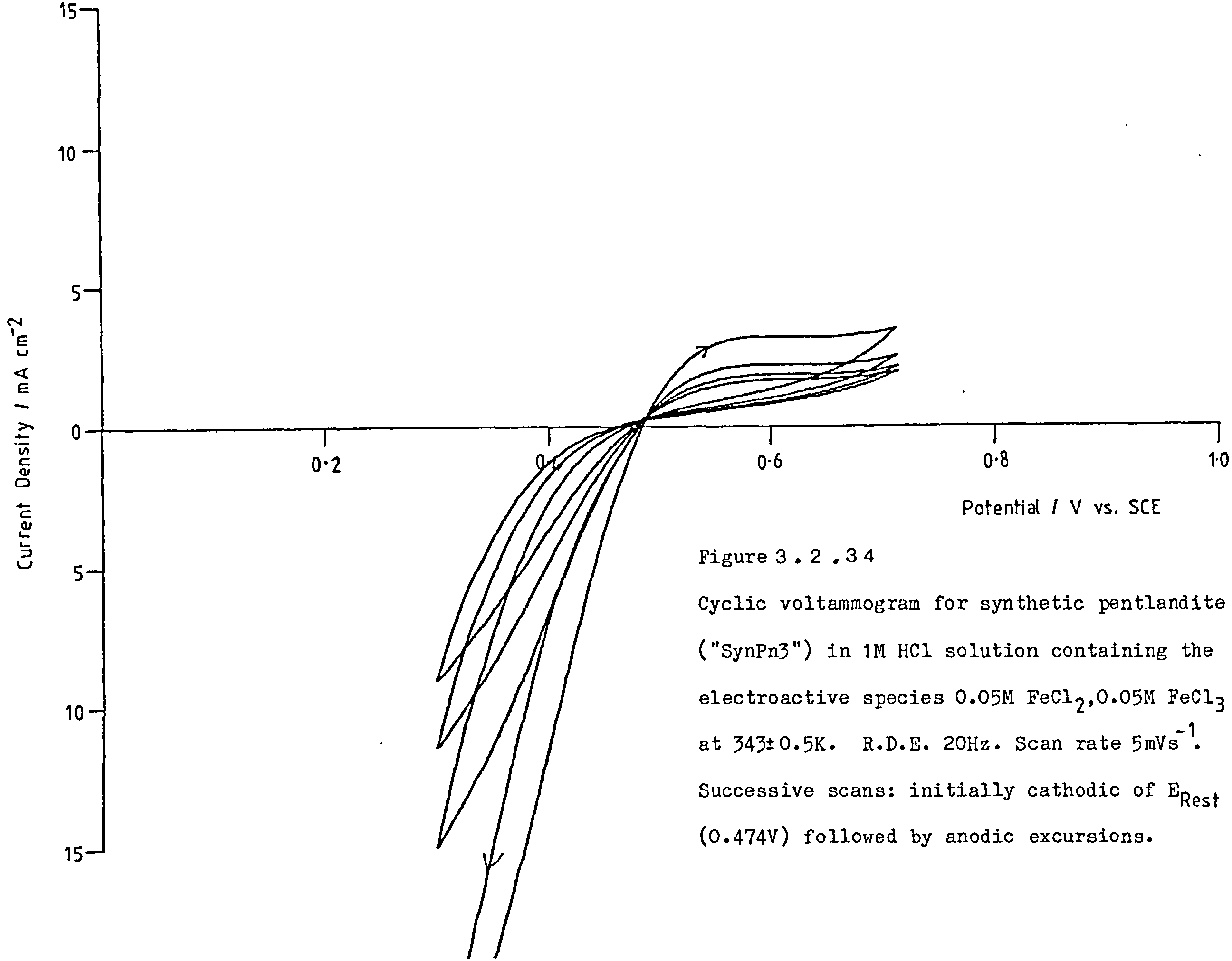

Figure 3.2.34

Cyclic voltammogram for synthetic pentlandite ("SynPn3") in 1M HCl solution containing the electroactive species 0.05M $FeCl_2$, 0.05M $FeCl_3$ at 343±0.5K. R.D.E. 20Hz. Scan rate $5mVs^{-1}$. Successive scans: initially cathodic of E_{Rest} (0.474V) followed by anodic excursions.

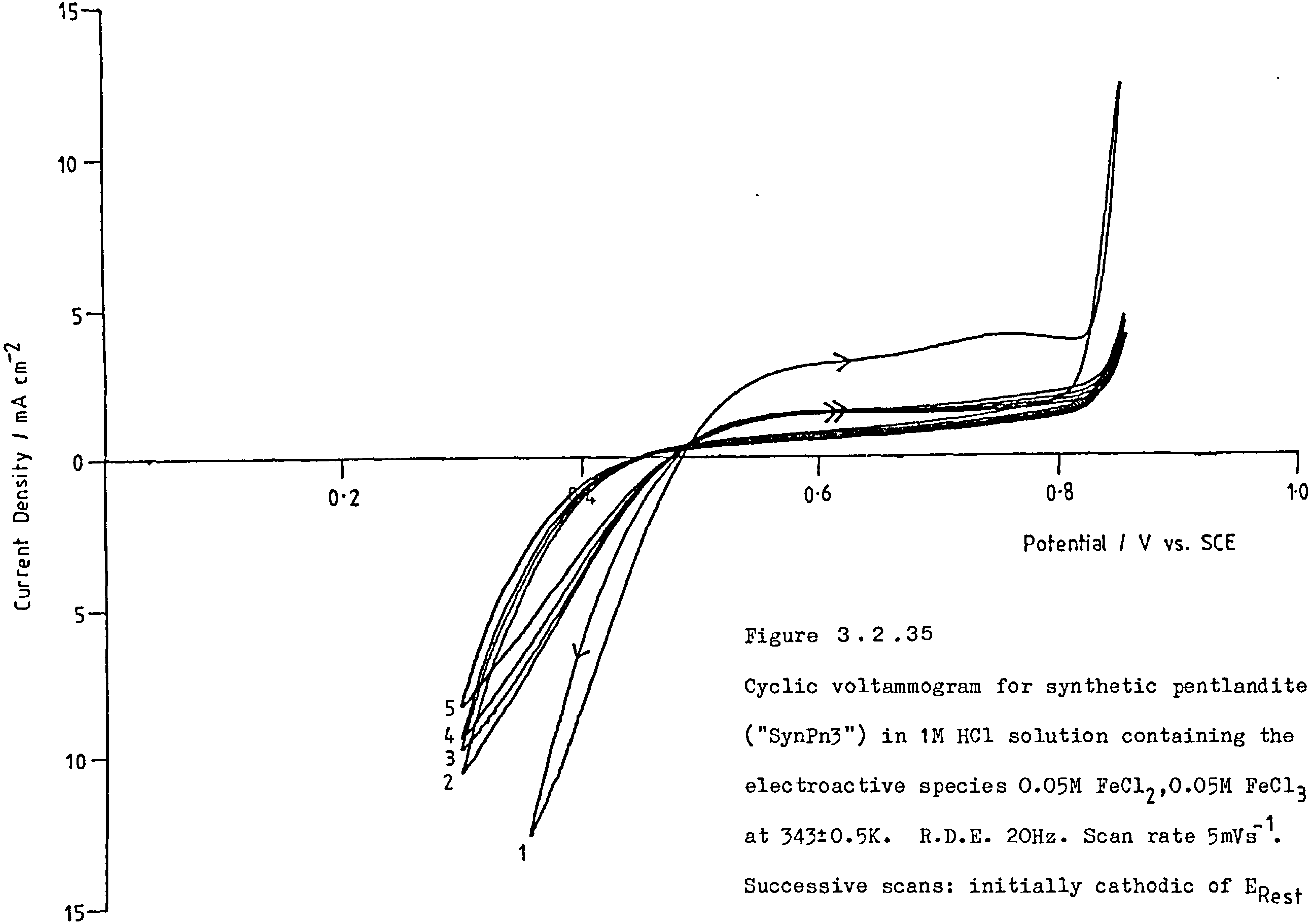

Figure 3.2.35

Cyclic voltammogram for synthetic pentlandite ("SynPn3") in 1M HCl solution containing the electroactive species 0.05M $FeCl_2$, 0.05M $FeCl_3$ at 343±0.5K. R.D.E. 20Hz. Scan rate $5 mVs^{-1}$. Successive scans: initially cathodic of E_{Rest} (0.447V) followed by anodic excursions.

Figure 3.2.36

Cyclic voltammograms for "SynPn3","SynVl1c", and Pt,in 1M HCl,0.5M KCl solution containing electroactive species 0.05M $CuCl_2$,0.05M CuCl at 295±0.5K. R.D.E. 20Hz. Scan rate 5mVs^{-1}. Successive scans: initially anodic of E_{Rest} (0.233V) followed by cathodic excursions.

Figure 3 . 2 . 37

Cyclic voltammograms for "SynPn3","SynVl1c", and Pt in 1M HCl,0.5M KCl solution containing electroactive species 0.05M $CuCl_2$,0.05M CuCl at 343±0.5K. R.D.E. 20Hz. Scan rate $5 mVs^{-1}$. Successive scans: initially anodic of E_{Rest} (0.289V) followed by cathodic excursions.

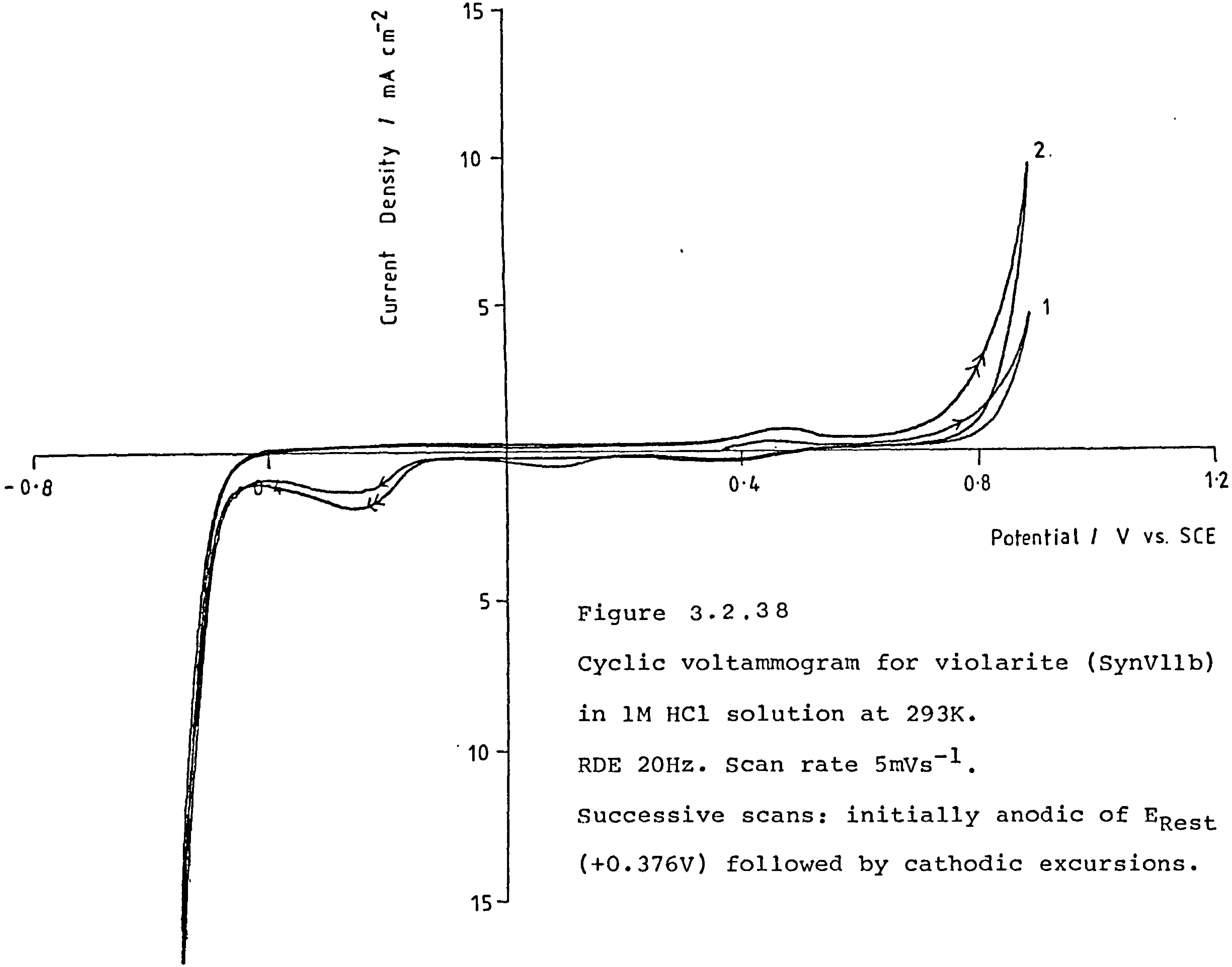

Figure 3.2.38

Cyclic voltammogram for violarite (SynV11b) in 1M HCl solution at 293K.

RDE 20Hz. Scan rate $5mVs^{-1}$.

Successive scans: initially anodic of E_{Rest} (+0.376V) followed by cathodic excursions.

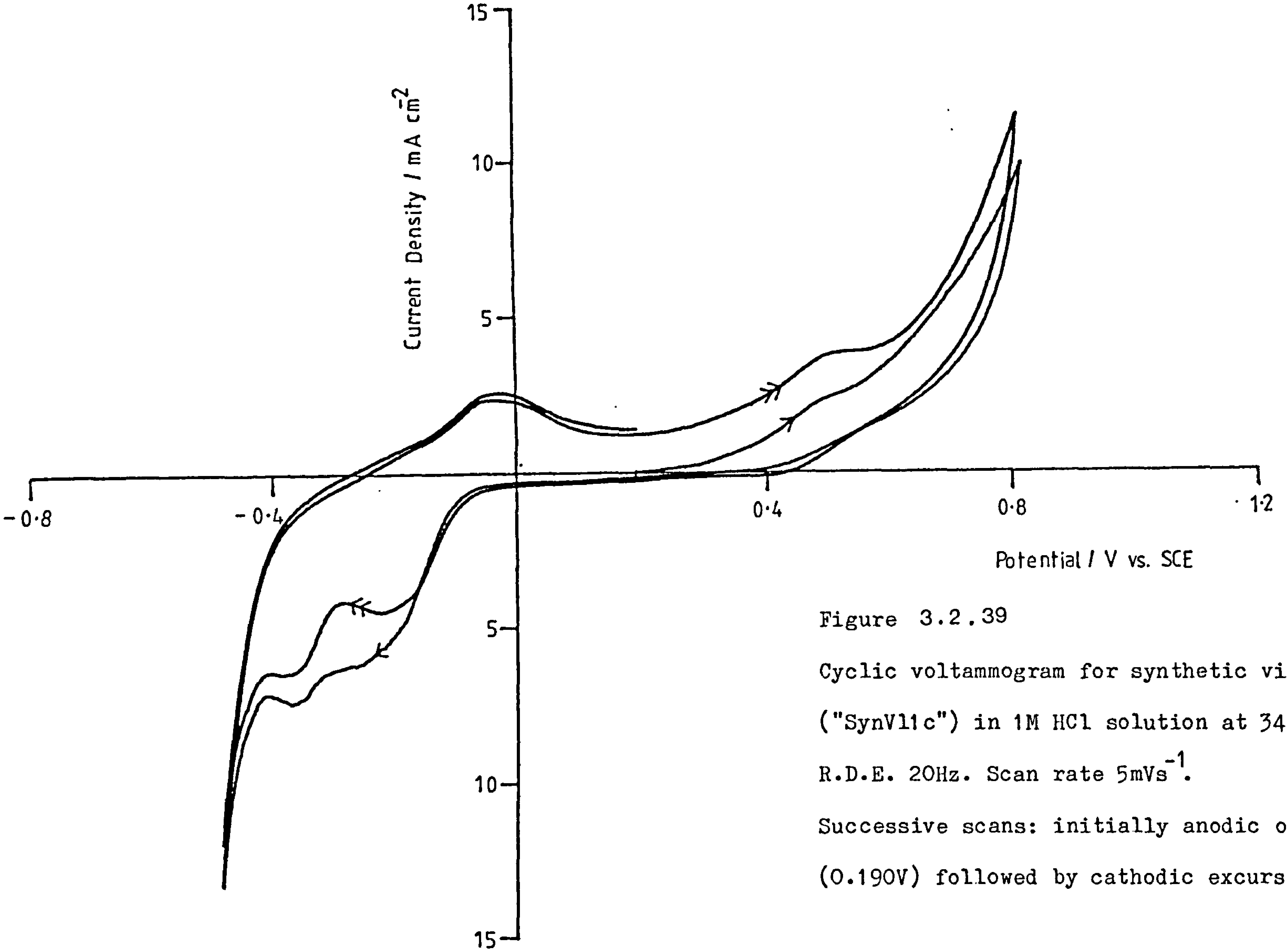

Figure 3.2.39

Cyclic voltammogram for synthetic violarite ("SynV11c") in 1M HCl solution at 343±0.5k. R.D.E. 20Hz. Scan rate 5mVs^{-1}.

Successive scans: initially anodic of E_{Rest} (0.190V) followed by cathodic excursions.

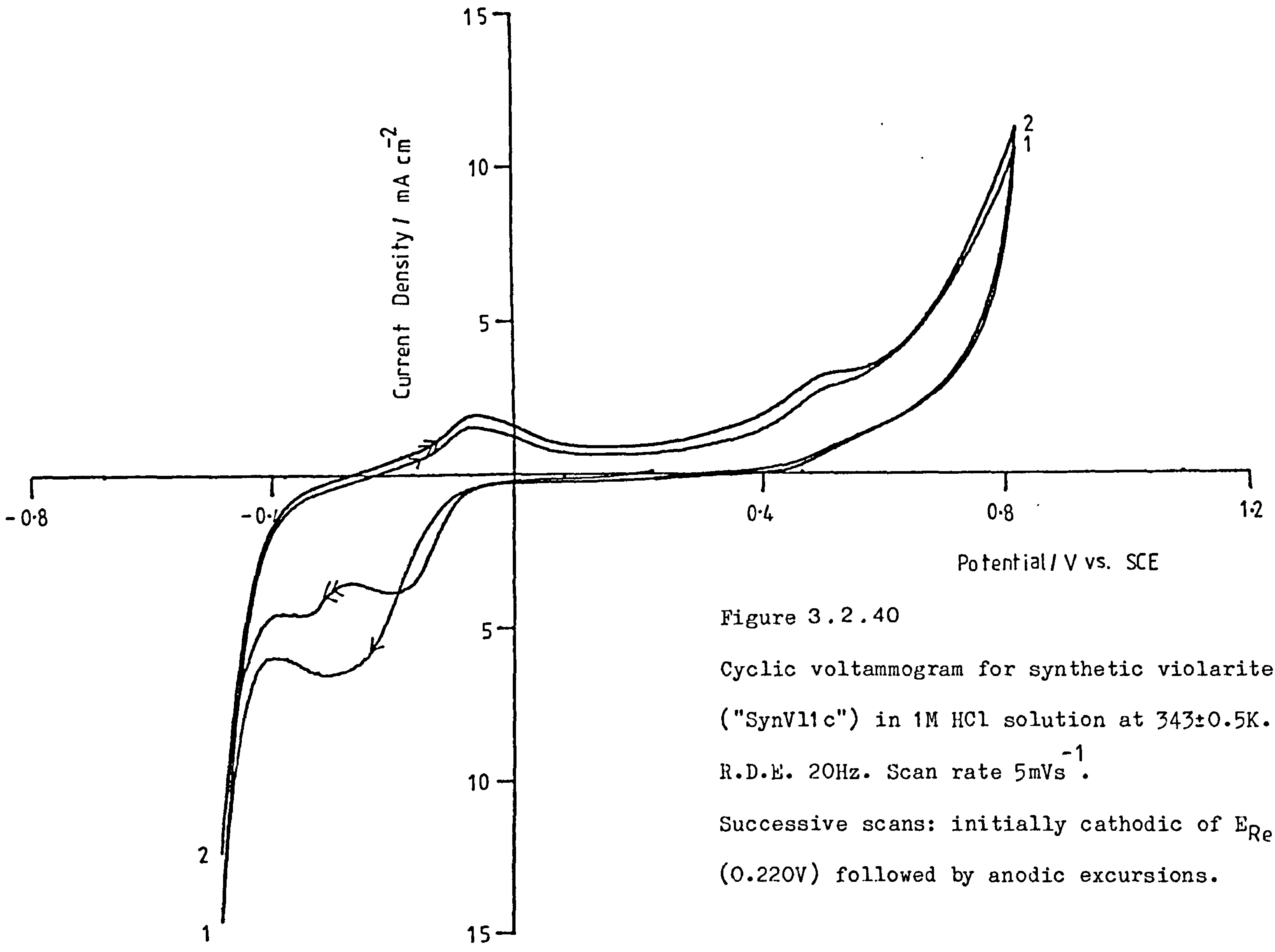

Figure 3.2.40

Cyclic voltammogram for synthetic violarite ("SynV11c") in 1M HCl solution at 343±0.5K. R.D.E. 20Hz. Scan rate 5mVs^{-1}.

Successive scans: initially cathodic of E_{Rest} (0.220V) followed by anodic excursions.

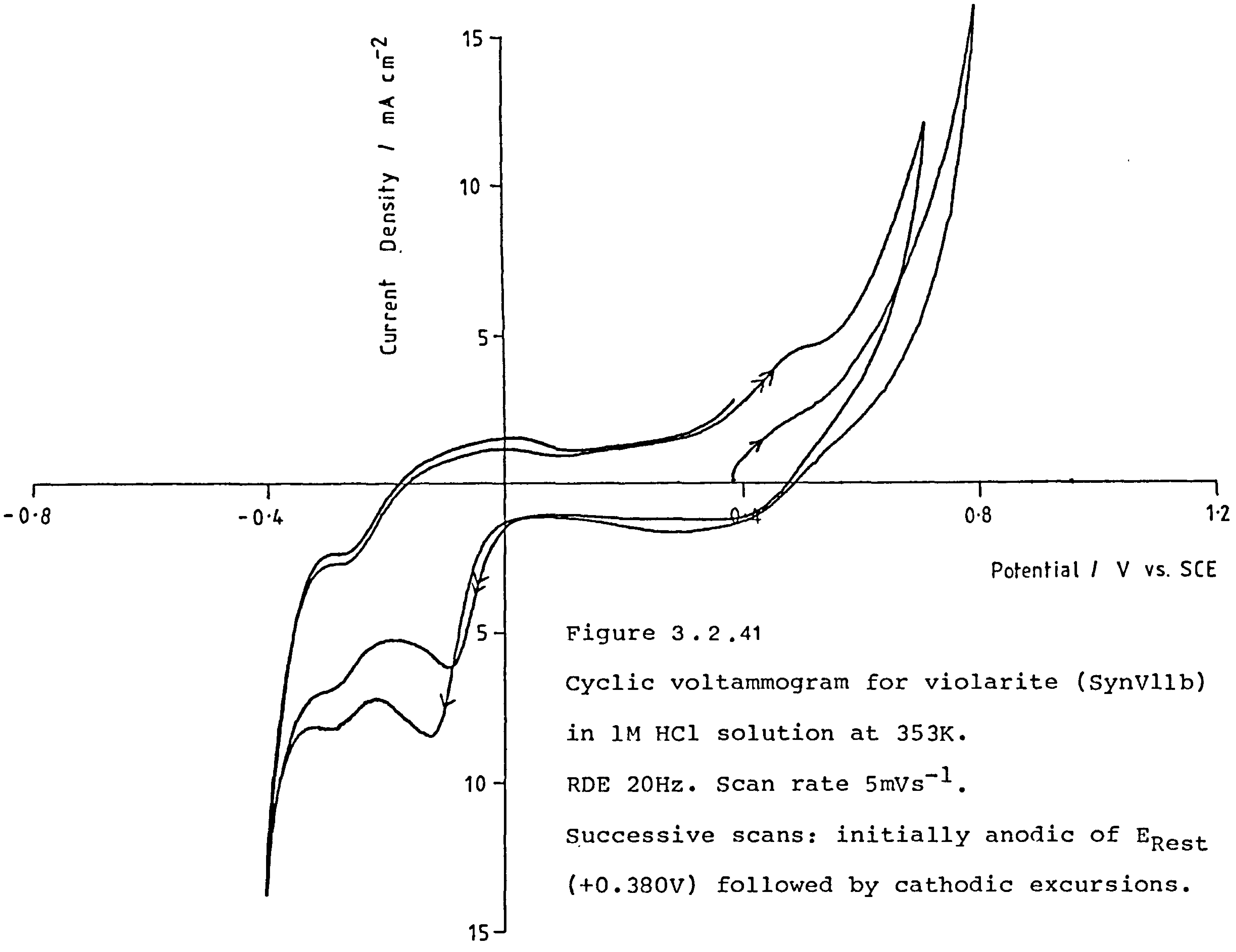

Figure 3.2.41

Cyclic voltammogram for violarite (SynV11b)

in 1M HCl solution at 353K.

RDE 20Hz. Scan rate 5mVs^{-1}.

Successive scans: initially anodic of E_{Rest}

(+0.380V) followed by cathodic excursions.

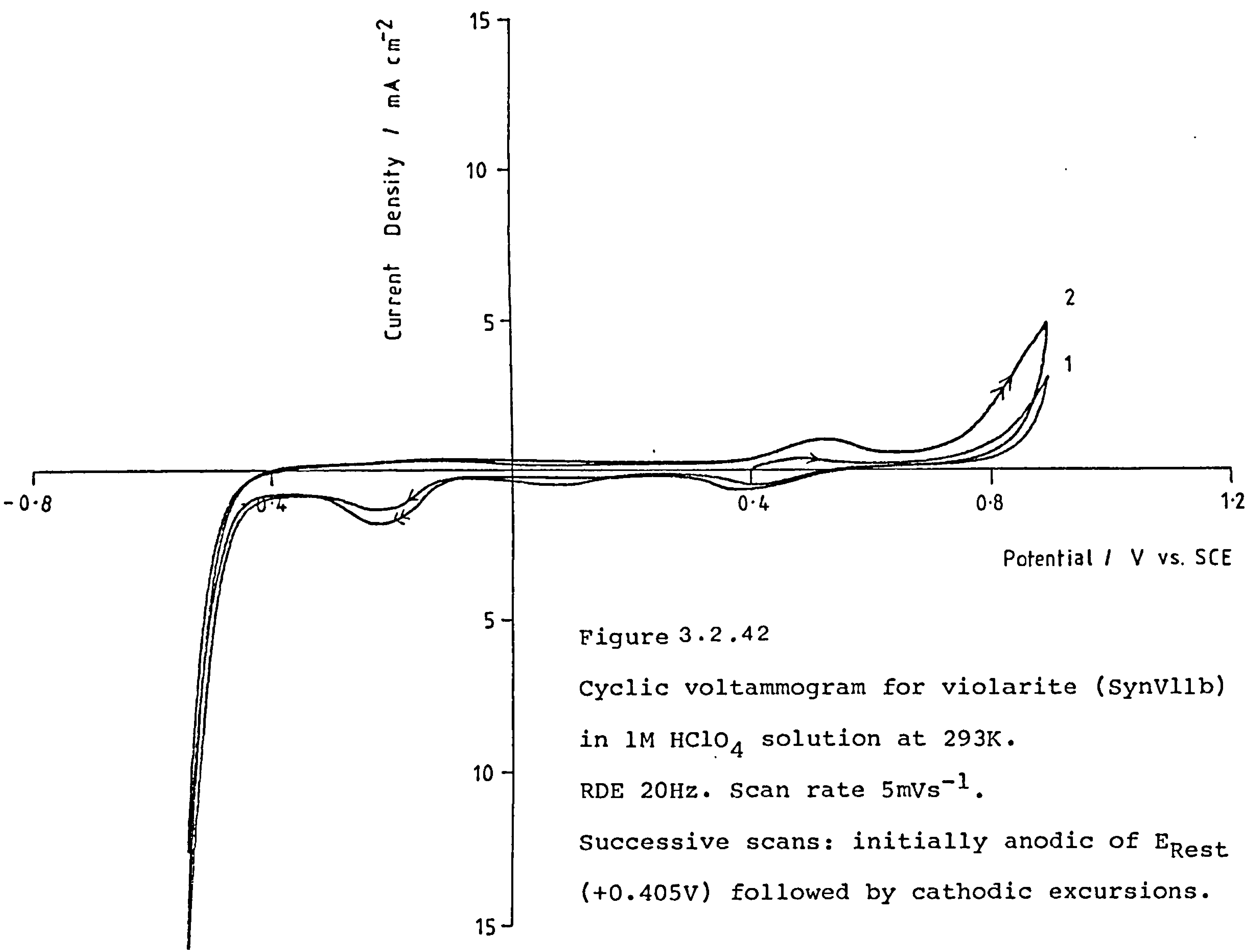

Figure 3.2.42

Cyclic voltammogram for violarite (SynV11b) in 1M $HClO_4$ solution at 293K.

RDE 20Hz. Scan rate 5mVs^{-1}.

Successive scans: initially anodic of E_{Rest} (+0.405V) followed by cathodic excursions.

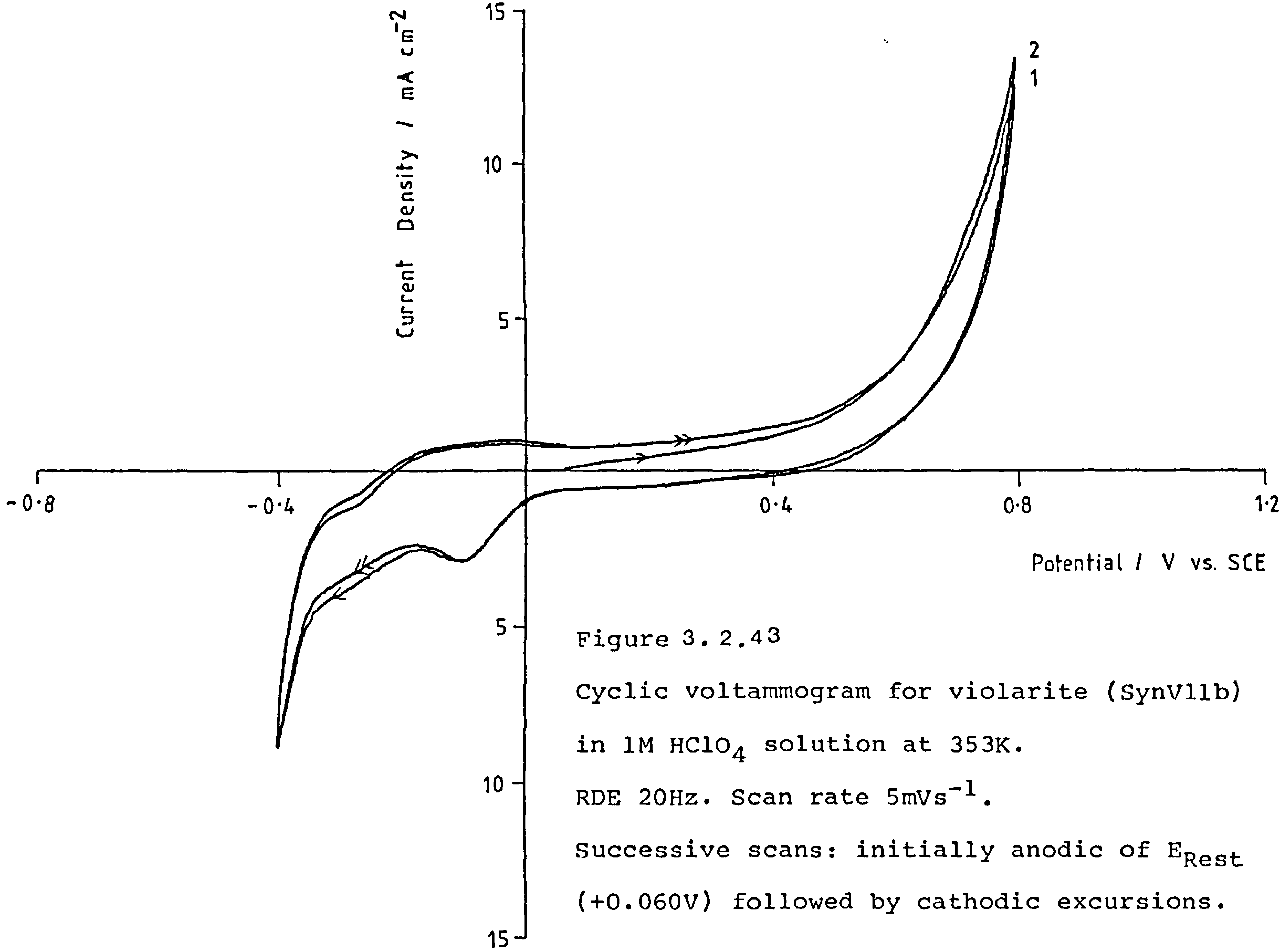

Figure 3.2.43

Cyclic voltammogram for violarite (SynV11b)

in 1M $HClO_4$ solution at 353K.

RDE 20Hz. Scan rate $5mVs^{-1}$.

Successive scans: initially anodic of E_{Rest}

(+0.060V) followed by cathodic excursions.

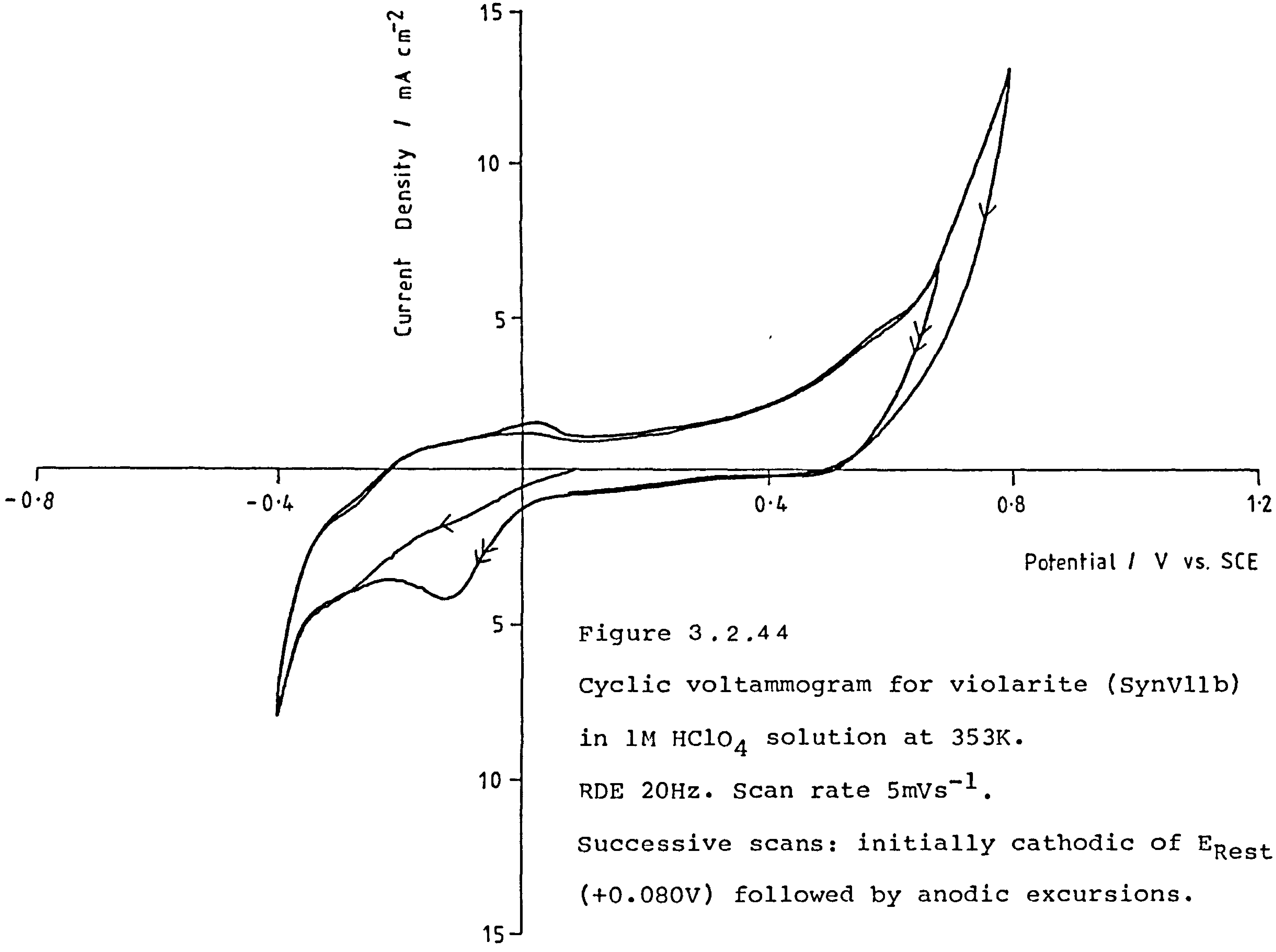

Figure 3.2.44

Cyclic voltammogram for violarite (SynV11b)

in 1M $HClO_4$ solution at 353K.

RDE 20Hz. Scan rate 5mVs^{-1}.

Successive scans: initially cathodic of E_{Rest}

(+0.080V) followed by anodic excursions.

Figure 3.2.45

Linear voltammogram for synthetic violarite ("SynV11c") in 1M HCl solution, 296±0.5K. R.D.E. 20Hz. Scan rate 50mVs^{-1}. Successive scans: anodic of E_{Rest} with open circuit between each scan.

Figure 3.2.46

Linear voltammogram for synthetic violarite ("SynVl1c") in 1M HCl solution, 343±0.5K.

R.D.E. 20Hz. Scan rate $50 mVs^{-1}$.

Successive scans: anodic of E_{Rest} with open circuit between each scan.

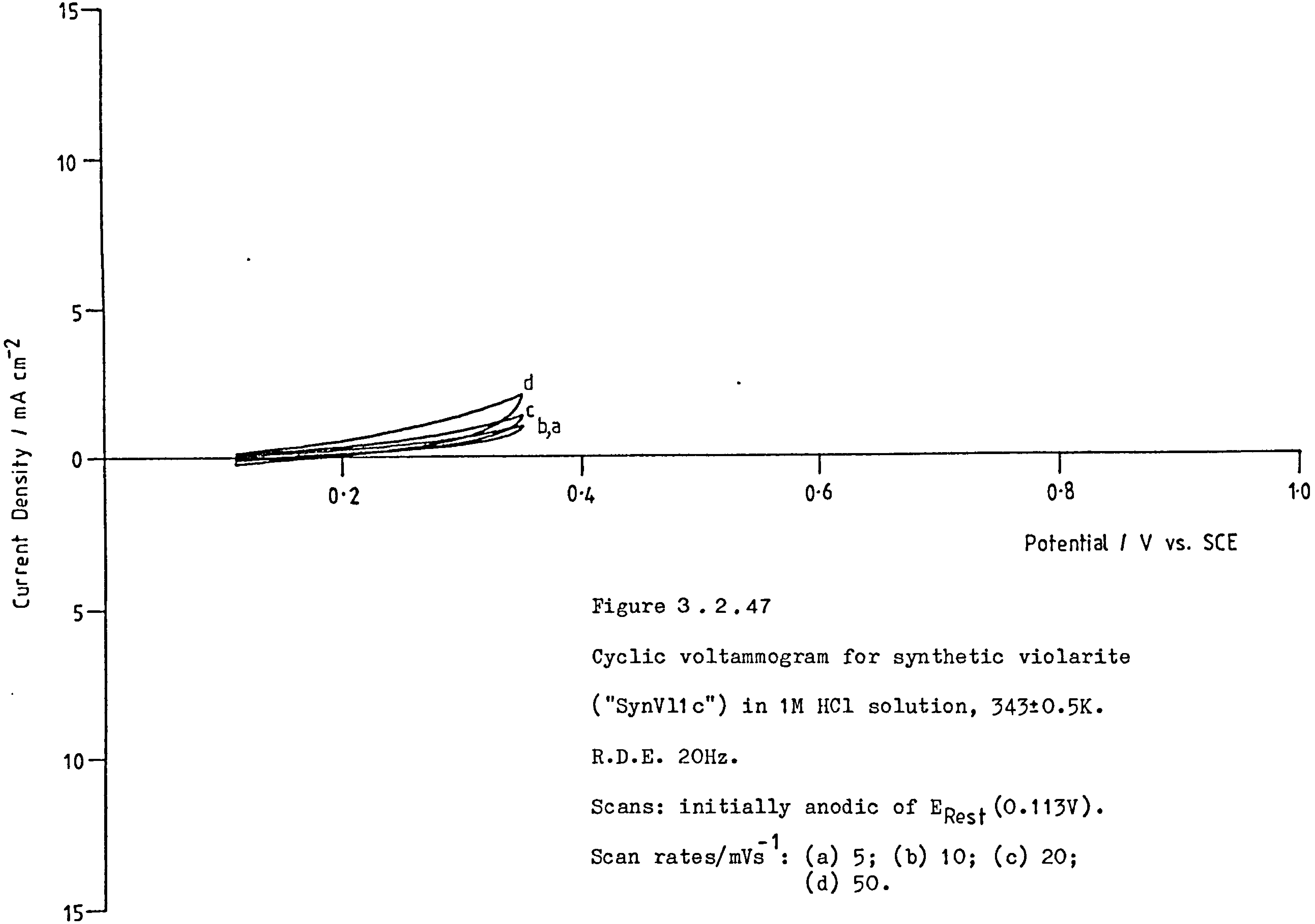

Figure 3 . 2 . 47

Cyclic voltammogram for synthetic violarite

("SynV11c") in 1M HCl solution, 343±0.5K.

R.D.E. 20Hz.

Scans: initially anodic of E_{Rest} (0.113V).

Scan rates/mVs^{-1}: (a) 5; (b) 10; (c) 20;
(d) 50.

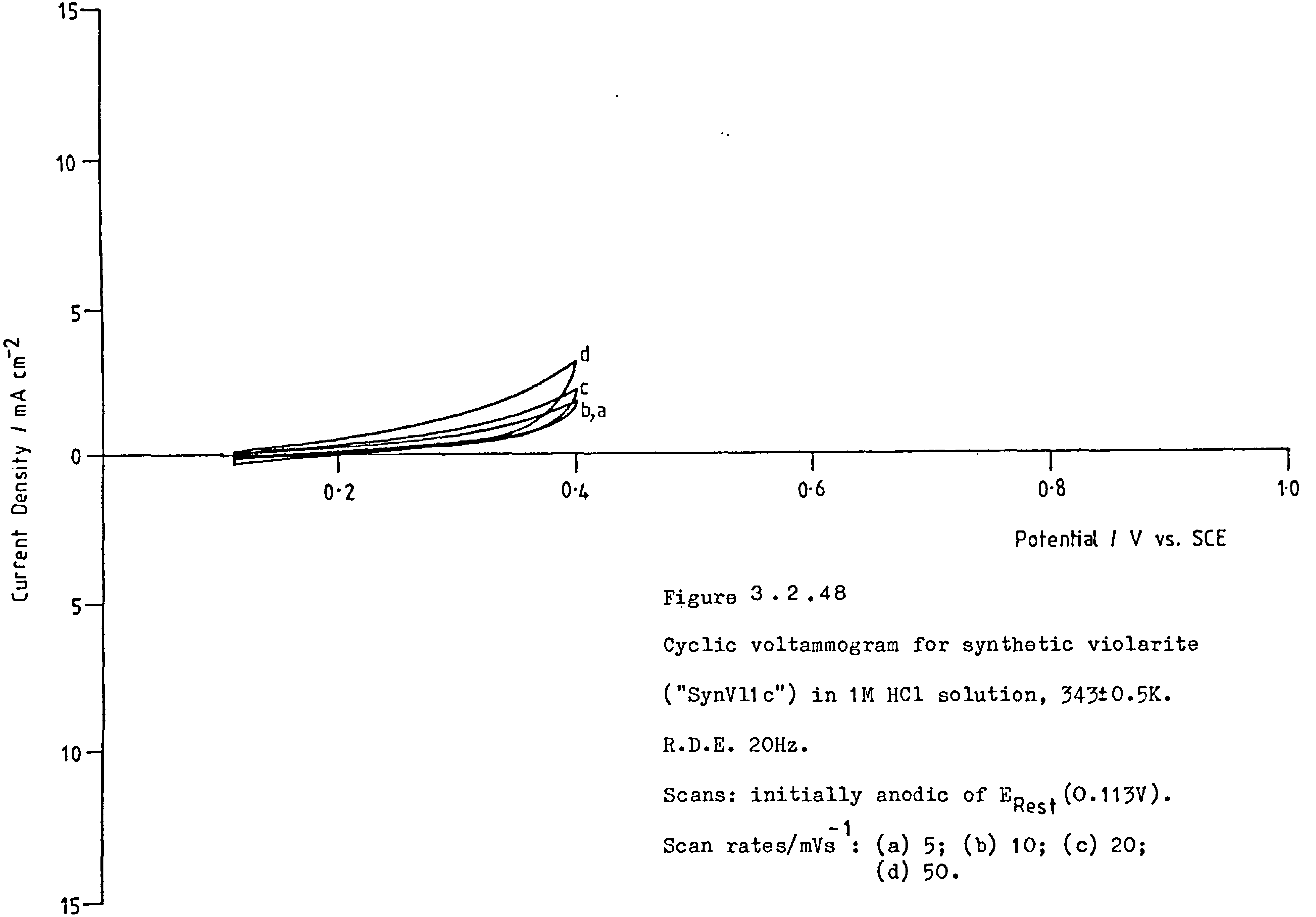

Figure 3.2.48

Cyclic voltammogram for synthetic violarite

("SynV11c") in 1M HCl solution, 343±0.5K.

R.D.E. 20Hz.

Scans: initially anodic of E_{Rest} (0.113V).

Scan rates/mVs^{-1}: (a) 5; (b) 10; (c) 20;
(d) 50.

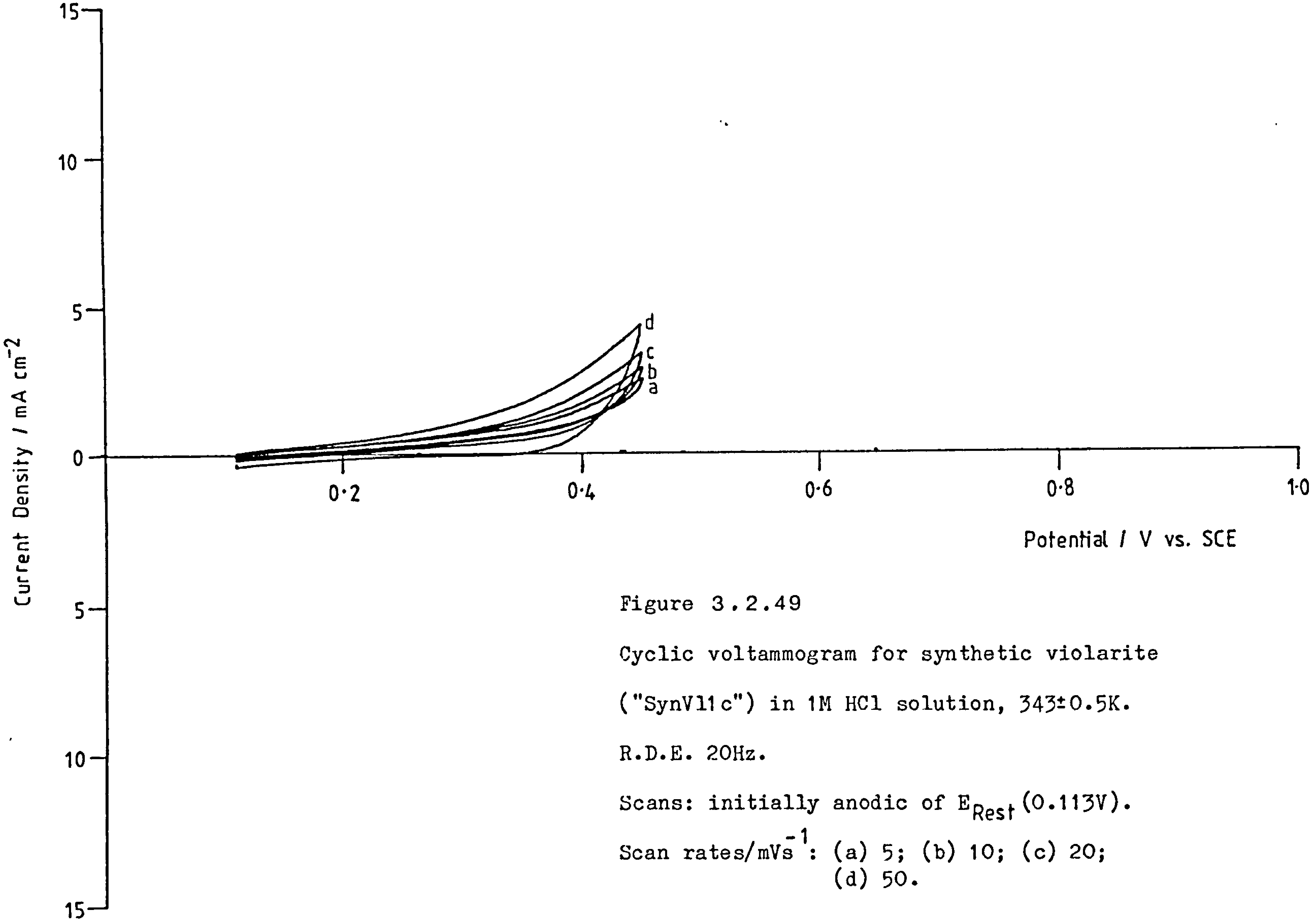

Figure 3.2.49

Cyclic voltammogram for synthetic violarite ("SynV11c") in 1M HCl solution, 343±0.5K.

R.D.E. 20Hz.

Scans: initially anodic of E_{Rest} (0.113V).

Scan rates/mVs^{-1}: (a) 5; (b) 10; (c) 20; (d) 50.

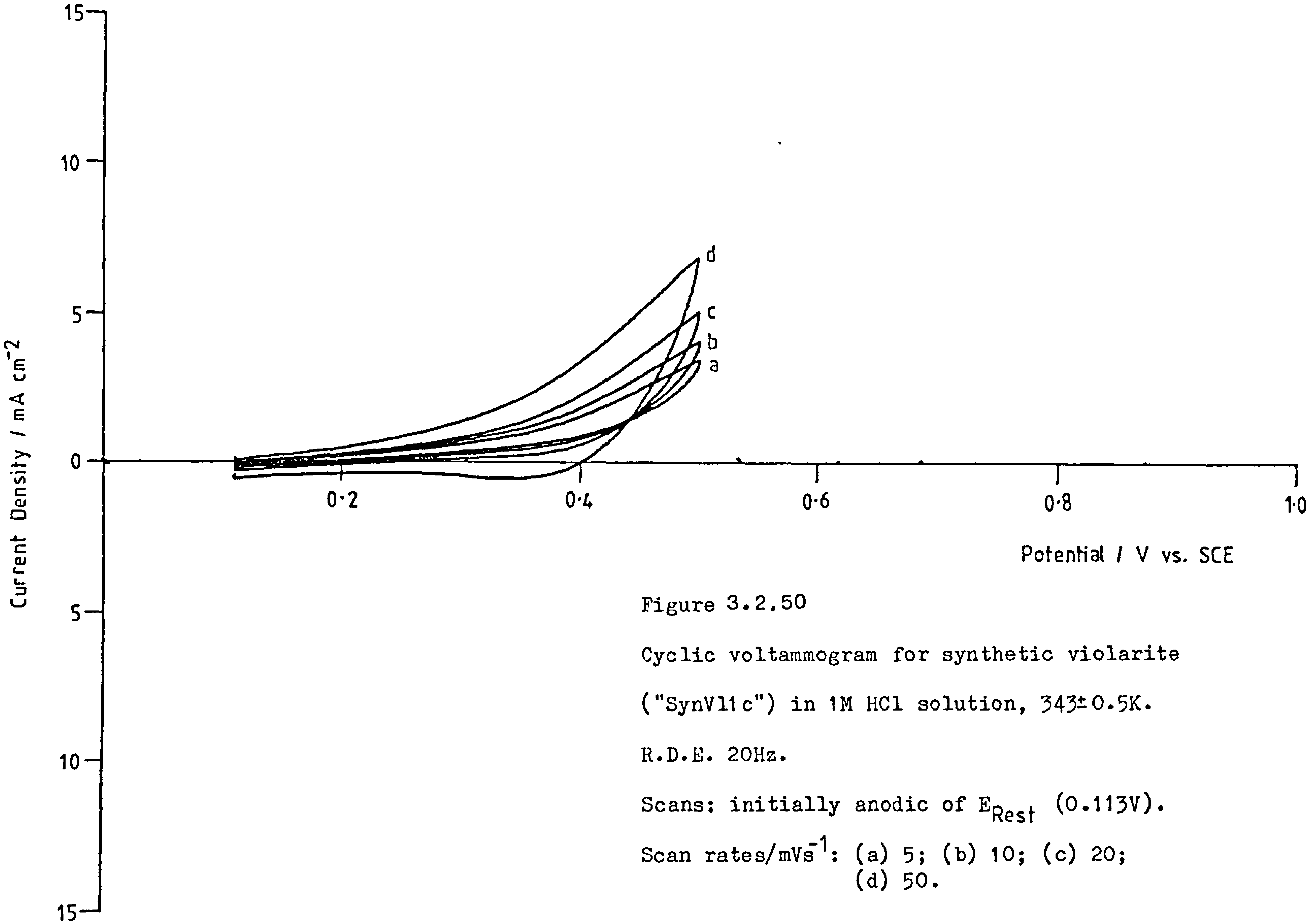

Figure 3.2.50

Cyclic voltammogram for synthetic violarite ("SynV11c") in 1M HCl solution, 343±0.5K.

R.D.E. 20Hz.

Scans: initially anodic of E_{Rest} (0.113V).

Scan rates/mVs^{-1}: (a) 5; (b) 10; (c) 20; (d) 50.

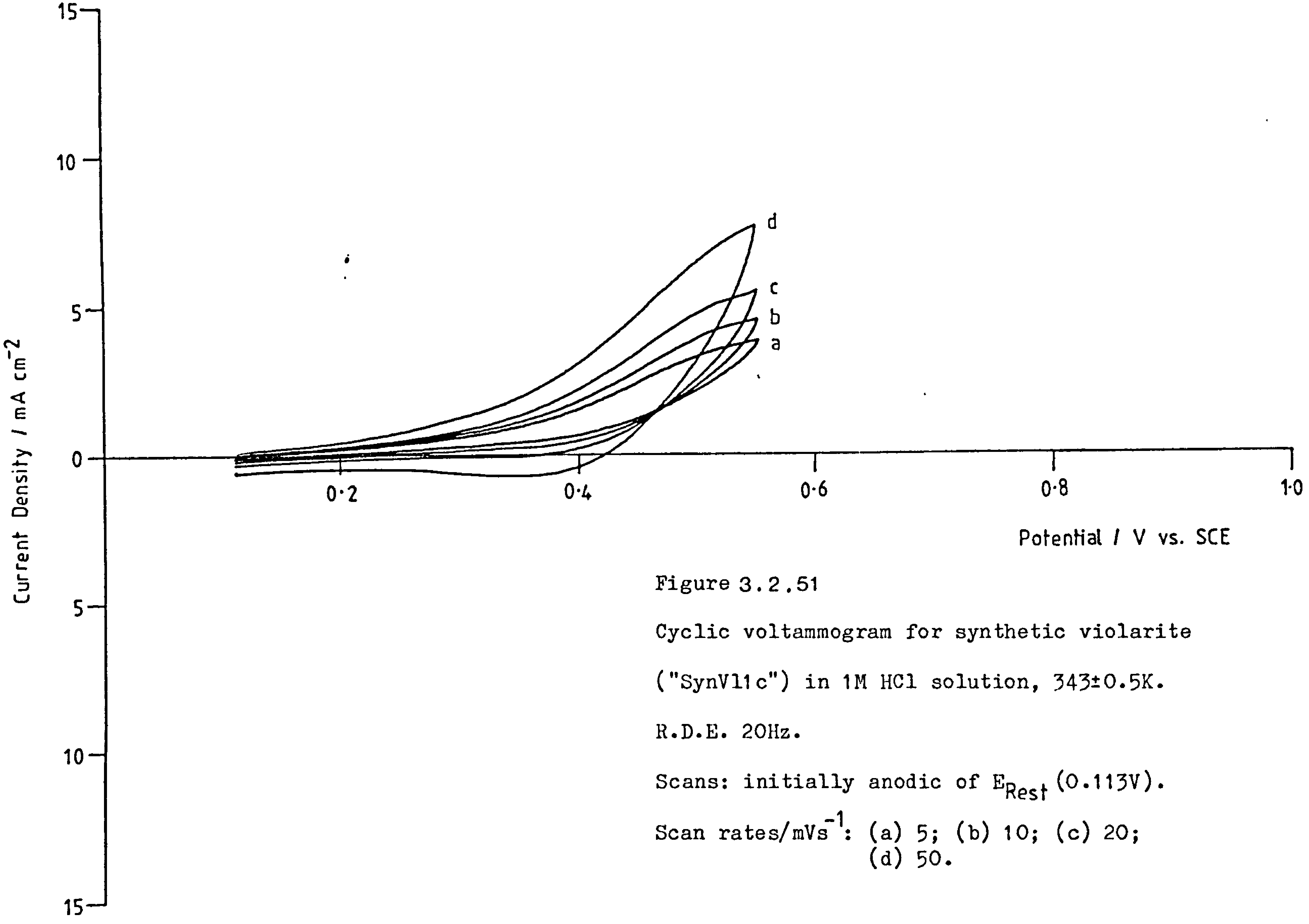

Figure 3.2.51

Cyclic voltammogram for synthetic violarite ("SynV11c") in 1M HCl solution, 343±0.5K.

R.D.E. 20Hz.

Scans: initially anodic of E_{Rest} (0.113V).

Scan rates/mVs^{-1}: (a) 5; (b) 10; (c) 20; (d) 50.

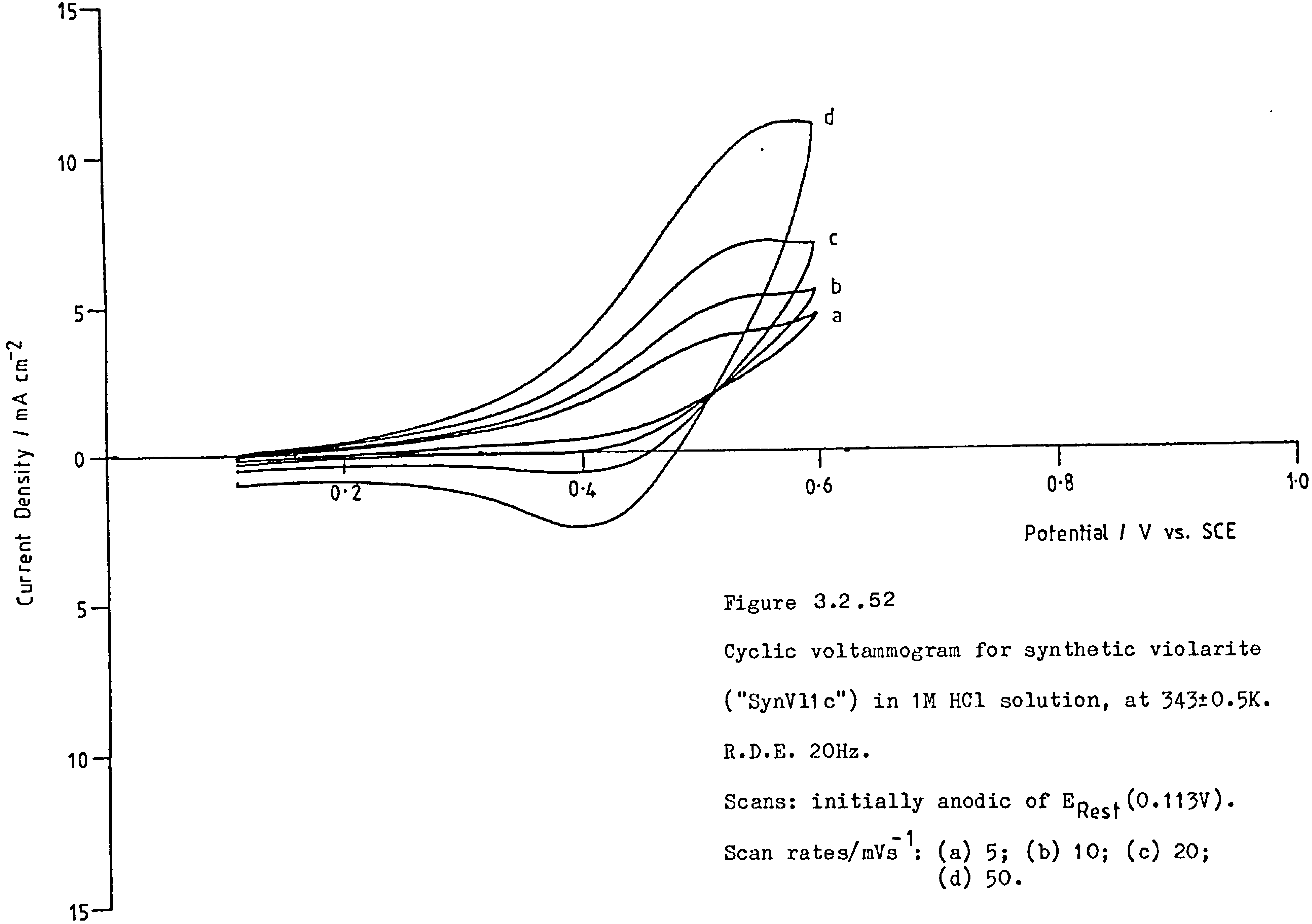

Figure 3.2.52

Cyclic voltammogram for synthetic violarite ("SynV11c") in 1M HCl solution, at 343±0.5K.

R.D.E. 20Hz.

Scans: initially anodic of E_{Rest}(0.113V).

Scan rates/mVs^{-1}: (a) 5; (b) 10; (c) 20; (d) 50.

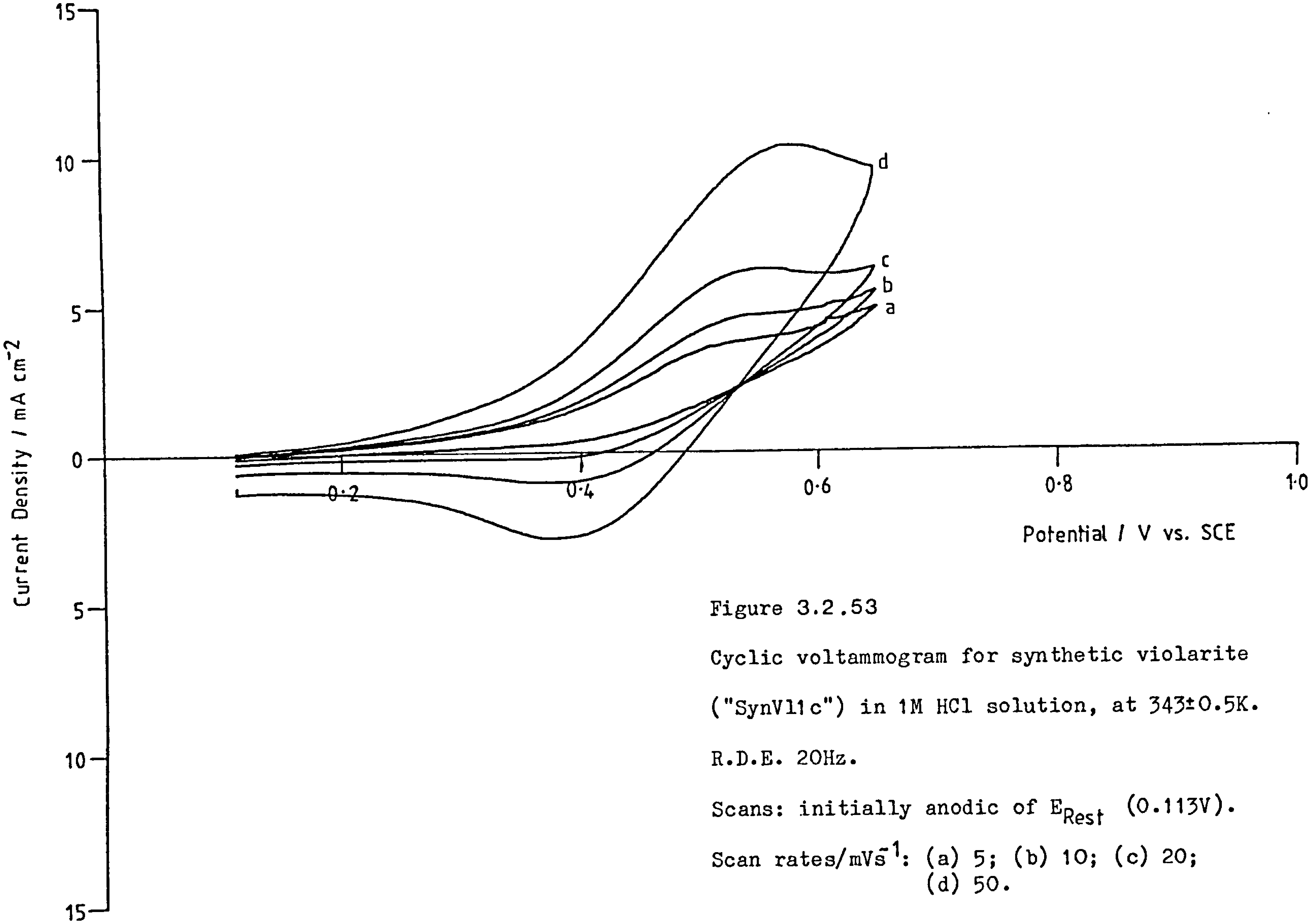

Figure 3.2.53

Cyclic voltammogram for synthetic violarite ("SynV11c") in 1M HCl solution, at 343±0.5K.

R.D.E. 20Hz.

Scans: initially anodic of E_{Rest} (0.113V).

Scan rates/mVs^{-1}: (a) 5; (b) 10; (c) 20; (d) 50.

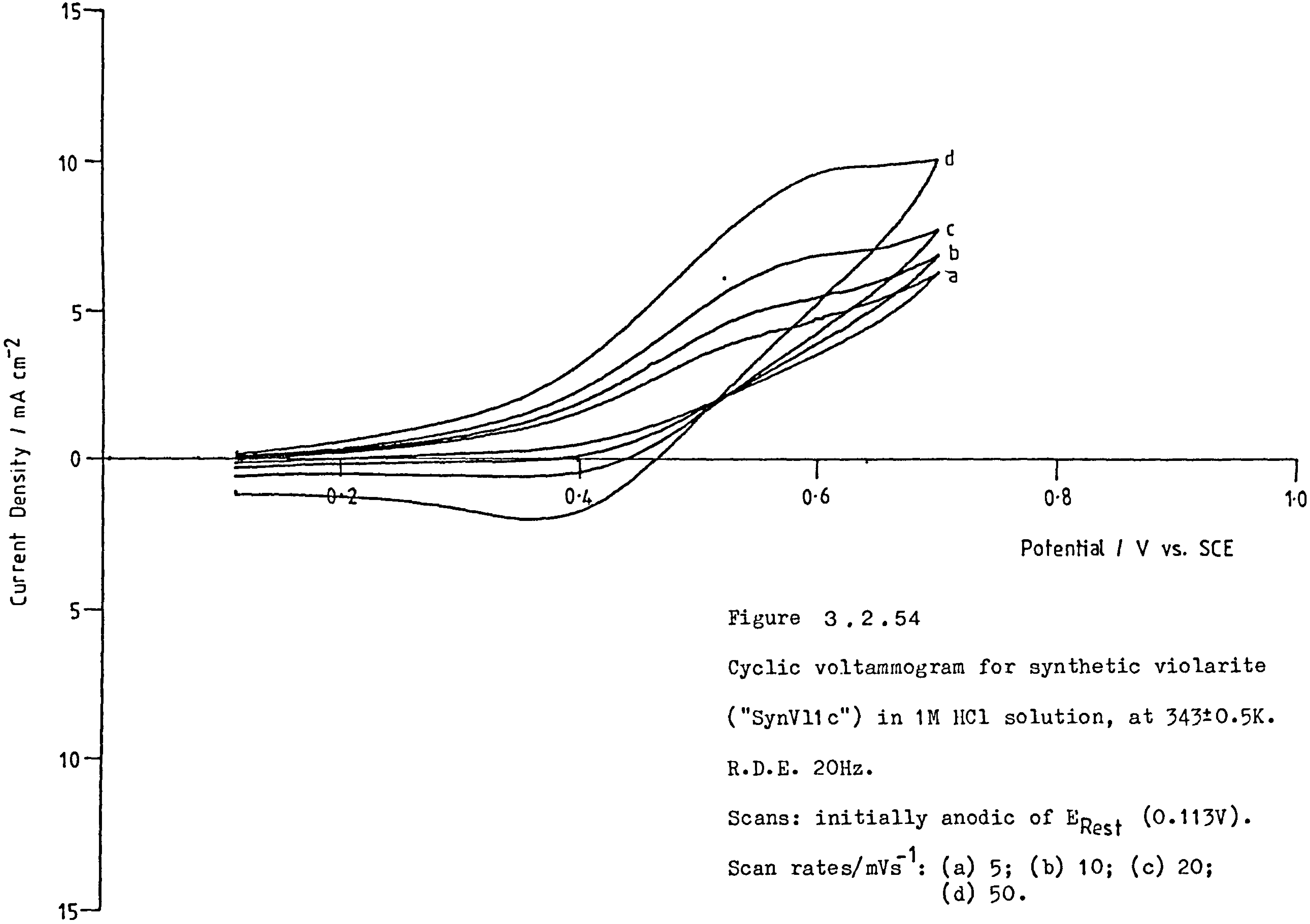

Figure 3.2.54

Cyclic voltammogram for synthetic violarite ("SynVl1c") in 1M HCl solution, at 343±0.5K.

R.D.E. 20Hz.

Scans: initially anodic of E_{Rest} (0.113V).

Scan rates/mVs^{-1}: (a) 5; (b) 10; (c) 20; (d) 50.

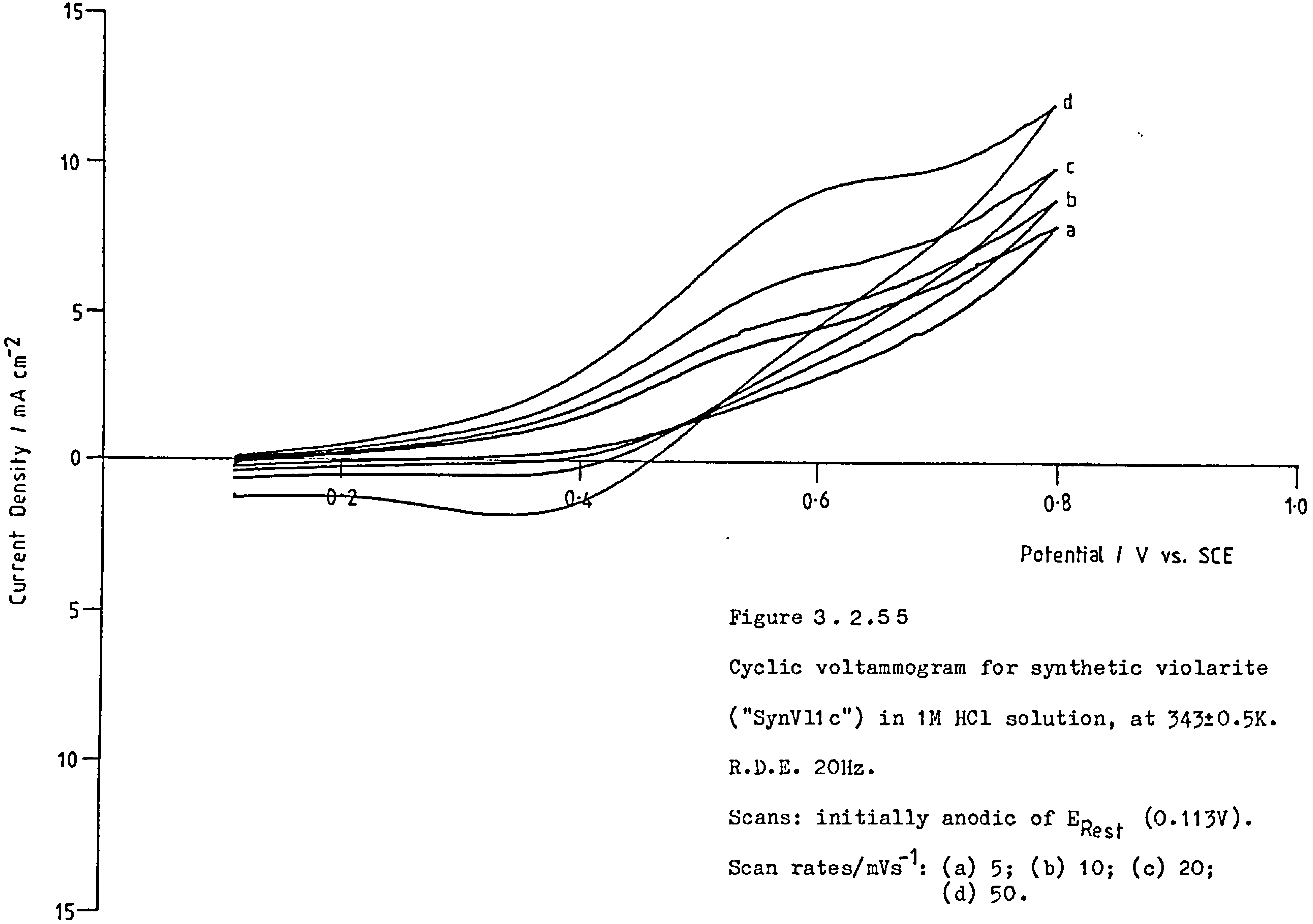

Figure 3 . 2.5 5

Cyclic voltammogram for synthetic violarite ("SynV11c") in 1M HCl solution, at 343±0.5K.

R.D.E. 20Hz.

Scans: initially anodic of E_{Rest} (0.113V).

Scan rates/mVs^{-1}: (a) 5; (b) 10; (c) 20; (d) 50.

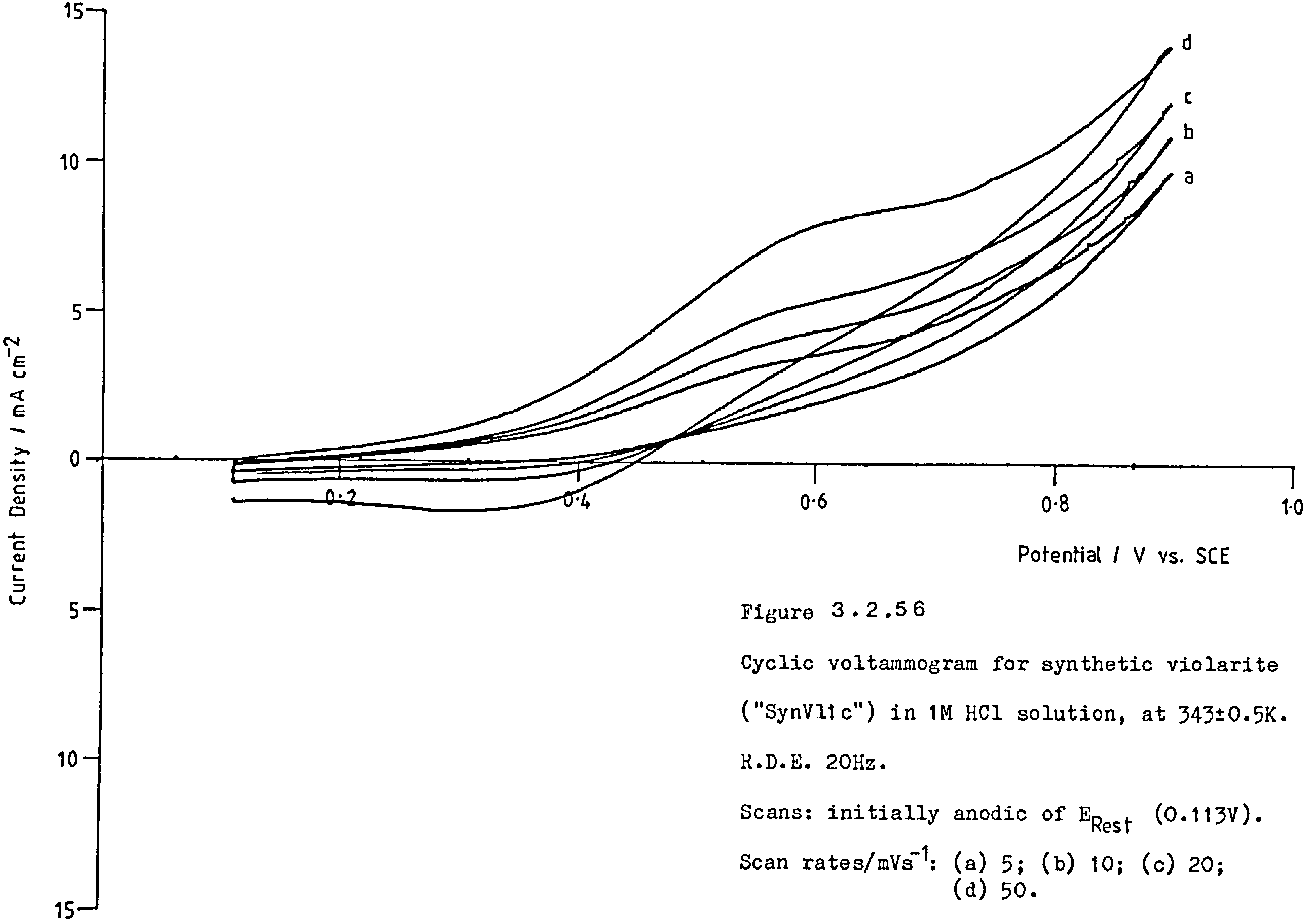

Figure 3.2.56

Cyclic voltammogram for synthetic violarite ("SynV11c") in 1M HCl solution, at 343±0.5K.

R.D.E. 20Hz.

Scans: initially anodic of E_{Rest} (0.113V).

Scan rates/mVs^{-1}: (a) 5; (b) 10; (c) 20; (d) 50.

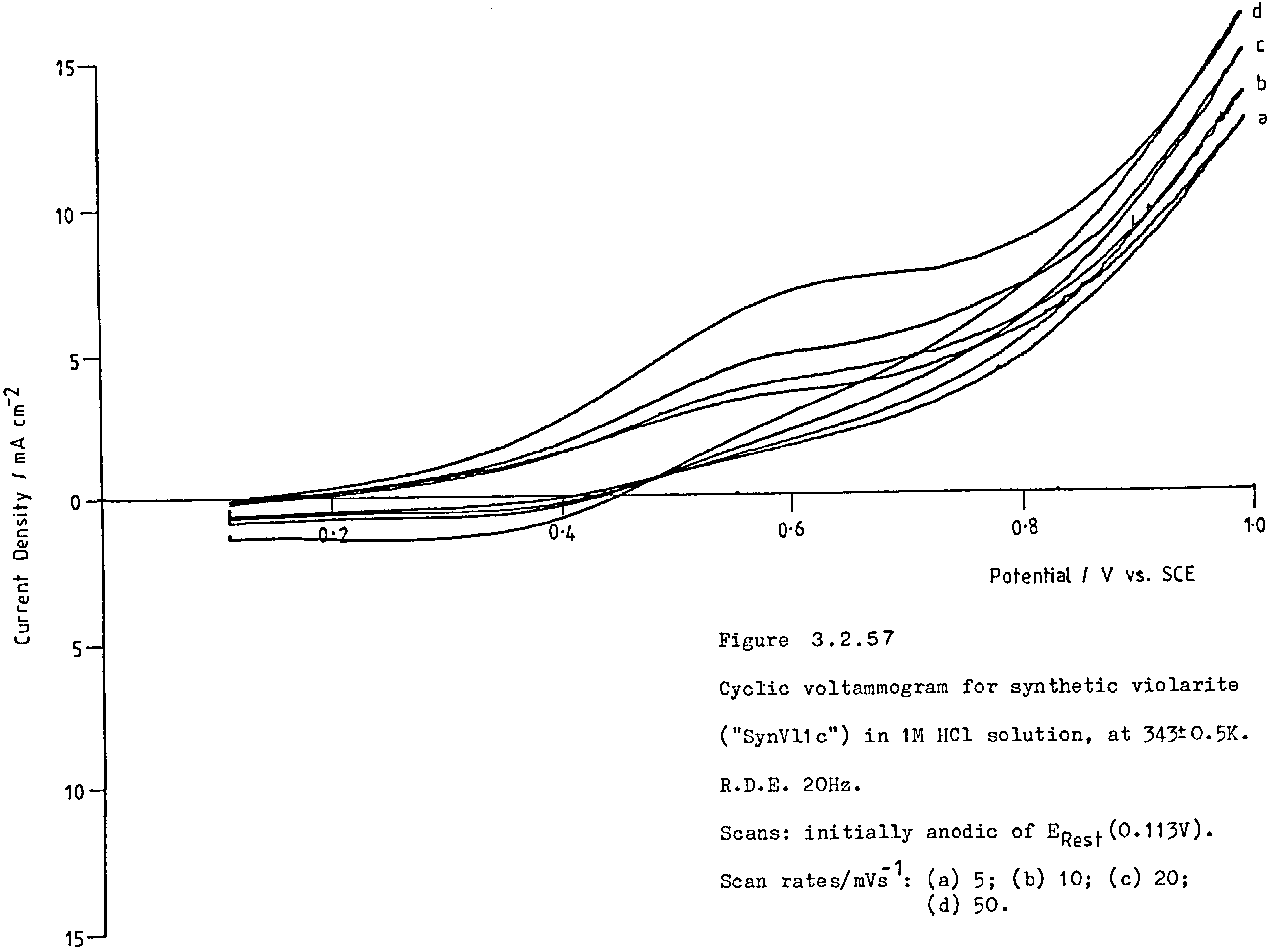

Figure 3.2.57

Cyclic voltammogram for synthetic violarite ("SynV11c") in 1M HCl solution, at 343±0.5K.

R.D.E. 20Hz.

Scans: initially anodic of E_{Rest} (0.113V).

Scan rates/mVs^{-1}: (a) 5; (b) 10; (c) 20; (d) 50.

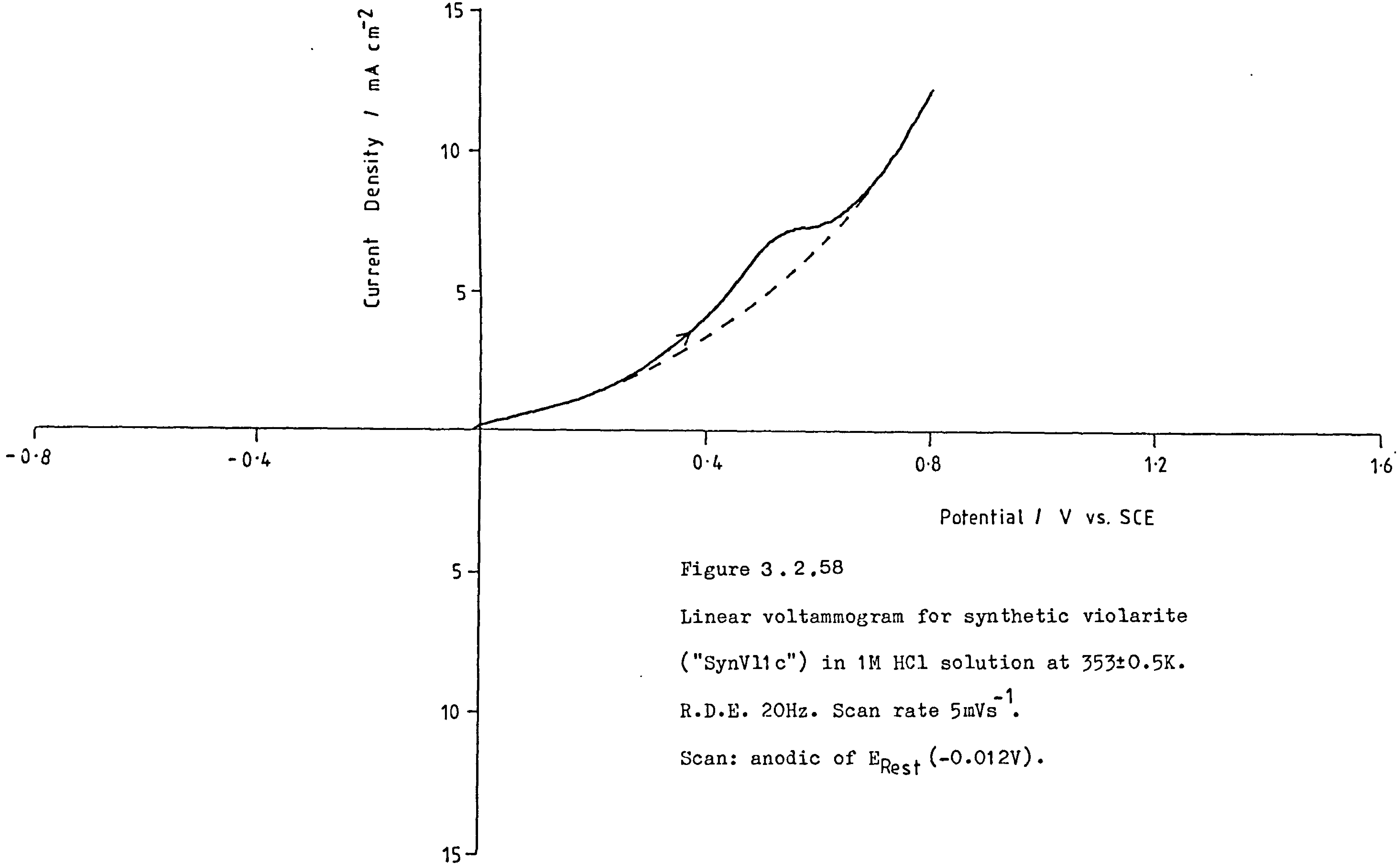

Figure 3.2.58

Linear voltammogram for synthetic violarite ("SynV11c") in 1M HCl solution at 353±0.5K.

R.D.E. 20Hz. Scan rate 5mVs^{-1}.

Scan: anodic of E_{Rest} (-0.012V).

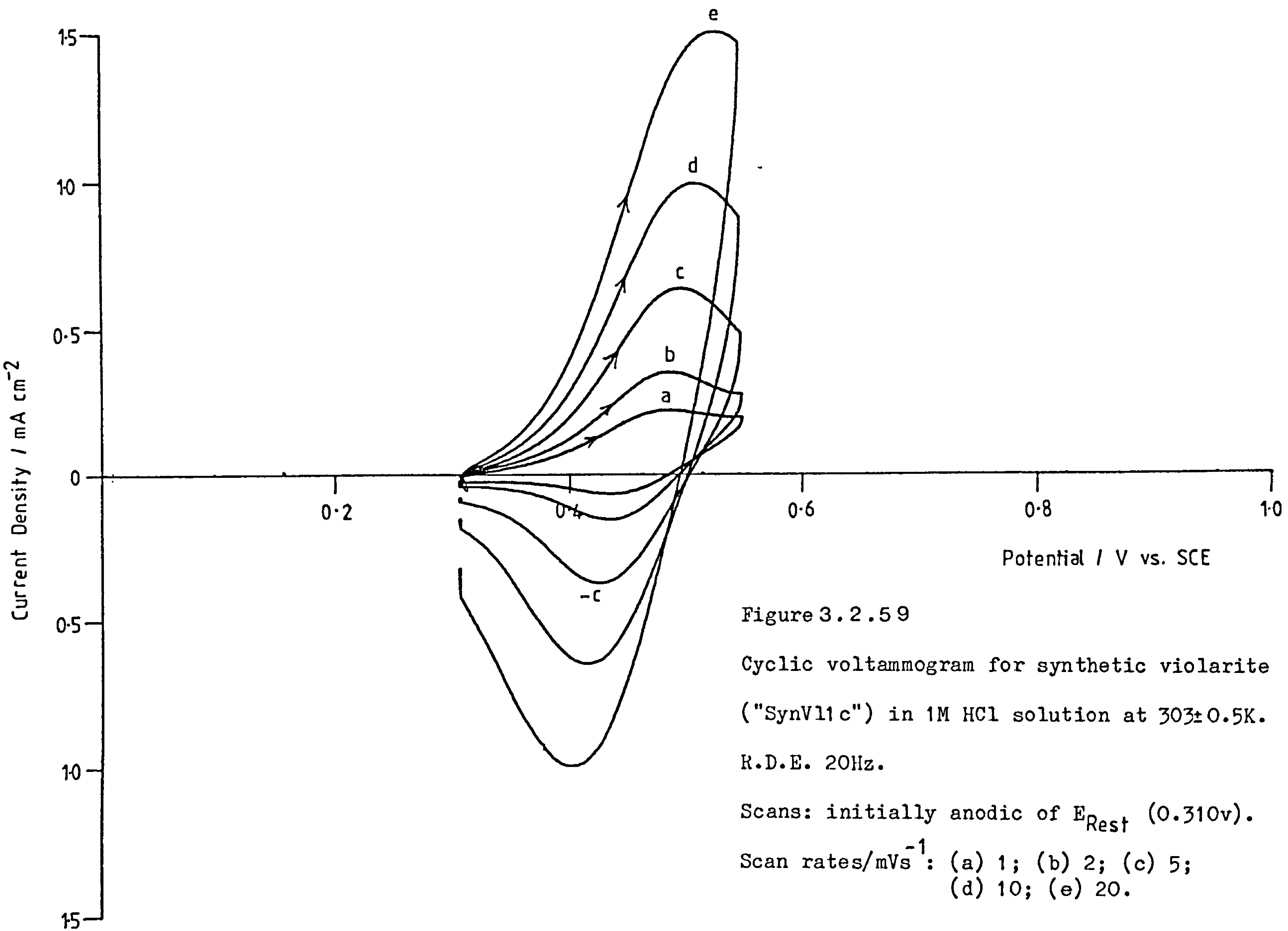

Figure 3.2.59

Cyclic voltammogram for synthetic violarite ("SynV11c") in 1M HCl solution at 303±0.5K.

R.D.E. 20Hz.

Scans: initially anodic of E_{Rest} (0.310v).

Scan rates/mVs^{-1}: (a) 1; (b) 2; (c) 5; (d) 10; (e) 20.

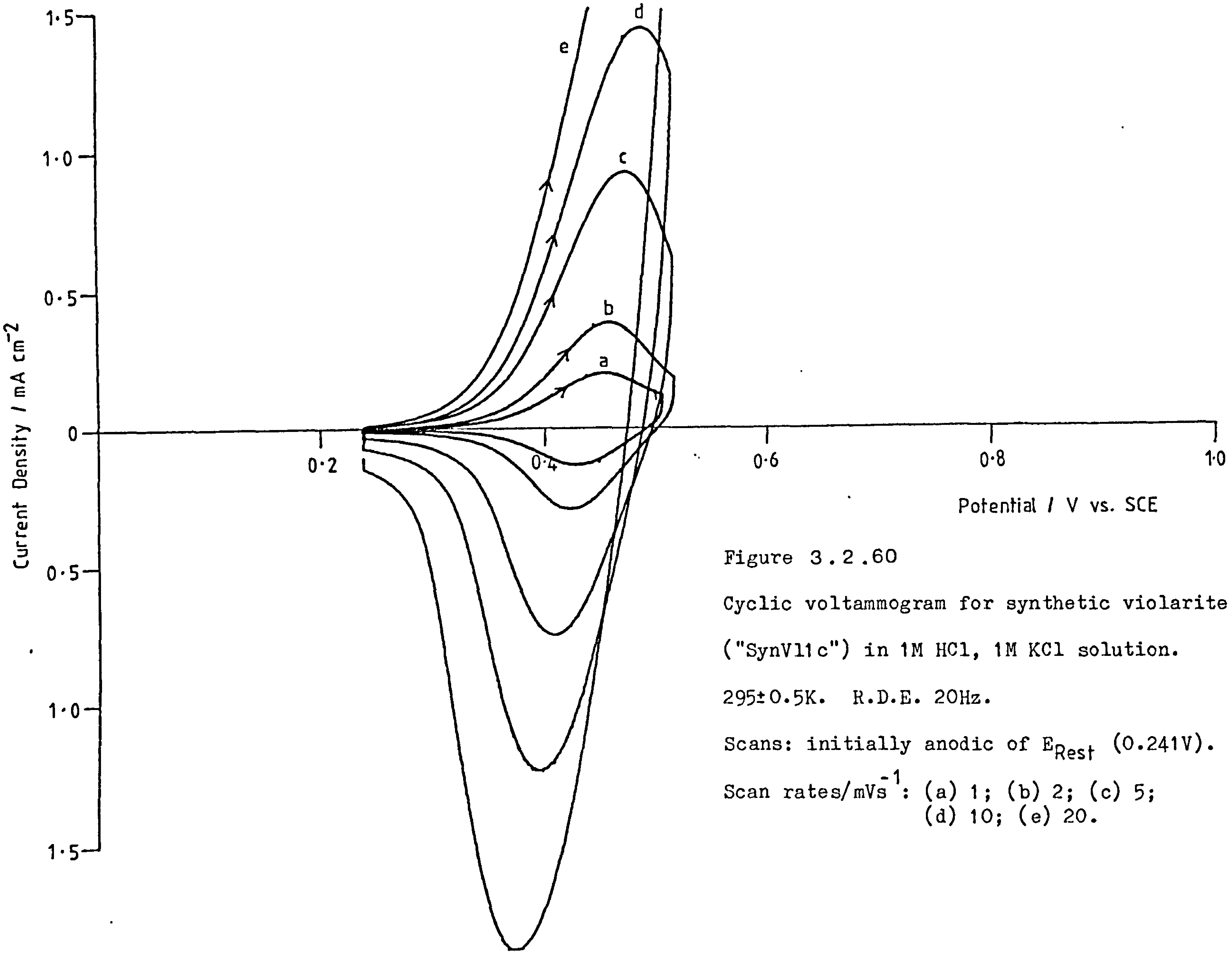

Figure 3.2.60

Cyclic voltammogram for synthetic violarite ("SynVl1c") in 1M HCl, 1M KCl solution.

295±0.5K. R.D.E. 20Hz.

Scans: initially anodic of E_{Rest} (0.241V).

Scan rates/mVs^{-1}: (a) 1; (b) 2; (c) 5; (d) 10; (e) 20.

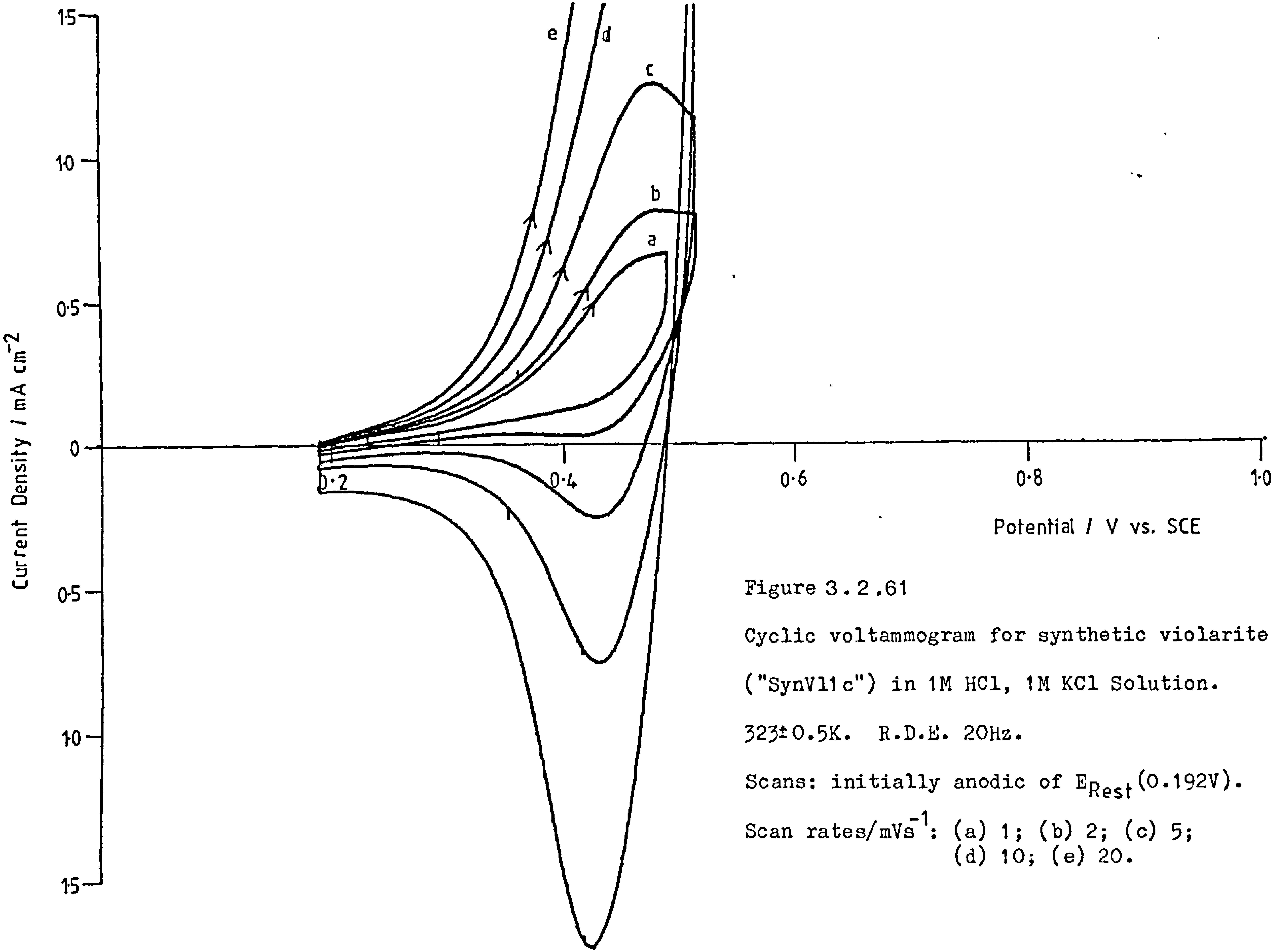

Figure 3.2.61

Cyclic voltammogram for synthetic violarite ("SynV11c") in 1M HCl, 1M KCl Solution.

323±0.5K. R.D.E. 20Hz.

Scans: initially anodic of E_{Rest}(0.192V).

Scan rates/mVs^{-1}: (a) 1; (b) 2; (c) 5; (d) 10; (e) 20.

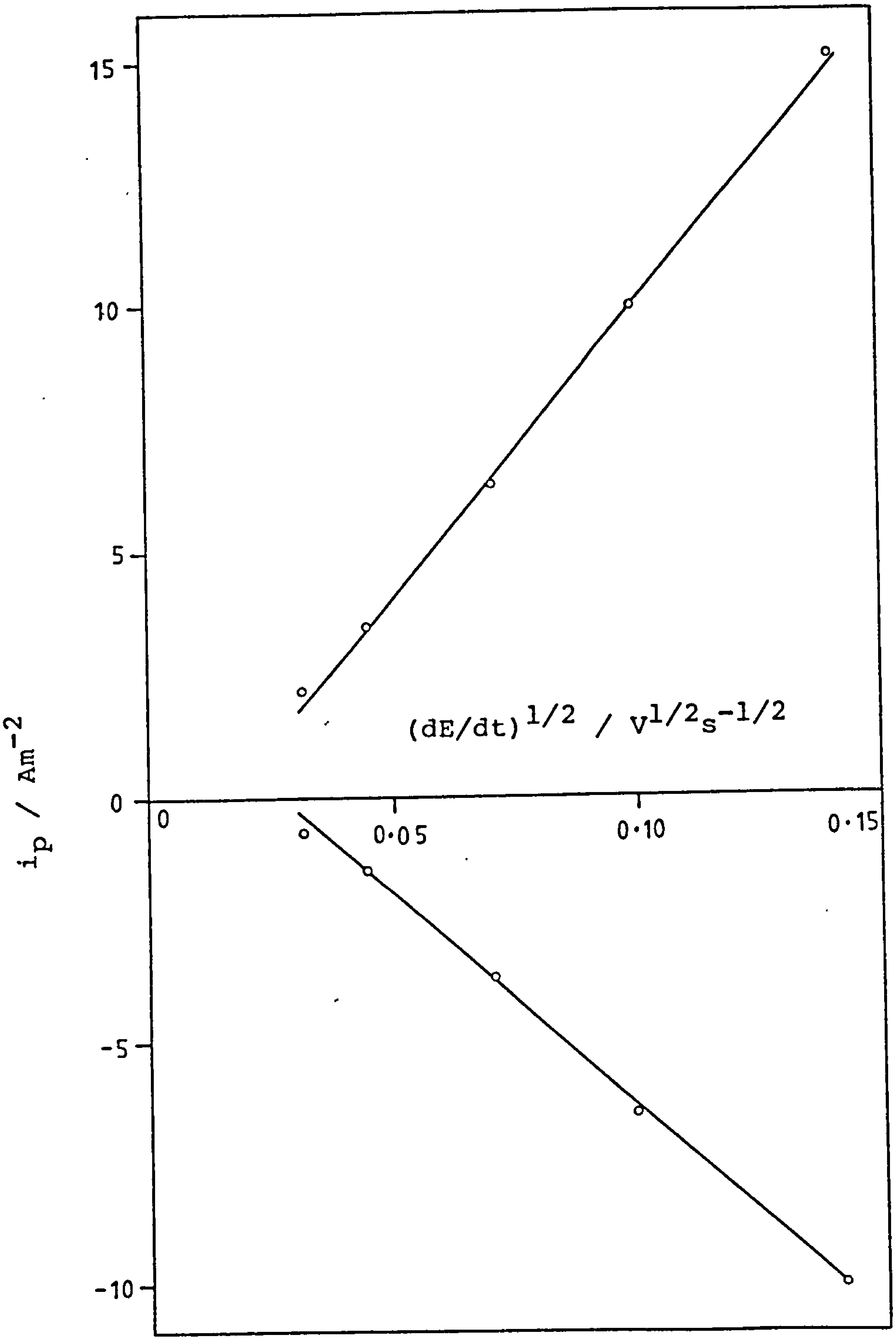

Figure 3.2.62

A plot of the dependence of the peak current density, on the square root of the potential scan rate, for the results obtained from cyclic voltammetry on violarite in Figure 3.2.59 (i.e. a test for fast electron transfer).

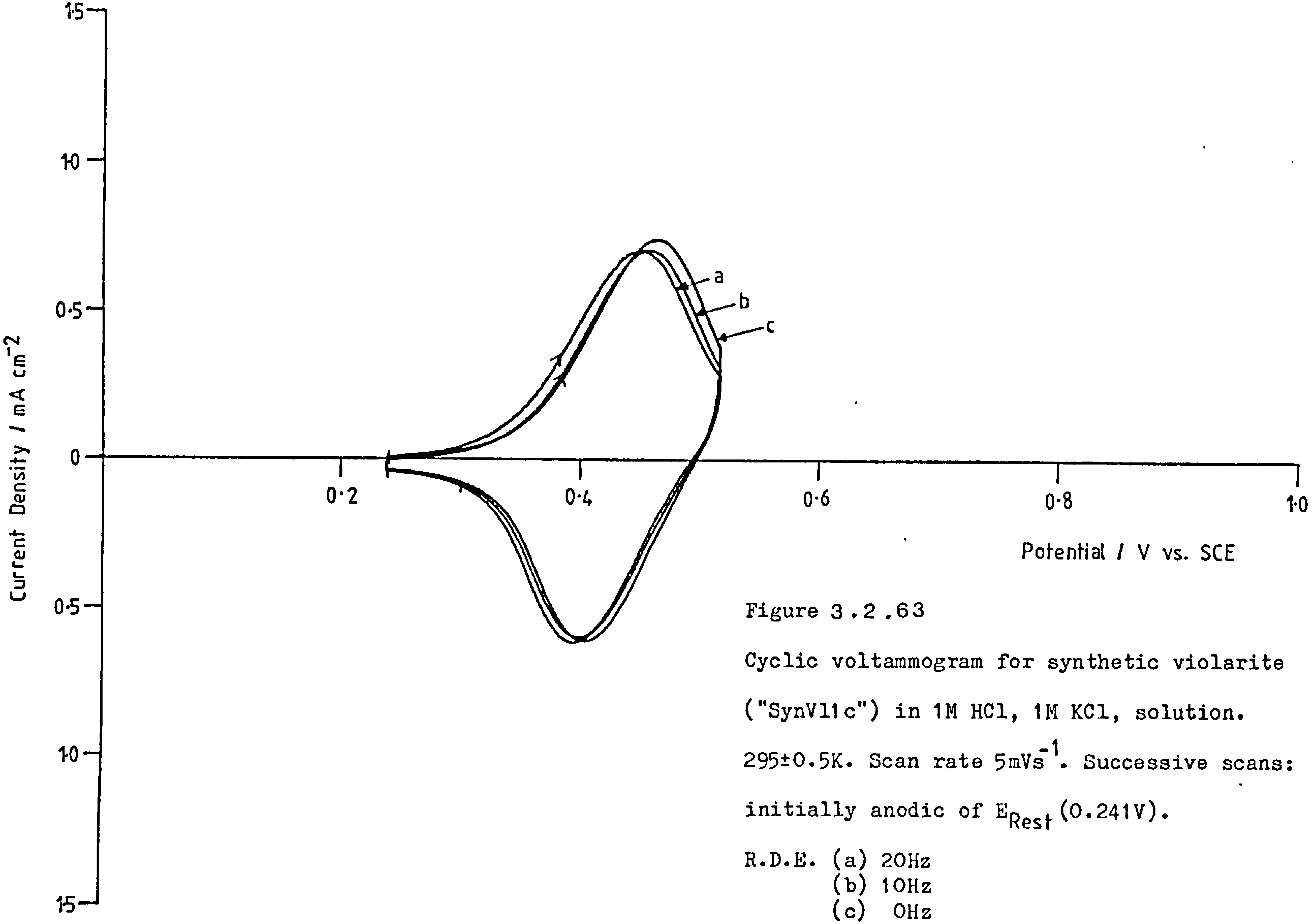

Figure 3.2.63

Cyclic voltammogram for synthetic violarite ("SynVl1c") in 1M HCl, 1M KCl, solution. 295±0.5K. Scan rate 5mVs^{-1}. Successive scans: initially anodic of E_{Rest} (0.241V).

R.D.E. (a) 20Hz
(b) 10Hz
(c) 0Hz

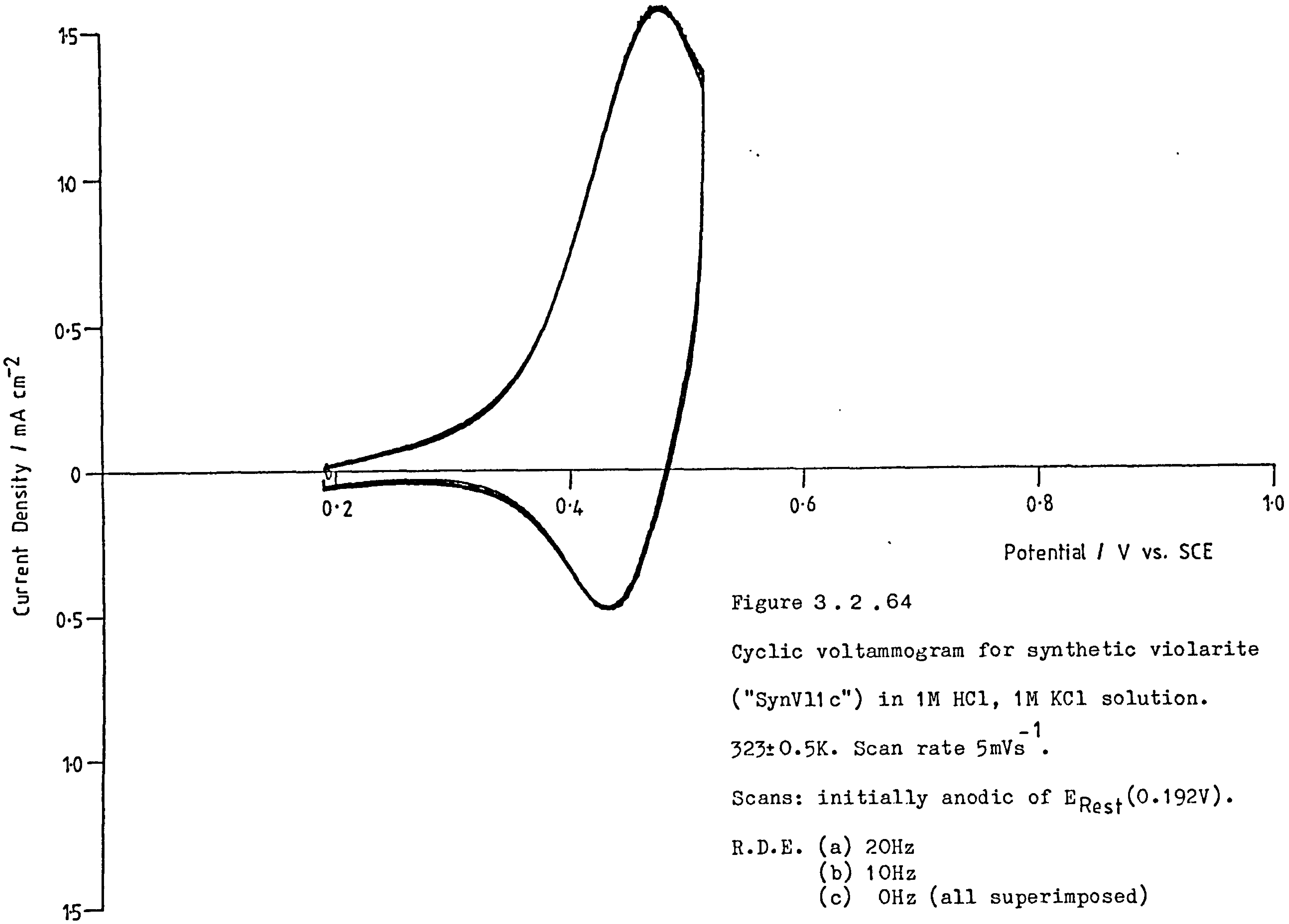

Figure 3 . 2 . 64

Cyclic voltammogram for synthetic violarite ("SynV11c") in 1M HCl, 1M KCl solution.

323±0.5K. Scan rate 5mVs^{-1}.

Scans: initially anodic of E_{Rest}(0.192V).

R.D.E. (a) 20Hz
(b) 10Hz
(c) 0Hz (all superimposed)

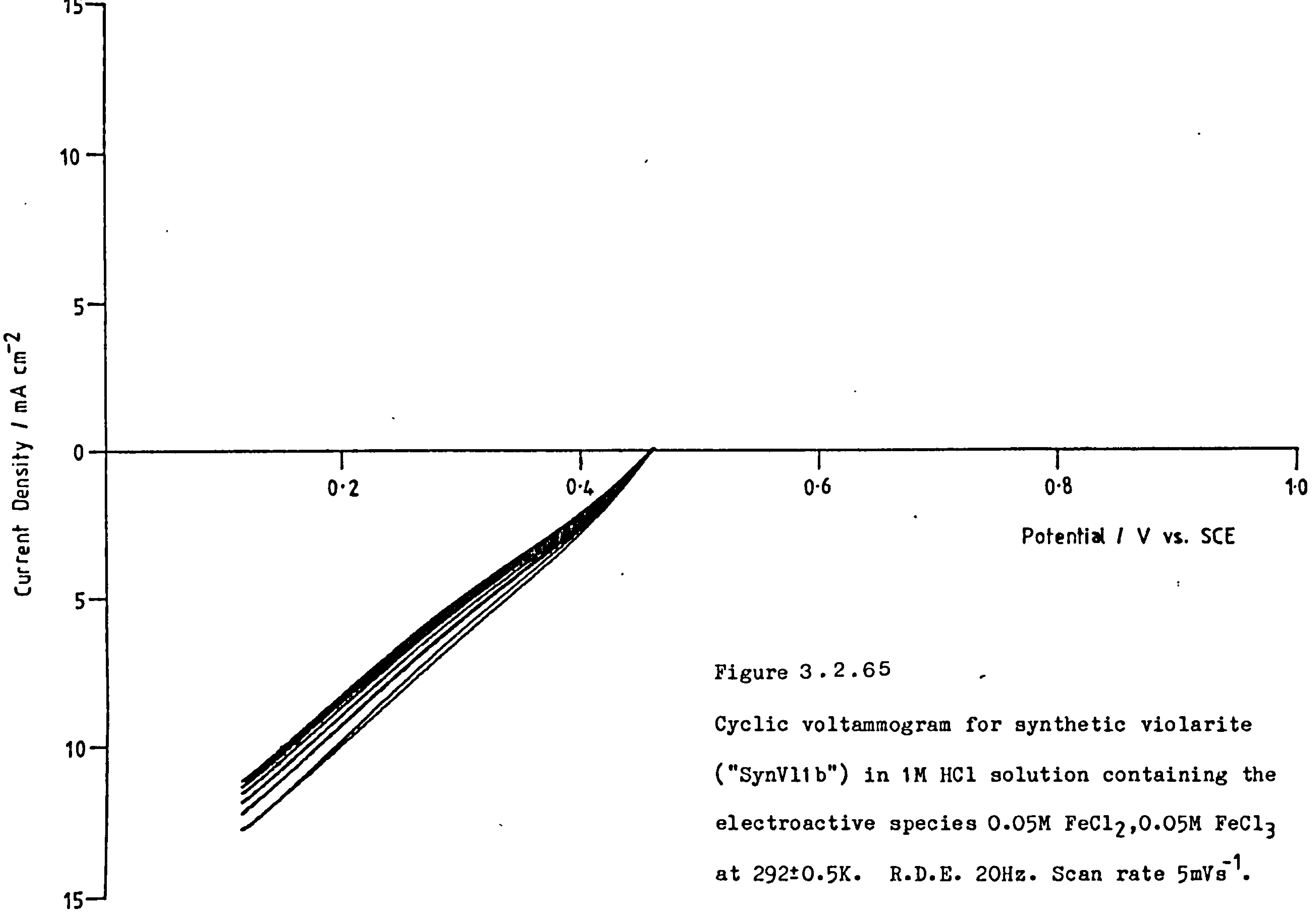

Figure 3.2.65

Cyclic voltammogram for synthetic violarite ("SynV11b") in 1M HCl solution containing the electroactive species 0.05M $FeCl_2$,0.05M $FeCl_3$ at 292±0.5K. R.D.E. 20Hz. Scan rate $5mVs^{-1}$. Successive scans: cathodic of E_{Rest} (0.450V).

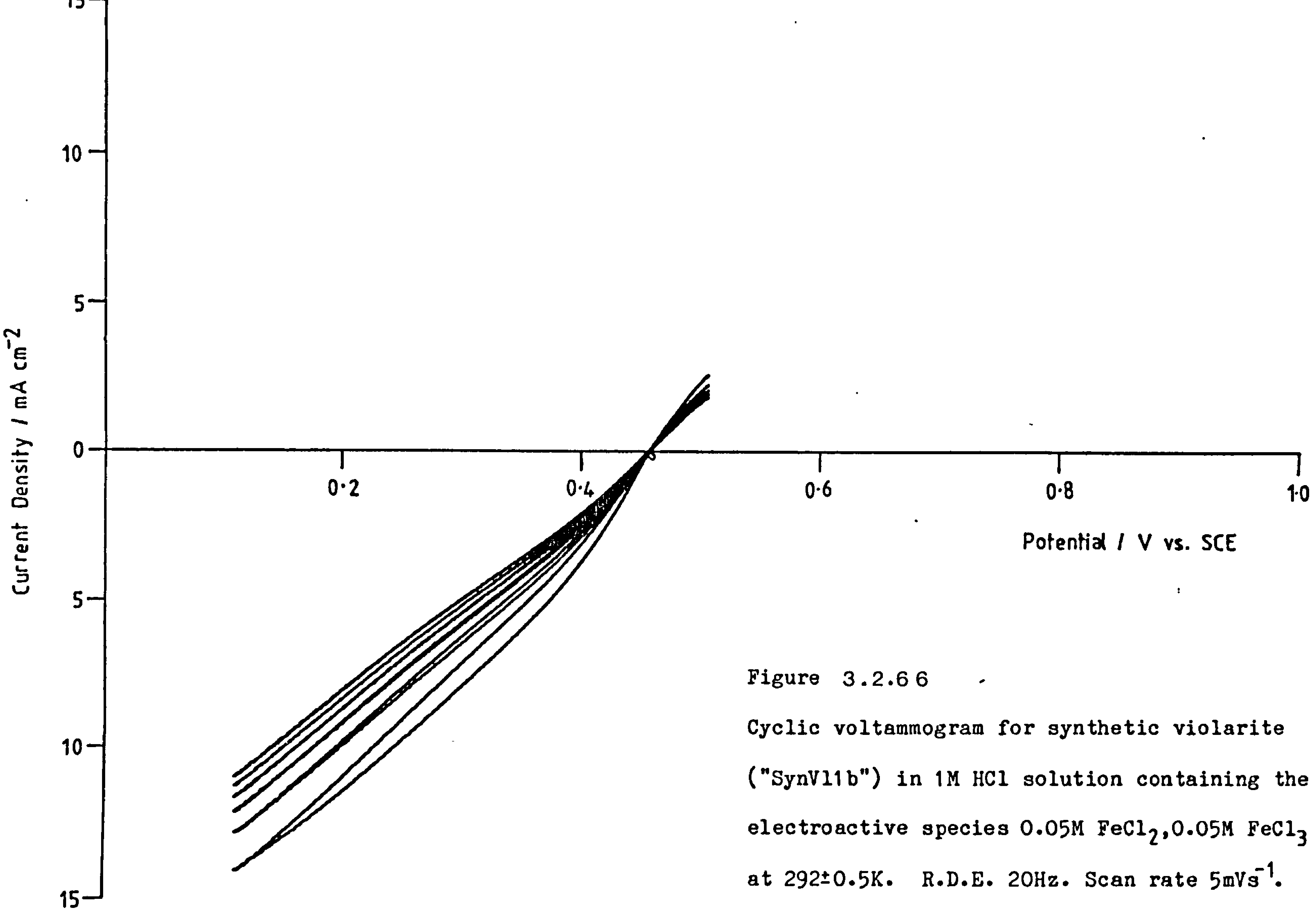

Figure 3.2.66

Cyclic voltammogram for synthetic violarite ("SynV11b") in 1M HCl solution containing the electroactive species 0.05M $FeCl_2$,0.05M $FeCl_3$ at 292±0.5K. R.D.E. 20Hz. Scan rate $5mVs^{-1}$. Successive scans: initially cathodic of E_{Rest} (0.450V) followed by anodic excursions.

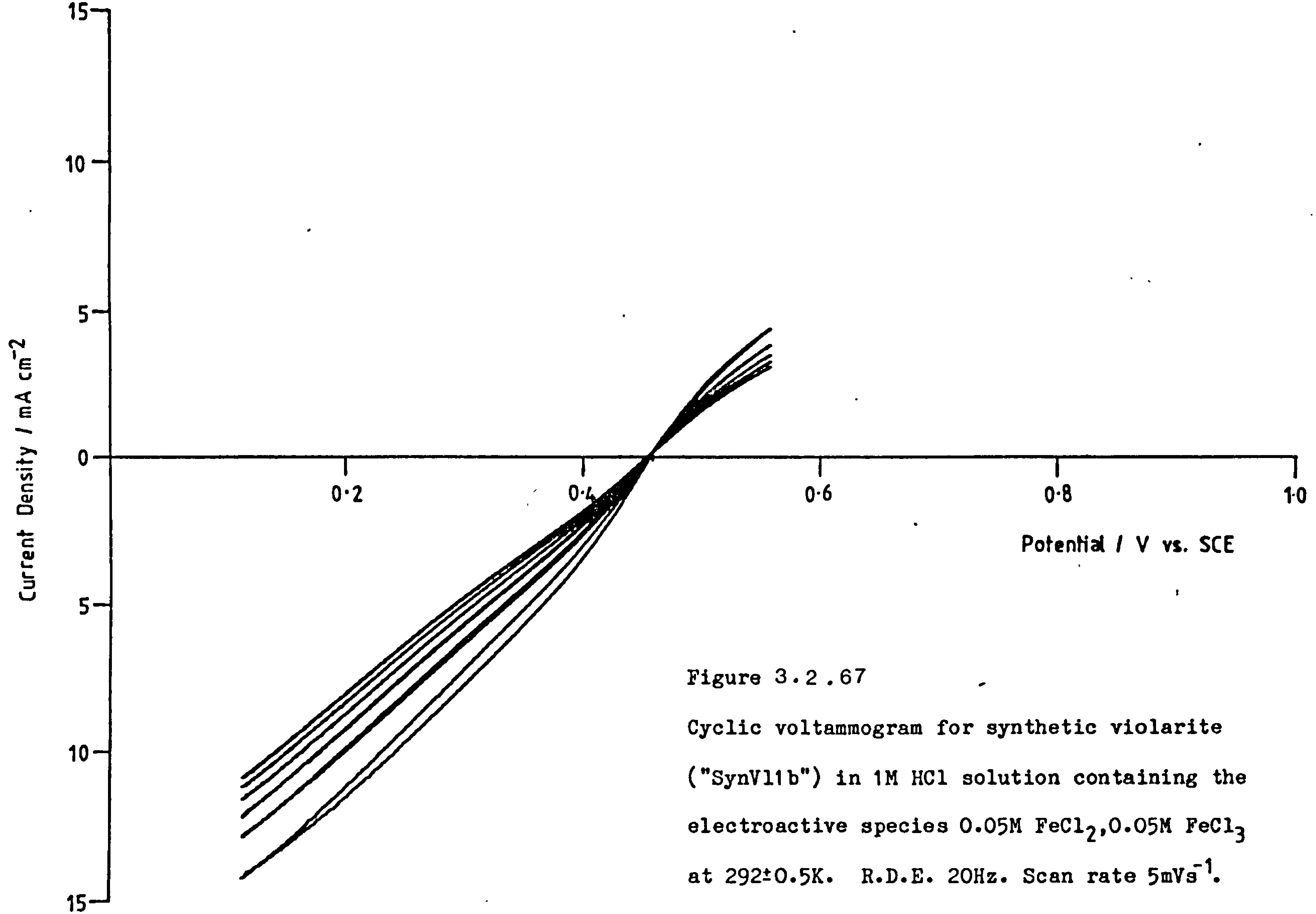

Figure 3.2.67

Cyclic voltammogram for synthetic violarite ("SynV11b") in 1M HCl solution containing the electroactive species 0.05M $FeCl_2$,0.05M $FeCl_3$ at 292±0.5K. R.D.E. 20Hz. Scan rate $5mVs^{-1}$. Successive scans: initially cathodic of E_{Rest} (0.450V) followed by anodic excursions.

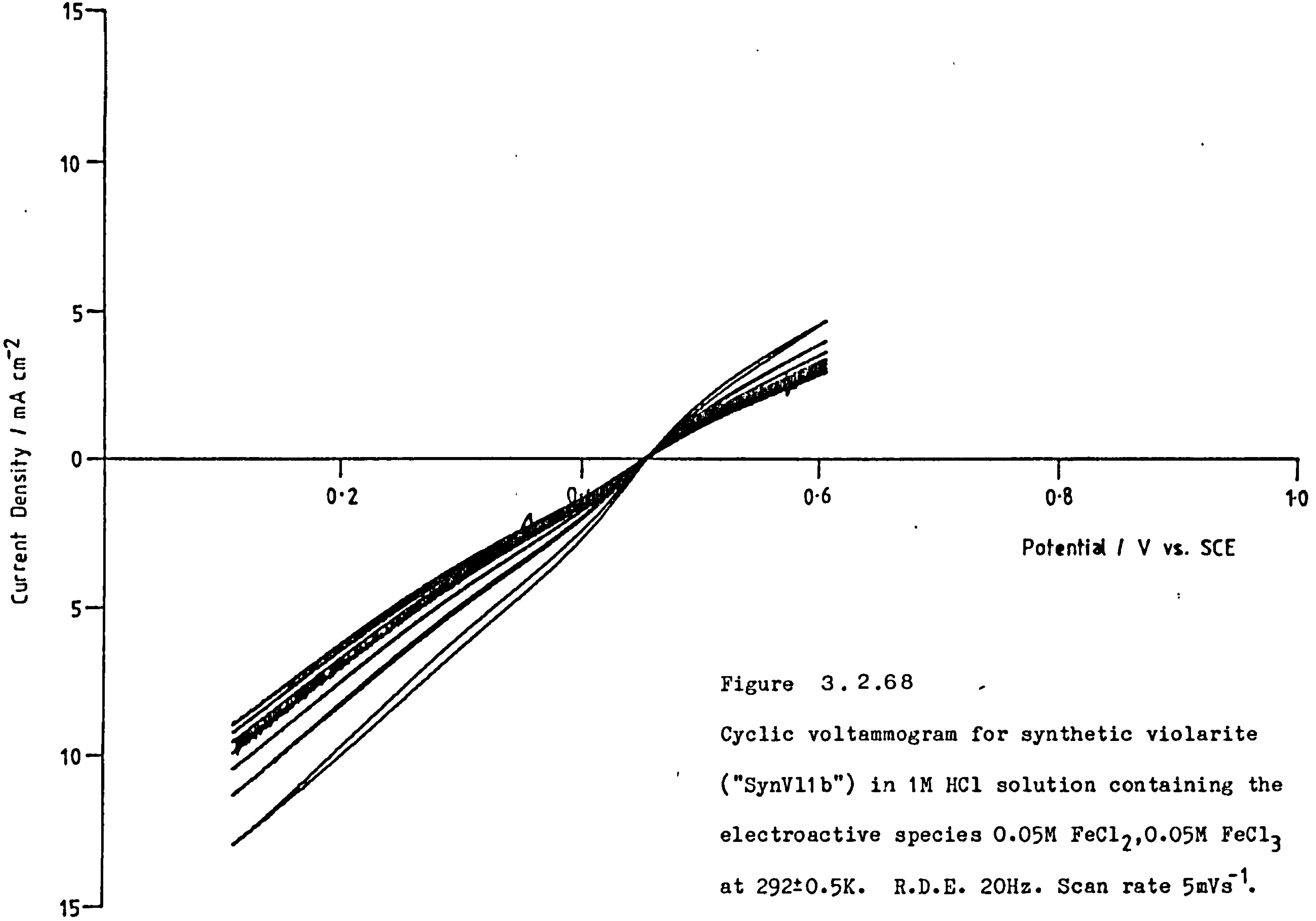

Figure 3.2.68

Cyclic voltammogram for synthetic violarite ("SynV11b") in 1M HCl solution containing the electroactive species 0.05M $FeCl_2$,0.05M $FeCl_3$ at 292±0.5K. R.D.E. 20Hz. Scan rate $5mVs^{-1}$. Successive scans: initially cathodic of E_{Rest} (0.450V) followed by anodic excursions.

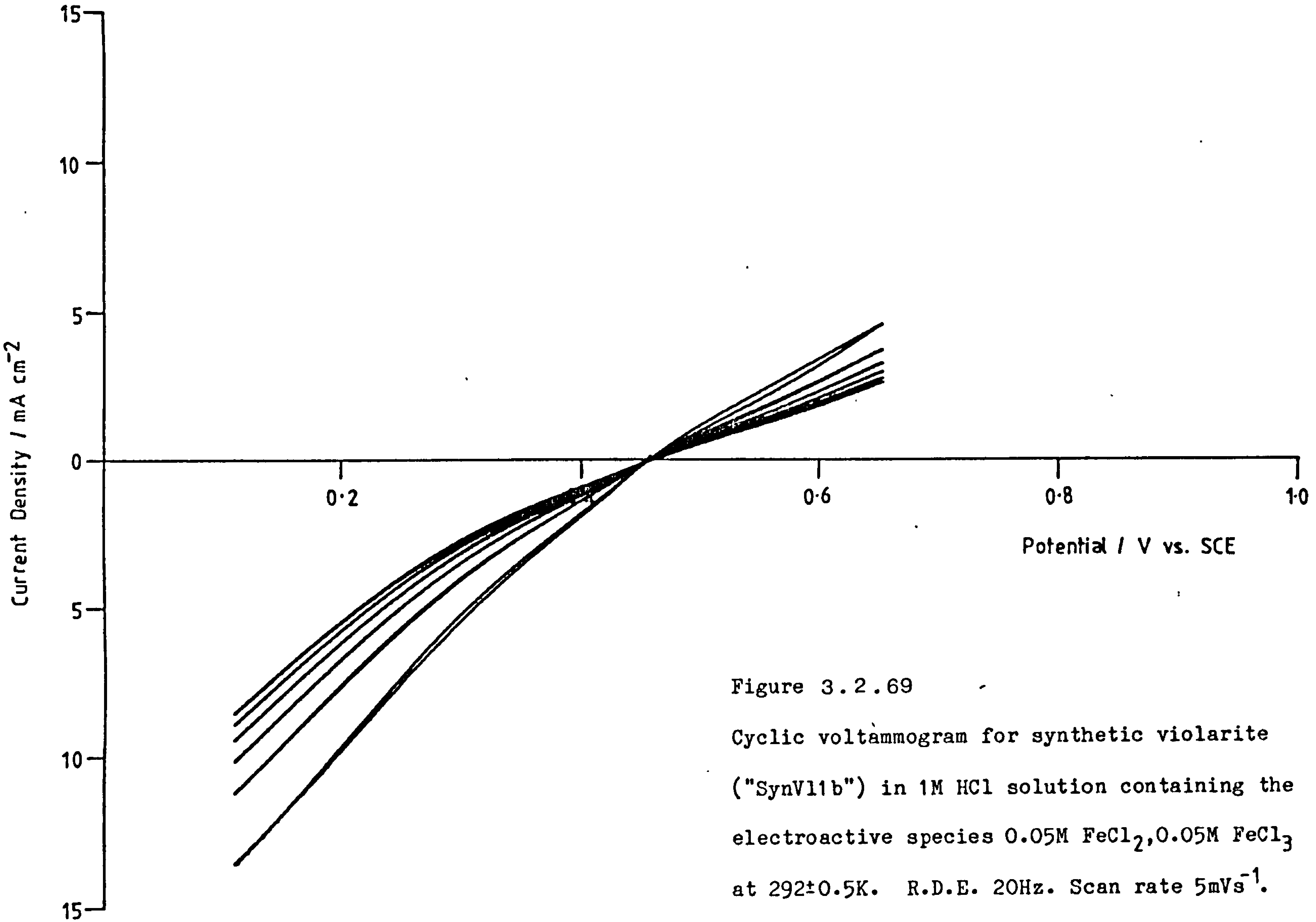

Figure 3.2.69

Cyclic voltammogram for synthetic violarite ("SynV11b") in 1M HCl solution containing the electroactive species 0.05M $FeCl_2$,0.05M $FeCl_3$ at 292±0.5K. R.D.E. 20Hz. Scan rate $5mVs^{-1}$. Successive scans: initially cathodic of E_{Rest} (0.450V) followed by anodic excursions.

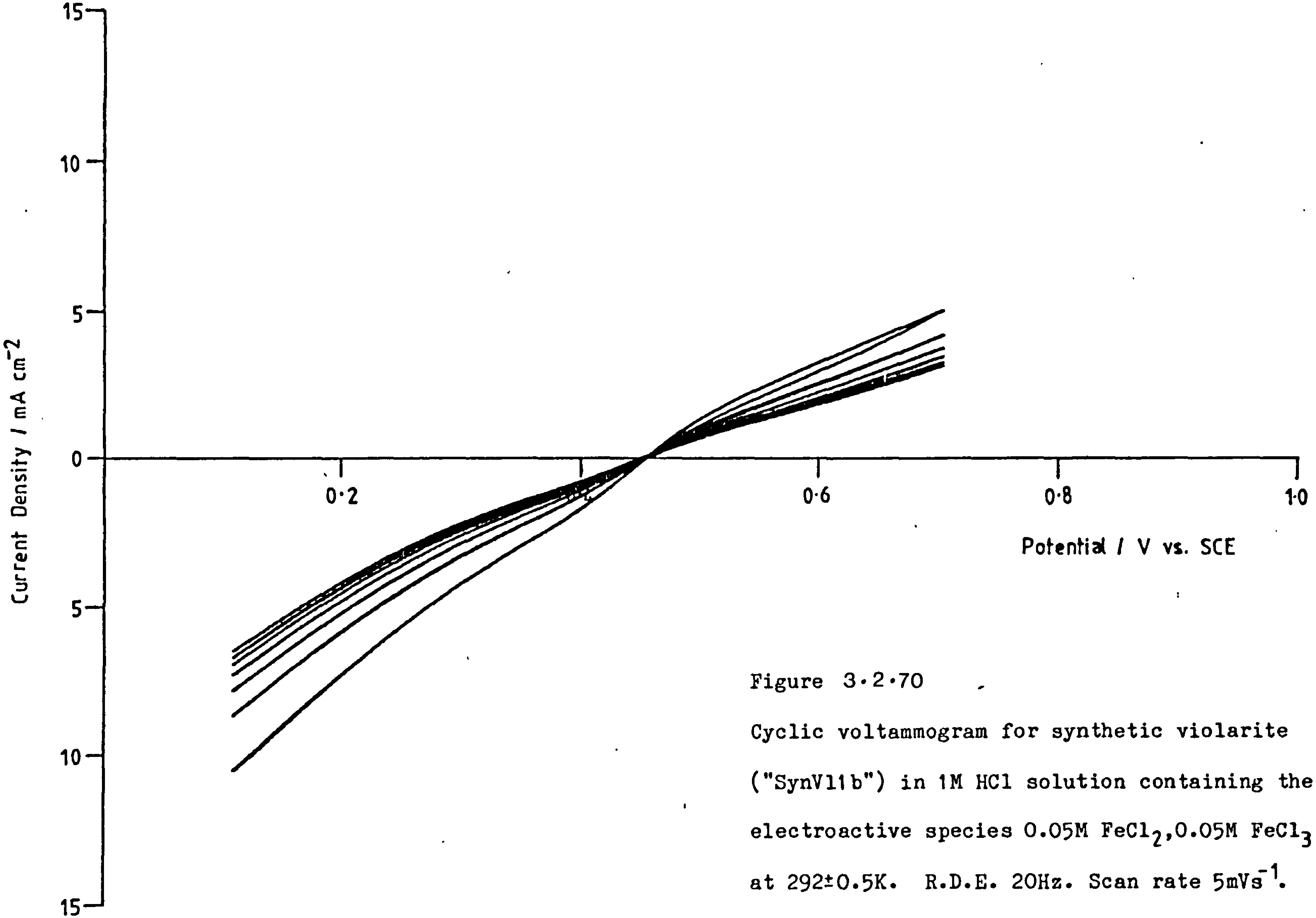

Figure 3·2·70

Cyclic voltammogram for synthetic violarite ("SynV11b") in 1M HCl solution containing the electroactive species 0.05M $FeCl_2$,0.05M $FeCl_3$ at 292±0.5K. R.D.E. 20Hz. Scan rate $5mVs^{-1}$. Successive scans: initially cathodic of E_{Rest} (0.450V) followed by anodic excursions.

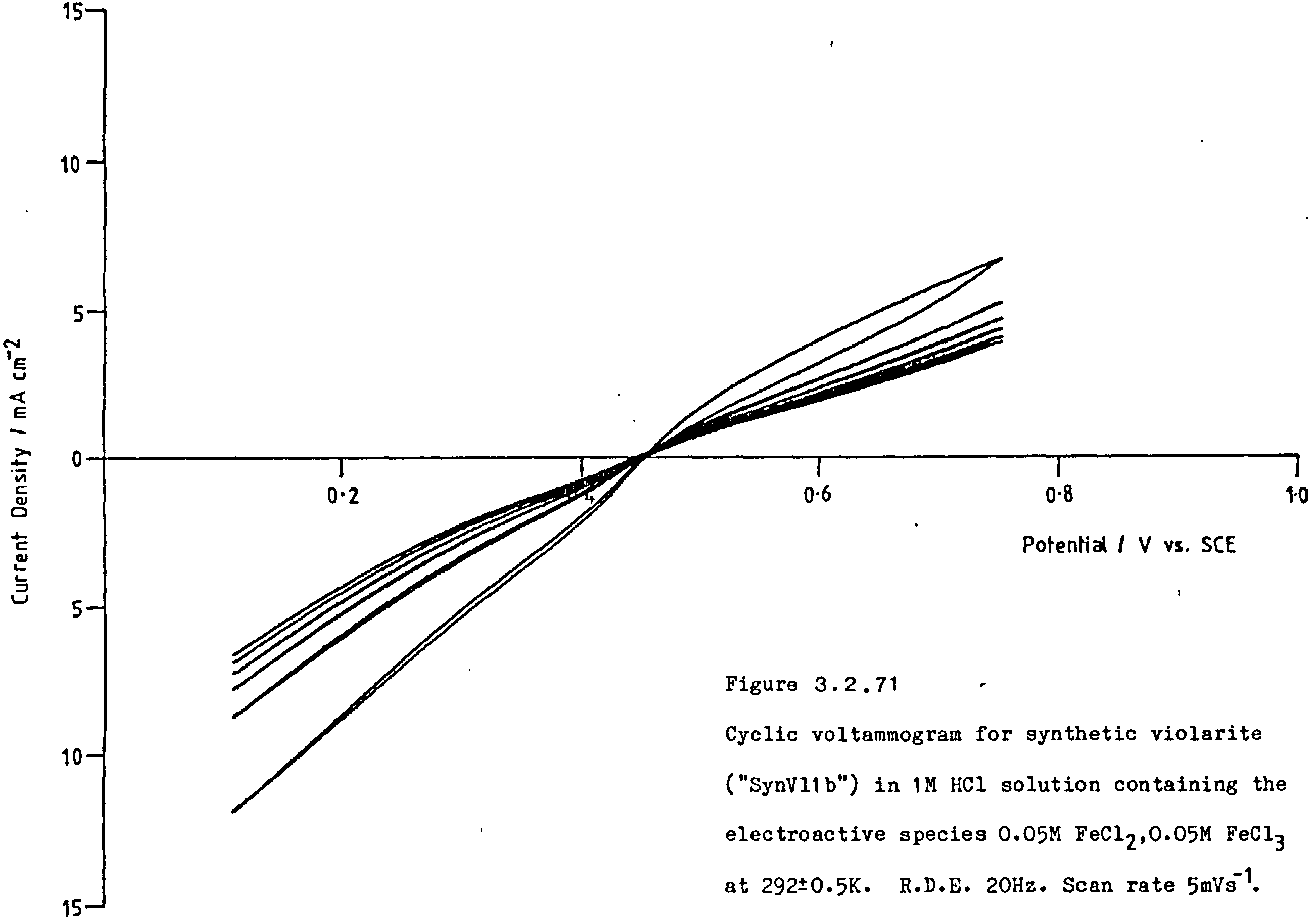

Figure 3.2.71

Cyclic voltammogram for synthetic violarite ("SynV11b") in 1M HCl solution containing the electroactive species 0.05M $FeCl_2$,0.05M $FeCl_3$ at 292±0.5K. R.D.E. 20Hz. Scan rate $5mVs^{-1}$. Successive scans: initially cathodic of E_{Rest} (0.450V) followed by anodic excursions.

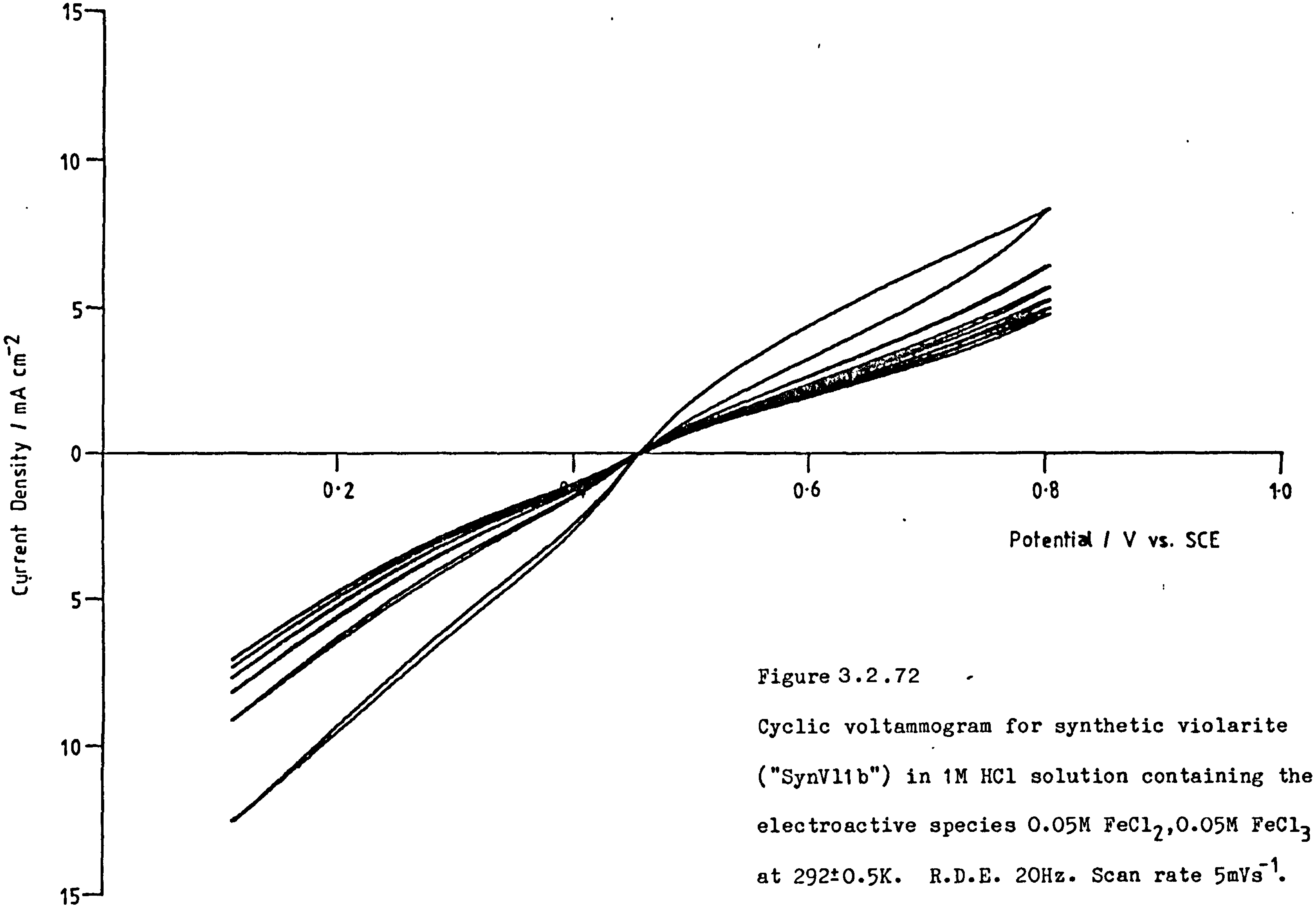

Figure 3.2.72

Cyclic voltammogram for synthetic violarite ("SynV11b") in 1M HCl solution containing the electroactive species 0.05M $FeCl_2$,0.05M $FeCl_3$ at 292±0.5K. R.D.E. 20Hz. Scan rate $5mVs^{-1}$. Successive scans: initially cathodic of E_{Rest} (0.450V) followed by anodic excursions.

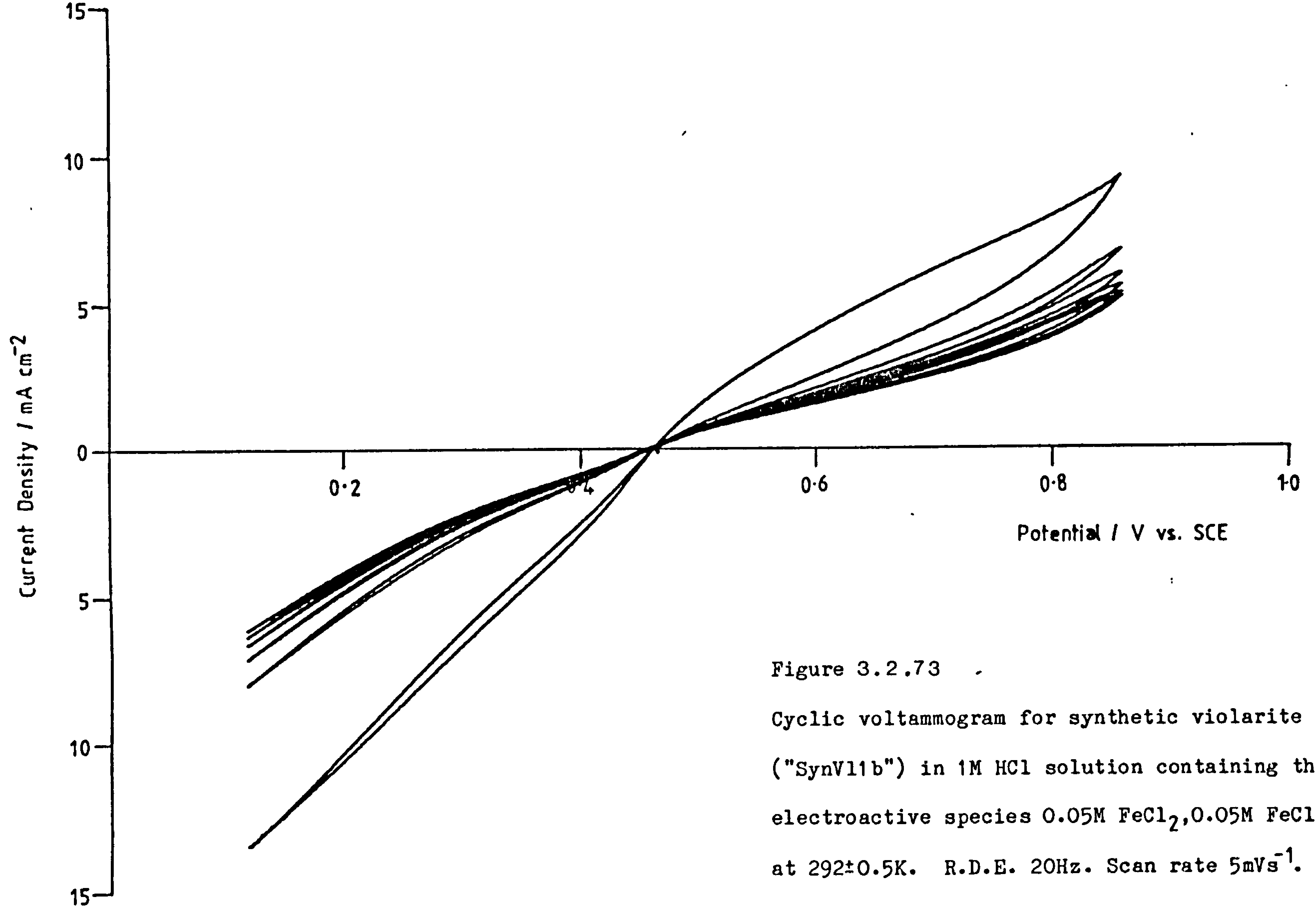

Figure 3.2.73

Cyclic voltammogram for synthetic violarite ("SynV11b") in 1M HCl solution containing the electroactive species 0.05M $FeCl_2$,0.05M $FeCl_3$ at 292±0.5K. R.D.E. 20Hz. Scan rate $5mVs^{-1}$. Successive scans: initially cathodic of E_{Rest} (0.450V) followed by anodic excursions.

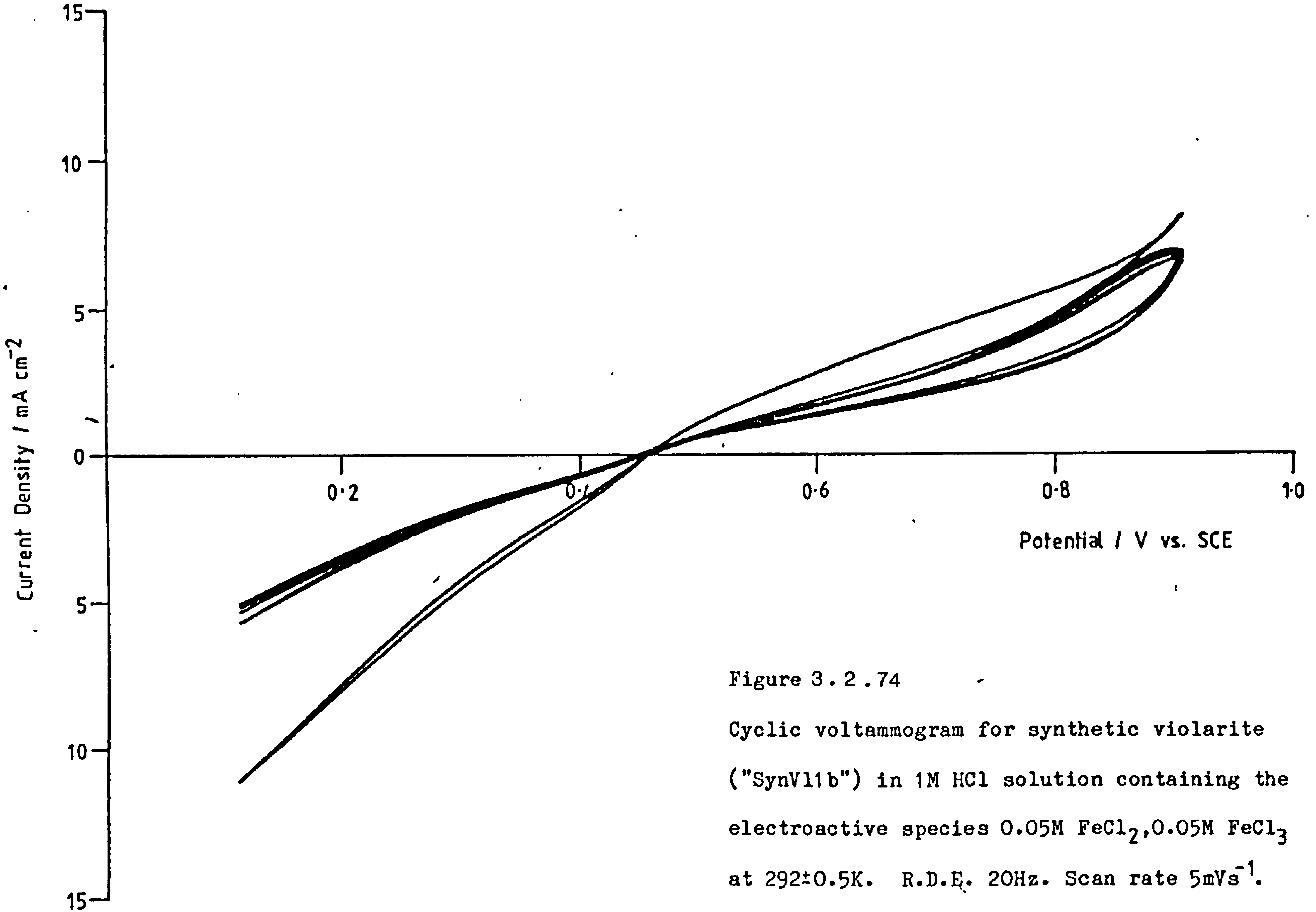

Figure 3.2.74

Cyclic voltammogram for synthetic violarite ("SynV11b") in 1M HCl solution containing the electroactive species 0.05M $FeCl_2$,0.05M $FeCl_3$ at 292±0.5K. R.D.E. 20Hz. Scan rate $5mVs^{-1}$. Successive scans: initially cathodic of E_{Rest} (0.450V) followed by anodic excursions.

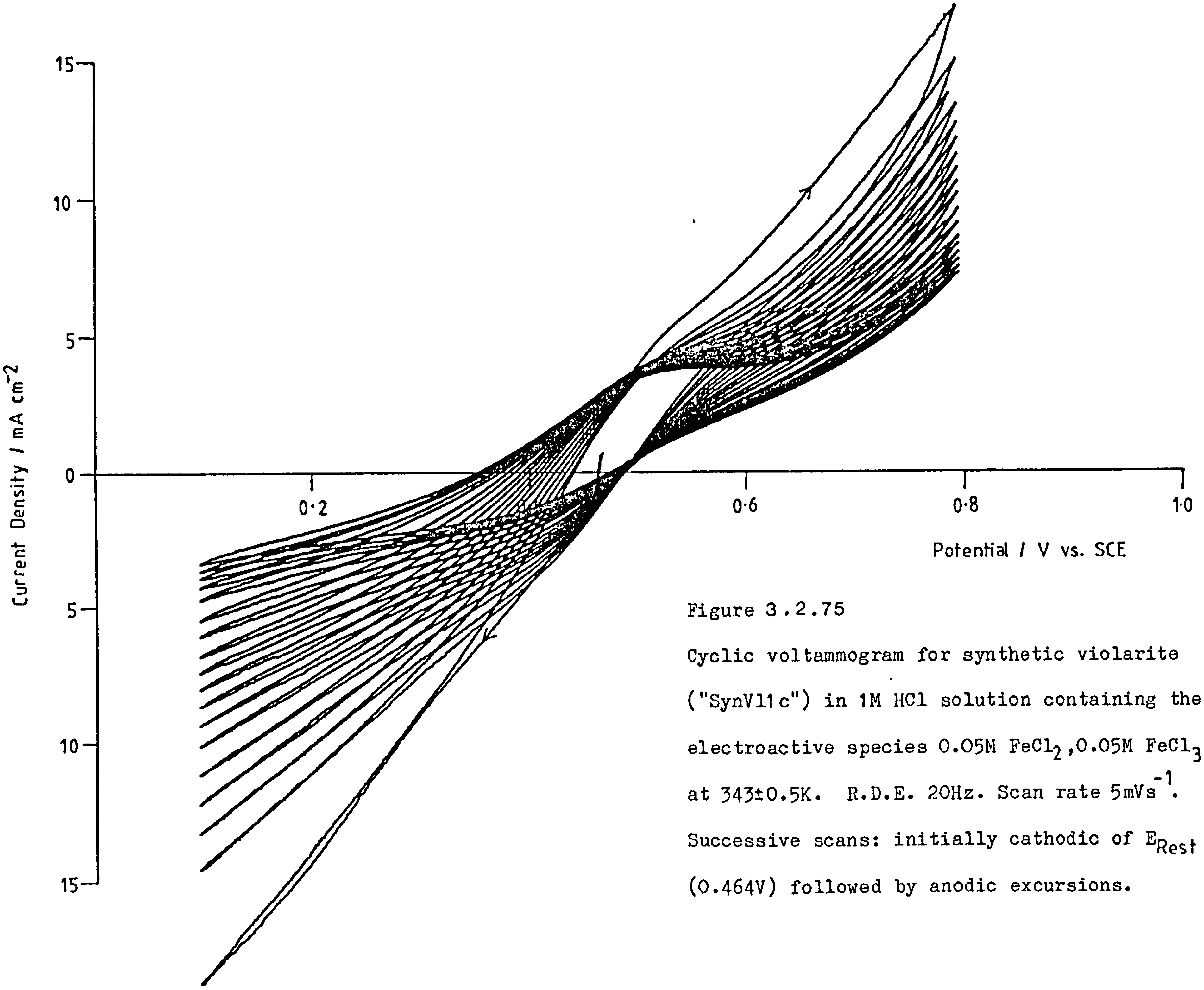

Figure 3.2.75

Cyclic voltammogram for synthetic violarite ("SynV11c") in 1M HCl solution containing the electroactive species 0.05M $FeCl_2$, 0.05M $FeCl_3$ at 343±0.5K. R.D.E. 20Hz. Scan rate $5 mVs^{-1}$. Successive scans: initially cathodic of E_{Rest} (0.464V) followed by anodic excursions.

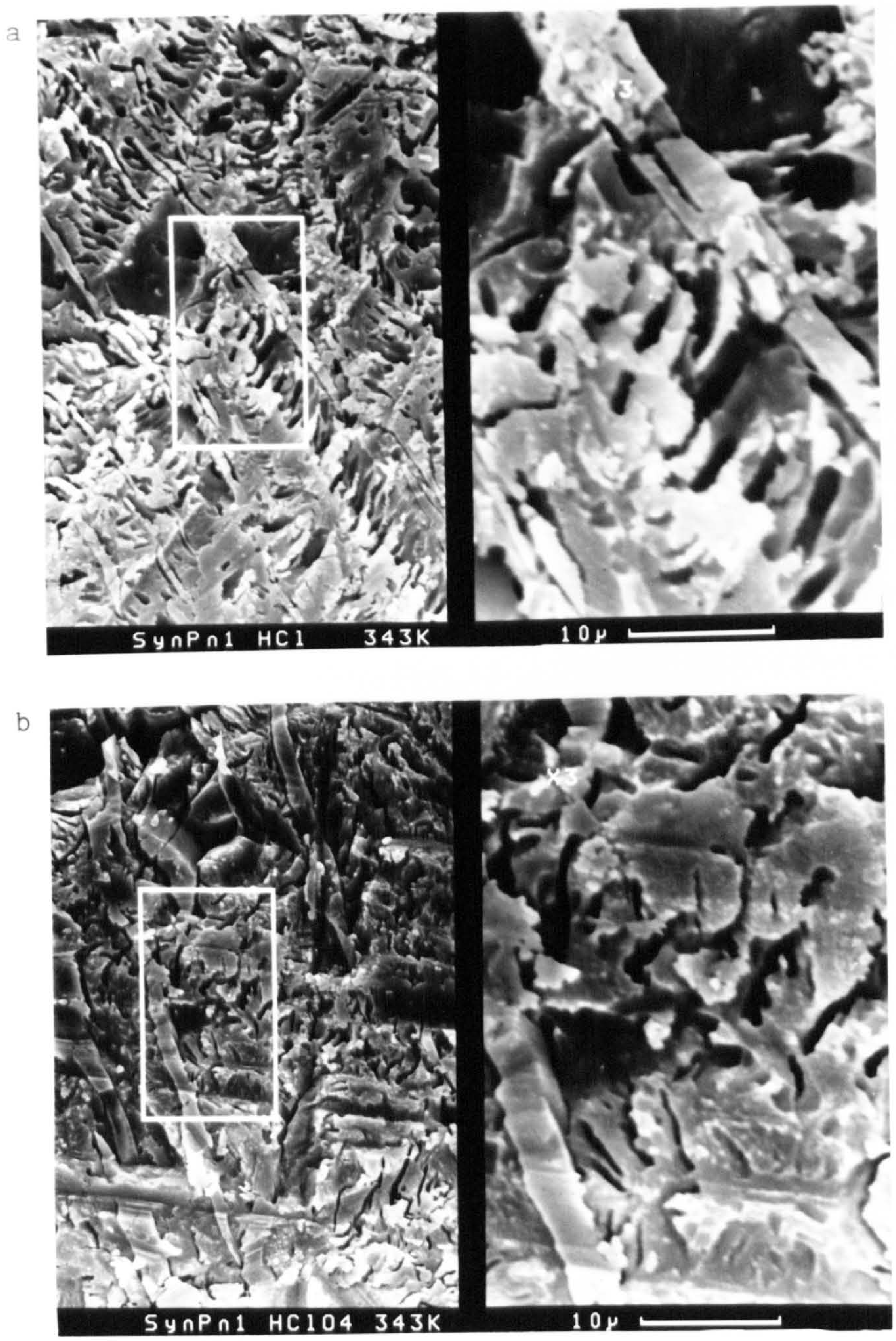

Figure 3.2.76

Scanning electron microscope (SEM) images of the pentlandite surface after an anodic excursion ($5mVs^{-1}$) from the rest-potential to 0.7V vs. SCE at 343K. (a) 1M HCl solution, (b) 1M $HClO_4$ solution. Surfaces appear significantly etched.

3.3 CATHODIC STRIPPING VOLTAMMETRY

Cathodic stripping voltammetry was performed on pentlandite in 1M HCl and 1M $HClO_4$ solutions at 293 and 343K (see Figures 3.3.1 to 3.3.4). Anodic polarization at various potentials was applied for 720s prior to the cathodic excursion. The cathodic currents can be divided into three regions.

The first of these occurs between 0.3 and 0V vs. SCE, in both HCl and $HClO_4$ solutions, where the currents are very small, although these increased slighty with an increase in temperature. It is tempting to apportion this potential region to the reduction of a metal deficient intermediate metal sulphide phase formed during the anodic polarization. However, a comparison with the voltammograms of violarite indicates that if such a phase does occur, it is unlikely to be violarite because of an insufficient similarity between these cathodic currents (cf. Figures 3.2.40 and 3.2.44). A more likely explaination is the reduction of certain allotropes of sulphur which are sufficiently unstable with respect to H_2S at these potentials.

The second region occurs between 0 and -0.4V vs. SCE. These currents are attributed to the reduction of elemental sulphur as previously inferred in Section 3.2.1, indicating that elemental sulphur is produced on pentlandite during polarization at potentials <0.8V vs. SCE. A significant difference on the effect which temperature has on this peak current is observed in comparing the reactions for the two solutions. In 1M HCl solution, the peak currents increase pro rata with temperature; whilst in 1M $HClO_4$ solution, the opposite occurs (at least for polarization at high potentials). This result is in agreement with those in Section 3.5 and 3.6, which show that the rate of oxidation of pentlandite in 1M $HClO_4$ (at relatively high potentials), decreases on increasing the temperature above approximately 293K.

Polarization at potentials <0.4V vs. SCE produces very little sulphur, whilst the small cathodic currents that do exist may be due to the formation of a "metal-rich" surface with the evolution of H_2S. (cf. Section 1.7.2).

The sharp peak at -0.1V vs. SCE in Figure 3.3.4 is typical of an adsorption process on the electrode surface (175). Adsorption peaks are normally sharp, since the peak current is largely determined by the surface excess of the reactant species prior to polarization, rather than by mass transport processes arising during polarization. A classic example of strong product adsorption is the reduction of aqueous hydrogen ions at a platinum electrode. This gives rise to a pre-wave adsorption, in which the adsorption of the reduced hydrogen atoms favour the forward reaction. A similar process of hydrogen adsorption may be implicated here, i.e. on sulphur coated pentlandite at high temperatures in 1M $HClO_4$ solution.

Currents below -0.4V vs. SCE correspond to H_2 evolution.

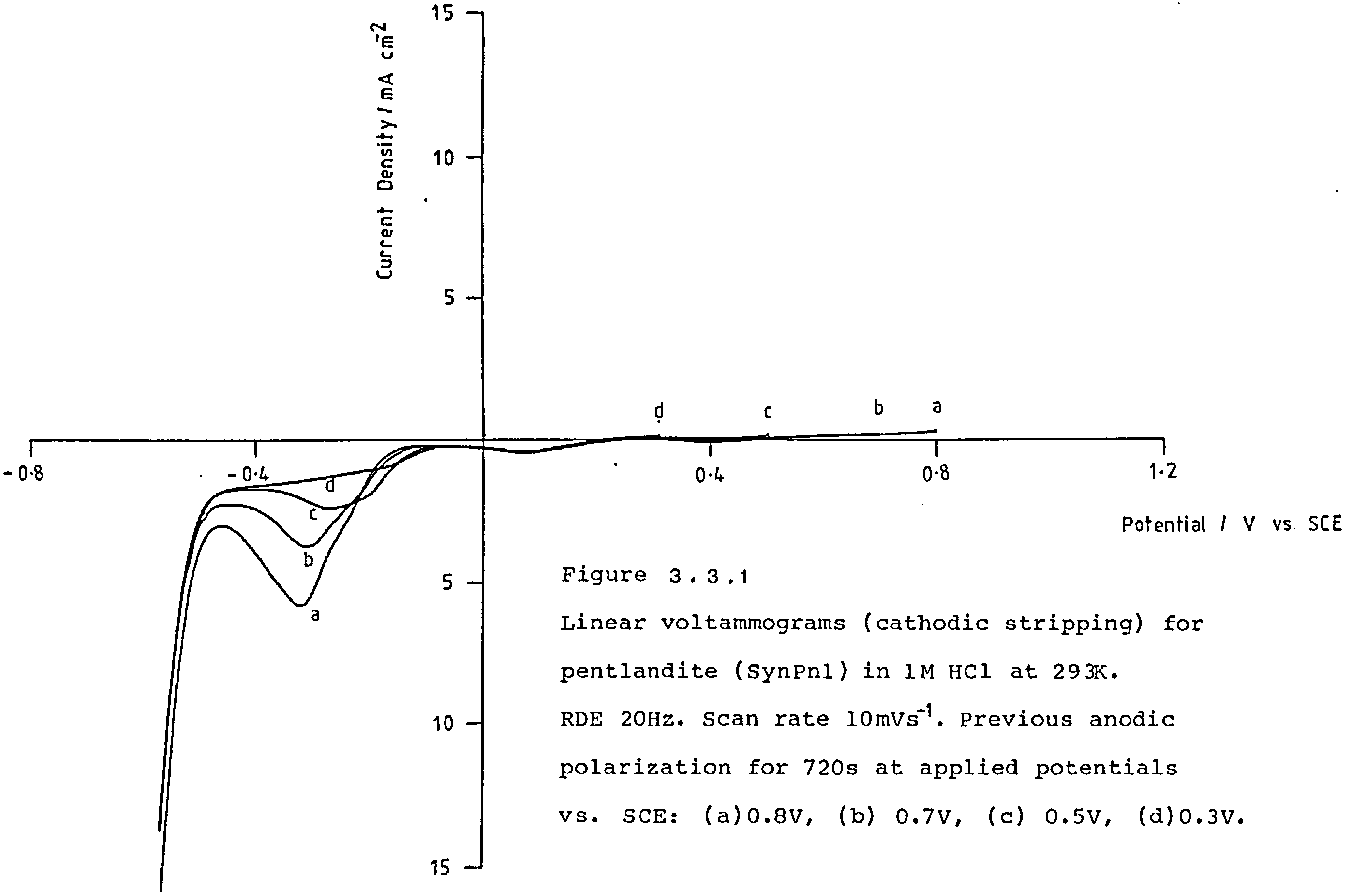

Figure 3.3.1

Linear voltammograms (cathodic stripping) for pentlandite (SynPn1) in 1M HCl at 293K. RDE 20Hz. Scan rate 10mVs^{-1}. Previous anodic polarization for 720s at applied potentials vs. SCE: (a)0.8V, (b) 0.7V, (c) 0.5V, (d)0.3V.

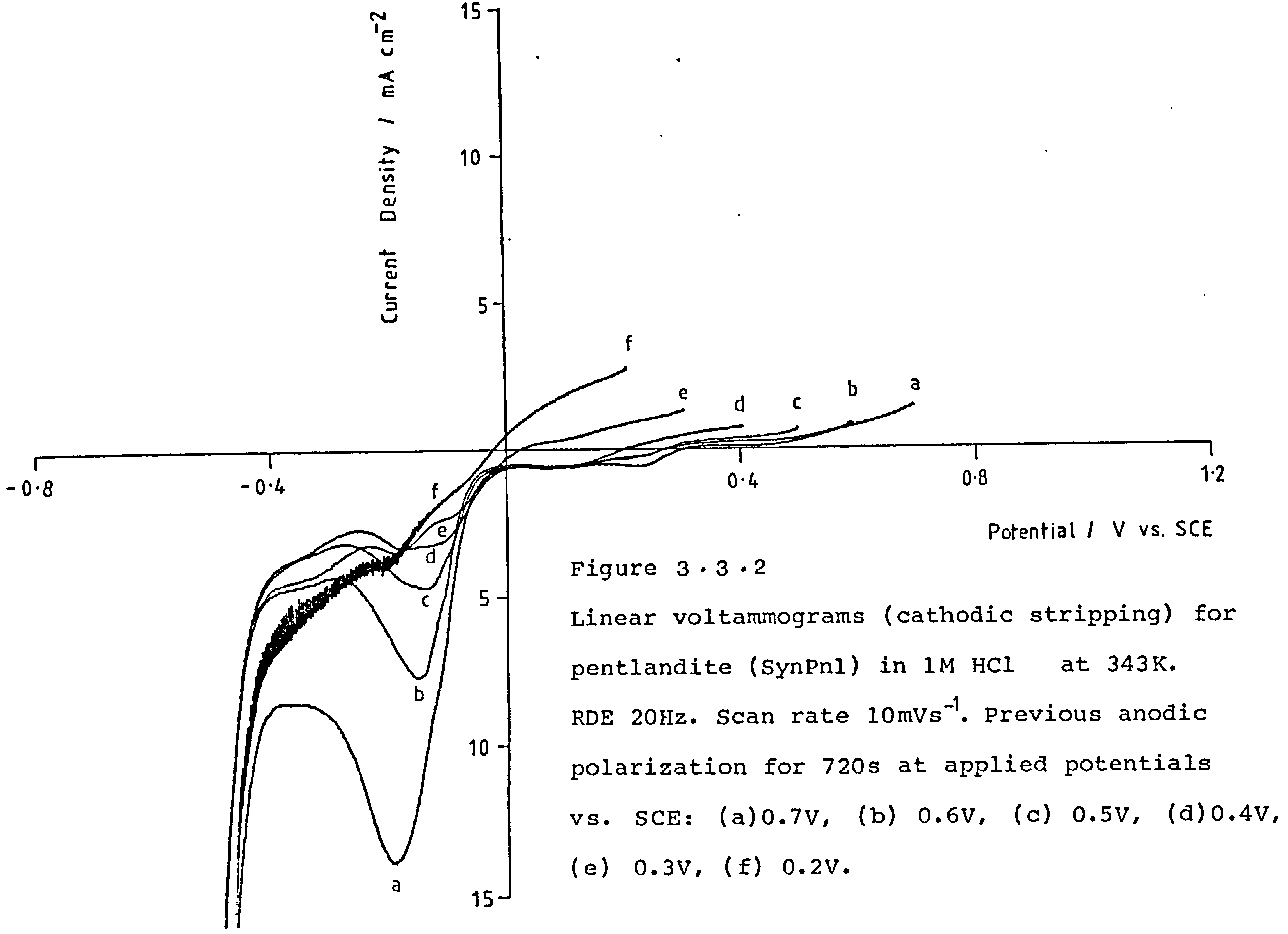

Figure 3·3·2

Linear voltammograms (cathodic stripping) for pentlandite (SynPn1) in 1M HCl at 343K. RDE 20Hz. Scan rate 10mVs^{-1}. Previous anodic polarization for 720s at applied potentials vs. SCE: (a)0.7V, (b) 0.6V, (c) 0.5V, (d)0.4V, (e) 0.3V, (f) 0.2V.

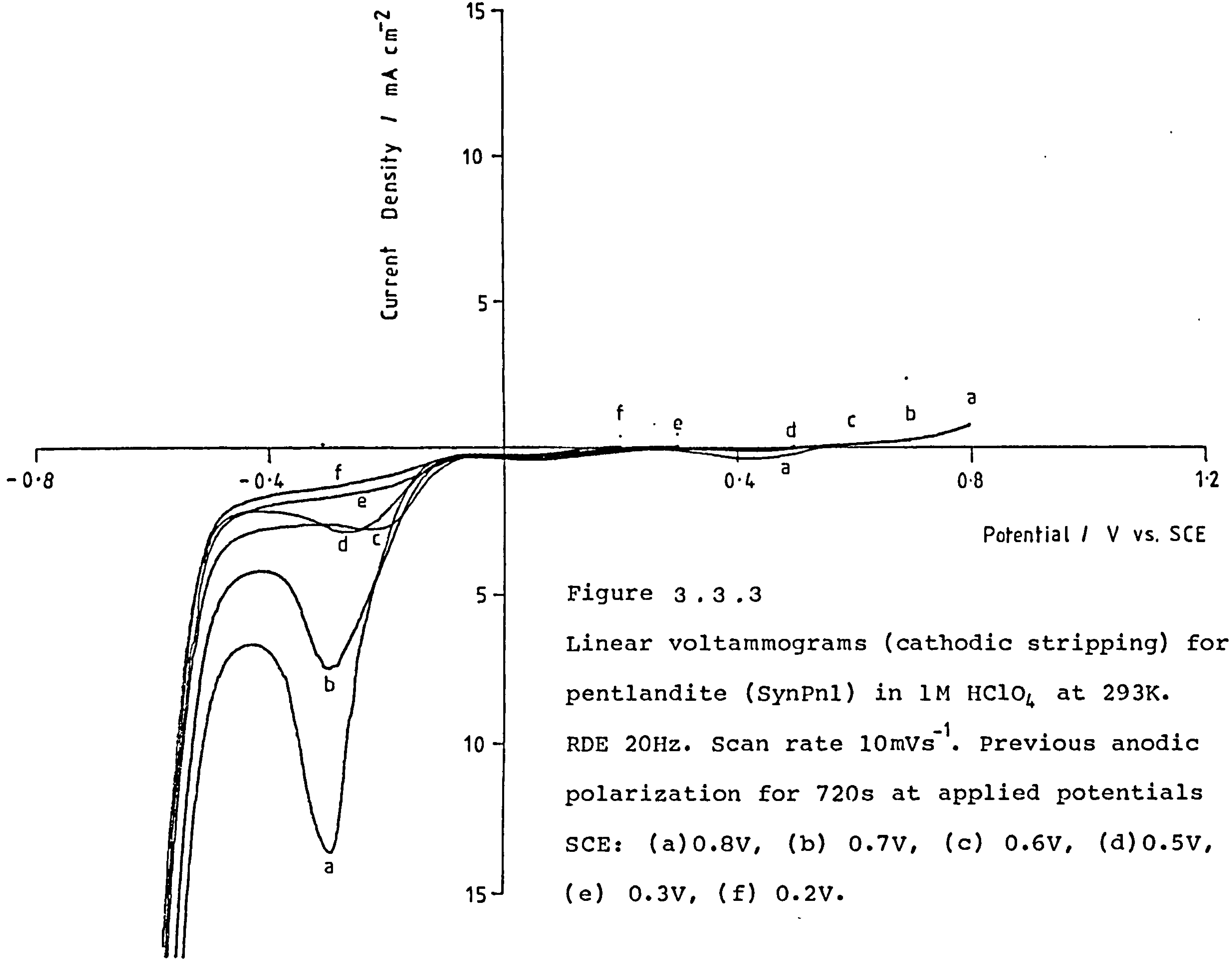

Figure 3 . 3 . 3

Linear voltammograms (cathodic stripping) for pentlandite (SynPn1) in 1M $HClO_4$ at 293K. RDE 20Hz. Scan rate $10mVs^{-1}$. Previous anodic polarization for 720s at applied potentials SCE: (a)0.8V, (b) 0.7V, (c) 0.6V, (d)0.5V, (e) 0.3V, (f) 0.2V.

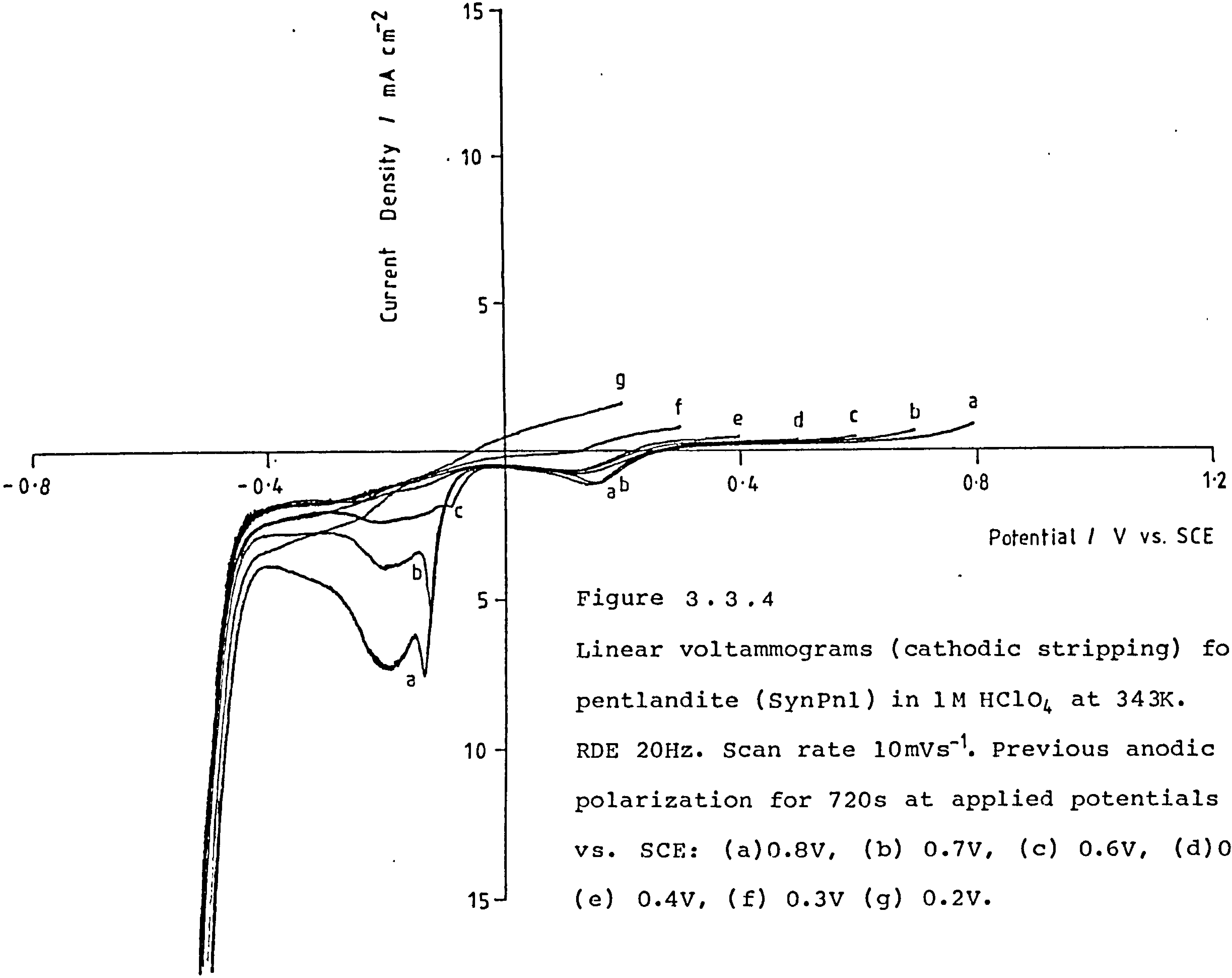

Figure 3.3.4

Linear voltammograms (cathodic stripping) for pentlandite (SynPn1) in 1 M $HClO_4$ at 343K. RDE 20Hz. Scan rate 10mVs^{-1}. Previous anodic polarization for 720s at applied potentials vs. SCE: (a)0.8V, (b) 0.7V, (c) 0.6V, (d)0.5V, (e) 0.4V, (f) 0.3V (g) 0.2V.

3.4 INTERMITTENT GALVANOSTATIC POLARIZATION

3.4.1 Pentlandite

Intermittent galvanostatic polarization (IGP) was performed on pentlandite in a further attempt to clarify the reaction sequence and indentify the product species through measurement of regularly interspersed open-circuit potentials. Comprehensive details of this technique are given in Section 2.2.3. Initially, experiments were performed along the lines described by Thornber (76), (cf. Section 1.7.3) i.e. a symmetric series of 2s on/off anodic current pulses were applied across the mineral/electrolyte interface. After a predetermined number of cycles the polarity of the IGP was reversed allowing a novel variant of "cathodic stripping". Figures 3.4.1 to 3.4.3 show the results for experiments at 343K in 1M HCl, 1M $HClO_4$, and 1M H_2SO_4 solutions. The various features on the IGP traces (numbers 1 to 11) are interpreted here according to the list of processes in Table 3.4.1.

The results are essentially similar for all three acid solutions. During anodic polarization a closed circuit potential of approximately 1.0V vs. SCE is required to maintain a current density of $177Am^{-2}$ as early as the second current pulse. This tallies with the voltammetric studies in Section 3.2, indicating a large overpotential requirement for the anodic dissolution of pentlandite. The amount of charge passed during the first two seconds is only $354Cm^{-2}$. Assuming that the removal of 2.25 moles of electrons is required for the liberation of 1 mole of sulphur atoms (as elemental sulphur), (cf. Equation 1.1.3) and taking the sulphur atom density in pentlandite as $51888molm^{-3}$ (cf.

Appendix B) one can calculate a sulphur film thickness (in terms of the pentlandite lattice parameters) of only 3.14×10^{-8}m (or 31 pentlandite unit cell parameters, see Figure 1.3.3).

It would seem unlikely that mass transport through such a thin film is rate determining. However, the potentials do continue to rise, particularly in perchloric acid solution, at 343K with succesive pulses (cf. Figure 3.4.2). Perhaps the effects of the sulphur film become kinetically important much earlier in the reaction than predicted at the close of Section 3.2.1 (at least in galvanostatically driven reactions). This hypothesis forms the focus of the study in Section 3.5.

The interspersed "open-circuit" potentials in Figures 3.4.1 to 3.4.3 gradually increase with successive anodic cycles to approximately 0.5V vs. SCE. These open-circuit potentials are transitory (as revealed by their drop in potential to approximately -0.10V vs. SCE in Figures 3.4.4 to 3.4.8, which comprise longer spells in open-circuit). Nonetheless, this transitory potential at 0.5V vs. SCE corresponds to a mixed potential regime between pentlandite and ferric iron generated during the preceeding faradaic reaction, i.e.

$$Fe^{3+} + e = Fe^{2+}$$

$$Fe_{4.5}Ni_{4.5}S_8 + 16H^+ = 4.5Fe^{2+} + 4.5Ni^{2+} + 8H_2S + 2e \qquad (3.4.1)$$

These experiments were repeated allowing a sufficient time in open-circuit to observe any "definite" potential arrests. Figures 3.4.4 to 3.4.6 show that such a potential arrest occurs at approximately -0.1V vs. SCE at 343K.

However, this to is a temporary arrest, and if the system is left for sufficient time (i.e. several minutes) in open-circuit, the initial rest-potential of -0.410V vs. SCE is resumed.

This "potential arrest" at -0.1V vs. SCE occurs in close proximity to the equilibrium potential for the reduction of orthorhombic sulphur to H_2S in acid solution, i.e.

$$S^o + 2H^+ + 2e = H_2S \qquad (3.4.2)$$

$$E_h(298K) = 0.144 - 0.0519pH - 0.0295lg[H_2S]$$

However, a mixed potential regime between amorphous sulphur and pentlandite in acid solution is inferred here, as described below.

Figures 3.4.7 and 3.4.8 show the dependency of this "potential arrest" on pH. Although dE_{rest}/dpH (291K) = -0.038V decade^{-1} does not exactly correspond to the thermodynamically predicted pH dependency for the above equilibrium involving elemental sulphur (see Equilibrium 3.4.2), i.e. dE_h/pH (298K) = -0.059pH (assuming a constant $H_2S(aq)$ activity at each pH), the trend is nonetheless in the right direction. The concentration of $H_2S(aq)$ is not known, but by assuming a concentration of 10^{-3}moldm^{-3}, a predicted value of $E_h(pH=0,298K) = 0.233V$ (-0.009V vs. SCE) can be calculated; compared with the observed value of $E_{rest}(pH=0,291K) = -0.071V$ vs. SCE. These values are only approximately equal, and furthermore, by considering the reductive potential for metastable amorphous sulphur visa vis orthorhombic sulphur, one would expect a higher thermodynamically derived potential, thus increasing the disparity still further.

This problem is resolved by inferring a mixed potential regime involving the "reduction" of elemental (amorphous) sulphur on the surface of the pentlandite to H_2S, together with the "oxidation" of pentlandite to H_2S, aqueous ferrous and nickel ions, i.e. by the interaction of the following two processes:

$$S^o + 2H^+ + 2e = H_2S$$
$$Fe_{4.5}Ni_{4.5}S_8 + 16H^+ = 4.5Fe^{2+} + 4.5Ni^{2+} + 8H_2S + 2e \qquad (3.4.3)$$

Thus, the mixed potential lies between the equilibium potentials for these two processes, albeit nearer the reduction equilibrium for $S^o,H^+/H_2S$ (indicating faster electron transfer for this couple); whilst the pH dependency is not expected to correspond to the Nernstian slope for either process.

Furthermore, once all the elemental sulphur has been reduced from the surface of the pentlandite by this mixed potential regime, the initial rest potential is resumed (i.e. a mixed-potential regime in which the oxidizing species for pentlandite dissolution is now provided by H^+(aq) rather than S^o). Therefore, this observed potential arrest at -0.1V vs.SCE is considered as evidence of the formation of elemental sulphur during the induced anodic oxidation.

More importantly, Figures 3.4.4 to 3.4.6 show by analogy that elemental sulphur is not formed until the closed-circuit potential (i.e. that accompanying the anodic process) is >0V vs. SCE. This is strong evidence that the alternative oxidative mechanism i.e.

$$Fe_{4.5}Ni_{4.5}S_8 + 16H^+ = 4.5Ni^{2+} + 4.5Fe^{2+} + 8H_2S + 2e \qquad (3.4.4)$$

predominates in this lower potential region, and in galvanostatically controlled experiments with an imposed current density of up to at least $18Am^{-2}$ at 343K.

The initial rest potential (-0.410V vs.SCE) is readily re-attained on reversal of the polarity (i.e. after the "induced reduction" of the elemental sulphur to H_2S). The amount of cathodic charge required to bring about this effect is proportional to the amount of "high-potential" oxidation incurred during the anodic cycles.

No evidence for the formation of an intermediate metal-sulphide phase, e.g. violarite can be drawn from these results.

3.4.2 Violarite

The results of IGP experiments on violarite are shown in Figures 3.4.9 to 3.4.13. The interpretation of the open-circuit potentials is less clearly understood than those of pentlandite. The results are similar for all three acid solutions (cf. Figures 3.4.9 to 3.4.11). Anodic potentials of approximately 1.0V vs. SCE are observed during the anodic polarization cycle, which is comparable to that for pentlandite. The formation of elemental sulphur is implicated here. The open-circuit potentials at approximately 0.5V vs. SCE are considered as a mixed-potential regime between ferric iron and violarite, as was inferred from the initial rest-potential, except at a greater ferric/ ferrous ratio, i.e.

$$\begin{aligned} &Fe^{3+} + e = Fe^{2+} \\ &FeNi_2S_4 = Fe^{2+} + 2Ni^{2+} + 4S^o + 6e \end{aligned} \qquad (3.4.5)$$

This open-circuit potential decays with time to values more akin to the initial rest-potential. It is considered that the presence of elemental sulphur does not significantly influence events here, unlike the case of pentlandite.

On the reversal of polarization, it is inferred that reduction of elemental sulphur and violarite occurs, i.e.

$$S^o + 2H^+ + 2e = H_2S \qquad (3.4.6)$$

$$FeNi_2S_4 + 8H^+ + 2e = Fe^{2+} + 2Ni^{2+} + 4H_2S \qquad (3.4.7)$$

with the accompanyment of H^+/H_2 reduction at large imposed cathodic current densities. During the intermittent spells in open-circuit, a transient potential arrest occurs at approximately -0.3V vs. SCE (cf. Figures 3.4.12 and 3.4.13). It is possible that this corresponds to a mixed-potential regime between a "metal-rich" sulphide surface formed during the preceeding faradaic reaction, and the H^+/H_2 couple (viz. E_{mixed} pentlandite in acid solution) i.e.

$$(Fe,Ni)_{1+x}S + 2H^+ = (1+x)(Fe,Ni)^{2+} + H_2S + 2xe \qquad (3.4.8)$$

A similar interpretation was offered by Thornber (76) in his work on violarite (cf. Figure 1.7.2). However, with the lack of additional analytical evidence (i.e. ESCA), this interaction must remain conjectural.

TABLE 3.4.1

Processes Denoted on the IGP Traces

No. Potential / Reaction

1. Mixed-potential

$Fe_{4.5}Ni_{4.5}S_8 = 4.5Ni^{2+} + 4.5Fe^{2+} + 8S^o + 18e$

$2H^+ + 2e = H_2$

2. Oxidation

$Fe_{4.5}Ni_{4.5}S_8 + 16H^+ = 4.5Ni^{2+} + 4.5Fe^{2+} + 8H_2S + 2e$

3. Oxidation

$Fe_{4.5}Ni_{4.5}S_8 = 4.5Ni^{2+} + 4.5Fe^{2+} + 8S^o + 18e$

4. Mixed-potential

$Fe_{4.5}Ni_{4.5}S_8 = 4.5Ni^{2+} + 4.5Fe^{2+} + 8S^o + 18e$

$Fe^{3+} = Fe^{2+} - e$

5. Mixed-potential

$Fe_{4.5}Ni_{4.5}S_8 + 16H^+ = 4.5Ni^{2+} + 4.5Fe^{2+} + 8H_2S + 2e$

$S^o + 2H^+ + 2e = H_2S$

6. Reduction

$S^o + 2H^+ + 2e = H_2S$

7. Reduction

$2H^+ + 2e = H_2$

8. Mixed-potential

$FeNi_2S_4 = Fe^{2+} + 2Ni^{2+} + 4S^o + 6e$

$Fe^{3+} = Fe^{2+} - e$

9. Oxidation

$FeNi_2S_4 = Fe^{2+} + 2Ni^{2+} + 4S^o + 6e$

10. Reduction

$FeNi_2S_4 + 8H^+ + 2e = Fe^{2+} + 2Ni^{2+} + 4H_2S$

11. Mixed-potential

$(Fe,Ni)_{1+x}S + 2H^+ = (1+x)(Fe,Ni)^{2+} + H_2S + 2xe$

$2H^+ + 2e = H_2$

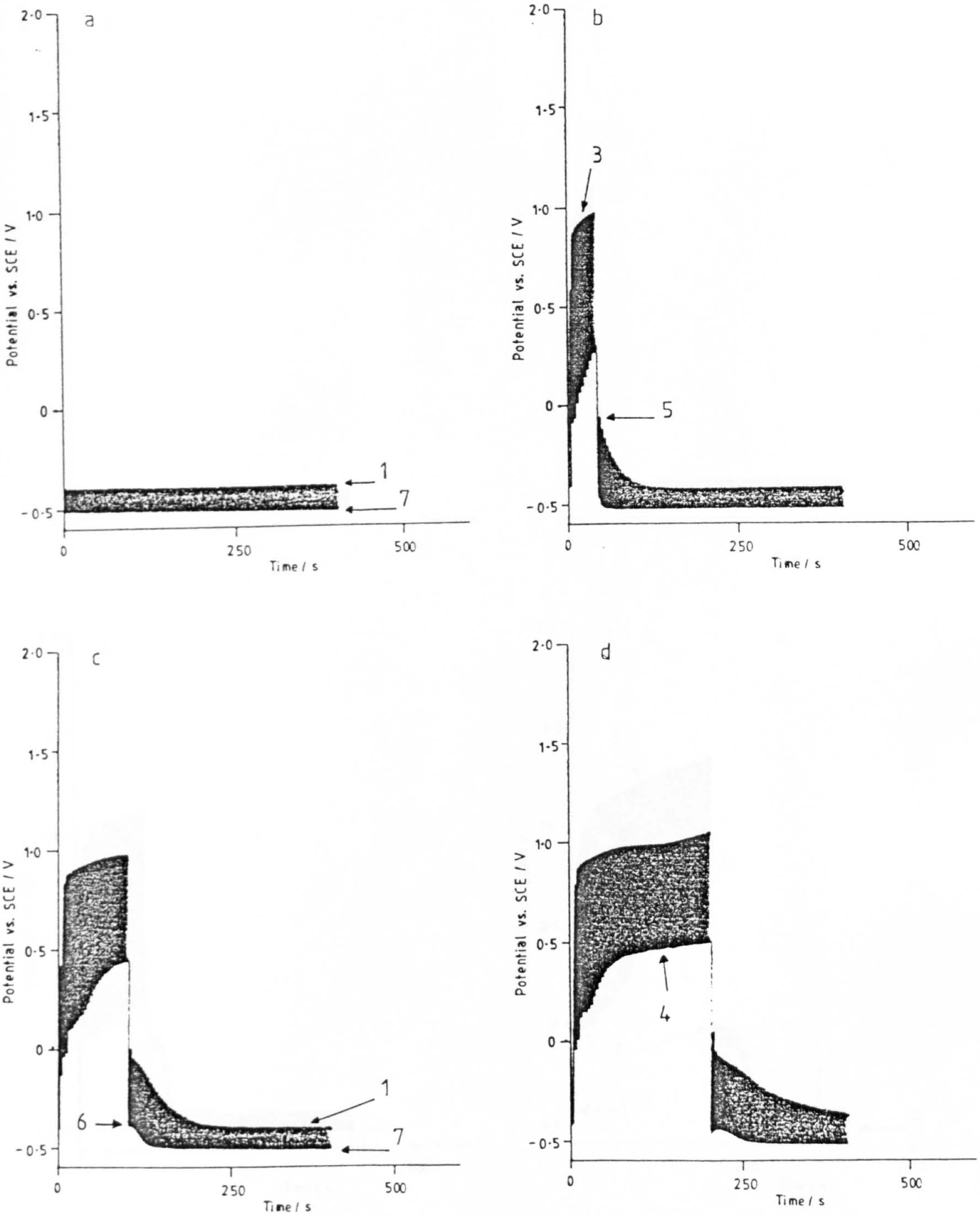

Figure 3.4.1

IGP diagrams for synthetic pentlandite ("SynPn2b") in an unstirred solution of 1M HCl at 343±0.5K. Current density = 17.7mAcm^{-2} with a square wave of 2s "on" and 2s "off". Initial anodic polarization: (a) 0s; (b) 40s; (c) 100s; (d) 200s; followed by cathodic polarization. Numbers on the traces refer to the anodic & cathodic processes as described in the text.

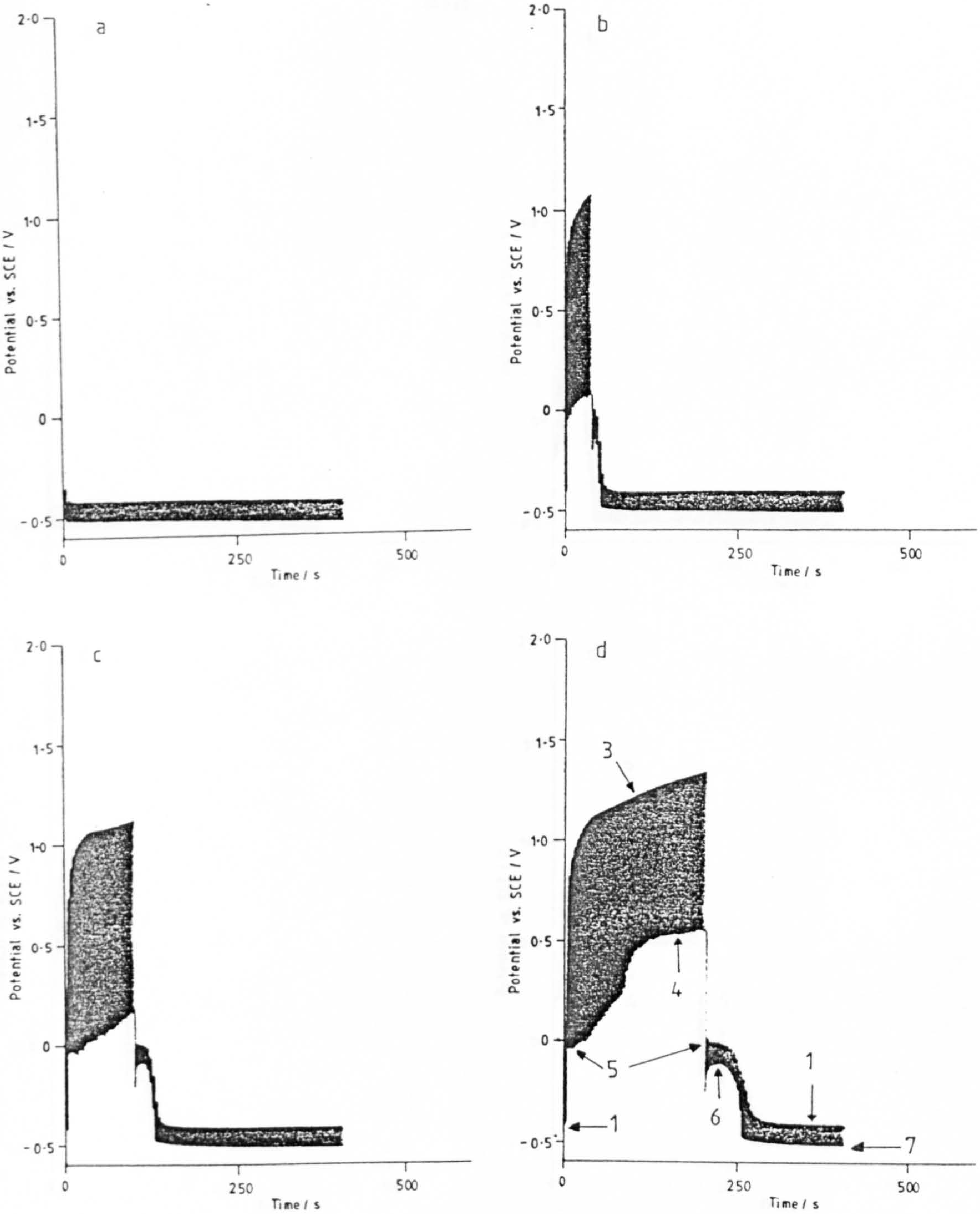

Figure 3.4.2

IGP diagrams for synthetic pentlandite ("SynPn2b") in an unstirred solution of 1M $HClO_4$ at 343±0.5K. Current density = $17.7 mAcm^{-2}$ with a square wave of 2s "on" and 2s "off". Initial anodic polarization: (a) 0s; (b) 40s; (c) 100s; (d) 200s; followed by cathodic polarization. Numbers on the traces refer to the anodic & cathodic processes as described in the text.

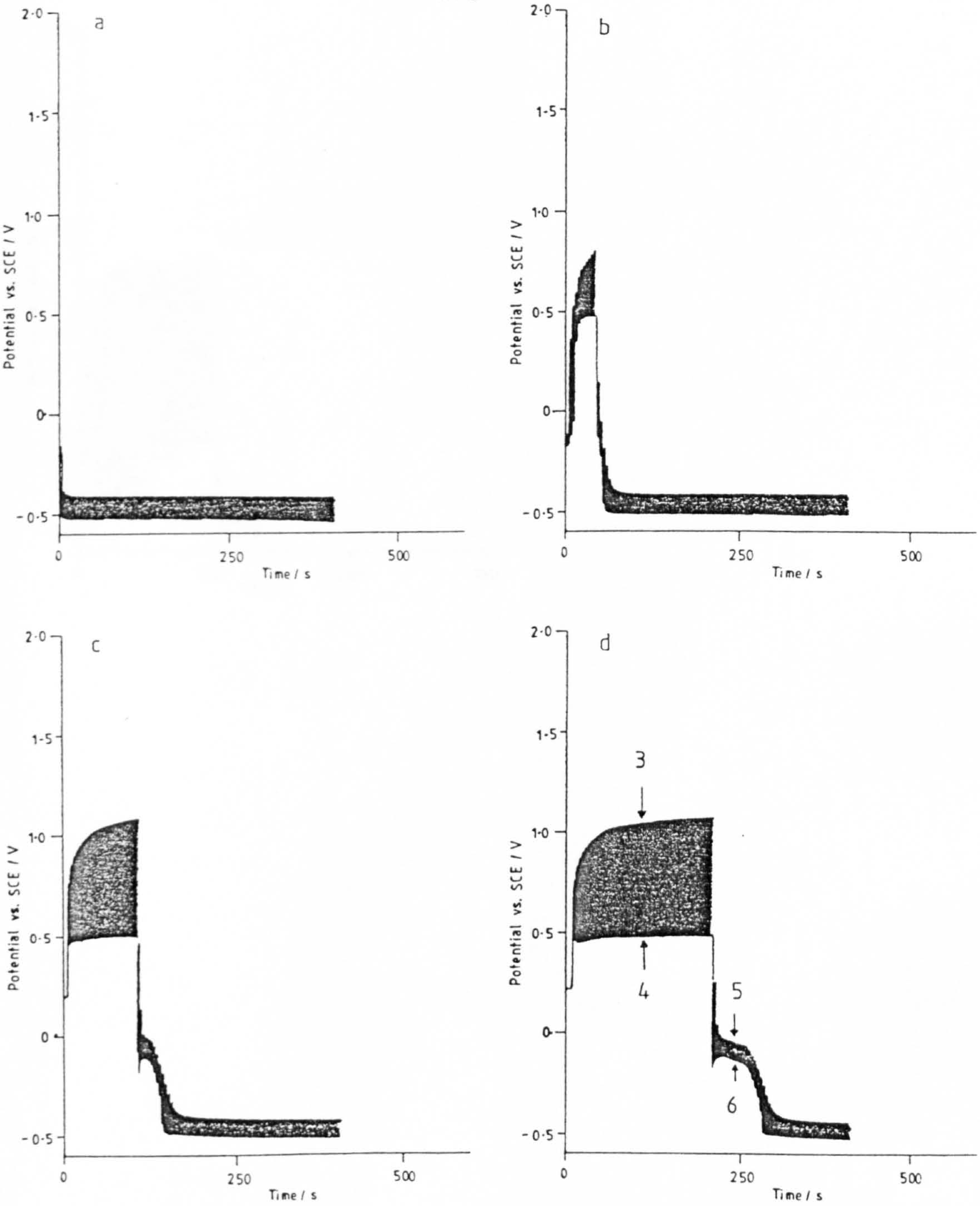

Figure 3 . 4 . 3

IGP diagrams for synthetic pentlandite ("SynPn2b") in an unstirred solution of 1M H_2SO_4 at 343±0.5K. Current density = 17.7mAcm^{-2} with a square wave of 2s "on" and 2s "off". Initial anodic polarization: (a) 0s; (b) 40s; (c) 100s; (d) 200s; followed by cathodic polarization. Numbers on the traces refer to the anodic & cathodic processes as described in the text.

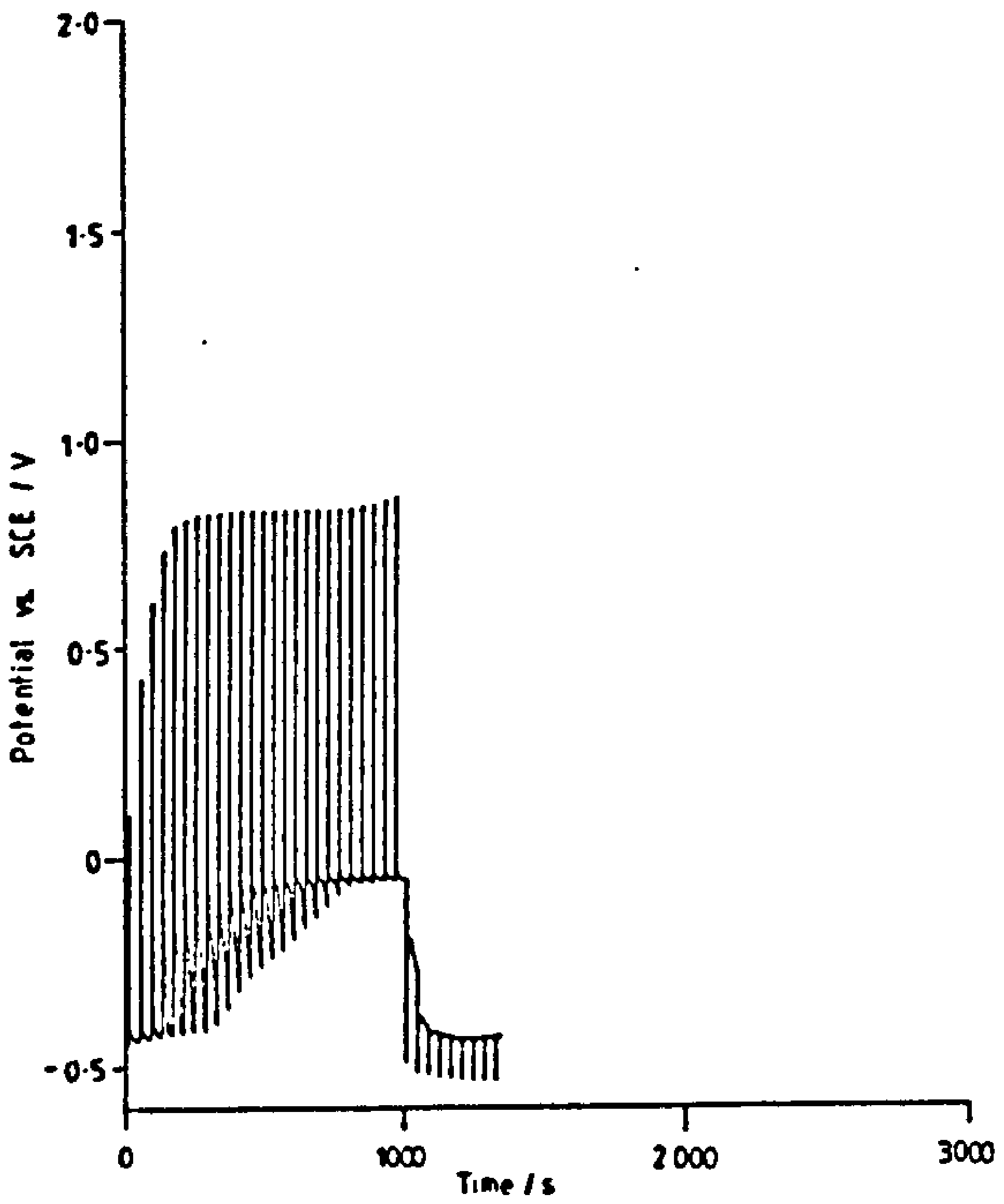

Figure 3.4.4

IGP diagram for synthetic pentlandite ("SynPn1") in an unstirred solution of 1M HCl at 343±0.5K. Initial anodic polarization for approximately 900s with a rectangular wave of 2s"on" and 38s"off"; followed by cathodic polarization. Current density 17.7mAcm^{-2}. Numbers on the traces refer to the anodic & cathodic processes as described in the text.

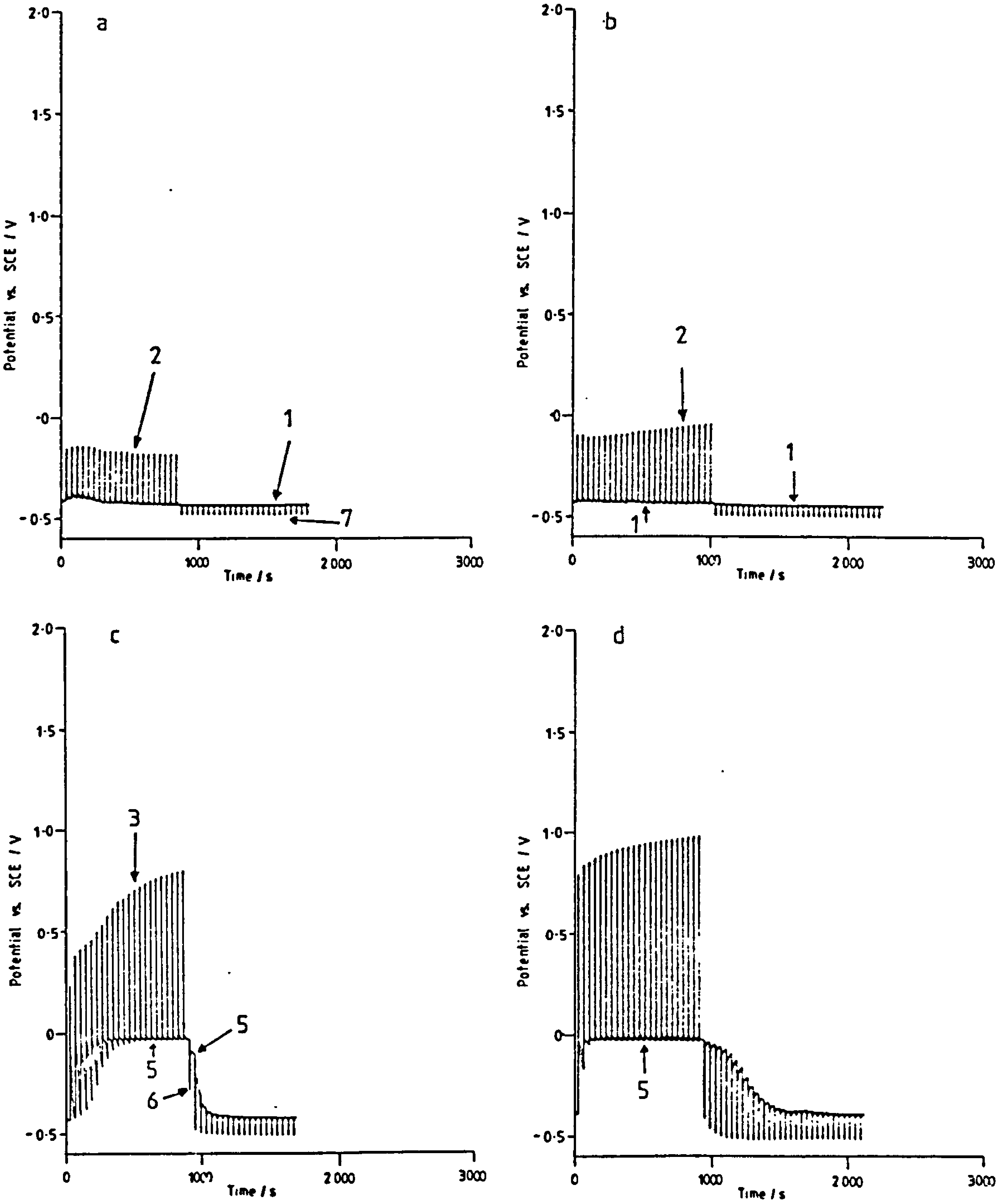

Figure 3.4.5

IGP diagrams for synthetic pentlandite ("SynPn2b") in an unstirred solution of 1M HCl at 343±0.5K. Initial anodic polarization for approximately 900s with a rectangular wave of 2s"on" and 38s"off"; followed by cathodic polarization. Current densities: (a) 1.77mAcm^{-2}; (b) 3.54mAcm^{-2}; (c) 7.07mAcm^{-2}; (d) 17.7mAcm^{-2}. Numbers on the traces refer to the anodic & cathodic processes as described in the text.

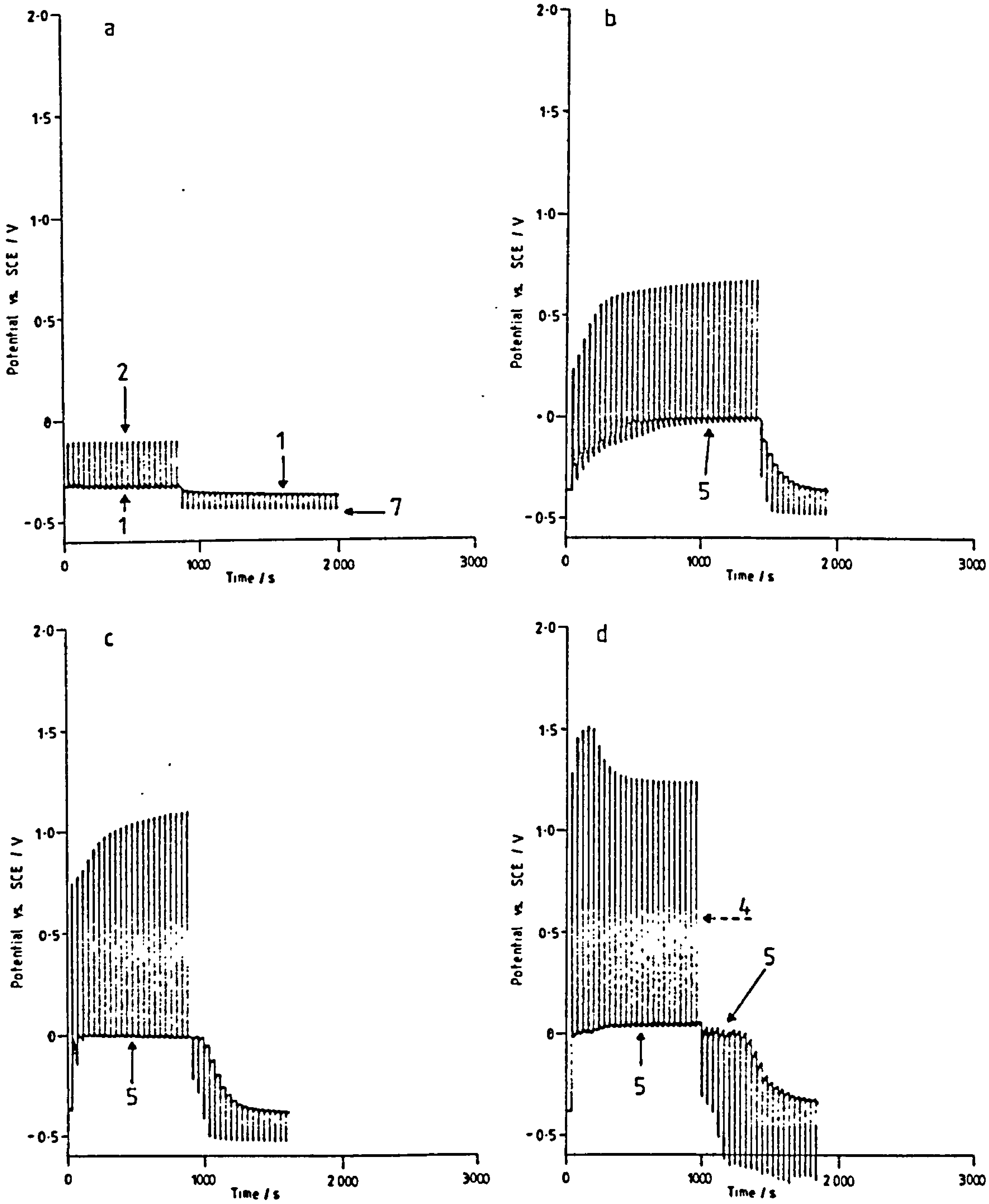

Figure 3.4.6

IGP diagrams for synthetic pentlandite ("SynPn2b") in an unstirred solution of 1M $HClO_4$ at 343±0.5K. Initial anodic polarization for approximately 900s with a rectangular wave of 2s"on" and 38s"off"; followed by cathodic polarization. Current densities: (a) $1.77mAcm^{-2}$; (b) $7.07mAcm^{-2}$; (c) $17.7mAcm^{-2}$; (d) $177mAcm^{-2}$. Numbers on the traces refer to the anodic & cathodic processes as described in the text.

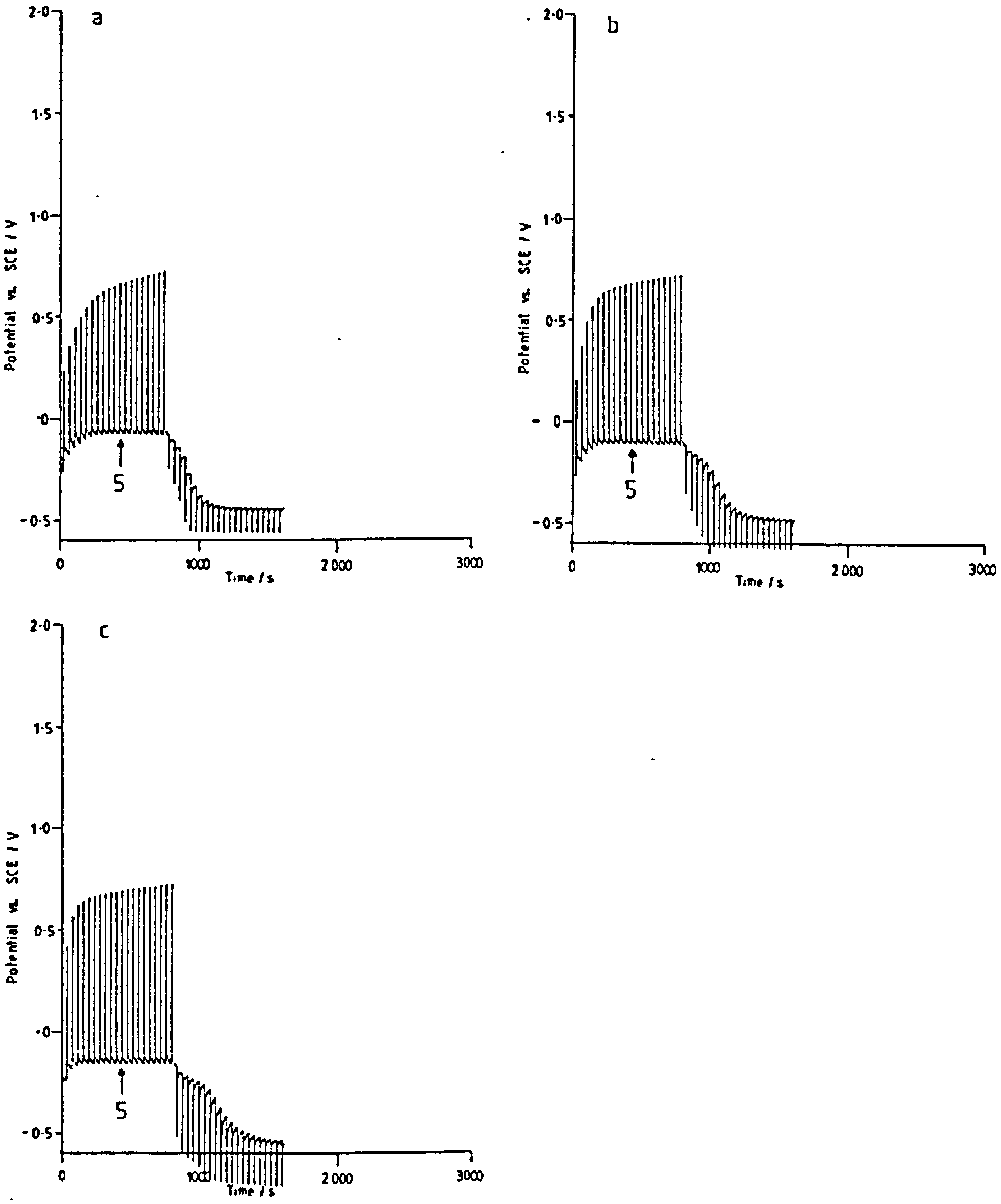

Figure 3.4.7

IGP diagrams for synthetic pentlandite ("SynPn3") in an unstirred solution of HCl/KCl at 291±0.5K. Initial anodic polarization for approximately 900s with a rectangular wave of 2s"on" and 38s"off"; followed by cathodic polarization. Current density 17.7mAcm^{-2}.
(a) 1M HCl; (b) 0.1M HCl, 0.9M KCl, (c) 0.01M HCl, 0.99M KCl.
Numbers on the traces refer to the anodic & cathodic processes as described in the text.

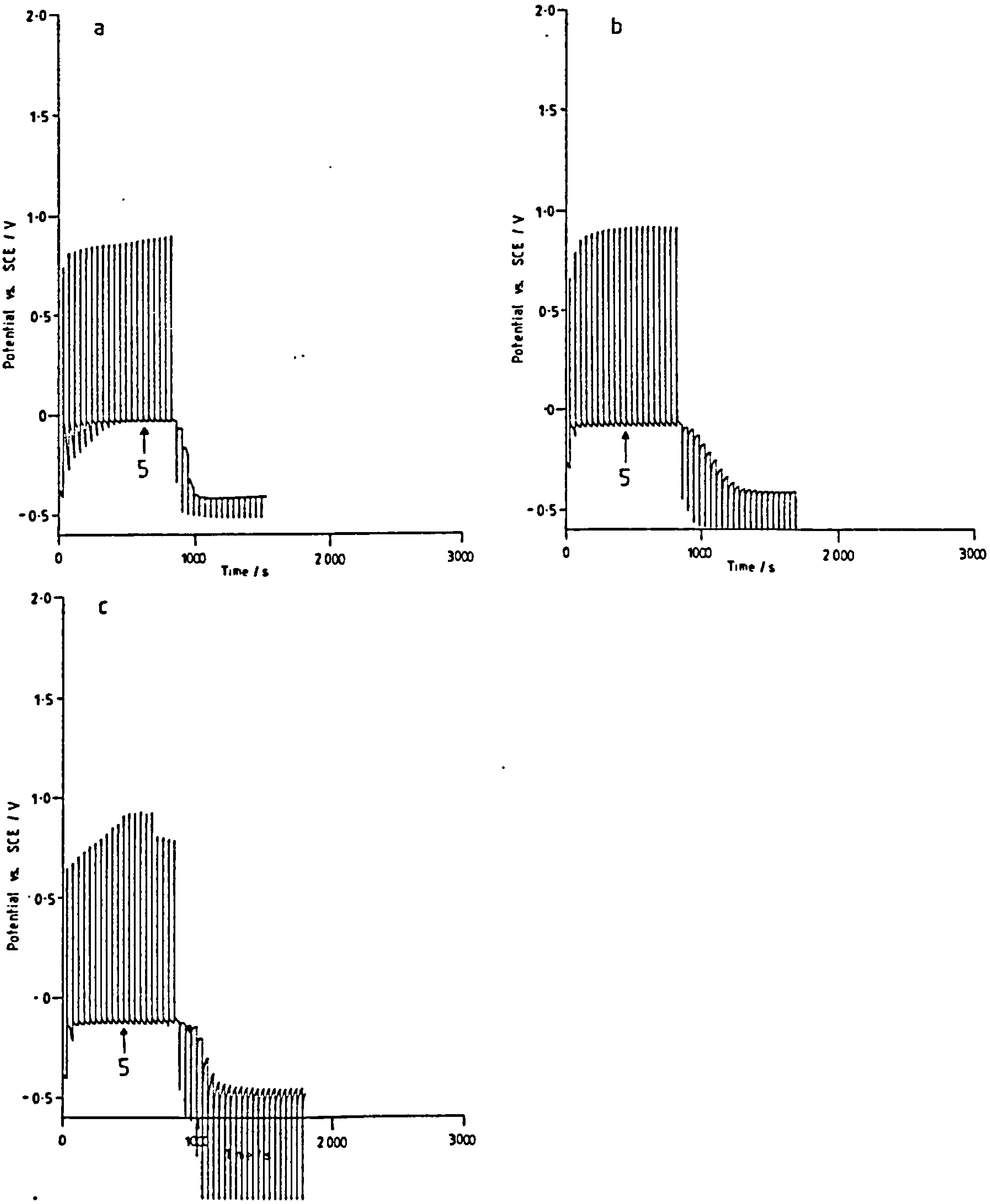

Figure 3.4.8

IGP diagrams for synthetic pentlandite ("SynPn3") in an unstirred solution of HCl/KCl at 343±0.5K. Initial anodic polarization for approximately 900s with a rectangular wave of 2s"on" and 38s"off"; followed by cathodic polarization. Current density 17.7mAcm^{-2}. (a) 1M HCl; (b) 0.1M HCl, 0.9M KCl, (c) 0.01M HCl, 0.99M KCl. Numbers on the traces refer to the anodic & cathodic processes as described in the text.

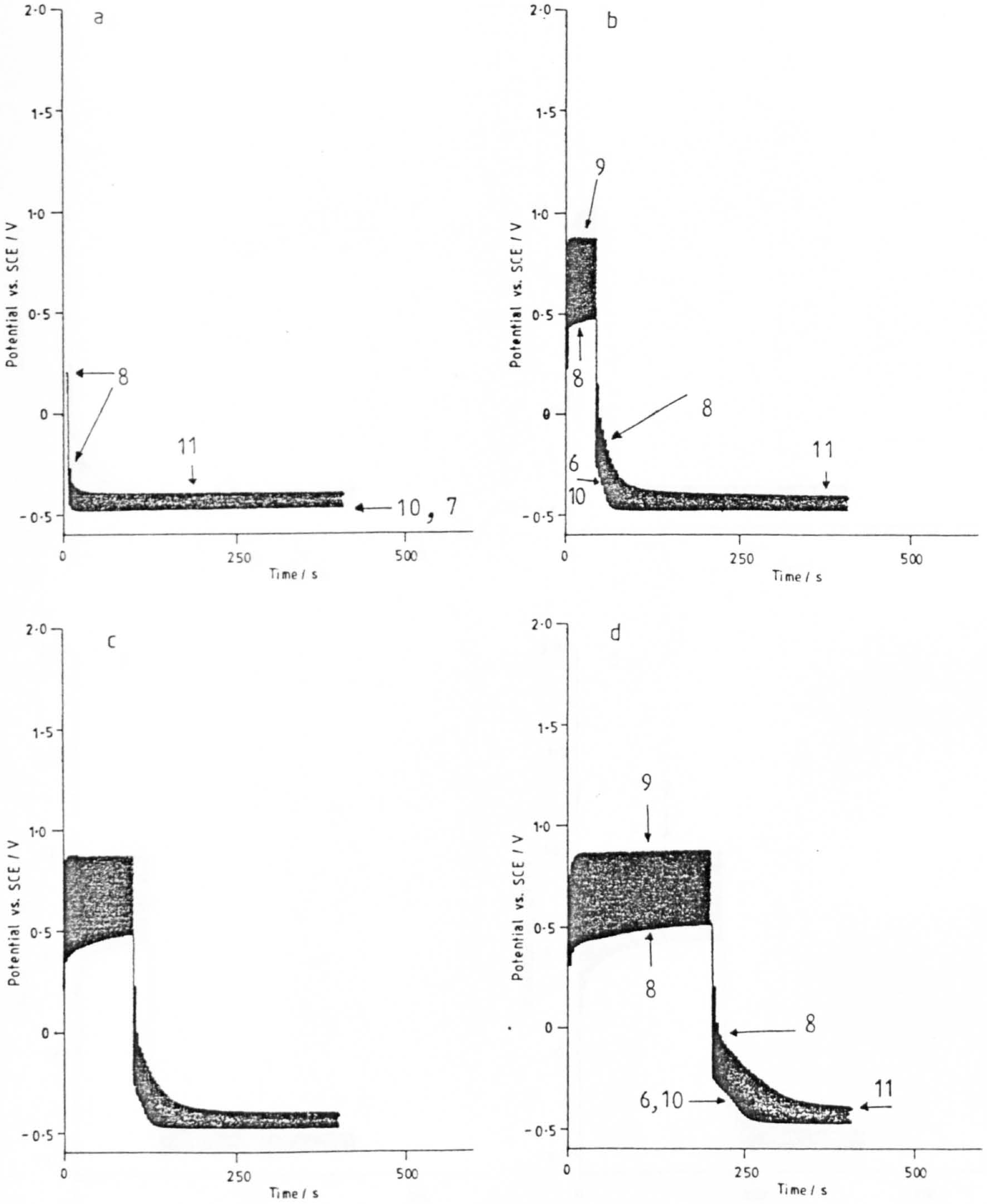

Figure 3.4.9

IGP diagrams for synthetic violarite ("SynVl1c") in an unstirred solution of 1M HCl at 343±0.5K. Current density = 17.7mAcm^{-2} with a square wave of 2s "on" and 2s "off". Initial anodic polarization: (a) 0s; (b) 40s; (c) 100s; (d) 200s; followed by cathodic polarization. Numbers on the traces refer to the anodic & cathodic processes as described in the text.

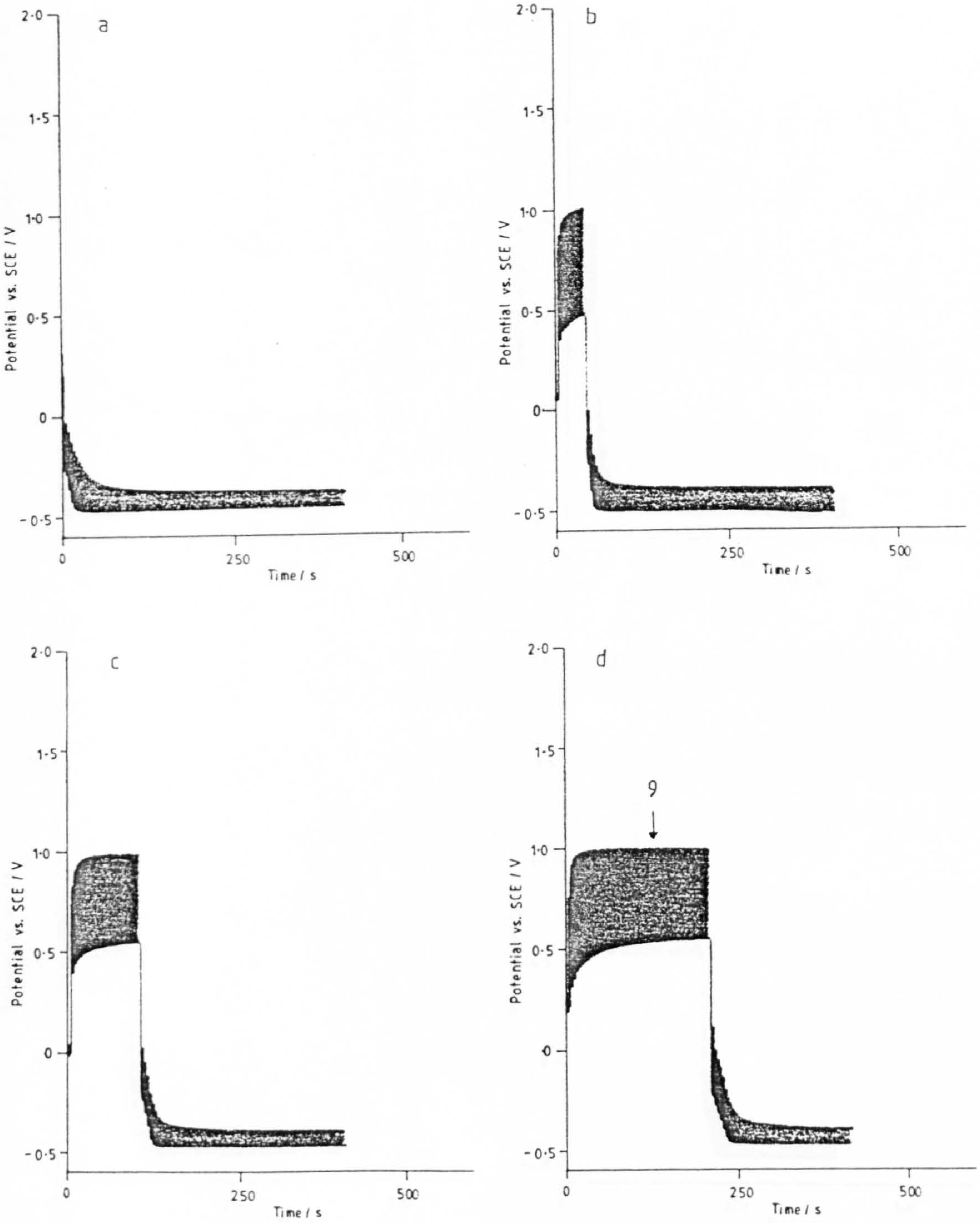

Figure 3 . 4 . 10

IGP diagrams for synthetic violarite ("SynV11c") in an unstirred solution of 1M $HClO_4$ at 343±0.5K. Current density = $17.7 mAcm^{-2}$ with a square wave of 2s "on" and 2s "off". Initial anodic polarization: (a) 0s; (b) 40s; (c) 100s; (d) 200s; followed by cathodic polarization. Numbers on the traces refer to the anodic & cathodic processes as described in the text.

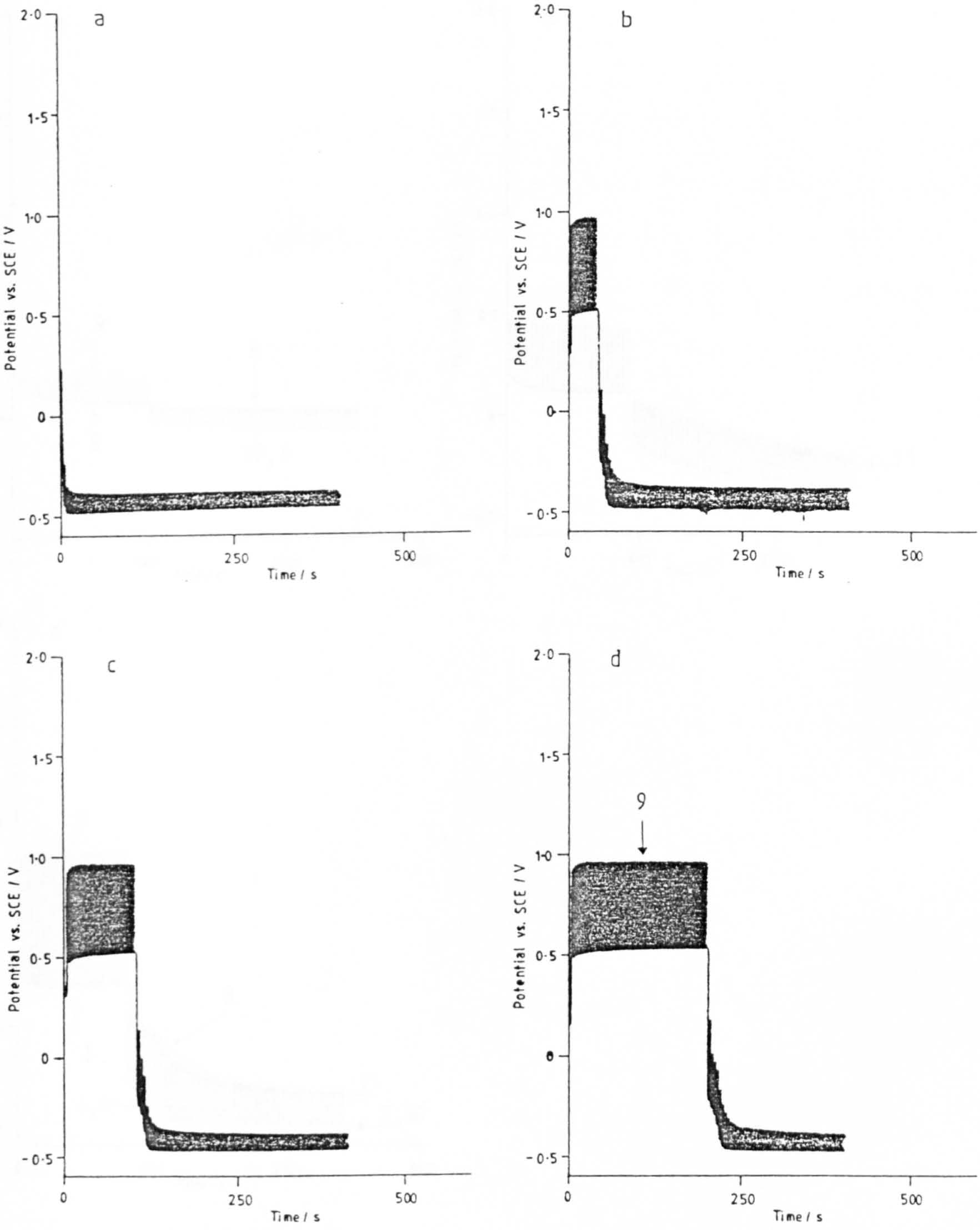

Figure 3 . 4.11

IGP diagrams for synthetic violarite ("SynVl1c") in an unstirred solution of 1M H_2SO_4 at 343±0.5K. Current density = $17.7 mAcm^{-2}$ with a square wave of 2s "on" and 2s "off". Initial anodic polarization: (a) 0s; (b) 40s; (c) 100s; (d) 200s; followed by cathodic polarization. Numbers on the traces refer to the anodic & cathodic processes as described in the text.

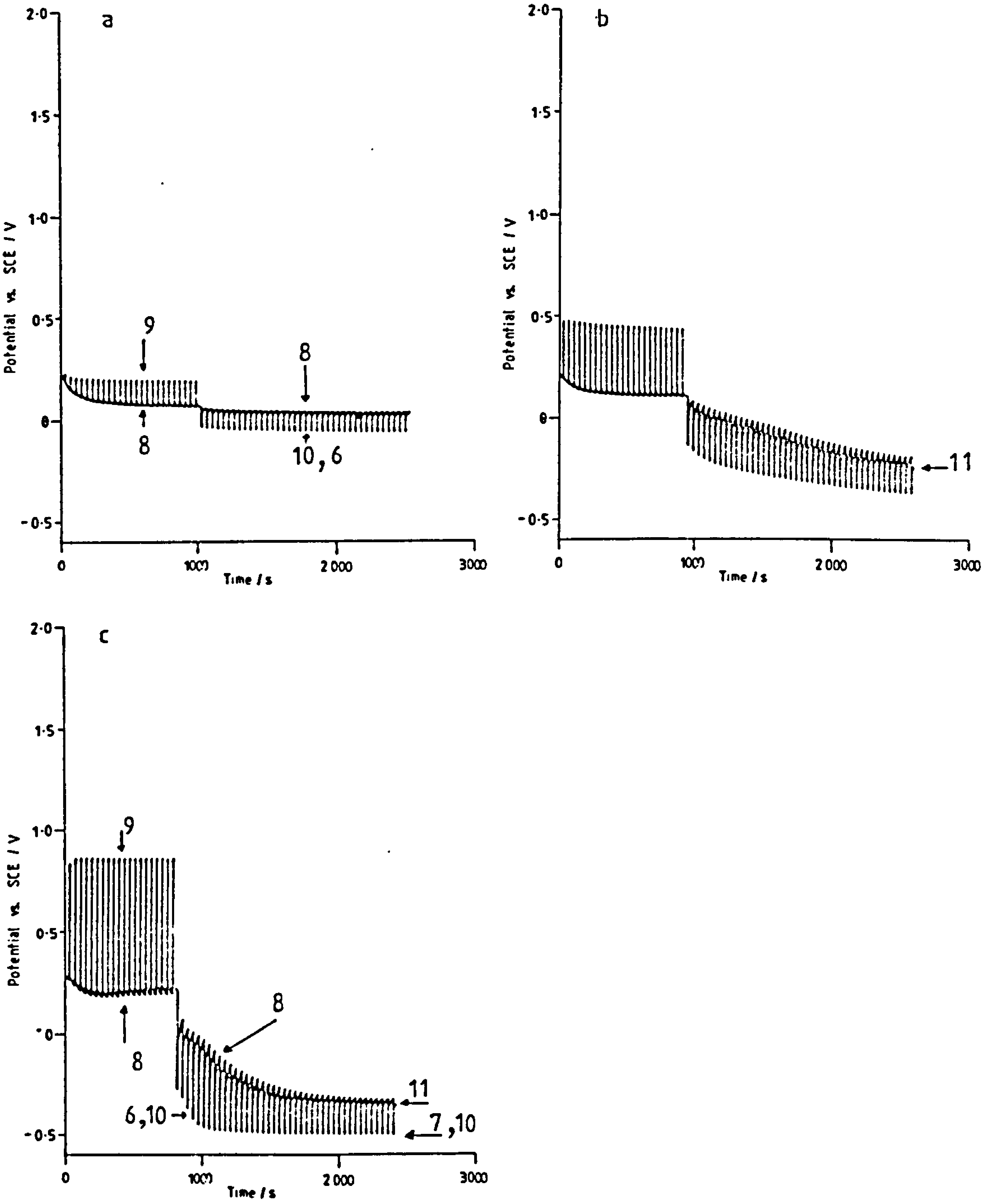

Figure 3.4.12

IGP diagrams for synthetic violarite ("SynV11c") in an unstirred solution of 1M HCl at 343±0.5K. Initial anodic polarization for approximately 900s with a rectangular wave of 2s"on" and 38s"off"; followed by cathodic polarization. Current densities: (a) 0.177mAcm^{-2}; (b) 1.77mAcm^{-2}; (c) 17.7mAcm^{-2}. Numbers on the traces refer to the anodic & cathodic processes as described in the text.

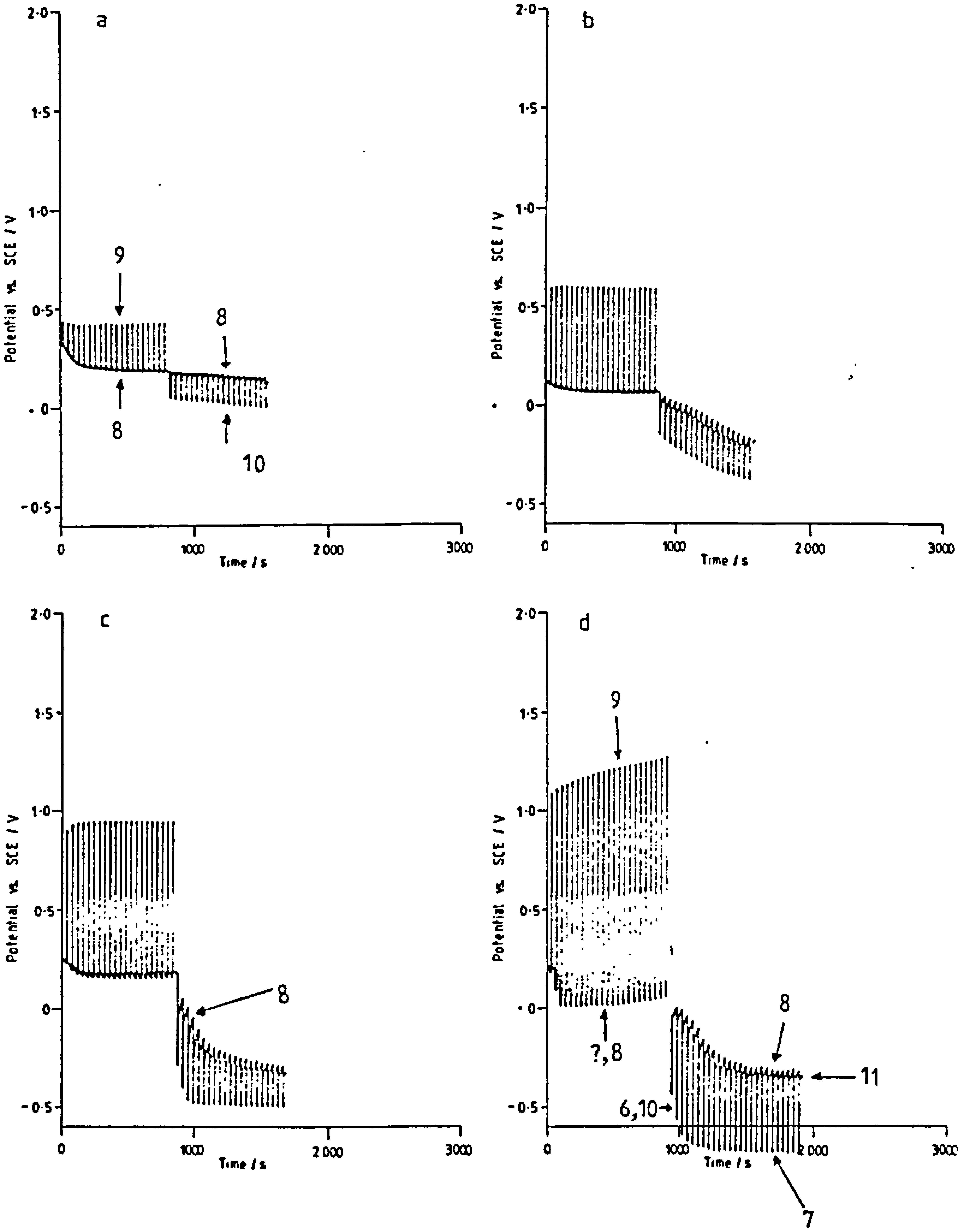

Figure 3.4.13

IGP diagrams for synthetic violarite ("SynVl1c") in an unstirred solution of 1M $HClO_4$ at 343±0.5K. Initial anodic polarization for approximately 900s with a rectangular wave of 2s"on" and 38s"off"; followed by cathodic polarization. Current densities: (a) $0.177mAcm^{-2}$; (b) $1.77mAcm^{-2}$; (c) $17.7mAcm^{-2}$; (d) $177mAcm^{-2}$. Numbers on the traces refer to the anodic & cathodic processes as described in the text.

3.5 CHRONOPOTENTIOMETRY

3.5.1 Pentlandite

Since intermediate solid-state phase changes are known to occur in pentlandite under geological conditions (cf. Section 1.4.2), constant current chronoamperometry was initially performed on pentlandite in acid media to investigate the possibile occurance of this alteration process under conditions more akin to hydrometallurgical extraction. The experimental results were later used to test a diffusion model (i.e. The Sand equation, cf. Sections 2.2.2 and 1.6.2), which has previously been applied by other workers to mechanistic studies of similar phenomena in other metal-sulphide aqueous systems.

A summary of such work in the Cu-S, Cu-Fe-S and Ni-S aqueous systems is appropriate here (156), (157), (158), (159), (172), (150). The chronopotentiometric results for a variety of metal sulphide phases in the above systems have at least one thing in common. When electrolysed at a constant anodic current in acid media, the potential rises steeply after a certain time (although the number of such potential rises depends on the experimental conditions and the compound being studied). The time required for the transitions to occur is observed to be a function of the applied current density, and thus ascribed to a diffusion process. However, it is the interpretation of these transition times in terms of various diffusion mechanisms which is at the centre of the controversy between different groups of workers.

Price (150), (158), (159), (157) performed constant current chronoamperometry on several metal sulphide phases, including chalcocite (Cu_2S), digenite (Cu_9S_5), bornite (Cu_5FeS_4), heazlewoodite (Ni_3S_2), and beta-millerite (NiS). He gave an account of how the solid electrode system, (i.e. the mineral crystal lattice) can be considered analogous to an unstirred convection free solution. Thus, the Sand equation (and its derived forms) can be applied to the diffusion of the mobile metal ions through the crystal lattice during electrolysis (157), (158).

However, Price was often rather vague about the nature (i.e. valency) of the mobile electroactive species, and hence the precise location of electron transfer process in this solid electrode system. This was further complicated by the lack of explicit details concerning the sequence of certain events (e.g. whether the diffusion processes occur prior to, or post, electron transfer), particularly during the formation of elemental sulphur. These processes are discussed in more detail below.

Taking the electrolysis of bornite as an example (158), the electroactive species is considered to be copper or cuprous ions, with the diffusion occuring through a "copper-deficient bornite phase" (although this description is often inadvertently interchanged with "bornite" during his account). The present author assumes that the copper-deficient bornite phase is the diffusion "medium", whilst the bornite is the "source" of the diffusing (electroactive) species. Nonetheless, it is quite plausible to accept that solid-state diffusion occurs, and is perhaps even rate determining, during this alteration, since the solid state diffusion process is considered as taking place through the solid sulphur sub-lattice of the copper-deficient bornite phase. These ideas were confirmed by Aguayo-Salinas (172), who in addition, concluded that the intermediate copper-deficient bornite phase was idaite (Cu_3FeS_4), through which the solid state diffusion of cuprous ions was rate determining (during stage I of the reaction) with a diffusion coefficient $D_{Cu^+} = 1.5 \times 10^{-11} m^2 s^{-1}$.

When the rate of solid state diffusion can no longer sustain the externally imposed current density at the mineral/aqueous interface, the second stage of electrolysis comes into effect. This results in all the copper and iron being leached out of the copper-deficient bornite phase with the formation of elemental sulphur. It is at this important stage of the reaction that ambiguity arises in Price's work.

Irrespective of Price's mathematical interpretation of the events here, he considered the diffusing species to be the same as in the first stage of the reaction (i.e. a copper species in the "solid state"), and assumed that its concentration gradient (presumably "within" the electrode) is maintained by an intimate mixture of the copper-deficient bornite phase and sulphur. It appears that he is trying to adopt a model in which "solid-state" diffusion continues through an evermore metal depleted solid sulphur prior to electron transfer at the "metal-depleted solid sulphur" / aqueous interface. He drew on a similar description of events during the second stage for the electrolysis of chalcocite (157), and also applied solid-state diffusion analysis to the liberation of elemental sulphur from millerite (150).

The adoption of a solid state diffusion theory to the stage where elemental sulphur is formed, seems rather implausible, whether credited to being rate-determining or not, for at least two reasons. Firstly, there is no experimental evidence for a concentration gradient,such as that proposed by Price. Secondly, solid-state diffusion of atomic species through what is essentially crystalline sulphur, "followed" by electron tranfer, is highly unlikely given a more credible alternative mechanism, i.e. electron transfer at the metal-deficient sulphide /aqueous interface, followed by aqueous pore diffusion of the "oxidized" metal species.

This latter mechanism, namely, aqueous pore diffusion was proposed by Biegler and Swift (156) and Peters (131) for the constant current electroysis of chalcocite and digenite.

Their critical observation in drawing this conclusion is the influence of the electrolyte composition on the transition time (t_s), which makes it clear that (t_s) is determined by transport processes occuring in the electrolyte rather than by solid-state diffusion. The rate-limiting transport process is the diffusion of copper dissolved in the electrolyte which fills pores and cracks in the reaction product layer (156). The constancy of the product $i_c t_s^{1/2}$ within this system implies that the thickness of the product layer at time t_s is inversely proportional to the imposed current density (131).

In this model the metal sulphide / aqueous interface (i.e. the place where electron transfer occurs) "moves" into the electrode. At this interface the electroactive species undergoes electron transfer and dissolves into the electrolyte, within the porous product. As the reaction proceeds, the diffusion path for the aqueous metal ions (i.e. the distance between the metal sulphide / aqueous interface where electron transfer occurs, and the bulk electrolyte) increases. The porosity of the product layer, together with the tortuosity of the diffusion path will influence events here (182), (183).

Eventually, the length of this diffusion path is such that the flux of the outwardly diffusing aqueous metal ions is no longer able to maintain the imposed current density in the electrode system. At this point (t_s), the potential rises rapidly until an additional process occurs which can provide an additional ionic flux to maintain the current. This would typically be a higher oxidation process, e.g. the oxidation of sulphur to sulphate, or even the oxidation of the electrolyte per se (cf. Section 2.2.2).

In this present work, the effects of the elemental sulphur product layer on mass transport at the pentlandite surface were studied by chronopotentiometry, and the results compared with the simple aqueous pore diffusion model described above.

Figures 3.5.1 and 3.5.2 show chronopotentiograms for pentlandite in stirred and unstirred 1M $HClO_4$ solution at 293K for various imposed current densities. At the onset of polarization the potential rose rapidly to approximately 1.0V vs. SCE, i.e. the potential region at which elemental sulphur is formed (cf. Section 3.4). The potential then continued to rise gradually until an abrupt increase to approximtely 1.6V vs. SCE at the designated time (t_s). This was followed by a steady state potential in the region 1.4 to 1.5V vs. SCE.

There was an insignificant difference in the transition time (t_s) of the first wave, between stirred and unstirred solution, indicating that agitation of the bulk aqueous phase near the mineral surface does not influence events here. The most striking feature of these results is that the product $i_c t_s^{1/2}$ is constant (at least within the range of i_c studied). This would therefore "appear" to correlate with the Sand equation, (at least in terms of the mechanistic model used by Price, as discussed above).

It was appropriate at this stage of the work to conduct a comprehensive analysis of the products of the reaction by a variety of techniques (cf. Section 2.4) in order to confirm the nature of the product species and to gain a knowledge of the reaction sequence. This was further compelled by the tantalizingly intense metallic violet/grey colour of the product layer (evident here and in previous experiments, cf. Sections 3.2 and 3.4), which was suggestive of the formation of violarite, although there was no electrochemical evidence of its occurance.

Scanning electron microscope (SEM) images of the surface of the mineral after electrolysis in 1M $HClO_4$ solution at 293K with a current density of $1000Am^{-2}$ are shown in Figures 3.5.3 and 3.5.4. After 10s of polarization (i.e. corresponding to a charge density of $1.03x10^4Cm^{-2}$), elemental sulphur had formed preferentially along grain boundaries and along certain (octahedral?) crystallographic plains, as portrayed by a series of parallel ridges of sulphur on the pentlandite surface (identified by EDXA). This feature is reminiscent of the supergene violarite from pentlandite alteration which occurs preferentially along the octahedral [111] planes of pentlandite (cf. Figure 1.4.1(d) and Section 1.4.2).

After 527s (i.e. just before the end of the first wave, corresponding to a charge density of $5.27x10^5Cm^{-2}$) the surface of the pentlandite was substantially covered with a layer of amorphous sulphur. The lack of crystalline structure is clearly evident in Figure 3.5.4. The surface contains elongated pores which suggests some degree of porosity within the layer (at least when formed under galvanostatic conditions). In the enlarged portion of Figure 3.5.4(a) tubercular structures of sulphur are observed. Although their genesis is unknown, their occurance testifies the formation of polymeric allotropes of sulphur. Even after attempting to dissolve the sulphur by boiling the electrode, first in carbon disulphide and then in tetrachloroethene, an amorphous layer was still evident; viz. insoluble (ω)S, (166). Furthermore, the electrode surface retained the metallic violet/grey coloured tarnish.

Electron microprobe analysis digitized maps (Ni, Fe, and S concentrations) of the pentlandite/sulphur reaction front (just after the first chronopotentiometric wave) are shown in Figure 3.5.5. The specimen was prepared by grinding and polishing normal to the electrode surface, to reveal the pentlandite/ sulphur reaction front (cf. Figure 3.5.7a). This was a more satisfactory method of preparation than the more orthodox method of preparing a perpendicular cross-section, in which plucking of product material had caused severe problems. These digitized maps confirm a distinct pentlandite/sulphur reaction front. No intermediate metal-deficient sulphide phase (i.e. violarite) was detected within the resolution limit of this analytical technique (i.e. approximately 10^{-6}m). Figure 3.5.6 shows the spectroscopic evidence for these two phases at the reaction front. The patches of elemental sulphur close to the pentlandite surface still retained a violet/grey colour.

Figure 3.5.7(b) shows a SEM image of a tear in the sulphur film. EMPA of this region shows that the surface of the film is predominantly elemental sulphur, whilst the surface beneath the tear is pentlandite (cf. Figure 3.5.8).

The violet coloured product layer was removed from the electrode and analysed. Destructive analysis (cf. Sections 2.4.5 and 2.4.6) gave the following elemental mass percentages: 19.3%Fe, 17.85%Ni, and 56.4%S; and hence a stoichiometry of $Fe_{2.0}Ni_{0.17}S$. Insufficient product material was available for analysis with a Philips X-ray powder diffractometer. However, ample material was available for the alternative XRD powder camera technique. Samples of synthetic violarite, pentlandite and orthorhombic sulphur were also analysed for "fingerprint" comparison. The atomic spacings from the product material only matched those of pentlandite (cf. Appendix D.6 and Figure 3.5.21). The slight haze on the film was probably due to the amorphous sulphur. Combining the results from these two analyses suggests that the product layer is comprised of a mixture of unreacted "islands" of pentlandite, and elemental sulphur.

The lack of formation of a metal-deficient sulphide phase (i.e. violarite or bravoite) under these conditions is inferred here in terms of very slow solid-state diffusion rates for nickel and iron atoms within the sulphur sublattice. This tallies with slow solid-state diffusion experienced during the synthesis of pentlandite and violarite (cf. Section 2.1), and also from exsolution studies (cf. Section 1.4.1). However, the colour of the product layer remains an intriguing mystery.

The author considers that the complementary analysis of the electrolyte for aqueous product species is important for a complete analysis of the system (cf. Sections 2.4.5 and 2.4.6); a procedure that is sometimes neglected by other workers (e.g. Price). Table 3.5.2 gives the results from this analysis.

An equal ratio of iron and nickel was introduced into the solution, which is consistent with a complete elemental decomposition of the mineral surface. By adopting iron(II) as the predominant iron species evolved in the dissolution reaction, an acceptable agreement is obtained between the amount of charge passed and the equivalent charge carried by the oxidized species. Based on this assumption, and by comparing the amount of sulphate vis à vis iron and nickel in solution, with the stoichiometry of pentlandite (viz. $Fe_{4.5}Ni_{4.5}S_8$), it can be shown that 32% of the sulphide sulphur is oxidized to sulphate, and 68% to elemental sulphur. It is therefore evident that, although no intermediate metal-deficient sulphide phase is formed (at least in any detectable amount), the formation of substantial amounts of sulphate accompanied with elemental sulphur means that the imposed current density needs to be proportioned between two processes. This casts a severe doubt on the application of a simple diffusion model (i.e. the Sand equation) to the analysis of the first chronopotentiometric wave. Furthermore, since the formation of 32% sulphate occurs both during and after the first wave, it is difficult to conceive of a method of proportioning the transition time (t_s) in terms of the two processes.

Nonetheless, the chronopotentiometric experiments were repeated at a variety of temperatures (cf. Table 3.5.1 and Figure 3.5.9). At temperatures <298K, the constancy of the product $i_c t_s^{1/2}$ makes it tempting to ignore sulphate formation and utilize the Sand equation to obtain the mean diffusion coefficient for Fe^{2+}(aq) and Ni^{2+}(aq) ions within the product layer (see Table 3.5.1); and hence by application of Arrhenius's equation obtain an activation energy (viz. $E_a = 18 kJmol^{-1}$), which would be in agreement with aqueous diffusion control. However, this approach is unacceptable here, for the reasons described above, and those discussed in further detail below.

Although the product $i_c t_s^{1/2}$ appears to correspond to the Sand equation, the "shape" of the chronopotentiometric waves does not correspond to the theoretical E-t trace (cf. Figure 1.6.3). This observation lead to an analysis of the chronopotentiometric wave by the convolutive techniques described in Section 1.6.2 (cf. Equation 1.6.42).

$$E(t) = E_{1/4} + \frac{RT}{(Z_B - Z_A)F} \ln \left\{ \frac{I_1}{2i(t_s/\pi)^{1/2} - I_1} \right\} \qquad (1.6.42)$$

Chronopotentiometric experiments were repeated for pentlandite in 1M $HClO_4$ solution at 293K for a variety of imposed current densities and for different fractions of t_s. The measurement of potential was continued for a further 200s in open-circuit so that a comparison could be made between the potential (as a function of the convoluted current) whilst in closed and open circuit. A test for

Nernstian behaviour and the applicability of the Sand equation is that these potentials remain a function of the convoluted current as given by Equation 1.6.42 (i.e. a plot of this equation should be linear and continuous).

The experimentally determined plots of this function are given in Figures 3.5.9 to 3.5.11. From these results it is evident that these requirements are not met, hence the Sand equation is not applicable here. Furthermore, the large potential drop of approximately 0.45V at the transition from closed to open circuit is important, and indicates that a large overpotential is required for the oxidative dissolution of pentlandite at the rates imposed by the applied current densities in these experiments.

At temperatures >298K, the constancy of the product $i_c t_s^{1/2}$ no longer holds. Furthermore, even if these results were applied to the Arrhenius equation as a function of reciprocal temperature, then anomolous behaviour would be observed (see Figures 3.5.12 to 3.5.14); such that by 343K, this characteristic wave has almost disappeared and the potentials rise rapidly to 1.5V vs. SCE.

Chronopotentiograms of pentlandite in 1M HCl solution at 293K are shown in Figure 3.5.15. The potential rises rapidly to approximately 1.6V vs. SCE, without the occurance of the characteristic waves observed in 1M $HClO_4$ under equivalent conditions. Figure 3.5.15 shows the progressive disappearance of this wave with increasing $HCl/HClO_4$ ratios. Figure 3.5.17 indicates that a large overpotential is required to drive the reaction in 1M HCl solution, even at moderate current densities. Analysis of the electrolyte shows that a greater yield of elemental sulphur is obtained in 1M HCl solution compared with 1M $HClO_4$ solution under equivalent conditions (cf. Table 3.5.2).

This work has shown that at low temperature there is a distinct difference in the oxidative dissolution kinetics of pentlandite in 1M $HClO_4$ solution compared with those in 1M HCl solution. However, it was shown that neither process can be "quantitatively" analysed in terms of the originally proposed model based on a simple diffusion process (i.e. the Sand equation).

The results suggest that the diffusion of aquo-complexed ferrous ions in 1M $HClO_4$ solution is easier than the larger chloro-complexed ferrous ions in 1M HCl solution, within the pores of the product layer. Alternatively, it is possible that different allotropes of sulphur are produced in 1M HCl solution, which yield a less permeable product layer.

The anomolous Arrenhius behaviour of pentlandite in 1M $HClO_4$ solution for temperatures >298K is explained here in terms of physical changes in the properties of the sulphur product layer. Amorphous sulphur (solid polycatenasulphur) can exist as a metastable mixture of many allotropes of sulphur including, helices, cyclo S_n molecules, and other molecular forms (166). The nature of the product sulphur was such that allotropes more akin to a viscous liquid might also be implicated here.

It is quite plausible that an increase in temperature will result in a change in the types of sulphur allotropes produced and also in their physical properties (i.e. density, elasticity, viscosity etc.). Thus, an enhanced ability of the sulphur to coat the surface of the pentlandite, coupled with a decreased permeability could explain the retardation of aqueous pore diffusion at temperatures >298K.

On the same account it would be difficult to correlate the diffusion of an ionic species with temperature, through such a sulphur layer. This is because the diffusion coefficient for a particular species is a function not only of its own intrinsic properties, but also of the medium through which it is diffusing. Therefore, in a system in which the properties of the diffusing medium (i.e. the amorphous sulphur) change profoundly with, and as a complex function of temperature, the activation energy for the diffusion process would need to be determined over a very narrow temperature range; ipso facto the activation energy would be temperature dependent.

Nonetheless, the "apparent" Sand behaviour of pentlandite in 1M $HClO_4$ solution at low temperature needs to be explained. It is possible that the transition time (t_s) corresponds to an additional mass transport process (i.e. migration). In classical anodic chronopotentiometry, the potential of the system always increases (unlike that observed just after t_s in this work, cf. Figure 3.5.1). Furthermore, the transition cannot be attributed to the onset of sulphate formation, since its rate of formation is unchanged by this event (cf. Table 3.5.2). Therefore it seems plausible that the electro-assisted "migration" of product aqueous metal ions in addition to the "diffusion" process plays an important role here in maintaining the required ionic flux through the product layer.

In these galvanostatically controlled electrolysis experiments, the overpotential is observed to be large, even for moderate current densities (viz. potential drop in Figure 3.5.17). Sections 3.1 and 3.2 conclude that electron transfer is slow, and would therefore require an appreciable overpotential for an observable rate of reaction. However, an iR drop in terms of the migration of product ions through the sulphur layer may also be important here, particularly in the post t_s region. The contribution from the resistance of the bulk mineral and bulk electrolyte are considered to be negligible, thus:

$$E_{applied} = E_{eq} + \eta_{E.T.} + \eta_{iR(migration)} \qquad (3.5.1)$$

To investigate this thesis further, experiments were performed to discover the influence of the sulphur layer on the mass transport of aqueous $FeCl_3$ from the bulk electrolyte to the pentlandite surface. Figure 3.5.18 shows that the reduction of $FeCl_3$ on a fresh pentlandite surface is similar to that on platinum at 293K. However, Figure 3.5.19 shows that there is a significant difference (0.2V) in the cathodic overpotential to drive this reaction on pentlandite which had been coated with sulphur (by previous anodic treatment). Figure 3.5.20 shows that at the higher temperatute of 343K this potential difference is smaller.

These results indicate that the amorphous sulphur layer produced in 1M HCl solution, reduces the ability of the surface of the pentlandite to undergo electron transfer with an additional aqueous redox couple (viz. Section 3.2.1). This is interpreted here as an impediment to mass transport from the bulk aqueous solution to the mineral surface. Migration within the aqueous pores of the sulphur layer is considered to play an important contribution to mass transport under galvanostatic conditions.

3.5.2 Violarite

Chronopotentiometry was performed on violarite in 1M HCl and 1M $HClO_4$ solutions. Steady state potentials of approximately 1.5V vs. SCE were rapidly obtained, indicating that diffusion processes are not rate limiting here. After prolonged electrolysis, elemental sulphur was visible on the violarite surface.

TABLE 3.5.1

Chronopotentiometric Data for Pentlandite in 1M $HClO_4$:

T/K	i/Am^{-2}	t_s/s	$i_c t_s^{1/2}/Am^{-2}s^{1/2}$	$\overline{D}_A/m^2s^{-1}$
279	1250	330	22700	
279	1000	450	21200	
279	750	780	20900	
279	500	1590	20000	
			21200 (mean)	4.51×10^{-12}
285	1000	516	22700	
285	900	636	22700	
285	800	774	22300	
285	700	996	22100	
			22500 (mean)	5.08×10^{-12}
293	1000	756	27500	
293	900	936	27500	
293	800	1116	26700	
293	700	1422	26400	
			27000 (mean)	7.32×10^{-12}

Determination of $\overline{D}_A$ from the Sand equation, based on the following data:

$C_{(Fe^o,Ni^o)} = 58374\ molm^{-3}$ (cf. Appendix B)

$z_B - z_A = 2$

TABLE 3.5.2

Chronopotentiometric Data for Pentlandite:

Aqueous Analysis Data

(a). Galvanostatic Polarization: $i = 1000\text{Am}^{-2}$
Area = $7.85\text{x}10^{-5}\text{m}^2$
t = 756s (end of 1st wave)
Q(applied) = 59.3C
1M $HClO_4$ solution
T = 293K

Element	No. moles dissolved	Equivalent Charge/C	
Iron	8.51x10-5	Fe(II)	16.4
Nickel	$8.03\text{x}10^{-5}$	Ni(II)	15.5
Sulphate	$4.75\text{x}10^{-5}$	S(VI)	27.5

Q(equivalent) = 59.4C

S^o = 67.7%(S), SO_4^{2-} = 32.3%(S)

(b). Galvanostatic Polarization: $i = 1000\text{Am}^{-2}$
Area = $7.85\text{x}10^{-5}\text{m}^2$
t = 1230s (beyond 1st wave)
Q(applied) = 96.6C
1M $HClO_4$ solution
T = 293K

Element	No. moles dissolved	Equivalent Charge/C	
Iron	$1.42\text{x}10^{-4}$	Fe(II)	27.4
Nickel	$1.42\text{x}10^{-4}$	Ni(II)	27.4
Sulphate	$8.05\text{x}10^{-5}$	S(VI)	46.6

Q(equivalent) = 101.4C

S^o = 68.1%(S), SO_4^{2-} = 31.9%(S)

(c). Galvanostatic Polarization: $i = 100\text{Am}^{-2}$
Area = $7.85\text{x}10^{-5}\text{m}^2$
t = 2330s
Q(applied) = 183C
1M HCl solution
T = 293K

Element	No. moles dissolved	Equivalent Charge/C	
Iron	$2.69\text{x}10^{-4}$	Fe(II)	51.9
Nickel	$2.84\text{x}10^{-4}$	Ni(II)	54.8
Sulphate	$8.54\text{x}10^{-5}$	S(VI)	49.4

Q(equivalent) = 156.1C

S^o = 82.6%(S), SO_4^{2-} = 17.4%(S)

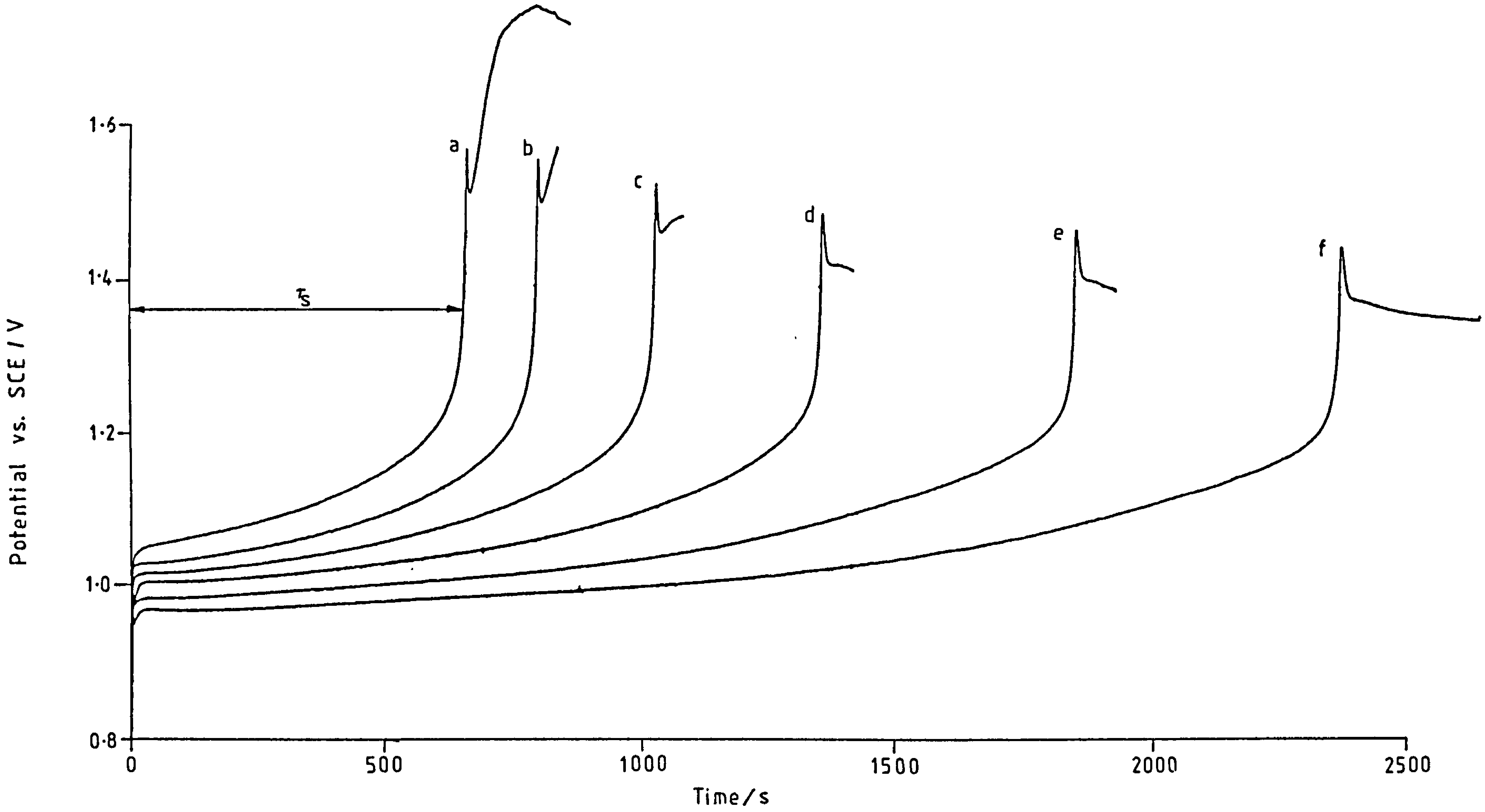

Figure 3.5.1

Chronopotentiograms for pentlandite (SynPn2b) in stirred 1M $HClO_4$ solution at 293K. Anodic polarization. Current density: (a) 100mAcm^{-2}, (b) 90mAcm^{-2}, (c) 80mAcm^{-2}, (d) 70mAcm^{-2} (e) 60mAcm^{-2}, (f) 50mAcm^{-2}.

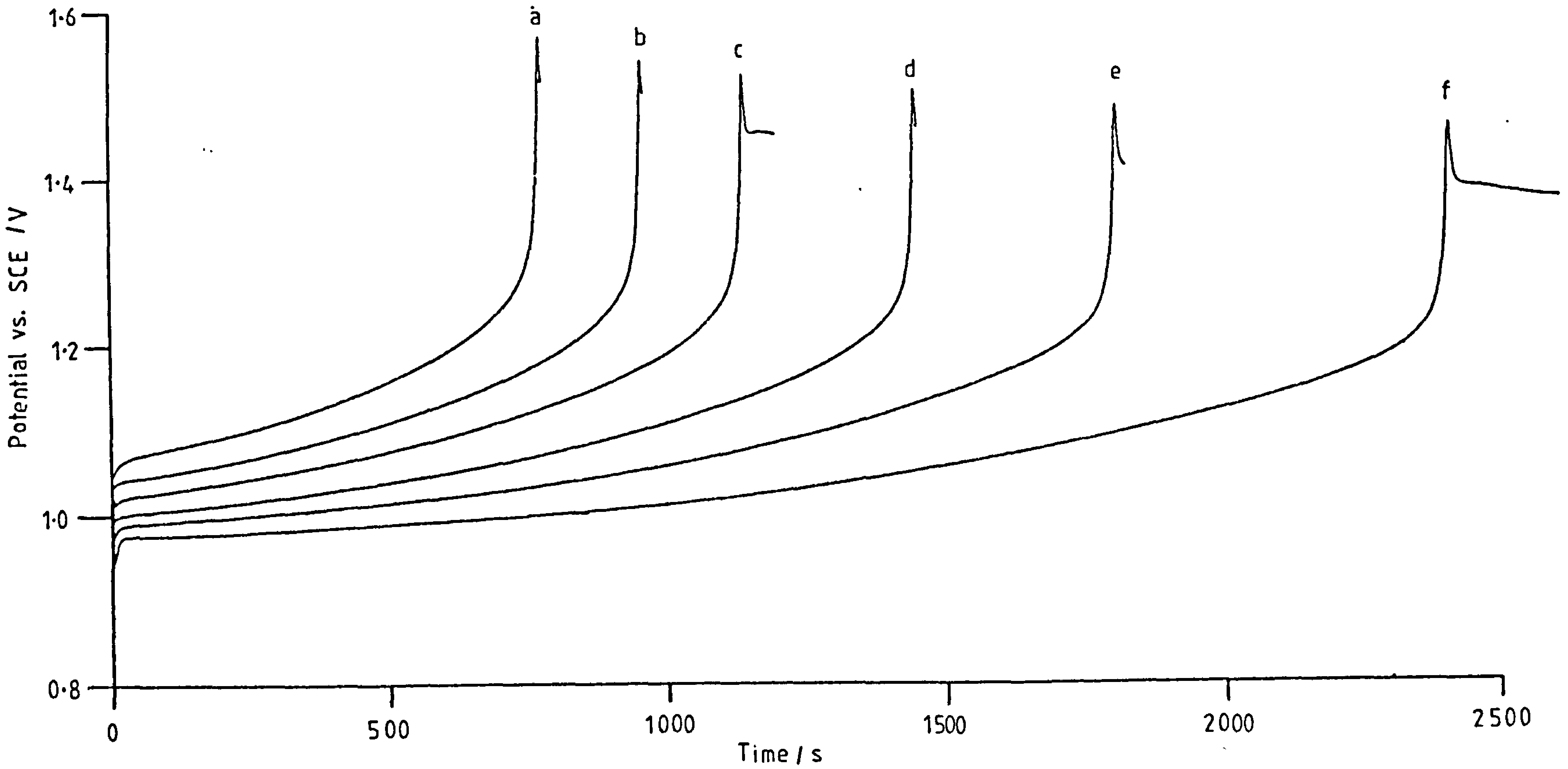

Figure 3.5.2

Chronopotentiograms for pentlandite (SynPn2b) in unstirred 1M $HClO_4$ solution at 293K. Anodic polarization. Current density: (a) $100 mAcm^{-2}$, (b) $90 mAcm^{-2}$, (c) $80 mAcm^{-2}$, (d) $70 mAcm^{-2}$ (e) $60 mAcm^{-2}$, (f) $50 mAcm^{-2}$.

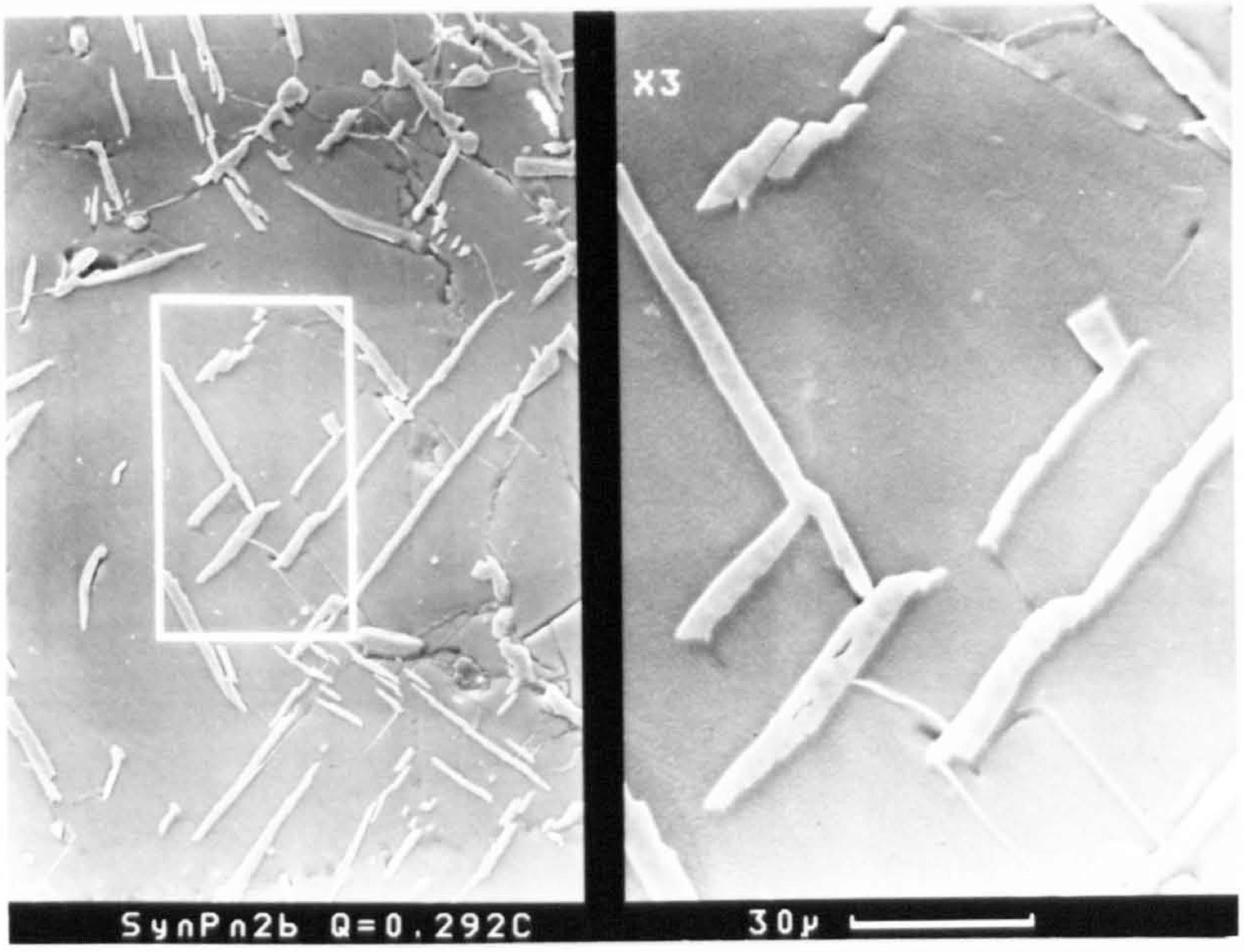

Figure 3.5.3

Scanning electron microscope (SEM) image (with a 10° tilt) of the pentlandite surface, after polarization in 1M $HClO_4$ solution at 293K, with an imposed anodic current density of $1000Am^{-2}$ for 10s. Elemental sulphur has formed preferentially along grain boundaries and along certain (octahedral ?) crystallographic planes, as portrayed by a series of parallel ridges of sulphur on the pentlandite surface (identified by EDXA).

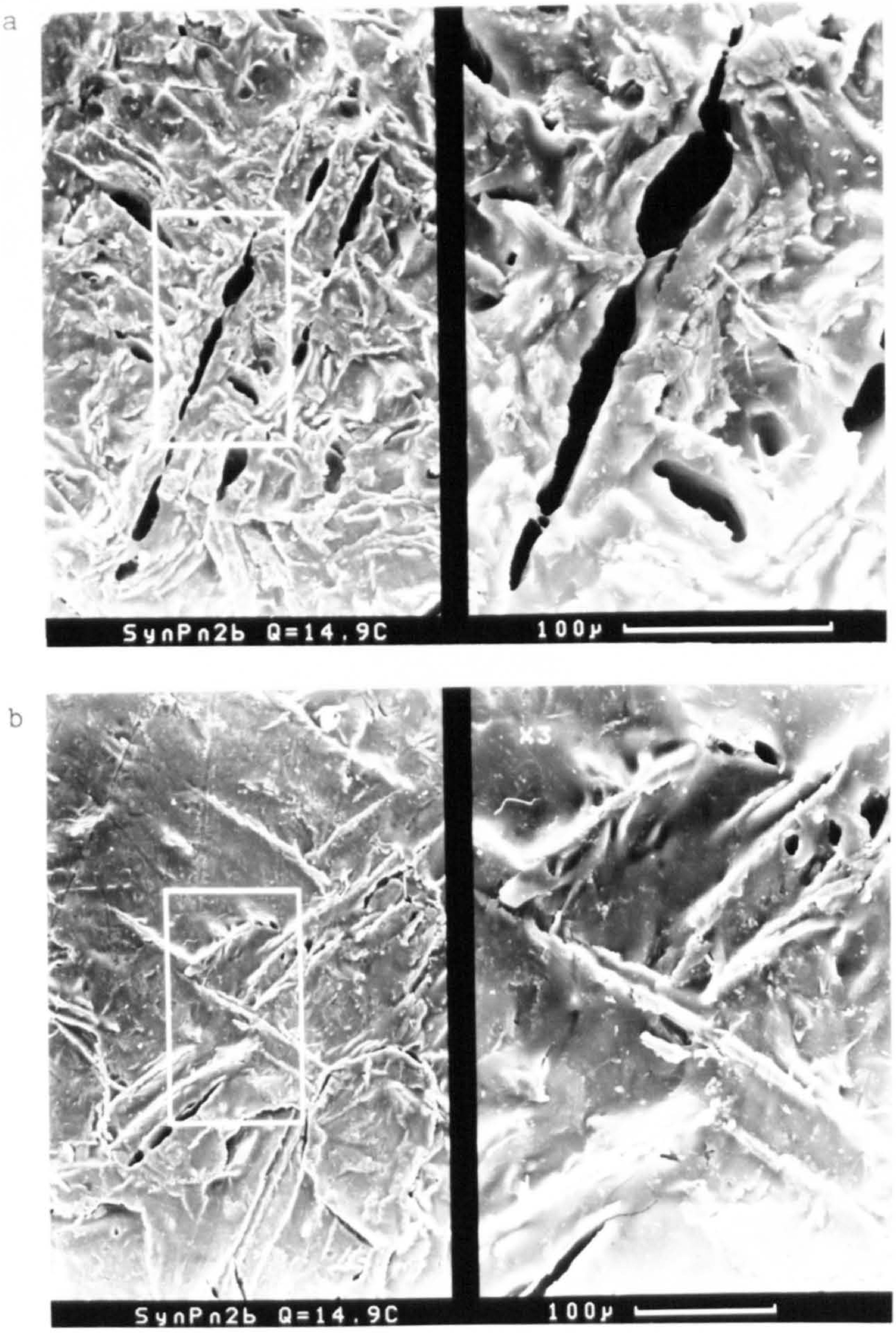

Figure 3.5.4

Scanning electron microscope (SEM) images (with 10° tilt) of the pentlandite surface after polarization in 1M $HClO_4$ solution at 293K, with an imposed anodic current density of $1000Am^{-2}$ for 527s (i.e. corresponding to just before the end of the first chronopotentiometric wave). (a) surface subsequently untreated, (b) surface subsequently washed with hot carbon disulphide, and hot tetrachloroethene.

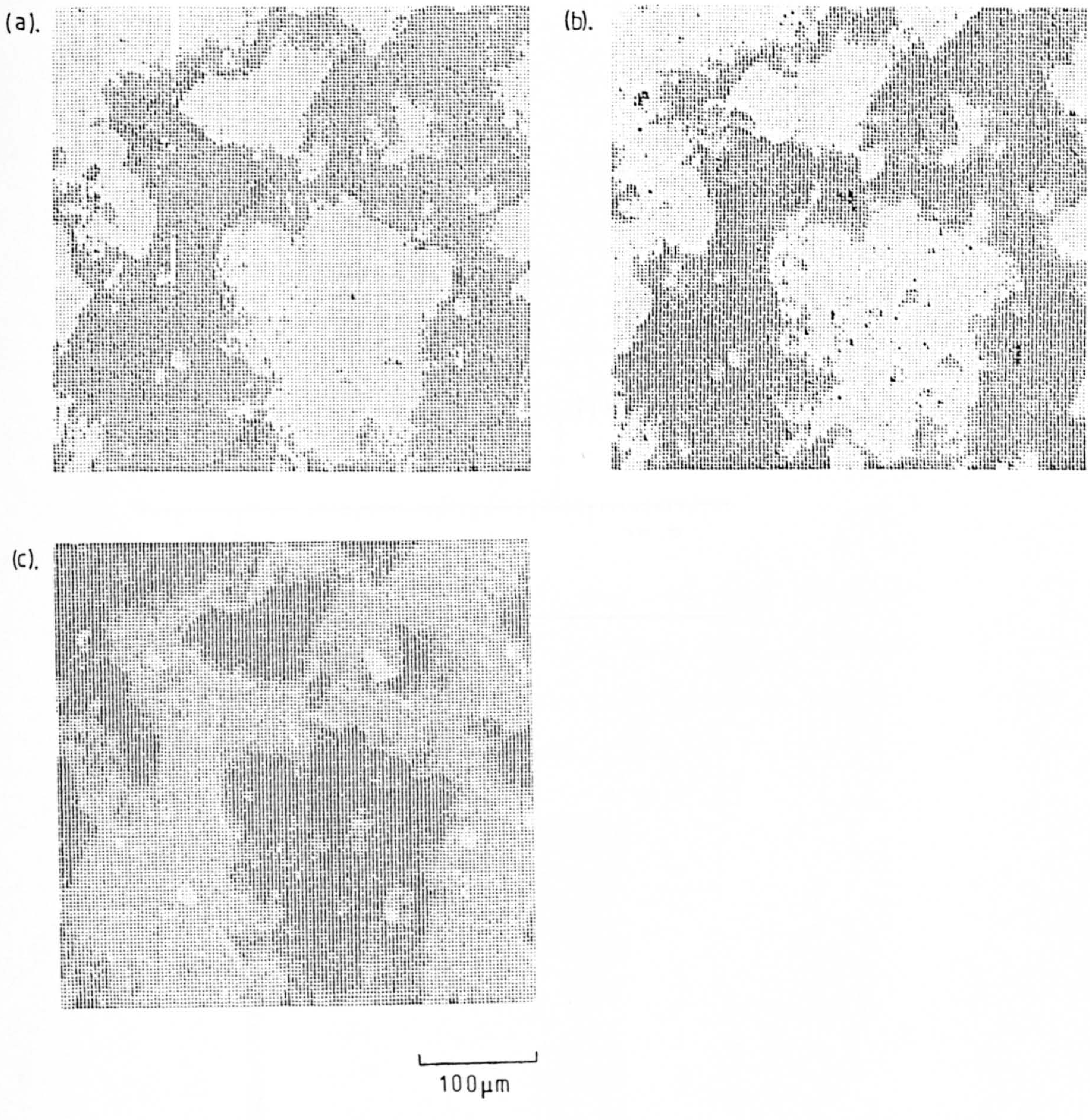

Figure 3.5.5
Electron microprobe analysis digitized maps of the pentlandite/sulphur reaction front after the first chronopotentiometric wave ($t = 648s$, $i = 100mAcm^{-2}$) in 1M $HClO_4$ solution at 293K. Specimen has been ground and polished normal to the electrode surface.(a) Ni-map, (b)Fe-map, (c) S-map. Shading is proportional to intensity.

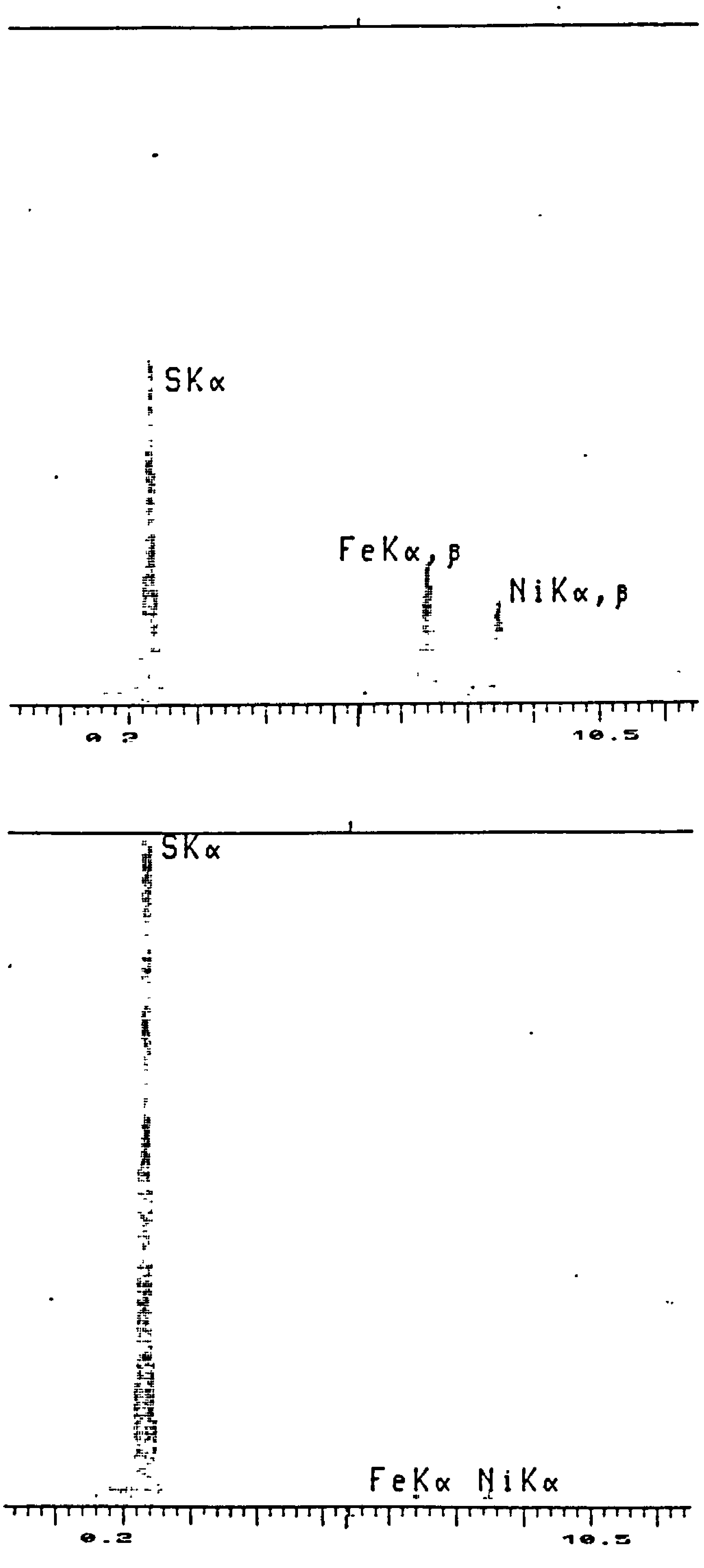

Figure 3.5.6

Electron microprobe analysis spectra of the phases present at the pentlandite/sulphur reaction front (cf. Figure 3.5.5), after the first chronopotentiometric wave ($t = 648s$, $i = 100mAcm^{-2}$) in 1M $HClO_4$ solution at 293K. Specimen has been ground and polished normal to the electrode surface. (a) Fe-Ni-S phase, (b) S-rich area.

a

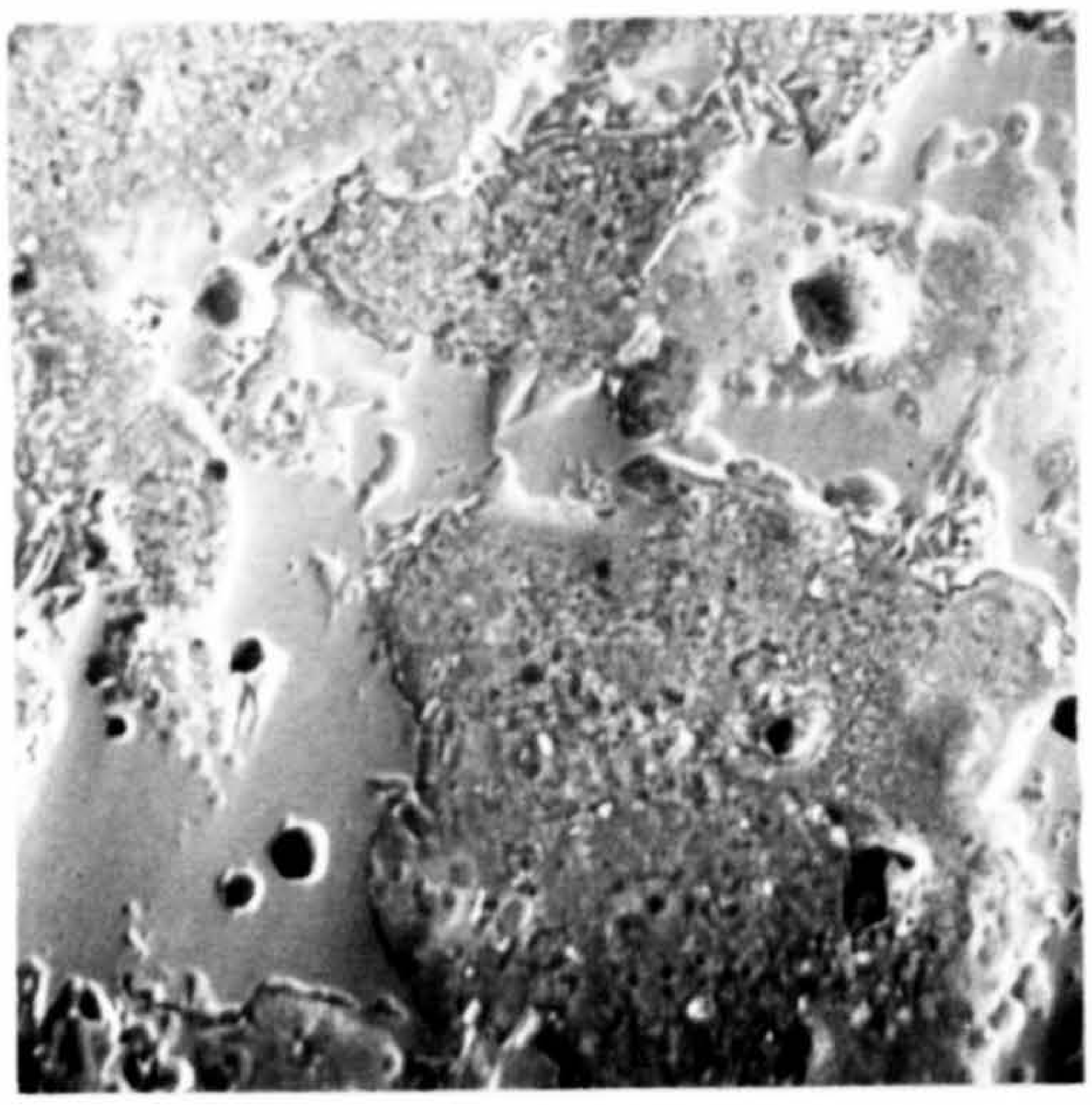

Figure 3.5.7(a)

SEM image of the pentlandite /sulphur reaction front after the first chronopotentiometric wave (t = 648s, i = 1000Am^{-2}) in 1M $HClO_4$ solution at 293K. Specimen has been ground and polished normal to the electrode surface (cf. Figure 3.5.5).

b

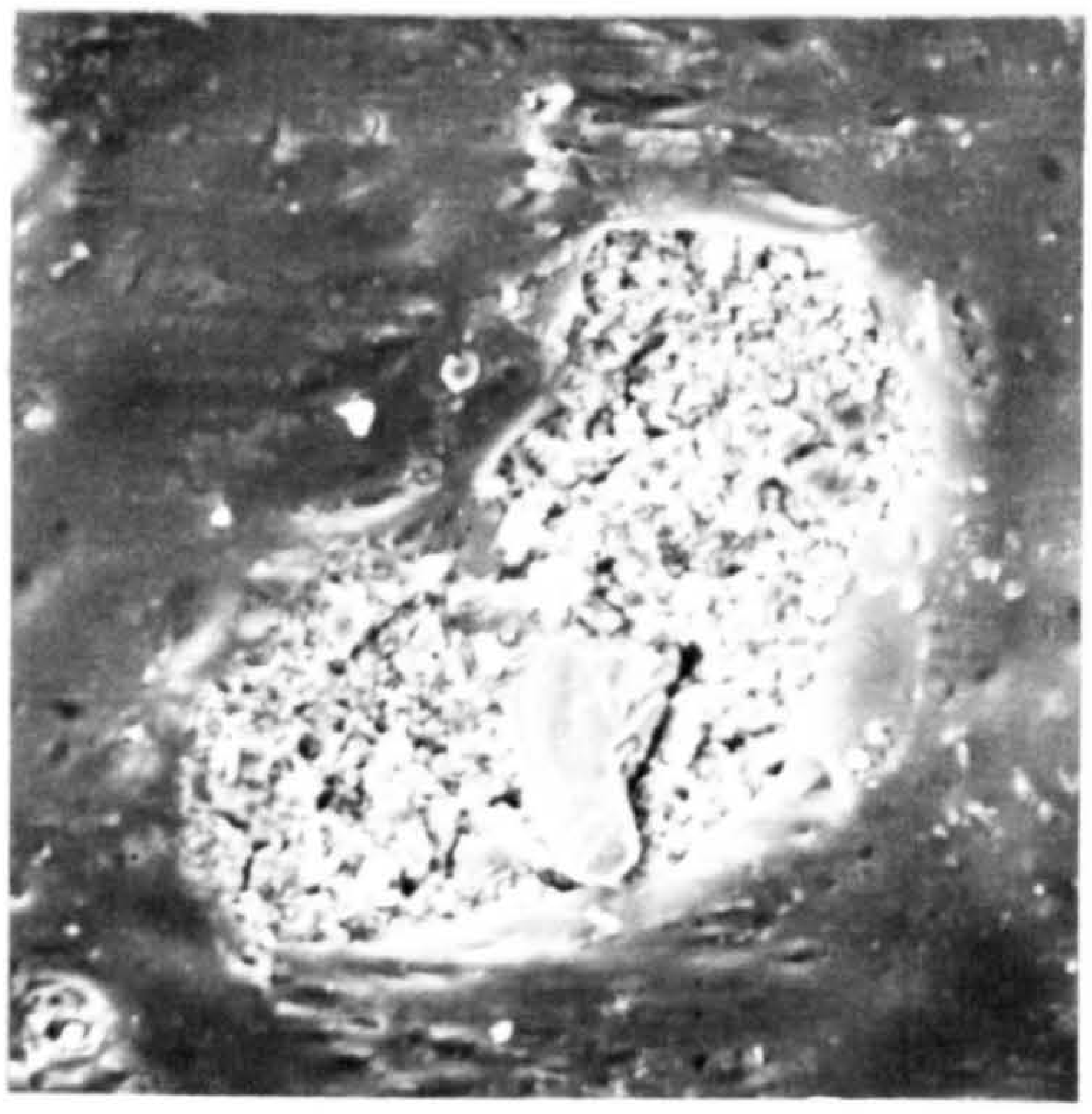

Figure 3.5.7(b)

SEM image of a tear in the sulphur film on the pentlandite surface, after anodic polarization (1000Am^{-2}, 1230s) in 1M $HClO_4$ solution at 293K. (cf. Figure 3.5.8 for EMPA).

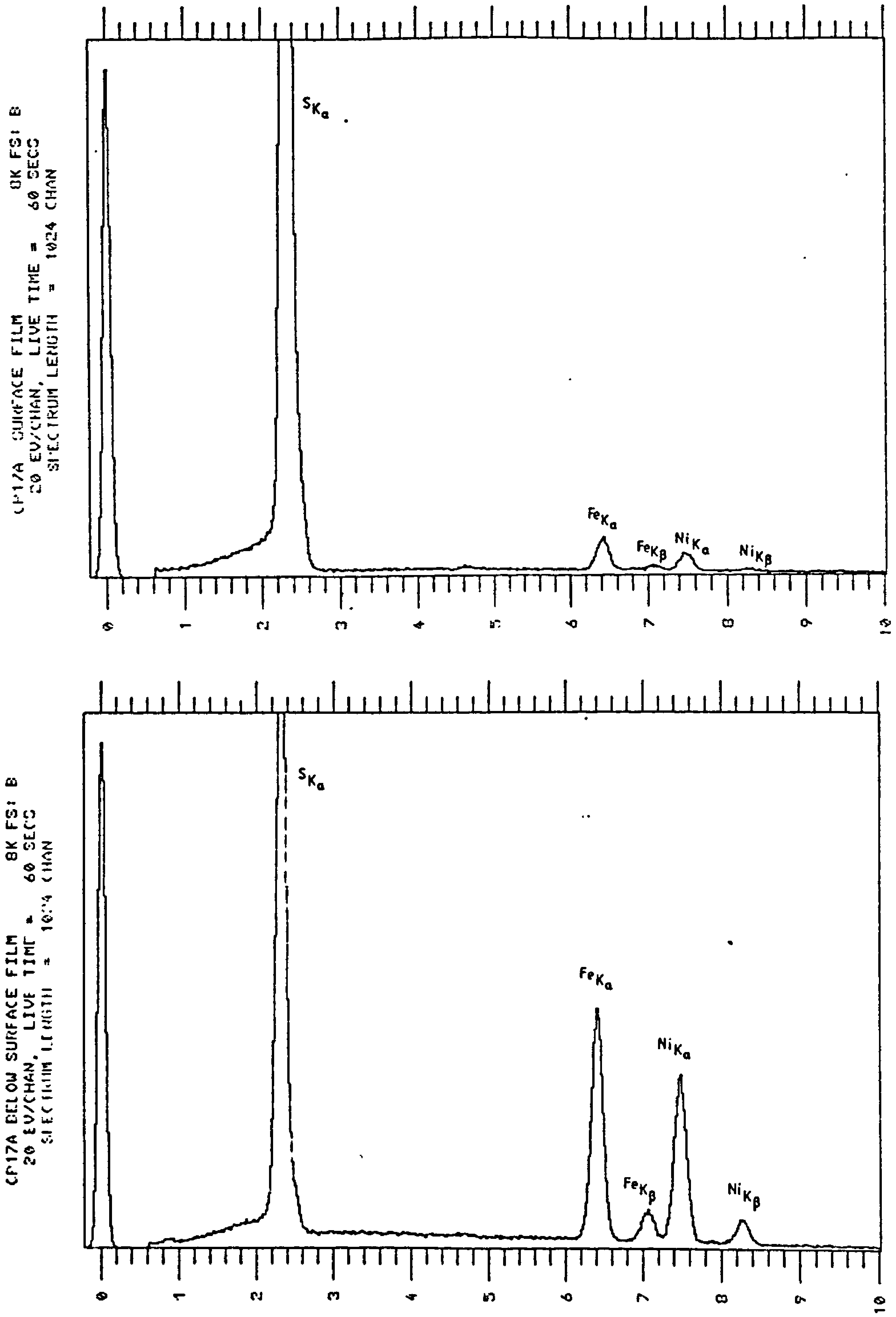

Figure 3.5.8

Electron microprobe analysis spectra of the pentlandite (SynPn2b) surface after polarization ($100mAcm^{-2}$, 1230s) in 1M $HClO_4$ solution at 293K. (a) Surface film, (b) Surface beneath a tear in the surface film.

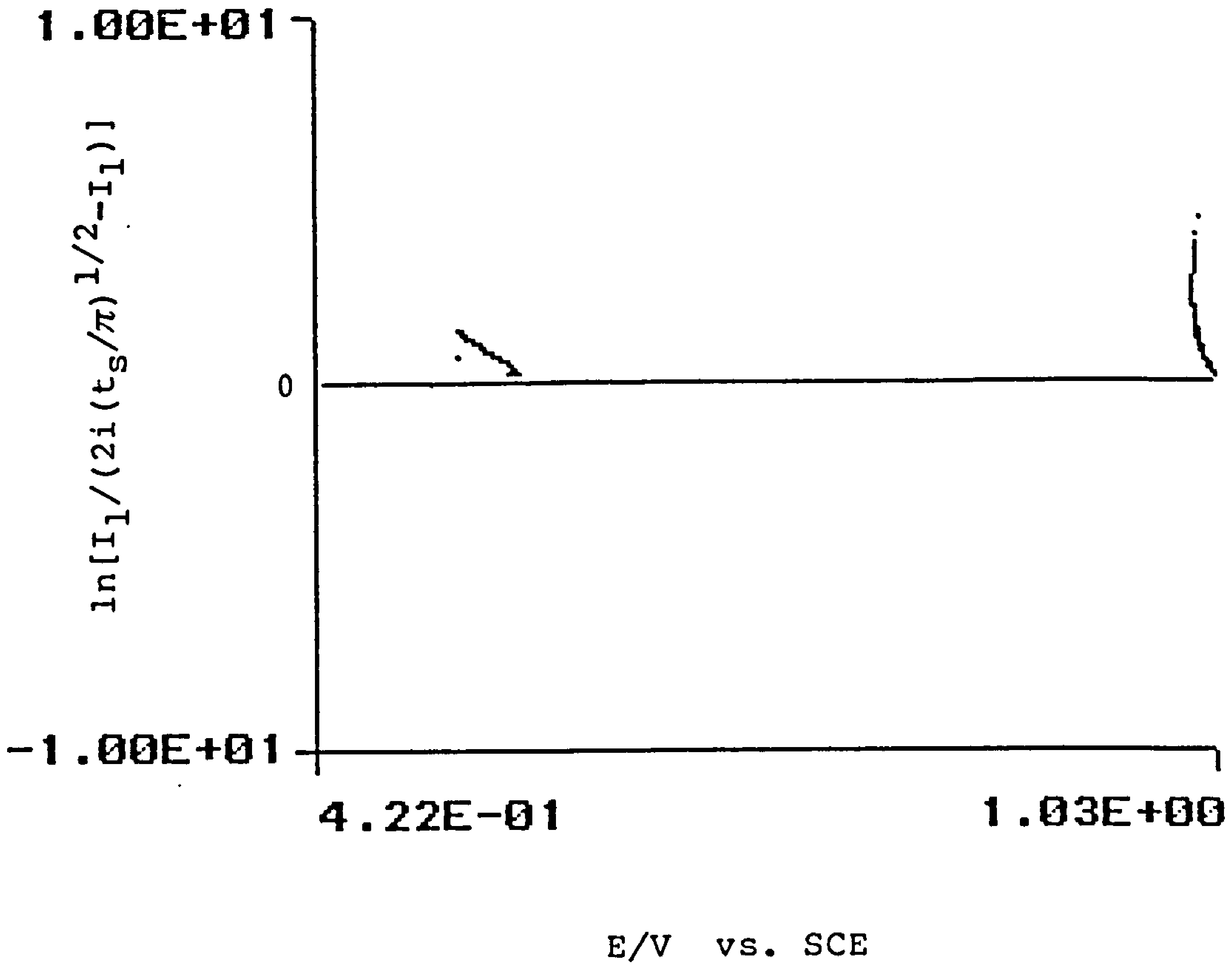

Figure 3.5.9

Plot of ln $[I_1/(2i(t_s/\pi)^{1/2}-I_1)]$ versus E vs. SCE, at 293K. I_{lim} = 2.37As$^{1/2}$ (calculated from Figure 3.5.1 for the chronopotentiometric wave: i = 0.0628A, t_s = 1116s, electrode area = 7.85x10^{-5}m^2). Closed-circuit = 250s, open-circuit = 200s.

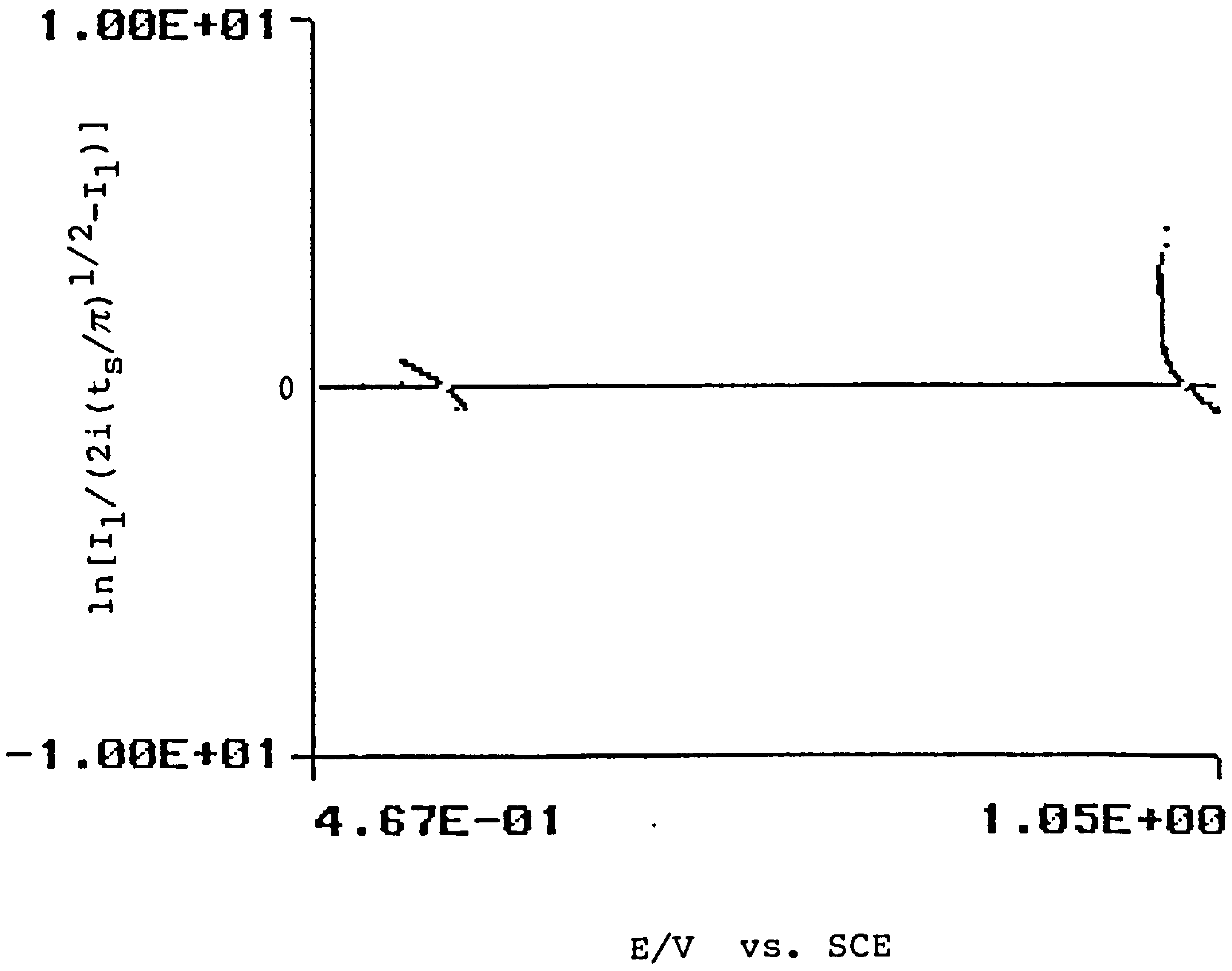

Figure 3.5.10

Plot of $\ln[I_1/(2i(t_s/\pi)^{1/2}-I_1)]$ versus E vs. SCE, at 293K. $I_{lim} = 2.37As^{1/2}$ (calculated from Figure 3.5.1 for the chronopotentiometric wave: $i = 0.0628A$, $t_s = 1116s$, electrode area = $7.85\times10^{-5}m^2$). Closed-circuit = 500s, open-circuit = 200s.

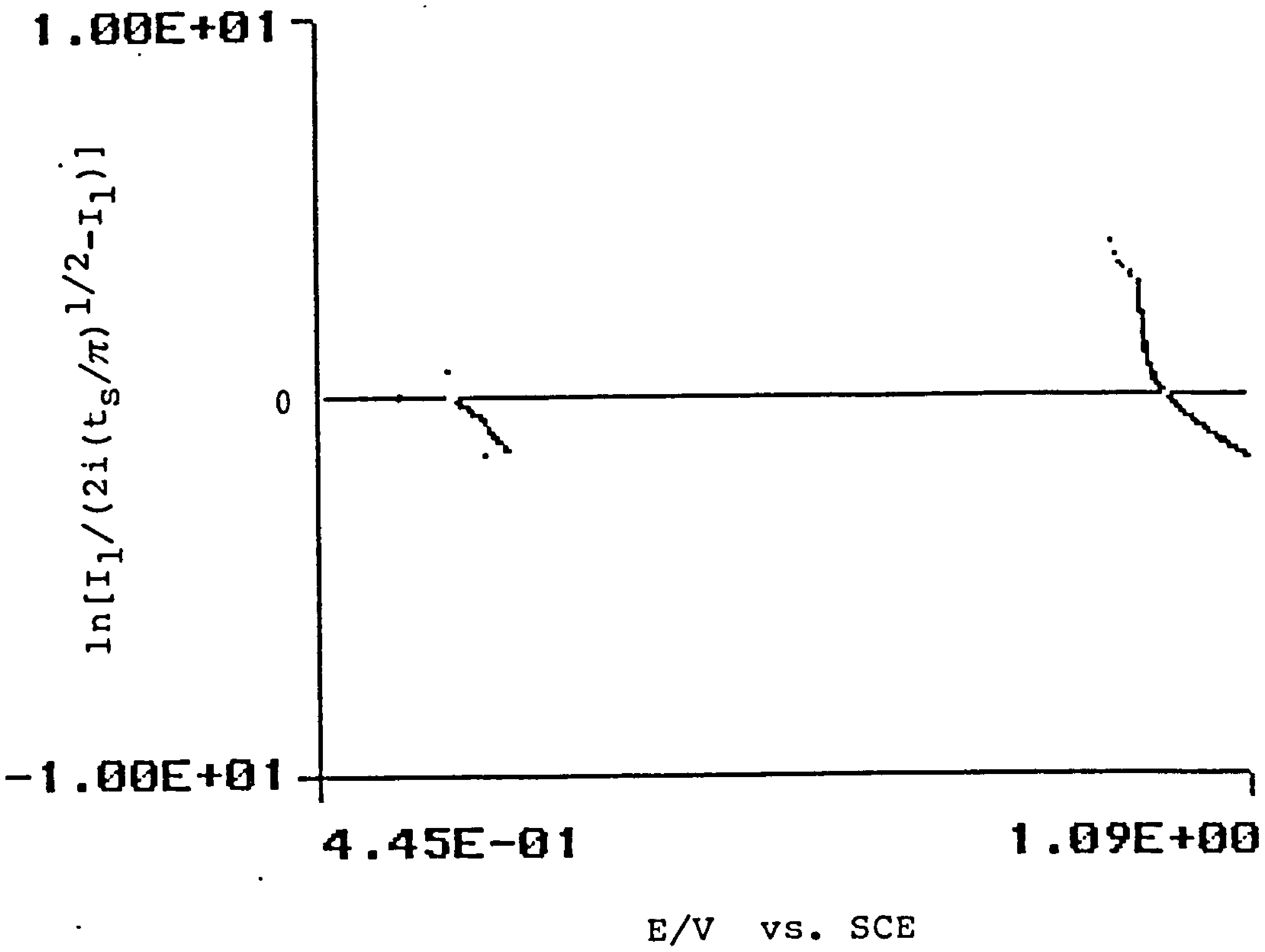

Figure 3.5.11

Plot of ln $[I_1/(2i(t_s/\pi)^{1/2}-I_1)]$ versus E vs. SCE, at 293K. I_{lim} = 2.37As$^{1/2}$ (calculated from Figure 3.5.1 for the chronopotentiometric wave: i = 0.0628A, t_s = 1116s, electrode area = 7.85x10^{-5}m^2). Closed-circuit = 750s, open-circuit = 200s.

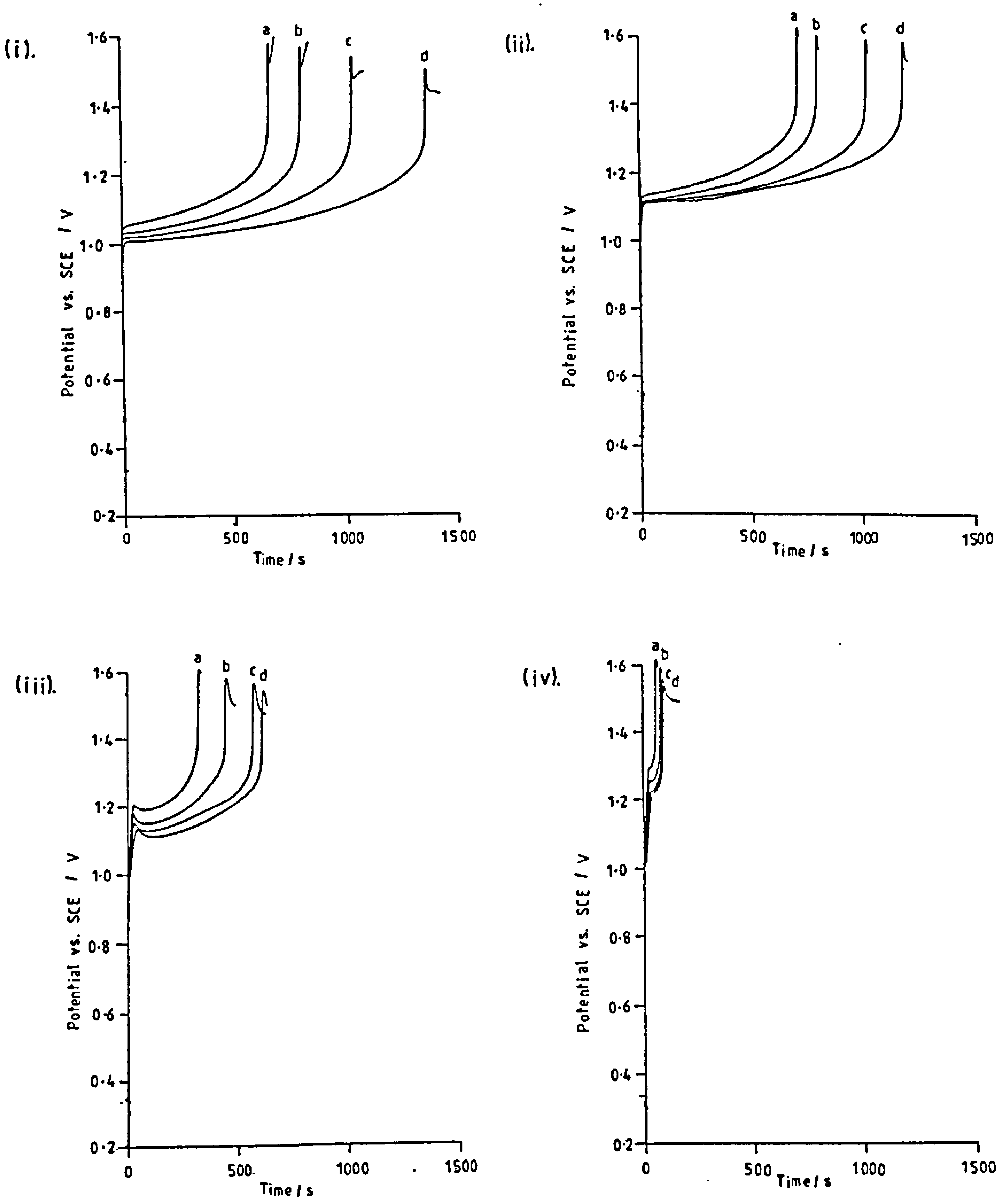

Figure 3.5.12

Chronopotentiograms for pentlandite (SynPn2b) in 1M $HClO_4$ solution. RDE 20Hz. Temperature: (i) 293K, (ii) 298K, (iii) 303K, (iv) 308K. Anodic polarization. Current density: (a) $100mAcm^{-2}$, (b) $90mAcm^{-2}$, (c) $80mAcm^{-2}$, (d) $70mAcm^{-2}$.

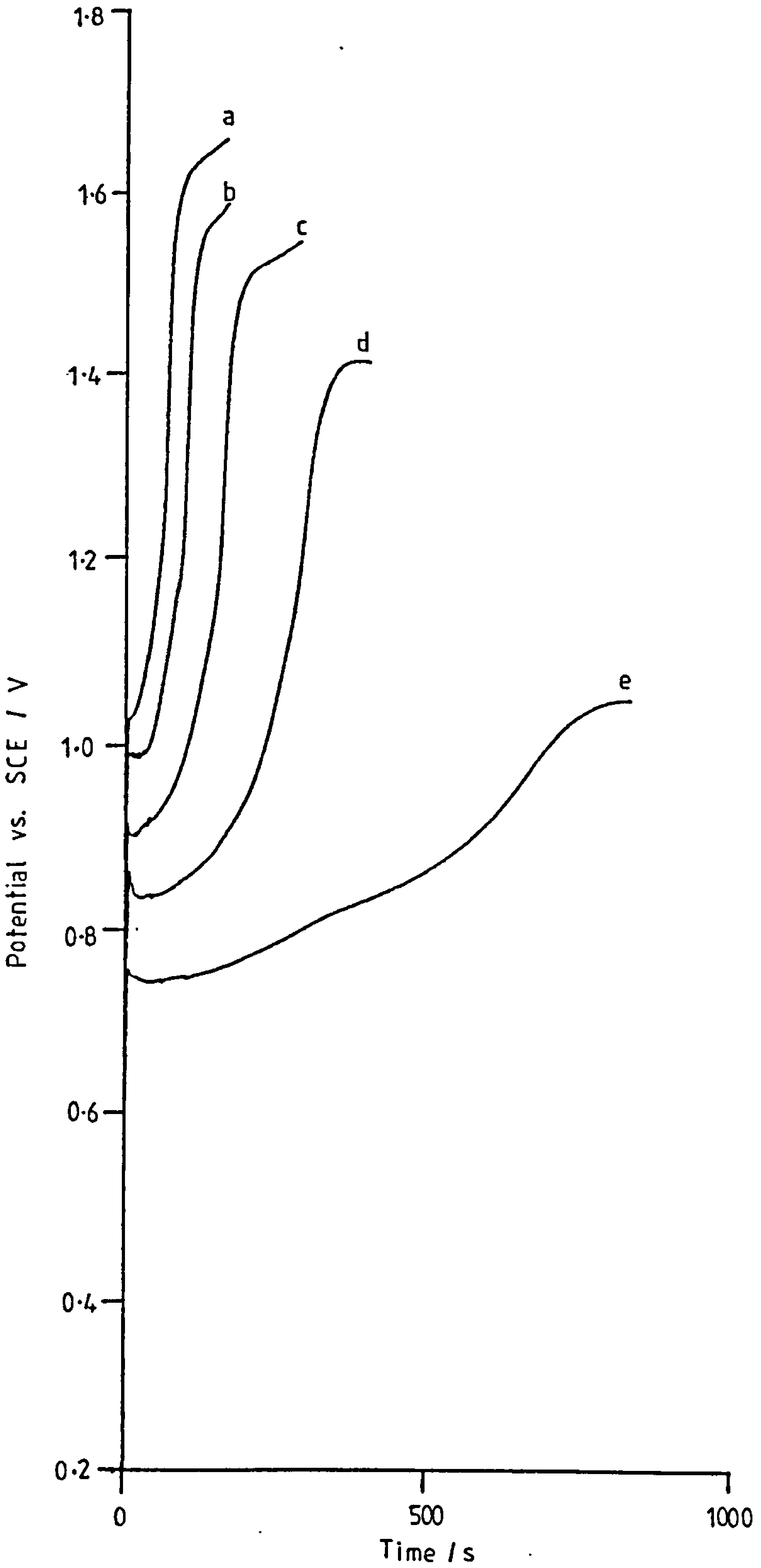

Figure 3.5.13

Chronopotentiograms for pentlandite (SynPn2b) in stirred 1M $HClO_4$ solution at 343K. Anodic polarization. Current density: (a)50mAcm^{-2}, (b)40mAcm^{-2}, (c)30mAcm^{-2}, (d)20mAcm^{-2}, (e)10mAcm^{-2}.

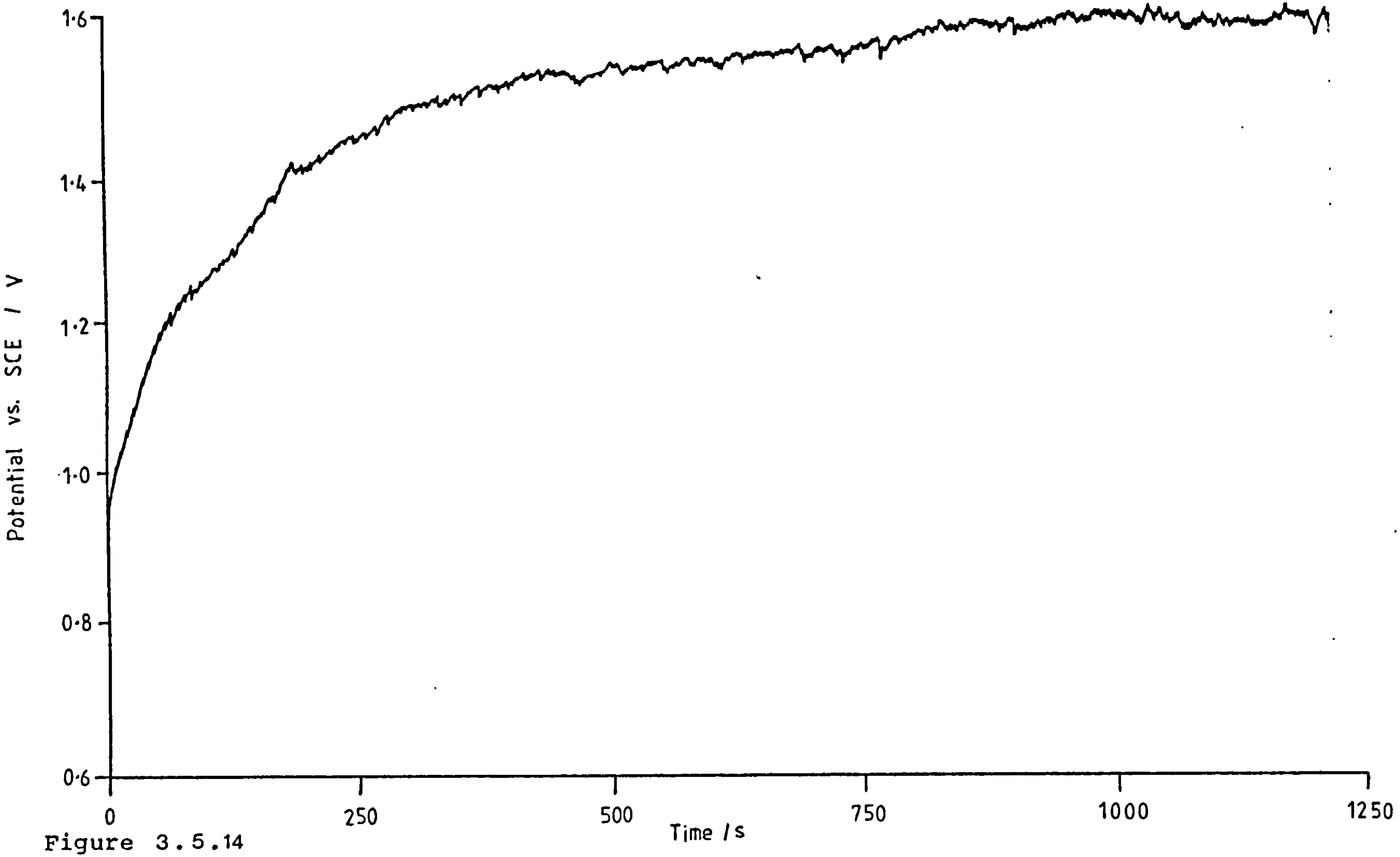

Figure 3.5.14

Chronopotentiogram for pentlandite (SynPn3) in stirred 1M $HClO_4$ solution at 343K. Anodic polarization. Current density $50mAcm^{-2}$

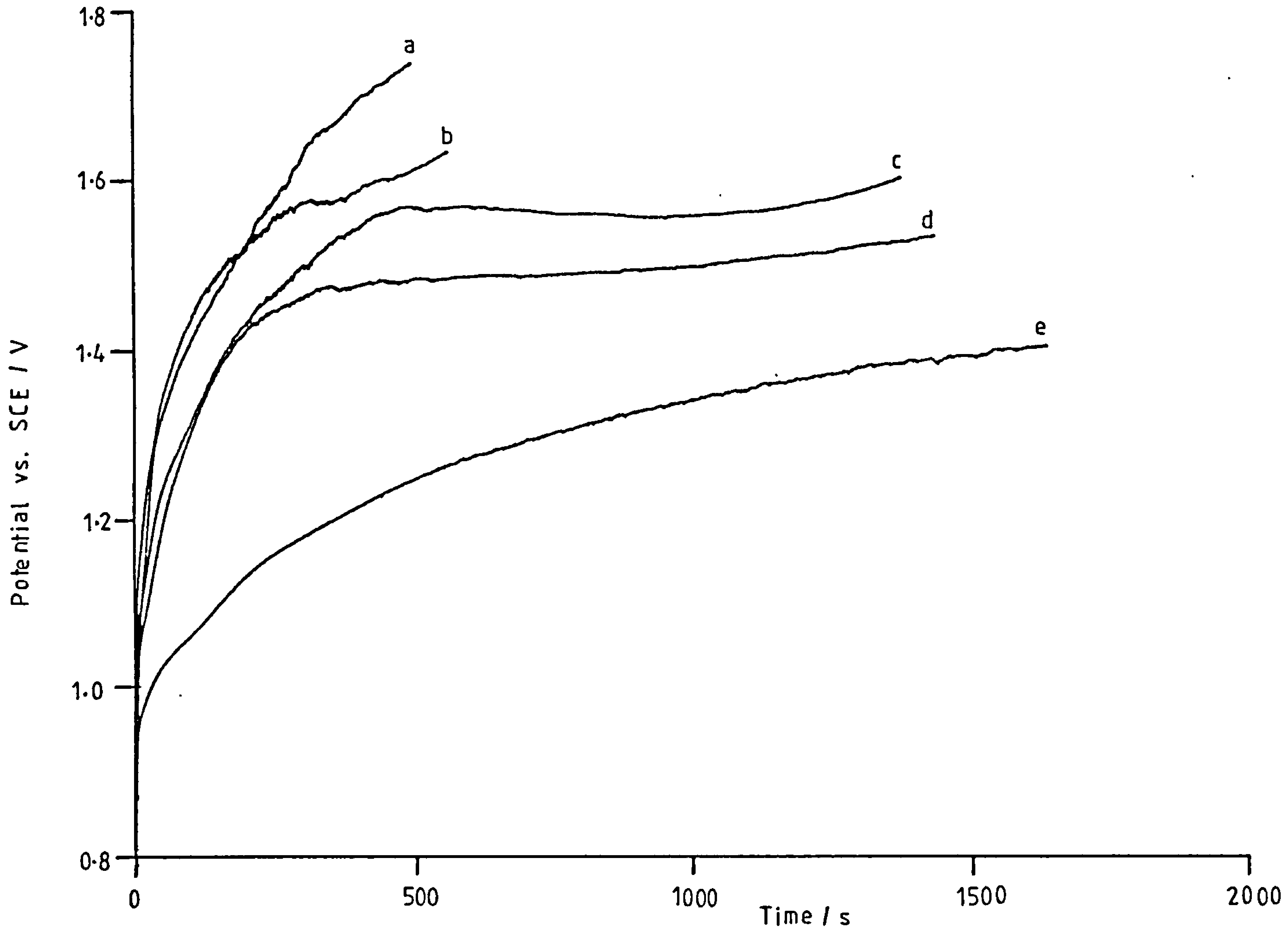

Figure 3.5.15

Chronopotentiograms for pentlandite (SynPn2b) in stirred 1M HCl solution at 293K. Anodic polarization. Current density: (a)50mAcm^{-2}, (b)40mAcm^{-2}, (c)30mAcm^{-2}, (d)20mAcm^{-2}, (e)10mAcm^{-2}

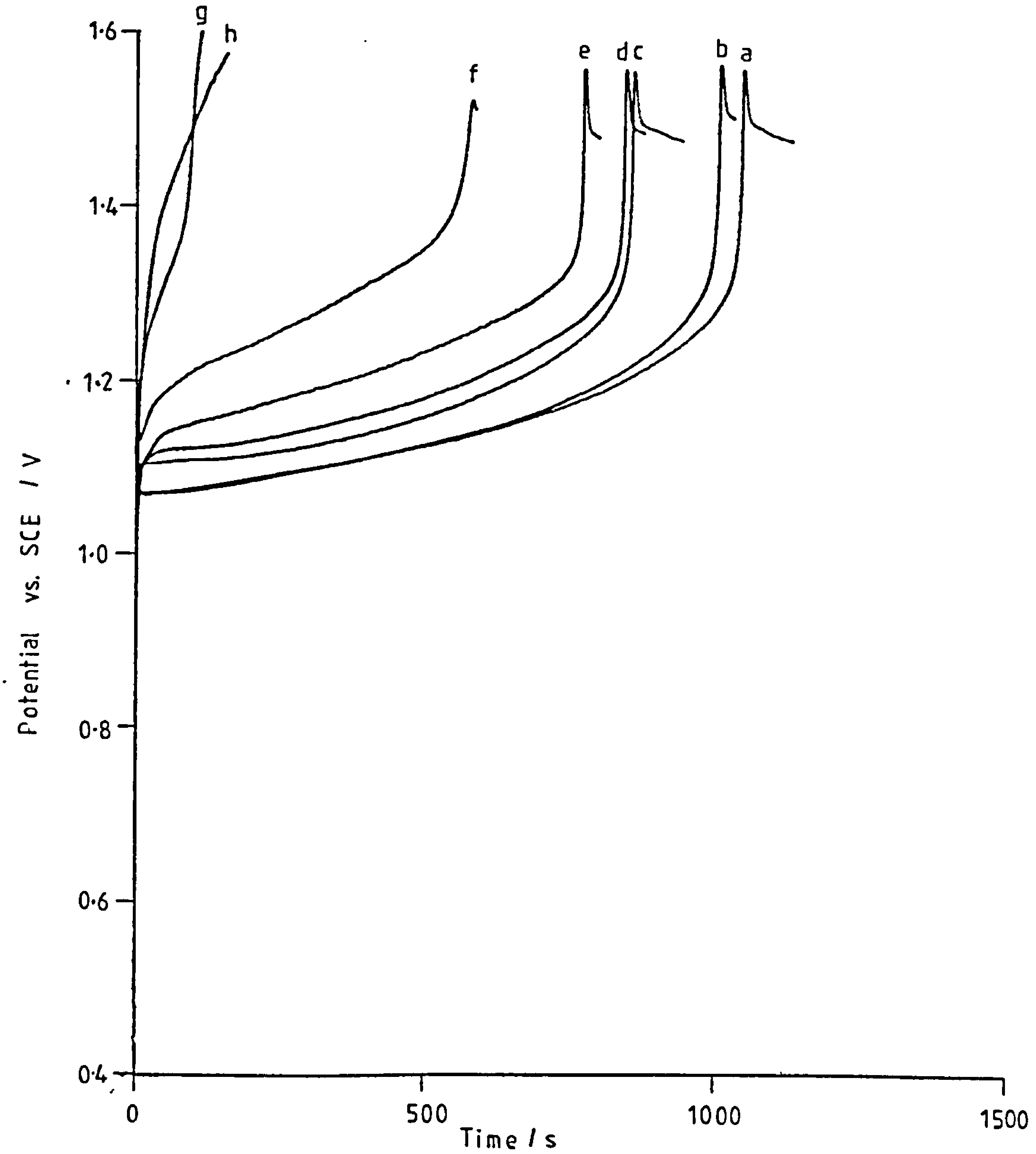

Figure 3.5.16

Chronopotentiograms for pentlandite (SynPn2b) in stirred 1M $HClO_4$/HCl solution at 293K. Current density $80mAcm^{-2}$. Effect of chloride addition on reducing the transition time. Volume percentages of 1M HCl: (a)0%, (b)1%, (c)5%, (d)9%, (e)17%, (f)33%, (g)50%, (h)100%.

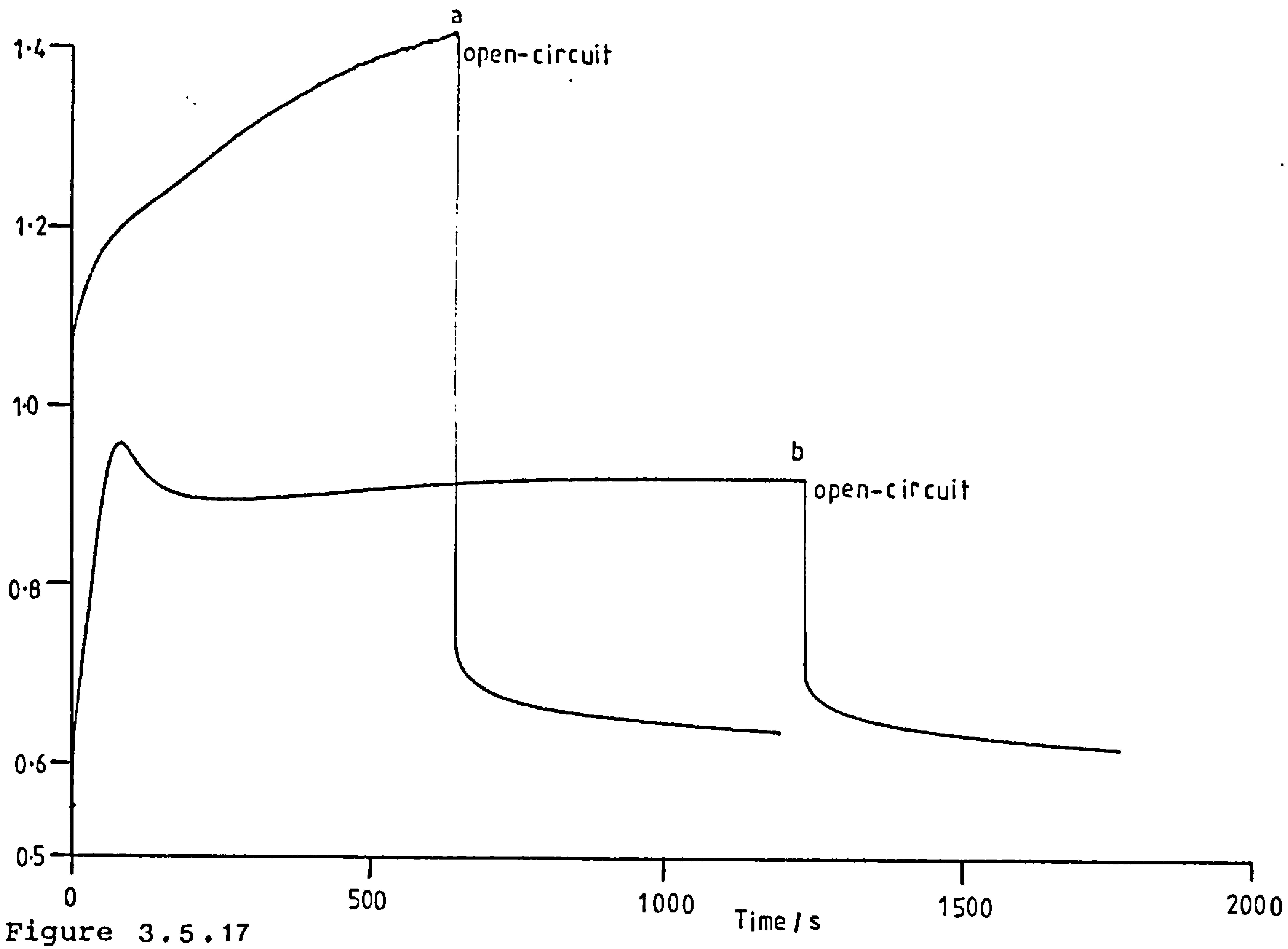

Figure 3.5.17

Chronopotentiograms for pentlandite (SynPn2b) in stirred 1M HCl solution at 293K. Anodic polarization. Current density: (a) 10mAcm^{-2}, (b) 1mAcm^{-2}; followed by period in open-circuit.

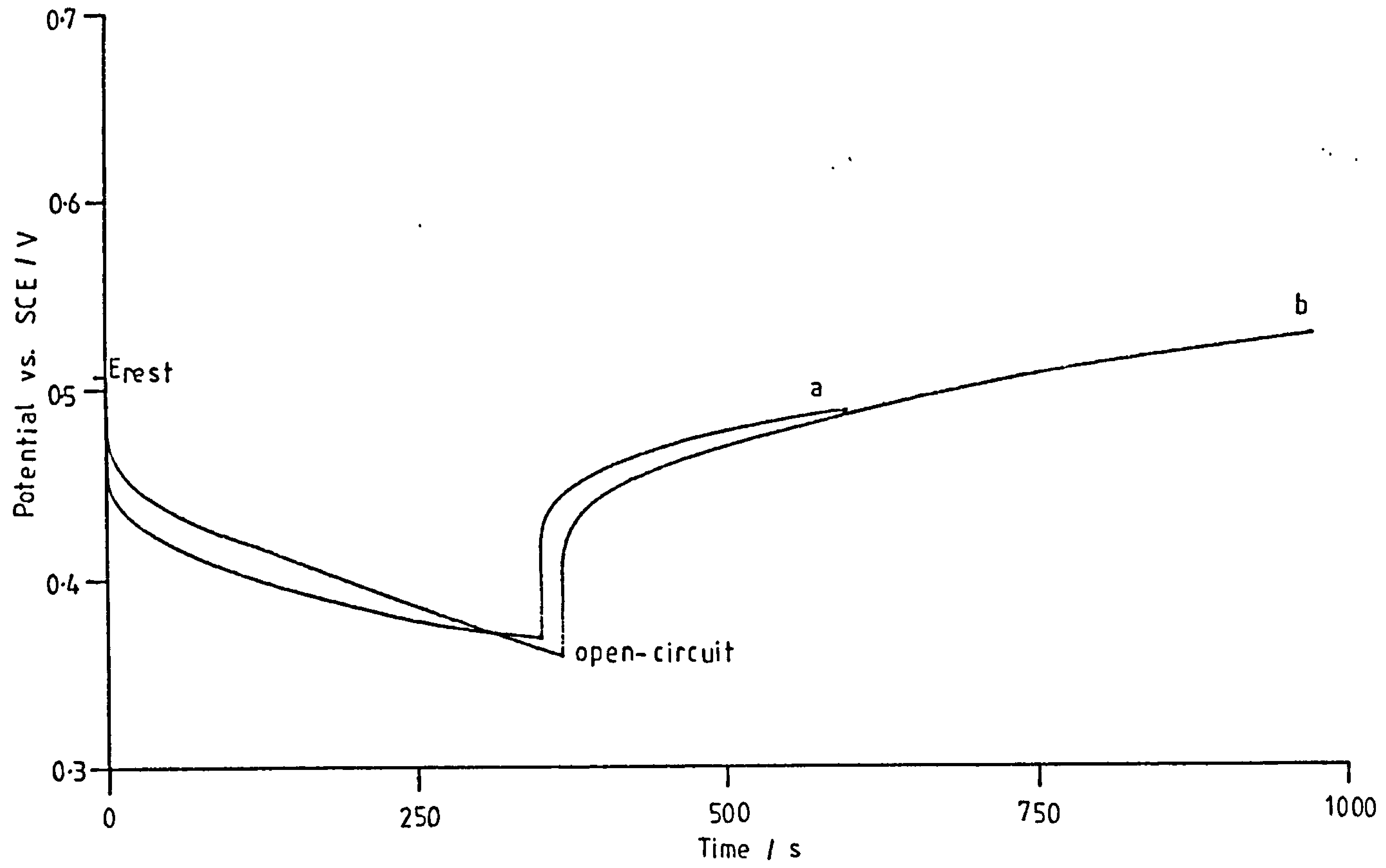

Figure 3.5.18

Chronopotentiograms for (a) pentlandite, (b) platinum, in 0.1M $FeCl_3$/1M HCl solution at 293K. RDE 20Hz. Cathodic polarization. Current density: $1mAcm^{-2}$, followed by open-circuit at approximately $E_{1/2}(Fe^{3+}/Fe^{2+})$.

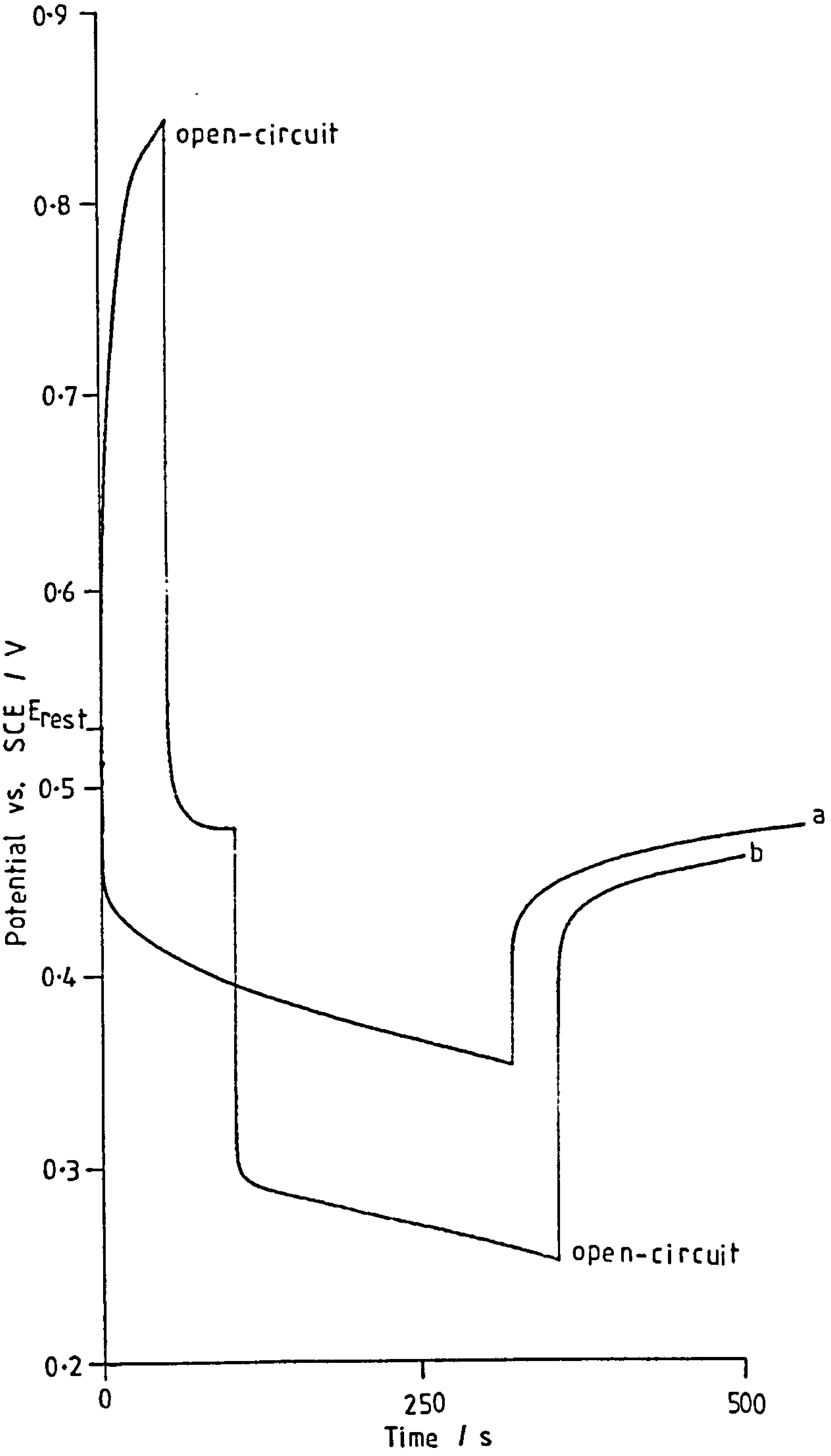

Figure 3 . 5 . 19

Chronopotentiograms for pentlandite in 0.1M $FeCl_3$/1M HCl solution at 293K. RDE 20Hz. (a) Cathodic polarization $1mAcm^{-2}$ followed by period in open-circuit. (b) Anodic polarization ($1mAcm^{-2}$) followed by period in open-circuit, followed by cathodic polarization ($1mAcm^{-2}$) followed by open-circuit.

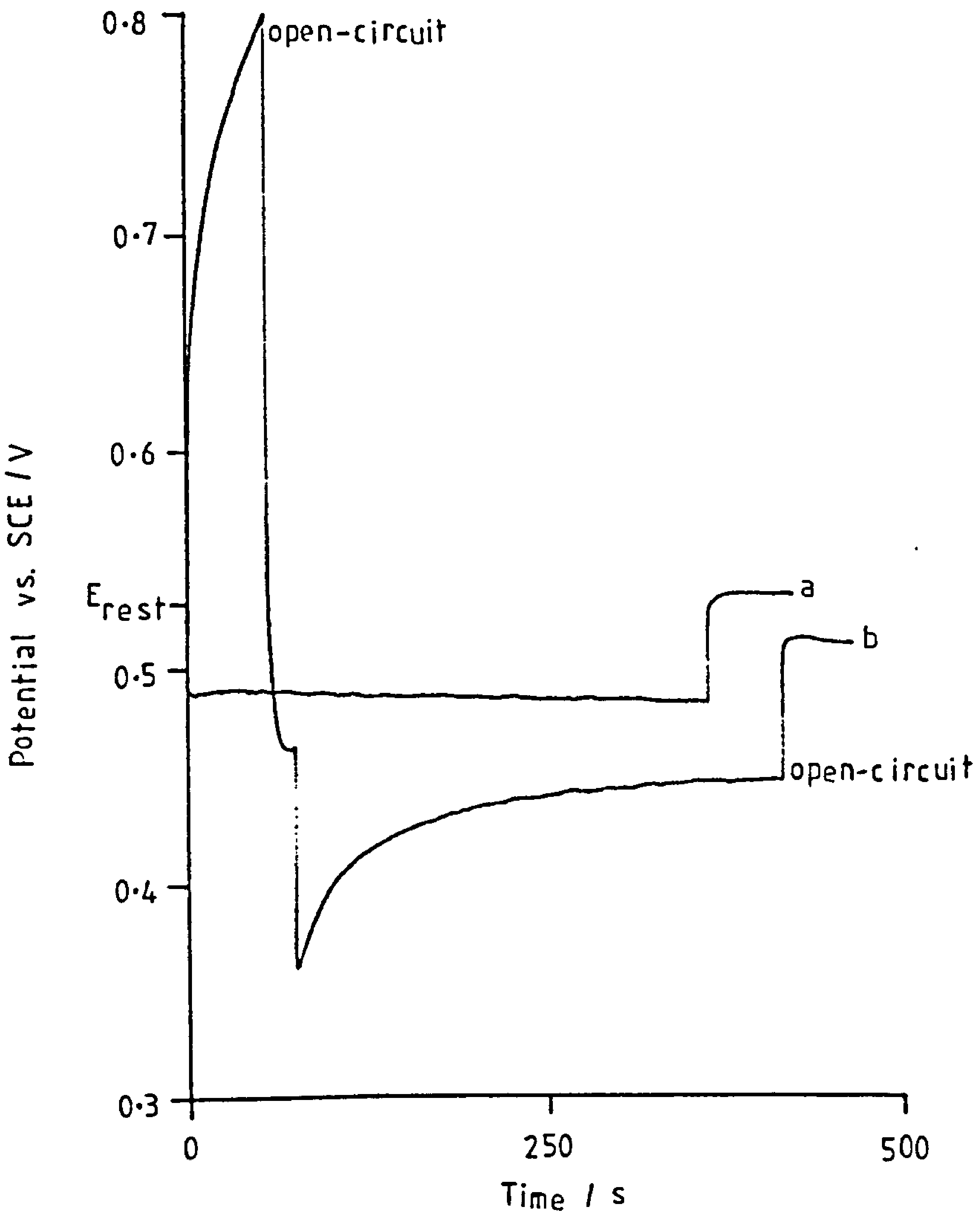

Figure 3.5.20

Chronopotentiograms for pentlandite in 0.1M $FeCl_3$/1M HCl solution at 343K. RDE 20Hz. (a) Cathodic polarization $1mAcm^{-2}$ followed by period in open-circuit. (b) Anodic polarization ($1mAcm^{-2}$) followed by period in open-circuit, followed by cathodic polarization ($1mAcm^{-2}$) followed by open-circuit.

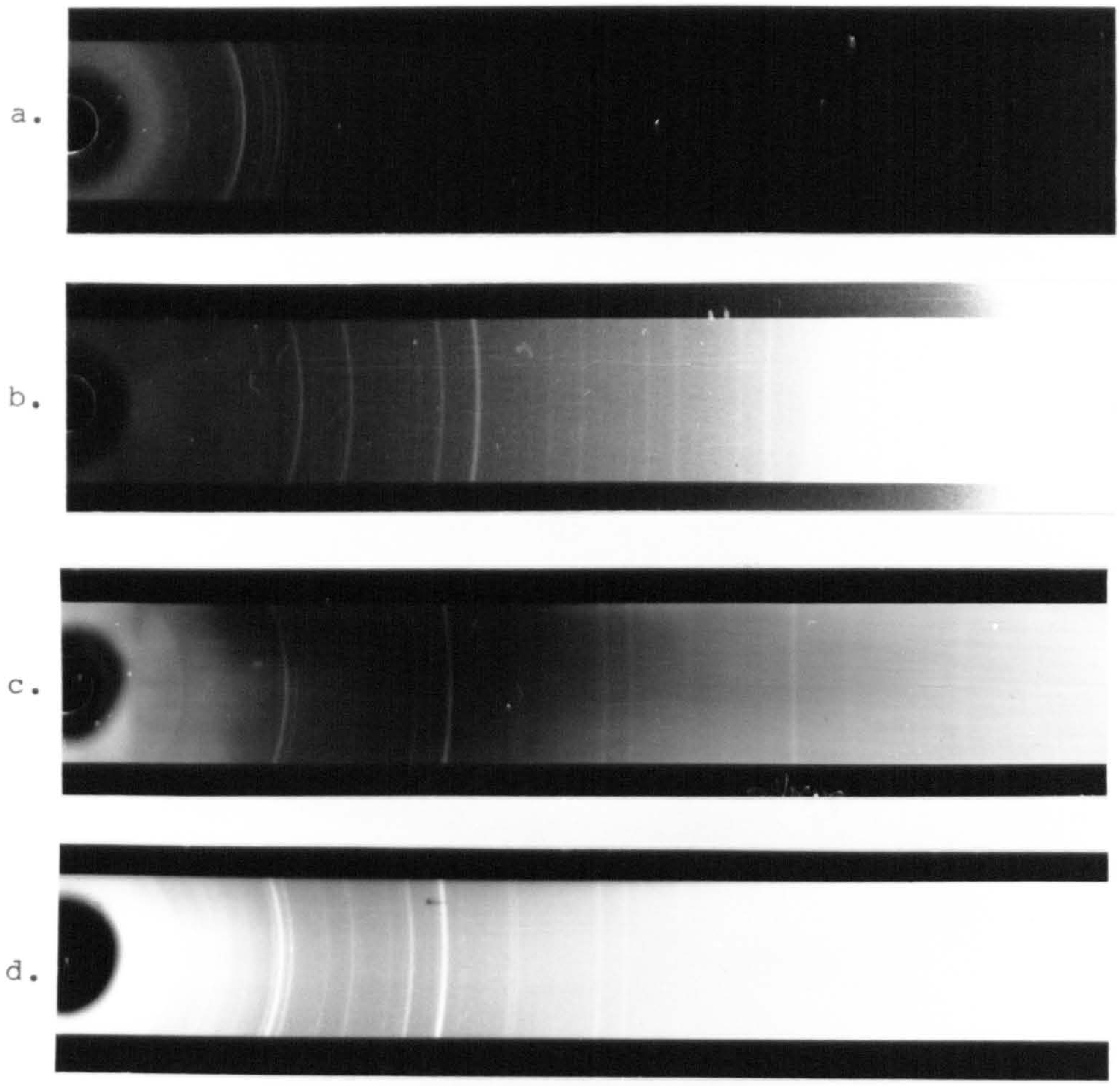

Figure 3.5.21

Siemens Kristalloflex 2 powder camera photographs of the product layer from the electrolysis of pentlandite in 1M $HClO_4$ (cf. Appendix D.6), for "fingerprint" comparison with known specimens of orthorhombic sulphur, pentlandite and violarite. These photographs indicate that the product layer contains unreacted pentlandite, but is devoid of orthorhombic sulphur and violarite.

a. Orthorhombic sulphur

b. Synthetic violarite

c. Synthetic pentlandite

d. Product layer material

3.6 CHRONOAMPEROMETRY

3.6.1 Pentlandite

Chronoamperometry was performed on pentlandite primarily to compare and confirm the conclusions drawn from the earlier voltammetric studies within this work.

Figures 3.6.1 to 3.6.5 show chronoamperograms for pentlandite in 1M HCl and 1M $HClO_4$ solution at temperatures within the range 293 to 353K. The reader may wish to compare the chronoamperograms at 293K in Figure 3.6.1 with the corresponding chronopotentiograms at the same temperature in 1M $HClO_4$ and 1M HCl solution, as shown in Figures 3.5.1 and 3.5.15 respectively (cf. Section 3.5). This comparison is important for the reasons described in Section 2.2.0 et seq.

The chronoamperograms for pentlandite in 1M $HClO_4$ solution at 293K show that reasonably large current densities (100 to 1700Am^{-2}) are sustained within the potential range 0.9 to 1.1 V vs. SCE, which tallies with the potentials obtained during the first chronopotentiometric wave at imposed current densities within the range 500 to 1000Am^{-2}. However, these chronoamperograms show non-Cottrell behaviour, which is consistent with the conclusions drawn in Section 3.5, in which it was shown that the Sand equation does not apply to this system. Furthermore, at temperatures >293K, these reasonably large current densities are no longer observed, which corresponds with the decrease in the transition time (t_s), and with the eventual disappearance of the first chronopotentiometric wave at higher potentials (cf. Figure 3.5.12).

The chronoamperograms for pentlandite in 1M HCl solution show that large anodic potentials are required in order to maintain an appreciable current density; which is in agreement with the results from chronopotentiometry (viz. Figure 3.5.15). Likewise, increasing the temperature results in larger current densities. Figure 3.6.10 shows SEM images of the electrode surface after polarization for 1260s at 2.2V vs. SCE in 1M HCl solution at 343K. The pentlandite surface was covered with elemental sulphur (confirmed by EDXA). The SEM images clearly reveal the amorphous nature of the sulphur product layer. One of the most striking features is the occurance of "strings" of sulphur, which appear to be growing from within the product layer. The surface also contains many pores, although their depth is unknown.

Figures 3.6.6 to 3.6.9 show chronoamperograms for pentlandite in the potential range relevant to ferric chloride leaching. These portray an initial rapid decay of current, followed by a tendency towards a steady state regime. At 293K the steady state currents increased pro rata with potential. However, at 343K, a partial reverse of this trend was observed, with substantial currents occuring in the low potential region of 0.2 to 0.3V vs. SCE. The anodic currents within this potential range are attributed to the oxidative dissolution of pentlandite accompanied with the formation of H_2S (cf. Sections 3.1 and 3.2.1, and Equation 3.1.1).

$$4.5Fe^{2+} + 4.5Ni^{2+} + 8H_2S + 2e = Fe_{4.5}Ni_{4.5}S_8 + 16H^+ \qquad (3.1.1)$$

The magnitude of these anodic currents alone, suggest that the oxidative dissolution of pentlandite at high potentials (with the formation of elemental sulphur), is kinetically more difficult than the alternative mechanism at lower potentials (with the formation of H_2S). Indeed, the small values for the steady state current density (viz. 8Am^{-2} in 1M HCl at 0.6V vs. SCE; and 5Am^{-2} in 1M $HClO_4$ at 0.6V vs. SCE), indicate that the exchange current density is small, and therefore suggests a slow electron transfer for the oxidative dissolution of pentlandite to elemental sulphur.

Unfortunately, the electrochemical kinetic parameters for this process are unobtainable from a Tafel plot of this data, since pentlandite is metastable in acid solution (cf. Section 1.5.2) and therefore an "equilibrium" potential for the Fe^{2+},Ni^{2+},S^o / $Fe_{4.5}Ni_{4.5}S_8$ couple does not exist. However, even if one adopts a "metastable" equilibrium potential (viz. approximately -0.2V vs. SCE (298K) cf. Figure 1.5.4), the system is further complicated by the occurance of the alternative oxidative mechanism (with the formation of H_2S) which predominates in this low potential region (viz.E_{rest} = -0.224V vs.SCE (293K),cf.Section 3.1).

Long term electrolysis experiments were performed on pentlandite in stirred 1M HCl solution at 343K at 0, 0.7 and 0.8V vs. SCE (cf. Table 3.6.1). After polarization at 0V vs. SCE, the electrode surface appeared to be etched, yet without a violet coloured tarnish. EMPA confirmed the presence of pentlandite, and the absence of elemental sulphur. The aqueous analysis indicated that iron and nickel were dissolved in approximately equal amounts. These results are consistent with the oxidative dissolution of pentlandite with the formation of H_2S at low potentials. The presence of sulphate in the aqueous solution is attributed to the ex-situ atmospheric oxidation of $H_2S(aq)$, and was therefore ignored in calculating the equivalent charge in Table 3.6.1.

When pentlandite was polarized at the higher potential of 0.7 or 0.8V vs. SCE, a steady state current was obtained within the first few minutes of polarization, and maintained for at least 22 hours. This indicates that an aqueous pore diffusion process through a thickening product layer is unlikely to be rate determining here. The electrode surface after polarization, had a metallic violet/grey coloured tarnish similar to that observed during chronopotentiometry. Unfortunately, EMPA was unavailable to determine the surface composition. A poor correlation of the anodic charge passed during the electroysis (obtained by intergrating the i-t trace) with that inferred from the aqueous analysis (cf. Table 3.6.1), is attributed to the difficulty in analysing low concentrations of sulphate in $0.02dm^3$ samples (viz. initial electrolyte volume = $0.75dm^3$, interfacial area = $7.85x10^{-5}m^2$), cf. Section 2.4.6. The aqueous nickel/iron concentration ratios were consistently low, which suggests that iron may be preferentially leached from pentlandite under these conditions, although no further evidence is available to support this possibility.

Chronoamperometry on pentlandite in acid solution at 343K has shown that low steady state current densities are established in the potential region relevant to ferric chloride leaching, within the first 250s, and then maintained over a long period of time. This indicates that the dissolution of pentlandite involves slow electron transfer, at least within the potential range 0.4 to 0.8V vs. SCE).

3.6.2 Violarite

Figures 3.6.11 to 3.6.20 show chronoamperograms for synthetic and natural violarite in 1M HCl and 1M $HClO_4$ solution at temperatures within the range 293 to 353K. These figures show that the behaviour of synthetic and natural violarite are essentially similar. A common feature of these results is that Cottrell behaviour is not observed. Steady state currents were rapidly obtained, indicating that diffusion processes are not rate limiting within the potential range 0.8 to 1V vs.SCE. Furthermore, these results are in qualitative agreement with those obtained from chronopotentiometry on violarite (cf. Section 3.5).

Figure 3.6.21 shows chronoamperograms for violarite in 1M $HClO_4$ solution at 353K, in the potential range relevant to ferric chloride leaching. Steady state currents were obtained within the first 30s of polarization (cf. Table 3.6.2). These data were used to construct a Tafel plot in which $\ln(i_{observed})$ was plotted as a function of $E_{applied}$ vs. SCE (cf. Equation 3.6.2 and Figure 3.6.22).

$$\ln i = \ln i_o + \frac{\alpha(Z_B - Z_A)F(E - E_{eq})}{RT} \qquad (3.6.2)$$

$$FeNi_2S_4 = Fe^{2+} + 2Ni^{2+} + 4S^o + 6e \qquad (3.6.3)$$

The Tafel slope (at 353K) = 7.77 decade V^{-1}. Equation 3.6.3 is assumed to represent the predominant process here (cf. Section 3.1). Therefore, by adopting $Z_B - Z_A = 2$, the Tafel slope gives an anodic charge transfer coefficient (α_a) = 0.12. Since the standard equilibrium potential (E^o) for the Fe^{2+}, Ni^{2+}, S^o / $FeNi_2S_4$ couple is unknown at 353K, together with the complications arising in its determination from open-circuit potential measurements (cf. Section 3.1), the corresponding overpotentials (i.e. $E - E_{eq}$) cannot be ascribed to this system. Therefore, the exchange current density (i_o) cannot be extrapolated from this data.

Nonetheless, it is evident from the Tafel plot (cf. Figure 3.6.22) that $\ln i_o < 0.2$ decade, (i.e. $i_o < 1.2 Am^{-2}$). Therefore, by adopting $Z_B - Z_A = 2$, and $\alpha_a = 0.12$, with a bulk metal concentration in violarite = $47373 moldm^{-3}$ (cf. Appendix B.2); indicates that the heterogeneous rate constant k^o ($Fe^{2+}, Ni^{2+}, S^o/FeNi_2S_4$) $<< 1.7x10^{-6} ms^{-1}$, which is in the domain of slow electron transfer.

TABLE 3.6.1

Chronoamperometric Data for Pentlandite:

Aqueous Analysis Data

(a). Potentiostatic Polarization: E = 0V vs. SCE
SynPn2b
1M HCl solution
T = 343K
Area = $7.85 \times 10^{-5} m^2$
i(steady state) = $0.8 Am^{-2}$

t/s	Q(obs.)/C	[Fe]/mol	[Ni]/mol	$[SO_4^{2-}]$/mol	Q(eqv.)/C
68000	4.1	1.9×10^{-5}	1.3×10^{-5}	4.0×10^{-5}	6.1

(b). Potentiostatic Polarization: E = 0.7V vs. SCE
SynPn1
1M HCl solution
T = 343K
Area = $7.85 \times 10^{-5} m^2$
i(steady state) = $2.5 Am^{-2}$

t/s	Q(obs.)/C	[Fe]/mol	[Ni]/mol	$[SO_4^{2-}]$/mol	Q(eqv.)/C
9360	2.3	4.4×10^{-5}	0	-	-
61560	12.8	5.9×10^{-5}	1.4×10^{-5}	4.3×10^{-5}	39
93960	19.3	5.9×10^{-5}	2.4×10^{-5}	5.3×10^{-5}	47
150960	28.4	6.9×10^{-5}	3.7×10^{-5}	1.8×10^{-4}	124
157320	29.7	7.4×10^{-5}	3.6×10^{-5}	4.0×10^{-4}	253

(c). Potentiostatic Polarization: E = 0.8V vs. SCE
SynPn1
1M HCl solution
T = 343K
Area = $7.85 \times 10^{-5} m^2$
i(steady state) = $29 Am^{-2}$

t/s	Q(obs.)/C	[Fe]/mol	[Ni]/mol	$[SO_4^{2-}]$/mol	Q(eqv.)/C
21000	48	1.2×10^{-4}	6.4×10^{-5}	-	-
80000	182	2.9×10^{-4}	2.1×10^{-4}	1.8×10^{-4}	201

Table 3.6.2

Chronoamperometric Data for Violarite in 1M $HClO_4$ at 353K

E/V vs. SCE	i/Am^{-2}	lni
-0.1	-1.41	-0.35
0	-1.06	-0.06
0.2	-0.07	-
0.3	1.06	0.06
0.325	1.41	0.35
0.35	1.77	0.57
0.4	2.12	0.75
0.45	4.95	1.60
0.5	3.54	1.26
0.55	10.6	2.36
0.6	8.84	2.18
0.65	19.4	2.97
0.7	23.0	3.14
0.75	37.1	3.61
0.8	56.6	4.04

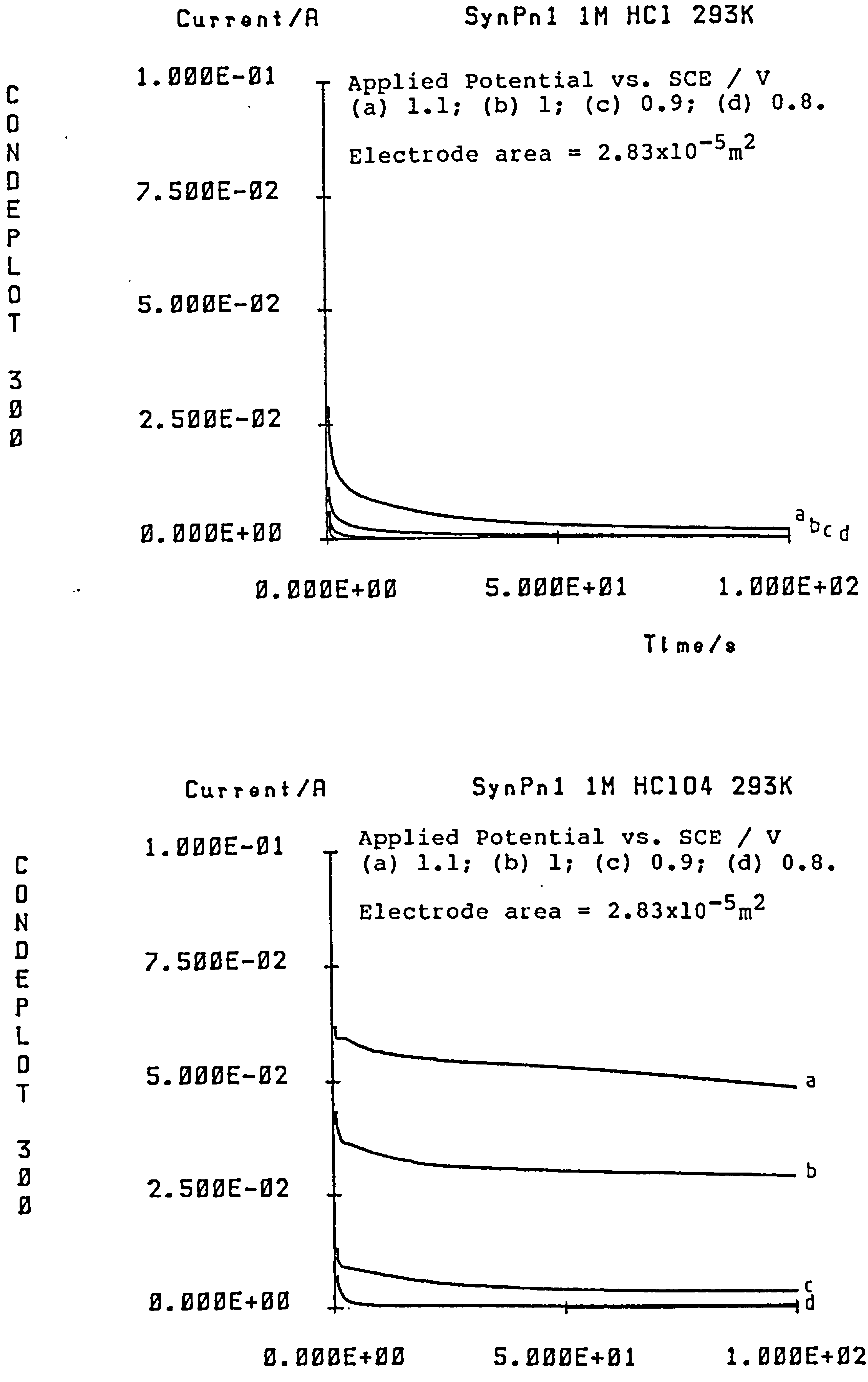

Figure 3.6.1

Chronoamperograms for pentlandite at 293K

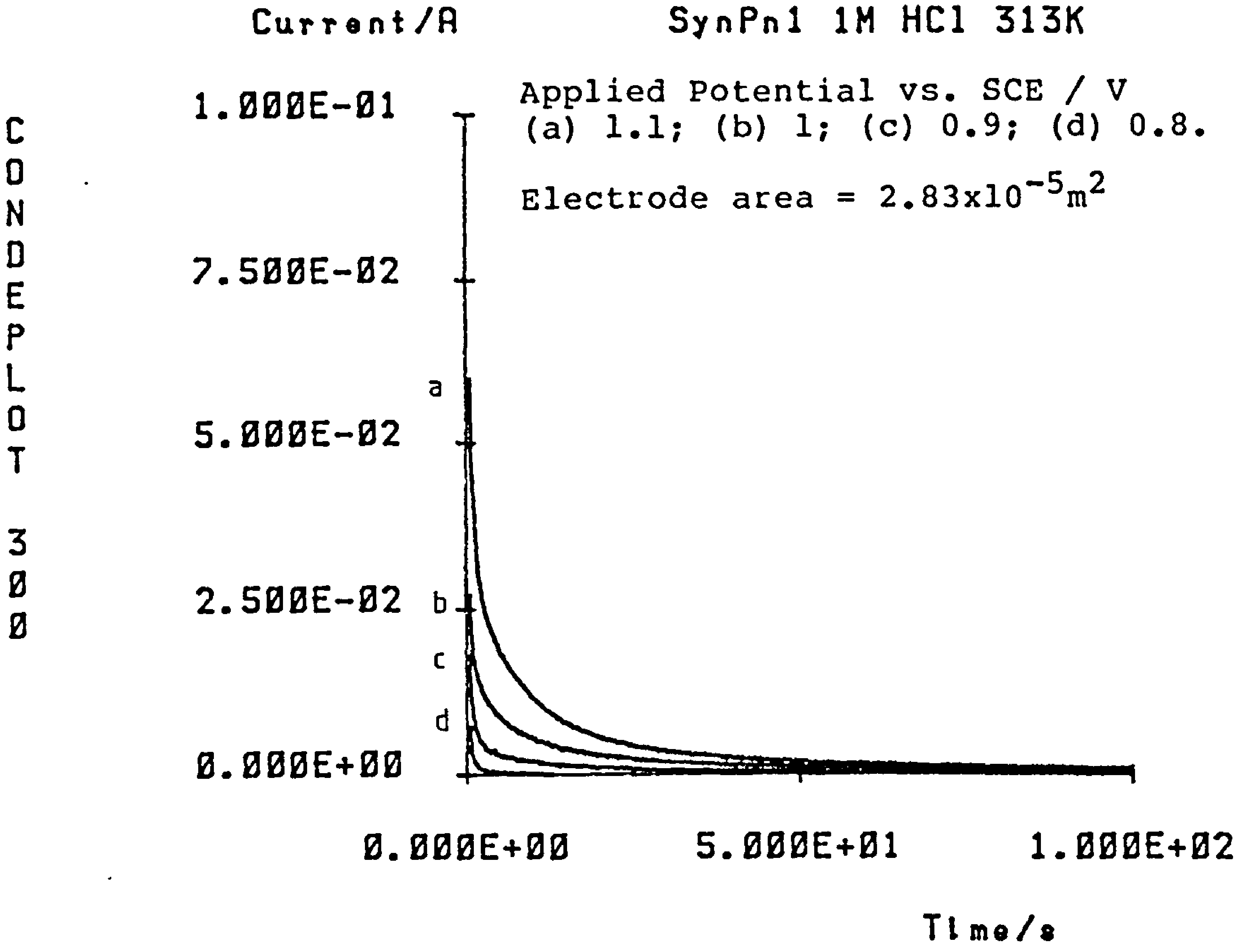

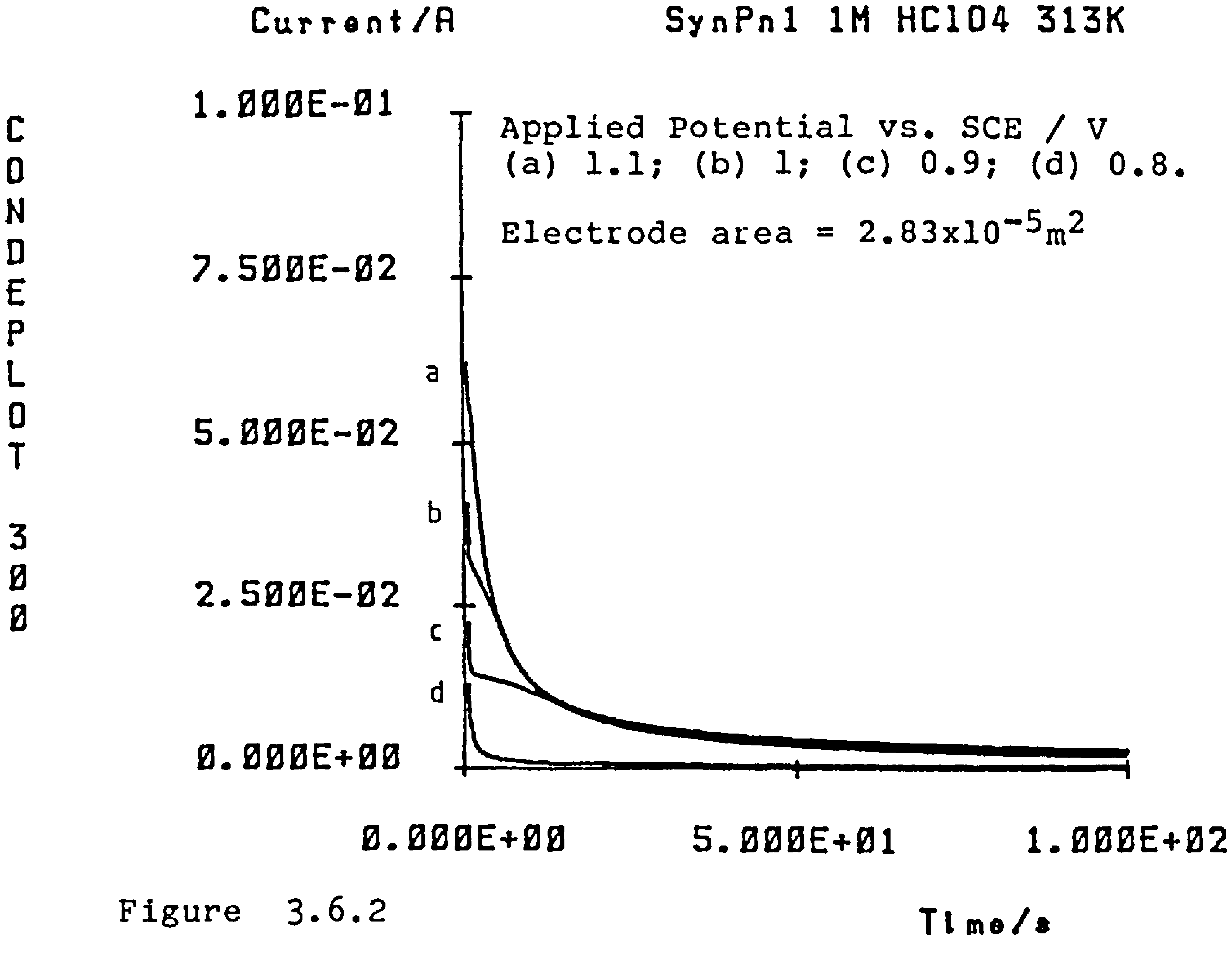

Figure 3.6.2

Chronoamperograms for pentlandite at 313K

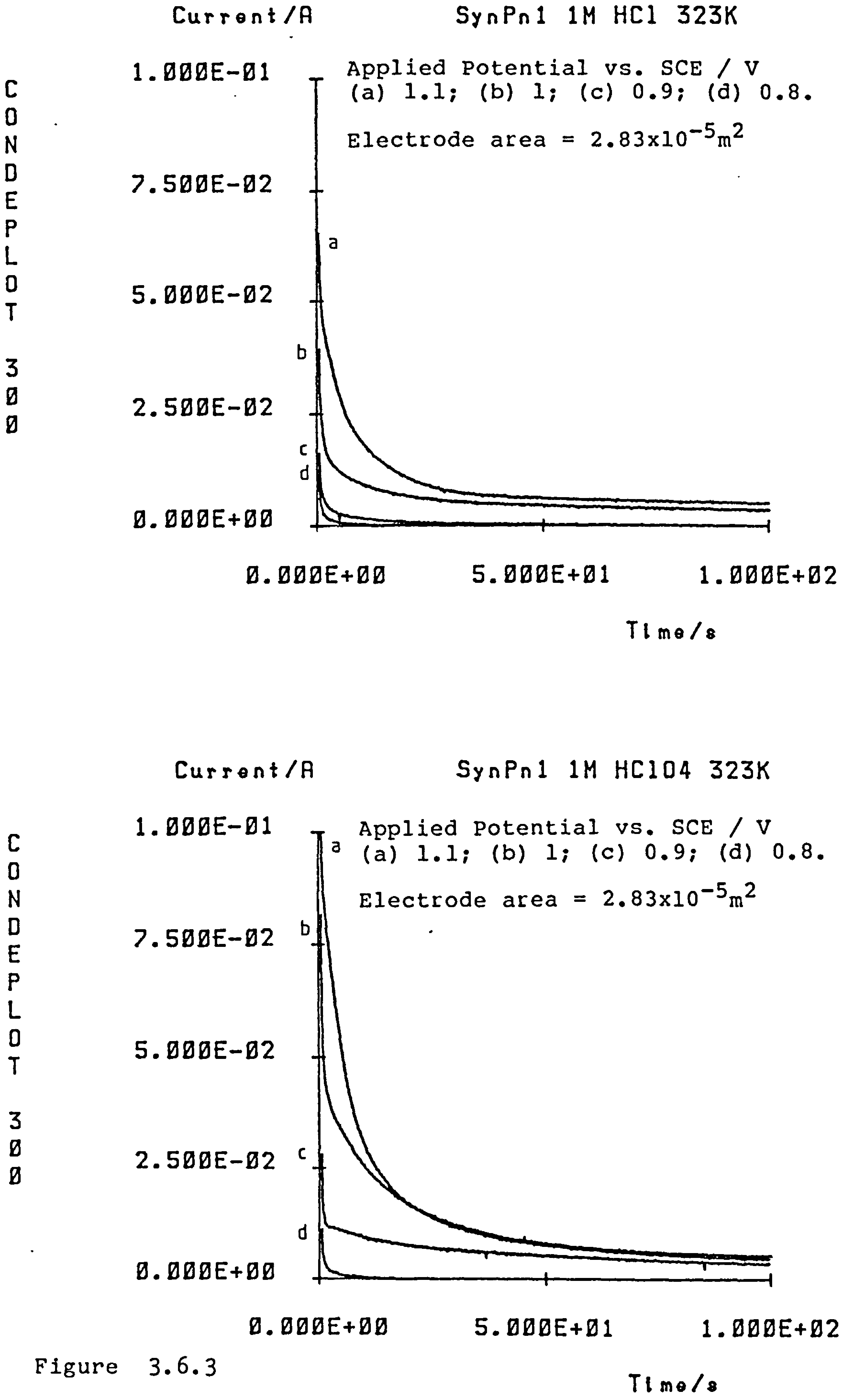

Figure 3.6.3

Chronoamperograms for pentlandite at 323K

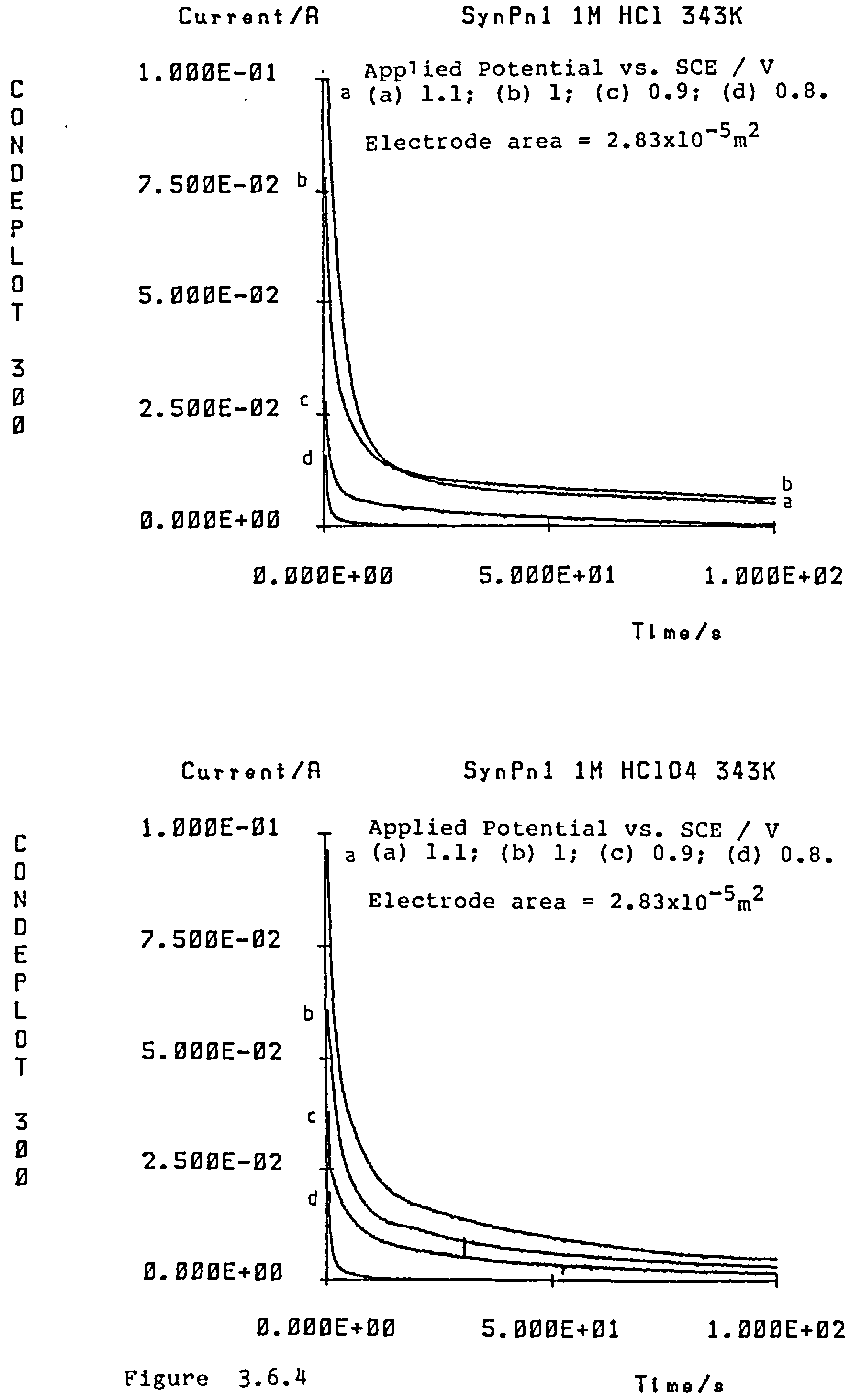

Figure 3.6.4

Chronoamperograms for pentlandite at 343K

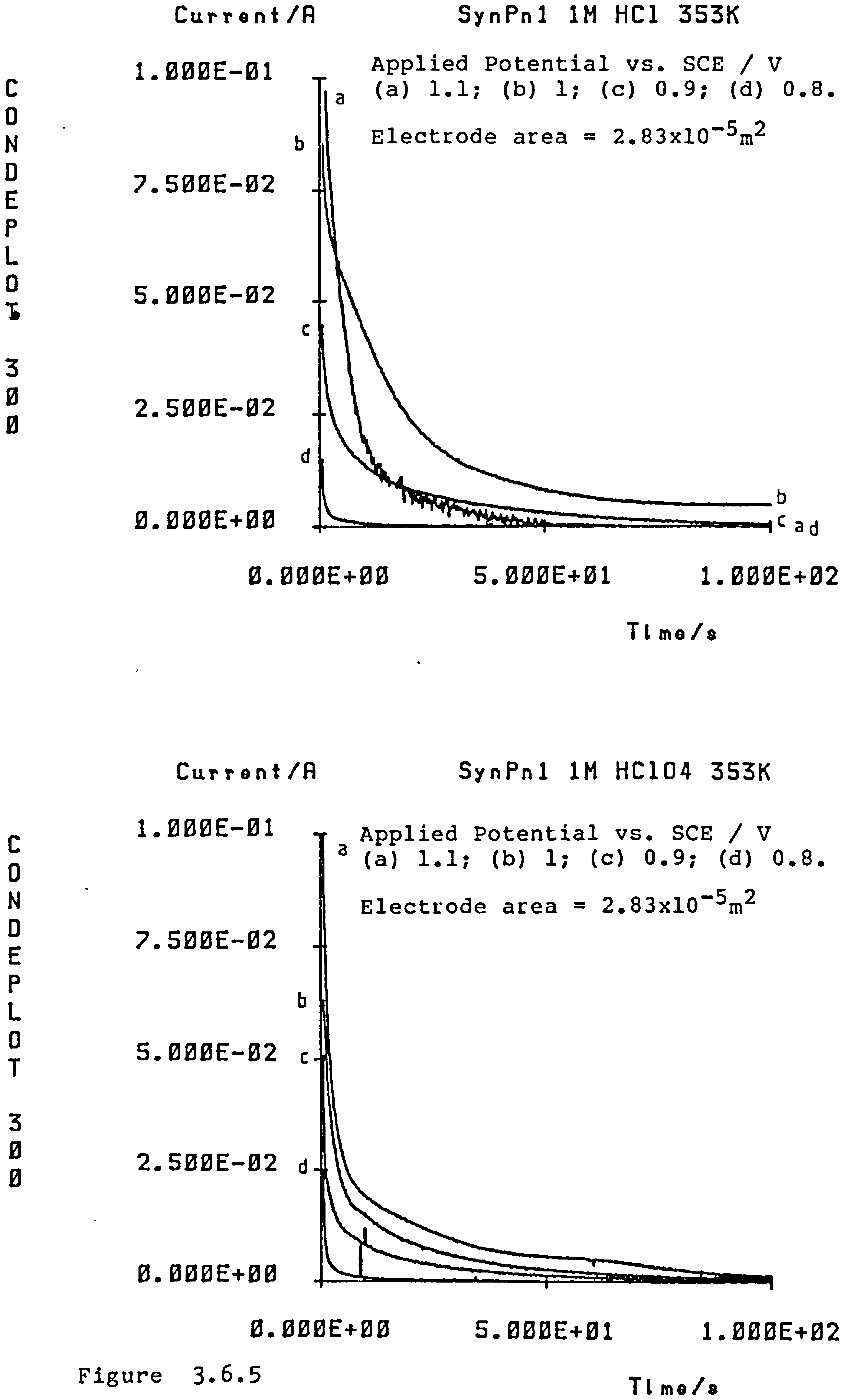

Figure 3.6.5

Chronoamperograms for pentlandite at 353K

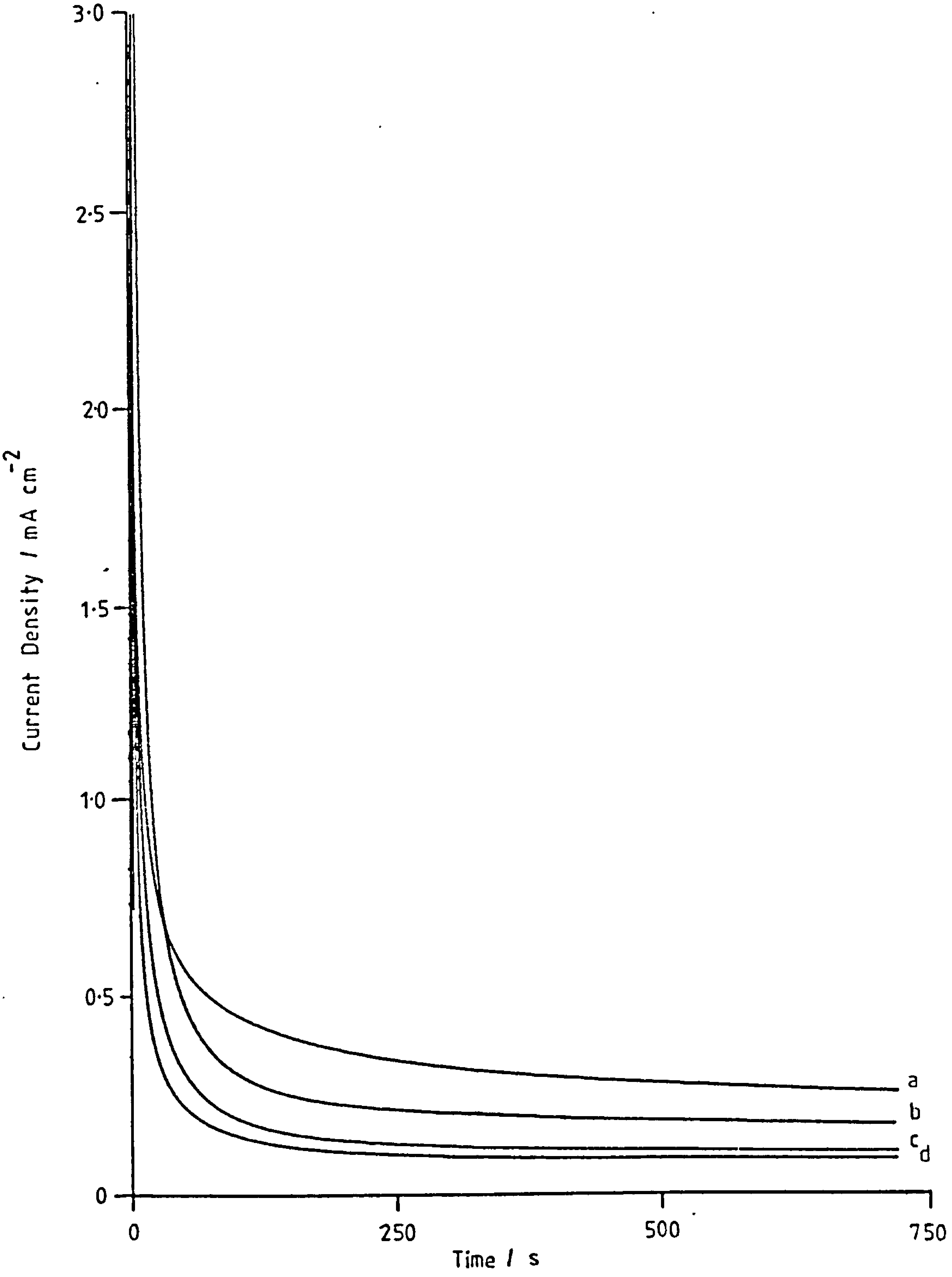

Figure 3.6.6

Chronoamperograms for pentlandite (SynPn1) in 1M HCl solution at 293K. RDE 20Hz. Anodic polarization for 720s at the applied potentials vs. SCE: (a) 0.8V, (b) 0.7V, (c) 0.5V, (d) 0.3V.

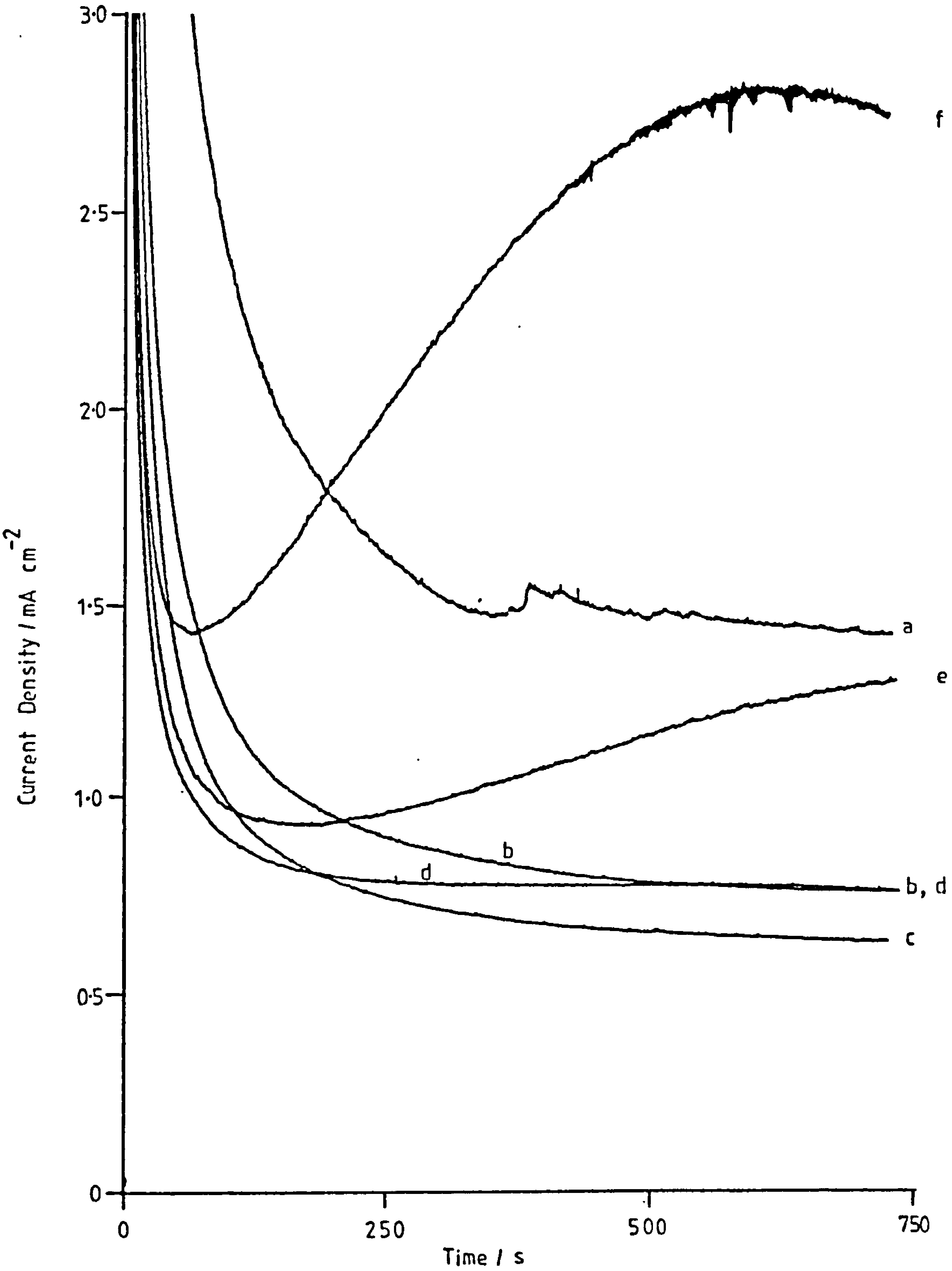

Figure 3.6.7

Chronoamperograms for pentlandite (SynPn1) in 1M HCl solution at 343K. RDE 20Hz. Anodic polarization for 720s at the applied potentials vs. SCE: (a) 0.7V, (b) 0.6V, (c) 0.5V, (d) 0.4V, (e) 0.3V, (f) 0.2V.

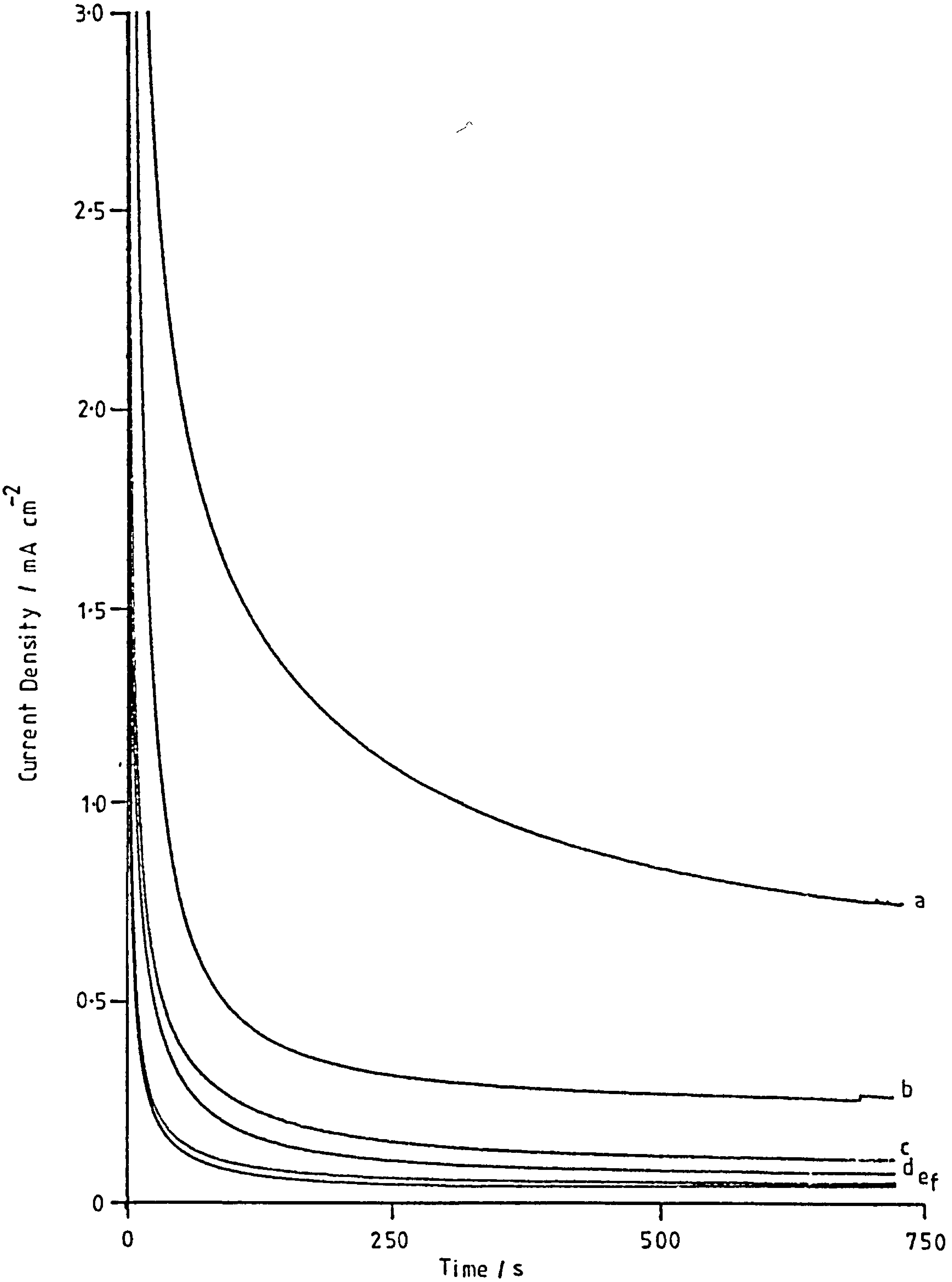

Figure 3.6.8

Chronoamperograms for pentlandite (SynPnl) in 1M $HClO_4$ solution at 293K. RDE 20Hz. Anodic polarization for 720s at the applied potentials vs. SCE: (a) 0.8V, (b) 0.7V, (c) 0.6V, (d) 0.5V, (e) 0.3V, (f) 0.2V.

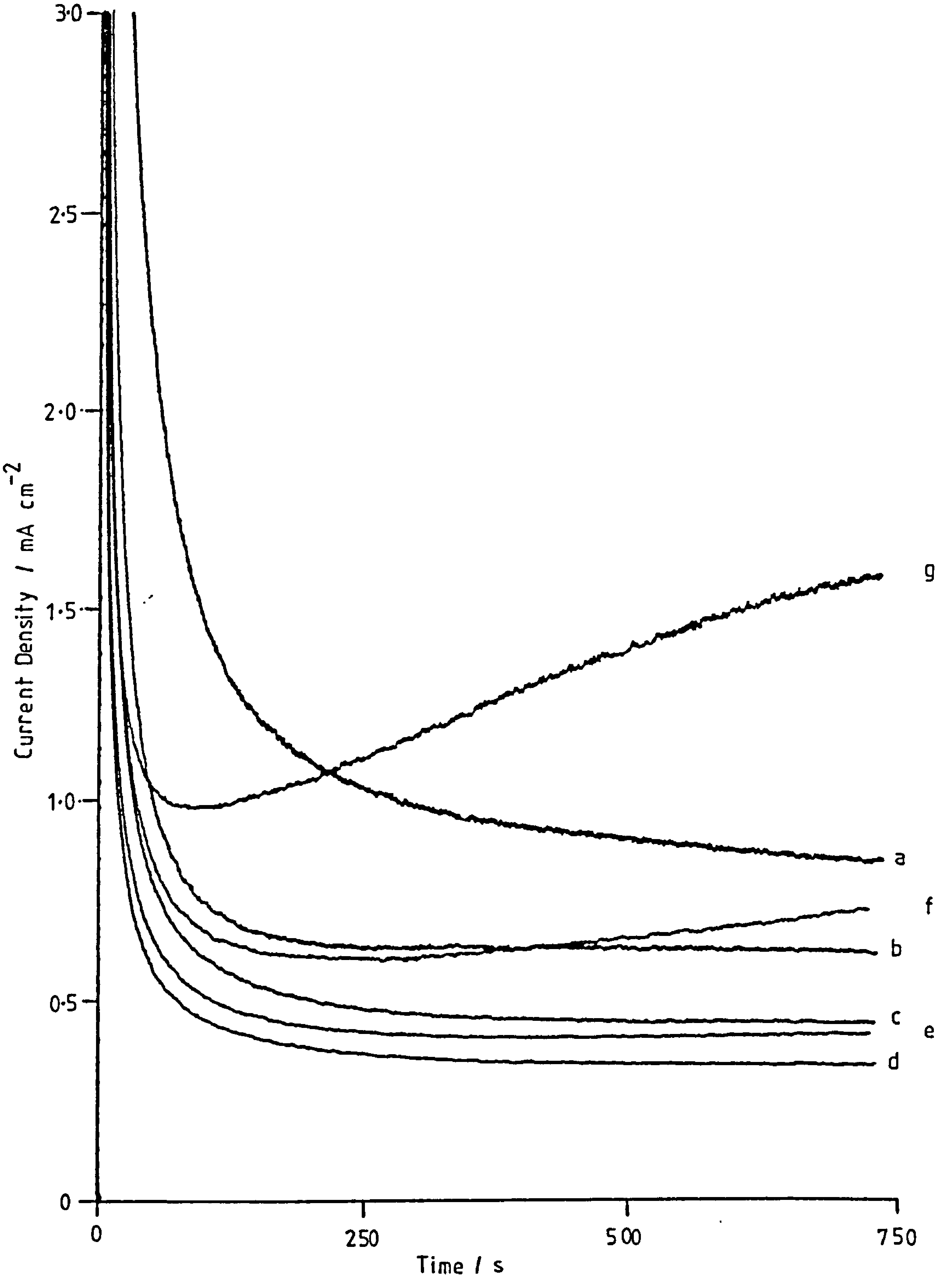

Figure 3.6.9

Chronoamperograms for pentlandite (SynPn1) in 1M $HClO_4$ solution at 343K. RDE 20Hz. Anodic polarization for 720s at the applied potentials vs. SCE: (a) 0.8V, (b) 0.7V, (c) 0.6V, (d) 0.5V, (e) 0.4V, (f) 0.3V, (g) 0.2V.

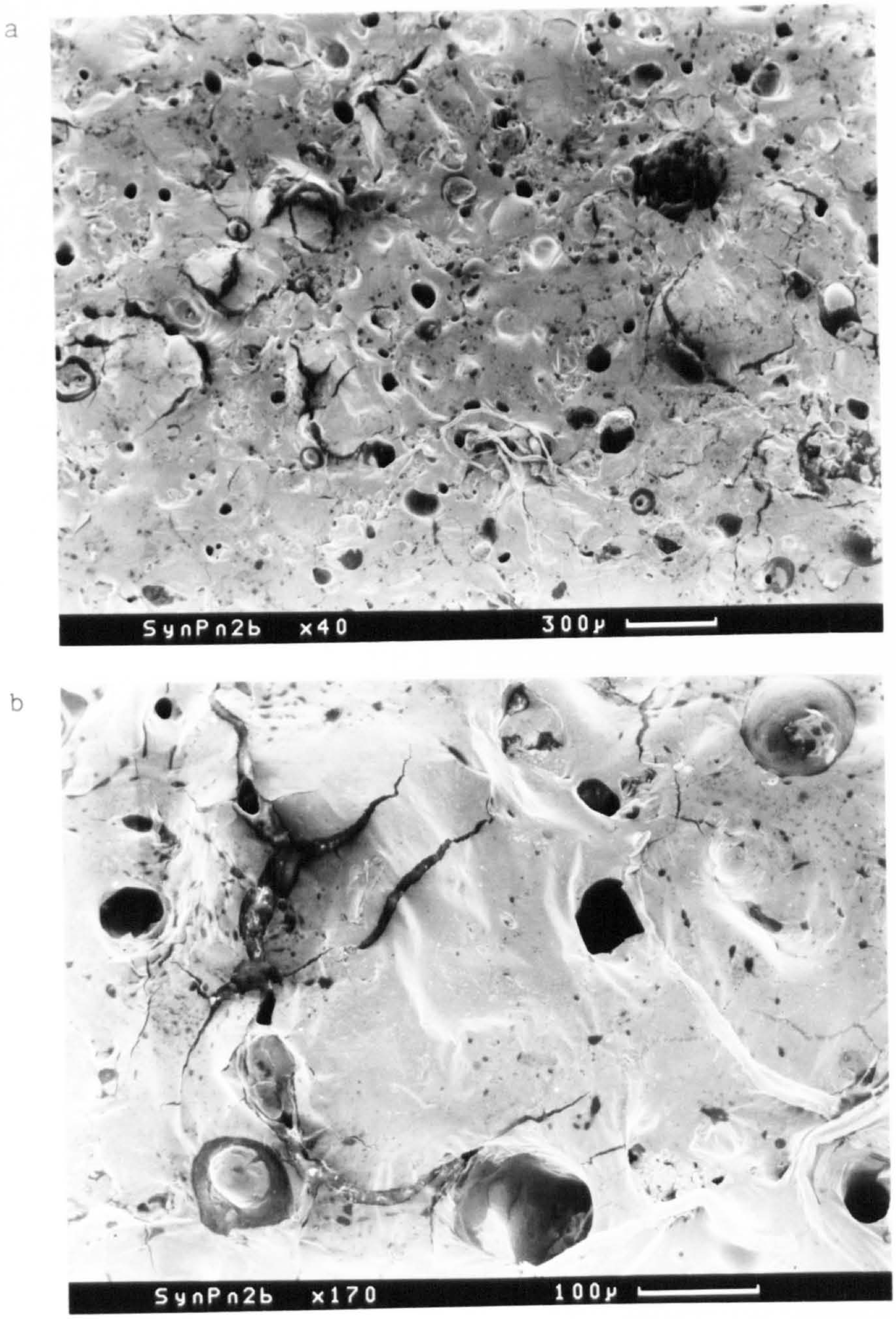

Figure 3.6.10

Scanning electron microscope (SEM) images of the pentlandite surface after polarization for 1260s at 2.2V vs. SCE, in 1M HCl solution at 343K. (a) Electrode surface covered with amorphous elemental sulphur (identified by EDXA). (b) Image shows "strings" of elemental sulphur, which appear to be growing from within the product layer.

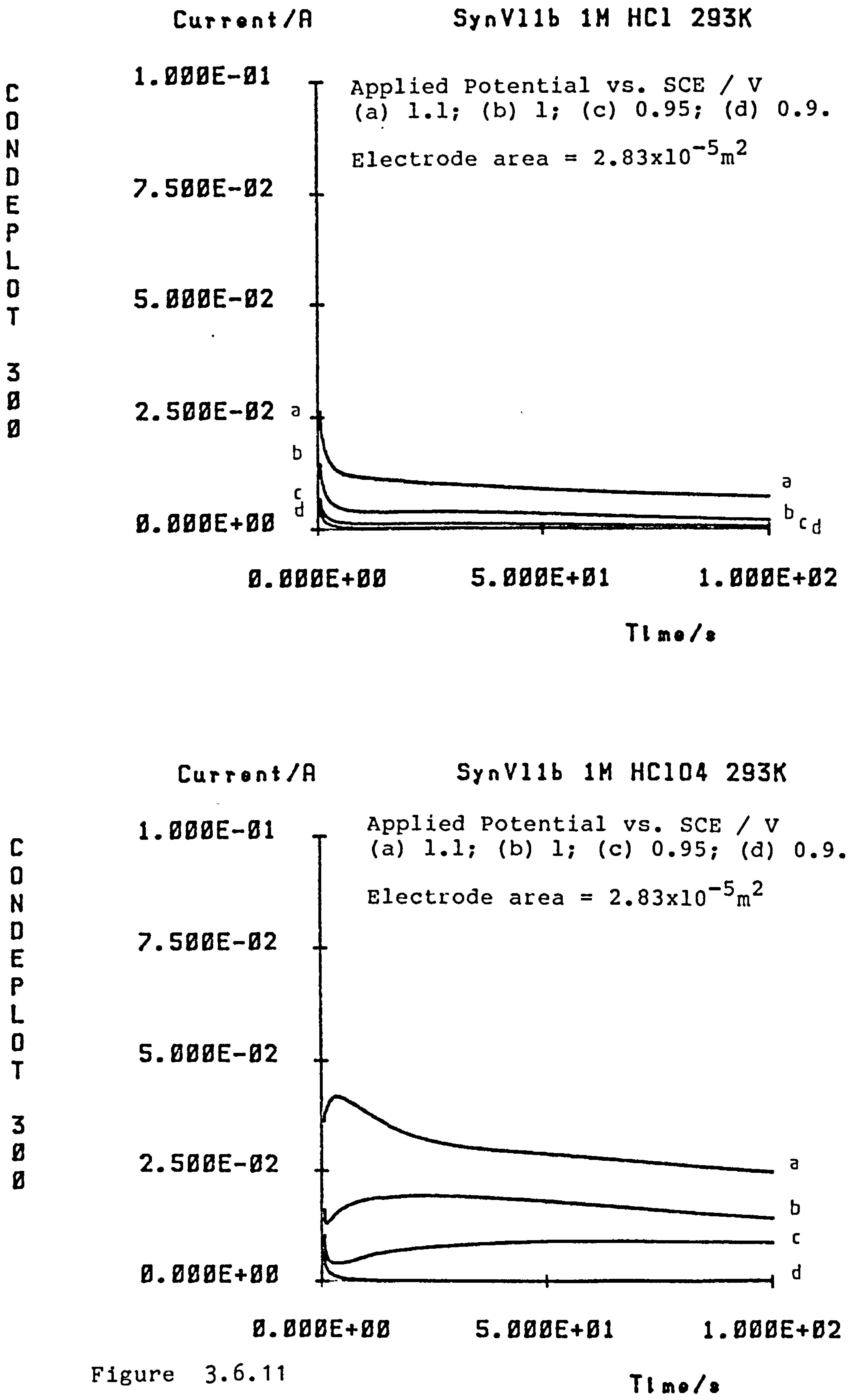

Figure 3.6.11

Chronoamperograms for synthetic violarite at 293K

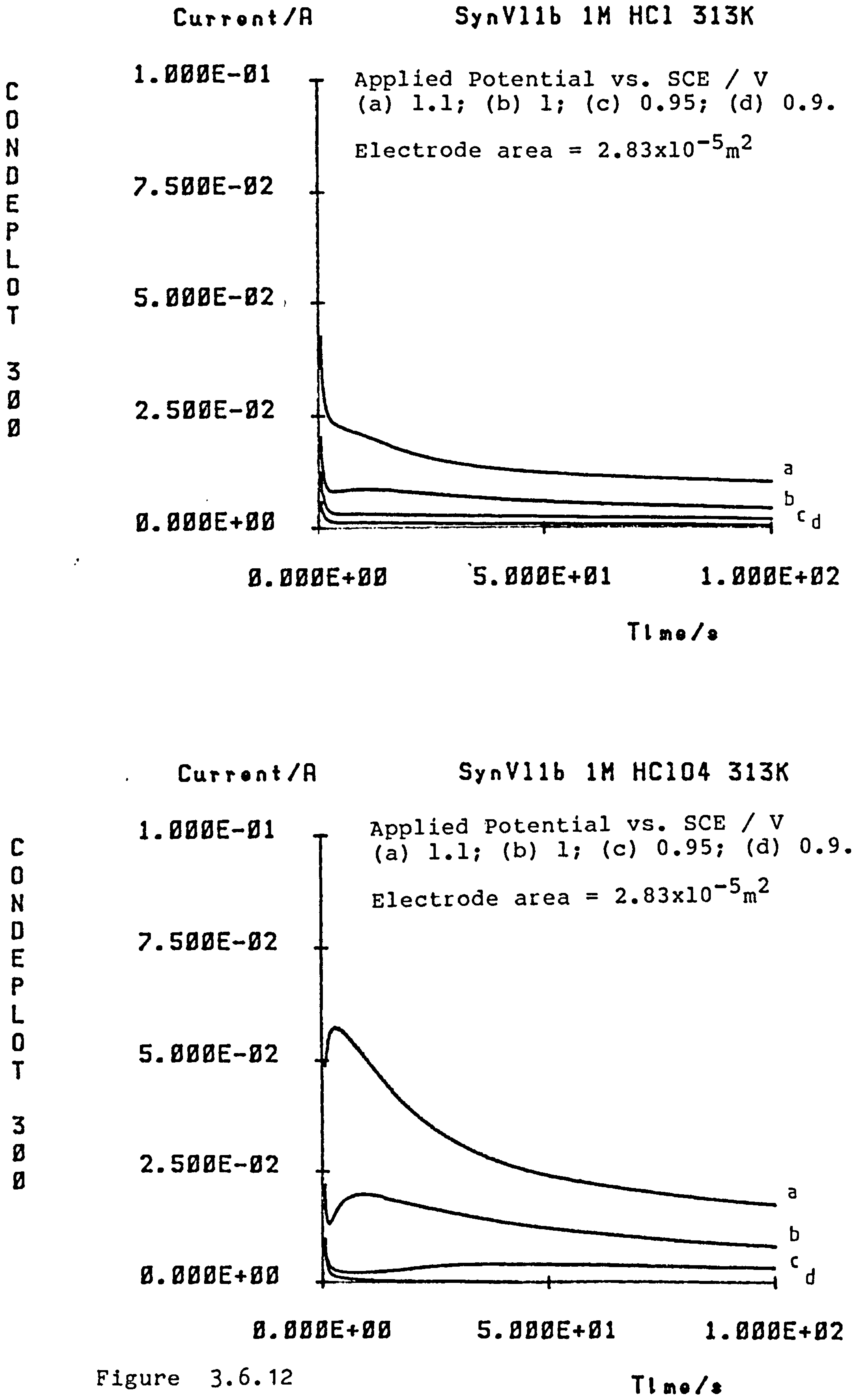

Figure 3.6.12

Chronoamperograms for synthetic violarite at 313K

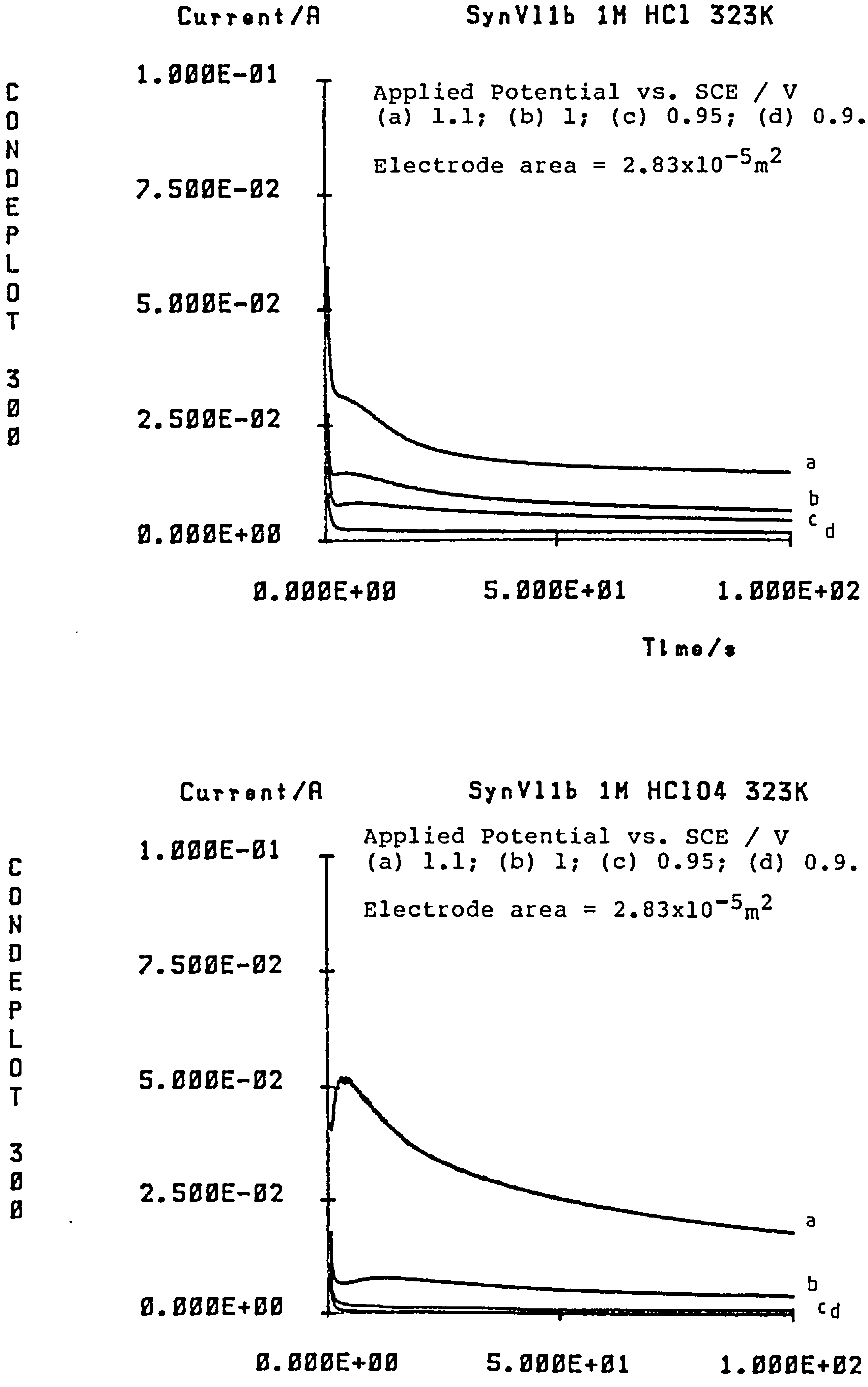

Figure 3.6.13

Chronoamperograms for synthetic violarite at 323K

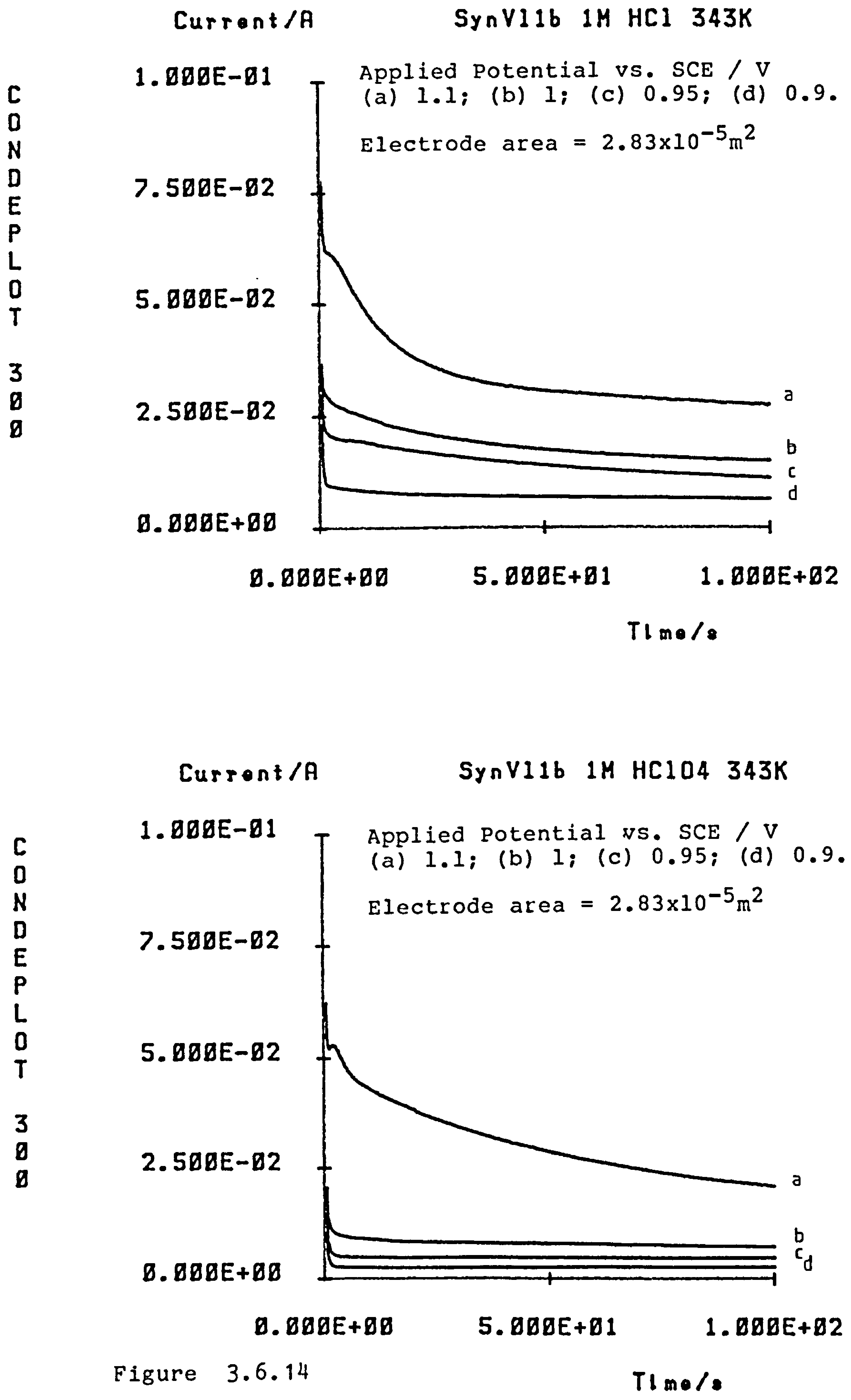

Figure 3.6.14

Chronoamperograms for synthetic violarite at 343K

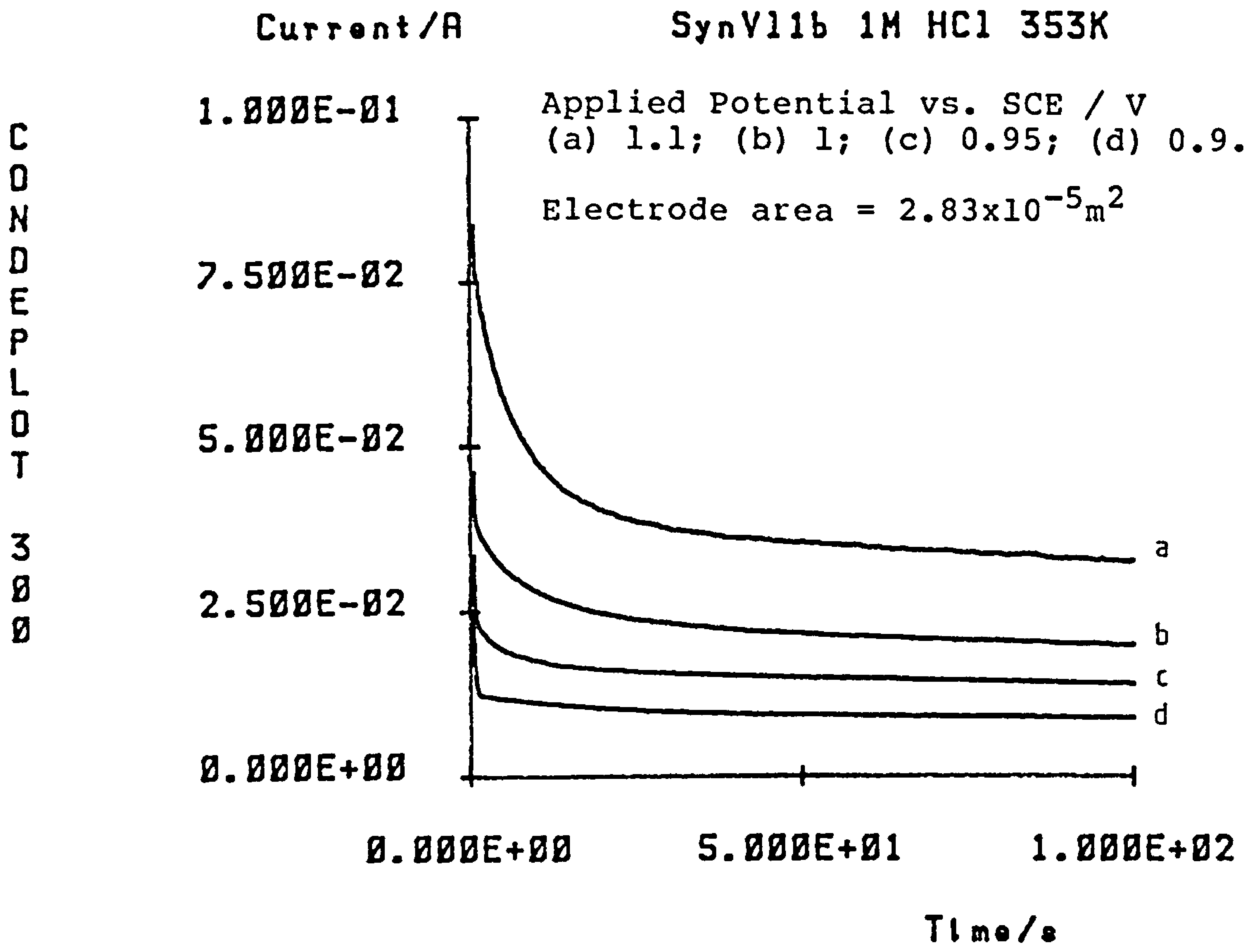

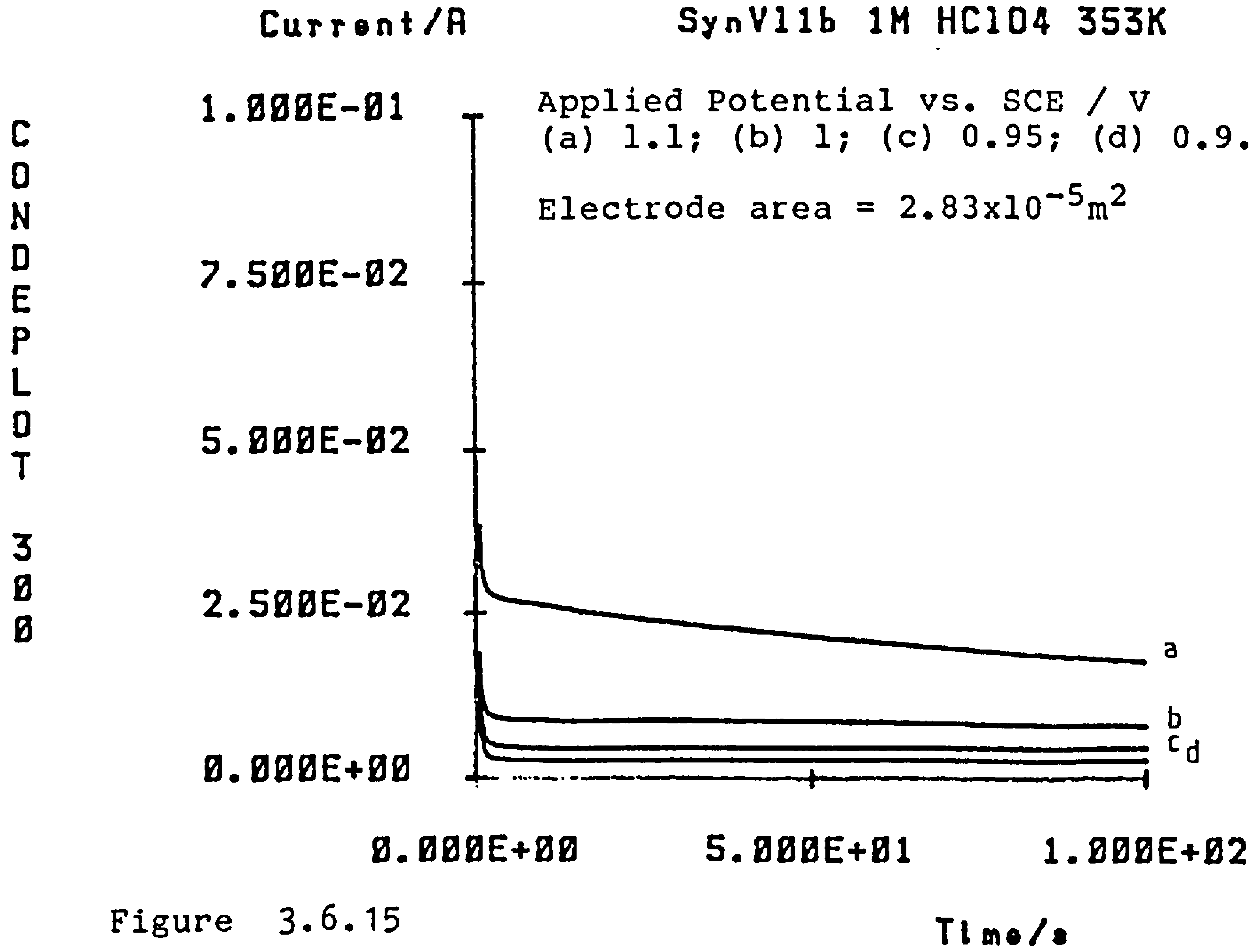

Figure 3.6.15

Chronoamperograms for synthetic violarite at 353K

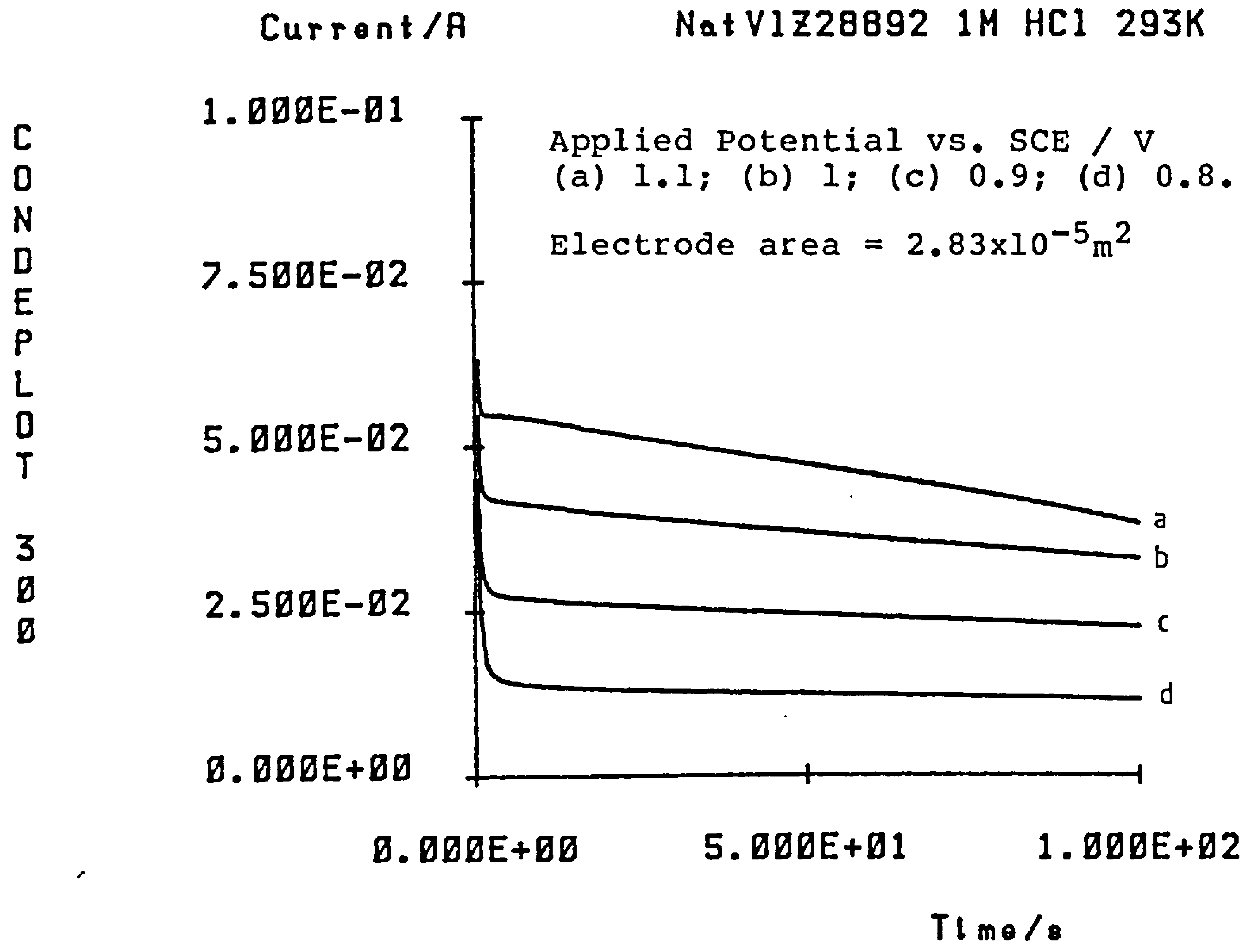

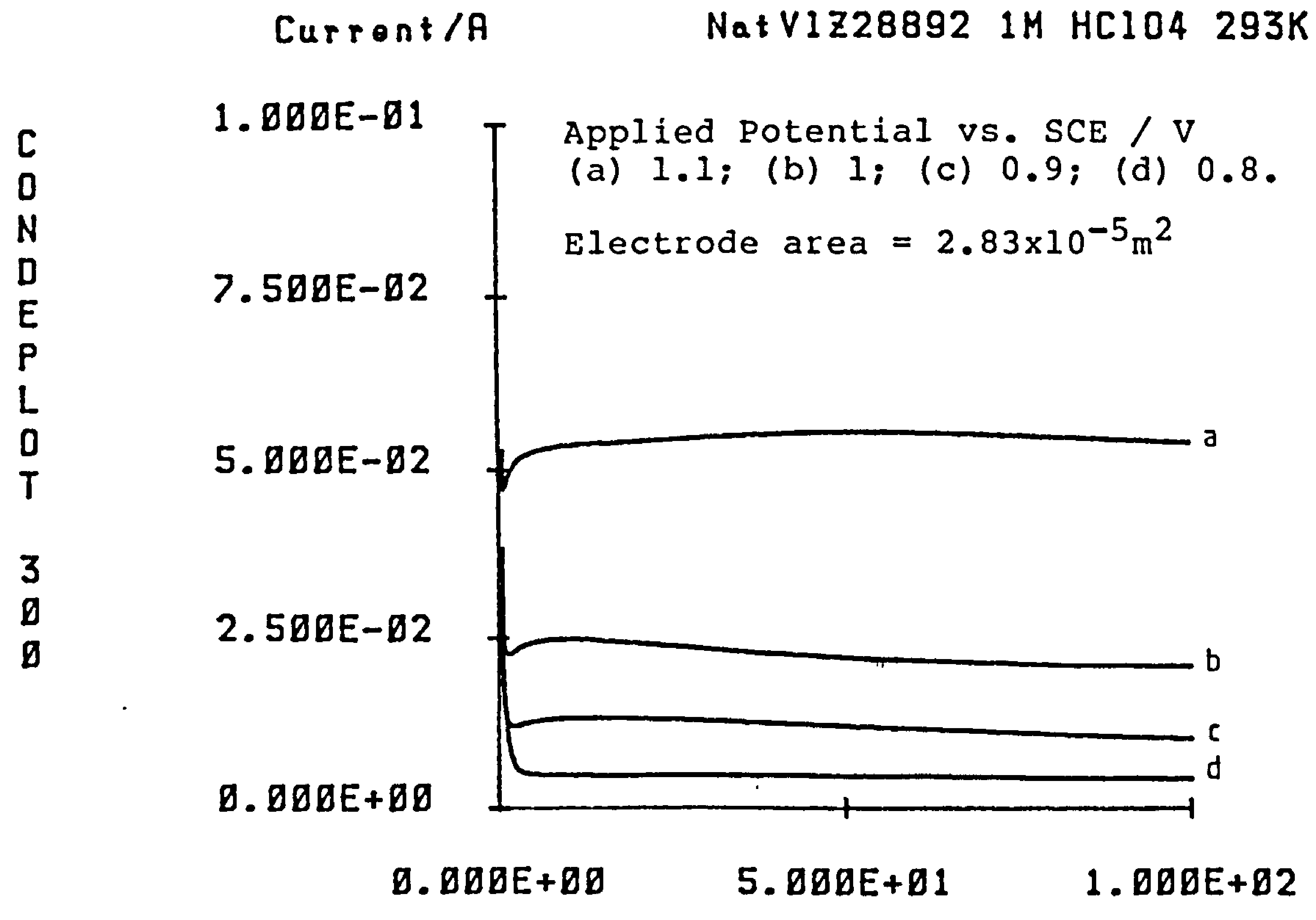

Figure 3.6.16

Chronoamperograms for natural violarite at 293K

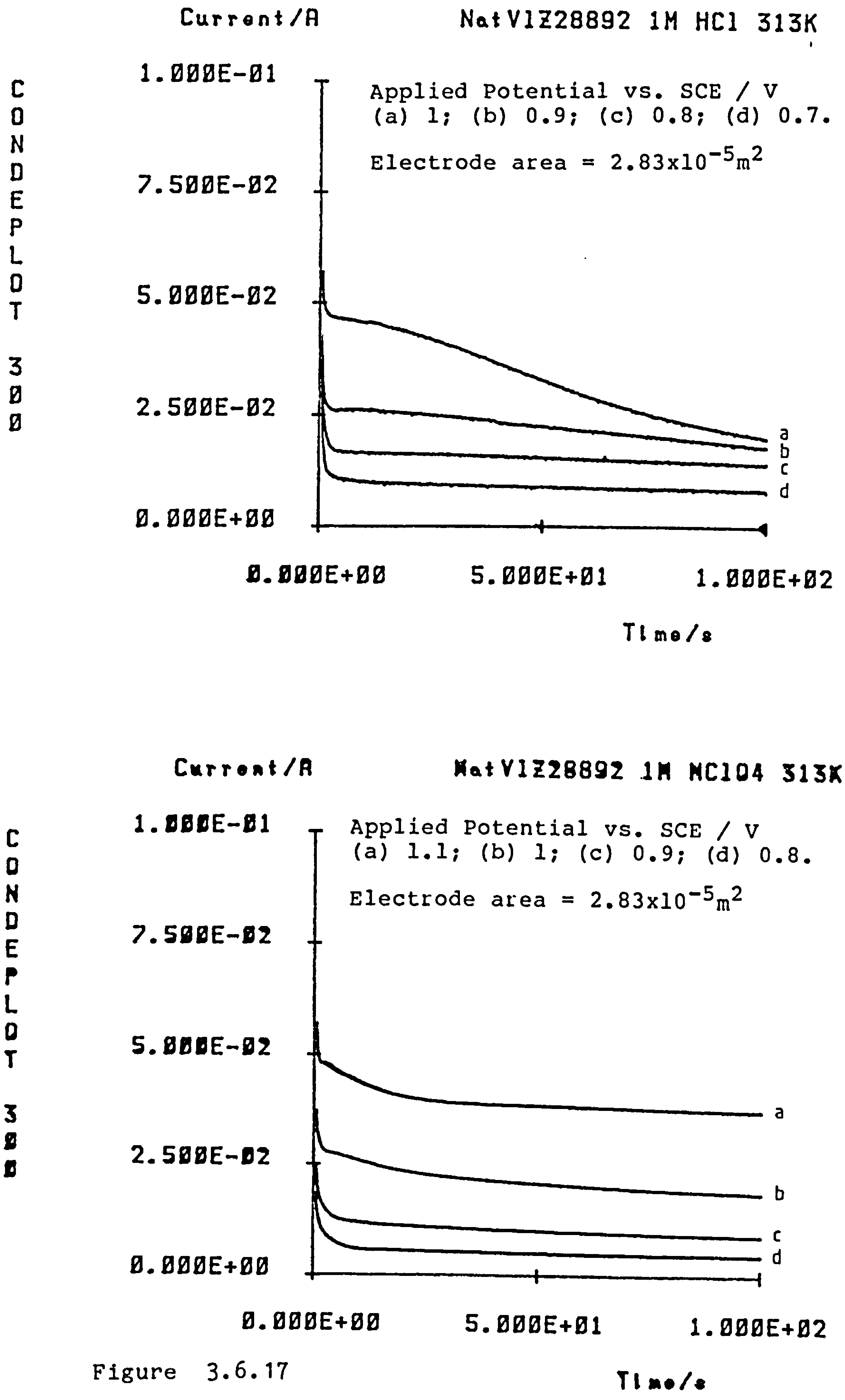

Figure 3.6.17

Chronoamperograms for natural violarite at 313K

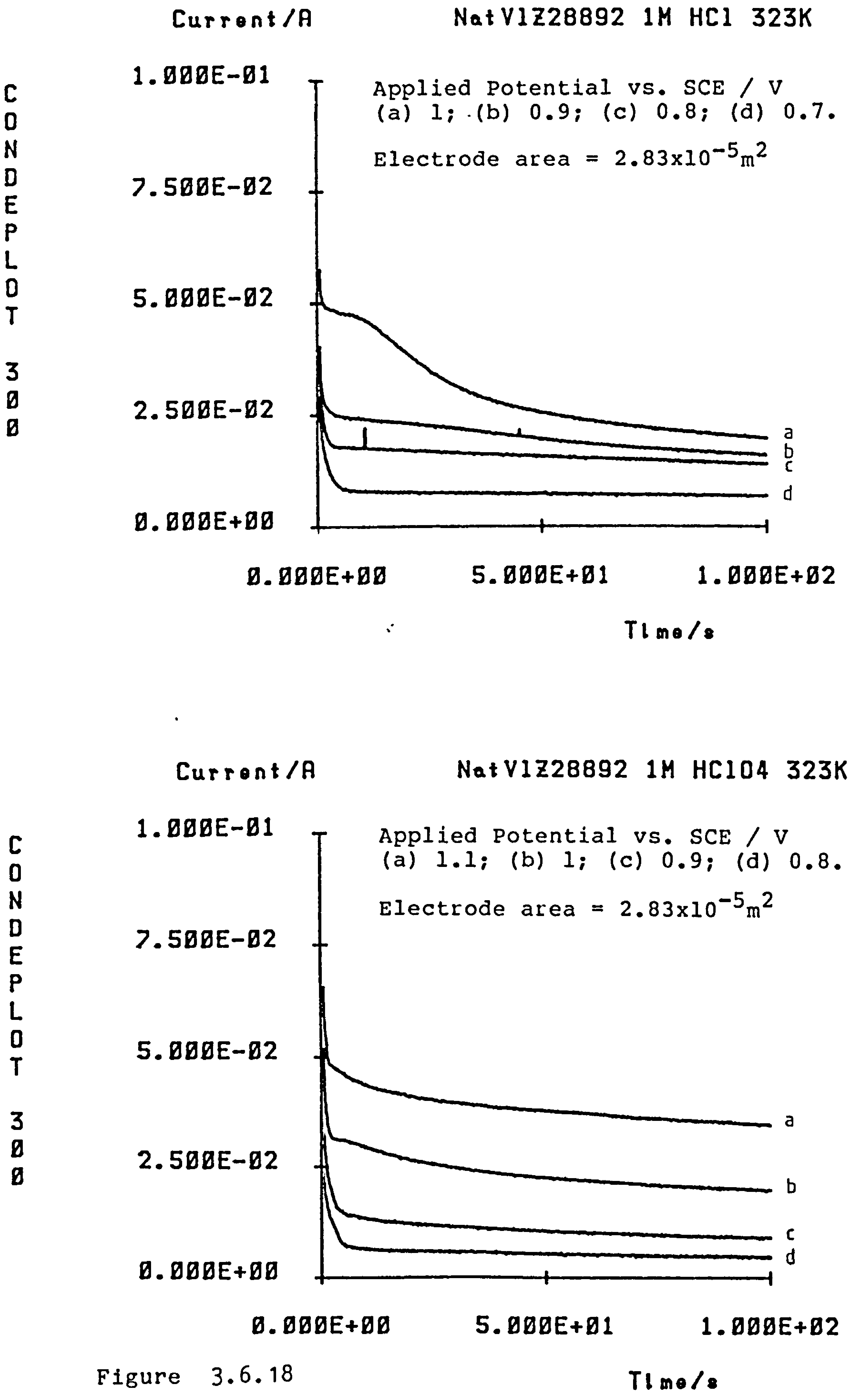

Figure 3.6.18

Chronoamperograms for natural violarite at 323K

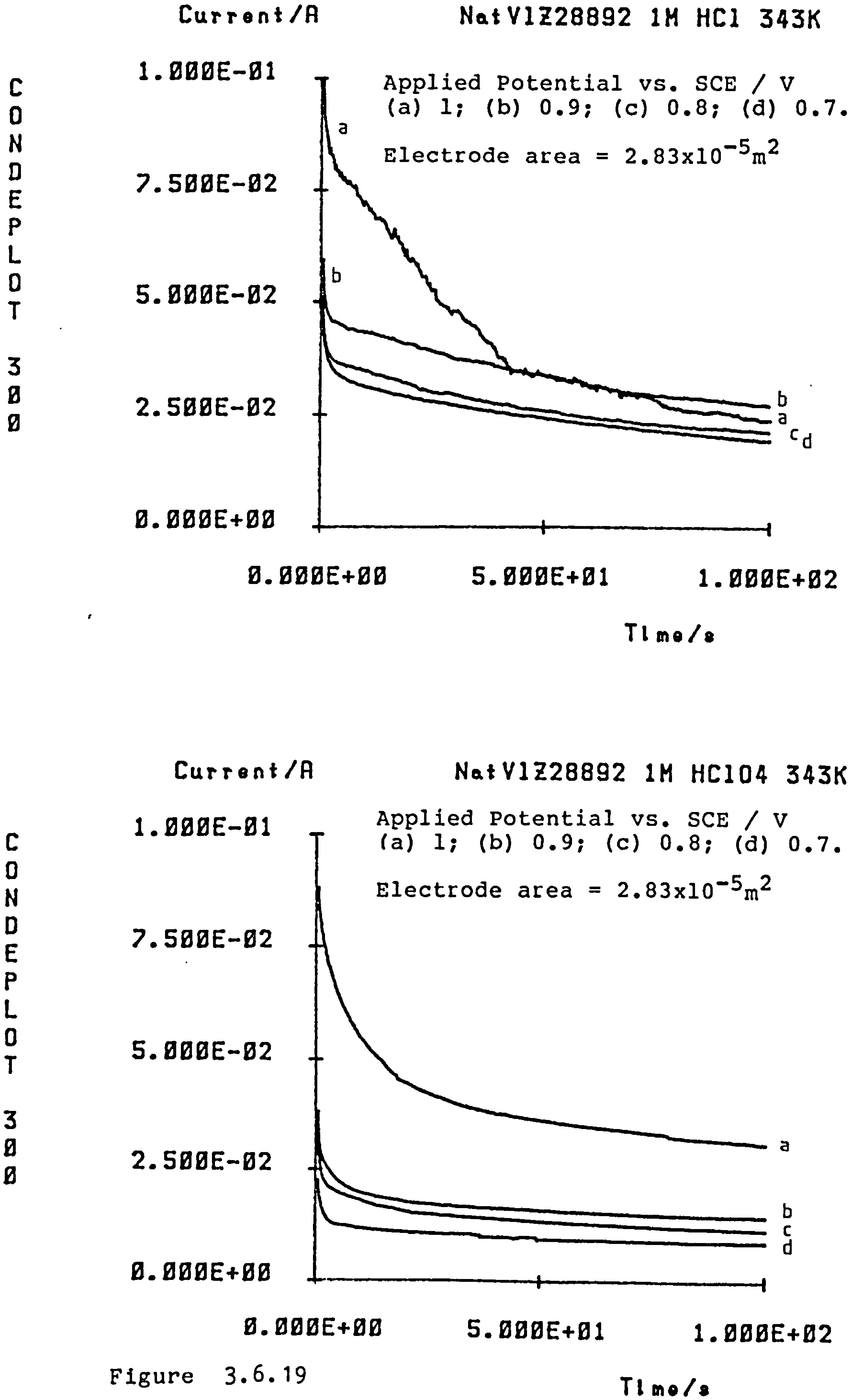

Figure 3.6.19

Chronoamperograms for natural violarite at 343K

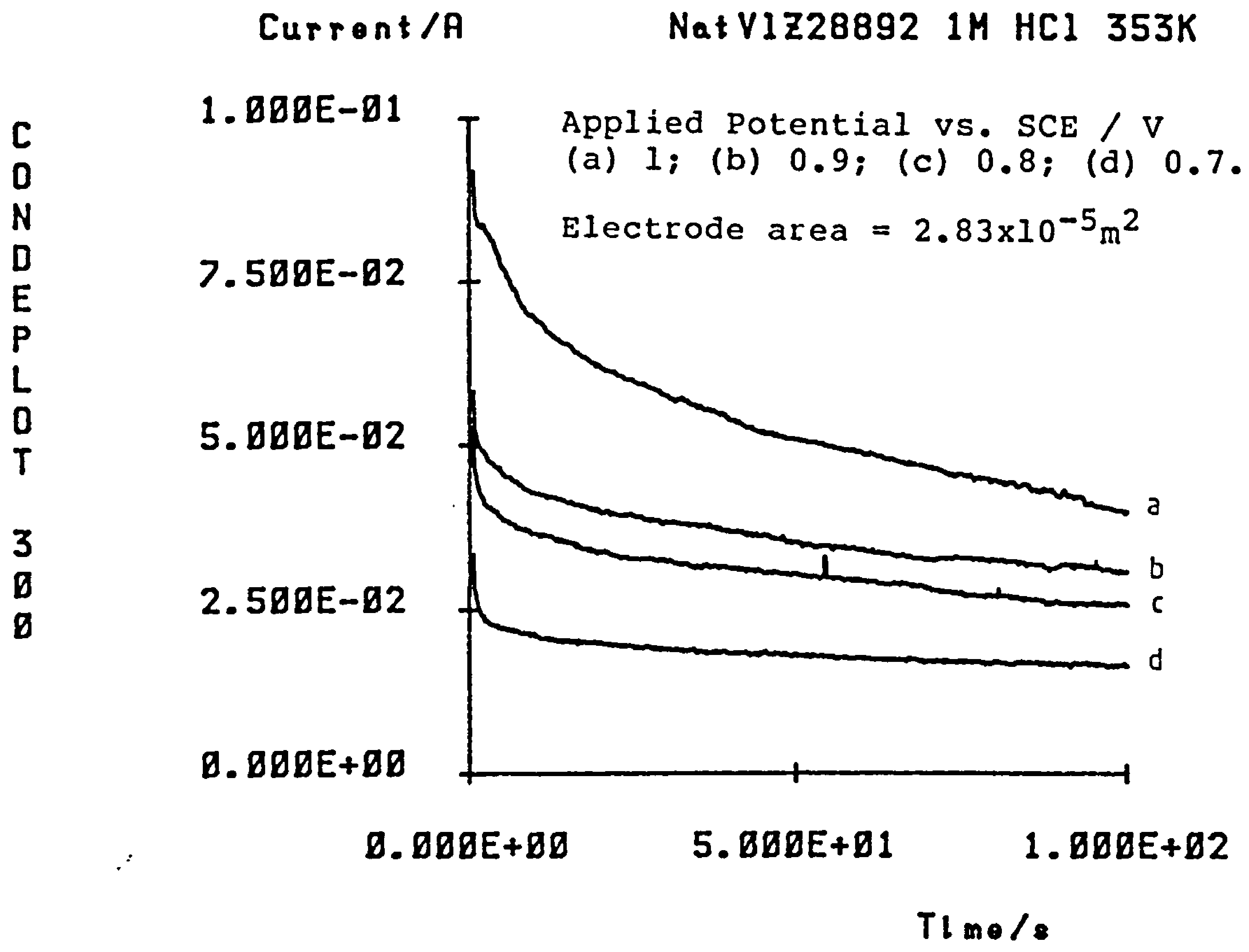

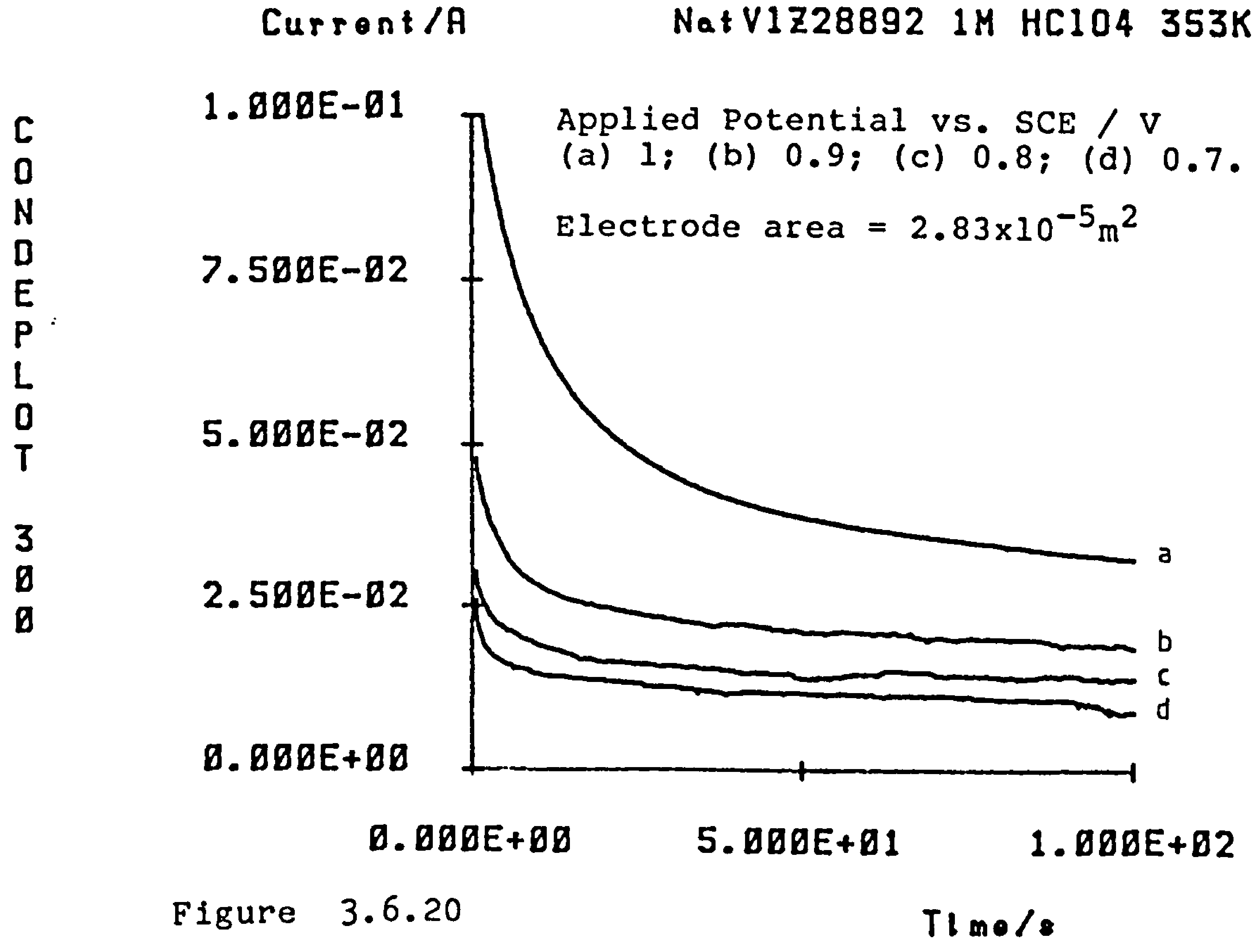

Figure 3.6.20

Chronoamperograms for natural violarite at 353K

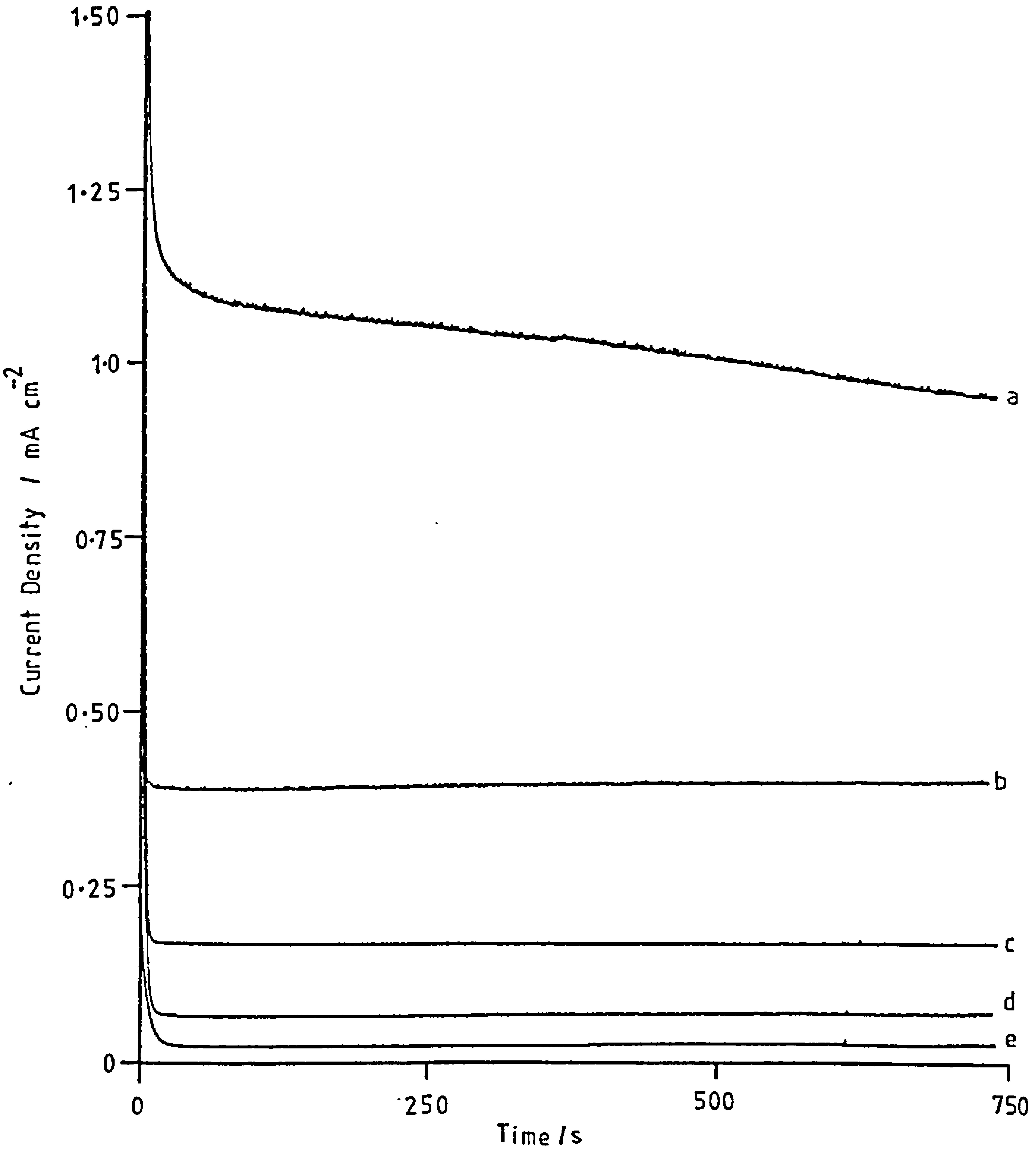

Figure 3 6 21

Chronoamperograms for violarite (SynVllb) in 1M $HClO_4$ solution at 353K. RDE 20Hz. Anodic polarization for 720s at the applied potentials vs. SCE: (a) 0.9V, (b) 0.8V, (c) 0.7V, (d) 0.6V, (e) 0.5V

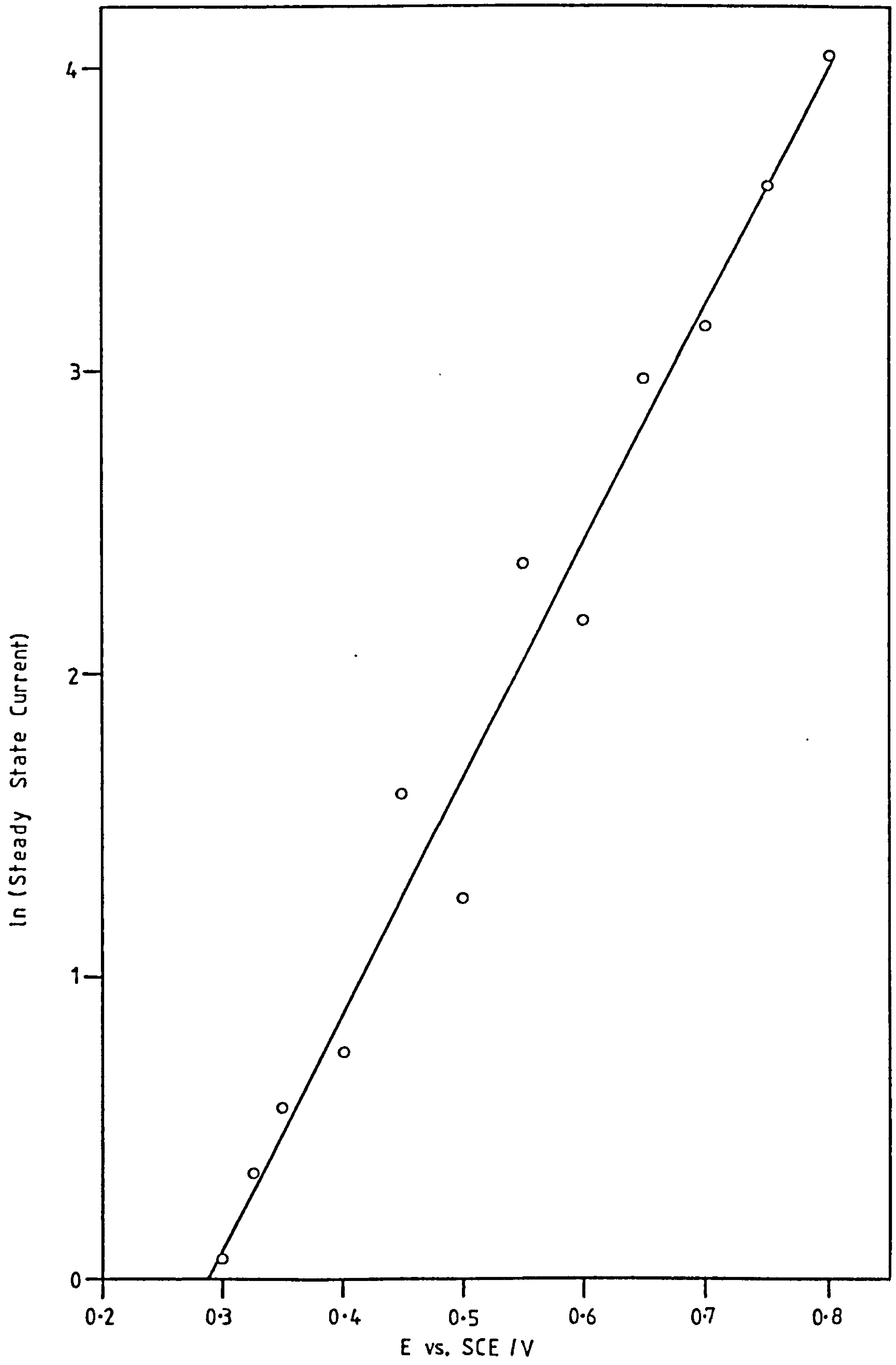

Figure 3.6.22

Tafel plot for the anodic oxidation of violarite in 1M $HClO_4$ solution at 353K (cf. Table 3.6.2).

3.7 THE $FeCl_3/FeCl_2$ COUPLE: DETERMINATION OF THE HETEROGENEOUS ELECTROCHEMICAL PARAMETERS BY CHRONOAMPEROMETRIC TECHNIQUES

The importance of acid ferric chloride as a leachant for the dissolution of base metal sulphide ore minerals and mattes (viz. the SLN and Cymet processes) was mentioned in Section 1.1.2. Previous kinetic studies on the dissolution of pentlandite in acid ferric chloride were discussed in Section 1.7.2, whilst the electrochemical involvement of ferric chloride within this context, was investigated in various parts of Section 3.

In this Section, a study was made to determine the heterogeneous electrochemical parameters (k^o and α) of the $FeCl_3/FeCl_2$ couple on platinum, using chronoamperometric techniques derived in Section 1.6.2. This included the treatment of chronoamperometric data via a novel method, as derived in Appendix G. Section 1.6.2 and Appendix G, play a complementary role to the discussion in this current section, and are where most of the equations and symbols used below, have been derived or defined.

Chronoamperometric experiments were performed on a stationary planar platinum electrode (area = $1.96 \times 10^{-5} m^2$), in an unstirred 1M HCl solution containing the electroactive species: $10 mol m^{-3}$ $FeCl_3$, and $10 mol m^{-3}$ $FeCl_2$, at 293K. Current/time data capture and subsequent treatment, was provided by the commercially available CONDECON software package (cf. Section 2.3.2). The optimal duration of polarization was between 0.2 and 2s. The lower limit was dictated by the logistics of collecting 2000 data points, whilst the upper time limit was imposed by the increasing contribution of convection within the electrolyte to the mass transport at long times. The current was electrically dampened prior to capture using a EG&G CONDECON 300 Signal Conditioning Unit, to reduce the charging current associated with the capacitance of the electrical double layer (cf. Section 1.6.1), and to improve the signal to noise ratio.

Figure 3.7.1 shows the profile of the captured chronoamperometric data at overpotentials 0.19V and -0.19V. Note, that the slow rise in current is due to a slight excess of damping. These results do not adhere to the Cottrell relationship as demonstrated by a plot of $i^2 t$ versus t in Figure 3.7.2 (cf. Equation 1.6.33 in Section 1.6.2).

In Section 1.6.2 it was shown that under conditions of constant potential chronoamperometry, the linearity of i(t) with I_1 in Equation 1.6.27 allows k_f, k_b, D_A, and D_B to be determined in principle in any regime of electron transfer. Therefore, the chronoamperometric data was explored via

$$i(t) = -\beta I_1 + \gamma. \qquad (1.6.27)$$

In the limiting case when $k_f >> k_b$ (i.e at sufficiently large overpotentials) it is found that

$$\gamma \sim I^A{}_{lim} \left\{ \frac{k_f}{D_A{}^{1/2}} \right\} \quad \text{and} \quad \beta \sim \left\{ \frac{k_f}{D_B{}^{1/2}} \right\}.$$

Therefore, measurement of the intercept, c, and the gradient m (i.e. $-\beta$), gives D_A and k_f (or, when $k_b >> k_f$, D_B and k_b). Plots of i(t) versus I_1 from captured i-t data are shown in Figure 3.7.3. This figure displays clearly, the characteristic features of this function. Firstly, the anodic and cathodic data show rotational symmetry about the

Cartesian axes. Secondly, if the i/I_1 data are extrapolated to $i = 0$, then a convergence is obtained, corresponding to I_{lim}, and therefore a direct route to the diffusion coefficients D_A or D_B. Thirdly, the gradients are proportional to $k_f(E)$ (or $K_b(E)$), such that at progressively larger overpotentials, the gradients approach negative infinity, and hence a trend towards Cottrell behaviour. Note, that this is true for either anodic or cathodic processes, because of the sign convention adopted in Section 1.6.2. Therefore, in the potential/time region where the overpotential is small enough to avoid Cottrell behaviour within the duration of the experiment, and yet sufficiently large to satisfy the requirement that $k_f \gg k_b$; then the potential dependent rate constant k_f can be calculated from the measurement of the gradient

$$m = -\beta = -k_f/D_A{}^{1/2}.$$

Furthermore, the variation of the gradient with overpotential is a route to k^o and α, and hence a test for the Butler-Volmer relationship.

Table 3.7.1 lists the intercepts (c), and the gradients (m), from the plots in Figure 3.7.3. I_{lim} is obtained directly from the mean value of the appropriate set of intercepts. Hence, via Equation 1.6.11 and 1.6.12 in Section 1.6.2; both of the diffusion coefficients were obtained. $D(FeCl_3) = 5.32\times10^{-10} \pm 0.19\times10^{-10}\ m^2s^{-1}$, and $D(FeCl_2) = 5.30\times10^{-10} \pm 0.02\times10^{-10}\ m^2s^{-1}$.

The Butler-Volmer relationship can be expressed in the form

$$\ln k = \alpha(Z_B-Z_A)F(E-E^o)/RT + \ln k^o \qquad (3.7.1)$$

which has the form of a linear relationship and yields the standard heterogeneous rate constant k^o and the charge transfer coefficient α .

A plot of Equation 3.7.1 is shown in Figure 3.7.4 for both anodic and cathodic processes. The following parameters were therefore determined. $\alpha_{anodic} = 0.30$, $\alpha_{cathodic} = 0.49$, and $k^o = 4.0\times10^{-6} +/- 2.1\times10^{-6}$ ms^{-1}.

The above analysis of i(t) with I_1 via Equation 1.6.27 is inherently prone to error because the charging current and damping, severely distort the initial currents, such that the convoluted current may not "forget" this region in the life-time of experimentally significant deviation from Cottrell behaviour, and / or before the onset of the effect of convection currents. An alternative treatment of the chronoamperometric data, is derived in Appendix G, and relates to Equation 1.6.35 in Section 1.6.2. This too, has a linear form, but one which is not distorted either by charging curents once these have died away, nor by the effects of damping on the initially rapidly varying currents.

The relevant equation is in the form of a step function, which is referred to here, for convenience, as the "chronoamperometric parameter plot".

$$\frac{\Delta Q}{\Delta i} = \left\{\frac{2 \quad \gamma}{\pi^{1/2} \beta}\right\} \frac{\Delta t^{1/2}}{\Delta i} + \frac{1}{\beta^2} \qquad (1.6.35)$$

The gradient and intercept allow parameter determination (cf. Appendix G). The arbitrary interval Δ allows the integration limits t_1 and t_2 to be chosen, so as to coincide with the least distorted part of the data, in this case the interval between the 500th and 1500th data point was chosen.

Plots of $\Delta Q/\Delta i$ versus $\Delta t^{1/2}/\Delta i$ (calculated from the same orignal data as used in the above analysis of i(t) with I_1), are shown in Figure 3.7.5.

This figure displays clearly the characteristic features of this function. Firstly, the anodic and cathodic data show near reflection symmetry in the $\Delta Q/\Delta i$ axis. Secondly, the of the gradient is a direct route to the diffusion coefficient D_A via Equation (G.12) in Appendix G. If the data on this plot are extrapolated to $\Delta t^{1/2}/\Delta i = 0$, then the variation in the corresponding intercept, c, (on the $\Delta Q/\Delta i$ axis) with the applied potential, is a route to the heterogeneous electrochemical parameters. Note that at progressively larger overpotentials, these intercepts approach $\Delta Q/\Delta i = 0$. The potential dependent rate constant (k_f) can be calculated from measurement of the gradient (m) and the intercept (c), and via Equation (G.13) in Appendix G.

Table 3.7.2 lists the intercepts (c) and gradients (m) from the plots in Figure 3.7.5. The diffusion coefficients were calculated from Equation G.12 using the mean value of the appropriate set of gradients. $D(FeCl_3) = 5.34\times10^{-10}$ +/- 0.24×10^{-10} m^2s^{-1}, and $(FeCl_2) = 5.23\times10^{-10}$+/- 0.02×10^{-10} m^2s^{-1}.

A plot of ln k versus $E-E^o$ (i.e. Equation 3.7.1) is given in Figure 3.7.6. The heterogeneous electrochemical parameters were obtained as follows. $\alpha_{anodic} = 0.41$, $\alpha_{cathodic} = 0.50$, and $k^o = 2.5\times10^{-6}$ +/- 0.8×10^{-6} ms^{-1}.

Because of the limiting conditions (i.e. $k_f >> k_b$ etc.) imposed during the determination of the potential dependent rate constants by the above techniques, the data in Figures 3.7.6 and 3.7.4 lie substantially removed from E^o. This creats a proportionately large error in the intercept of the ln k axis (at $E-E^o = 0$). It would, for this reason, be better to capture and treat chronoamperometric data within the vicinity of the polarographic wave (i.e. near E^o). The treatment of such data in terms of the "chronoamperometric parameter plot" is given in Appendix G, and relates to Equations (G.14 to G.21). Chronamperometric data obtained at relatively low overpotentials are given in Table 3.7.3. The treatment of this data initially involved the determination of half-wave potential $E_{1/2}$ and D_A (and hence D_B through a knowledge of E^o) by the construction of the "diffusion coefficient plot" (cf. Equation G.17 in Appendix G) as shown in Figure 3.7.7. Measurement of the gradient (M), and intercept (C), enabled the calculation of $E_{1/2}$ from Equation (G.20), from both the cathodic and anodic data. $E_{1/2}$(cathodic) = 0.4613V, $E_{1/2}$(anodic) = 0.4666V vs. SCE.

Within the limits of experimental error (as indicated by the standard deviation in the gradient and intercept of the "diffusion coefficient plot", cf. Table 3.7.3), these results indicate that $E_{1/2}$ is approximately equal to E^o. This is in agreement with the results from the previous analysis at larger potentials (cf. Table 3.7.2). For this reason, $E_{1/2}$ was taken as being equal to E^o in the subsequent calculation of k_f via Equation (G.22) in Appendix G. Similarly, the values for the diffusion coefficients as determined from the large overpotential data (via Equation G.11), were considered more accurate than those determined from the small overpotential data (via Equation G.19), because at larger overpotentials, the system at a given time is closer to Cottrell behaviour, i.e. diffusion control. For this reason, the diffusion coefficients for both $FeCl_3$ and $FeCl_2$ were taken as $5.3x10^{-10}m^2s^{-1}$ in calculating k_f via Equation (G.22). The values of ln k_f as calculated from the above data are given in Table 3.7.3. The corresponding plot of ln k_f versus $E-E^o$ (i.e. Equation 3.7.1) is shown in Figure 3.7.8. The heterogeneous electrochemical parameters were obtained as follows. $\alpha_{anodic} = 0.34$, $\alpha_{cathodic} = 0.50$, and $k^o = 2.0x10^{-5}$ +/- $1.0x10^{-5}$ ms^{-1}.

The above results from the chronoamperometric analyses are in general agreement with the Butler-Volmer relationship, and therefore support the above model of simple electron transfer. However, the consistent departure of the sum $\alpha_a + \alpha_c$ from unity is noted, but unexplained here.

The numerical value for the standard heterogeneous rate constant was compared with that obtained from the measurement of the peak separation in cyclic voltammograms of the $FeCl_3/FeCl_2$ couple, via the use of the "working curve" for the kinetic parameter Ψ as described by Nicholson (176).

Cyclic voltammograms of the $FeCl_3/FeCl_2$ couple on platinum are shown in Figure 3.7.9 and 3.7.10. At dE/dt = $0.005Vs^{-1}$, the peak potential separation $\Delta E_p = 0.114V$, whilst at dE/dt = $0.05Vs^{-1}$, $\Delta E_p = 0.237V$. The charge transfer parameter Ψ, was calculated from the relationship

$$\Psi = \frac{k^o(D_A/D_B)^{\alpha/2}}{[\pi(Z_B-Z_A)F(dE/dt)D_A/RT]^{1/2}} \qquad (3.7.2)$$

Taking $D_A = D_B = 5.3x10^{-10}ms^{-1}$, and adopting $\alpha = 0.5$, gave $\Psi = 79861k^o$ (at dE/dt = $0.005Vs^{-1}$) and $\Psi = 25254k^o$ (at dE/dt

$= 0.05Vs^{-1}$). By comparing these values with those shown in the working curve (176) for the variation of ΔE_p with Ψ , gave a mean value of $k^o = 6x10^{-6}ms^{-1}$; which is in approximate agreement with those obtained from the chronoamperometric analysis within this Section.

Table 3.7.1

Data from plots of the function $i = mI_1 + c$

500th - 1500th point data.

$[FeCl_3] = [FeCl_2] = 10 mol m^{-3}$

$T = 293K$

$E^o = 0.457V$ vs. SCE

(cf. Section 1.6.2, Equation 1.6.27).

$E-E^o/V$	c/V	m/V^{-1}	s.d. (m)	ln k
0.19	$4.38x10^{-4}$	-2.44	$1.43x10^{-3}$	-9.787
0.18	$4.37x10^{-4}$	-2.38	$1.25x10^{-3}$	-9.812
0.17	$4.36x10^{-4}$	-2.05	$9.39x10^{-4}$	-9.961
0.16	$4.35x10^{-4}$	-1.74	$7.05x10^{-4}$	-10.125
0.15	$4.34x10^{-4}$	-1.57	$6.35x10^{-4}$	-10.228
-0.15	$-4.46x10^{-4}$	-4.08	$6.42x10^{-3}$	-9.271
-0.16	$-4.35x10^{-4}$	-1.84	$1.40x10^{-3}$	-10.067
-0.17	$-4.35x10^{-4}$	-2.10	$1.80x10^{-3}$	-9.935
-0.18	$-4.36x10^{-4}$	-2.76	$2.75x10^{-3}$	-9.662
-0.19	$-4.35x10^{-4}$	-3.20	$3.56x10^{-3}$	-9.514

$I_{lim}(FeCl_2) = 4.36x10^{-4} As^{1/2}$ s.d. $= 1.41x10^{-6}$

$I_{lim}(FeCl_3) = -4.37x10^{-4} As^{1/2}$ s.d. $= 4.32x10^{-6}$

$D(FeCl_2) = 5.30x10^{-10} m^2 s^{-1}$

$D(FeCl_3) = 5.32x10^{-10} m^2 s^{-1}$

$E_{1/2} = 0.4569V$ vs. SCE

$k^o = 4.0x10^{-6} +/- 2.1x10^{-6} ms^{-1}$

$\alpha_a = 0.30 +/- 0.03$

$\alpha_c = 0.49 +/- 0.05$

Table 3.7.2

Data from plots of the function $\Delta Q/\Delta i = m\Delta t^{1/2}/\Delta i + c$

500th - 1500th point data

$[FeCl_3] = [FeCl_2] = 10 mol m^{-3}$

T = 293K

$E^o = 0.457V$ vs. SCE

(cf. Appendix G, Equation G.8).

$E-E^o/V$	c/s	s.d. (c)	$m/As^{1/2}$	ln k
0.19	0.109	$3.90x10^{-4}$	$4.91x10^{-4}$	-9.577
0.18	0.120	$4.17x10^{-4}$	$4.89x10^{-4}$	-9.626
0.17	0.183	$5.60x10^{-4}$	$4.88x10^{-4}$	-9.837
0.16	0.282	$9.53x10^{-4}$	$4.88x10^{-4}$	-10.053
0.15	0.358	$1.38x10^{-3}$	$4.87x10^{-4}$	-10.172
-0.15	0.082	$4.93x10^{-4}$	$-5.03x10^{-4}$	-9.425
-0.16	0.318	$1.37x10^{-3}$	$-4.92x10^{-4}$	-10.102
-0.17	0.239	$1.04x10^{-3}$	$-4.91x10^{-4}$	-9.960
-0.18	0.155	$7.90x10^{-4}$	$-4.94x10^{-4}$	-9.743
-0.19	0.098	$5.16x10^{-4}$	$-4.89x10^{-4}$	-9.514

$\overline{m}$ $(FeCl_2)$ = $4.89x10^{-4}As^{1/2}$ s.d. = $1.36x10^{-6}$

$\overline{m}$ $(FeCl_3)$ = $-4.94x10^{-4}As^{1/2}$ s.d. = $4.87x10^{-6}$

$D(FeCl_2) = 5.23x10^{-10}m^2s^{-1}$

$D(FeCl_3) = 5.34x10^{-10}m^2s^{-1}$

$E_{1/2} = 0.4567V$ vs. SCE

$k^o = 2.5x10^{-6}$ +/- $0.8x10^{-6}$ ms^{-1}

α_a = 0.41 +/- 0.04

α_c = 0.50 +/- 0.04

Table 3.7.3

Data from plots of the function $\Delta Q/\Delta i = m\Delta t^{1/2}/\Delta i + c$

500th - 1500th point data

$[FeCl_3] = [FeCl_2] = 10 mol m^{-3}$, T = 293K, E^o = 0.460V vs. SCE

(cf. Appendix G, Equation G.8).

$E-E^o/V$	c/s	$m/As^{1/2}$	theta	$\ln k_f$
0.010	0.1609	7.66×10^{-4}	42678	-10.280
0.020	0.1656	1.50×10^{-4}	36404	-10.153
0.030	0.1497	2.19×10^{-4}	31796	-9.995
0.040	0.1301	2.73×10^{-4}	29069	-9.846
0.050	0.1141	3.22×10^{-4}	26763	-9.723
0.060	0.1050	3.48×10^{-4}	26051	-9.641
0.070	0.0874	3.77×10^{-4}	24841	-9.521
0.080	0.0688	3.94×10^{-4}	24326	-9.382
0.090	0.0469	4.13×10^{-4}	23539	-9.177
0.100	0.0378	4.19×10^{-4}	23420	-9.060

$M = 29800 mol m^{-3} A^{-1} s^{-1/2}$ s.d. = 307

$C = 22900 mol m^{-3} A^{-1} s^{-1/2}$ s.d. = 88

$D(FeCl_2) = 4.2\times10^{-10} m^2 s^{-1}$

$E_{1/2}$ = 0.4666V vs. SCE

$k^o = 3.02\times10^{-5} ms^{-1}$

α_a = 0.34 +/- 0.01

$E-E^o/V$	c/s	$m/As^{1/2}$	theta	$\ln k_f$
-0.010	1.851	-9.12×10^{-5}	-35860	-11.501
-0.020	1.460	-1.79×10^{-4}	-30566	-11.242
-0.030	1.014	-2.70×10^{-4}	-25750	-10.952
-0.040	0.777	-3.25×10^{-4}	-24459	-10.739
-0.050	0.578	-3.70×10^{-4}	-23297	-10.534
-0.060	0.441	-4.03×10^{-4}	-22509	-10.359
-0.070	0.345	-4.26×10^{-4}	-22007	-10.208
-0.080	0.243	-4.43×10^{-4}	-21619	-10.013
-0.090	0.173	-4.45×10^{-4}	-21816	-9.830
-0.100	0.125	-4.53×10^{-4}	-21630	-9.658

$M = -21700 mol m^{-3} A^{-1} s^{-1/2}$ s.d. = 1060

$C = -20600 mol m^{-3} A^{-1} s^{-1/2}$ s.d. = 3060

$D(FeCl_3) = 5.2\times10^{-10} m^2 s^{-1}$

$E_{1/2}$ = 0.4613V vs. SCE

$k^o = 9.16\times10^{-6} ms^{-1}$

α_c = 0.50 +/- 0.02

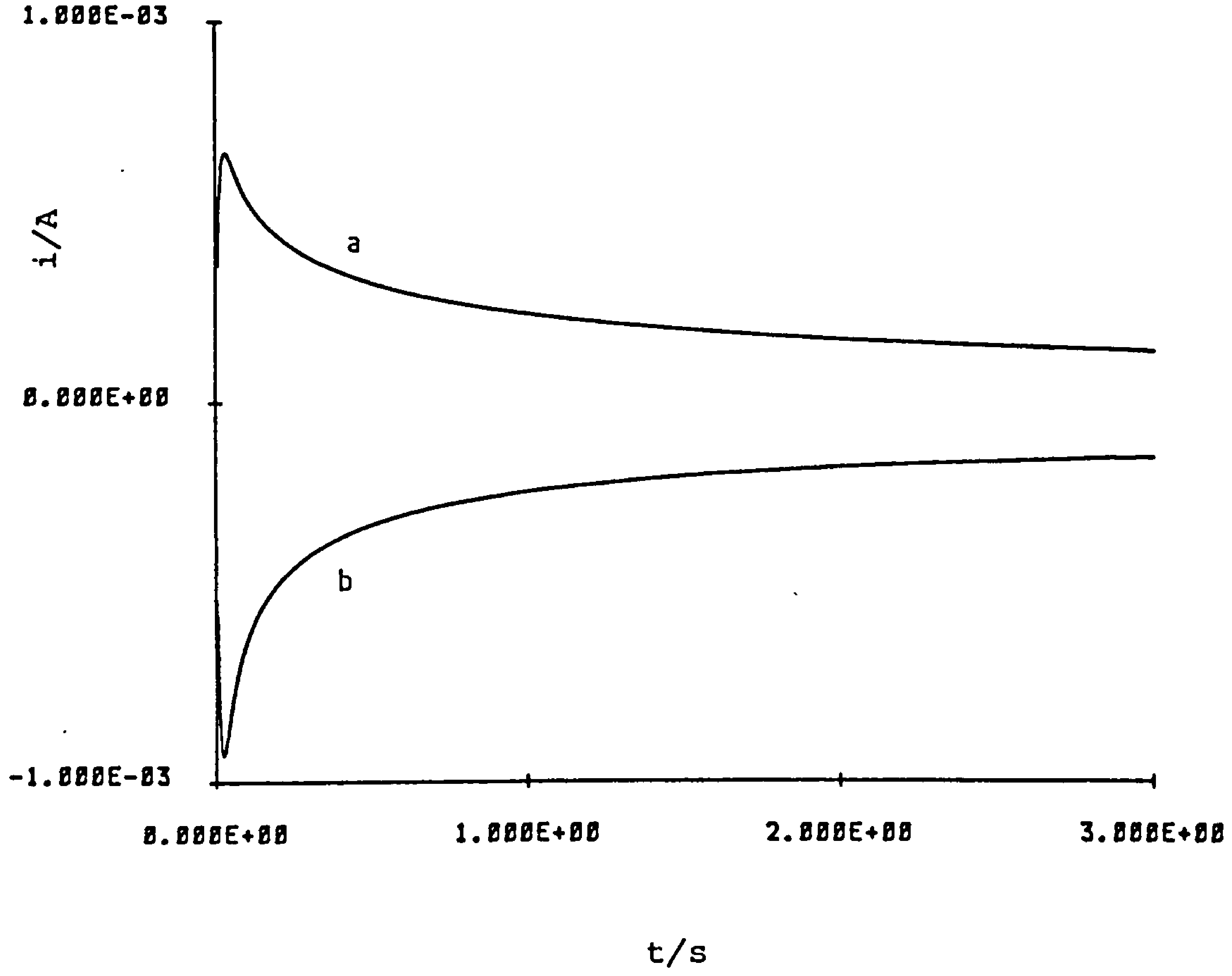

Figure 3.7.1

Chronoamperograms for the $FeCl_3/FeCl_2$ couple in unstirred 1M HCl solution containing $10molm^{-3}$ $FeCl_3$ and $10molm^{-3}$ $FeCl_2$, on a stationary platinum electrode (area = $2.83x10^{-5}m^2$) at 293K. E_{eq} = 0.457V vs. SCE.

Polarization: (a) 0.647V (η= 0.19V), (b) 0.267V (η= -0.19V).

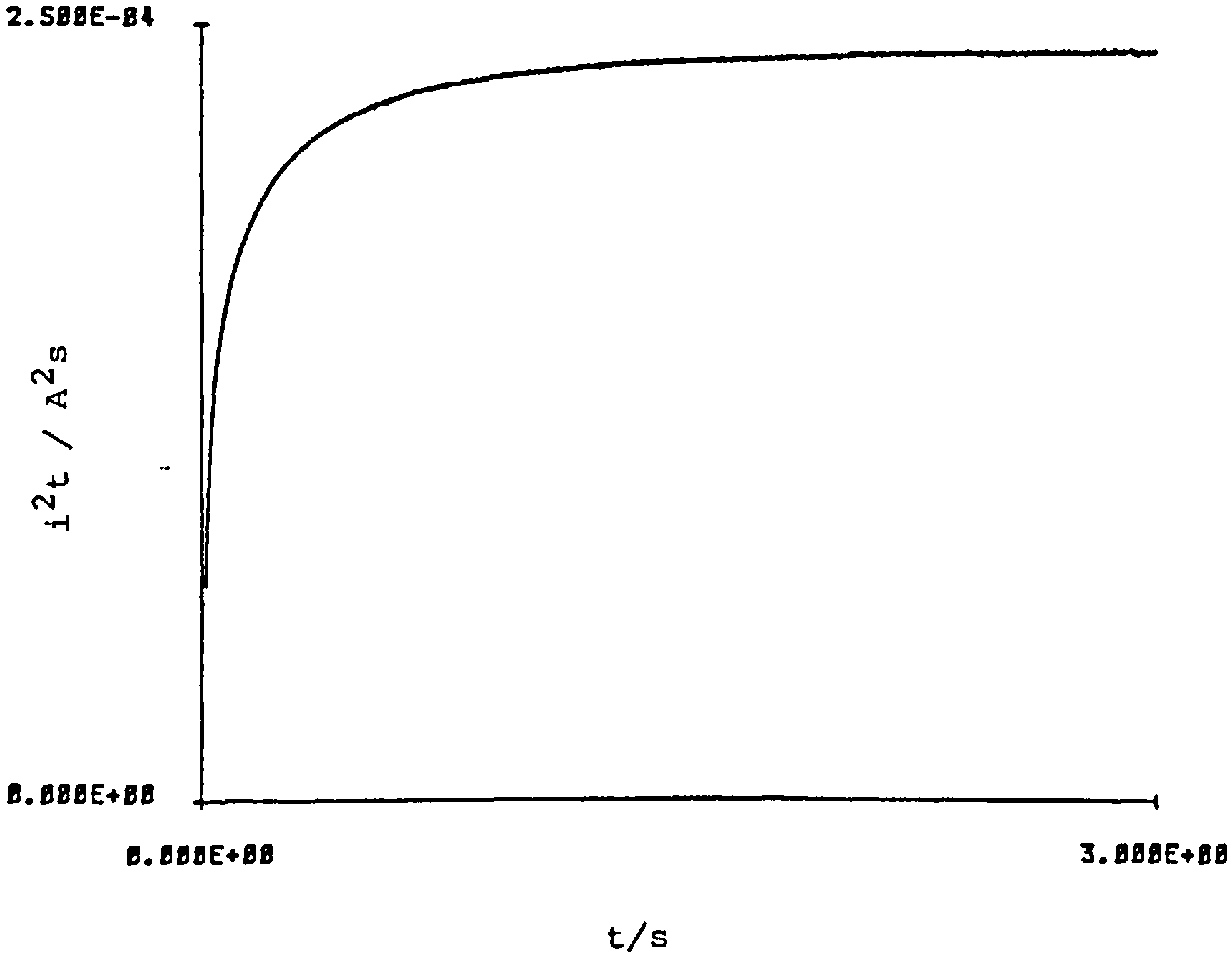

Figure 3.7.2
Plot of i^2 t versus t (i.e. test for Cottrell behaviour), on chronoamperometric data at $E-E^o$ = 0.19V.

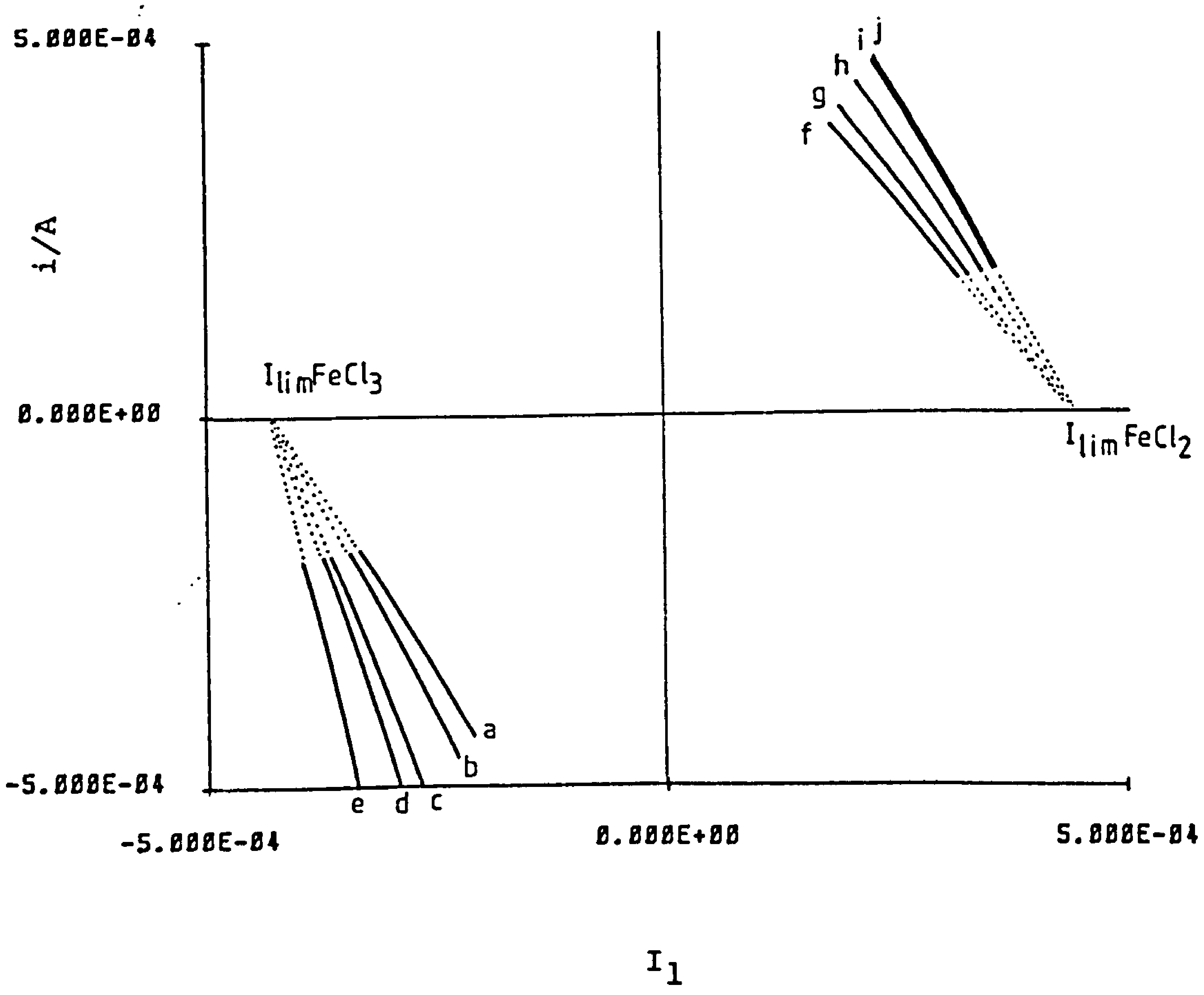

Figure 3.7.3

Plots of i vs. I_1, from captured i-t data for the $FeCl_3$/$FeCl_2$ couple. Overpotentials:

(a) -0.15V, (b) -0.16V, (c) -0.17V, (d) -0.18V, (e) -0.19V, (f) 0.15V, (g) 0.16V, (h) 0.17V, (i) 0.18V, (j) 0.19V.

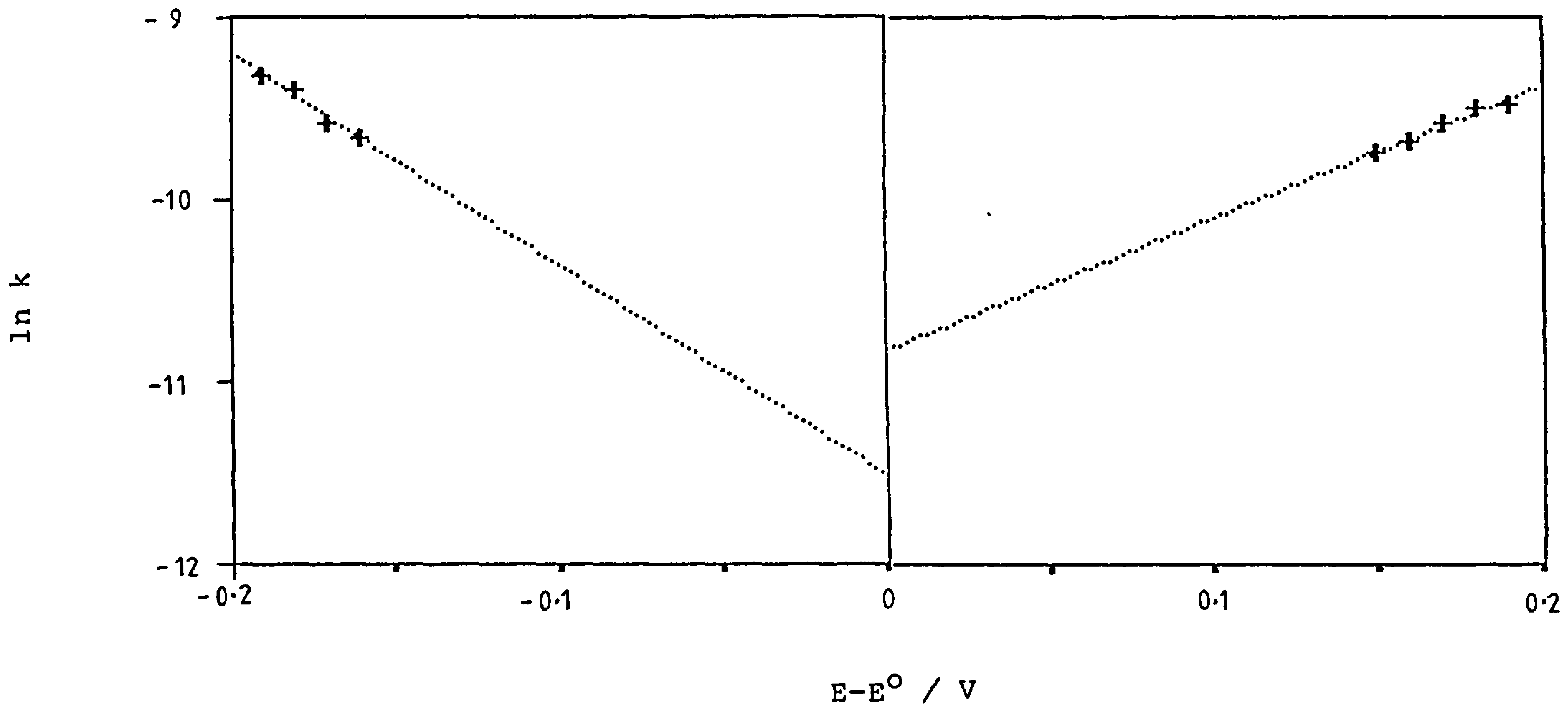

Figure 3.7.4

Plot of ln k vs. $(E-E_{eq})$ for the determination of the electrochemical parameters for the $FeCl_3/FeCl_2$ couple based on k_f and k_b data obtained from the i vs. I_1 plots in Figure 3.7.2.

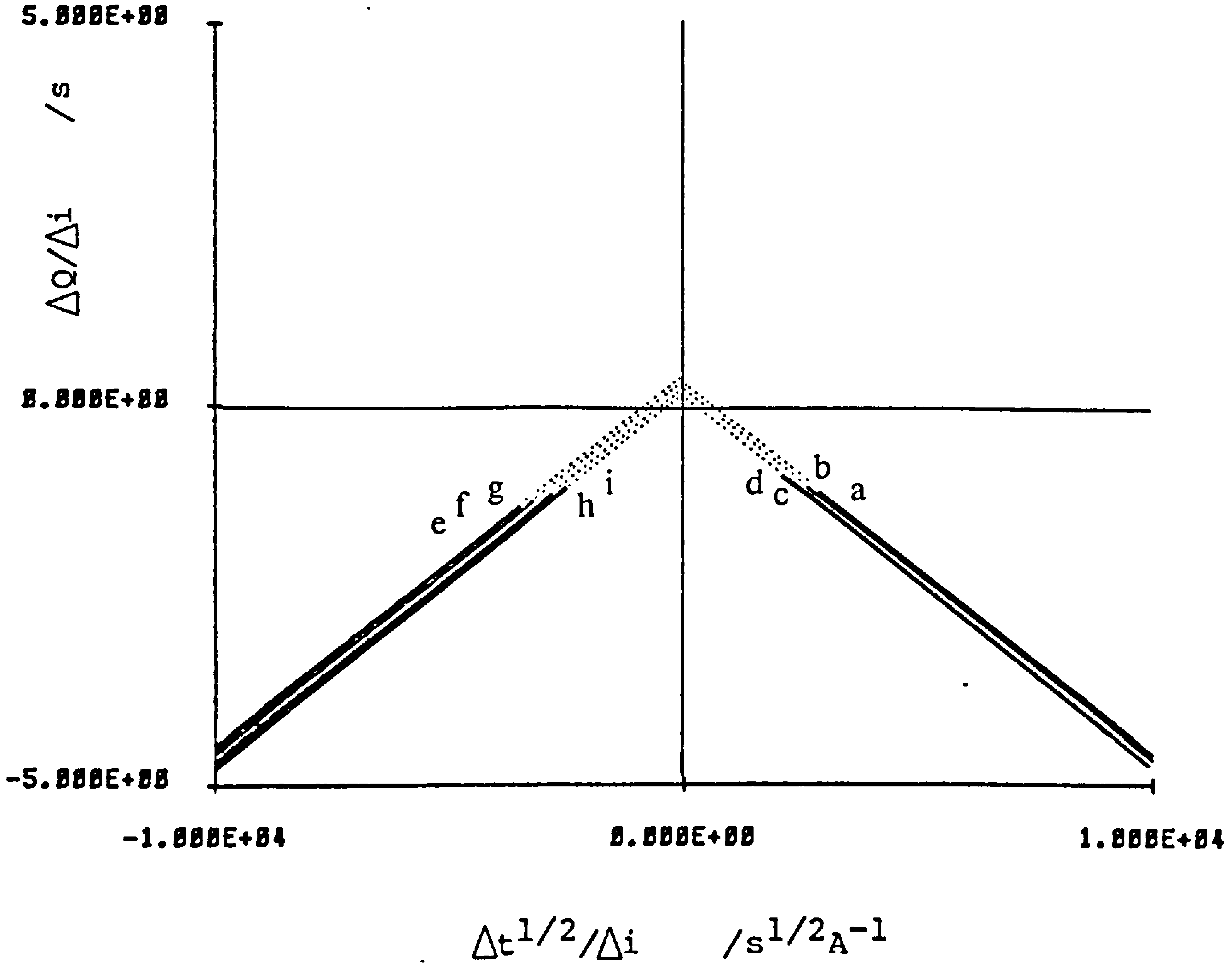

Figure 3.7.5

Plots of $\Delta Q/\Delta i$ vs. $\Delta t^{1/2}/\Delta i$ from captured i-t data for the $FeCl_3/FeCl_2$ couple. Overpotentials:

(a) -0.16V, (b) -0.17V, (c) -0.18V, (d) -0.19V, (e) 0.15V, (f) 0.16V, (g) 0.17V, (h) 0.18V, (i) 0.19V.

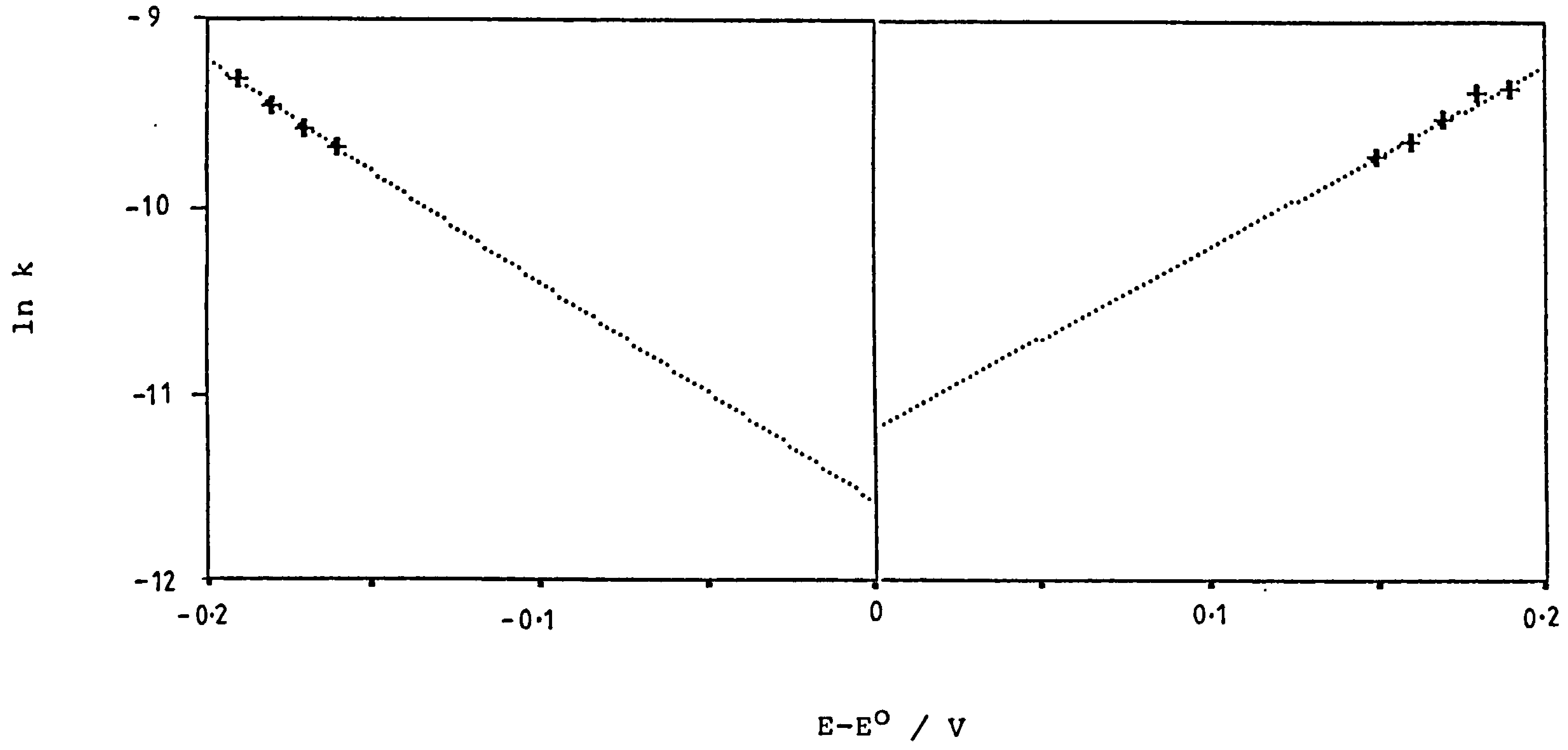

Figure 3.7.6

Plot of ln k vs. $(E-E_{eq})$ for the determination of the electrochemical parameters for the $FeCl_3/FeCl_2$ couple based on k_f and k_b data obtained from the $\Delta Q/\Delta i$ vs. $\Delta t^{1/2}/\Delta i$ plots in Figure 3.7.4.

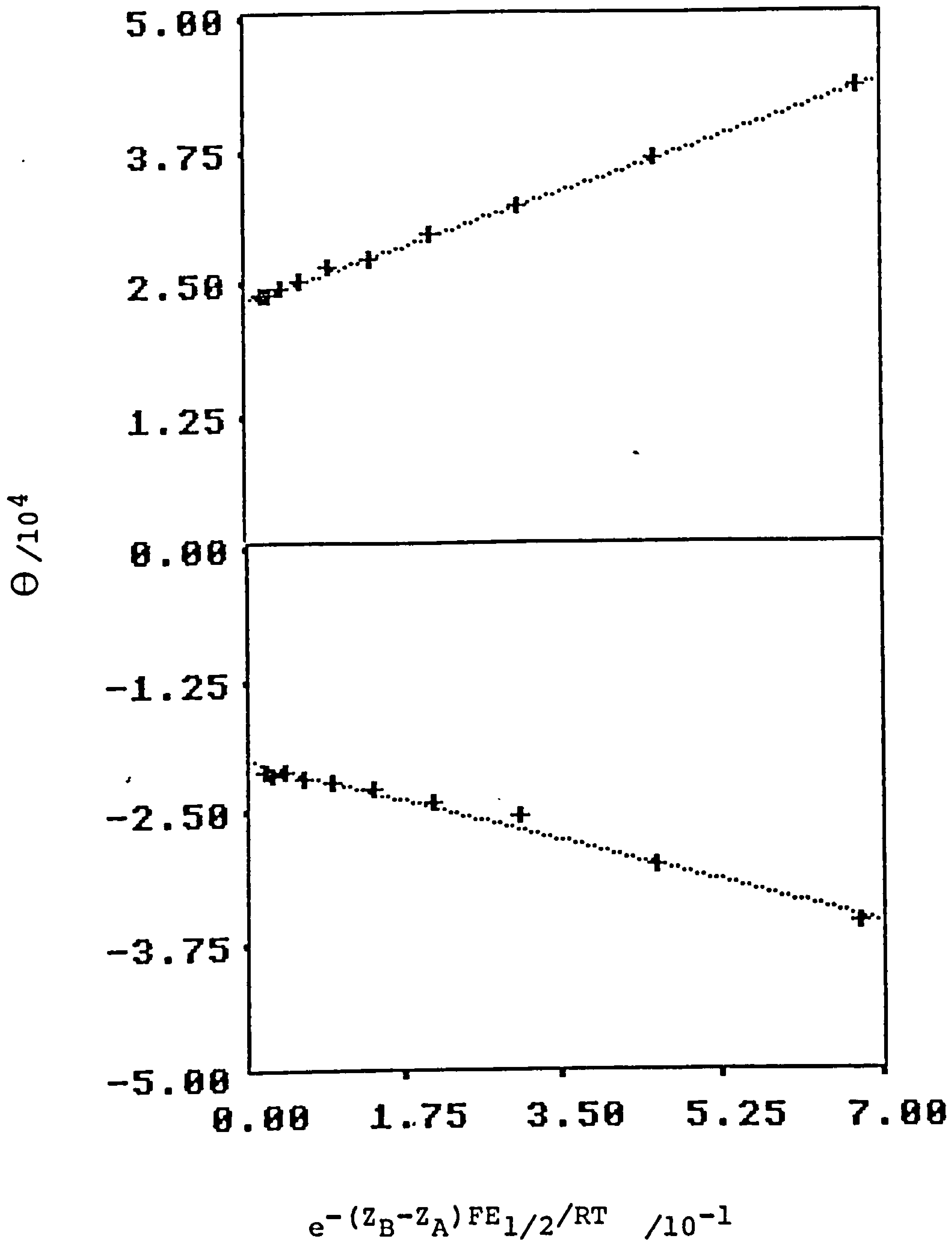

Figure 3.7.7

Diffusion Coefficient Plot,

Θ versus $e^{-(Z_B-Z_A)FE_{1/2}/RT}$ for the chronoamperometric data at low overpotentials (cf. Table 3.7.3).

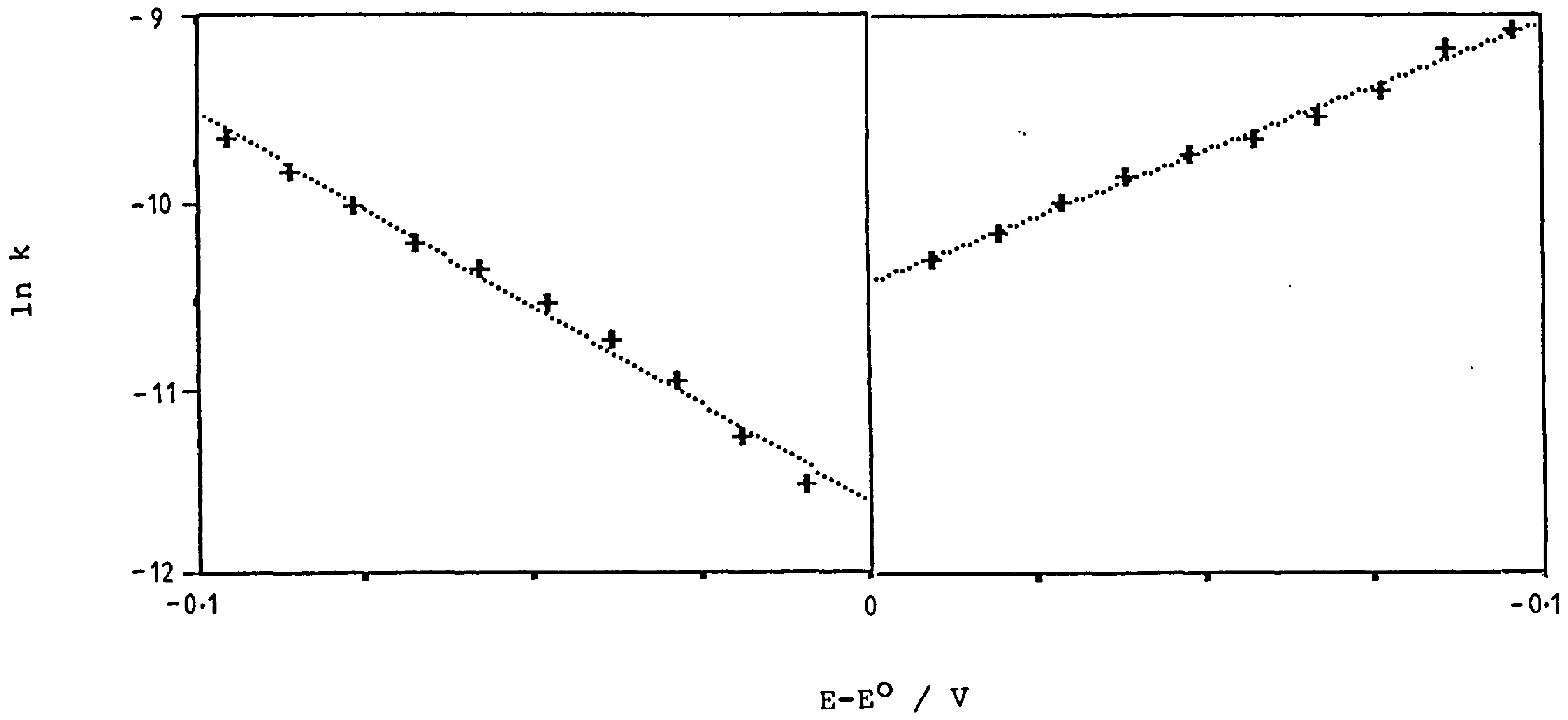

Figure 3.7.8

Plot of ln k vs. (E-E_{eq}) for the determination of the electrochemical parameters for the $FeCl_3/FeCl_2$ couple based on k_f and k_b data obtained from the $\Delta Q/\Delta i$ vs. $\Delta t^{1/2}/\Delta i$ plots at low overpotentials (cf. Table 3.7.2).

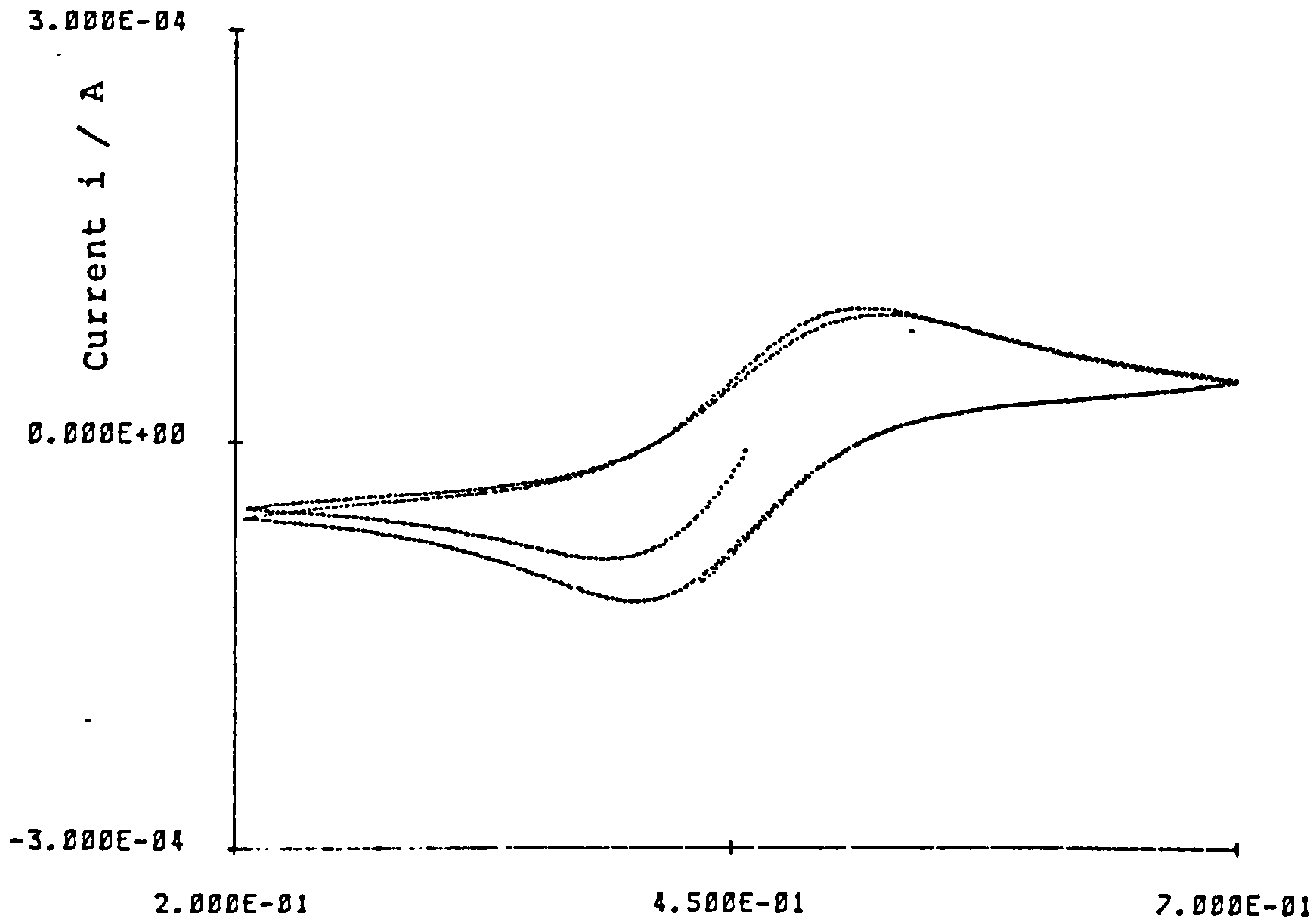

Potential E / V vs. SCE

Figure 3.7.9
Cyclic Voltammogram for the $FeCl_3/FeCl_2$ couple in unstirred 1M HCl solution containing $10molm^{-3}$ $FeCl_3$ and $10molm^{-3}$ $FeCl_2$ on a stationary platinum electrode (area = $2.83x10^{-5}m^2$) at 293K. Scan rate = $0.005Vs^{-1}$. Initially cathodic of E_{eq} (0.457V vs. SCE).

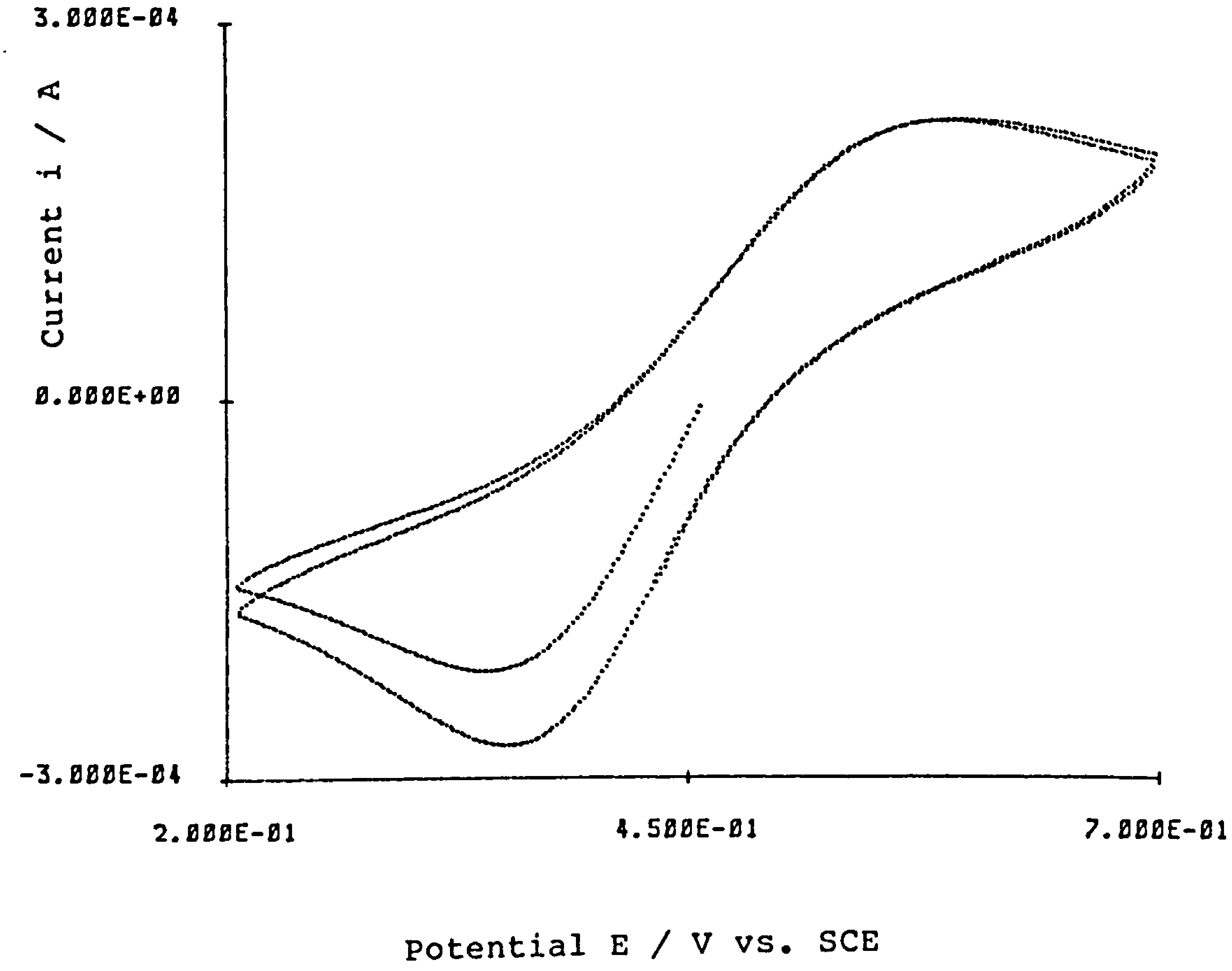

Figure 3.7.10

Cyclic Voltammogram for the $FeCl_3/FeCl_2$ couple in unstirred 1M HCl solution containing $10molm^{-3}$ $FeCl_3$ and $10molm^{-3}$ $FeCl_2$ on a stationary platinum electrode (area = $2.83x10^{-5}m^2$) at 293K. Scan rate = $0.05Vs^{-1}$. Initially cathodic of E_{eq} (0.457V vs. SCE).

4 SUMMARY AND CONCLUSIONS

4.1 SUMMARY OF RESULTS

This section includes a brief review of certain parts of Section 1 together with a summary of the results from Section 3.

With regard to the thermodynamic properties of the Fe-Ni-S system, both pentlandite ($Fe_{4.5}Ni_{4.5}S_8$) and Fe-deficient violarite ($Fe_{1-x}Ni_{2+x}S_4$) are considered as stable phases at 298K and 101kPa. However, their coexistence, which often occurs in natural material, appears to represent a metastable assemblage due to the construction of a tie line between pyrite (FeS_2) and millerite (NiS) in the corresponding isothermal phase diagram. The intimate occurance of violarite with pentlandite in such deposits is attributed to the supergene alteration of violarite from pentlandite. Furthermore, there is much evidence in the literature to suggest an electrochemical mechanism for this process on account of the appreciable electrical conductivity vis a vis metallic bonding of these two phases. Indeed, measurements from this present work give the electrical resistivites of pentlandite as $5.2x10^{-4}\Omega m$ and violarite as $6.5x10^{-4}$ Ωm respectively.

From a critical review of the thermodynamic data in the literature, speculative estimates of the standard free energies of formation at 298K were proposed as follows: pentlandite = $-813kJmol^{-1}$, and violarite = $-346kJmol^{-1}$. These values were used in the construction of several E_h-pH diagrams at 298K for the Fe-Ni-S aqueous system relevant to this work. These diagrams indicate that pentlandite is unstable in acid media with respect to nickel and ferrous ions, and hydrogen sulphide, violarite, orthorhombic sulphur, or sulphate, in order of increasing oxidative conditions.

Pentlandite adopts a definite rest-potential of approximately -0.410V vs. SCE in 1M HCl solution at 353K. This is interpreted in terms of a mixed-potential regime incorporating the following two processes:

$$Fe_{4.5}Ni_{4.5}S_8 + 16H^+ = 4.5Fe^{2+} + 4.5Ni^{2+} + 8H_2S + 2e \qquad (4.1.1)$$

$$2H^+ + 2e = H_2 \qquad (4.1.2)$$

By comparison, violarite adopts an ill-defined open-circuit potential in the same solution, within the range 0.1 to 0.4V vs. SCE. This is attributed to the interaction of trace oxidants (via a Fe^{3+}/Fe^{2+} couple) with the following disproportionation reaction:

$$4FeNi_2S_4 + 23H^+ + 4H_2O = 8Ni^{2+} + 4Fe^{2+} + 15H_2S + HSO_4^- \qquad (4.1.3)$$

Pentlandite and violarite both adopt the same rest-potential in 1M HCl solution containing an equal ratio of $FeCl_3$ and $FeCl_2$ at 298K, as that for platinum (i.e. 0.450V vs. SCE). This similarity between mixed and equilibrium potentials (even at 353K) is compelling evidence that the oxidative dissolution of pentlandite or violarite in acid media involves (at least during the initial stages of reaction and in the temperature range 293 to 343K) slow electron transfer for the S^o,Ni^{2+},Fe^{2+} / $Fe_{4.5}Ni_{4.5}S_8$ and S^o,Fe^{2+},Ni^{2+} / $FeNi_2S_4$ couples per se.

Cyclic voltammetric experiments in electrochemically inert 1M HCl solution have shown that reasonable rates of dissolution by either pentlandite or violarite (i.e. $100Am^{-2}$) were not obtained until relatively high potentials (i.e. >0.8V vs. SCE), irrespective of temperature or solution composition. This implies that a large anodic overpotential is required for the oxidation of these minerals, which is in agreement with the conclusions from the open-circuit potential measurements with $FeCl_3$ as described above. In this high potential region, the anodic currents were accompanied with the visible formation of amorphous sulphur. In the case of pentlandite, this was accompanied by a metallic violet/grey coloured tarnish, which from purely visual observations was tantalizingly suggestive of the formation of violarite as an intermediate phase.

Cyclic voltammetric experiments for the reduction / oxidation of the $FeCl_3/FeCl_2$ couple on the corroding pentlandite surface showed a progressive drop in current on successive cycles. This apparent passivation of the pentlandite surface was explained in terms of a semi-permeable amorphous sulphur product film, which hindered ionic mass transport in the aqueous phase adjacent to the mineral surface. This conclusion does not retract from that given above. It merely creates an additional kinetic problem for the dissolution mechanism. It is therefore possible that at a later stage of the reaction, this mass transport process becomes comparable with, and ultimately predominates over the electron transfer process and thereby becomes rate determining.

Similar features also occured on corroding violarite, although the drop in currents were less rapid.

Intermittent galvanostatic polarization (IGP) experiments on pentlandite showed a temporary potential arrest whilst in open-circuit at approximately -0.1V vs. SCE (343K). This was interpreted in terms of a mixed-potential regime between elemental sulphur and pentlandite in acid solution. This phenomenon was used to show that elemental sulphur was not formed during anodic polarization until the closed-circuit potential exceeded approximately 0V vs. SCE. Furthermore, no evidence for the formation of an intermediate metal-sulphide phase, e.g. violarite, could be drawn from these results.

The results from similar experiments on violarite were less clearly understood than those of pentlandite. Nonetheless, the lack of any similarity in the open-circuit potential arrests may be adopted as further evidence for the lack of formation of violarite on the pentlandite surface.

Chronopotentiometric experiments with pentlandite in 1M $HClO_4$ solution yielded a first wave in the high potential region of 0.8 to 1V vs. SCE. The transition time (t_s) for this wave at various imposed current densities only corresponds to the Sand equation at temperatures <298K. Furthermore, the product $i_c^2t_s$ when applied to the Arrhenius equation as a function of reciprocal temperature yielded anomalous behaviour. Likewise, an analysis of the chronopotentiometric wave by convolutive techniques (for a Nernstian system) yielded results inconsistent with this model. Furthermore, the formation of substantial amounts of sulphate accompanied by elemental sulphur means that the imposed current density would need to be proportioned between two processes. These findings collectively, cast a severe doubt on using a model solely based on simple diffusional processes.

Substantial differences in the behaviour between experiments in $HClO_4$ and HCl solution add to the complexity of the mechanistic problem, but nonetheless illustrate clearly that solid state diffusional processes are not rate determining here. However, sufficient evidence was available to suggest that electro-assisted migration of product aqueous metal ions, in addition to the diffusional process, play an important role in maintaining the required ionic flux through the product layer under galvanostatic conditions, i.e.

$$E_{applied} = E_{eq} + \eta_{E.T.} + \eta_{iR(migration)} \qquad (4.1.4)$$

EMPA and SEM of the electrode surface at various stages of anodic polarization revealed increasing amounts of sulphur. The amorphous nature of the product sulphur was clearly observed by SEM. EMPA failed to detect any intermediate phases (e.g. violarite) as was confirmed by its absence in powder camera XRD analysis of the product layer. Aqueous analysis also showed that an equal ratio of iron and nickel was introduced into the solution, suggesting complete "elemental" decomposition of the mineral surface. Nonetheless, the layer has an intense violet/grey colour, which is yet to be explained. The presence of trace amounts of iron and/or nickel atoms within the polymeric sulphur may create a "colour centre" (184) and cause this effect. The lack of formation of violarite under these conditions can be inferred in terms of very slow solid-state diffusion rates within the bulk phase, which would tally with those experienced during synthesis and also in exolution studies (11). However, the colour of the product remains an intriguing mystery.

Chronoamperometric experiments on pentlandite in acid solution at 343K have shown that low steady state current densities are established in the potential region relevant to ferric chloride leaching within the first 250s, and then maintained over a long period of time. This indicates that the dissolution of pentlandite involves slow electron transfer, at least within the potential range 0.4 to 0.8V vs. SCE. Steady state currents on violarite also indicate very slow electron transfer for the S^o,Fe^{2+},Ni^{2+} / $FeNi_2S_4$ couple. A crude estimate of the heterogeneous electrochemical parameters for this couple gave $\alpha_a = 0.12$ and $k^o << 1.7x10^{-6}ms^{-1}$.

The determination of the heterogeneous electrochemical parameters for the $FeCl_3/FeCl_2$ couple in 1M HCl solution on platinum at 293K using convolutive chronoamperometric techniques and other derived functional forms, gave encouraging results.

The "chronoamperometric parameter plot" was considered to be more accurate for parameter determination rather than the analogous $i(t) = f(I_1)$ function.

The diffusion coefficients as determined from the large overpotential data were considered more accurate than those determined from the small overpotential data, because at large overpotentials, the system at a given time is closer to Cottrell behaviour, i.e. diffusion control. This yielded the following diffusion coefficients:

$D(FeCl_3) = 5.34x10^{-10}$ +/- $0.24x10^{-10}$ m^2s^{-1}, and

$D(FeCl_2) = 5.23x10^{-10}$ +/- $0.02x10^{-10}$ m^2s^{-1}.

However, it was considered better to capture and treat chronoamperometric data within the vicinity of the polarographic wave (i.e. near E^o) for the purposes of heterogeneous electrochemical parameter determination. This approach yielded:

$\alpha_a = 0.34$, $\alpha_c = 0.50$, and $k^o = 2.0\times10^{-5} \pm 1.0\times10^{-5}\ ms^{-1}$.

The above results from the chronoamperometric analysis are in general agreement with the Butler-Volmer relationship, and therefore support the above model of simple electron transfer. However, the consistent departure of the sum $\alpha_a + \alpha_c$ from unity is noted but unexplained here.

4.2 PROPOSED MECHANISMS FOR THE OXIDATIVE DISSOLUTION OF PENTLANDITE AND THE IMPLICATION FOR HYDROMETALLURGY

4.2.1 Acid Decomposition

Pentlandite in acid media (free from any extraneous oxidizing influences) spontaneously decomposes via a corrosion mechanism (i.e. a mixed-potential regime) incorporating the reduction of hydrogen ions in the acid solution to hydrogen, together with the oxidation of pentlandite to hydrogen sulphide, aqueous ferrous and nickel ions, i.e.

$$2H^+ + 2e = H_2 \qquad (4.2.1)$$

$$4.5Fe^{2+} + 4.5Ni^{2+} + 8H_2S + 2e = Fe_{4.5}Ni_{4.5}S_8 + 16H^+ \qquad (4.2.2)$$

4.2.2 Supergene Alteration

Under the relatively mild oxidizing / near neutral pH conditions akin to a supergene environment, the solid state phase transformation of pentlandite to violarite occurs on account of the similarity of the sulphur sub-lattice for these two crystal structures, and the slow rates of change imposed by the near equilibrium conditions at the mineral / solution interface; i.e.

$$(O_2 + 2H_2O + 4e = 4OH^-) \qquad (4.2.3)$$

$$2FeNi_2S_4 + 0.5Ni^{2+} + 2.5Fe^{2+} + 6e = Fe_{4.5}Ni_{4.5}S_8 \qquad (4.2.4)$$

4.2.3 Oxidative Dissolution of Pentlandite by Electrolysis and Acid Ferric Chloride Leaching

Under potentiostatic conditions with applied potentials / acid media akin to acid ferric chloride leaching and in the temperature range 293 to 353K, the formation of H_2S is no longer thermodynamically favoured as a product species vis à vis more oxidized sulphur containing species i.e. violarite, bravoite, orthorhombic sulphur and sulphate etc. Under such conditions one might predict from thermodynamic and crystallographic knowledge, a solid state transformation of pentlandite to violarite as in Section 4.2.2. However, this work has shown that under these conditions, pentlandite is oxidized directly to elemental sulphur without the formation of any intermediate metal sulphide phase, i.e.

$$4.5Fe^{2+} + 4.5Ni^{2+} + 8S + 18e = Fe_{4.5}Ni_{4.5}S_8 \qquad (4.2.5)$$

The lack of formation of violarite under these conditions, indicates that the system is substantially perturbed from equilibrium due to slow solid state diffusion of metal atoms within the sulphur sub lattice. The actual formation of metastable amorphous sulphur as the alternative product is further evidence to this respect. Furthermore, the slow rates of solid-state diffusion experienced during the synthesis and from exsolution studies within the Fe-Ni-S system (even at substantially elevated temperatures) are in agreement with this conclusion.

The physical properties of the amorphous sulphur product layer cause an impediment to mass transport for the oxidant species as in chemical leaching (eg. $FeCl_3$) from the bulk aqueous solution to the mineral surface; and for the mass transport of the product aqueous metal ions from the mineral surface to the bulk aqueous solution. However, the latter are only kinetically important under either galvanostatic conditions with current densities >10Am^{-2}, or under potentiostatic conditions with imposed potentials >0.8V vs. SCE).

The conclusions from this work suggest the thesis that within the potential range relevant to acid ferric chloride leaching (i.e. 0.4 to 0.7V vs. SCE) and in the temperature range 293 to 343K, and with a sufficient concentration of $FeCl_3$, the oxidation of pentlandite involves slow electron transfer for the S^o,Fe^{2+},Ni^{2+} / $Fe_{4.5}Ni_{4.5}S_8$ couple per se, and is rate determining. However, it is possible that at a later stage of the reaction, the mass transport of $FeCl_3$ from the bulk aqueous phase to the pentlandite surface through the semi-permeable amorphous sulphur product layer becomes comparable with, and ultimately predominates, the electron transfer process, and thereby becomes rate determining.

The heterogeneous rate constant for the $FeCl_3/FeCl_2$ couple (on platinum) is sufficiently large ($2x10^{-5}ms^{-1}$ at 293K) so as to contribute a negligible effect to the rate of acid $FeCl_3$ leaching of pentlandite.

The implication for extractive hydrometallurgy is that high potentials are required for appreciable rates of dissolution. This therefore strongly suggests that $FeCl_3$ would be an inappropriate oxidant. Chemical oxidants of a sufficiently high potential would be required (eg. persulphate) although these might result in further oxidation with the formation of appreciable amounts of undesirable sulphate. In the alternative process of electrolysis of cast pentlandite anodes, severe passivation will occur via the limitation of mass transport through an amourphous sulphur film. The present practice of converting pentlandite to an intermediate Ni-matte is concluded as the most feasible route for nickel extraction from sulphide ore.

4.3 COMPARISON OF THE PRESENT STUDY WITH PREVIOUS WORK

4.3.1 Synthesis of nickel-iron-sulphides

In the synthesis of pentlandite a partial phase segregation of pentlandite into heazlewoodite and/or pyrrhotite was observed. This was particularly acute in vertically annealed charges, in which pyrrhotite was predominant at the top, and pentlandite/heazlewoodite at the bottom. This phenomenon was attributed to the influence of gravity on the phase relationships at 950^{o}C. However, in the horizontally annealed charges small amounts of pyrrhotite (approx. 5%) were observed within the pentlandite matrix. These results are typical of those of other workers, namely: Kelt (4), Tzamtzis (14), Thornber (76), and Kullerud (3), though none of these offer any explanation as to the apparent inadvertent metal deficiency of this assemblage (i.e. the absence of heazlewoodite vis a vis pyrrhotite/mss). Although this phenomenon was discussed in this present work, no conclusive explanation could be offered.

In the synthesis of violarite, EMPA revealed a distinct compositional segregation between two violarite phases within the individual violarite grains; i.e. a Ni-deficient violarite ($Fe_{1.2}Ni_{1.8}S_4$) core, and a Ni-rich violarite ($Fe_{0.5}Ni_{2.5}S_4$) rim. Since $Fe_{1.2}Ni_{1.8}S_4$ is regarded as a metastable phase, this textural feature is considered to be a kinetic phenomenon, and a possible explanation was offered in terms of the effects of internal friction during cooling. It is interesting to note that Vaughan and Craig (53) emphasise that compositions more Fe-rich than $FeNi_2S_4$ have not yet been synthesized.

In the synthesis of argentopentlandite, severe inhomogeneity within the product was encountered, even after annealing at 400°C for 66 days. The product comprised of approximately 85% Fe-deficient argentopentlandite, with an average composition of $Fe_{4.75}Ni_{3.25}AgS_8$. The remainder of the product was comprised of elemental silver and an Fe-rich mss with a stoichiometry approximating to $Fe_{0.71}Ni_{0.23}S$. The failure in obtaining an homogeneous product has been ascribed by other workers (Mandziuk and Scott (16)) to the very sluggish nucleation of this phase.

The inhomogeneity within these synthetic minerals are largely attributed to the intrinsic behaviour of the Fe-Ni-S ternary system. The preparative techniques, namely the use of a double bulbed "96%" silica glass vessel is highly recommended for the synthesis of metal-sulphides. However, the author emphasises that appropriate precautions must be taken to protect the charge from oxidation etc., especially during cooling, where fracture of the vessel is often imminent.

4.3.2 The oxidation of nickel-iron-sulphide minerals in aqueous media

Jibiki (143) observed that the acid decomposition of pentlandite in 1M HCl solution at 313K was retarded by the introduction of molecular oxygen into the system. He proposed that the formation of an oxide-film on the sulphide surface may be responsible for this behaviour.

The present author considers this explaination highly implausible on account of the solution having a pH = 0. The results from this current work suggest that a change in the dissolution mechanism by the introduction of molecular oxygen, may account for the drop in reaction rate, i.e. from

$Fe_{4.5}Ni_{4.5}S_8 + 18H^+ = 4.5Fe^{2+} + 4.5Ni^{2+} + 8H_2S + H_2$ (4.3.1)

to

$Fe_{4.5}Ni_{4.5}S_8 = 4.5Fe^{2+} + 4.5Ni^{2+} + 8S^o + H_2 + 18e$ (4.3.2)

This conclusion is based on evidence from the present work in which it was shown that this latter anodic reaction involves slow electron transfer. Furthermore, although the driving force for this reaction would originate from the reduction of oxygen, the actual electron transfer at the mineral surface would more probably involve the reduction of an oxidant species such as $FeCl_3$(aq) (ferrous iron being re-oxidized to ferric via the "oxygen pump"). A very low concentration of aqueous iron might influence matters here also.

The results of this current electrochemical study are in general agreement with those from the studies of the acid $FeCl_3$ leaching of pentlandite by Kelt (4) and Tzamtzis (14). However, by virtue of the electrochemical nature of the techniques used in this current work, the conclusions derived here help to clarify some of the results obtained from the purely chemical approach adopted by these two workers.

The lack of formation of any intermediate Fe-Ni-S phase is consistent with the observations of Kelt and Tzamtzis. However, neither worker reports the occurrence of metastable allotropes of sulphur, which have important mechanistic implications as discussed in Section 4.2. Both workers concluded that the reaction involves a mixed kinetic regime with two stages of reaction, namely: a predominance of chemical control during the initial stage, followed by a predominance of diffusion control in the latter stage. Nonetheless, they are rather vague in ascribing any detail to the nature of the chemically controlled reaction. Kelt surmises the possibility of the nucleation of orthorhombic sulphur, or a surface reaction between $FeCl_3$ and pentlandite. Tzamtzis insists that "electrochemical corrosion is not important in the dissolution of pentlandite by ferric chloride", without offering any evidence for this assertion. In this current work, slow electron transfer for the S^o, Ni^{2+}, Fe^{2+} / $Fe_{4.5}Ni_{4.5}S_8$ couple is inferred as the rate determining step, from a variety of experimental evidence.

From some of the evidence described by Tzamtzis concerning his own experiments (i.e. the provision of an insufficient quantity of $FeCl_3$ in the bulk solution to even enable complete dissolution of the pentlandite) it is likely that little mechanistic value can be derived from the latter stages of these experiments.

Thornber's electrochemical studies on the Fe-Ni-S aqueous system have been discussed in much detail in Sections 1.4.2, 1.5.1, 1.7.2 and 3.4. Thornber's (76) unaccounted quasi-reversible reaction near the rest potential on violarite at low pH (corresponding to the prewave on similar cyclic voltammograms in this current work) is explained here in terms of the oxidation of ferrous iron released by a preceeding reaction at the violarite surface.

Thornber's conclusion that the slow solid-state diffusion of metal atoms within the pentlandite/violarite lattice plays an important mechanistic role in determining the reaction pathway is acknowledged here, and is in agreement with the results obtained from this present work.

The simple diffusional model as applied by Price to the Cu-Fe-S and Cu-S and Ni-S aqueous systems (150), (157), (158), (159), (viz. the Sand equation), was tested in this current work. This was found to be unapplicable to the chronopotentiometric analysis of the oxidative dissolution of pentlandite in acid solution (at least within the range of imposed curent densities here). Furthermore, any mass transport applied to this system under such conditions would be more likely to involve aqueous diffusion/migration processes across a semi-permeable layer, rather than by solid-state diffusion within substrate material as implied by Price's work. Nonetheless, solid-state diffusion processes might be applicable under certain condition, to other systems which display more facile behaviour.

4.3.3 The $FeCl_3/FeCl_2$ Couple: Determination of the heterogeneous electrochemical parameters

Sharma and Dutt (177) determined these in 1M HCl solution at 294K on graphite, using the technique of direct current polarography in flowing media. Results were as follows:

$\alpha_c = 0.59$, $k^o = 1.2x10^{-6} ms^{-1}$.

Suzuki (178) determined these in 0.1M $HClO_4$ solution at 298K on platinum using hydrodynamic voltammetry. Results were as follows:

$\alpha_c = 0.63 +/- 0.02$, $k^o = 7.6x10^{-5} +/- 1.5x10^{-5} ms^{-1}$.

4.4 RECOMMENDATIONS FOR FUTURE WORK

(a). Concerning the synthesis of metal sulphides, the observation of a compositional segregation between a Ni-deficient and a Ni-rich violarite phase within the individual synthetic violarite grains, warrants further study. This phenomenon is particularly interesting since it is reported in the literature that violarite compositions more Fe-rich than $FeNi_2S_4$ have never been synthesized (although such compositions are found in natural material).

(b). The use of electron spectroscopy for chemical analysis (ESCA) for the identification of surface species, may provide a stimulating area for future work with regards to the identification of the violet/grey coloured tarnish formed on the surface of anodically polarized pentlandite in acid media.

(c). The intermittent galvanostatic polarization (IGP) techniques developed in this work for the identification of product species obtained during the early stages of the reaction, might be useful in the study of similar systems.

(d). Chronopotentiometric analysis of pentlandite in aqueous solution of neutral pH at very low current densities may provide further information on the pentlandite/violarite supergene alteration process.

(e). The chronoamperometric techniques developed in this work provide the opportunity for the determination of the diffusion coefficients and heterogeneous electrochemical parameters for other systems, including those on different electrode surfaces and at a variety of temperatures.

APPENDICES

A LIQUID JUNCTION POTENTIALS

A.1 Origin of the Liquid Junction Potential E_J

When two mutually miscible solutions (a and b) are brought into contact with each other, the solute and solvent species will undergo spontaneous diffusion across the interface. The net effect is that a species (i) will diffuse in a direction which will tend to reduce, and ultimately eliminate, the difference in its chemical potential between the two solutions. When both of the solutions comprise of the same solvent (eg. water), the direction of the decrease in chemical potential of solute (i) coincides with the direction of the decrease in ionic activity of (i) across the diffuse zone. Thus, a net diffusion occurs from regions of higher to those of lower ionic activity for a given solute species (138).

If one of the ionic species has a greater mobility than its counterpart in the adjacent solution eg. $H^+ > K^+$, then it will tend to diffuse more rapidly and set up an electrical double layer involving charge separation and the establishment of an electrical field. The polarity of this field will be such, so as to retard the diffusion of the more mobile ions (H^+) whilst hasten the slower ones (K^+). If the junction is constructed so that a stable diffusion geometry is established (eg. use of a porous ceramic plug) a kinetic steady state is rapidly established in which both ionic species diffuse at the same rate. Thus, there is a constant potential difference across the diffusion zone, which can be regarded as the "liquid junction potential". Furthermore, since this diffusion process is irreversible, the liquid junction results in an irreversible contribution to the cell emf; i.e. a cell with a liquid junction can never be an equilibrium system (138).

An essential point is that there is no way of completely eliminating a liquid-junction potential; and that a priori calculation of E_J requires a knowledge of the "single" ionic activity coefficients of the "individual" ions concerned. This information is not available, and experimental evaluation of such coefficients is impossible without a knowledge of the value of E_J, and vice versa for the determination of E_J and in perpetualis. Therefore, these values by their nature remain inaccessible (163) although there is no doubt about the reality of liquid junction potentials, nor of the basic mechanism by which they are established (154).

A.2 Estimation of E_J: Henderson's Equation

The electrical work expended in transferring an infinitesimal quantity of charge (which is carried by cations and anions in proportion to their transport numbers) is equated to the increase in Gibbs free energy which accompanies it, i.e.

$$- dF \, . \, dE_J \; = \; dG$$

where dF is an infinitesimal quantity of charge transfered and dE_J is the infinitesimal difference of electrical potential across the interfacial layer. There is also, for each ion, an infinitesimal difference of chemical potential across the interfacial layer, such that the sum of these gives rise to dG. Thus per "equivalent" Faraday of charge transfered:

$$- F \cdot dE_J = \sum_i \frac{t_i}{z_i} du_i$$

(where t_i is the transport number of the ionic species i)

Since

$$du_i = RT \, d\ln a_i$$

$$- dE_J = \frac{RT}{F} \sum_i \frac{t_i}{z_i} d\ln a_i$$

which is the basic differential equation for the liquid junction potential. Strictly, this equation should include the term $t_w d\ln a_w$ for the transference of water. However, its magnitude is uncertain since t_w is unknown, although it is considered to become negligible with increasing dilution of the solutions (154).

Since

$$a_i = \gamma_i C_i$$

the above differential equation can be split into two terms: $E_J(\gamma)$, (a function of t_i and γ_i); and $E_J(C)$, (a function of t_i and C_i). As mentioned above, the former is apparently incalculable. However, an approximate evaluation of E_J can be made by ignoring this term, (i.e. by adopting $\gamma_i = 1$); whilst determining the concentration component $E_J(C)$ by means of Henderson's equation, coupled with a knowledge of the appropriate ionic mobilities (or transport numbers).

$$- dE_J(C) = \frac{RT}{F} \sum_i \frac{t_i}{z_i} d\ln C_i$$

To solve this differential equation for $E_J(C)$ requires a knowledge of the boundary conditions (i.e. integration limits) for the concentration componants C_i and, a knowledge of the concentration dependancies of the various transport numbers (t_i), which for simplicity is assumed to be independant. The former can be obtained by assuming that at every point across the transition zone, the interfacial solution will have a fractional composition, i.e. a fraction (x) of solution (a) mixed with a fraction (1-x) of solution (b), such that the integral limits become: $0 < x < 1$. Thus, the concentration of each ionic species will be given by:

$$C_i = xC_i(a) + (1-x)C_i(b)$$

$$C_i = C_i(a) + (C_i(b) - C_i(a))\,x$$

Hence

$$d\ln C_i = \frac{dC_i}{C_i} = \frac{(C_i(b) - C_i(a))\,dx}{C_i}$$

The transport number of each ionic species is defined by

$$t_i = \frac{C_i u_i\,|z_i|}{x \sum_i C_i(b) u_i\,|z_i| + (1-x) \sum_i C_i(a) u_i\,|z_i|}$$

where u_i and $|z_i|$ represent the ionic mobility ($m^2 s^{-1} V^{-1}$) and the magnitude of the charge respectivly, for the various ionic species (i). Combination and rearrangement with the above, gives:

$$\frac{t_i}{|z_i|} d\ln C_i = \frac{u_i\,(C_i(b) - C_i(a))\,dx}{\sum_i C_i(a) u_i\,|z_i| + x \sum_i u_i\,|z_i|\,(C_i(b) - C_i(a))}$$

Substitution into the above differential equation gives on integration:

$$- E_J = \frac{RT}{F} \int_{x=0}^{x=1} \frac{\sum u_i (C_i(b) - C_i(a))\,dx}{\sum_i C_i(a) u_i\,|z_i| + x \sum_i u_i\,|z_i|\,(C_i(b) - C_i(a))}$$

$$E_J = \frac{RT}{F}\,\frac{\sum (u_i/z_i).(C_i(b) - C_i(a))}{\sum_i (u_i).(C_i(b) - C_i(a))}\,\ln\left\{\frac{\sum u_i\,|z_i|\,C_i(a)}{\sum_i u_i\,|z_i|\,C_i(b)}\right\}$$

which is the Henderson equation for E_J.

As mentioned above with reference to transport numbers (t_i), the ionic mobilities (λ_i or u_i) are assumed to be independent of concentration, and therefore taken as remaining constant across the transition zone. Furthermore, the more readily available limiting ionic mobilities ($\lambda^o{}_i$) (i.e. those at infinite dilution) are often adopted, for which the temperature dependance is also known in some cases.

Since E_J is in many cases inherently small, Henderson's equation may introduce more error than is achieved merely by assuming that E_J is negligible. However,it is useful for estimating the order of magnitude of E_J for changes in the composition of the working electrolyte (cf. Section 2.3.3.1 on the use of the reference electrode).

B MINERAL DENSITIES AND METAL ATOM CONCENTRATIONS

B.1 Pentlandite

From powder-XRD data for SynPn3 (cf. Appendix D.1):

d_{002} = 0.5033nm

d_{004} = 0.2522nm

unit cell parameter = 1.008nm

unit cell volume = $1.024\times10^{-27}m^3$

unit cell mass (cf. Section 1.3.1) = $5.128\times10^{-24}kg$

density = $5007kgm^{-3}$

molar concentration ($Fe_{4.5}Ni_{4.5}S_8$) = $6486molm^{-3}$

molar concentration (metal atom) = $58374molm^{-3}$

molar concentration (sulphur atom) = $51888molm^{-3}$

B.2 Violarite

From powder-XRD data for SynVl1b (cf. Appendix D.4):

d_{400} = 0.236nm

unit cell parameter = 0.944nm

unit cell volume = $8.4123\times10^{-28}m^3$

unit cell mass (cf. Section 1.3.2) = $4.005\times10^{-24}kg$

density = $4761kgm^{-3}$

molar concentration ($FeNi_2S_4$) = $15791molm^{-3}$

molar concentration (metal atom) = $47373molm^{-3}$

molar concentration (sulphur atom) = $63164molm^{-3}$

C PHYSICOCHEMICAL DATA

C.1 Thermodynamic Properties at 298.15K and 101.325kPa

Species	$\Delta H^o{}_f/kJmol^{-1}$	$S^o/JKmol^{-1}$	$\Delta G^o{}_f/kJmol^{-1}$	Ref.
H_2(g)	0	130.57	0	120
H^+(aq)	0	0	0	**
O_2(g)	0	205.04	0	120
S(c)	0	31.88 ∓ 0.17	0	118
S_2(g)	+128.7	228.0 ∓ 0.42	+79.73	118
Fe(c)	0	27.28	0	120
Fe^{2+}(aq)	-89.1	-138	-78.87	119
Fe^{3+}(aq)	-48.5	-316	-4.60	119
Ni(c)	0	29.87	0	120
Ni^{2+}(aq)	-54.0	-129	-45.6	119
Ag(c)	0	42.55	0	120
Ag^+(aq)	+105.58	72.68	77.124	119
$FeNi_3$(s)	-16.74	-0.52		129
FeNi(c)			<0 (?)	*
H_2S(g)	-20.5 ∓ 0.42	205.7 ∓ 0.42	-33.4	118
H_2S(aq)	-39.7		-27.86	118
HS^-(aq)	-17.66	61.09	12.59	121
S^{2-}(aq)	35.81	-26.78	92.47	121
$S_2{}^{2-}$(aq)	38.9	0.0	91.2	121
$S_3{}^{2-}$(aq)	32.6	21	88.3	121
$S_4{}^{2-}$(aq)	22.2	42	81.2	121
FeS(c)	-100.4 ∓ 0.42	60.312	-100.7	118
Fe_7S_8(c)	-736.3	485.8	-748.5	119
FeS_2(c)	-171.5 ∓ 8.4	52.93	-160.1	118
$Fe_{4.5}Ni_{4.5}S_8$(c)	-837.3	505.43	-835.2 -779.0 <-790.1 -813 (?)	85 76 * *

Species	ΔH^o_f/kJmol^{-1}	S^o/JKmol^{-1}	ΔG^o_f/kJmol^{-1}	Ref.
$FeNi_2S_4$(c)	-324.8	192.46	-319.0 -348.4	85,7 76
$Fe_{1-x}Ni_{2+x}S_4$(c)			<-343.1 -346 (?)	* *
Ni_3S_2(c)	-215.9∓12.5	133.9∓2.5	-210.1	118
Ni_7S_6(c)	-577.0∓29.3	342.7∓29.3	-559.8	118
NiS(c)	-94.14∓4.2	52.97∓0.84	-91.5	118
Ni_3S_4(c)	-326.4∓25.1	171.3∓25.1	-312.7	118
NiS_2(c)	-133.9∓8.4	67.78∓8.4	-126.2	118
Ag_2S(c)	-31.59∓0.42	143.5∓1.2	-39.50	118
$AgFe_5Ni_3S_8$(c)			<-778 (?)	*
H_2O(l)	-285.83	69.948	-237.19	120
$Fe_{0.947}O$(c)	-266.27	57.488	-245.14	120
Fe_3O_4(c)	-1118.4	146.15	-1015.3	120
Fe_2O_3(c)	-824.25	87.404	-742.34	120
FeO(OH)(c)	-559.0	59.41∓5.0	-488.0	122
$Fe(OH)_2$(c)	-569.0	87.9	-486.6	119
$Fe(OH)_3$(c)	-823.0	107	-696.6	119
NiO(c)	-239.74	37.99	-211.60	120
Ni_3O_4(c)			-712.1	121
Ni_2O_3(c)	-489.5		-469.9	119
NiO_2(c)			-198.7	121
$Ni(OH)_2$(c)	-529.7	87.9	-447.3	119
$Ni(OH)_3$(c)	-678.2	81.6	-541.8	121
Ag_2O(c)	-31.05	121.3	-11.28	120
Ag_2O_2(c)	-24.27	117.2	+27.31	120
H_2SO_4(aq)	-907.51	17.15	-741.99	121
HSO_4^-(aq)	-885.75	126.9	-752.87	121
SO_4^{2-}(aq)	-907.51	17.15	-742.0	121

---

* Speculative data, cf. Section 1.5.1

** By definition, cf. Section 1.5.2

C.2 Equilibria with corresponding Nernst Functions* with respect to the Standard Hydrogen Electrode (SHE) for the Fe-Ni-S Aqueous System at 298K and 101kPa, (based on data given in Appendix C.1).

H_2O System:

1. $2H^+ + 2e = H_2$

   $E = -0.0591pH$

2. $O_2 + 4H^+ + 4e = 2H_2O$

   $E = 1.229 - 0.0591pH$

S-H_2O System:

3. $HSO_4^- + 7H^+ + 6e = 4H_2O + S$

   $E = 0.338 - 0.0693pH + 0.0099lg[HSO_4^-]$

4. $SO_4^{2-} + 8H^+ + 6e = 4H_2O + S$

   $E = 0.357 - 0.0792pH + 0.0099lg[SO_4^{2-}]$

5. $S + 2H^+ + 2e = H_2S$

   $E = 0.144 - 0.0591pH - 0.0295lg[H_2S]$

6. $S + H^+ + 2e = HS^-$

   $E = -0.065 - 0.0295pH - 0.0295lg[HS^-]$

7. $SO_4^{2-} + 9H^+ + 8e = HS^- + 4H_2O$

   $E = 0.251 - 0.0665pH - 0.0074lg[HS^-] + 0.0074lg[SO_4^{2-}]$

8. $HSO_4^- = H^+ + SO_4^{2-}$

   $pH = 1.90 - lg[HSO_4^-] + lg[SO_4^{2-}]$

9. $H_2S = H^+ + HS^-$

   $pH = 7.09 - lg[H_2S] + lg[HS^-]$

---

* Terms in square parantheses represent activities.

Fe-S-H_2O System:

10\. $Fe^{2+} + 2e = Fe$

$E = -0.409 + 0.0295lg[Fe^{2+}]$

11\. $Fe^{3+} + e = Fe^{2+}$

$E = 0.770 - 0.0591lg[Fe^{2+}] + 0.0591lg[Fe^{3+}]$

12\. $FeS + 2H^+ + 2e = Fe + H_2S$

$E = -0.378 - 0.0591pH - 0.0295lg[H_2S]$

13\. $FeS + H^+ + 2e = Fe + HS^-$

$E = -0.587 -0.0295pH - 0.0295lg[HS^-]$

14\. $FeS_2 + 4H^+ + 2e = Fe^{2+} + 2H_2S$

$E = -0.132 - 0.1183pH - 0.0296lg[Fe^{2+}] - 0.0592lg[H_2S]$

15\. $FeS_2 + 2H^+ + 2e = FeS + H_2S$

$E = -0.163 - 0.0591pH - 0.0295lg[H_2S]$

16\. $FeS_2 + H^+ + 2e = FeS + HS^-$

$E = -0.373 -0.0295pH - 0.0295lg[HS^-]$

17\. $2S + Fe^{2+} + 2e = FeS_2$

$E = 0.421 + 0.0296lg[Fe^{2+}]$

18\. $Fe^{2+} + 2HSO_4^- + 14H^+ + 14e = FeS_2 + 8H_2O$

$E = 0.350 - 0.0591pH + 0.0084lg[HSO_4^-] + 0.0042lg[Fe^{2+}]$

19\. $FeS + 2H^+ = Fe^{2+} + H_2S$

$pH = 0.528 - 0.5lg[Fe^{2+}] - 0.5lg[H_2S]$

20\. $Fe^{2+} + 2SO_4^{2-} + 16H^+ + 14e = FeS_2 + 8H_2O$

$E = 0.366 - 0.0676pH + 0.0042lg[Fe^{2+}] + 0.0085lg[SO_4^{2-}]$

21. $Fe_2O_3 + 6H^+ = 2Fe^{3+} + 3H_2O$

$pH = -0.630 - 0.333\lg[Fe^{3+}]$

22. $Fe_2O_3 + 6H^+ + 2e = 2Fe^{2+} + 3H_2O$

$E = 0.658 - 0.177pH - 0.0591\lg[Fe^{2+}]$

23. $Fe_2O_3 + 4SO_4{}^{2-} + 38H^+ + 30e = 2FeS_2 + 19H_2O$

$E = 0.386 - 0.075pH + 0.0079\lg[SO_4{}^{2-}]$

24. $3Fe_2O_3 + 2H^+ + 2e = 2Fe_3O_4 + H_2O$

$E = 0.211 - 0.0591pH$

25. $Fe_3O_4 + 6SO_4{}^{2-} + 56H^+ + 44e = 3FeS_2 + 28H_2O$

$E = 0.390 - 0.075pH + 0.0080\lg[SO_4{}^{2-}]$

Ni-S-H_2O System:

26. $Ni^{2+} + 2e = Ni$

$E = -0.236 + 0.0295\lg[Ni^{2+}]$

27. $Ni^{2+} + H_2O = NiO + 2H^+$

$pH = 6.236 - 0.5\lg[Ni^{2+}]$

28. $Ni_3O_4 + 8H^+ + 2e = 3Ni^{2+} + 4H_2O$

$E = 1.935 - 0.2364pH - 0.0886\lg[Ni^{2+}]$

29. $Ni_2O_3 + 6H^+ + 2e = 2Ni^{2+} + 3H_2O$

$E = 1.725 - 0.1773pH - 0.0591\lg[Ni^{2+}]$

30. $Ni_3O_4 + 2H^+ + 2e = 3NiO + H_2O$

$Eh = 0.828 - 0.0591pH$

31. $3Ni_2O_3 + 4H^+ + 4e = 2Ni_3O_4 + 2H_2O$

$E = 1.270 - 0.0591pH$

32. $2S + Ni^{2+} + 2e = NiS_2$

$E = 0.418 + 0.0296lg[Ni^{2+}]$

33. $Ni^{2+} + 2HSO_4^- + 14H^+ + 14e = NiS_2 + 8H_2O$

$E = 0.350 - 0.0591pH + 0.0084lg[HSO_4^-] + 0.0042lg[Fe^{2+}]$

34. $Ni^{2+} + 2SO_4^{2-} + 16H^+ + 114e = NiS_2 + 8H_2O$

$E = 0.366 - 0.0676pH + 0.0042lg[Fe^{2+}] + 0.0085lg[SO_4^{2-}]$

35. $3Ni^{2+} + 4SO_4^{2-} + 32H^+ + 30e = Ni_3S_4 + 16H_2O$

$E = 0.347 - 0.0630pH + 0.0079lg[SO_4^{2-}] + 0.0059lg[Ni^{2+}]$

36. $Ni^{2+} + SO_4^{2-} + 8H^+ + 8e = NiS + 4H_2O$

$E = 0.327 - 0.0591pH + 0.0074lg[SO_4^{2-}] + 0.0074lg[Ni^{2+}]$

37. $NiO + SO_4^{2-} + 10H^+ + 8e = NiS + 5H_2O$

$E = 0.420 - 0.0739pH + 0.0074lg[SO_4^{2-}]$

38. $3NiO + 2SO_4^{2-} + 22H^+ + 18e = Ni_3S_2 + 11H_2O$

$E = 0.403 - 0.0722pH + 0.0066lg[SO_4^{2-}]$

39. $Ni_3S_4 + 2SO_4^{2-} + 16H^+ + 12e = 3NiS_2 + 8H_2O$

$E = 0.414 - 0.0788pH + 0.0099lg[SO_4^{2-}]$

40. $3NiS + SO_4^{2-} + 8H^+ + 6e = Ni_3S_4 + 4H_2O$

$E = 0.423 - 0.0788pH + 0.0099lg[SO_4^{2-}]$

41. $Ni_3S_2 + SO_4^{2-} + 8H^+ + 6e = 3NiS + 4H_2O$

$E = 0.468 - 0.0788pH + 0.0099lg[SO_4^{2-}]$

42. $NiS + 4H^+ + 2e = Ni^{2+} + 2H_2S$

$E = -0.129 - 0.1183pH - 0.0296lg[Ni^{2+}] - 0.0592lg[H_2S]$

43. $Ni_3S_4 + 8H^+ + 2e = 3Ni^{2+} + 4H_2S$

$E = -0.334 - 0.2364pH - 0.0887lg[Ni^{2+}] - 0.1182lg[H_2S]$

44. $NiS + 2H^+ = Ni^{2+} + H_2S$
$pH = -1.580 - 0.5lg[Ni^{2+}] - 0.5lg[H_2S]$

45. $3Ni^{2+} + 2H_2S + 2e = Ni_3S_2 + 4H^+$
$E = 0.091 + 0.1182pH + 0.0887lg[Ni^{2+}] + 0.0591lg[H_2S]$

46. $3NiS_2 + 4H^+ + 4e = Ni_3S_4 + 2H_2S$
$E = -0.026 - 0.0591pH - 0.0296lg[H_2S]$

47. $Ni_3S_4 + 2H^+ + 2e = 3NiS + H_2S$
$E = -0.054 - 0.0591pH - 0.0296lg[H_2S]$

48. $3NiS + 2H^+ + 2e = Ni_3S_2 + H_2S$
$E = -0.189 - 0.0591pH - 0.0296lg[H_2S]$

49. $Ni_3S_2 + 4H^+ + 4e = 3Ni + 2H_2S$
$E = -0.400 - 0.0591pH - 0.0296lg[H_2S]$

50. $3NiS + 2H^+ + 4e = Ni_3S_4 + 2HS^-$
$E = -0.236 - 0.0296pH - 0.0296lg[HS^-]$

51. $Ni_3S_4 + H^+ + 2e = 3NiS + HS^-$
$E = -0.263 - 0.296pH - 0.0296lg[HS^-]$

52. $3NiS + H^+ + 2e = Ni_3S_2 + HS^-$
$E = -0.399 - 0.0296pH - 0.0296lg[HS^-]$

53. $Ni_3S_2 + 2H^+ + 4e = 3Ni + 2HS^-$
$E = -0.610 - 0.0296pH - 0.0296lg[HS^-]$

Fe-Ni-S-H_2O System:

54. $Fe_{4.5}Ni_{4.5}S_8 + H^+ + e = 1.5Ni_3S_2 + 4.5FeS + 0.5H_2S$
$E = -0.324 - 0.0591pH - 0.0296lg[H_2S]$

55. $4.5FeNi_2S_4 + 11H^+ + 11e = Fe_{4.5}Ni_{4.5}S_8 + 5.5H_2S + 4.5NiS$
$E = -0.167 - 0.0591pH - 0.0296lg[H_2S]$

56. $1.5FeS_2 + Ni_3S_4 + 2H^+ + 2e = 1.5FeNi_2S_4 + H_2S$
$E = -0.033 - 0.0591pH - 0.0296lg[H_2S]$

57. $4.5FeS_2 + 1.5Ni_3S_4 + 14H^+ + 14e = Fe_{4.5}Ni_{4.5}S_8 + 7H_2S$
$E = -0.134 -0.0591pH -0.0295lg[H_2S]$ (metastable)

58. $2Fe_{4.5}Ni_{4.5}S_8 + H^+ + 2e = 3Ni_3S_2 + 9FeS + HS^-$
$E = -0.529 - 0.0296pH - 0.0296lg[HS^-]$

59. $9FeNi_2S_4 + 11H^+ + 22e = 2Fe_{4.5}Ni_{4.5}S_8 + 11HS^- + 9NiS$
$E = -0.377 - 0.0296pH - 0.0296lg[HS^-]$

60. $1.5FeS_2 + Ni_3S_4 + H^+ + 2e = 1.5FeNi_2S_4 + HS^-$
$E = -0.243 - 0.0296pH - 0.0296lg[HS^-]$

61. $Fe_{4.5}Ni_{4.5}S_8 + 10H^+ + e = 1.5Ni_3S_2 + 4.5Fe^{2+} + 5H_2S$
$E = -0.043 - 0.591pH - 0.266lg[Fe^{2+}] - 0.2955lg[H_2S]$

62. $4.5NiS + 4.5Fe^{2+} + 3.5H_2S + 2e = Fe_{4.5}Ni_{4.5}S_8 + 7H^+$
$E = -0.263 + 0.2068pH + 0.1330lg[Fe^{2+}] + 0.1034lg[H_2S]$

63. $FeNi_2S_4 + 4H^+ + 2e = 2NiS + Fe^{2+} + 2H_2S$
$E = 0.146 - 0.1182pH - 0.0296lg[Fe^{2+}] - 0.0591lg[H_2S]$

64. $3FeNi_2S_4 + 8H^+ + 2e = 2Ni_3S_4 + 3Fe^{2+} + 4H_2S$
$E = -0.330 - 0.2364pH - 0.0887lg[Fe^{2+}] - 0.1182lg[H_2S]$

65. $4Ni_3S_4 + 3Fe_2O_3 + 8SO_4^{2-} + 82H^+ + 66e = 6FeNi_2S_4 + 41H_2O$

$E = 0.375 - 0.0734pH + 0.0072lg[SO_4^{2-}]$

66. $2NiS + 0.5Fe_2O_3 + 2SO_4^{2-} + 19H^+ + 15e = FeNi_2S_4 + 9.5H_2O$

$E = 0.388 - 0.0749pH + 0.0079lg[SO_4^{2-}]$

67. $4Ni_3S_4 + 2Fe_3O_4 + 8SO_4^{2-} + 80H^+ + 64e = 6FeNi_2S_4 + 40H_2O$

$E = 0.380 - 0.0739pH + 0.0074lg[SO_4^{2-}]$

68. $2Ni_3S_4 + 1.5Fe_2O_3 + 4SO_4^{2-} + 41H^+ + 33e =$

$3FeNi_2S_4 + 20.5H_2O$

$E = 0.375 - 0.0734pH + 0.0072lg[SO_4^{2-}]$

Metastable Equilibria: with $Fe_{4.5}Ni_{4.5}S_8$ and $FeNi_2S_4$ as the only metal-sulphide phases. H_2S not consumed. β-FeO(OH) and $Ni(OH)_2$ as metastable products.

69. $FeO(OH) + 3H^+ + e = Fe^{2+} + 2H_2O$

$E = 0.676 - 0.1773pH - 0.0591lg[Fe^{2+}]$

70. $Ni(OH)_2 + 2H^+ = Ni^{2+} + 2H_2O$

$pH = 6.367 - 0.5lg[Ni^{2+}]$

71. $FeO(OH) + 3H^+ = Fe^{3+} + 2H_2O$

$pH = -0.527 - 0.333lg[Fe^{3+}]$

72. $4.5Ni^{2+} + 4.5Fe^{2+} + 8S + 18e = Fe_{4.5}Ni_{4.5}S_8$

$E = 0.146 + 0.0148lg[Ni^{2+}] + 0.0148lg[Fe^{2+}]$

73. $Fe^{2+} + 2Ni^{2+} + 4S + 6e = FeNi_2S_4$

$E = 0.303 + 0.0197lg[Ni^{2+}] + 0.0099lg[Fe^{2+}]$

74. $2FeNi_2S_4 + 0.5Ni^{2+} + 2.5Fe^{2+} + 6e = Fe_{4.5}Ni_{4.5}S_8$

$E = -0.169 + 0.0049lg[Ni^{2+}] + 0.0246lg[Fe^{2+}]$

75. $Fe^{2+} + 2Ni^{2+} + 4HSO_4^- + 28H^+ + 30e = FeNi_2S_4 + 16H_2O$

$E = 0.331 - 0.0552pH + 0.0020lg[Fe^{2+}] + 0.0039lg[Ni^{2+}] + 0.0079lg[HSO_4^-]$

76. $Fe^{2+} + 2Ni^{2+} + 4SO_4^{2-} + 32H^+ + 30e = FeNi_2S_4 + 16H_2O$

$E = 0.346 - 0.0630pH + 0.0020lg[Fe^{2+}] + 0.0039lg[Ni^{2+}] + 0.0079lg[SO_4^{2-}]$

77. $FeO(OH) + 2Ni^{2+} + 4SO_4^{2-} + 35H^+ + 31e = FeNi_2S_4 + 18H_2O$

$E = 0.357 - 0.0667pH + 0.0038lg[Ni^{2+}] + 0.0076lg[SO_4^{2-}]$

78. $FeO(OH) + 2Ni(OH)_2 + 4SO_4^{2-} + 39H^+ + 31e =$

$FeNi_2S_4 + 22H_2O$

$E = 0.406 - 0.0744pH + 0.0076lg[SO_4^{2-}]$

79. $4.5Fe^{2+} + 4.5Ni^{2+} + 8SO_4^{2-} + 64H^+ + 66e =$

$Fe_{4.5}Ni_{4.5}S_8 + 32H_2O$

$E = 0.347 - 0.0574pH + 0.0072lg[SO_4^{2-}] + 0.0040lg[Fe^{2+}] + 0.0040lg[Ni^{2+}]$

80. $4.5FeO(OH) + 4.5Ni^{2+} + 8SO_4^{2-} + 77.5H^+ + 70.5e =$

$Fe_{4.5}Ni_{4.5}S_8 + 41H_2O$

$E = 0.324 - 0.0650pH + 0.0038lg[Ni^{2+}] + 0.0067lg[SO_4^{2-}]$

81. $4.5FeO(OH) + 4.5Ni(OH)_2 + 8SO_4^{2-} + 86.5H^+ + 70.5e =$

$Fe_{4.5}Ni_{4.5}S_8 + 50H_2O$

$E = 0.372 - 0.0725pH + 0.0067lg[SO_4^{2-}]$

82. $2FeNi_2S_4 + 0.5Ni^{2+} + 2.5FeO(OH) + 7.5H^+ + 8.5e =$

$Fe_{4.5}Ni_{4.5}S_8 + 5H_2O$

$E = 0.080 - 0.0522pH + 0.0049lg[Ni^{2+}]$

83. $2FeNi_2S_4 + 0.5Ni(OH)_2 + 2.5FeO(OH) + 8.5H^+ + 8.5e =$

$Fe_{4.5}Ni_{4.5}S_8 + 6H_2O$

$E = 0.124 - 0.0591pH$

84. $FeNi_2S_4 + 8H^+ + 2e = 2Ni^{2+} + Fe^{2+} + 4H_2S$

$E = -0.333 - 0.2364pH - 0.05911lg[Ni^{2+}] - 0.0296lg[Fe^{2+}]$

$- 0.1182lg[H_2S]$

85. $4.5Fe^{2+} + 4.5Ni^{2+} + 8H_2S + 2e = Fe_{4.5}Ni_{4.5}S_8 + 16H^+$

$E = 0.158 + 0.4728pH + 0.1330lg[Fe^{2+}] + 0.1330lg[Ni^{2+}] +$

$0.2364lg[H_2S]$

86. $Fe_{4.5}Ni_{4.5}S_8 + 16H^+ + 7e = 4.5Ni + 4.5Fe^{2+} + 8H_2S$

$E = -0.349 - 0.1351pH - 0.0380lg[Fe^{2+}] - 0.0675lg[H_2S]$

87. $Fe_{4.5}Ni_{4.5}S_8 + 16H^+ + 16e = 4.5Fe + 4.5Ni + 8H_2S$

$E = -0.383 - 0.0591pH - 0.0296lg[H_2S]$

88. $Fe_{4.5}Ni_{4.5}S_8 + 8H^+ + 16e = 4.5Fe + 4.5Ni + 8HS^-$

$E = -0.592 - 0.0296pH - 0.0296lg[HS^-]$

Metastable Equilibrium: with FeS_2, NiS_2, $Fe_{4.5}Ni_{4.5}S_8$ and $FeNi_2S_4$ as the only metal-sulphide phases. H_2S and SO_4^{2-} neither consumed nor produced.

89. $FeS_2 + NiS_2 + Ni^{2+} + 2e = FeNi_2S_4$

$E = 0.072 + 0.0295lg[Ni^{2+}]$

90. $4FeS_2 + 0.5Fe^{2+} + 4.5Ni^{2+} + 10e = Fe_{4.5}Ni_{4.5}S_8$

$E = -0.074 + 0.0030lg[Fe^{2+}] + 0.0266lg[Ni^{2+}]$

D POWDER X-RAY DIFFRACTION DATE

D.1 Synthetic pentlandite ($Fe_{4.5}Ni_{4.5}S_8$)

D.1.1 SynPn1 (annealed vertically)

SynPn1(bottom)			Pentlandite(ASTM8-90)			Minor Phases
2θ	d/nm	I	d/nm	I	hkl	
15.28	0.580	40	0.578	30	111	
17.60	0.504	5	0.501	5	002	
21.73	0.409	t				$(Ni,Fe)_{3\mp x}S_2$ ref.(7)
25.01	0.356	5	0.355	5	022	
29.38	0.304	100	0.303	80	113	
30.72	0.291	50	0.290	40	222	
31.16	0.287	t				$(Ni,Fe)_{3\mp x}S_2$ ref.(7)
35.63	0.252	5	0.251	5	004	
38.99	0.231	20	0.230	30	133	
40.07	0.225	5	0.225	5	024	
44.18	0.205	5				$(Ni,Fe)_{3\mp x}S_2$ ref.(7)
46.83	0.194	30	0.1931	50	115,333	
51.02	0.179	90	0.1775	100	044	
53.93	0.170	5	0.1697	5	135	
55.34	0.166	5				$(Ni,Fe)_{3\mp x}S_2$ ref.(7)
60.08	0.154	10	0.1530	10	335	
60.95	0.152	10	0.1514	10	226	
66.29	0.141	5	0.1412	5	117,155	ref.(7)
72.10	0.131	15	0.1307	20	355,731	
75.22	0.126	10	0.1255	20	008	
77.26	0.123	5				$(Ni,Fe)_{3\mp x}S_2$ ref.(7)

D.1.2 SynPn2a (annealed vertically)

SynPn2a(top)			Pentlandite(ASTM8-90)			Minor Phases
2θ	d/nm	I	d/nm	I	hkl	
15.25	0.5810	70	0.578	30	111	
17.60	0.5039	t	0.501	5	002	
24.98	0.3565	5	0.355	5	022	
29.35	0.3043	90	0.303	80	113	
30.02	0.2977	30				mss
30.70	0.2912	100	0.290	40	222	
34.00	0.2637	15				mss
35.60	0.2522	t	0.251	5	004	
38.91	0.2315	10	0.230	30	133	
39.97	0.2256	t				?
41.83	0.2160	t				?
44.00	0.2058	60				mss
46.75	0.1943	40	0.1931	50	115.333	
51.17	0.1785	80	0.1775	100	044	
53.30	0.1719	10				?
53.70	0.1707	t	0.1697	5	135	
57.75	0.1596	t				?
60.13	0.1539	5	0.1530	10	335	
60.90	0.1521	5	0.1514	10	226	
64.70	0.1441	t				?
66.00	0.1415	t	0.1412	5	117,155	ref.(7)
71.85	0.1314	10				mss
75.28	0.1262	t	0.1307	20	355,731	
82.80	0.1166	5	0.1255	20	008	

D.1.3 SynPn2b (re-annealed horizontal)

SynPn2b(middle)			Pentlandite(ASTM8-90)			Minor Phases
2θ	d/nm	I	d/nm	I	hkl	
15.30	0.5791	30	0.578	30	111	
17.60	0.5039	5	0.501	5	002	
24.98	0.3562	5	0.355	5	022	
29.38	0.3037	100	0.303	80	113	
30.72	0.2910	50	0.290	40	222	
33.98	0.2638	t				mss
35.60	0.2522	5	0.251	5	004	
38.94	0.2314	10	0.230	30	133	
40.98	0.2202	t	0.225	5	024	
44.01	0.2057	10				mss
46.81	0.1941	20	0.1931	50	115,333	
51.25	0.1783	90	0.1775	100	044	
53.70	0.1707	t	0.1697	5	135	
60.10	0.1538	10	0.1530	10	335	
60.91	0.1520	5	0.1514	10	226	
66.00	0.1415	t	0.1412	5	117,155	ref.(7)
75.30	0.1262	10	0.1307	20	355,731	
82.80	0.1166	5	0.1255	20	008	

D.1.4 SynPn3 (annealed horizontally)

SynPn3(middle)			Pentlandite(ASTM8-90)			minor Phases
2θ	d/nm	I	d/nm	I	hkl	
15.23	0.5817	30	0.578	30	111	
17.62	0.5033	5	0.501	5	002	
24.99	0.3563	5	0.355	5	022	
29.37	0.3041	70	0.303	80	113	
30.70	0.2912	40	0.290	40	222	
33.90	0.2644	t				mss
35.60	0.2522	5	0.251	5	004	
38.92	0.2315	20	0.230	30	133	
39.91	0.2259	t	0.225	5	024	
43.91	0.2062	5				mss
46.76	0.1943	30	0.1931	50	115,333	
51.18	0.1785	100	0.1775	100	044	
53.25	0.1721	5				mss
53.76	0.1706	5	0.1697	5	135	
54.47	0.1685	t				mss
60.09	0.1504	5	0.1530	10	335	
60.87	0.1500	5	0.1514	10	226	
65.98	0.1416	t	0.1412	5	117,155	ref.(7)
71.79	0.1315	10	0.1307	20	355,731	
75.27	0.1263	5	0.1255	20	008	

D.2 Argentopentlandite

D.2.1 SynAgPnlb (re-annealed horizontally)

SynAgPnlb(middle)			Natural AgPn (71)			Minor Phases
2θ	d/nm	I	d/nm	I	hkl	
14.70	0.6026	10	0.606	20	111	
16.96	0.5228	10	0.525	20	002	
24.06	0.3699	10	0.371	20	022	
28.25	0.3159	100	0.3170	100	113	
29.52	0.3026	20	0.3024	20	222	
30.05	0.2974	t				mss
34.01	0.2636	5	0.2610	5	004	
37.38	0.2406	t	0.241	10	133	
38.38	0.2345	10	0.2350	10	024	
42.44	0.2129	5	0.2150	20	224	
44.06	0.2055	5				mss
44.88	0.2041	30	0.2018	40	115,333	
49.10	0.1854	80	0.1858	100	044	
52.29	0.1750	t	0.1758	5	244	ref.(52)
53.36	0.1717	15				mss
57.60	0.1601	5	0.1602	20	335	
58.33	0.1583	t	0.1584	10	226	
68.70	0.1367	10	0.1369	20	137,355	
71.99	0.1312	5	0.1315	10	008	
79.00	0.1213	5	0.1212	5	157,555	

D.3 Synthetic monosulphide solid solution (FeNi2S3.25)

SynMss(middle)			Fe0.29Ni0.64S (2)	Minor Phases
2θ	d/nm	I	d/nm	
30.16	0.2963	40	0.2970	None detected
34.27	0.2614*		0.2769*	
		60	0.2738	
34.35	0.2615*		0.2701*	
34.55	0.2596	60	0.2614	
44.98	0.2015*		0.2024*	
		100	0.2013	
45.50	0.1994*		0.1999*	
53.51	0.1712*			
		30	0.1713	
53.68	0.1707*			
			0.1573*	
59.18	0.1561	t	0.1563	
			0.1554*	
60.27	0.1536	t		
65.02	0.1434	5	0.1434	
65.20	0.1431	5	?*	
72.34	0.1306	10		
86.69	0.0771	t		

---

* denotes "diffuse side-bands"

D.4 Synthetic Violarite ($FeNi_2S_4$)

D.4.1 SynV11a

SynV11a(middle)			violarite(ASTM11-95)			minor Phases
2θ	d/nm	I	d/nm	I	hkl	
16.31	0.5435	20	0.547	20	111	
26.71	0.3338	30	0.335	30	220	
30.25	0.2955	10				NiS
31.99	0.2798	100	0.285	100	311	
32.89	0.2723	t				FeS_2
34.36	0.2591	5				NiS
38.11	0.2361	50	0.236	50	400	
45.52	0.1993	20				NiS
47.11	0.1929	5	0.1931	20	422	
50.15	0.1819	20	0.1820	60	511,333	
53.61	0.1710	10				NiS
54.98	0.1617	80	0.1674	80	440	
64.62	0.1442	5	0.1445	20	533	
68.81	0.1364	5	0.1365	20	444	
72.90	0.1298	t				NiS
75.25	0.1263	t	0.1261	10	642	
77.51	0.1232	5	0.1233	30	731,553	
81.43	0.1182	5	0.1183	40	800	

D.4.2 SynV11b (sintered/re-annaeled)

SynV11b(middle)			violarite(ASTM11-95)			Minor Phases
2θ	d/nm	I	d/nm	I	hkl	
16.30	0.5438	15	0.547	20	111	
26.72	0.3336	30	0.335	30	220	
30.28	0.2952	t				NiS
31.45	0.2844	100	0.285	100	311	
32.98	0.2716	t				FeS_2
34.65	0.2589	t				NiS
37.03	0.2428	t				FeS_2
38.13	0.2360	60	0.236	50	400	
44.69	0.2028	t				NiS
47.11	0.1929	10	0.1931	20	422	
50.18	0.1817	40	0.1820	60	511,333	
53.65	0.1708	t				NiS
54.94	0.1671	70	0.1674	80	440	
56.05	0.1641	t				FeS_2
57.70	0.1598	5	0.1602	30	531	
62.10	0.1495	t				?
64.62	0.1442	5	0.1445	20	533	
68.76	0.1365	10	0.1365	20	444	
71.22	0.1324	t				?
75.12	0.1265	t				NiS
75.35	0.1261	t	0.1261	10	642	
77.50	0.1232	10	0.1233	30	731,553	
81.39	0.1182	15	0.1183	40	800	

D.5 Natural violarite ($FeNi_2S_4$) (Kambalda, Z28890)

NatVl (Z28890)			violarite(ASTM11-95)			Minor Phases
2θ	d/nm	I	d/nm	I	hkl	
16.26	0.545	20	0.547	20	111	
21.31	0.417	5				?
26.69	0.334	30	0.335	30	220	
28.61	0.312	t				?
31.39	0.285	100	0.285	100	311	
32.08	0.279	5				?
33.18	0.270	10				FeS_2
37.15	0.242	5				FeS_2
38.13	0.236	50	0.236	50	400	
41.03	0.220	5				?
47.61	0.191	5	0.1931	20	422	
50.12	0.182	30	0.1820	60	511,333	
54.98	0.167	70	0.1674	80	440	
56.45	0.163	5				FeS_2
not detected			0.1602	30	531	
59.23	0.156	t				?
64.24	0.145	t	0.1445	20	533	
69.06	0.136	5	0.1365	20	444	
81.58	0.118	t	0.1261	10	642	
not detected			0.1233	30	731,553	
not detected			0.1183	40	800	

D.6 Product layer (anodic polarization of pentlandite)

(from synthetic pentlandite SynPn3 anodic polarization in 1M $HClO_4$ 293K i = $1000Am^{-2}$ t =648s washed in tertrachloroethene and carbondisulphide to remove amorphous and orthorhombic sulphur respectively prior to analysis).

Product Layer			Pentlandite (ASTM 8-90)			
4θ	d/nm	I	d/nm	I	hkl	
29.2	0.607	w			113	2nd Order ?
31.0	0.572	m	0.578	30	111	
35.8	0.496	w	0.501	5	002	
39.5	0.450	w			133	2nd Order ?
41.5	0.428	m				?
44.9	0.396	w			115,333	2nd Order ?
50.5	0.353	m	0.355	5	022	
57.4	0.311	w			335	2nd Order ?
59.2	0.302	s	0.303	80	113	
62.1	0.288	m	0.290	40	222	
71.5	0.251	w	0.251	5	004	
78.3	0.230	m	0.230	30	133	
80.2	0.225	w	0.225	5	024	
87.9	0.206	w				mss
94.2	0.193	s	0.1931	50	115,333	
103.3	0.177	s	0.1775	100	044	
107.9	0.170	w	0.1697	5	135	
120.2	0.154	m	0.1530	10	335	
122.8	0.151	m	0.1514	10	226	
131.5	0.142	w	0.1412	5	177,155	ref.(7)
144.2	0.131	m	0.1307	20	355,731	
150.9	0.126	m	0.1255	20	008	
155.2	0.123	w				?
164.9	0.117	w	0.1160	5	157,555	
?			0.1105	5	119,357	
186.6	0.106	w	0.1052	5	139	
193.8	0.103	s	0.1025	20	448	

* Intensities (I) w = weak, m = medium, s = strong

E Electron microprobe analysis data

E. 1 Synthetic pentlandite

E. 1.1 SynPn2a (bottom),(vertically annealed)
Specimen from middle to lower section of rod

	Element	%Elememt	Atomic%	ratio
Major phase Grain 1	Fe	31.404	25.976	4.384
	Ni	33.834	26.623	4.493
	S	32.895	47.400	8.000
	Total	98.133	100.00	
Major phaes Grain 1	Fe	32.019	26.373	4.472
	Ni	33.759	26.452	4.486
	S	32.878	47.175	8.000
	Total	98.656	100.000	
Major phase Grain 1	Fe	32.036	26.269	4.434
	Ni	33.762	26.336	4.445
	S	33.179	47.395	8.000
	Total	98.976	100.000	
Major phase Grain 2	Fe	31.721	26.033	4.415
	Ni	34.314	26.790	4.543
	S	32.997	47.176	8.000
	Total	99.032	100.000	
Minor phase Grain 1	Fe	4.934	4.193	0.207
	Ni	68.446	55.335	2.734
	S	27.338	40.473	2.000
	Total	100.717	100.000	
Minor phase Grain 2	Fe	5.075	4.356	0.216
	Ni	67.667	55.251	2.736
	S	27.014	40.393	2.000
	Total	99.756	100.000	

Stoichiometry
SynPn2a(bottom) major phase: $Fe_{4.5}Ni_{4.5}S_8$

minor phase: $Fe_{0.2}Ni_{2.7}S_2$

E. 1.2 SynPn2a (top),(vertically annealed)
Specimen from top section of rod

	Element	%Element	Atomic%	ratio
Major phase Grain 1	Fe	48.485	37.971	0.738
	Ni	14.167	10.555	0.205
	S	37.730	51.475	1.000
	Total	100.383	100.000	
Minor phase Grain 1	Fe	30.876	25.197	4.240
	Ni	35.108	27.255	4.586
	S	33.445	47.547	8.000
	Total	99.429	100.000	

Minor phase	Fe	30.982	25.514	4.327
Grain 2	Ni	34.863	27.312	4.632
	S	32.883	47.174	8.000
	Total	98.728	100.000	
Minor phase	Fe	31.221	25.769	4.357
Grain 2	Ni	34.283	26.917	4.551
	S	32.907	47.314	8.000
	Total	98.411	100.000	

Stoichiometry
SynPn2a(top) major phase: $Fe_{0.74}Ni_{0.21}S$

minor phase: $Fe_{4.4}Ni_{4.6}S_8$

E. 1.3 SynPn3 (annealed horizontally)

Sample from middle of rod

	Element	%Element	Atomic%	ratio
Major phase				
(bottom of	Fe	31.106	25.326	4.300
X-section)	Ni	35.586	27.562	4.680
Grain 1	S	33.217	47.112	8.000
	Total	99.908	100.00	
Grain 2	Fe	30.939	25.393	4.301
	Ni	35.070	27.381	4.638
	S	33.032	47.227	8.000
	Total	99.041	100.000	
Grain 3	Fe	30.902	25.293	4.310
	Ni	35.650	27.758	4.730
	S	32.926	46.949	8.000
	Total	99.478	100.000	
Grain 4	Fe	30.851	25.481	4.342
	Ni	35.088	27.570	4.698
	S	32.630	46.949	8.000
	Total	98.569	100.000	
Grain 5	Fe	30.959	25.451	4.345
	Ni	35.407	27.690	4.727
	S	32.721	46.860	8.000
	Total	99.086	100.000	
Major phase	Fe	31.302	25.554	4.347
(top of X-section)	Ni	35.303	27.416	4.664
Grain 1	S	33.070	47.030	8.000
	Total	99.675	100.000	
Grain 2	Fe	31.537	25.795	4.385
	Ni	34.880	27.140	4.613
	S	33.031	47.065	8.000
	Total	99.448	100.000	
Grain 3	Fe	31.636	25.804	4.429
	Ni	35.559	27.591	4.736
	S	32.800	46.606	8.000
	Total	99.995	100.000	

Minor phase (top of X-section) Grain 1	Fe	49.137	38.905	0.760
	Ni	13.143	9.899	0.193
	S	37.118	51.196	1.000
	Total	99.398	100.000	
Grain 2	Fe	51.278	40.435	0.785
	Ni	10.710	8.034	0.156
	S	37.513	51.531	1.000
	Total	99.502	100.000	
Grain 3	Fe	51.938	40.343	0.781
	Ni	10.837	8.008	0.155
	S	38.169	51.649	1.000
	Total	100.944	100.000	
Grain 4	Fe	51.463	40.267	0.779
	Ni	10.813	8.049	0.156
	S	37.918	51.685	1.000
	Total	100.195	100.000	
Grain 5	Fe	50.752	39.984	0.779
	Ni	11.555	8.660	0.169
	S	37.420	51.356	1.000
	Total	99.727	100.000	

Stoichiometry
SynPn3 major phase: $Fe_{4.3}Ni_{4.7}S_8$ to $Fe_{4.4}Ni_{4.6}S_8$

minor phase: $Fe_{0.78}Ni_{0.17}S_8$

E. 2 Synthetic Argentopentlandite

E. 2.1 SynAgPnla (annealed vertically)

Specimen from bottom section of rod

	Element	%Element	Atomic%	ratio
Minor phase Grain 2	Fe	30.839	24.965	4.253
	Ni	35.823	27.587	4.700
	Ag	1.164	0.488	0.083
	S	33.300	46.961	8.000
	Total	101.125	100.000	
Minor phase Grain 2	Fe	30.244	24.914	4.260
	Ni	35.317	27.676	4.733
	Ag	1.468	0.626	0.107
	S	32.601	46.784	8.000
	Total	99.629	100.000	

Stoichiometry
SynAgPnla minor phase: $Fe_{4.3}Ni_{4.7}Ag_{0.1}S_8$

E. 2.2 SynAgPnlb (re-annealled horizontally)
Specimen from central section of rod

	Element	%Element	Atomic %	ratio
Major phase (bottom of X-section Grain 1	Fe	31.516	27.300	4.664
	Ni	24.116	19.872	3.395
	Ag	13.388	6.004	1.026
	S	31.029	46.824	8.000
	Total	100.049	100.000	
Grain 2	Fe	31.953	27.695	4.752
	Ni	24.069	19.845	3.405
	Ag	13.004	5.835	1.001
	S	30.880	46.625	8.000
	Total	99.906	100.000	
Grain 3	Fe	32.231	27.698	4.734
	Ni	23.985	19.608	3.351
	Ag	13.238	5.890	1.007
	S	31.264	46.804	8.000
	Total	100.719	100.000	
Grain 4	Fe	32.430	27.965	4.762
	Ni	23.489	19.268	3.281
	Ag	12.970	5.791	0.986
	S	31.272	46.977	8.000
	Total	100.162	100.000	
Grain 5	Fe	32.669	28.350	4.874
	Ni	23.153	19.113	3.286
	Ag	13.358	6.002	1.032
	S	30.783	46.535	8.000
	Total	99.963	100.000	
Major phase (Top of X-section) Grain 1	Fe	33.197	28.447	4.870
	Ni	23.447	19.113	3.272
	Ag	12.861	5.706	0.977
	S	31.306	46.733	8.000
	Total	100.810	100.000	
Grain 2	Fe	32.891	28.141	4.766
	Ni	23.169	18.857	3.194
	Ag	13.016	5.766	0.976
	S	31.692	47.236	8.000
	Total	100.768	100.000	
Grain 3	Fe	32.832	28.330	4.837
	Ni	23.280	19.109	3.262
	Ag	12.762	5.702	0.973
	S	31.173	46.859	8.000
	Total	100.046	100.000	
Grain 4	Fe	32.512	28.130	4.789
	Ni	23.279	19.160	3.262
	Ag	12.770	5.721	0.974
	S	31.175	46.989	8.000
	Total	99.736	100.000	

Grain 5	Fe	32.198	27.933	4.743
	Ni	23.278	19.211	3.262
	Ag	12.778	5.739	0.974
	S	31.177	47.117	8.000
	Total	99.432	100.000	
Minor phase	Fe	46.372	36.508	0.703
Grain 1	Ni	15.417	11.546	0.222
	Ag	0.000	0.000	0.000
	S	37.875	51.946	1.000
	Total	99.664	100.000	
Grain 2	Fe	45.419	35.932	0.699
	Ni	16.765	12.617	0.245
	Ag	0.048	0.020	0.000
	S	37.318	51.431	1.000
	Total	99.550	100.000	
Grain 3	Fe	46.280	36.859	0.718
	Ni	15.399	11.666	0.227
	Ag	0.279	0.115	0.002
	S	37.018	51.359	1.000
	Total	98.976	100.000	
Grain 4	Fe	46.624	36.687	0.715
	Ni	16.023	11.994	0.234
	Ag	0.000	0.000	0.000
	S	37.438	51.319	1.000
	Total	100.085	100.000	
Grain 5	Fe	46.785	36.574	0.705
	Ni	15.493	11.522	0.222
	Ag	0.153	0.062	0.001
	S	38.068	51.843	1.000
	Total	100.499	100.000	
Metallic phase	Fe	0.414	0.795	
	Ni	0.247	0.452	
	Ag	98.914	98.302	
	S	0.135	0.451	
	Total	99.711	100.000	

Stoichiometry:
SynAgPn1b major phase (bottom) = $Fe_{4.7}Ni_{3.3}AgS_8$

major phase (top) = $Fe_{4.8}Ni_{3.2}AgS_8$

minor phase = $Fe_{0.71}Ni_{0.23}S$

metallic phase = Ag

E. 3 Synthetic monosulphide solid solution (mss): SynMss

	Element	%Element	Atomic%	Ratio
Grain 1	Fe	19.998	15.635	0.975
	Ni	43.323	32.221	2.008
	S	38.286	52.145	3.250
	Total	101.607	100.000	
Grain 2	Fe	20.657	16.182	1.016
	Ni	43.032	32.067	2.014
	S	37.923	51.751	3.250
	Total	101.612	100.000	

Stoichiometry SynMss = $Fe_{1.0}Ni_{2.0}S_{3.25}$

E. 4 Synthetic violarite

E. 4.1 SynV11a (annealed horizontally)
Specimen taken from centre of rod.

	Element	%Element	Atomic%	Ratio
Core Grain 1	Fe	21.865	16.875	1.182
	Ni	35.465	26.037	1.824
	S	42.463	57.088	4.000
	Total	99.793	100.000	
Core Grain 2	Fe	21.908	16.880	1.181
	Ni	35.421	25.962	1.817
	S	42.583	57.158	4.000
	Total	99.912	100.000	
Core Grain 3	Fe	21.191	16.320	1.149
	Ni	36.683	26.874	1.892
	S	42.343	56.806	4.000
	Total	100.217	100.000	
Core Grain 4	Fe	22.576	17.350	1.225
	Ni	35.507	25.958	1.832
	S	42.329	56.669	4.000
	Total	100.412	100.000	
Core Grain 5	Fe	21.001	16.312	1.146
	Ni	36.149	26.710	1.876
	S	42.084	56.944	4.000
	Total	99.234	100.000	
Core Grain 6	Fe	20.966	16.152	1.136
	Ni	36.825	26.989	1.899
	S	42.365	56.859	4.000
	Total	100.156	100.000	
Small Grain 1	Fe	15.115	11.726	0.829
	Ni	42.934	31.686	2.240
	S	41.871	56.588	4.000
	Total	99.920	100.000	

Small Grain 2	Fe	17.998	13.813	0.975
	Ni	40.423	29.512	2.083
	S	42.392	56.676	4.000
	Total	100.813	100.000	
Large Grain 1 (rim)	Fe	9.616	7.459	0.527
	Ni	48.761	35.976	2.544
	S	41.864	56.563	4.000
	Total	100.241	100.000	
Large Grain 1 (core)	Fe	21.141	16.390	1.165
	Ni	37.024	27.304	1.941
	S	41.655	56.256	4.000
	Total	99.819	100.000	

Stoichiometry
SynVlla: Core Grain = $Fe_{1.2}Ni_{1.8}S_4$

Rim Grain = $Fe_{0.5}Ni_{2.5}S_4$

E. 4.2 SynVllb (re-annealed horizontally)

	Element	%Element	%Atomic	Ratio
Core Grain 1	Fe	20.961	16.111	1.148
	Ni	37.931	27.735	1.976
	S	41.932	56.146	4.000
	Total	100.824	100.000	
Core Grain 1	Fe	20.547	15.840	1.125
	Ni	37.937	27.822	1.975
	S	41.950	56.338	4.000
	Total	100.434	100.000	
Core Grain 2	Fe	19.320	14.877	1.045
	Ni	38.454	28.169	1.978
	S	42.456	56.954	4.000
	Total	100.230	100.000	
Core Grain 3	Fe	19.853	15.226	1.072
	Ni	38.304	27.945	1.967
	S	42.536	56.829	4.000
	Total	100.693	100.000	
Core Grain 4	Fe	19.357	15.024	1.058
	Ni	38.149	28.166	1.983
	S	42.018	56.810	4.000
	Total	99.524	100.000	
Core Grain 5	Fe	20.530	15.891	1.128
	Ni	37.728	27.781	1.973
	S	41.772	56.327	4.000
	Total	100.030	100.000	
Rim Grain 4	Fe	15.395	11.967	0.846
	Ni	42.523	31.444	2.223
	S	41.790	56.589	4.000
	Total	99.708	100.000	

Rim Grain 5	Fe	17.865	13.716	0.965
	Ni	40.260	29.405	2.068
	S	42.526	56.879	4.000
	Total	100.651	100.000	

Stoichiometry
SynV11b Core = $Fe_{1.1}Ni_{1.9}S_4$

Rim = $Fe_{0.90}Ni_{2.1}S_4$

E.5 Natural violarite (Kambalda Z28892)

	Element	%Element	%Atomic	Ratio
Major phase Grain 1	Fe	11.087	8.648	0.607
	Ni	46.357	34.398	2.416
	S	41.913	56.954	4.000
	Total	99.358	100.000	
Grain 2	Fe	11.919	9.271	0.659
	Ni	46.583	34.468	2.451
	S	41.522	56.261	4.000
	Total	100.024	100.000	
Grain 3	Fe	12.900	10.017	0.710
	Ni	45.382	33.522	2.375
	S	41.740	56.461	4.000
	Total	100.023	100.000	
Grain 4	Fe	10.127	7.919	0.561
	Ni	47.869	35.611	2.522
	S	41.452	56.470	4.000
	Total	99.448	100.000	
Sulphide vein	Fe	36.047	26.627	0.831
	Ni	13.254	9.313	0.291
	S	49.783	64.060	2.000
	Total	99.084	100.000	

Stoichiometry
Major phase = $Fe_{0.6}Ni_{2.4}S_4$ (cobalt below detection limit)

Sulphide vein = $Fe_{0.83}Ni_{0.29}S_2$ Bravoite (?)

F MINERALS AND PHASES IN THE Fe-Ni-S SYSTEM

FeNi	Taenite	stable ?
$FeNi_3$	Awaruite	metastable
FeS_2	Pyrite (cubic)	
FeS_2	Marcasite (orthorhombic)	metastable
Fe_3S_4	Greigite (cubic)	metastable
$Fe_{1-x}S$	Pyrrhotite (anomalous)	
$\sim Fe_7S_8$	Pyrrhotite (monoclinic)	
$\sim Fe_9S_{10}$	Pyrrhotite (hexagonal)	
FeS	Troilite (hexagonal)	
$Fe_{1+x}S$	Mackinawite (tetragonal)	metastable
Fe_9S_8	Iron-pentlandite	metastable
Fe_2S_3	gamma iron sulphide	metastable
NiS_2	Vaesite (cubic)	
Ni_3S_4	Polydymite (cubic)	
NiS	beta Millerite (hexagonal)	<282°C
$Ni_{1-x}S$	alpha Millerite (hexagonal)	985-379°C
Ni_7S_6	Godlevskite (orthorhomic)	
$Ni_{7+x}S_6$	alpha Godlevskite (orthorhomic)	400-573°C
$Ni_{3+x}S_2$	High heazlewoodite (cubic)	>556°C
Ni_3S_2	Heazlewoodite (hexagonal)	
$(Fe,Ni)S_2$	Bravoite (cubic)	(metastable)
$Fe_{1-x}Ni_{2+x}S_4$	Violarite (cubic)	
$\sim(Fe,Ni)_9S_{11}$	Smythite (hexagonal)	(metastable)
$(Ni,Fe)_{3\mp x}S_2$	non-quenchable s.s.	862-500°C
$(Fe,Ni)_{1-x}S$	momosulphide s.s. (mss) (nickeliferous pyrrhotite)	(complete 992-282°C)
$(Fe,Ni)_9S_8$	Pentlandite (cubic)	

G DERIVATION OF THE CHRONOAMPEROMETRIC PARAMETER PLOT AND THE TREATMENT OF CHRONOAMPEROMETRIC DATA*

In the case of simple electron transfer at planar electrodes, the variation of current (i) with time (t) for a chronoamperometric experiment turns out to be:

$$i(t) = \gamma e^{\beta^2 t} \operatorname{erfc} \beta t^{1/2}, \qquad \text{(G.1)}$$

where $\gamma = I^A{}_{\lim} \left\{\frac{k_f}{D_A{}^{1/2}}\right\} + I^B{}_{\lim} \left\{\frac{k_b}{D_B{}^{1/2}}\right\}$

and $\beta = \frac{k_f}{D_A{}^{1/2}} + \frac{kb}{D_B{}^{1/2}}$

(cf. Section 1.6.2)

This can conveniently be represented in the form

$$i = \gamma g(z), \quad z = \beta t^{1/2}, \quad g(z) = e^{z^2} \operatorname{erfc} z,$$

where $\operatorname{erfc} z = 1 - \frac{2}{\pi^{1/2}} \int_0^z e^{-z^2} dz$.

First consider g(z). Taking natural logarithms yields

$$\ln g = z^2 + \ln \operatorname{erfc} z, \qquad \text{(G.2)}$$

and hence

$$\frac{d\ln g}{dz} = 2z - \frac{2 \quad g^{-1}}{\pi^{1/2}},$$

or alternatively

$$\frac{dg}{dz} = 2gz - \frac{2}{\pi^{1/2}}. \qquad \text{(G.3)}$$

---

* The equations and symbols used within this Appendix relate to those used in Sections 1.6.2 and 3.7.

Of the many functions defined by equation (G.3) it can be shown that only that one corresponding to $g(z=0) = 1$, remains finite (in fact zero) at $z = \infty$. It is this function which corresponds to equation (G.1). (Note that all other values of $g(z=0)$, cause $g(z)$ to have a minimum or a zero at finite z.)

The expression for $dg(z)/dz$ in equation (G.3) leads to a suitable test for experimental data via $di/dt^{1/2}$ in terms of i and t, as will be shown below.

By integrating equation (G.3) one obtains the step relationship

$$\Delta g = \int_{z_1}^{z_2} g \, d(z^2) - \frac{2 \quad \Delta z}{\pi^{1/2}}. \tag{G.4}$$

Expressing g in terms of i, and z in terms of t, gives

$$\frac{\Delta i}{\gamma} = \frac{\beta^2}{\gamma} \int_{t_1}^{t_2} i \, dt - \frac{2\beta \quad \Delta t^{1/2}}{\pi^{1/2}}. \tag{G.5}$$

Simple algebraic manipulation of (G.5) yields

$$\frac{\int_{t_1}^{t_2} i \, dt}{\Delta i} = \frac{2 \quad \gamma \, \Delta t^{1/2}}{\pi^{1/2} \beta \, \Delta i} + \frac{1}{\beta^2}, \tag{G.6}$$

or

$$\frac{\Delta Q}{\Delta i} = \frac{2 \quad \gamma \, \Delta t^{1/2}}{\pi^{1/2} \beta \, \Delta i} + \frac{1}{\beta^2}. \tag{G.7}$$

This equation is referred to here, for convenience, as the "chronoamperometricparameter plot", and has the form of a linear relationship

$$y = mx + c, \tag{G.8}$$

where $Q = \int_0^t i\,dt$, $y = \Delta Q/\Delta i$, and $x = \Delta t^{1/2}/\Delta i$ are all easily calculable from the i/t data. The unknown values of γ and β can be calculated from the intercept

$$c = \beta^{-2}, \qquad \text{i.e.} \qquad \beta = c^{-1/2} \tag{G.9}$$

and the gradient

$$m = \frac{2\gamma}{\pi^{1/2}\beta} \qquad \text{i.e.} \qquad \gamma = \frac{\pi^{1/2} m c^{-1/2}}{2}. \tag{G.10}$$

In the above treatment the Δ interval is entirely arbitrary and hence the integration limits t_1 and t_2 can be chosen so as to correspond to the least distorted part of the data. This might typically be the region where the effects of charging or damping in the initially rapidly varying curents have died away, and where the effects of convection are not yet observed.

In the limiting case when $k_f >> k_b$ one finds that

$$\gamma \longrightarrow I^A{}_{lim} \left\{\frac{k_f}{D_A{}^{1/2}}\right\} \qquad \text{and} \qquad \beta \longrightarrow \frac{k_f}{D_A{}^{1/2}},$$

so that

$$\frac{\gamma}{\beta} \longrightarrow I^A{}_{lim} = (Z_B - Z_A) F A D_A{}^{1/2} C_A{}^{\infty}.$$

Hence the diffusion coefficient D_A can be calculated from

$$D_A = \left\{\frac{\pi^{1/2} m}{2(Z_B - Z_A) F A C_A^{\infty}}\right\}^2, \tag{G.11}$$

for a final potential corresponding to a negligible back reaction. Note that the gradient, m is independent of the potential-dependent rate constants (k_f and k_b) in this limiting case. Furthermore, a route to k_f is achieved through a knowledge of the intercept, c and gradient, m in equation (G.8). Thus

$$k_f = \frac{\pi^{1/2}m}{2c^{1/2}(Z_B-Z_A)FAC_A^\infty} = (D_A/c)^{1/2}. \qquad (G.12)$$

Note that as $k_f \longrightarrow \infty$, then $c \longrightarrow 0$.

For chronoamperometric experiments in which the imposed potential lies within the vicinity of the polarographic wave, the above limiting relationships (G.11 and G.12) no longer apply, since $E \sim E_{1/2}$ and $k_f/k_b \sim 1$. Nonetheless, the kinetic parameters D_A, D_B, k_f and k_b can be determined from chronoamperometric experiments within this potential region, through use of the relationships derived below.

Since by definition (cf. Equation G.1)

$$\gamma = I^A{}_{\text{lim}} \left\{\frac{k_f}{D_A{}^{1/2}}\right\} + I^B{}_{\text{lim}} \left\{\frac{k_b}{D_B{}^{1/2}}\right\},$$

one may write

$$\gamma = \frac{\pi^{1/2}mc^{-1/2}}{2} = (Z_B-Z_A)FAk_f[C_A^\infty - C_B^\infty e^{-(Z_B-Z_A)F(E-E^o)/RT}], \qquad (G.13)$$

where E is the applied potential (versus a reference electrode), such that $E = E^o$ when $C_A{}^o/C_B{}^o = 1$.

Similarly from the definition of β,

$$\beta = \frac{k_f}{D_A{}^{1/2}} + \frac{k_b}{D_B{}^{1/2}}, \qquad (G.14)$$

one finds

$$\beta = c^{-1/2} = \frac{k_f}{D_A{}^{1/2}}[1 + e^{-(Z_B-Z_A)F(E-E_{1/2})/RT}], \qquad (G.15)$$

where m and c are the known quantities obtained from the linear plots of equation (G.7) and relate to (G.8), and where $E_{1/2}$ is the half-wave potential.

Combining equations (G.13) and (G.15) one obtains

$$\frac{\gamma}{\beta} = \frac{\pi^{1/2}m}{2} = \frac{(Z_B-Z_A)FAD_A{}^{1/2}[C_A{}^{\infty}-C_B{}^{\infty}e^{-(Z_B-Z_A)F(E-E^{o})/RT}]}{[\,1 + e^{-(Z_B-Z_A)F(E-E_{1/2})/RT}]} , \tag{G.16}$$

which can be written in the convenient linear form

$$\Theta = \Lambda^{-1} + [\Lambda^{-1}\, e^{(Z_B-Z_A)FE_{1/2}/RT}]\; e^{-(Z_B-Z_A)FE/RT} , \tag{G.17}$$

or,

where $y = Mx + C,$ (G.18)

$$y = \Theta = [C_A{}^{\infty}-C_B{}^{\infty}e^{-(Z_B-Z_A)F(E-E^{o})/RT}]/m$$

and

$$x = e^{-(Z_B-Z_A)FE/RT}$$

are both known experimental variables and the parameters of the line are given by

$$C = \Lambda^{-1} = \pi^{1/2}/2(Z_B-Z_A)FAD_A{}^{1/2}$$

and

$$M = \Lambda^{-1}\, e^{(Z_B-Z_A)FE_{1/2}/RT} .$$

It follows that a plot of Θ versus $e^{-(Z_B-Z_A)FE/RT}$ enables the diffusion coefficient D_A to be determined from the intercept, C in equation (G.17) which relates to (G.18). For This plot is referred to here, for convenience, as the "diffusion coefficient parameter plot".

Explicitly we have

$$D_A = \pi/[2(Z_B-Z_A)FAC]^2. \qquad (G.19)$$

Furthermore, $E_{1/2}$ may be calculated from

$$E_{1/2} = \frac{RT}{(Z_B-Z_A)F} \ln(M/C) \qquad (G.20)$$

and hence D_B from

$$E_{1/2} = E^o + \frac{RT}{(Z_B-Z_A)F} \ln(D_A/D_B)^{1/2} \qquad (G.21)$$

Algebraic manipulation of equation (G.15) yields

$$k_f = \frac{D_A^{1/2} c^{-1/2}}{1 + e^{-(Z_B-Z_A)F(E-E_{1/2})/RT}} \qquad (G.22)$$

where all the quantities on the right hand side of equation (G.22) are now known. Therefore, a route to k_f is achieved through a knowledge of the intercept, c in equation (G.8), and from a knowledge of D_A and $E_{1/2}$ (either as determined from equations (G.20) and (G.21), or otherwise i.e. equation (G.12).

Finally, the heterogeneous electrochemical parameters (k^o and α) can be determined from an appropriate plot of the Butler-Volmer relationship, i.e. a plot of ln k_f versus $E-E^o$. The linearity of this plot is in effect also a test of the Butler-Volmer relationship.

Since

$$\ln k_f = \ln k^o + \alpha(Z_B-Z_A)F(E-E^o)/RT , \qquad (G.23)$$

the charge transfer coefficient α can be calculated from measurement of the gradient; whilst the standard heterogeneous rate constant (k^o) can be determined from measurement of the intercept at $E-E^o = 0$.

REFERENCES

1. Ferreira,R.C.H., Leaching of Chalcopyrite, Ph.D. Thesis (1972) University of London.
2. Shewman,R.W. and Clark,L.A., Canadian Journal of Earth Sciences (1970) vol.7 p67-85.
3. Kullerud,G., Canadian Mineralogist (1963) vol.7 p353-366.
4. Kelt,S.M., The Leaching of Certain Nickel Sulphides, Ph.D. Thesis (1975) University of London.
5. Burkin,A.R., Personal Communication (February,1986).
6. Knop,O. et al, Journal of Solid State Chemistry (1976) vol.16 p97-116.
7. Craig,J.R., The American Mineralogist (1971) vol.56 p1303-1311.
8. Keele,R.A. and Nickel,E.H., Economic Geology (1974) vol.69 p1102-1117.
9. Francis,C.A. et al, The American Mineralogist (1976) vol.61 p913-920.
10. Naldrett,A.J. et al, Economic Geology (1967) vol.62 p826-847.
11. Craig,J.R., Carnegie Institution of Washington Year Book 66 (1966) p434-436.
12. Kullerud,G.,Carnegie Institution of Washington Year Book 62 (1962) p175-189.
13. Misra,K.C. and Fleet,M.E., Economic Geology (1973) vol.68 p518-539.
14. Tzamtzis,G., Leaching of Some Sulphide Minerals of Nickel Under Acidic Oxidizing Conditions, Ph.D. Thesis (1976) University of London.
15. Kullerud,G., Experimental Techniques in Dry Sulphide Research, in Research Techniques for High Pressure and High Temperature (1971) p288-315; Ed. G.C. Ulmer, Pub. Springer-Verlag, Berlin.
16. Mandziuk,Z.l. and Scott,S.D., Canadian Mineralogist (1977) vol.15 p349-364.
17. Riply,L.G., Crystal Growth Part(III): The Sulphides of Cobalt, Iron and Nickel (1972) Dept. Energy Mines Research; Mines Branch. Research Paper R237.
18. Vaughan,D.J. and Craig,J.R., Mineral Chemistry of Metal Sulphides (1978) Pub. Cambridge University Press.
19. Clark,L.A. and Kullerud,G., Carnegie Institution of Washington Year Book 58 (1959) p142-145.
20. Kullerud,G. and Yund,R.A., Journal of Petrology (1962) vol.3 p126-175.
21. Shimazahi,H., Economic Geology (1971) vol.66 p1080-1082.
22. Townsend,M.G. et al, Physica Status Solidi (a), (1977) vol.44 K25-29.
23. Misra,K.C. and Fleet,M.E., Economic Geology (1974) vol.69 p391-403.
24. Watmuff,I.D., Mineralium Diposita (1974) vol.9 p199-221.
25. Vaughan,D.J. and Craig,J.R., American Mineralogist (1985) vol.70 p1036-1043.
26. Hulliger,F., Crystal Chemistry of the Chalcogenides and Pnictides of the Transition Elements: Stucture and Bonding (1968) vol.4 p83-299.
27. Clark,L.A. and Kullerd,G., Economic Geology (1963) vol.58 p853-885.

28. Bannister,M.A., Mineralogical Magazine (1940) vol.25 p609-615.
29. Kullerud,G., Carnegie Institution of Washington Year Book 60 (1960) p174-176.
30. Kullerud,G., Carnegie Institution of Washington Year Book 61 (1961) p144-149.
31. Graterol,M. and Naldrett,A.J.,Economic Geology (1971) vol.66 p886-900.
32. Craig,J.R., American Journal of Science,(1973) vol.273-A p496-510.
33. Ludqvist,D., Arkiv For Kemi, Mineralogi och Geologi, (1947) Band 24A No.22 p1-12.
34. Taylor,L.A., American Mineralogist,(1972) vol.57 p1571-1577.
35. Rudashevskiy,N.S. et al, International Geology Review, (19 ?) vol.21 p695-698.
36. Kullerud,G. et al, Magmatic Ore Deposits, A Symposium Economic Geology Monograph 4,(1969) Ed.Wilson,H.D.B. p323-343.
37. Lindqvist,M et al, Svensk Kem Tidsk,(1936) vol.48 p156-160.
38. Rajamani,V and Prewitt,C.T., Canadian Mineralogist, (1973) vol.12 p178-187.
39. Hall,S.R. and Stewart,J.M., Canadian Mineralogist, (1973) vol.12 p169-177.
40. Pearson,A.D. and Buerger,M.J., American Mineralogist, (1956) vol.41 p804-805.
41. Knop,O and Ibrahium,M.A., Canadian Journal of Chemistry, (1961) vol.39 p297-317.
42. Knop,O et al, American Mineralogist,(1970) vol.55 p1115-1130.
43. Vaughan,D.J. and Ridout,M.S., Journal of Inorganic Nuclear Chemistry,(1971) vol.33 p741-746.
44. Knop,O. et al, Journal of Solid State Chemistry,(1976) vol.16 p97-116.
45. Tsukimura,K. and Nakazawa,H., Acta Crystallographica, (1984) B40 p364-367.
46. Riley,J.F., Mineralogical Magazine,(1977) vol.41 p345-349.
47. Rajamani,V and Prewitt,C.T., American Mineralogist, (1975) vol.60 p39-48.
48. Craig,J.R. and Vaughan,D.J., Ore Microscopy and Ore Petrology (1981), Pub. Wiley-Interscience, New York.
49. Kelly,D.P. Pentlandite exsolution in the Fe-Ni-S system: A mechanistic approach to pentlandite/pyrrhotite ore textures, Ph.D. Thesis (1985), University of Aston in Birmingham.
50. Kelly,D.P. and Vaughan,D.J. Mineralogical Magazine, (1983) vol.47 p453-463.
51. Harris,D.C. and Nickel,E.H., Canadian Mineralogist, (1972) vol.11 p861-878.
52. Scott,S.D. and Gasparrini,E., Canadian Mineralogist, (1973) vol.12 p165-168.
53. Vaughan,D.J. and Craig,J.R., American Mineralogist, (1985) vol.70 p1036-1043.
54. Higgins,J.B. et al, The Philosophical Magazine,(1975) vol.32 p683-685.
55. Craig,J.R. and Higgins,J.B., American Mineralogist, (1975) vol.60 p35-38.

56. Nickel,E.H., Perth Conference, (May,1973) The Australian I.M.M., p111-116.
57. Thornber,M.R., Newcastle Conference,(May-June,1972) The Australian I.M.M. p51-58.
58. Ripley,J.F., Mineralogical Magazine,(1980) vol.43 p733-739.
59. Desborough,G.A. and Czamanske,G.K., American mineralogist,(1973) 58 p195-202.
60. Imbert,P. et al Comptes Rendus Academie Des Sciences (France), (1963) vol.256, p4391-4393.
61. Greenwood,N.N. and Whitfield,H.J., Journal of the Chemical Society, (1968) A, p1697-1699.
62. Vaughan,D.J. et al, Geochemica et Cosmochimica Acta, (1971) vol.35 p365-381.
63. Vaughan,D.J. and Tossell,J.A., American Mineralogist, (1981) vol.66 p1250-1253.
64. Lundvist,D., Arkiv For Kemi, Mineralogi och Geologi, (1947) Band 24A No.23 p1-7.
65. Nickel,E.H. et al, Economic Geology,(1974) vol.69 p93-107.
66. Vaughan,D.J.,Personal Communication (May,1986).
67. Hudson,D.R. and Groves,D.I.,Economic Geology,(1974) vol.69 p1335-1340.
68. Ramdohr,P., The Ore Minerals and their Intergrowths, (1979) 2nd Edt. Pub. Pergamon Press, Oxford.
69. Michener,C.E. and Yates,A.B., Economic Geology,(1944) vol.39 p506-514.
70. Craig,J.R. et al, Carnegie Institute of Washington Year Book 66,(1968) p440-441.
71. Vuorelainen,Y. et al, American Mineralogist,(1972) vol.57 p137-145.
72. Barton,P.B. and Skinner,B.J., Sulphide Mineral Stabilities, in Geochemistry of Hydrothermal Ore Deposits, Ed. Barnes,H.L.,(1979) 2nd Edt. Chapter 7, p278-403. Pub. Wiley-Interscience.
73. Vaughan,D.J., A review with special reference to phases of interest in hydrometallurgy. In Hydrometallurgical Process Fundamentals, VI Materials Science (1984) vol.10 p1-22. Ed. Bautista,R.G.,Nato Conference Series.
74. Vaughan,D.J., ibid. Electronic structures of sulphides and leaching behaviour. p23-40.
75. Burkin,A.R., ibid.,Composition and phase changes during oxidative acid leaching reactions. p113-123.
76. Thornber,M.R., Journal of Applied Electrochemistry, (1983) vol.13 p253-267.
77. Bouchard,R.J., Journal of Crystal Growth,(1968) vol.2 p40-44.
78. Butler,S.R. and Bouchard,R.J., ibid.,(1971) vol.10 p163-169.
79. Shick,L.K. and A.R.von Neida, ibid.,(1969) vol.5 p313-314.
80. Thornber,M.R., Chemical Geology,(1975) vol.15 p1-14.
81. Thornber,M.R., ibid.,p117-144.
82. Thornber,M.R., ibid.,(1985) vol.53 p279-301.
83. Thornber,M.R. et al, Economic Geology,(1981) vol.76 p1764-1774.
84. Nickel,E.H. and Thornber,M.R., Journal of Geochemical Exploration, (1977) vol.8 p235-245.
85. Craig,J.R. and Naldrett,A.J.,`GAL-MAC Conference', Sudbury 16 (1971).

86. Buddington,A.F., Economic Geology,(1924) vol.19 p521-541.

87. Sato,M. and Mooney,H.M., Geophysics,(1960) vol.25, p226-249.

88. Sato,M., Economic Geology,(1960) vol.55, p929-961.

89. Sato,M., ibid., p1202-1231.

90. Folwell,A.J.S., The Anodic Behaviour of Some Metallic Compounds, Ph.D. Thesis,(1971) University of Cambridge.

91. Woodall,R. and Travis,G.A., The Kambalda Nickel Deposits, Western Australia, Ninth Commonwealth Mining and Metallurgical Congress, Mining and Petroleum Section.(1969) Paper 26, p517-533.

92. Goncharov,G.N. and Tomilov,S.B., Nuclclear Gamma Resonance Spectroscopic Study of Pentlandite, Zap. Vses. Mineral. O-va., (1975), 104(2), p238-240.

93. Ramdohr,P.,"The Opaque minerals in stony meteorites" (1973) Pub. Elsevier, Amsterdam.

94. Buchanan,D.L.,"Nickel: A Commodity Review"(1982) Pub. The Institution of Mining and Metallurgy, London.

95. Cowden,A.,Personal Communication (April,1986); Geological Research Laboratory, Western Mining Corporation Ltd., Kambalda, W.Australia.

96. Peters,E.,"Direct Leaching of Sulphides: Chemistry and Application", The Metallurgical Society of AIME, Metallurgical Transactions B (1976) vol.7B pp505-517.

97. Alcock,R.A.,Personal Communication (January,1986); Geological Research and Exploration Laboratories, INCO Ltd., Ontario, Canada.

98. Stensholt,E.O. et al,"Falconbridge Chlorine Leach Process", Transactions of the Institution of Mining and Matallurgy, Section C, (1986) vol.95 ppC10-C16.

99. Williams,C.J.,"Nickel smelting at the Kalgoorlie nickel smelter of Western Mining Corporation Ltd.",Mining and Metallurgical Practices in Australasia, Monograph Series No.10, Ed. Woodcock,J.T.(1980) pp594-598 Pub. The Australasian Institution of Mining and Metallurgy.

100. Dyson,N.F. and Scott,T.R., Hydrometallurgy (1976) vol.1 pp361-372.

101. Muir,D.M. et al.,"Recent Developments in Chloride Hydrometallurgy", The Australian I.M.M. Melbourne Branch, Symposium on "Extractive Metallurgy",(November, 1984) pp153-160.

102. Ottery,A.H., Personal Communication (July,1986); Kwina Nickel Refinery Kwina, W.Australia.

103. Forward,F.A., Transactions Canadian I.M.M. (1953) vol.56 pp

104. Forward,F.A. and Machiw,V.N., Journal of Metals,(1955) vol.7 No.3 pp457-463.

105. Warner,J.P., The Industrial Chemist,(1956) vol.32 pp359-368.

106. Jansz,J.J.C.,"Chloride Hydrometallurgy for Pyrite Zinc-Lead Sulphide Ores. The non-oxidative leaching routes. (1984)

107. Archibald,F.R., Journal of Metals,(1962) vol.14 pp648-652.

108. Thornhill,W.P.G. et al, Journal of Metals,(1971) vol.23 No.7 pp13-18.

109. Sale,F.R., Minerals Science and Engineering,(1971) vol.3 pp3-12. No.4

110. Roscoe,H.E. and Schorlemmer,C.,"A Treatise on Chemistry" vol.II The Metals. Pub. Macmillan & Co. Ltd., London,(1907).

111. Gilchrist,J.D.,"Extractive Metallurgy", 2nd ed. (1980) Pub. Pergamon Press, Oxford. pp378-380.

112. Damarthe,J.M. et al, "Hydrometallurgical Process for the treatment of nickel matte" Societe Metallurgique le nickel, Ger. offen. 2,601,534. (Cl. C22B23/04 2nd December,1976) Fr. Appl. 75/1,264, 16th January,1975. 70pp

113. Renzoui,L.S. et al, Journal of Metals,(1958) vol.10 pp414-418.

114. Spence,W.W. and Cook,W.R.,"The Thompson Refinery", Symposium on the Thompson Operation. Transactions C.I.M.,(1964) vol.67 pp257-267.

115. Cook,W.R.,"Current Practice at the Thompson Nickel Refinery", (February,1973) INCO unpublished material.

116. Kruesi,P.R. et al, The Canadian Mining and Metallurgical (C.I.M.) Bulletin, (June,1973) pp81-87.

117. Barbour,R.,"Glassblowing for Laboratory Technicians", 2nd ed. (1978) Pub. Pergomon Press, Oxford.

118. Mills,K.C.,"Thermodynamic Data for Inorganic Sulphides, Selenides and Tellurides"(1974), Butterworths.

119. Wagman,D.D. et al,"Selected Values of Chemical Thermodynamic Properties", Technical Note 270-4 (May,1969) National Bureau of Standards, United States Department of Commerce.

120. Pankratz,L.B.,"Thermodynamic Properties of Elements and Oxides", Bulletin 672, (1982) Bureau of Mines, United States Department of the Interior.

121. Latimer,W.M.,"The Oxidation States of the Elements and their Potentials in Aqueous Solutions",(1952) 2nd.ed., Prentice-Hall, Inc.

122. Barry,T.I.,"Coexistance or Predominance Area Diagrams", DCS Internal Report 2/78, National Physical Laboratory, Department of Industry (March, 1978) p14

123. Kubaschewski,O.,Alcock,C.B.,"Metallurgical Thermochemistry",(1979) 2nd.ed., Pergamon Press.

124. Milazzo,G.,Caroli,S.,"Tables of Standard Electrode Potentials", Project of the IUPAC Electrochemistry Commision (1978) Wiley.

125. Thornber,M.R., Personal Communication (August,1986).

126. Atkins,P.W.,"Physical Chemistry",(1978) Oxford University Press.

127. Cottrell,A.,"An Introduction to Metallurgy",(1975) ed., Edward Arnold, p515.

128. Hansen,M.,"Constitution of Binary Alloys",(1958) 2nd.ed. Mcgraw-Hill, p677-683.

129. Kubaschewski,O.,Catterall,J.A.,"Metal Physics and Physical Metallurgy", (1956) Pergamon Press, p46-48.

130. Albertsen,J.F.,Knudsen,J.M.,"Meteorites and Thermodynamic Equilibria in f.c.c. Iron-Nickel Alloys (25-50% Ni)",Physica Scripta (1980)) vol.22, p171-175.

131. Peters.E.,"The Electrochemistry of Sulphide Minerals" in "Trends in Electrochemistry" (1977) Edt. Bockris, J.O'M. et al. Plenum. pp267-290.

132. Sillen,L.G.,"Stability Constants, Inorganic Ligands", Supplement No.1 Special Publication 25, The Chemical Society, London (1971).

133. Rajamani,V. and Prewitt,C.T., Canadian Mineralogist (1975) vol.13 pp75-78.
134. Huheey,J.E.,"Inorganic Chemistry", Chapter 9, Coordination Chemistry, 2nd Edition (1978) Harper & Row, pp332-424.
135. Natarajan,F.A. and Iwasaki,I., Minerals Science Engineering, vol.6, No.1 (1974) pp35-44.
136. CSIRO, Division of Mineral Chemistry, Research Report (1984) p3.
137. Bockris,J.O'M. amd Reddy,A.K.N.,"Modern Electrochemistry" (1970) Plenum Press.
138. Denbigh,K."The Principles of Chemical Equilibrium" 4th edt. Cambridge (1981).
139. Vogel,A.L."A Textbook of Quantitative Inorganic Analysis"
140. Greig,J.A.,"Separation Processes in Hydrometallurgy", ed.Davies,G.A., Society of Chemistry Industry (1987), chap.3, pp35-48,"Oxidative Chlorine Leaching of Sulphide Concentrates".
141. Hubli,R.C. et al, Hydrometallurgy vol.10 (1983) pp359-366.
142. Reddy,P.L.N. et al, " Electrochemical Dissolution of a chalcopyrite concentrate", Proc. Electrochem. Soc. (1984) - 10 (Proc. Int. Symp. Electrochem. Miner. Met. Process.), pp 447-468.
143. Jibiki,K. "Acid Decomposition Reaction on Compounds and Minerals in the Fe-Ni Sulphide System",Ph.D. Thesis, Department of Metallurgy, University of British Columbia, May, (1974).
144. Subramanian,K.N. and Ferrajuolo,R., Hydrometallurgy vol.2 (1976) pp117-125.
145. Wells,R.C.,"Electric Activity in Ore Deposits, Dept. of the Interior, U.S. Geological Survey, Bulletin 548 (1914).
146. Sato,M., Economic Geology vol.55 (1960) pp1202-1231.
147. Woodcock,J.T.,"Some Aspects of the Oxidation of Sulphide Minerals in Aqueous Solution", Proceedings The Aus. IMM No.198 (1961) pp47-84.
148. Wadsworth,M.E., Materials Sci Engng, vol.4 No.4 (1972) pp36-47.
149. Muir,D.M. et al, Hydrometall. 81, Proc. Soc. Chem Ind Symp B3/1-B3/14, London (1981).
150. Price,D.C. and Davenport,W.G., J. Applied Electrochemistry, vol.12 (1982) pp281-290.
151. Dry,M.J. and Bryson,A.W., Hydrometallurgy, vol.18 (1987) pp155-181.
152. Burkin,A.R.,"Extractive Metallurgy of Nickel" editor Critical Reports on Applied Chemistry, vol. 17 (1987) Society of Chemical Industry, Wiley.
153. Luo,R., Ph.D. Thesis (to be submitted) University of Leeds, U.K.
154. Ives,D.J.G. and Janz,G.J. (Edt.) "Reference Electrodes - Theory and Practice" (1961) Academic Press.
155. ASTM Handbook, Powder Diffraction File Search Manual (1975) Joint Committee on Powder Diffraction Standards.
156. Biegler,T. and Swift,D.A., Hydrometallurgy, Vol.2 (1976/1977) pp335-349.
157. Price,D.C., Metallurgical Transactions, vol.12B (1981) pp231-239.

158. Price,D.C. and Chilton,J.P., Hydrometallurgy vol.7 (1981) pp117-133.
159. Price,D.C. and Chilton,J.P. Hydrometallurgy vol.5 (1980) pp381-394.
160. Pritzker,M.D. and Yoon,R.H., International Journal of Mineral Processing, vol.20 (1987) pp267-290.
161. Horvath,J. and Hackl,L., Corrosion Science vol.5 (1965) pp525-538.
162. Nagel,K., et al, Z. Elektrochem, vol.61 (1957) pp795-803.
163. Robinson,R.A. and Stokes,R.H.,"Electrolyte Solutions", 2nd edition (1958) Butterworths.
164. Liao Pinjum, " An electrochemical study of the oxidation of violarite surface and the interaction of violarite surface with the reagents", (Journal of Central-South Institute of Mining and Metallurgy) Zhongnan Kuangye Xueyuan Xuebao (1981) No.2 pp1-8 (Chinese).
165. Parker,A.J. et al Aust. J. Chem (1981) vol.34 pp13-34.
166. Greemwod,N.N. and Earnshaw,A.,"Chemistry of the Elements", Pergamon Press, Section 15.1.4 "Allotrops of Sulphur" pp769-781.
167. Parker,A.J. et al, J. Electroanal. Chem. (1981) vol.118 pp305-316.
168. McMillan,R.S., et al, J.Applied Electrochemistry (1982) vol.12 pp743-757.
169. Hirato,T. et al, Metallurgical Transactions B (1986) vol.17B pp19-28.
170. Hirato,T. et al, ibid. (1987) vol.18B pp31-39.
171. Biegler,T. and Swift,D.A., J of Applied Electrochemistry (1979) vol.9 pp545-554.
172. Aguago-Salinas,S.,"A study of the leaching of bornite by electrochemical techniques", Ph.D. Thesis (1985), University of London.
173. Bard,A.J. anf Faulkner,L.R. "Electrochemical Methods-Fundamentals and Applications" (1980) Wiley.
174. Boldt,J.R. and Queneau,P."The Winning of Nickel", Methuem, London (1967).
175. Southampton Electrochemistry Group, "Instrumental Methods in Electrochemistry",(1985) Ellis Horwod.
176. Nicholson,R.S., "Theory and Application of Cyclic Voltammetry for Measurement of Electrode Reaction Kinetics", Analytical Chemistry (1965) vol.37 No.11 pp1351-1355.
177. Sharma,L.R. and Dutt,J. Indian J. Chem, (1970) vol.8 p170.
178. Suzuki,J., Bull. Chem. Soc. Japan (1970) vol.43 p755.
179. Rosenqvist,T."Principles of Extractive Metallurgy" 2nd edt. (1983) McGraw-Hill p418.
180. Burkin,A.R.,"The Chemistry of Hydrometallurgical Processes", Spon (1966).
181. Hydrometallurgy (1983) vol.9 pp349-369.
182. Roach,G.I.D. and Prosser,A.P., Hydrometallurgy (1975) vol.1, pp79-91.
183. Roach,G.I.D. and Prosser,A.P., Hydrometallurgy (1976/1977) vol.2, pp211-218.
184. Nassan,K,"The causes of colour", Scientific American (October, 1980) vol.243, pp124-154.

BIBLIOGRAPHY

Extractive Hydrometallurgy: Leaching

Bautista,R.G., (Editor) "Hydrometallurgical Process Fundamentals", NATO Conference Series VI Materials Science vol.10 (1984) Plenum Press.

Burkin,A.R., "The Chemistry of Hydrometallurgical Processes" Spon (1966).

Burkin,A.R., (Editor) "Leaching and Reduction in Hydrometallurgy", The Institution of Mining and Metallurgy (1975).

Burkin,A.R., "Extractive Metallurgy of Nickel" (Editor), Critical Reports on Applied Chemistry Vol.17 (1987) Society of Chemical Industry, Wiley.

Wadsworth,M.E., (Editor) "Rate Processes of Extractive Metallurgy", (1979) Plenum Press.

Mineralogy

Vaughan,D,J, and Craig,J.C., "Mineral Chemistry of Metal Sulfides", (1978) Cambridge University Press.

Ramdohr,P.,"The Ore Minerals and their Intergrowths" (1979) 2nd edition, Pergamon.

Electrochemistry

Bard,A.J. and Faulkner,L.R., "Electrochemical Methods - Fundamentals and Apllications", (1980) Wiley.

Southampton Electrochemistry Group, "Instrumental Methods in Electrochemistry", (1985) Ellis Horwood.

West,J.M., "Basic Corrosion and Oxidation", 2nd. Edition (1980) Ellis Horwood.

Ives,D.J.G. and Janz,G.J. (Editors) "Reference Electrodes, Theory and Practice" (1961) Academic Press.

Vetter,K.J.,"Electrochemical Kinetics- Theoretical and Experimental Aspects" (1967) Academic Press.

Thermodynamic Data

Mills,K.C., "Thermodynamic Data for Inorganic Sulphides, Selenides and Tellurides", (1974) Butterworths.

Wagman,D.D. at al, "Selected Values of Chemical Thermodynamic Properties", Technical Note 270-4 (May,1969) National Bureau of Standards, United States Department of Commerce.

Milazzo,G., and Caroli,S., "Tables of Standard Electrode Potentials", Project of the IUPAC Electrochemistry Commision (1978) Wiley.